รายงานวิจัยฉบับสมบูรณ์

อิทธิพลของความเค้นแบบแกนเดี่ยวต่อสมบัติไดอิเล็กตริกของสารเซรามิกเฟร์โรอิเล็กตริก

โดย

ผศ. ดร. รัตติกร ยิ้มนิรัญ

สิงหาคม 2550

สัญญาเลขที่ RSA4780002

รายงานวิจัยฉบับสมบูรณ์

อิทธิพลของความเค้นแบบแกนเดี่ยวต่อสมบัติไดอิเล็กตริกของสารเซรามิกเฟร์โรอิเล็กตริก

ผศ. ดร. รัตติกร ยิ้มนิรัญ
ภาควิชาฟิสิกส์ คณะวิทยาศาสตร์
มหาวิทยาลัยเชียงใหม่

สนับสนุนโดยสำนักงานกองทุนสนับสนุนการวิจัย

(ความเห็นในรายงานนี้เป็นของผู้วิจัย สกว.ไม่จำเป็นต้องเห็นด้วยเสมอไป)

กิตติกรรมประกาศ

ผู้วิจัยใคร่ขอขอบพระคุณ สำนักงานกองทุนสนับสนุนการวิจัย (สกว.) ที่ได้ให้การสนับสนุนงานวิจัยและพัฒนาครั้งนี้ ผ่านทางทุนพัฒนานักวิจัย ประจำปี พ.ศ. 2547 ขอขอบพระคุณศาสตราจารย์ ดร. ทวี ตันฆศิริ และบุคลากรของห้องปฏิบัติการวิจัยอิเล็กโทรเซรามิกส์ที่ได้ให้การสนับสนุนและคำแนะนำในทุกด้าน ขอขอบคุณภาควิชาฟิสิกส์ คณะวิทยาศาสตร์ มหาวิทยาลัยเชียงใหม่ ที่ช่วยอำนวยความสะดวกในการใช้เครื่องมือ อุปกรณ์ และสถานที่ จนทำให้งานวิจัยเรื่องนี้สามารถดำเนินการจนสำเร็จผลได้ด้วยดี ขอขอบคุณผู้ร่วมงานและนักศึกษาทุกท่าน ที่มีส่วนช่วยเหลือผู้วิจัยให้ดำเนินงานชิ้นนี้สำเร็จลุล่วงได้ดี โดยเฉพาะ ดร. วรรณวิลัย ไชยสาร คุณสุพัตรา วงศ์แสนใหม่ คุณอธิพงศ์ งามจารุโรจน์ คุณสวรินทร์ ฉมังลาภ คุณเรวดี วงศ์มณีรุ่ง คุณเมืองใจ อุ่นเรือน และคุณนฤทธ์ ตรีอำนรรค ขอขอบคุณผู้ช่วยศาสตราจารย์ ดร.ยงยุทธ เหล่าศิริถาวร สำหรับด้านงานคำนวณและงานด้านฟิสิกส์อื่นๆ ขอขอบคุณรองศาสตราจารย์ ดร.สุพล อนันตา ที่ได้ให้ความช่วยเหลือส่งเสริมเกื้อกูลในการทำงานเสมอมานับตั้งแต่วันเริ่มต้น ตลอดจนเป็นกำลังใจให้กันเสมอที่จะสู้และอยู่รอดในการทำวิจัย ผู้วิจัยต้องขอบคุณความร่วมมือที่ได้รับอย่างดีจากนักวิจัยที่ปรึกษาและเพื่อนร่วมงานในต่างประเทศ ได้แก่ Prof. Robert Newnham Prof. Kenji Uchino และ Prof. Amar Bhalla แห่ง The Pennsylvania State University Prof. Xiaoli Tan แห่ง Iowa State University และ Prof. David Cann แห่ง Oregon State University

ท้ายที่สุดนี้ขอมอบความดีทั้งหมดให้แทนคำขอบคุณสำหรับ คุณวิภา ยิ้มนิรัญ ภรรยา และด.ช. รัญชน์ ยิ้มนิรัญ ลูกชาย คงไม่มีความสำเร็จใดๆเกิดขึ้นได้ถ้าปราศจากความรักและความเข้าใจ รอยยิ้มแห่งความสุข คำปลอบเมื่อยามท้อ ตลอดจนกำลังใจและความอดทนที่ครอบครัวมอบให้ผู้วิจัยตลอดมาจนสามารถมาถึง ณ วันนี้ได้

(ผศ.ดร. รัตติกร ยิ้มนิรัญ)
หัวหน้าโครงการ

บทคัดย่อ

รหัสโครงการ : RSA4780002

ชื่อโครงการ : อิทธิพลของความเค้นแบบแกนเดี่ยวต่อสมบัติไดอิเล็กตริกของสารเซรามิกเฟร์โรอิเล็กตริก

ชื่อนักวิจัย : ผศ.ดร. รัตติกร ยิ้มนิรัญ

ภาควิชาฟิสิกส์ คณะวิทยาศาสตร์ มหาวิทยาลัยเชียงใหม่

E-mail Address : rattikornyimnirun@yahoo.com

ระยะเวลาโครงการ : 31 สิงหาคม 2547 ถึง 30 สิงหาคม 2550

ในการวิจัยนี้ได้ทำการศึกษาอิทธิพลของความเค้นแบบแกนเดี่ยวต่อสมบัติไดอิเล็กตริกของสารเซรามิกเฟร์โรอิเล็กตริกที่สำคัญ กล่าวคือ BT PT PZT PZN PMN PIN PZT-BT PMN-PT PZN-PZT PIN-PT และ PZTBT-PMNT โดยสามารถแบ่งผลงานที่ได้จากโครงการวิจัยนี้ออกเป็น 3 กลุ่มใหญ่ กล่าวคือ 1. กระบวนการเตรียมผงและเซรามิก 2. สมบัติไดอิเล็กตริกและทางไฟฟ้าอื่นๆของสารเซรามิก และ 3. อิทธิพลของความเค้นแบบแกนเดี่ยวต่อสมบัติไดอิเล็กตริกและทางไฟฟ้าอื่นๆของสารเซรามิกทั้งหมดที่กล่าวมาข้างต้น ซึ่งกลุ่มผู้วิจัยได้ประสบความสำเร็จในการเตรียมผงและเซรามิกด้วยการใช้เทคนิคผสมออกไซด์ร่วมกับเทคนิคการบดย่อยละเอียด โดยได้ทราบถึงเงื่อนไขที่เหมาะสมต่อการเตรียมผงให้มีความบริสุทธิ์สูง และพบเงื่อนไขในการเผาที่เหมาะสมต่อการเตรียมเซรามิกแต่ละชนิดที่กล่าวมาเหล่านี้ให้มีความบริสุทธิ์และความหนาแน่นสูง และจากการตรวจสอบคุณลักษณะเฉพาะและคุณสมบัติทางไฟฟ้าต่างๆของเซรามิกที่เตรียมได้ก็พบว่าสารเซรามิกที่เตรียมได้นั้นแสดงคุณลักษณะเฉพาะเป็นสารเซรามิกเฟร์โรอิเล็กตริกแบบปกติ หรือสารเซรามิกเฟร์โรอิเล็กตริกกลุ่มรีแลกเซอร์ หรือสารเซรามิกที่แสดงลักษณะผสมกันระหว่างเซรามิกเฟร์โรอิเล็กตริกแบบปกติและสารเซรามิกเฟร์โรอิเล็กตริกกลุ่มรีแลกเซอร์ ทั้งนี้ขึ้นกับชนิดของสารเซรามิกและอัตราส่วนผสม และจากการศึกษาอิทธิพลของความเค้นแบบแกนเดี่ยวต่อสมบัติไดอิเล็กตริกและทางไฟฟ้าอื่นๆของสารเซรามิกก็พบว่าความเค้นมีผลอย่างชัดเจนในการเปลี่ยนแปลงสมบัติต่างๆในสารเซรามิกทุกระบบ โดยมีทิศทางและอัตราการเปลี่ยนแปลงที่ขึ้นอยู่กับชนิดของสารเซรามิกและอัตราส่วนผสม ท้ายที่สุดนั้นผลการศึกษาในโครงการวิจัยนี้ได้นำไปสู่ผลงานการตีพิมพ์ในระดับนานาชาติแล้วกว่า 40 เรื่อง

คำหลัก: ความเค้นแบบแกนเดี่ยว; สมบัติไดอิเล็กตริก; สารเซรามิกเฟร์โรอิเล็กตริก

Abstract

Project Code : RSA4780002

Project Title : Effects of Uniaxial Stress on Dielectric Properties of Ferroelectric Ceramics

Investigators : Asst. Prof. Dr. Rattikorn Yimnirun

Department of Physics, Faculty of Science, Chiang Mai University

E-mail Address : rattikornyimnirun@yahoo.com

Project Period : August 31, 2004 to August 30, 2007

In this study, effects of uniaxial stress on the dielectric properties of important ceramics in BT PT PZT PZN PMN PIN PZT-BT PMN-PT PZN-PZT PIN-PT และ PZTBT-PMNT systems were investigated. The outputs of this project can be divided into 3 main groups; namely, 1. powder and ceramic fabrication, 2. dielectric and other electrical properties, and 3. effects of uniaxial stress on dielectric and other electrical properties of all the prepared ceramics. We have successfully prepared powders and ceramics by using the mixed-oxide technique in conjunction with the vibro-milling technique and found suitable conditions for preparing high purity powders and for fabricating each ceramic to high purity and density. From the characterization and electrical properties measurements, the prepared ceramics exhibit either normal or relaxor or mixed ferroelectric characteristics, depending upon the type of ceramics and composition ratio. Similarly, the uniaxial stress studies also indicate that the applied stress impose significant influence on the electrical properties with the direction and rate of change depending on the type of ceramics and composition ratio. Finally, the results from this project has resulted in more than 40 international publications.

Keywords : Uniaxial Stress; Dielectric Properties; Ferroelectric Ceramics

Executive Summary

สารเซรามิกเฟร์โรอิเล็กตริก (ferroelectrics) เช่น แบเรียมไทเทเนต ($BaTiO_3$) หรือ BT เลดไทเทเนต ($PbTiO_3$) หรือ PT เลดเซอร์โคเนตไทเทเนต ($Pb(Zr,Ti)O_3$) หรือ PZT เลดซิงค์ไนโอเบต ($Pb(Zn_{1/3}Nb_{2/3})O_3$) หรือ PZN เลดแมกนีเซียมไนโอเบต ($Pb(Mg_{1/3}Nb_{2/3})O_3$) หรือ PMN และ เลดอินเดียมไนโอเบต ($Pb(In_{1/2}Nb_{1/2})O_3$) หรือ PIN ล้วนแล้วแต่เป็นสารที่ถูกพัฒนาขึ้นมาเพื่อใช้ประโยชน์ในอุปกรณ์อิเล็กทรอนิกส์ประเภทต่างๆ อย่างไรก็ตามโดยทั่วไปแล้ว ในสภาวะการใช้งานจริงของอุปกรณ์อิเล็กทรอนิกส์ที่ผลิตจากสารเซรามิกเฟร์โรอิเล็กตริกดังที่กล่าวมาแล้วนั้น สารเซรามิกมักจะอยู่สภาวะภายใต้ความเค้น ซึ่งอาจจะเกิดจากความเค้นเชิงกลภายนอกระหว่างการใช้งาน หรือความเค้นเชิงกลภายในอันเกิดจากการที่สารเซรามิก เหล่านี้ ดังนั้นข้อมูลเกี่ยวกับสมบัติไดอิเล็กตริกภายใต้อิทธิพลของความเค้น จึงมีความสำคัญอย่างมากต่อการออกแบบ การจัดสร้างและการใช้งานของอุปกรณ์อิเล็กทรอนิกส์ที่ผลิตจากสารเซรามิกเฟร์โรอิเล็กตริกเหล่านี้ ดังนั้นผู้วิจัยจึงทำการศึกษาอย่างเป็นระบบถึงอิทธิพลของความเค้นต่อสมบัติไดอิเล็กตริกของสารเซรามิกเฟร์โรอิเล็กตริกที่สำคัญ กล่าวคือ BT PT PZT PZN PMN PIN PZT-BT PMN-PT PZN-PZT PIN-PT และ PZTBT-PMNT โดยสามารถแบ่งผลงานที่ได้จากโครงการวิจัยนี้ออกเป็น 3 กลุ่มใหญ่ กล่าวคือ 1. กระบวนการเตรียมผงและเซรามิก 2. สมบัติไดอิเล็กตริกและทางไฟฟ้าอื่นๆของสารเซรามิก และ 3. อิทธิพลของความเค้นแบบแกนเดี่ยวต่อสมบัติไดอิเล็กตริกและทางไฟฟ้าอื่นๆของสารเซรามิกทั้งหมดที่กล่าวมาข้างต้น ซึ่งกลุ่มผู้วิจัยได้ประสบความสำเร็จในการเตรียมผงและเซรามิกด้วยการใช้เทคนิคผสมออกไซด์ร่วมกับเทคนิคการบดย่อยละเอียด โดยได้ทราบถึงเงื่อนไขที่เหมาะสมต่อการเตรียมผงให้มีความบริสุทธิ์สูง และพบเงื่อนไขในการเผาที่เหมาะสมต่อการเตรียมเซรามิกแต่ละชนิดที่กล่าวมาเหล่านี้ให้มีความบริสุทธิ์และความหนาแน่นสูง และจากการตรวจสอบคุณลักษณะเฉพาะและคุณสมบัติทางไฟฟ้าต่างๆของเซรามิกที่เตรียมได้ก็พบว่าสารเซรามิกที่เตรียมได้นั้นแสดงคุณลักษณะเฉพาะเป็นสารเซรามิกเฟร์โรอิเล็กตริกแบบปกติ หรือสารเซรามิกเฟร์โรอิเล็กตริกกลุ่มรีแลกเซอร์ หรือสารเซรามิกที่แสดงลักษณะผสมกันระหว่างเซรามิกเฟร์โรอิเล็กตริกแบบปกติและสารเซรามิกเฟร์โรอิเล็กตริก กลุ่มรีแลกเซอร์ ทั้งนี้ขึ้นกับชนิดของสารเซรามิกและอัตราส่วนผสม และจากการศึกษาอิทธิพลของความเค้นแบบแกนเดี่ยวต่อสมบัติไดอิเล็กตริกและทางไฟฟ้าอื่นๆของสารเซรามิกก็พบว่าความเค้นมีผลอย่างชัดเจนในการเปลี่ยนแปลงสมบัติต่างๆในสารเซรามิกทุกระบบ โดยมีทิศทางและอัตราการเปลี่ยนแปลงที่ขึ้นอยู่กับชนิดของสารเซรามิกและอัตราส่วนผสม

เนื้อหางานวิจัย

ปรากฏการณ์พิโซอิเล็กตริก (piezoelectric effect) เป็นปรากฏการณ์ที่วัสดุสามารถเปลี่ยนพลังงานกลไปเป็นพลังงานไฟฟ้าหรือเปลี่ยนพลังงานไฟฟ้าไปเป็นพลังงานกลในผลึกเชิงเดี่ยว (single crystal compounds) และในสารประเภทเฟร์โรอิเล็กตริก ความเป็นเฟร์โรอิเล็กตริกของวัสดุจะขึ้นอยู่กับสมบัติของหน่วยเซลล์ (unit cell) พื้นฐานของโครงสร้างพื้นฐานของวัสดุจากการแบ่งกลุ่มผลึกเป็น 32 คลาส (class) ตามสมมาตร (symmetry) มี 21 คลาสเป็นประเภทที่ไม่มีศูนย์กลางสมมาตร (non-centrosymmetry) แต่มีเพียง 20 คลาส ที่มีสมบัติพิโซอิเล็กตริกและมี 10 คลาสที่เป็นเฟร์โรอิเล็กตริก

สารเซรามิกเฟร์โรอิเล็กตริกสามารถแบ่งได้เป็น 2 ประเภทใหญ่ๆ จากลักษณะของการเปลี่ยนแปลงเฟสและการตอบสนองต่อความถี่ คือ สารเซรามิกเฟร์โรอิเล็กตริกแบบปกติ (normal ferroelectrics) และสารเซรามิกเฟร์โรอิเล็กตริกกลุ่มรีแลกเซอร์ (relaxor ferroelectrics) ซึ่งในกลุ่มแรกนั้นการเปลี่ยนเฟสจะเกิดขึ้นอย่างรวดเร็ว (sharp transition) บริเวณอุณหภูมิคูรี (Curie temperature: T_C) และมีสมบัติไดอิเล็กตริกที่ไม่ค่อยขึ้นกับความถี่ ในขณะที่สารเซรามิกในกลุ่มที่สองนั้นจะเกิดการเปลี่ยนเฟสแบบช้าๆ (diffuse phass transition) และมีสมบัติไดอิเล็กตริกที่เปลี่ยนแปลงกับความถี่อย่างชัดเจน ตัวอย่างสารเซรามิกเฟร์โรอิเล็กตริกแบบปกติที่สำคัญได้แก่ แบเรียมไทเทเนต ($BaTiO_3$) หรือ BT เลดไทเทเนต ($PbTiO_3$) หรือ PT และเลดเซอร์โคเนตไทเทเนต ($Pb(Zr,Ti)O_3$) หรือ PZT ในขณะตัวอย่างของสารเซรามิกเฟร์โรอิเล็กตริกกลุ่มรีแลกเซอร์ ที่สำคัญประกอบด้วย เลดแมกนีเซียมไนโอเบต ($Pb(Mg_{1/3}Nb_{2/3})O_3$) หรือ PMN เลดซิงค์ไนโอเบต ($Pb(Zn_{1/3}Nb_{2/3})O_3$) หรือ PZN และ เลดอินเดียมไนโอเบต ($Pb(In_{1/2}Nb_{1/2})O_3$) หรือ PIN

1. ที่มาและความสำคัญของปัญหา

สืบเนื่องจากนโยบายของรัฐบาลที่ต้องการที่จะพัฒนาประเทศให้เป็นศูนย์กลางของภูมิภาคในด้านอุตสาหกรรมอิเล็กทรอนิกส์ อุตสาหกรรมยานยนต์และการแพทย์ รวมทั้งการพัฒนาด้านการเกษตรอันเป็นอาชีพหลักของประชาชนส่วนใหญ่ของประทศให้มีความก้าวหน้าและสามารถเพิ่มผลผลิตให้ได้ตามความต้องการ เพื่อนำประเทศไปสู่การเป็นครัวของโลก ซึ่งการพัฒนาด้านต่างๆเหล่านี้จะเป็นพื้นฐานในการพัฒนาประเทศอย่างยั่งยืนต่อไป อย่างไรก็ตาม เป็นที่ทราบกันดีว่า ในอุตสาหกรรมทุกด้านที่กล่าวมานั้น ช่วงที่ผ่านมาประเทศของเราได้มีการพัฒนาไปได้ค่อนข้างช้าและส่วนใหญ่เป็นไปในลักษณะของการนำชิ้นส่วนเข้ามาจากประเทศผู้ผลิตหลักโดยผู้ประกอบการต่างชาติมาประกอบเป็นอุปกรณ์และขายในประเทศหรือส่งออกไปขายยังประเทศอื่น ซึ่งลักษณะเช่นนี้คงไม่สามารถที่จะทำให้เกิดการพัฒนาประเทศอย่างยั่งยืนได้ ดังนั้นจึงควรต้องมีการพัฒนาอุตสาหกรรมเหล่านั้นขึ้นมาในประเทศโดยให้มีลักษณะแบบครบวงจร ถึงกระนั้น ในความเป็นจริงแล้วในอุตสาหกรรมบางประเภท ยกตัวอย่างเช่น อุตสาหกรรมทางด้านชิ้นส่วนอิเล็กทรอนิกส์ เช่น ตัวต้านทานและตัวเก็บประจุที่ใช้ทั่วไปในวงจรไฟฟ้าและ

อิเล็กทรอนิกส์นั้น การแข่งขันค่อนข้างสูงและโอกาสค่อนข้างต่ำที่ประเทศของเราจะประสพความสำเร็จในตลาดโลก ในขณะที่อุตสาหกรรมที่เน้นตลาดเฉพาะทางนั้นยังมีโอกาสที่เปิดกว้าง (niche market) ยกตัวอย่างเช่น ตัวเก็บประจุไฟฟ้าและตัวต้านทานที่ใช้ในวงจรควบคุมในรถยนต์ เทอร์มิสเตอร์ที่ใช้ควบคุมอุณหภูมิในรถยนต์ เซนเซอร์ที่สามารถใช้ตรวจวัดความชื้นในอาหารหรือผลไม้ หรือเซนเซอร์ที่ใช้ควบคุมการเผาไหม้ของเชื้อเพลิงในรถยนต์ แอกทัวเอเทอร์ที่ใช้ในการผลิตทางอุปกรณ์อิเล็กทรอนิกส์ที่ต้องการความละเอียดสูง ทรานสดิวเซอร์ที่สามารถใช้ในการตรวจหาฝูงปลาในทะเลและในอุปกรณ์ตรวจสอบตำหนิหรือรอยร้าวในวัสดุแบบไม่ทำลาย หม้อแปลงไฟฟ้า บัซเซอร์ในลำโพง ตัวบังคับการสั่นของหัวเข็มในเครื่องมือขูดหินปูน อุปกรณ์ทำความสะอาดเครื่องมือทางการแพทย์ด้วยอัลตร้าโซนิกส์ หัวตรวจวัดอัลตร้าซาวด์ หัวตรวจวัดความดันโลหิต และหุ่นยนต์ขนาดจิ๋วสำหรับใช้ในการตรวจอวัยวะภายในแบบไร้สาย เป็นต้น

วัสดุที่เป็นพื้นฐานในการผลิตอุปกรณ์ที่กล่าวมาทั้งหมดนั้นคือสารเซรามิกเฟร์โรอิเล็กตริก (ferroelectrics) เช่น แบเรียมไทเทเนต ($BaTiO_3$) หรือ BT เลดไทเทเนต ($PbTiO_3$) หรือ PT เลดเซอร์โคเนตไทเทเนต ($Pb(Zr,Ti)O_3$) หรือ PZT เลดซิงค์ไนโอเบต ($Pb(Zn_{1/3}Nb_{2/3})O_3$) หรือ PZN เลดแมกนีเซียมไนโอเบต ($Pb(Mg_{1/3}Nb_{2/3})O_3$) หรือ PMN และ เลดอินเดียมไนโอเบต ($Pb(In_{1/2}Nb_{1/2})O_3$) หรือ PIN ล้วนแล้วแต่เป็นสารที่ถูกพัฒนาขึ้นมาเพื่อใช้ประโยชน์ในอุปกรณ์อิเล็กทรอนิกส์ประเภทต่างๆ ที่กล่าวมาข้างต้น [1-9] ซึ่งโดยหลักการพื้นฐานแล้ววัสดุที่มีศักยภาพเหมาะสมสำหรับการนำมาประยุกต์ใช้ในงานต่างๆเหล่านี้นั้น จะต้องมีคุณลักษณะที่สำคัญอันได้แก่ การมีค่าสภาพยอมสัมพัทธ์ที่เหมาะสม ในช่วงของอุณหภูมิและความถี่สำหรับการทำงานของอุปกรณ์ มีค่าสัมประสิทธิ์ไพฟ้าเชิงกลคู่ควบสูง สามารถทำการจัดเรียงไดโพลภายในเนื้อสารได้ง่าย มีการสูญเสียของพลังงานในระหว่างการใช้งานที่ต่ำ มีอายุการใช้งานนาน และที่สำคัญต้องสามารถทำการเตรียมได้ง่าย โดยมีค่าใช้จ่ายไม่มากและปลอดภัย สามารถหาวัตถุดิบได้ง่าย และต้องการอุณหภูมิเผาที่ไม่สูงมากนัก เป็นต้น [1-9] ซึ่งโดยทั่วไปแล้วนั้น การผสมผสานของคุณสมบัติที่ดีต่างๆเหล่านี้ไม่สามารถพบได้ในวัสดุเดี่ยวๆตัวใดตัวหนึ่งที่กล่าวมาในข้างต้นได้ เนื่องจากวัสดุแต่ละชนิดต่างก็มีข้อดีและข้อเสียที่แตกต่างกันไปในลักษณะที่มีความเฉพาะตัวมาก ดังนั้นการศึกษาวิจัยเพื่อค้นหาวัสดุชนิดใหม่ๆ ที่อาศัยหลักการนำเอาวัสดุหลักๆที่มีอยู่เดิมมารวมเข้าด้วยกัน ที่สามารถจะผสมผสานข้อดีและช่วยบรรเทาข้อเสียของแต่ละวัสดุที่เป็นองค์ประกอบหลักได้อย่างลงตัว จึงเป็นวิธีการหนึ่งที่ได้รับความสนใจอย่างมากทั้งในแวดวงวิชาการและในวงการอุตสาหกรรม ทำให้ในปัจจุบันมีสารเซรามิกเฟร์โรอิเล็กตริกชนิดใหม่ๆที่มีความสลับซับซ้อนยิ่งขึ้นจำนวนมากเกิดขึ้นมาเช่น BT-PT, BT-PZT, PZT-PZN, PMN-PT, PMN-PZN, PMN-PZT, PIN-PT, PIN-PMN, PIN-PZN, BT-PMN-PZN, PT-PMN-PZN, PMN-PT-BT, PZT-PZN-PMN และ PMN-PT-PIN เป็นต้น [1-3,10-20] และงานวิจัยทางด้านนี้ส่วนใหญ่เน้นถึงการศึกษาถึงอิทธิพลของปัจจัยหลักในกระบวนการผลิตที่มีต่อพฤติกรรมการเกิดเฟส โครงสร้างจุลภาคและสมบัติไดอิเล็กตริกและสมบัติไพฟ้าเชิงกลของสารเซรามิกที่ผลิตขึ้น [10-24]

อย่างไรก็ตามโดยทั่วไปแล้ว ในสภาวะการใช้งานจริงของอุปกรณ์อิเล็กทรอนิกส์ที่ผลิตจากสารเซรามิกเฟร์โรอิเล็กตริกดังที่กล่าวมาแล้วนั้น สารเซรามิกมักจะอยู่สภาวะภายใต้ความเค้น ซึ่งอาจจะเกิดจากความเค้นเชิงกลภายนอกระหว่างการใช้งาน เช่น แอกทัวเอเทอร์และทรานสดิวเซอร์ เป็นต้น หรือความเค้นเชิงกลภายในอันเกิดจากการที่สารเซรามิกเหล่านี้ซึ่งมีสมบัติพิโซอิเล็กตริกจะเกิดการเปลี่ยนแปลงรูปร่างภายใต้อิทธิพลของสนามไฟฟ้าซึ่งส่งผลให้เกิดความเค้นกระทำต่อสารเซรามิก เช่น ตัวเก็บประจุไฟฟ้า เทอร์มิสเตอร์ เซนเซอร์ หม้อแปลงไฟฟ้า และหัวตรวจวัดอัลตร้าซาวด์ เป็นต้น ดังนั้นข้อมูลเกี่ยวกับสมบัติต่างๆ เช่น สมบัติไดอิเล็กตริกและสมบัติไฟฟ้าเชิงกล ภายใต้อิทธิพลของความเค้น จึงมีความสำคัญอย่างมากต่อการออกแบบ การจัดสร้างและการใช้งานของอุปกรณ์อิเล็กทรอนิกส์ที่ผลิตจากสารเซรามิกเฟร์โรอิเล็กตริกเหล่านี้ ซึ่งการศึกษาเหล่านี้นอกจากจะช่วยเสริมข้อมูลที่จำเป็นในการพัฒนาและการนำไปประยุกต์ใช้ของสารเซรามิกเฟร์โรอิเล็กตริกแล้ว ยังสามารถเสริมองค์ความรู้พื้นฐานในเรื่องโครงสร้างของโดเมน (domain structure) และการเคลื่อนที่ของโดเมน (domain motion) [25,26] ซึ่งเป็นกลไกที่สำคัญที่มีอิทธิพลต่อสมบัติไดอิเล็กตริกและสมบัติไฟฟ้าเชิงกลในสารเซรามิกเฟร์โรอิเล็กตริก ส่งผลให้ในช่วงที่ผ่านมาได้เริ่มมีการศึกษาถึงอิทธิพลของความเค้นต่อสมบัติทางไดอิเล็กตริกและไฟฟ้าเชิงกลของสารเซรามิกในระบบต่างๆ เช่น PZT PMN-PT และ PMN-PZT เป็นต้น แต่ยังคงอยู่ในวงที่จำกัดเมื่อเปรียบเทียบกับจำนวนของสารเซรามิกเฟร์โรอิเล็กตริกใหม่ๆที่ได้รับการพัฒนาขึ้นมา ทำให้งานวิจัยที่เป็นระบบในประเด็นของอิทธิพลของความเค้นต่อสมบัติต่างๆของสารเซรามิกเฟร์โรอิเล็กตริกที่สำคัญที่ปรากฏในวารสารงานวิจัยในระดับนานาชาติยังมีจำนวนที่ค่อนข้างน้อย [20,25-33]

ด้วยเหตุผลดังกล่าวมาข้างต้น ดังนั้นทางผู้วิจัยจึงได้เกิดแนวคิดที่จะทำการศึกษาอย่างเป็นระบบถึงอิทธิพลของความเค้นต่อสมบัติทางไฟฟ้าของสารเซรามิกเฟร์โรอิเล็กตริกที่สำคัญกล่าวคือ สารเซรามิกเฟร์โรอิเล็กตริกระบบเดี่ยว เช่น BT PT PZT PZN PMN PIN เป็นต้น สารเซรามิกเฟร์โรอิเล็กตริกระบบคู่ที่สำคัญที่เกิดจากการผสมสารในระบบเดี่ยว เช่น PZT-BT PMN-PT PZN-PZT PIN-PT เป็นต้น และ สารเซรามิกเฟร์โรอิเล็กตริกที่มีความซับซ้อนมากและไม่เป็นที่ปรากฏมาก่อน คือ PZTBT-PMNT โดยในเบื้องต้นโครงการวิจัยนี้จะมุ่งเน้นความสำคัญไปที่การศึกษาถึงสมบัติไดอิเล็กตริกของสารเหล่านี้ภายใต้อิทธิพลของความเค้นแบบแกนเดี่ยว ซึ่งการศึกษานี้มีความสำคัญในแง่ของการสร้างองค์ความรู้พื้นฐานใหม่ที่จำเป็นสำหรับการทำความเข้าใจในธรรมชาติของสมบัติไดอิเล็กตริกของสารเซรามิกเฟร์โรอิเล็กตริกระบบเดี่ยวภายใต้ความเค้น และอิทธิพลของสมบัติดังกล่าวของแต่ละองค์ประกอบต่อสมบัติไดอิเล็กตริกของสารเซรามิกในระบบที่มีความซับซ้อนมากขึ้น เพื่อเป็นแนวทางในการนำองค์ความรู้ที่ได้รับจากการวิจัยนี้ไปใช้ในภาคปฏิบัติเพื่อพัฒนาการออกแบบ การจัดสร้างและการใช้งานของอุปกรณ์อิเล็กทรอนิกส์ที่ผลิตจากสารเซรามิกเฟร์โรอิเล็กตริกเหล่านี้ให้มีประสิทธิภาพสูงขึ้น นอกจากนี้แล้ว โครงการวิจัยนี้ยังเป็นการสร้างผลงานวิจัยแบบต่อเนื่องซึ่งมุ่งเน้นการใช้องค์ความรู้ที่ได้รับจากโครงการวิจัยจากทุนส่งเสริมนักวิจัยรุ่นใหม่ของผู้วิจัยซึ่งได้ทำการศึกษาเกี่ยวกับอิทธิพลของความเค้นแบบ

แกนเดี่ยวต่อสมบัติไดอิเล็กตริกและไฟฟ้าเชิงกลของสารเซรามิกในระบบ PMN-PZT มาประยุกต์ใช้ ซึ่งโครงการดังกล่าวได้รับความสำเร็จเป็นอย่างดีและได้รับความสนใจและยอมรับโดยสามารถตีพิมพ์ผลงานทั้งในระดับชาติและนานาชาติ [20,36-40] และโครงการวิจัยนี้ยังเป็นการส่งเสริมให้เกิดการเชื่อมโยงด้านการวิจัยระหว่างนักวิจัยในประเทศโดยการนำผลการวิจัยจากนักวิจัยที่ได้รับทุนพัฒนานักวิจัยมาใช้ประโยชน์ [24,35] ซึ่งโครงการดังกล่าวนั้นได้มุ่งเน้นไปที่การการศึกษาถึงอิทธิพลของปัจจัยหลักในกระบวนการผลิตที่มีต่อพฤติกรรมการเกิดเฟสโครงสร้างจุลภาคและสมบัติไดอิเล็กตริกของสารเซรามิกในระบบ PZBT-PMNT โดยได้ศึกษารายละเอียดของสารเซรามิกเฟร์โรอิเล็กตริกระบบเดี่ยว BT PT PZT PZN PMN สารเซรามิกเฟร์โรอิเล็กตริกระบบคู่ PZT-BT PMN-PT และสารเซรามิกเฟร์โรอิเล็กตริกที่มีความซับซ้อนมาก PZTBT-PMNT ซึ่งผลการศึกษาเหล่านี้สามารถนำมาใช้โดยตรงในการเลือกเงื่อนไขที่เหมาะสมในการเตรียมสารเซรามิกที่มีความบริสุทธิ์และความหนาแน่นสูง รวมทั้งสมบัติไดอิเล็กตริกที่ดีมาใช้ในการศึกษาในโครงการวิจัยนี้ต่อไป นอกจากนี้โดยอาศัยความรู้เบื้องต้นจากระบบพื้นฐาน PT และ PZT ที่ศึกษามาก่อน ผู้วิจัยยังจะได้ขยายขอบเขตของงานวิจัยไปศึกษาสารเซรามิกเฟร์โรอิเล็กตริกระบบเดี่ยว PIN และ PZN รวมทั้งสารเซรามิกเฟร์โรอิเล็กตริกระบบคู่ PIN-PT และ PZN-PZTที่มีความสำคัญมากและในช่วง 5 ปีที่ผ่านมานี้ได้รับความสนใจอย่างแพร่หลายเนื่องจากมีสมบัติไดอิเล็กตริก สมบัติพิโซอิเล็กตริกและสมบัติเฟร์โรอิเล็กตริกที่โดดเด่นมากและกำลังได้รับการพัฒนาทางการค้าอย่างจริงจัง [8,9,14,15,17,41-43] จะเห็นได้ว่าโครงการวิจัยนี้นอกจากจะให้องค์ความรู้ที่สามารถนำไปใช้ในภาคปฏิบัติแล้ว ยังจะนำไปสู่ความรู้ความเข้าใจพื้นฐานใหม่ๆเกี่ยวกับสารเซรามิกเฟร์โรอิเล็กตริกที่สำคัญอันจะเป็นพื้นฐานในการพัฒนาประเทศและผลงานที่ได้ยังสามารถที่จะตีพิมพ์ในวารสารวิชาการระดับนานาชาติได้

2. วัตถุประสงค์ของการวิจัย

1. เพื่อศึกษากระบวนการเตรียมสารเซรามิกในระบบ BT PT PZT PZN PMN PIN PZT-BT PMN-PT PZN-PZT PIN-PT และ PBZT-PMNT
2. เพื่อศึกษาอิทธิพลของความเค้นแบบแกนเดี่ยวต่อสมบัติไดอิเล็กตริกของสารเซรามิก ระบบเดี่ยว BT PT PZT PZN PMN และ PIN
3. เพื่อศึกษาอิทธิพลของความเค้นแบบแกนเดี่ยวต่อสมบัติไดอิเล็กตริกของสารเซรามิก ระบบคู่ PZT-BT PMN-PT PZN-PZT และ PIN-PT
4. เพื่อศึกษาอิทธิพลของความเค้นแบบแกนเดี่ยวต่อสมบัติไดอิเล็กตริกของสารเซรามิกระบบ PBZT-PMNT
5. เพื่อศึกษาความสัมพันธ์ระหว่างสมบัติไดอิเล็กตริกภายใต้ความเค้นแบบแกนเดี่ยวของแต่ละองค์ประกอบและสมบัติดังกล่าวของสารเซรามิกระบบคู่
6. เพื่อศึกษาความสัมพันธ์ระหว่างสมบัติไดอิเล็กตริกภายใต้ความเค้นแบบแกนเดี่ยวของแต่ละองค์ประกอบและสมบัติดังกล่าวของสารเซรามิกระบบ PBZT-PMNT

3. ระเบียบวิธีวิจัย

ขั้นตอนการวิจัยในโครงการนี้ถูกแบ่งออกเป็น 3 ส่วนหลัก คือ 1) การศึกษาอิทธิพลอิทธิพลของความเค้นแบบแกนเดี่ยวต่อสมบัติไดอิเล็กตริกของสารเซรามิกระบบเดี่ยว BT PT PZT และ PMN สารเซรามิกระบบคู่ PZT-BT และ PMN-PT และสารเซรามิกระบบ PBZT-PMNT โดยใช้องค์ความรู้พื้นฐานในส่วนของเงื่อนไขในการเตรียมสารเซรามิกที่มีความบริสุทธิ์และความหนาแน่นสูงที่ได้จากการศึกษาอย่างละเอียดในโครงการวิจัยที่ได้รับทุนพัฒนานักวิจัยของรองศาสตราจารย์ ดร. สุพล อนันตา 2) การศึกษาการเตรียมเซรามิกในระบบ PZN PIN PZN-PZT และ PIN-PT ด้วยการใช้เทคนิคผสมออกไซด์ และ 3) การศึกษาอิทธิพลอิทธิพลของความเค้นแบบแกนเดี่ยวต่อสมบัติไดอิเล็กตริกของสารเซรามิกระบบเดี่ยว PZN และ PIN และสารเซรามิกระบบคู่ PZN-PZT และ PIN-PT ที่เตรียมขึ้นได้

ดังนั้นเพื่อให้เกิดความต่อเนื่องของการดำเนินการวิจัยที่สอดคล้องกับโครงการวิจัยทุนพัฒนานักวิจัยของรองศาสตราจารย์ ดร. สุพล อนันตา จึงต้องมีการวางแผนงานการวิจัยโดยมีรายละเอียดของระเบียบวิธีวิจัยดังนี้

ปีที่ 1

1. ศึกษาค้นคว้ารวบรวมข้อมูลจากผลงานวิจัยและเอกสารทางวิชาการที่เกี่ยวข้อง
2. ทำการติดตั้งและตรวจสอบเครื่องมืออัดแรงแบบแกนเดี่ยวเพื่อใช้ในการวัดสมบัติไดอิเล็กตริกของสารเซรามิกภายใต้ความเค้นแบบแกนเดี่ยว โดยชุดเครื่องมือดังกล่าวได้รับการพัฒนาและทดสอบแล้วจากโครงการวิจัยทุนส่งเสริมนักวิจัยรุ่นใหม่ (2545) และทำการติดตั้งและตรวจสอบอุปกรณ์อื่นๆที่จะใช้งานให้มีความพร้อม
3. เตรียมผงและเซรามิกในระบบ $BaTiO_3$ (BT) และ $Pb(Zr_{0.52}Ti_{0.48})O_3$ ด้วยการใช้เทคนิคผสมออกไซด์
4. ทำการตรวจสอบคุณลักษณะเฉพาะและคุณสมบัติของเซรามิกที่เตรียมได้
5. ทดสอบอิทธิพลของความเค้นแบบแกนเดี่ยวต่อสมบัติไดอิเล็กตริก (ค่าคงที่ไดอิเล็กตริก (ε_r) และการสูญเสียทางไดอิเล็กตริก (tan δ)) ของสารเซรามิกระบบเดี่ยว BT และ PZT ด้วยเครื่องมืออัดแรงแบบแกนเดี่ยว
6. เตรียมผงและเซรามิกในระบบ $PbTiO_3$ (PT) และ $Pb(Mg_{1/3}Nb_{2/3})O_3$ (PMN) ด้วยการใช้เทคนิคผสมออกไซด์
7. ทำการตรวจสอบคุณลักษณะเฉพาะและคุณสมบัติของเซรามิกที่เตรียมได้

8. ทดสอบอิทธิพลของความเค้นแบบแกนเดี่ยวต่อสมบัติไดอิเล็กตริก (ค่าคงที่ไดอิเล็กตริก (ε_r) และการสูญเสียทางไดอิเล็กตริก (tan δ)) ของสารเซรามิกระบบเดี่ยว PT และ PMN ด้วยเครื่องมืออัดแรงแบบแกนเดี่ยว
9. อภิปรายผลการศึกษาและสรุปผลการวิจัย ตลอดจนข้อเสนอแนะในรูปแบบการเขียนรายงานความก้าวหน้า และการเตรียมผลงานเพื่อการตีพิมพ์

ปีที่ 2

10. เตรียมผงและเซรามิกในระบบ (1-x)PZT-xBT และ (1-x)PMN-xPT เมื่อ x มีค่าเป็น 0.1, 0.2, 0.3, 0.4, 0.5, 0.6, 0.7, 0.8 และ 0.9 ด้วยเทคนิคมิกซ์ออกไซด์โดยใช้สารที่เตรียมได้จาก ข้อ 8.3 และ 8.6 ที่มีความบริสุทธิ์สูงเป็นสารตั้งต้น
11. ทำการตรวจสอบคุณลักษณะเฉพาะและคุณสมบัติของเซรามิกที่เตรียมได้
12. ทดสอบอิทธิพลของความเค้นแบบแกนเดี่ยวต่อสมบัติไดอิเล็กตริก (ค่าคงที่ไดอิเล็กตริก (ε_r) และการสูญเสียทางไดอิเล็กตริก (tan δ)) ของสารเซรามิกระบบคู่ PZT-BT และ PMN-PT ด้วยเครื่องมืออัดแรงแบบแกนเดี่ยว
13. สรุปความสัมพันธ์ระหว่างสมบัติไดอิเล็กตริกภายใต้ความเค้นแบบแกนเดี่ยวของ BT PZT PT และ PMN และสมบัติดังกล่าวของสารเซรามิกระบบ PZT-BT และ PMN-PT
14. ศึกษาการเตรียมผงและเซรามิกในระบบ $Pb(Zn_{1/3}Nb_{2/3})O_3$ (PZN) และ $Pb(In_{1/2}Nb_{1/2})O_3$ (PIN) ด้วยการใช้เทคนิคผสมออกไซด์ โดยศึกษาหาเงื่อนไขที่เหมาะสมต่อการเตรียมผงให้มีความบริสุทธิ์สูง และศึกษาหาเงื่อนไขในการเผาที่เหมาะสมต่อการเตรียมเซรามิกเหล่านี้ให้มีความบริสุทธิ์และความหนาแน่นสูง
15. ทำการตรวจสอบคุณลักษณะเฉพาะและคุณสมบัติของเซรามิกที่เตรียมได้
16. เตรียมเซรามิกในระบบ PZBT-PMNT ด้วยเทคนิคมิกซ์ออกไซด์โดยใช้สารที่เตรียมได้จาก ข้อ 8.10 ที่มีความบริสุทธิ์สูงเป็นสารตั้งต้น
17. ทำการตรวจสอบคุณลักษณะเฉพาะและคุณสมบัติของเซรามิกที่เตรียมได้
18. ทดสอบอิทธิพลของความเค้นแบบแกนเดี่ยวต่อสมบัติไดอิเล็กตริก (ค่าคงที่ไดอิเล็กตริก (ε_r) และการสูญเสียทางไดอิเล็กตริก (tan δ)) ของสารเซรามิกระบบ PZBT-PMNT ด้วยเครื่องมืออัดแรงแบบแกนเดี่ยว

19. สรุปความสัมพันธ์ระหว่างสมบัติไดอิเล็กตริกภายใต้ความเค้นแบบแกนเดี่ยวของ PZBT และ PMNT และสมบัติดังกล่าวของสารเซรามิกระบบ PZBT-PMNT
20. อภิปรายผลการศึกษาและสรุปผลการวิจัย ตลอดจนข้อเสนอแนะในรูปแบบการเขียนรายงานความก้าวหน้า และการเตรียมผลงานเพื่อการตีพิมพ์

ปีที่ 3

21. ทดสอบอิทธิพลของความเค้นแบบแกนเดี่ยวต่อสมบัติไดอิเล็กตริก (ค่าคงที่ไดอิเล็กตริก (ε_r) และการสูญเสียทางไดอิเล็กตริก (tan δ)) ของสารเซรามิกระบบเดี่ยว PZN และ PIN ด้วยเครื่องมืออัดแรงแบบแกนเดี่ยว
22. ศึกษาการเตรียมผงและเซรามิกในระบบ (1-x)PZN-xPZT และ (1-x)PIN-xPT เมื่อ x มีค่าเป็น 0.1, 0.2, 0.3, 0.4, 0.5, 0.6, 0.7, 0.8 และ 0.9 ด้วยเทคนิคมิกซ์ออกไซด์ โดยใช้สารที่เตรียมได้จาก ข้อ 8.14 ที่มีความบริสุทธิ์สูงเป็นสารตั้งต้น ด้วยการใช้เทคนิคผสมออกไซด์ โดยศึกษาหาเงื่อนไขที่เหมาะสมต่อการเตรียมผงให้มีความบริสุทธิ์สูง และศึกษาหาเงื่อนไขในการเผาที่เหมาะสมต่อการเตรียมเซรามิกเหล่านี้ให้มีความบริสุทธิ์และความหนาแน่นสูง
23. ทำการตรวจสอบคุณลักษณะเฉพาะและคุณสมบัติของเซรามิกที่เตรียมได้
24. ทดสอบอิทธิพลของความเค้นแบบแกนเดี่ยวต่อสมบัติไดอิเล็กตริก (ค่าคงที่ไดอิเล็กตริก (ε_r) และการสูญเสียทางไดอิเล็กตริก (tan δ)) ของสารเซรามิกระบบ PZN-PZT และ PIN-PT ด้วยเครื่องมืออัดแรงแบบแกนเดี่ยว
25. สรุปความสัมพันธ์ระหว่างสมบัติไดอิเล็กตริกภายใต้ความเค้นแบบแกนเดี่ยวของ PT PZT PZN และ PIN และสมบัติดังกล่าวของสารเซรามิกระบบ PZN-PZT และ PIN-PT
26. อภิปรายผลการศึกษาและสรุปผลการวิจัย ตลอดจนข้อเสนอแนะในรูปแบบการเขียนรายงานฉบับสมบูรณ์ และการเตรียมผลงานเพื่อการตีพิมพ์

4. ประโยชน์ที่ได้รับจากโครงการวิจัยนี้

1. องค์ความรู้ใหม่ในเรื่องกระบวนการเตรียมเซรามิกในระบบ BT PT PZT PZN PMN PIN PZT-BT PMN-PT PZN-PZT PIN-PT และ PBZT-PMNT
2. องค์ความรู้ใหม่ในเรื่องของอิทธิพลของความเค้นแบบแกนเดี่ยวต่อสมบัติไดอิเล็กตริกของสารเซรามิกระบบเดี่ยว BT PT PZT PZN PMN และ PIN
3. องค์ความรู้ใหม่ในเรื่องของอิทธิพลของความเค้นแบบแกนเดี่ยวต่อสมบัติไดอิเล็กตริกของสารเซรามิกระบบคู่ PZT-BT PMN-PT PZN-PZT และ PIN-PT
4. ความรู้ความเข้าใจถึงความสัมพันธ์ระหว่างสมบัติไดอิเล็กตริกภายใต้ความเค้นแบบแกนเดี่ยวของแต่ละองค์ประกอบและสมบัติดังกล่าวของสารเซรามิกระบบคู่
5. องค์ความรู้ใหม่ในเรื่องของอิทธิพลของความเค้นแบบแกนเดี่ยวต่อสมบัติไดอิเล็กตริกของสารเซรามิกระบบ PBZT-PMNT
6. ความรู้ความเข้าใจถึงความสัมพันธ์ระหว่างสมบัติไดอิเล็กตริกภายใต้ความเค้นแบบแกนเดี่ยวของ PZT-BT และ PMN-PTและสมบัติดังกล่าวของสารเซรามิกระบบ PBZT-PMNT
7. ผลงานวิจัยในรูปของสิ่งตีพิมพ์ ได้แก่สิ่งตีพิมพ์ในวารสารทางวิชาการต่างๆ การนำเสนอผลงานในการประชุมวิชาการและสัมมนา หรือหนังสือตำราวิชาการเฉพาะด้าน กล่าวคือ ตำราเรื่อง สมบัติทางไฟฟ้าของเซรามิกเฟร์โรอิเล็กทริก
8. องค์ความรู้ใหม่ที่จะนำไปใช้ประกอบการเรียนการสอนและการปรับปรุงกระบวนวิชาในหลักสูตรวัสดุศาสตร์ทั้งในระดับปริญญาตรีและระดับบัณฑิตศึกษาที่ผู้วิจัยรับผิดชอบอยู่ต่อไป
9. นักวิจัยรุ่นใหม่และรุ่นกลางที่มีความรู้ทางด้านสารเซรามิกเฟร์โรอิเล็กตริกกลุ่มเพอรอพสไกต์และแนวทางในการกำหนดหัวข้อวิทยานิพนธ์สำหรับการพัฒนาบุคลากรทางด้านวัสดุศาสตร์ที่เกี่ยวข้องทั้งในระดับปริญญาโท และเอก สาขาวัสดุศาสตร์อย่างต่อเนื่อง
10. แนวทางการพัฒนาชุดโครงการวิจัยและการสร้างความร่วมมือของกลุ่มนักวิจัยภายในสถาบันต้นสังกัดและระหว่างกลุ่มวิจัยต่างๆที่สนใจในเรื่องที่เกี่ยวข้องกันทั้งในและต่างประเทศ

5. สรุปผลที่ได้จากโครงการวิจัยนี้

โดยสรุปแล้วสามารถแบ่งองค์ความรู้ใหม่ที่ได้จากโครงการวิจัยนี้ออกเป็น 3 กลุ่มใหญ่ กล่าวคือ

1. องค์ความรู้ใหม่ในเรื่องกระบวนการเตรียมผงและเซรามิกในระบบ BT PT PZT PZN PMN PIN PZT-BT PMN-PT PZN-PZT PIN-PT และ PBZT-PMNT
2. องค์ความรู้ใหม่ในเรื่องของสมบัติไดอิเล็กตริกและทางไฟฟ้าอื่นๆของสารเซรามิก ในระบบ BT PT PZT PZN PMN PIN PZT-BT PMN-PT PZN-PZT PIN-PT และ PBZT-PMNT
3. องค์ความรู้ใหม่ในเรื่องของอิทธิพลของความเค้นแบบแกนเดี่ยวต่อสมบัติไดอิเล็กตริกและทางไฟฟ้าอื่นๆของสารเซรามิกในระบบ BT PT PZT PZN PMN PIN PZT-BT PMN-PT PZN-PZT PIN-PT และ PBZT-PMNT

ซึ่งผลงานที่ได้ใน 3 กลุ่มในเบื้องต้นนั้น ถือเป็นผลงานที่เกี่ยวข้อง*โดยตรง*กับโครงการวิจัยนี้ ดังจะได้กล่าวถึงในรายละเอียดต่อไป

ส่วนที่ 1: สำหรับองค์ความรู้ใหม่ในเรื่องกระบวนการเตรียมผงและเซรามิกในระบบ BT PT PZT PZN PMN PIN PZT-BT PMN-PT PZN-PZT PIN-PT และ PBZT-PMNT นั้น กลุ่มผู้วิจัยได้ประสบความสำเร็จในการเตรียมผงและเซรามิกในระบบ $BaTiO_3$(BT) $Pb(Zr_{0.52}Ti_{0.48})O_3$ $PbTiO_3$(PT) $Pb(Mg_{1/3}Nb_{2/3})O_3$(PMN) $Pb(Zn_{1/3}Nb_{2/3})O_3$(PZN) และ $Pb(In_{1/2}Nb_{1/2})O_3$(PIN) ด้วยการใช้เทคนิคผสมออกไซด์ โดยศึกษาหาเงื่อนไขที่เหมาะสมต่อการเตรียมผงให้มีความบริสุทธิ์สูง และศึกษาหาเงื่อนไขในการเผาที่เหมาะสมต่อการเตรียมเซรามิก เหล่านี้ให้มีความบริสุทธิ์และความหนาแน่นสูง นอกจากนี้ก็ได้เตรียมผงและเซรามิกในระบบ (1-x)PZT-xBT (1-x)PMN-xPT (1-x)PZN-xPZT และ (1-x)PIN-xPT เมื่อ x มีค่าเป็น 0.1, 0.2, 0.3, 0.4, 0.5, 0.6, 0.7, 0.8 และ 0.9 และทำการเตรียมเซรามิกในระบบ PZBT-PMNT ด้วยการใช้เทคนิคผสมออกไซด์เช่นกัน ผลงานที่ได้รับนั้นได้ถูกนำไปตีพิมพ์ในวารสารทางวิชาการต่างๆ ดังต่อไปนี้ (ทั้งนี้ รายละเอียดได้ถูกนำเสนอในแต่ละผลงานแล้ว)

1. R. Wongmaneerung, **R. Yimnirun** and S. Ananta, “Effects of Vibro-Milling Time on Phase Formation and Particle Size of Lead Titanate Nanopowders”, *Materials Letters,* 60(12), pp 1447-1452 (2006).
2. R. Wongmaneerung, T. Sarnkonsri, **R. Yimnirun** and S. Ananta “Effects of milling method and calcination condition on phase and morphology characteristics of $Mg_4Nb_2O_9$ powders”, *Materials Science and Engineering B*, 130(1-3), pp 246-253 (2006).

3. R. Wongmaneerung, **R. Yimnirun** and S. Ananta, “Effects of Milling Time and Calcination Condition on Phase Formation and Particle Size of Lead Titanate Nanopowders Prepared by Vibro-milling”, *Materials Letters*, 60, pp 2666-2671 (2006)
4. R. Wongmaneerung, T. Sarnkonsri, **R. Yimnirun** and S. Ananta “Effects of magnesium niobate precursor and calcination condition on phase formation and morphology of lead magnesium niobate powders”, *Materials Science and Engineering B,* 132, pp 292-299 (2006).
5. A. Ngamjarurojana, O. Khamman, **R. Yimnirun** and S. Ananta, “Effect of Calcination Conditions on Phase Formation and Particle Size of Zinc Niobate Powders Synthesized by Solid-State Reaction”, *Materials Letters*, 60, pp 2867-2872 (2006).
6. S. Wongsaenmai, **R. Yimnirun** and S. Ananta, “Effects of Calcination Conditions on Phase Formation and Particle Size of Indium Niobate Powders Synthesized by the Solid-State Reaction”, *Materials Letters* (2007) *in press.*
7. O. Khamman, **R. Yimnirun** and S. Ananta,”Effect of Vibro-Milling Time on Phase Formation and Particle Size of Lead Zirconate Nanopowders” *Materials Letters* (2007) *in press.*
8. A. Prasatkhetragarn, **R. Yimnirun** and S. Ananta, “Effect of calcination conditions on phase formation and particle size of $Zn_3Nb_2O_8$ powders synthesized by solid-state reaction”, *Materials Letters* (2007) *in press*
9. S. Wongsaenmai, **R. Yimnirun** and S. Ananta, “Influence of Calcination Conditions on Phase Formation and Particle Size of Indium Niobate Powders Synthesized by the Solid-State Reaction”, *Journal of Materials Science* (2007) *in press*
10. W. Chaisan, O. Khamman, **R. Yimnirun** and S. Ananta,, “Effects of Calcination Conditions on Phase and Morphology Evolution of Lead Zirconate Powders Synthesized by Solid-State Reaction”, *Journal of Materials Science* (2007) *in press*
11. Orawan Khamman, Rewadee Wongmaneerung, Wanwilai Chaisan, **Rattikorn Yimnirun** and Supon Ananta, “Potential of Vibro-Milling Technique for Preparation of Electroceramic Nanopowders” *Journal of Alloys and Compounds* (2007) *in press.*

12. Athipong Ngamjarurojana, Orawan Khamman, Supon Ananta, and **Rattikorn Yimnirun**, “Synthesis and Characterizations of Lead Zinc Niobate-Lead Zirconate Titanate Powders” *Journal of Electroceramics* (2007) *accepted.*
13. Supattra Wongsaenmai, Orawan Khamman, Supon Ananta, and **Rattikorn Yimnirun**, “Synthesis and Characterizations of Lead Indium Niobate-Lead Titanate Powders” *Journal of Electroceramics* (2007) *accepted.*
14. Rewadee Wongmaneerung, Orawan Khamman, **Rattikorn Yimnirun**, and Supon Ananta, “Synthesis and Characterizations of Lead Titanate Powders” *Journal of Electroceramics* (2007) *accepted.*
15. O. Khamman, **R. Yimnirun** and S. Ananta,”Effect of Vibro-Milling Time and Calcination n Phase Formation and Particle Size of Lead Zirconate Nanopowders” *Ferroelectrics (2007) accepted*
16. A. Prasatkhetragarn, **R. Yimnirun** and S. Ananta, “Effects of Calcination Conditions on Phase Formation of Zirconium Titanate Powders Synthesized by the Solid-State Reaction”, *Ferroelectrics* (2007) *accepted*
17. W. Chaisan, A. Prasatkhetragarn**, R. Yimnirun**, S. Ananta, *“*Two-Stage Solid-State Reaction of Lead Zirconate Titanate Powders” *Ferroelectrics (2007) accepted*
18. O. Khamman, T. Sarakonsri, A. Rujiwatra, Y. Laosiritaworn, **R. Yimnirun**, and S. Ananta. “Effects of Milling Time and Calcination Condition on Phase Formation and Particle Size of Lead Zirconate Nanopowders Prepared by Vibro-milling“ *Journal of Materials Science* (2007) *accepted.*

ส่วนที่ 2: ในส่วนขององค์ความรู้ใหม่ในเรื่องของสมบัติไดอิเล็กตริกและทางไฟฟ้าอื่นๆ ของสารเซรามิกในระบบ BT PT PZT PZN PMN PIN PZT-BT PMN-PT PZN-PZT PIN-PT และ PBZT-PMNT นั้น ได้รับโดยตรงจากการทำการตรวจสอบคุณลักษณะเฉพาะและคุณสมบัติต่างๆของเซรามิกที่เตรียมได้ และผลงานที่ได้นั้นก็ได้ถูกนำไปตีพิมพ์ในวารสารทางวิชาการต่างๆ ดังต่อไปนี้ (รายละเอียดได้ถูกนำเสนอในแต่ละผลงานแล้ว)

1. W. Chaisan, **R. Yimnirun**, S. Ananta and D.P. Cann, “Dielectric properties of solid solutions in the lead zirconate titanate-barium titanate system prepared by a modified mixed-oxide method ,” *Materials Letters,* 59(28), pp 3732-3737 (2005).
2. **Rattikorn Yimnirun**, Rungnapa Tipakontitikul and Supon Ananta, “Effect of Sintering Temperature on Densification and Dielectric Properties of

$Pb(Zr_{0.44}Ti_{0.56})O_3$ Ceramics" *International Journal of Modern Physics B*, 20(16), pp 2415-2424 (2006).

3. W. Chaisan, **R. Yimnirun**, S. Ananta and D.P. Cann, "Phase Development and Dielectric Properties of $(1-x)Pb(Zr_{0.52}Ti_{0.48})O_3–xBaTiO_3$ ceramics ," *Materials Science and Engineering B,*132, pp 300-306 (2006).
4. R. Wongmaneerung, **R. Yimnirun**, S. Ananta, R. Guo, and A.S. Bhalla, "Polarization Behavior in the Two Stage Sintered Lead Titanate Ceramics" *Ferroelectric Letters*, 33(5-6), pp 137-146 (2006).
5. **Rattikorn Yimnirun**, Yongyut Laosiritaworn, Supattra Wongsaenmai and Supon Ananta, "Scaling Behavior of Dynamic Hysteresis in Soft PZT Bulk Ceramics", *Applied Physics Letters,* 89(16), pp 162901-3 (2006)
6. R. Wongmaneerung, **R. Yimnirun** and S. Ananta, "Effects of Sintering Condition on Phase Formation, Microstructure and Dielectric Properties of Lead Titanate Ceramics", *Applied Physics A*, 86(2), pp 249-255 (2007).
7. **R. Yimnirun**, R. Wongmaneerung, S. Wongsaenmai, A. Ngamjarurojana, S. Ananta, and Y. Laosiritaworn, "Temperature Scaling of Dynamic Hysteresis in Soft Lead Zirconate Titanate Bulk Ceramic" *Applied Physics Letters*, 90(11), pp 112906 (2007).
8. **R. Yimnirun**, R. Wongmaneerung, S. Wongsaenmai, A. Ngamjarurojana, S. Ananta, and Y. Laosiritaworn, "Dynamic Hysteresis and Scaling Behavior of Hard Lead Zirconate Titanate Bulk Ceramic" *Applied Physics Letters*, 90(11), pp 112908 (2007).
9. Supattra Wongsaenmai, Xiaoli Tan, Supon Ananta, and **Rattikorn Yimnirun**, "Dielectric and Ferroelectric Properties of Fine Grains $Pb(In_{1/2}Nb_{1/2})O_3–PbTiO_3$ Ceramics" *Journal of Alloys and Compounds* (2007) *in press*
10. W. Chaisan, **R. Yimnirun**, S. Ananta, "Two-Stage Sintering of Barium Titanate and Resulting Characteristics" *Ferroelectrics (2007) in press*
11. **Rattikorn Yimnirun**, Xiaoli Tan, Supon Ananta, and Supattra Wongsaenmai, "Preparation of Fine-Grain Lead Indium Niobate Ceramics with Wolframite Precursor Method and Resulting Electrical Properties" *Applied Physics A* (2007) *in press*
12. W. Chaisan, **R. Yimnirun**, S. Ananta and D.P. Cann, "Dielectric and Ferroelectric Properties of Ceramics in PZT-BT System," *Materials Chemistry and Physics* (2007) *in press.*

13. **R. Yimnirun** “Dielectric Properties of PMN-PT Prepared by Mixed Oxide Method” *International Journal of Modern Physics B* (2007) *accepted*
14. P. Ketsuwan, Y. Laosiritaworn, S. Ananta, and **R. Yimnirun**, “Effect of Sintering Temperature on Phase Formation, Dielectric, Piezoelectric, and Ferroelectric Properties of Nb-doped $Pb(Zr_{0.52}Ti_{0.48})O_3$ Ceramics” *Ferroelectrics* (2007) *accepted.*
15. S. Wongsaenmai, A. Bhalla, R. Guo, S. Ananta, and **R. Yimnirun**, “Effect of Addition BT on Relaxor Behavior of PIN-PT Ceramics” *Integrated Ferroelectrics* (2007) *accepted*.
16. S. Wongsaenmai, A. Bhalla, X. Tan, S. Ananta, and **R. Yimnirun**, “Dielectric Properties and Relaxor Behavior of PIN-Based System” *Ferroelectrics Letters* (2007) *accepted.*

ส่วนที่ 3: ในส่วนนี้นั้นถือเป็นผลงานหลักของโครงการวิจัยนี้ โดยองค์ความรู้ใหม่ในเรื่องของอิทธิพลของความเค้นแบบแกนเดี่ยวต่อสมบัติไดอิเล็กตริกและทางไฟฟ้าอื่นๆของสารเซรามิกในระบบ BT PT PZT PZN PMN PIN PZT-BT PMN-PT PZN-PZT PIN-PT และ PBZT-PMNT นั้นได้จากการใช้เครื่องมืออัดแรงแบบแกนเดี่ยวประกอบในการวัดสมบัติไดอิเล็กตริก เช่น ค่าคงที่ไดอิเล็กตริก (ε_r) และการสูญเสียทางไดอิเล็กตริก (tan δ) และสมบัติอื่นๆ เช่น สมบัติเฟร์โรอิเล็กทริกฮิสเทอรีซิส (วงวน P-E) ของสารเซรามิกในทุกระบบที่กล่าวมาภายใต้ความเค้นแบบแกนเดี่ยว และผลงานที่ได้นั้นก็ได้ถูกนำไปตีพิมพ์ในวารสารทางวิชาการต่างๆ ดังต่อไปนี้ (รายละเอียดได้ถูกนำเสนอในแต่ละผลงานแล้ว)

1. **Rattikorn Yimnirun**, Yongyut Laosiritaworn, and Supattra Wongsaenmai, “Effects of Uniaxial Compressive Pre-Stress on Ferroelectric Properties of Soft PZT Ceramic” *Journal of Physics D: Applied Physics*, 39, pp 759-764 (2006).
2. **R. Yimnirun**, S. Ananta, A. Ngamjarurojana, and S. Wongsaenmai, “Effects of Uniaxial Stress on Dielectric Properties of Ferroelectric Ceramics”, *Current Applied Physics,* 6(3), pp 520-524 (2006).
3. **Rattikorn Yimnirun**, Muangjai Unruan, Yongyut Laosiritaworn, and Supon Ananta, “Change of Dielectric Properties of Ceramics in Lead Magnesium Niobate-Lead Titanate System With Compressive Stress”, *J. Physics D: Applied Physics*, 39, pp 3097-3102 (2006)

4. **R. Yimnirun**, “Change in Dielectric Properties of Normal and Relaxor Ferroelectric Ceramic Composites in BT-PZT and PMN-PZT Systems by Uniaxial Compressive Stress” *Ferroelectrics,* 331, pp 9-18 (2006)
5. **Rattikorn Yimnirun**, “Contributions of Domain-Related Phenomena on Dielectric Constant of Lead-Based Ferroelectric Ceramics Under Uniaxial Compressive Pre-Stress” *International Journal of Modern Physics B*, 20(23), pp 3409-3417 (2006).
6. **Rattikorn Yimnirun**, Supattra Wongsaenmai, Supon Ananta, and Yongyut Laosiritaworn “Stress-Dependent Scaling Behavior of Dynamic Hysteresis in Bulk Soft Ferroelectric Ceramics”, *Applied Physics Letters*, 89(24), pp 242901-3 (2006).
7. **R. Yimnirun**, S. Ananta, and S. Chamunglap, “Dielectric Properties of (1-x)PZT-xBT Ceramics Under Uniaxial Compressive Pre-Stress” *Materials Chemistry and Physics*, 102(2-3), pp 165-170 (2007).
8. Narit Triumnak, Muangjai Unruan, Supon Ananta, and **Rattikorn Yimnirun**, “Uniaxial Stress Dependence of Dielectric Properties of 0.9PMN-0.1PT Ceramics” *Journal of Electroceramics* (2007) *accepted.*
9. **R. Yimnirun,** A. Ngamjarurojana, Y. Laosiritaworn, Supon Ananta, and Narit Triamnak, “Dielectric Properties of PZT-PZN Ceramics Under Compressive Stress” *Ferroelectrics* (2007) *accepted.*

หนังสืออ้างอิง

1. B. Jaffe, W.R. Cook Jr., and H. Jaffe, *Piezoelectric Ceramics*, Academic Press, 1971.
2. Y. Xu, *Ferroelectric Materials and Their Applications*, North-Holland, 1991.
3. A.J. Moulson and J.M. Herbert, *Electroceramics*, Chapman and Hall, 1993.
4. R.E. Newnham and G.R. Ruschau, *Am. Ceram. Soc. Bull*. **75**[10] 51 (1996).
5. K. Uchino, *Piezoelectric Actuators and Ultrasonic Motors*, Kluwer Academic, 1997.
6. J.F. Scott, *Ferroelectrics*, **206/207**, 365 (1998).
7. G.H. Haertling, *J. Am. Ceram. Soc.* **82**[4] 797 (1999).
8. A.S. Bhalla, R. Guo and R. Roy, Mat. Res. Innovat. **4**, 3 (2000)
9. S.E.E Park and W. Hackenberger, *Current Opinion Sol. State Mat. Sci.* **6**, 11 (2002).
10. H. Chen, X. Guo and Z. Meng, *Mater. Chem.Phys.* **75**, 202 (2002).
11. R. Zuo, L. Li, X. Hu and Z. Gui, *Mater. Lett*. **54**, 185 (2002).
12. Y. H. Chen, K. Uchino, M. Shen and D. Viehland, *J. Appl. Phys.* **90(3)**, 1455 (2001).
13. H. Chen, J. Long and Z. Meng, *Mater. Sci. Eng*. **B99**, 433 (2003).
14. S. Priya, K. Uchino and D. Viehland, *Appl. Phys. Lett*. **81(13)**, 2430 (2002).
15. N. Yasuda, H. Ohwa, M. Kume, K. Hayashi, Y. Hosono and Y. Yamashita, *J. Cryst. Growth*. **229**, 299 (1999).
16. E. F. Alberta and A. S. Bhalla, *Mater. Lett*. **40**, 114 (1999).
17. E. F. Alberta and A. S. Bhalla, *Mater. Lett*. **29**, 127 (1996).
18. H. Ouchi, *J. Am. Ceram. Soc.* **51** 169 (1968).
19. C.H. Wang, *J. Eur. Ceram. Soc*. **22** 2033 (2002).
20. R. Yimnirun, S. Ananta, E. Meechoowas and S. Wongsaenmai, *J. Phys. D: Appl. Phys*. **36** 1615 (2003).
21. R. Yimnirun, S. Ananta and P. Laoratanakul, *J. Eur. Ceram. Soc.* **25** 3225 (2005).
22. W. Chaisan, S. Ananta and T. Tunkasiri, *Curr. Appl. Phys*. **4** 182 (2004).
23. S. Ananta, R. Tipakorntitikul and T. Tunkasiri, *Mater. Lett.* **57** 2637 (2003).
24. สุพล อนันตา, การพัฒนากระบวนการเตรียมสาร PZT โดยวิธีการประยุกต์กระบวนการผสมออกไซด์แบบ 2 ขั้นตอน, รายงานฉบับสมบูรณ์โครงการทุนวิจัยหลังปริญญาเอก, สนับสนุนโดยสำนักงานกองทุนสนับสนุนการวิจัย (สกว.) พ.ศ. 2545.
25. S. Sherrit, D.B. Van Nice, J.T. Graham, B.K. Mukherjee and H.D. Wiederick, *Proc. IEEE ISAF* 167 (1992).
26. Q.M. Zhang, J. Zhao, K. Uchino and J. Zheng, *J. Mater. Res.* **12[1]** 226 (1997).

27. D. Viehland, J.F. Li, E. McLaughlin, J. Powers, R. Janus and H. Robinson, *J. Appl. Phys.* **95(4)**, 1969 (2004).
28. I.J. Fritz, *J. Appl. Phys.* **49(9)**, 4922 (1978).
29. D. Viehland and J. Powers, *Appl. Phys. Lett.* **78(20)**, 3112 (2001).
30. D. Viehland, F. Tito, E. McLaughlin, H. Robinson, R. Janus, L Ewart and J. Powers, and, *J. Appl. Phys.* **90(3)**, 1496 (2001).
31. J. Zhao, A.E. Glazounov and Q.M. Zhang, *Appl. Phys. Lett.* **74(3)**, 4362 (1999).
32. D. Viehland, L. Ewart, J. Powers, and L.F. Li, *J. Appl. Phys.* **90(5)**, 2479 (2001).
33. D. Audigier, C. Richard, C. Descamps, M. Troccaz and L. Eyraud, *Ferroelectrics,* **154** 219 (1994).
34. รัตติกร ยิ้มนิรัญ, อิทธิพลของความเค้นแบบแกนเดี่ยวต่อสมบัติไดอิเล็กตริกและไฟฟ้าเชิงกลของสารเซรามิกในระบบ PMN-PZT, รายงานฉบับสมบูรณ์โครงการทุนส่งเสริมนักวิจัยรุ่นใหม่, สนับสนุนโดยสำนักงานกองทุนสนับสนุนการวิจัย (สกว.) พ.ศ. 2547.
35. สุพล อนันตา, อิทธิพลของปัจจัยในกระบวนการเตรียมต่อการเกิดเฟส โครงสร้างจุลภาค และสมบัติไดอิเล็กตริกของสารเซรามิก PBZT-PMNT, รายงานฉบับสมบูรณ์โครงการทุนพัฒนานักวิจัย, สนับสนุนโดยสำนักงานกองทุนสนับสนุนการวิจัย (สกว.) พ.ศ. 2549.
36. R. Yimnirun, S. Ananta, E. Meechoowas, S. Wongsaenmai, *Chiang Mai J. Sci.* **30**, 81 (2003).
37. S. Wongsaenmai, S. Ananta and R. Yimnirun, *Chiang Mai J. Sci.*, *in press* (2004).
38. สุพัตรา วงศ์แสนใหม่, สุพล อนันตา และ **รัตติกร ยิ้มนิรัญ,** *วารสารสงขลานครินทร์วิทยาศาสตร์และเทคโนโลยี***, 25(5)**, 629 (2546).
39. สุพัตรา วงศ์แสนใหม่, สุพล อนันตา และ **รัตติกร ยิ้มนิรัญ,** *วารสารวิทยาศาสตร์ มข***, 31(2)**, 73 (2546).
40. สุพัตรา วงศ์แสนใหม่, สุพล อนันตา และ **รัตติกร ยิ้มนิรัญ,** *วารสารเทคโนโลยีสุรนารี***, 10(3)**, (2546).
41. Y.D. Hou, M.K. Zhu, H. Wang, B. Wang, H. Yan and C.S. Tian, *Mater. Lett.*, *In Press* (2003).
42. S. Priya and K. Uchino, *J. Appl. Phys*. **91(7)**, 4515 (2002).
43. T. Bove, W. Wolny, E. Ringgaard and A. Pedersen, *J. Eur. Ceram. Soc*. **21**, 1469 (2001).

Output จากโครงการวิจัยที่ได้รับทุนจาก สกว.

1. ผลงานตีพิมพ์ในวารสารวิชาการนานาชาติ จำนวนทั้งสิ้น 70 เรื่องได้แก่

1.1 ผลงานวิจัยโดยตรงที่ได้ตีพิมพ์แล้ว 44 เรื่อง (รายละเอียดในภาคผนวก)

1. W. Chaisan, **R. Yimnirun**, S. Ananta and D.P. Cann, “Dielectric properties of solid solutions in the lead zirconate titanate-barium titanate system prepared by a modified mixed-oxide method ,” *Materials Letters,* 59(28), pp 3732-3737 (2005).
2. **Rattikorn Yimnirun**, Yongyut Laosiritaworn, and Supattra Wongsaenmai, “Effects of Uniaxial Compressive Pre-Stress on Ferroelectric Properties of Soft PZT Ceramic” *Journal of Physics D: Applied Physics*, 39, pp 759-764 (2006).
3. R. Wongmaneerung, **R. Yimnirun** and S. Ananta, “Effects of Vibro-Milling Time on Phase Formation and Particle Size of Lead Titanate Nanopowders”, *Materials Letters,* 60(12), pp 1447-1452 (2006).
4. **R. Yimnirun**, S. Ananta, A. Ngamjarurojana, and S. Wongsaenmai, “Effects of Uniaxial Stress on Dielectric Properties of Ferroelectric Ceramics”, *Current Applied Physics,* 6(3), pp 520-524 (2006).
5. R. Wongmaneerung, T. Sarnkonsri, **R. Yimnirun** and S. Ananta “Effects of milling method and calcination condition on phase and morphology characteristics of $Mg_4Nb_2O_9$ powders”, *Materials Science and Engineering B*, 130(1-3), pp 246-253 (2006).
6. **Rattikorn Yimnirun**, Muangjai Unruan, Yongyut Laosiritaworn, and Supon Ananta, “Change of Dielectric Properties of Ceramics in Lead Magnesium Niobate-Lead Titanate System With Compressive Stress”, *J. Physics D: Applied Physics*, 39, pp 3097-3102 (2006)
7. **R. Yimnirun**, “Change in Dielectric Properties of Normal and Relaxor Ferroelectric Ceramic Composites in BT-PZT and PMN-PZT Systems by Uniaxial Compressive Stress” *Ferroelectrics,* 331, pp 9-18 (2006)
8. R. Wongmaneerung, **R. Yimnirun** and S. Ananta, “Effects of Milling Time and Calcination Condition on Phase Formation and Particle Size of Lead Titanate Nanopowders Prepared by Vibro-milling”, *Materials Letters*, 60, pp 2666-2671 (2006)

9. **Rattikorn Yimnirun**, Rungnapa Tipakontitikul and Supon Ananta, "Effect of Sintering Temperature on Densification and Dielectric Properties of $Pb(Zr_{0.44}Ti_{0.56})O_3$ Ceramics" *International Journal of Modern Physics B*, 20(16), pp 2415-2424 (2006).
10. R. Wongmaneerung, T. Sarnkonsri, **R. Yimnirun** and S. Ananta "Effects of magnesium niobate precursor and calcination condition on phase formation and morphology of lead magnesium niobate powders", *Materials Science and Engineering B,* 132, pp 292-299 (2006).
11. W. Chaisan, **R. Yimnirun**, S. Ananta and D.P. Cann, "Phase Development and Dielectric Properties of $(1-x)Pb(Zr_{0.52}Ti_{0.48})O_3–xBaTiO_3$ ceramics ," *Materials Science and Engineering B,*132, pp 300-306 (2006).
12. A. Ngamjarurojana, O. Khamman, **R. Yimnirun** and S. Ananta, "Effect of Calcination Conditions on Phase Formation and Particle Size of Zinc Niobate Powders Synthesized by Solid-State Reaction", *Materials Letters*, 60, pp 2867-2872 (2006).
13. **Rattikorn Yimnirun**, "Contributions of Domain-Related Phenomena on Dielectric Constant of Lead-Based Ferroelectric Ceramics Under Uniaxial Compressive Pre-Stress" *International Journal of Modern Physics B*, 20(23), pp 3409-3417 (2006).
14. **Rattikorn Yimnirun**, Yongyut Laosiritaworn, Supattra Wongsaenmai and Supon Ananta, "Scaling Behavior of Dynamic Hysteresis in Soft PZT Bulk Ceramics", *Applied Physics Letters,* 89(16), pp 162901-3 (2006)
15. R. Wongmaneerung, **R. Yimnirun**, S. Ananta, R. Guo, and A.S. Bhalla, "Polarization Behavior in the Two Stage Sintered Lead Titanate Ceramics" *Ferroelectric Letters*, 33(5-6), pp 137-146 (2006).
16. **Rattikorn Yimnirun**, Supattra Wongsaenmai, Supon Ananta, and Yongyut Laosiritaworn "Stress-Dependent Scaling Behavior of Dynamic Hysteresis in Bulk Soft Ferroelectric Ceramics", *Applied Physics Letters*, 89(24), pp 242901-3 (2006).
17. R. Wongmaneerung, **R. Yimnirun** and S. Ananta, "Effects of Sintering Condition on Phase Formation, Microstructure and Dielectric Properties of Lead Titanate Ceramics", *Applied Physics A*, 86(2), pp 249-255 (2007).

18. **R. Yimnirun**, S. Ananta, and S. Chamunglap, “Dielectric Properties of (1-x)PZT-xBT Ceramics Under Uniaxial Compressive Pre-Stress” *Materials Chemistry and Physics*, 102(2-3), pp 165-170 (2007).
19. **R. Yimnirun**, R. Wongmaneerung, S. Wongsaenmai, A. Ngamjarurojana, S. Ananta, and Y. Laosiritaworn, “Temperature Scaling of Dynamic Hysteresis in Soft Lead Zirconate Titanate Bulk Ceramic” *Applied Physics Letters*, 90(11), pp 112906 (2007).
20. **R. Yimnirun**, R. Wongmaneerung, S. Wongsaenmai, A. Ngamjarurojana, S. Ananta, and Y. Laosiritaworn, “Dynamic Hysteresis and Scaling Behavior of Hard Lead Zirconate Titanate Bulk Ceramic” *Applied Physics Letters*, 90(11), pp 112908 (2007).
21. S. Wongsaenmai, **R. Yimnirun** and S. Ananta, “Effects of Calcination Conditions on Phase Formation and Particle Size of Indium Niobate Powders Synthesized by the Solid-State Reaction”, *Materials Letters* (2007) *in press.*
22. O. Khamman, **R. Yimnirun** and S. Ananta, ”Effect of Vibro-Milling Time on Phase Formation and Particle Size of Lead Zirconate Nanopowders” *Materials Letters* (2007) *in press.*
23. Supattra Wongsaenmai, Xiaoli Tan, Supon Ananta, and **Rattikorn Yimnirun**, “Dielectric and Ferroelectric Properties of Fine Grains $Pb(In_{1/2}Nb_{1/2})O_3$–$PbTiO_3$ Ceramics” *Journal of Alloys and Compounds* (2007) *in press*
24. A. Prasatkhetragarn, **R. Yimnirun** and S. Ananta, “Effect of calcination conditions on phase formation and particle size of $Zn_3Nb_2O_8$ powders synthesized by solid-state reaction”, *Materials Letters* (2007) *in press*
25. S. Wongsaenmai, **R. Yimnirun** and S. Ananta, “Influence of Calcination Conditions on Phase Formation and Particle Size of Indium Niobate Powders Synthesized by the Solid-State Reaction”, *Journal of Materials Science* (2007) *in press*
26. W. Chaisan, **R. Yimnirun**, S. Ananta, “Two-Stage Sintering of Barium Titanate and Resulting Characteristics” *Ferroelectrics (2007) in press*
27. W. Chaisan, O. Khamman, **R. Yimnirun** and S. Ananta,, “Effects of Calcination Conditions on Phase and Morphology Evolution of Lead

Zirconate Powders Synthesized by Solid-State Reaction", *Journal of Materials Science* (2007) *in press*

28. **Rattikorn Yimnirun**, Xiaoli Tan, Supon Ananta, and Supattra Wongsaenmai, "Preparation of Fine-Grain Lead Indium Niobate Ceramics with Wolframite Precursor Method and Resulting Electrical Properties" *Applied Physics A* (2007) *in press*
29. Orawan Khamman, Rewadee Wongmaneerung, Wanwilai Chaisan, **Rattikorn Yimnirun** and Supon Ananta, "Potential of Vibro-Milling Technique for Preparation of Electroceramic Nanopowders" *Journal of Alloys and Compounds* (2007) *in press.*
30. W. Chaisan, **R. Yimnirun**, S. Ananta and D.P. Cann, "Dielectric and Ferroelectric Properties of Ceramics in PZT-BT System," *Materials Chemistry and Physics* (2007) *in press.*
31. Narit Triumnak, Muangjai Unruan, Supon Ananta, and **Rattikorn Yimnirun**, "Uniaxial Stress Dependence of Dielectric Properties of 0.9PMN-0.1PT Ceramics" *Journal of Electroceramics* (2007) *accepted.*
32. Athipong Ngamjarurojana, Orawan Khamman, Supon Ananta, and **Rattikorn Yimnirun**, "Synthesis and Characterizations of Lead Zinc Niobate-Lead Zirconate Titanate Powders" *Journal of Electroceramics* (2007) *accepted.*
33. Supattra Wongsaenmai, Orawan Khamman, Supon Ananta, and **Rattikorn Yimnirun**, "Synthesis and Characterizations of Lead Indium Niobate-Lead Titanate Powders" *Journal of Electroceramics* (2007) *accepted.*
34. Rewadee Wongmaneerung, Orawan Khamman, **Rattikorn Yimnirun**, and Supon Ananta, "Synthesis and Characterizations of Lead Titanate Powders" *Journal of Electroceramics* (2007) *accepted.*
35. **R. Yimnirun** "Dielectric Properties of PMN-PT Prepared by Mixed Oxide Method" *International Journal of Modern Physics B* (2007) *accepted*
36. O. Khamman, **R. Yimnirun** and S. Ananta,"Effect of Vibro-Milling Time and Calcination n Phase Formation and Particle Size of Lead Zirconate Nanopowders" *Ferroelectrics (2007) accepted*

37. A. Prasatkhetragarn, **R. Yimnirun** and S. Ananta, “Effects of Calcination Conditions on Phase Formation of Zirconium Titanate Powders Synthesized by the Solid-State Reaction”, *Ferroelectrics* (2007) *accepted*
38. W. Chaisan, A. Prasatkhetragarn**, R. Yimnirun**, S. Ananta, *“*Two-Stage Solid-State Reaction of Lead Zirconate Titanate Powders” *Ferroelectrics (2007) accepted*
39. **R. Yimnirun,** A. Ngamjarurojana, Y. Laosiritaworn, Supon Ananta, and Narit Triamnak, “Dielectric Properties of PZT-PZN Ceramics Under Compressive Stress” *Ferroelectrics* (2007) *accepted.*
40. P. Ketsuwan, Y. Laosiritaworn, S. Ananta, and **R. Yimnirun**, “Effect of Sintering Temperature on Phase Formation, Dielectric, Piezoelectric, and Ferroelectric Properties of Nb-doped $Pb(Zr_{0.52}Ti_{0.48})O_3$ Ceramics” *Ferroelectrics* (2007) *accepted.*
41. **R. Yimnirun**, Y. Laosiritaworn, S. Ananta, and S. Wongsaenmai, “Scaling Behavior of Dynamic Ferroelectric Hysteresis in Soft PZT Ceramics: Stress Dependence” *Ferroelectrics* (2007) *accepted.*
42. S. Wongsaenmai, A. Bhalla, R. Guo, S. Ananta, and **R. Yimnirun**, “Effect of Addition BT on Relaxor Behavior of PIN-PT Ceramics” *Integrated Ferroelectrics* (2007) *accepted*.
43. S. Wongsaenmai, A. Bhalla, X. Tan, S. Ananta, and **R. Yimnirun**, “Dielectric Properties and Relaxor Behavior of PIN-Based System” *Ferroelectrics Letters* (2007) *accepted.*
44. O. Khamman, T. Sarakonsri, A. Rujiwatra, Y. Laosiritaworn, **R. Yimnirun**, and S. Ananta. “Effects of Milling Time and Calcination Condition on Phase Formation and Particle Size of Lead Zirconate Nanopowders Prepared by Vibro-milling“ *Journal of Materials Science* (2007) *accepted.*

1.2 ผลงานวิจัยที่อยู่ระหว่างการส่งไปเพื่อตีพิมพ์ 26 เรื่อง

1. **Rattikorn Yimnirun**, Muangjai Unruan, Rewadee Wongmaneerung, Orawan Khamman, Wanwilai Chaisan, and Supon Ananta, “Dielectric Properties of Complex Perovskite PZBT-PMNT Ceramic Under Compressive Stress” submitted to *International Journal of Modern Physics B* (2007)

2. S. Wongsaenmai, S. Ananta, **R. Yimnirun**, W. Qu, and X. Tan, "Ferroelectric Properties and Phase Transitions of PBINT Ceramics" submitted to *Applied Physics A* (2007)
3. **R. Yimnirun**, R. Wongmaneerung, S. Wongsaenmai, A. Ngamjarurojana, S. Ananta, and Y. Laosiritaworn, "Temperature Scaling of Dynamic Hysteresis in Hard Lead Zirconate Titanate Bulk Ceramic" submitted to *Applied Physics A* (2007)
4. R. Wongmaneerung, **R. Yimnirun**, S. Ananta, "Processing and Properties of $Pb(Mg_{1/3}Nb_{2/3})O_3$-$PbTiO_3$ Based Ceramics" submitted to *Current Applied Physics* (2007)
5. **Rattikorn Yimnirun**, Narit Triamnak, Muangjai Unruan, Athipong Ngamjarurojana, Yongyut Laosiritaworn, and Supon Ananta, "Ferroelectric Properties of $Pb(Zr_{1/2}Ti_{1/2})O_3$—$Pb(Zn_{1/3}Nb_{2/3})O_3$ Ceramics Under Compressive Stress" submitted to *Current Applied Physics* (2007)
6. N. Triamnak, S. Wongsaenmai, S. Ananta, **R. Yimnirun**, "Dielectric Properties of PIN-PT Ceramics Under Compressive Stress" submitted to *Current Applied Physics* (2007)
7. N. Wongdamnern, N. Triamnak, A. Ngamjarurojana, Y. Laosiritaworn, S. Ananta, and **R. Yimnirun**, "Effects of Temperature and Stress on Ferroelectric Properties of Hard and Soft PZT Ceramics" submitted to *Current Applied Physics* (2007)
8. S. Wongsaenmai, A. Bhalla, R. Guo, S. Ananta, and **R. Yimnirun**, "Thermal Expansion Measurement in the Relaxor Ferroelectric PIN-PT System" submitted to *Materials Letters* (2007)
9. **Rattikorn Yimnirun**, Narit Triamnak, Muangjai Unruan, Athipong Ngamjarurojana, Yongyut Laosiritaworn, and Supon Ananta, "Stress-Dependent Ferroelectric Properties of $Pb(Zr_{1/2}Ti_{1/2})O_3$—$Pb(Zn_{1/3}Nb_{2/3})O_3$ Ceramic Systems" submitted to *Ceramics International* (2007)
10. Supattra Wongsaenmai, Supon Ananta, Xiaoli Tan, **Rattikorn Yimnirun**, "Dielectric and Ferroelectric Properties of Lead Indium Niobate Ceramic Prepared by Wolframite Method" submitted to *Ceramics International* (2007)

11. N. Wongdamnern, N. Triamnak, A. Ngamjarurojana, Y. Laosiritaworn, S. Ananta, and **R. Yimnirun**, "Comparative Studies of Dynamic Hysteresis Responses in Hard and Soft PZT Ceramics" submitted to *Ceramics International* (2007)
12. R. Wongmaneerung, A. Rittidech, O. Khamman, **R. Yimnirun** and S. Ananta, "Processing and Properties of $Pb(Mg_{1/3}Nb_{2/3})O_3$-$PbTiO_3$ Based Ceramics" submitted to *Ceramics International* (2007)
13. A. Ngamjarurojana, S. Ural, S. Ananta, **R. Yimnirun**, and K. Uchino, "Effects of Mn-Doping on PZN-PZT Ceramics" submitted to *Ceramics International* (2007)
14. A. Ngamjarurojana, S. Ural, S. Ananta, **R. Yimnirun**, and K. Uchino, "Low Sintering Temperature PZN-PZT Based-Ceramics" submitted to *Ceramics International* (2007)
15. W. Chaisan, **R. Yimnirun**, and S. Ananta, "Synthesis and Properties of PZT-BT Nanocomposites" submitted to *Ceramics International* (2007)
16. W. Chaisan, **R. Yimnirun**, and S. Ananta, "Synthesis of BT Nanopowders" submitted to *Ceramics International* (2007)
17. R. Wongmaneerung, O. Khamman, **R. Yimnirun** and S. Ananta, "Potential of Vibro-Milling in Nanopowders Production" submitted to *Ceramics International* (2007)
18. P. Ketsuwan, S. Ananta, **R. Yimnirun**, and Y. Laosiritaworn, "Effect of Porosity on Hysteresis Properties of Ferroelectrics" submitted to *Ceramics International* (2007)
19. Y. Laosiritaworn, S. Ananta, and **R. Yimnirun**, " Monte-Carlo Simulation on Stress Dependence on Ferroelectric Properties" submitted to *Ceramics International* (2007)
20. W. Suktomya, S. Ananta, **R. Yimnirun**, and Y. Laosiritaworn, "Neural Network Approach to Prediction of Powder Processing" submitted to *Ceramics International* (2007)
21. Piyachon Ketsuwan , Yongyut Laosiritaworn , Supon Ananta, and **Rattikorn Yimnirun**, "Effect of Nb-Doping on Electrical Properties of $Pb(Zr_{0.52}Ti_{0.48})O_3$ Ceramics" submitted to *Ceramics International* (2007)

22. N. Triamnak, S. Wongsaenmai, S. Ananta, **R. Yimnirun**, “Effects of Compressive Stress on the Dielectric Properties of PIN-PT Ceramics” submitted to *Ceramics International* (2007)
23. W. Chaisan, **R. Yimnirun**, and S. Ananta, “Synthesis and Properties of PZT-BT Nanocomposites” submitted to *J. Materials Science* (2007)
24. W. Chaisan, **R. Yimnirun**, and S. Ananta, “Synthesis of BT Nanopowders” submitted to *J. Materials Science* (2007)
25. **R. Yimnirun**, S. Wongsaenmai, R. Wongmaneerung, N. Wongdamnern, A. Ngamjarurojana, S. Ananta, and Y. Laosiritaworn, “ Stress- and Temperature-Dependent Scaling Behavior of Dynamic Hysteresis in Soft PZT Bulk Ceramics” submitted to *Physica Scripta* (2007)
26. **R. Yimnirun**, N. Triamnak, M. Unruan, S. Wongsaenmai, A. Ngamjarurojana, Y. Laosiritaworn, and S. Ananta, “Dielectric and Ferroelectric Properties of Complex Perovskite Ceramics Under Compressive Stress” submitted to *Physica Scripta* (2007)

2. การนำผลงานวิจัยไปใช้ประโยชน์

2.1 เชิงพาณิชย์

ในการวิจัยนี้ถึงแม้ไม่ได้มุ่งหวังในด้านการนำผลงานไปใช้ประโยชน์ในเชิงพาณิชย์ แต่มุ่งเน้นในการสร้างองค์ความรู้ใหม่ แต่อุปกรณ์ที่ถูกพัฒนาขึ้นมาใช้ประกอบการศึกษา ซึ่งได้แก่ ชุดอุปกรณ์ในการวัดสมบัติไดอิเล็กตริกภายใต้ความเค้นนั้น สามารถนำไปประยุกต์ใช้ในการวัดสมบัติดังกล่าวทั้งในกรณีที่ไม่มีความเค้นและกรณีที่มีความเค้นในวัสดุตัวอื่นๆได้ ซึ่งสามารถที่จะลดการสั่งซื้ออุปกรณ์ที่มีความคล้ายคลึงจากต่างประเทศได้

2.2 เชิงนโยบาย

ผลการวิจัยที่ได้จากโครงการนี้ได้ถูกนำไปใช้ในการกำหนดแผนและทิศทางการวิจัยของผู้วิจัยที่ชัดเจนขึ้น ดังจะเห็นได้จากการเสนอหัวข้อวิจัยเพื่อขอรับทุนพัฒนาศักยภาพการทำงานวิจัยของอาจารย์รุ่นกลาง ประจำปี 2550 จากสำนักงานกองทุนสนับสนุนการวิจัยและสำนักงานคณะกรรมการการอุดมศึกษา ซึ่งเป็นการวิจัยต่อเนื่องจากโครงการวิจัยนี้ เพื่อเป็นการส่งเสริมให้เกิดการวิจัยแบบมีทิศทางมากขึ้น

2.3 เชิงสาธารณะ

โครงการวิจัยนี้ได้ก่อให้เกิดเครือข่ายความร่วมมือในการวิจัยมากขึ้นระหว่างนักวิจัยรุ่นกลางและนักวิจัยรุ่นใหม่ทั้งในและต่างประเทศ เช่นความร่วมมืออย่างใกล้ชิดในการวิจัยกับ รศ. ดร. สุพล อนันตา ภาควิชาฟิสิกส์ คณะวิทยาศาสตร์ มหาวิทยาลัยเชียงใหม่ ซึ่งเน้นการวิจัยด้านกระบวนการผลิตเซรามิก ในขณะที่ผู้วิจัยได้มีส่วนร่วมในการวัดสมบัติทางไฟฟ้าของเซรามิกที่ผลิตขึ้น นอกจากนี้ก็มีความร่วมมือกับ ผศ. ดร. ยงยุทธ เหล่าศิริถาวร ภาควิชาฟิสิกส์ คณะวิทยาศาสตร์ มหาวิทยาลัยเชียงใหม่ ที่นำความรู้เรื่องฟิสิกส์คณานามาประกอบการคำนวณหลายๆอย่าง นอกจากนี้ยังได้มีการสร้างความร่วมมือด้านการวิจัยกับนักวิจัยในต่างประเทศคือ Prof. David Cann แห่ง Oregon State University และ Prof. Xiaoli Tan แห่ง Iowa State University สหรัฐอเมริกา และที่สำคัญที่สุดผู้วิจัยได้รับความรู้ในการวิจัยจากนักวิจัยอาวุโสจากทั้งในประเทศและต่างประเทศคือ ศ. ดร. ทวี ตันฑศิริ แห่งภาควิชาฟิสิกส์ คณะวิทยาศาสตร์ มหาวิทยาลัยเชียงใหม่ และ Prof. Robert Newnham Prof. Kenji Uchino และ Prof. Amar Bhalla แห่ง The Pennsylvania State University สหรัฐอเมริกา

2.4 เชิงวิชาการ (พัฒนาการเรียนการสอน/สร้างนักวิจัยใหม่)

ผลงานที่ได้จากการวิจัยนี้ได้ถูกนำไปใช้ประกอบการเรียนการสอนในหลายๆ กระบวนวิชาของสาขาวิชาวัสดุศาสตร์ ทั้งในระดับปริญญาตรีและระดับบัณฑิตศึกษา เช่น MATS 743 Electroceramics MATS 701 Characterization and Properties of Materials MATS 703 Fabrication Processes of Materials และ MATS 723 Ferroelectric Materials นอกจากนี้ผู้วิจัยยังนำผลงานบางส่วนไปประกอบการเขียนตำราเรื่อง สมบัติทางไฟฟ้าของเซรามิกเฟร์โรอิเล็กทริก (Electrical Properties of Ferroelectric Ceramics) สำหรับในส่วนของการสร้างนักวิจัยใหม่นั้น นอกจากประโยชน์โดยตรงที่เกิดกับผู้วิจัยเองแล้ว โครงการวิจัยนี้ได้มีส่วนในการฝึกฝนทักษะการวิจัยและการเผยแพร่ผลงานให้กับนักศึกษาทั้งในระดับปริญญาตรีและระดับบัณฑิตศึกษาในฐานะผู้ช่วยวิจัยร่วมกับหัวหน้าโครงการ และผลงานวิจัยที่ได้สามารถนำไปตีพิมพ์ในวารสารทางวิชาการทั้งในและต่างประเทศ รวมทั้งการนำเสนอผลงานในที่ประชุมทางวิชาการระดับนานาชาติ (ดังแสดงใน output และผลงานอื่นๆ) ซึ่งมีผลให้เกิดการพัฒนานักวิจัยรุ่นใหม่มากขึ้น

3. อื่น ๆ (ผลงานตีพิมพ์ในวารสารวิชาการและการเสนอผลงานในที่ประชุมวิชาการนานาชาติ)

3.1 ผลงานตีพิมพ์ในวารสารวิชาการในประเทศจำนวนทั้งสิ้น 9 เรื่องได้แก่

1. S. Chamunglap, S. Ananta and **R. Yimnirun**, "Effect of Uniaxial Stress on Dielectric Properties of PZT, BT and 0.55PZT-0.45BT Ceramics," *Naresuan University Science Journal*, 2004, 1(2), 15-21.
2. A. Ngamjarurojana, S. Wongsaenmai, O. Khamman, S. Ananta and **R. Yimnirun**, "Hysteresis Properties of Lead Zirconate Titanate Ceramic Under Uniaxial compressive Pre-Stress," *Chiang Mai Journal of Science*, 2005, 32(3), 355-359.
3. R. Tipakontitikul, S. Ananta and **R. Yimnirun**, "Effect of Sintering Conditions on Densification and Dielectric Properties of PZT Ceramics," *Chiang Mai Journal of Science*, 2005, 32(3), 323-329.
4. S. Chamunglap, S. Ananta and **R. Yimnirun**, "Uniaxial Stress Dependence of Dielectric Properties of PZT and 0.95PZT-0.05BT Ceramics," *Chiang Mai Journal of Science*, 2005, 32(3), 337-342.
5. R. Wongmaneerung, **R. Yimnirun** and S. Ananta, "Synthesis and Characterizations of Lead Titanate Nano-Sized Powders via a Rapid Vibro-milling," *Chiang Mai Journal of Science*, 2005, 32(3), 399-404.
6. A. Ngnamjarurojana, Y. Laosiritaworn, S. Ananta, and **R. Yimnirun**, " Synthesis and Characterization of Zinc Niobate Nanopowder via a Vibro-Milling Method" *Chiang Mai University Journal*, 2005, 4(1), 47-52.
7. R. Wongmaneerung, Y. Laosiritaworn, **R. Yimnirun** and S. Ananta, "A Mixed Oxide Synthetic Route to $Mg_4Nb_2O_9$ Nanopowders in a Corundum-Like Phase," *Chiang Mai University Journal*, 2005, 4(1), 41-46.
8. R. Wongmaneerung, S. Ananta, **R. Yimnirun** and Y. Laosiritaworn, "Monte Carlo Simulation of Nano-Powder from Mechanical Milling," *Chiang Mai University Journal*, 2005, 4(1), 169-175.
9. **R. Yimnirun**, "Roles of Nano-Domains on Uniaxial Stress Dependence of Dielectric Properties of Ferroelectric Ceramics", *Chiang Mai University Journal*, 2006 *in press*

3.2 การเสนอผลงานในที่ประชุมวิชาการนานาชาติจำนวนทั้งสิ้น 34 เรื่องได้แก่

1. **R. Yimnirun**, S. Ananta, A. Ngamjarurojana, and S. Wongsaenmai, “Effects of Uniaxial Stress on Dielectric Properties of Ferroelectric Ceramics”, *The 2nd International Conference on Advanced Materials and Nanotechnology*, Queenstown, New Zealand (February 2005)
2. Rungnapa Tipakontitikul, Supon Ananta, **Rattikorn Yimnirun**, “Formation and Transitions in Lead Zirconate Titanate-Lead Magnesium Niobate System” *The 2nd International Conference on Advanced Materials and Nanotechnology*, Queenstown, New Zealand (February 2005)
3. A. Ngamjarurojana, S. Wongsaenmai, R. Tipakontitikul, S. Ananta and **R. Yimnirun**, “Hysteresis Properties of Lead Zirconate Titanate Ceramic Under Uniaxial compressive Pre-Stress,” *The International Conference on Smart Materials: Smart/Intelligent Materials and Nanotechnology*, 1-3 Dec. 2004, Chiang Mai, Thailand.
4. R. Tipakontitikul, S. Ananta and **R. Yimnirun**, “Effect of Sintering Conditions on Densification and Dielectric Properties of PZT Ceramics,” *The International Conference on Smart Materials: Smart/Intelligent Materials and Nanotechnology*, 1-3 Dec. 2004, Chiang Mai, Thailand.
5. S. Chamunglap, S. Ananta and **R. Yimnirun**, “Uniaxial Stress Dependence of Dielectric Properties of PZT and 0.95PZT-0.05BT Ceramics,” *The International Conference on Smart Materials: Smart/Intelligent Materials and Nanotechnology*, 1-3 Dec. 2004, Chiang Mai, Thailand.
6. R. Wongmaneerung, **R. Yimnirun** and S. Ananta, “Synthesis and Characterizations of Lead Titanate Nano-Sized Powders via a Rapid Vibro-milling”, *The International Conference on Smart Materials: Smart/Intelligent Materials and Nanotechnology*, 1-3 Dec. 2004, Chiang Mai, Thailand.
7. Narit Triumnak, Supon Ananta, and **Rattikorn Yimnirun**, “Uniaxial Stress Dependence of Dielectric Properties of 0.9PMN-0.1PT Ceramics” *The 4th Asian Meeting on Electroceramics,* Hangzhou, China (June 2005)
8. Athipong Ngamjarurojana, Supon Ananta, and **Rattikorn Yimnirun**, “Synthesis and Characterizations of Lead Zinc Niobate-Lead Zirconate

Titanate Powders" *The 4th Asian Meeting on Electroceramics,* Hangzhou, China (June 2005)

9. Supattra Wongsaenmai, Supon Ananta, and **Rattikorn Yimnirun**, "Synthesis and Characterizations of Lead Indium Niobate-Lead Titanate Powders" *The 4th Asian Meeting on Electroceramics,* Hangzhou, China (June 2005)
10. Rewadee Wongmaneerung, **Rattikorn Yimnirun**, and Supon Ananta, "Synthesis and Characterizations of Lead Titanate Powders" *The 4th Asian Meeting on Electroceramics,* Hangzhou, China (June 2005)
11. O. Khamman, **R. Yimnirun** and S. Ananta,"Effect of Vibro-Milling Time and Calcination n Phase Formation and Particle Size of Lead Zirconate Nanopowders" AMF-5, Japan (September 2006)
12. A. Prasatkhetragarn, **R. Yimnirun** and S. Ananta, "Effects of Calcination Conditions on Phase Formation of Zirconium Titanate Powders Synthesized by the Solid-State Reaction", AMF-5, Japan (September 2006)
13. W. Chaisan, A. Prasatkhetragarn**, R. Yimnirun**, S. Ananta, "Two-Stage Solid-State Reaction of Lead Zirconate Titanate Powders" AMF-5, Japan (September 2006)
14. **R. Yimnirun,** A. Ngamjarurojana, Y. Laosiritaworn, Supon Ananta, and Narit Triamnak, "Dielectric Properties of PZT-PZN Ceramics Under Compressive Stress" AMF-5, Japan (September 2006)
15. P. Ketsuwan, Y. Laosiritaworn, S. Ananta, and R. Yimnirun, "Effect of Sintering Temperature on Phase Formation, Dielectric, Piezoelectric, and Ferroelectric Properties of Nb-doped $Pb(Zr_{0.52}Ti_{0.48})O_3$ Ceramics" AMF-5, Japan (September 2006)
16. **R. Yimnirun**, Y. Laosiritaworn, S. Ananta, and S. Wongsaenmai, "Scaling Behavior of Dynamic Ferroelectric Hysteresis in Soft PZT Ceramics: Stress Dependence" AMF-5, Japan (September 2006)
17. **Rattikorn Yimnirun**, Supattra Wongsaenmai, Yongyut Laosiritaworn and Supon Ananta , "Uniaxial Stress Dependence and Scaling Behavior of Dynamic Hysteresis Responses in Soft PZT Ceramics" ISAF-2006, North Carolina, USA (August 2006)

18. Wanwilai Chaisan**, Rattikorn Yimnirun**, and Supon Ananta , “Two-Stage of Barium Titanate” ISAF-2006, North Carolina, USA (August 2006)
19. Rewadee Wongmaneerung, Amar Bhalla, Ryan Guo, Supon Ananta, and **Rattikorn Yimnirun**, “Thermal Expansion Investigation of PMN-PT Ceramics” ISAF-2006, North Carolina, USA (August 2006)
20. Supattra Wongsaenmai, Xiaoli Tan, Supon Ananta, and Rattikorn Yimnirun, “Investigation of New PBINT Ceramic Systems” ISAF-2006, North Carolina, USA (August 2006)
21. **Rattikorn Yimnirun**, Narit Triamnak, Muangjai Unruan, Athipong Ngamjarurojana, Yongyut Laosiritaworn, and Supon Ananta, “Stress-Dependent Ferroelectric Properties of $Pb(Zr_{1/2}Ti_{1/2})O_3$—$Pb(Zn_{1/3}Nb_{2/3})O_3$ Ceramic Systems” *The 5th Asian Meeting on Electroceramics,* Bangkok, Thailand (December 2006)
22. Supattra Wongsaenmai, Supon Ananta, Xiaoli Tan, **Rattikorn Yimnirun**, “Dielectric and Ferroelectric Properties of Lead Indium Niobate Ceramic Prepared by Wolframite Method” *The 5th Asian Meeting on Electroceramics,* Bangkok, Thailand (December 2006)
23. N. Wongdamnern, N. Triamnak, A. Ngamjarurojana, Y. Laosiritaworn, S. Ananta, and **R. Yimnirun**, “Comparative Studies of Dynamic Hysteresis Responses in Hard and Soft PZT Ceramics” *The 5th Asian Meeting on Electroceramics,* Bangkok, Thailand (December 2006)
24. R. Wongmaneerung, A. Rittidech, O. Khamman, **R. Yimnirun** and S. Ananta, “Processing and Properties of $Pb(Mg_{1/3}Nb_{2/3})O_3$-$PbTiO_3$ Based Ceramics” *The 5th Asian Meeting on Electroceramics,* Bangkok, Thailand (December 2006)
25. A. Ngamjarurojana, S. Ural, S. Ananta, **R. Yimnirun**, and K. Uchino, “Effects of Mn-Doping on PZN-PZT Ceramics” *The 5th Asian Meeting on Electroceramics,* Bangkok, Thailand (December 2006)
26. A. Ngamjarurojana, S. Ural, S. Ananta, **R. Yimnirun**, and K. Uchino, “Low Sintering Temperature PZN-PZT Based-Ceramics” *The 5th Asian Meeting on Electroceramics,* Bangkok, Thailand (December 2006)
27. W. Chaisan, **R. Yimnirun**, and S. Ananta, “Synthesis and Properties of PZT-BT Nanocomposites” *The 5th Asian Meeting on Electroceramics,* Bangkok, Thailand (December 2006)

28. W. Chaisan, **R. Yimnirun**, and S. Ananta, “Synthesis of BT Nanopowders” *The 5th Asian Meeting on Electroceramics,* Bangkok, Thailand (December 2006)
29. R. Wongmaneerung, O. Khamman, **R. Yimnirun** and S. Ananta, “Potential of Vibro-Milling in Nanopowders Production” *The 5th Asian Meeting on Electroceramics,* Bangkok, Thailand (December 2006)
30. P. Ketsuwan, S. Ananta, **R. Yimnirun**, and Y. Laosiritaworn, “Effect of Porosity on Hysteresis Properties of Ferroelectrics” *The 5th Asian Meeting on Electroceramics,* Bangkok, Thailand (December 2006)
31. Y. Laosiritaworn, S. Ananta, and **R. Yimnirun**, “ Monte-Carlo Simulation on Stress Dependence on Ferroelectric Properties” *The 5th Asian Meeting on Electroceramics,* Bangkok, Thailand (December 2006)
32. W. Suktomya, S. Ananta, **R. Yimnirun**, and Y. Laosiritaworn, “Neural Network Approach to Prediction of Powder Processing” *The 5th Asian Meeting on Electroceramics,* Bangkok, Thailand (December 2006)
33. Piyachon Ketsuwan , Yongyut Laosiritaworn , Supon Ananta, and **Rattikorn Yimnirun**, “Effect of Nb-Doping on Electrical Properties of $Pb(Zr_{0.52}Ti_{0.48})O_3$ Ceramics” *The 5th Asian Meeting on Electroceramics,* Bangkok, Thailand (December 2006)
34. N. Triamnak, S. Wongsaenmai, S. Ananta, **R. Yimnirun**, “Effects of Compressive Stress on the Dielectric Properties of PIN-PT Ceramics” *The 5th Asian Meeting on Electroceramics,* Bangkok, Thailand (December 2006)

ภาคผนวก

Re-Print หรือ Pre-Print หรือ Accepted Manuscript

ของ

ผลงานตีพิมพ์ในวารสารวิชาการนานาชาติ

Available online at www.sciencedirect.com
SCIENCE DIRECT
ELSEVIER
Materials Letters 59 (2005) 3732 – 3737
materials letters
www.elsevier.com/locate/matlet

Dielectric properties of solid solutions in the lead zirconate titanate–barium titanate system prepared by a modified mixed-oxide method

Wanwilai Chaisan [a,*], Rattikorn Yimnirun [a], Supon Ananta [a], David P. Cann [b]

[a] *Department of Physics, Faculty of Science, Chiang Mai University, Chiang Mai, Thailand*
[b] *Materials Science and Engineering Department, Iowa State University, Ames, IA, USA*

Received 13 January 2005; accepted 30 June 2005
Available online 22 July 2005

Abstract

Ceramic solid solutions within the system $(1-x)Pb(Zr_{0.52}Ti_{0.48})O_3-xBaTiO_3$, where x ranged from 0.0 to 1.0, were prepared by a modified mixed-oxide method. The crystal structure, microstructure and dielectric properties of the ceramics were investigated as a function of composition via X-ray diffraction (XRD), scanning electron microscopy (SEM) and dielectric spectroscopy. While pure BT and PZT ceramics exhibited sharp phase transformation expected for normal ferroelectrics, the $(1-x)$PZT–xBT solid solutions showed that with increasing solute concentration (BT or PZT), the phase transformation became more diffuse. This was primarily evidenced by an increased broadness in the dielectric peak, with a maximum peak width occurring at $x=0.4$.

Keywords: Dielectric properties; Barium titanate (BT); Lead zirconate titanate (PZT)

1. Introduction

Currently lead-based perovskite ferroelectric ceramics are widely applied in multilayer capacitors and sensors because of their excellent electrical properties [1]. Many of these applications require materials with superior dielectric and piezoelectric properties. Both $BaTiO_3$ (BT) and $Pb(Zr,Ti)O_3$ (PZT) are among the most common ferroelectric materials and have been studied extensively since the late 1940s [2,3]. These two ceramics have distinct characteristics that make each ceramic suitable for different applications. The compound $Pb(Zr_{0.52}Ti_{0.48})O_3$ (PZT) has great piezoelectric properties which can be applied in transducer applications. Furthermore, it has a high T_C of 390 °C which allows piezoelectric devices to be operated at relatively high temperatures. Barium titanate (BT) is a normal ferroelectric material which exhibits a high dielectric constant, a lower T_C (~120 °C) and better mechanical properties [1–3]. However, sintering temperature of BT is higher than PZT. Thus, mixing PZT with BT is expected to decrease the sintering temperature of BT-based ceramics, a desirable move towards electrode of lower cost [4]. Moreover, since PZT–BT is not a pure-lead system, it is easier to prepare single phase ceramics with significantly lower amount of undesirable pyrochlore phases, usually associated with lead-based system [5,6]. With their complimentary characteristics, it is expected that excellent properties with preparation ease can be obtained from ceramics in PZT–BT system. In addition, the Curie temperature of PZT–BT system can be engineered over a wide range of temperature by varying the composition in this system. Therefore, this study is aimed at investigating dielectric properties of PZT–BT system over the whole composition range in hope to identify compositions with desirable properties.

* Corresponding author.
E-mail address: wanwilai_chaisan@yahoo.com (W. Chaisan).

0167-577X/$ - see front matter © 2005 Elsevier B.V. All rights reserved.
doi:10.1016/j.matlet.2005.06.045

BT has been mixed into solid solutions with $SrTiO_3$ (BST) and with $PbTiO_3$ (BPT) to adjust the Curie temperature and to optimize the dielectric and piezoelectric response [1,2,7,8]. PZT ceramics are always modified with other chemical constituents, such as Nb and La, to improve the physical properties for specific applications [2,3,9]. Moreover, solid solutions between normal and relaxor ferroelectric materials such as PZN–BT [10], PMN–PZT [11], PZT–PNN [12], PMN–PT [13] and PZN–PT [14] have been widely studied for dielectric applications and to examine the order–disorder behavior. However the superior dielectric properties of these relaxor systems have been associated with the presence of unwanted phase, densification behavior and microstructure development [15]. It is well known that the single phase of relaxor materials is very difficult to prepare and these systems always exhibit high dielectric loss and strong frequency dependence which is not suitable for some applications [2,16]. Even though there have been extensive work on PZT-based and BT-based solid solutions, there are only a few studies on PZT–BT solid solutions [5,6,17]. Chaisan et al. [5] prepared perovskite powders in the whole series of the solid solutions in PZT–BT system. The phase formation characteristics, cell parameters and the degree of tetragonality were examined as a function of composition. It was found that complete solid solutions of perovskite-like phase in the $(1-x)$PZT–xBT system occurred across the entire composition range. Lattice parameters of the tetragonal phase and of the rhombohedral phase were found to vary with chemical composition. The degree of tetragonality increased, while optimum firing temperatures decreased continuously with decreasing BT content. Moreover, pseudo-binary system of PZN–BT–PZT was previously studied and the effect of processing conditions on the piezoelectric and dielectric properties of this system was also discussed [17].

Thus far, from these literatures, there have been no systematic studies on the dielectric properties of the whole series of PZT–BT compositions. Therefore, as an extension of our earlier work on structural studies of the PZT–BT system [5], the overall purpose of this study is to investigate the dielectric properties of the solid solution between two normal ferroelectrics with the aim of identifying excellent electrical properties within this system. Although the conventional mixed-oxide method has attracted interest to prepare normal ferroelectric PZT and BT materials for many decades, several methods such as mechanical activation [6] and sol–gel-hydrothermal technique [18] still have been developed for better approach. A number of chemical routes has also been used as alternatives [19–21]. However these techniques are more complicated and expensive than the conventional mixed-oxide route, which limits its commercial applicability for mass powder synthesis. In this respect, it is desirable to develop a method based on the mixed-oxide method for preparation of PZT–BT ferroelectric materials. Therefore, this paper presents the dielectric properties of compositions in the PZT–BT binary system prepared via a modified mixed-oxide method, in which PZT powders are prepared through lead zirconate ($PbZrO_3$) precursor to eliminate pyrochlore phase usually found in powders from a conventional mixed-oxide method [5].

2. Experimental procedures

The compositions $(1-x)Pb(Zr_{0.52}Ti_{0.48})O_3-xBaTiO_3$ or $(1-x)$PZT–xBT, where $x=0.0$, 0.1, 0.3, 0.4, 0.5, 0.7, 0.9 and 1.0, were prepared by a modified mixed-oxide method [5]. Reagent grade PbO, ZrO_2, TiO_2 and $BaCO_3$ powders (Fluka, >99% purity) were used as starting materials. Powder of each end member (PZT and BT) was first formed in order to avoid unwanted pyrochlore phases. For the preparation of BT, $BaCO_3$ and TiO_2 powders were homogeneously mixed via ball-milling for 24 h with zirconia media in ethanol. The well-mixed powder was calcined at 1300 °C for 2 h in an alumina crucible. With a modified mixed-oxide method [5], the PZT powders were prepared by using a lead zirconate ($PbZrO_3$) as precursor in order to reduce the occurrence of undesirable phase. Pure $PbZrO_3$ phase was first formed by reacting PbO with ZrO_2 at 800 °C for 2 h. $PbZrO_3$ powder was then mixed with PbO and TiO_2 and milled, dried and calcined at 900 °C for 2 h to form single phase PZT. The $(1-x)$PZT–xBT powders were then formulated from the BT and PZT components by employing the similar mixed-oxide procedure and calcining at various

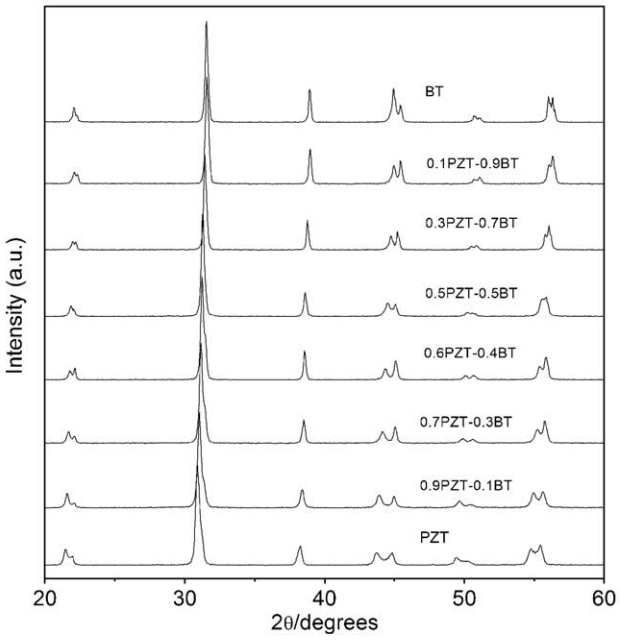

Fig. 1. XRD diffraction patterns of sintered $(1-x)$PZT–xBT ceramics.

Table 1
Characteristics of (1 − x)PZT–xBT ceramics with optimized processing conditions

Compositions	Sintering temperature (°C)	Density (g/cm^3)	Average grain size (μm)
PZT	1100	7.7	2.36
0.9PZT–0.1BT	1200	7.6	2.86
0.7PZT–0.3BT	1200	7.2	1.97
0.6PZT–0.4BT	1250	6.9	2.31
0.5PZT–0.5BT	1250	6.6	3.87
0.3PZT–0.7BT	1250	5.7	3.71
0.1PZT–0.9BT	1300	5.3	5.72
BT	1350	5.8	2.42

temperatures between 900 and 1300 °C for 2 h in order to obtain single phase $(1-x)$PZT–xBT powders [5].

The calcined $(1-x)$PZT–xBT powders were then isostatically cold-pressed into pellets with a diameter of 15 mm and a thickness of 2 mm at a pressure of 4 MPa and sintered for 2 h over a range of temperatures between 1050 and 1350 °C depending upon the composition. Densities of sintered ceramics were measured by Archimedes method and X-ray diffraction (XRD using CuK_α radiation) was employed to identify the phases formed. The grain morphology and size were directly imaged using scanning electron microscopy (SEM) and the average grain size was determined by using a mean

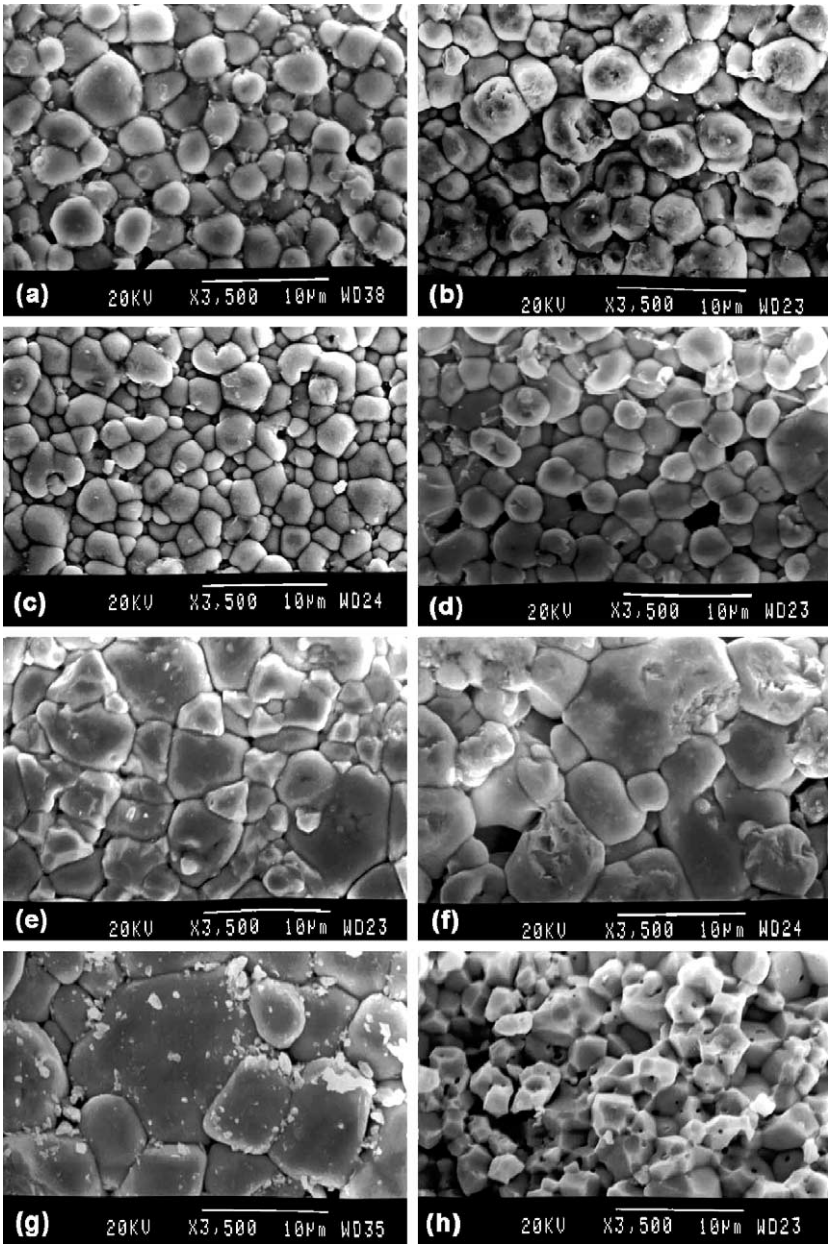

Fig. 2. SEM micrographs of $(1-x)$PZT–xBT ceramics: (a) PZT, (b) 0.9PZT–0.1BT, (c) 0.7PZT–0.3BT, (d) 0.6PZT–0.4BT, (e) 0.5PZT–0.5BT, (f) 0.3PZT–0.7BT, (g) 0.1PZT–0.9BT and (h) BT.

linear intercept method [22]. For electrical measurements, silver paste was fired on both sides of the polished samples at 550 °C for 30 min as the electrodes. A dimension of ceramics after sintered and polished is about 12.5 mm in diameter and 1 mm in thickness. Dielectric properties of the sintered ceramics were studied as a function of both temperature and frequency. The capacitance was measured with a HP4284A LCR meter in connection with a Delta Design 9023 temperature chamber and a sample holder (Norwegian Electroceramics) capable of high temperature measurement. Dielectric constant (ε_r) was calculated using the geometric area and thickness of the discs.

3. Results and discussion

The phase formation behavior of the sintered $(1-x)$PZT–xBT ceramics is revealed by XRD as shown in Fig. 1. The $BaTiO_3$ ceramic sintered at 1350 °C was identified as single phase perovskite having tetragonal symmetry. With increasing PZT content, the diffraction peaks shifted towards lower angle and the diffraction peak around 2θ of 43°–46° was found to split at composition $x=0.5$. This observation suggests that this composition may lead to a diffuse MPB between the tetragonal and rhombohedral PZT phases [23]. In this case, the peak of tetragonal phase is much stronger than that of rhombohedral phase. However, the (200) peak splitting for the PZT–BT system exhibited more clearly in powders as reported in our earlier work [5]. Additionally, the PZT–BT ceramics showed single diffraction peaks which indicate good homogeneity and complete solid solution within the $(1-x)$PZT–xBT system [24]. The pure $Pb(Zr_{0.52}Ti_{0.48})O_3$ ceramic sintered at 1100 °C showed a co-existence of both tetragonal and rhombohedral phases which can be matched with the JCPDS file no. 33-0784 and 73-2022, respectively.

The optimized sintering temperatures at which ceramics with single phase and highest densification are obtained, densities, and average grain sizes of the sintered $(1-x)$PZT–xBT ceramics are listed in Table 1. Higher firing temperatures were necessary for compositions containing a large fraction of BT. Compositions with $x=0.7$ and $x=0.9$ could not be sintered to sufficient densities and the theoretical densities of ceramics in this range were about 86%–89%. It is possible that volatilization of PbO during firing is the main reason for the failure in preparing dense ceramics over this composition range [25,26]. As shown in Fig. 2, SEM micrographs reveal that the compositions with $0.0 \le x \le 0.4$ exhibit good densification and homogenous grain size. For the compositions with $0.5 \le x \le 0.9$, the grain size varies greatly from 1 to 15 μm and defective grains and some degree of porosity are clearly seen; these matched with the density data. The reason for the variation of grain sizes in this composition range is not clearly understood. However, it can be assumed that since sintering temperatures for highest

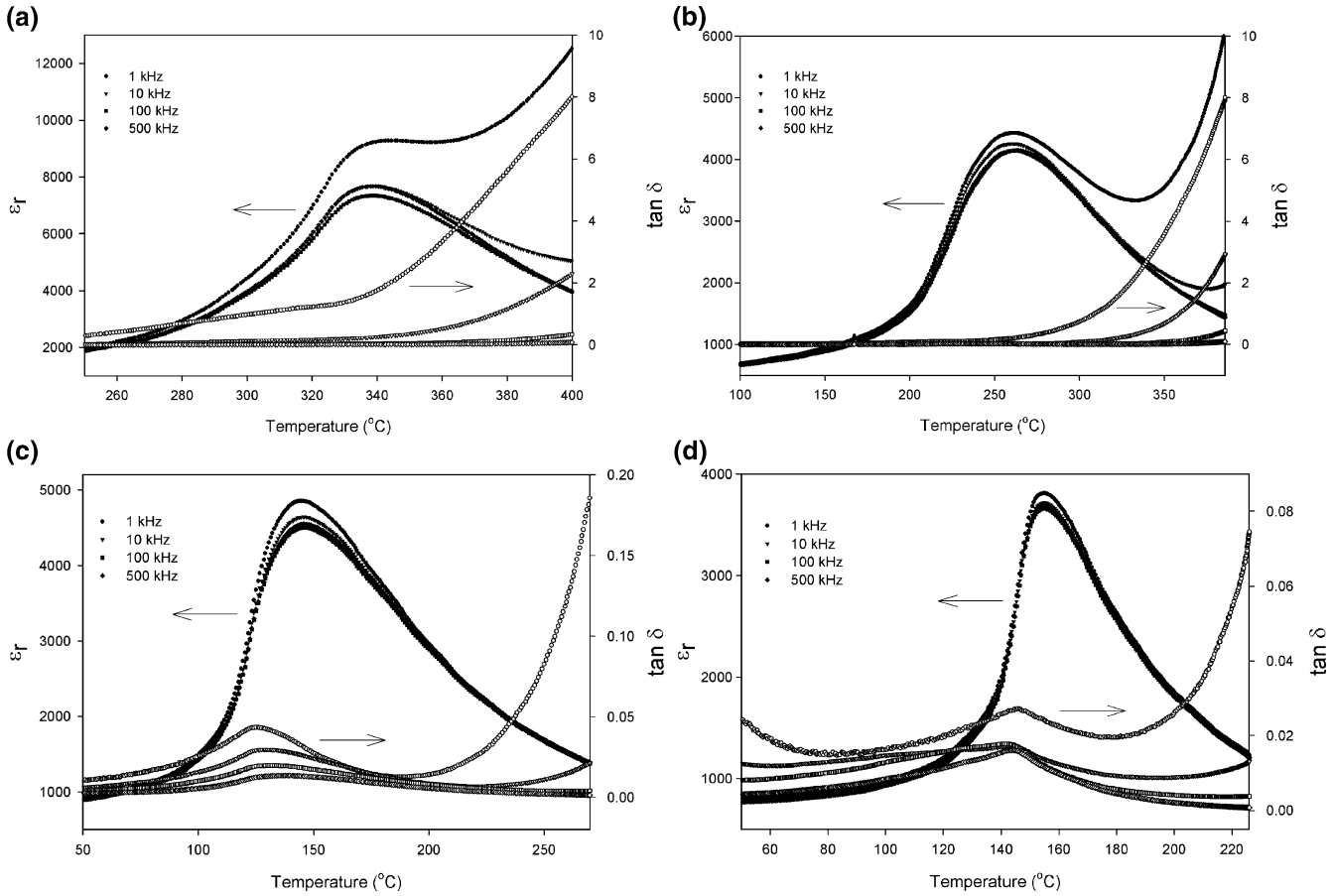

Fig. 3. Temperature and frequency dependence of dielectric properties of (a) 0.9PZT–0.1BT, (b) 0.7PZT–0.3BT, (c) 0.3PZT–0.7BT and (d) 0.1PZT–0.9BT ceramics.

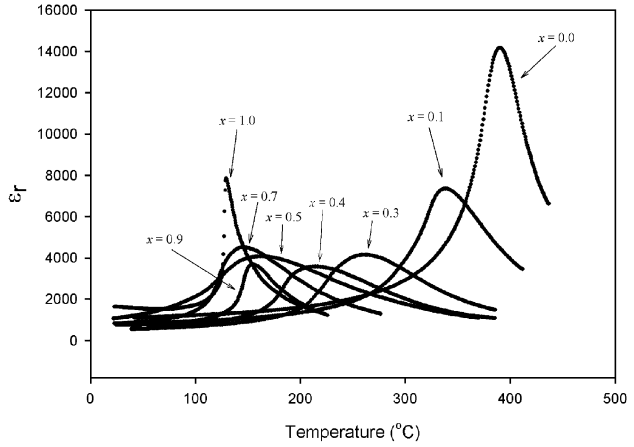

Fig. 4. Temperature dependence of dielectric constant (ε_r) of $(1-x)$PZT–xBT ceramics at 100 kHz.

densification of PZT and BT ceramics are very different (900 °C and 1300 °C, respectively), this could lead to different grain growth behaviors between two phases, hence heterogeneous microstructure [27].

Fig. 3 shows the temperature dependence of dielectric constant (ε_r) and dissipation factor (tan δ) at various frequencies for compositions with $x=0.1$, 0.3, 0.7 and 0.9. All compositions show indication of a diffuse phase transition of dielectric constant with rather weak frequency dependence. In addition, Curie temperatures (T_C) are also noticeably frequency independent [28]. It should be noted that the dielectric loss tangent of all ceramics increases rapidly at high temperature as a result of thermally activated space charge conduction [11]. The representative temperature dependence of the dielectric constant (ε_r) measured at 100 kHz for $(1-x)$PZT–xBT samples with $0.0 \le x \le 1.0$ is shown in Fig. 4. The Curie temperatures and maximum dielectric constants of the pure PZT and BT ceramics in this work were, respectively, 390 °C and 14,200 for PZT, and 129 °C and 7800 for BT. Therefore, a solid solution between PZT and BT is expected to show a transition temperature between 390 and 129 °C. The variation of T_C with compositions and dielectric data are listed in Table 2. The Curie temperature significantly decreases with increasing BT content up to 50 mol%. However, for the compositions $0.5 \le x \le 0.9$, T_C is not clearly depending on composition and remains at a nearly constant value between 140 and 160 °C. Even though the presence of Pb is known to shift T_C to higher temperatures [2,3], the nearly constant T_C with increasing Pb content in the composition with $0.5 \le x \le 0.9$ is likely caused by PbO loss due to the high sintering temperatures required for these compositions [25,26]. For pure PZT, the ε_r peak is sharp and approaches 15,000. However, the ε_r peaks become broader with increasing BT content, and the broadest peak occurs at the $x=0.4$ composition. It is very interesting to observe that the ε_r peak becomes more sharp as the BT content further increases.

Table 2
Dielectric properties of $(1-x)$PZT–xBT ceramics

Compositions	T_C (°C)	ε_m	γ	δ
PZT	390	14,200	1.74	16.1
0.9PZT–0.1BT	338	7300	1.76	16.2
0.7PZT–0.3BT	262	4100	1.86	16.6
0.6PZT–0.4BT	214	3600	1.97	17.1
0.5PZT–0.5BT	162	4100	1.91	17.3
0.3PZT–0.7BT	146	4500	1.74	15.9
0.1PZT–0.9BT	155	3700	1.63	14.4
BT	129	7800	1.16	12.5

To understand the interesting dielectric behavior of the PZT–BT system, we look at the different behaviors of normal and relaxor ferroelectric. For a normal ferroelectric such as PZT and BT, above the Curie temperature the dielectric constant follows the Curie–Weiss law:

$$\varepsilon = \frac{c}{T - T_0} \tag{1}$$

where c is the Curie constant and T_0 is the Curie–Weiss temperature [2,11,29]. For a ferroelectric with a diffuse phase transition, the following equation:

$$\frac{1}{\varepsilon} \approx (T - T_m)^2 \tag{2}$$

has been shown to be valid over a wide temperature range instead of the normal Curie–Weiss law (Eq. (1)) [10,30]. In Eq. (2), T_m is the temperature at which the dielectric constant is maximum. If the local Curie temperature distribution is Gaussian, the reciprocal permittivity can be written in the form [10,12]:

$$\frac{1}{\varepsilon} = \frac{1}{\varepsilon_m} + \frac{(T - T_m)^\gamma}{2\varepsilon_m \delta^2} \tag{3}$$

where ε_m is maximum permittivity, γ is diffusivity, and δ is diffuseness parameter. For $(1-x)$PZT–xBT compositions, the diffusivity (γ) and diffuseness parameter (δ) can be estimated from the slope and intercept of the dielectric data shown in Fig. 5, and tabulated in Table 2.

For the PZT-rich ceramics, the values of γ and δ increase with increasing BT content, confirming the diffuse phase transitions in PZT–BT solid solutions. It is clear that the addition of BT raises the degree of disorder in $(1-x)$PZT–xBT over the compositional range $0.1 \le x \le 0.5$. The highest degree of diffuseness is exhibited in the 0.5PZT–0.5BT ceramic. Similarly, from the BT end member, the values of both γ and δ exhibit the same trend with

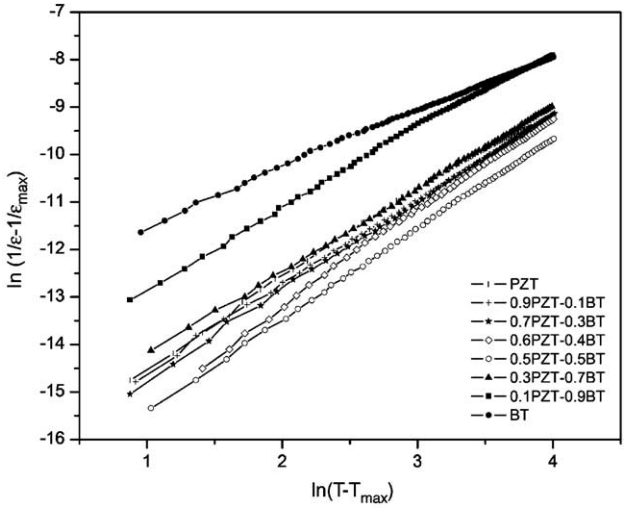

Fig. 5. Plots of $\ln\left(\frac{1}{\varepsilon} - \frac{1}{\varepsilon_m}\right)$ vs. $\ln(T - T_m)$ for $(1-x)$PZT–xBT ceramics.

increasing PZT content. This observation indicates that PZT addition also induces disorder in BT-rich compositions. It should also be mentioned here that different dielectric behaviors could also be caused by grain size variation [11]. However, the grain size, as shown in Table 1, in this study does not differ significantly enough to cause such a variation in the dielectric properties. Finally, it should be noted here that with comparison to other solid solution systems, such as PMN–PT, PZN–PT, PZT–PNN [12–14], ceramics in PZT–BT are much easier to prepare with minimized pyrochlore phases, lower dielectric loss and weak frequency dependence.

4. Conclusions

The dielectric properties of solid solutions in the $(1-x)$PZT–xBT system prepared via the mixed-oxide method are reported. All compositions in this study were single phase perovskite with tetragonal symmetry. The results indicated that the dielectric behavior of pure PZT and BT follows a Curie–Weiss law, while solid solutions of $(1-x)$PZT–xBT ($0.1 \leq x \leq 0.9$) exhibited a diffuse phase transition behavior with a Curie temperature ranging between 390 °C to 129 °C. In $(1-x)$PZT–xBT solid solutions, the degree of diffuseness increased with increased solute content up to a maximum at $x=0.5$.

Acknowledgements

This work was supported by the Thailand Research Fund (TRF), Graduate School of Chiang Mai University and the Ministry of University Affairs.

References

[1] A.J. Moulson, J.M. Herbert, Electroceramics: Materials, Properties, Applications, 2nd edition, John Wiley & Sons, Ltd., 2003, p. 243.
[2] G.H. Haertling, J. Am. Ceram. Soc. 82 (1999) 797–818.
[3] B. Jaffe, W.R. Cook, Piezoelectric Ceramics, R.A.N. Publishers, 1971, p. 317.
[4] J. Chen, Z. Shen, F. Liu, X. Liu, J. Yun, Scr. Mater. 49 (2003) 509–514.
[5] W. Chaisan, S. Ananta, T. Tunkasiri, Cur. Appl. Phys. 4 (2004) 182–185.
[6] B.K. Gan, J.M. Xue, D.M. Wan, J. Wang, Appl. Phys., A 69 (1999) 433–436.
[7] K. Uchino, Acta Mater. 46 (1998) 3745–3753.
[8] A.D. Polli, F.F. Lange, C.G. Levi, J. Am. Ceram. Soc. 83 (2000) 873–881.
[9] H. Jaffe, D.A. Berlincourt, Proc. IEEE 53 (1965) 1372–1386.
[10] A. Halliyal, U. Kumar, R.E. Newnham, L.E. Cross, Am. Ceram. Soc. Bull. 66 (1987) 671–676.
[11] R. Yimnirun, S. Ananta, P. Laoratanakul, Mater. Sci. Eng., B, Solid-State Mater. Adv. Technol. 112 (2004) 79–86.
[12] N. Vittayakorn, G. Rujijanagul, X. Tan, M.A. Marquardt, D.P. Cann, J. Appl. Phys. 96 (2004) 5103–5109.
[13] K. Babooram, H. Tailor, Z.-G. Ye, Ceram. Int. 30 (2004) 1411–1417.
[14] J.J. Lima-Silva, I. Guedes, J.M. Filho, A.P. Ayala, M.H. Lente, J.A. Eiras, D. Garcia, Solid State Commun. 131 (2004) 111–114.
[15] J.P. Guha, J. Eur. Ceram. Soc. 23 (2003) 133–139.
[16] L.E. Cross, Ferroelectrics 151 (1994) 305–320.
[17] F. Xia, X. Yao, J. Mater. Sci. 34 (1999) 3341–3343.
[18] J. Zeng, M. Zhang, Z. Song, L. Wang, J. Li, K. Li, C. Lin, Appl. Surf. Sci. 148 (1999) 137–141.
[19] R.N. Das, R.K. Pati, P. Pramanik, Mater. Lett. 45 (2000) 743–748.
[20] A. Abreu, S.M. Zanetti, M.A.S. Oliveira, G.P. Thim, J. Eur. Ceram. Soc. 25 (2005) 743–748.
[21] R.N. Das, P. Pramanik, Mater. Lett. 40 (1999) 251–254.
[22] D.G. Brandon, W.D. Kaplan, Microstructural Characterization of Materials, John Wiley & Sons, Ltd., 1999, p. 409.
[23] A.K. Arora, R.P. Tandon, A. Mansingh, Ferroelectrics 132 (1992) 9.
[24] B.D. Cullity, Elements of X-ray Diffraction, Addison-Wesley Publishing Company, Inc., 1978, p. 32.
[25] A. Garg, D.C. Agrawal, Mater. Sci. Eng., B, Solid-State Mater. Adv. Technol. 56 (1999) 46–50.
[26] C.H. Wang, S.J. Chang, P.C. Chang, Mater. Sci. Eng., B, Solid-State Mater. Adv. Technol. 111 (2004) 124–130.
[27] Y.-M. Chiang, D.P. Birnie, W.D. Kingery, Physical Ceramics, John Wisley & Sons, Inc., 1997, p. 522.
[28] T.R. Shrout, J. Fielding, Proc. IEEE Ultrasonics Symposium, 1990, pp. 711–720.
[29] L.E. Cross, Mater. Chem. Phys. 43 (1996) 108–115.
[30] R.D. Shannon, C.T. Prewitt, Acta Crystallogr., B Struct. Crystallogr. Cryst. Chem. 25 (1969) 925–945.

INSTITUTE OF PHYSICS PUBLISHING JOURNAL OF PHYSICS D: APPLIED PHYSICS
J. Phys. D: Appl. Phys. **39** (2006) 759–764 doi:10.1088/0022-3727/39/4/025

Effect of uniaxial compressive pre-stress on ferroelectric properties of soft PZT ceramics

Rattikorn Yimnirun, Yongyut Laosiritaworn and Supattra Wongsaenmai

Department of Physics, Faculty of Science, Chiang Mai University, Chiang Mai 50200, Thailand

Received 21 October 2005, in final form 11 January 2006
Published 3 February 2006
Online at stacks.iop.org/JPhysD/39/759

Abstract
The effect of uniaxial compressive pre-stress on the ferroelectric properties of commercial soft PZT ceramics is investigated. The ferroelectric properties under the uniaxial compressive pre-stress of the ceramics are observed at stress up to 24 MPa using a compressometer in conjunction with a modified Sawyer–Tower circuit. The results show that the ferroelectric characteristics, i.e. the area of the ferroelectric hysteresis (P–E) loops, the saturation polarization (P_{sat}), the remanent polarization (P_r), and the loop squareness (R_{sq}) decrease with increasing compressive pre-stress, while the coercive field (E_c) is virtually unaffected by the applied stress. The stress-induced domain wall motion suppression and non-180° ferroelectric domain switching processes are responsible for the changes observed. In addition, a significant decrease in these parameters after a full cycle of stress application has been observed and attributed to the stress-induced decrease in the switchable part of the spontaneous polarization at high stress. Furthermore, the permittivity calculated from the P–E loops is found to decrease with increasing applied pre-stress. This finding differs considerably from the results in the low-field experimental condition. Finally, this study clearly shows that the applied stress has a significant influence on the ferroelectric properties of soft PZT ceramics.

(Some figures in this article are in colour only in the electronic version)

1. Introduction

Lead zirconate titanate ($Pb(Zr_{1-x}Ti_x)O_3$ or PZT) ceramics are among the lead-based complex perovskites that have been investigated extensively, from both the academic and commercial viewpoints. They are employed extensively in sensor and actuators applications, as well as smart systems [1–6]. The most widely studied and used PZT compositions are in the vicinity of the morphotropic phase boundary (MPB) between the tetragonal and rhombohedral ferroelectric phases [1, 4, 6–8]. However, to meet the requirements for specific applications, PZT ceramics are usually modified with dopants [1, 4, 9–12]. Generally, donor (higher-valency) additives induce 'soft' piezoelectric behaviours with higher dielectric and piezoelectric activities suitable for sensor and actuator applications. On the other hand, acceptor (lower-valency) additives result in 'hard' piezoelectric behaviours particularly suitable for ultrasonic motor applications [1, 2, 4–6].

However, in these applications PZT ceramics are often subjected to mechanical loading, either deliberately in the design of the device itself or because the device is used to changing shapes as in many smart structure applications or the device is used under environmental stresses [1–7]. A prior knowledge of how the material properties change under different load conditions is therefore crucial for proper design of a device and for suitable selection of materials for a specific application. Despite that fact, material constants used in many design calculations are often obtained from a stress-free measuring condition, which in turn may lead to incorrect or inappropriate actuator and transducer designs. It is therefore important to determine the properties of these materials as

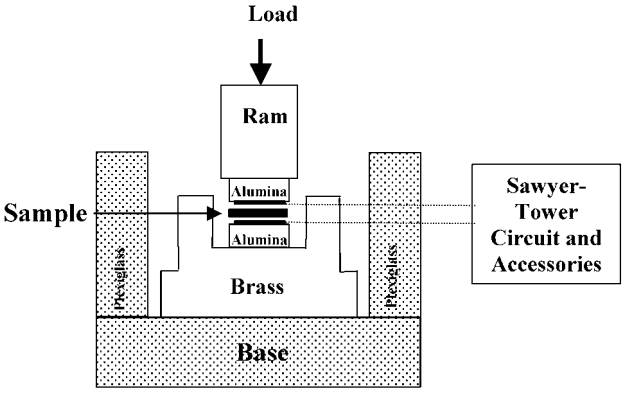

Figure 1. A schematic of the experimental set-up.

a function of applied stress. Previous investigations on the stress-dependence of dielectric and electrical properties of many ceramic systems, such as undoped-PZT, PLZT, BT, PMN-PT, PZT-BT and PMN-PZT, have clearly emphasized the importance of the subject [13–21]. The present study is aimed at studying technically important and commercially available soft PZT ceramics. Many investigations have already revealed interesting results on the dielectric and piezoelectric properties of the soft PZT ceramics under applied stress [15–17, 21]. However, there has been no work on the stress dependence of the ferroelectric properties of the ceramics. Therefore, this study is undertaken to investigate the influences of the uniaxial compressive pre-stress on the ferroelectric properties of the soft PZT ceramics.

2. Experiments and measurements

A commercially available soft PZT ceramic (PKI-552, Piezo Kinetics Inc., USA) was used in this study. Denoted as Navy Type VI, this ceramic is designed for applications that require high electromechanical activity and high dielectric constant. Its properties are (measured by the supplier) longitudinal charge coefficient $d_{33} = 550\,\mathrm{pm\,V^{-1}}$; planer coupling factor $k_p = 0.63$, dielectric constant (1 kHz) $\varepsilon_r = 3400$, Curie temperature $T_C = 200\,^{\circ}\mathrm{C}$ and bulk density $= 7.6\,\mathrm{g\,cm^{-3}}$. The disc-shaped samples with diameter of 10 mm and thickness of 1 mm were pre-poled by the supplier.

The ferroelectric hysteresis (P–E) loops were characterized by using a computer controlled modified Sawyer–Tower circuit. The electric field was applied to a sample by a high voltage ac amplifier (Trek, model 610D) with the input sinusoidal signal with a frequency of 100 Hz from a signal generator (Goodwill, model GAG-809). The detailed descriptions of this system are explained elsewhere [22, 23]. To study the effects of the uniaxial stress on the ferroelectric properties, the uniaxial compressometer was constructed [24]. As shown in figure 1, the compressometer was developed for simultaneous applications of the mechanical stress and the electric field. The compressometer cell consisting of a cylindrical brass cell with a heavy brass base, a brass ram and a precisely guided loading platform provides true uniaxial stress during mechanical loading. The prepared specimen was carefully placed between the two alumina blocks and the electric field was applied to the specimen via the copper shims attached to the alumina blocks. With this setting, the uniaxial compressive stress was applied parallel to the electric field direction. During the measurements, the specimen was immersed in silicone oil to prevent high-voltage arcing during electric loading. The uniaxial compressive stress was supplied by the servohydraulic load frame and the applied stress was monitored with the pressure gauge of the load frame. Measurements were performed as a function of mechanical pre-stress applied discretely between 0 and 24 MPa. During the measurements, a desired pre-stress was first applied to the sample and then the electric field was applied. The ferroelectric hysteresis (P–E) loop was recorded at room temperature (25 °C) for both loading and unloading conditions. The parameters obtained from the loops were the saturation polarization (P_{sat}), the remanent polarization (P_r) and the coercive field (E_c), which are defined as the points where the loops reach the maximum polarization, cross the zero field and cross the zero polarization, respectively. The measurements reported were for the samples during their first mechanical stress cycle. It should also be noted that the reported ferroelectric parameters were obtained after a total of 10 cycles of the electric field were applied to the sample at each constant pre-stress.

3. Results and discussion

The polarization versus electric field (P–E) hysteresis loops of the soft PZT ceramics under different compressive pre-stress during loading and unloading are shown in figures 2 and 3, respectively. It should first be noticed that the area of the P–E loops decreases steadily with increasing the pre-stress (figure 2) and then increases when the stress is gradually removed (figure 3). The P–E loop area indicates the polarization dissipation energy of a ferroelectric material subjected to one full cycle of electric field application [25]. This amount of energy loss is directly related to volume involved in the switching process during the application of electric field [21]. Therefore, the decrease in the loop area with increasing pre-stress is a result of the stress-induced domain wall motion suppression [21]. The polarization dissipation energy is consequently found to decrease non-linearly with increasing applied pre-stress, as plotted in figure 4, indicating that the sample volume contributing to polarization reversal decreases with the increasing pre-stress. In the stress-free state, the dissipation energy is $\sim 8.1 \times 10^5\,\mathrm{J\,m^{-3}}$; while at 24 MPa, the dissipation energy decreases to $3.8 \times 10^5\,\mathrm{J\,m^{-3}}$ ($< 50\%$ of the stress-free state). A similar observation has also been found in previous investigations [13, 14, 21, 26–28]. In addition, even though the P–E loop expands when the stress is being removed, the loop does not return to its original form after the stress cycle, as shown in figure 3. Correspondingly, the dissipation energy increases at a slower rate during the unloading, and eventually the stress-free value of the dissipation energy after a full stress cycle drops to $\sim 5.6 \times 10^5\,\mathrm{J\,m^{-3}}$, as displayed in figure 4. The difference in the dissipation energy during stress loading and unloading is believed to be caused by the decrease in the switchable part of spontaneous polarization of the ceramic after being subjected to the high pre-stress, as will be supported by the following discussions [17, 29].

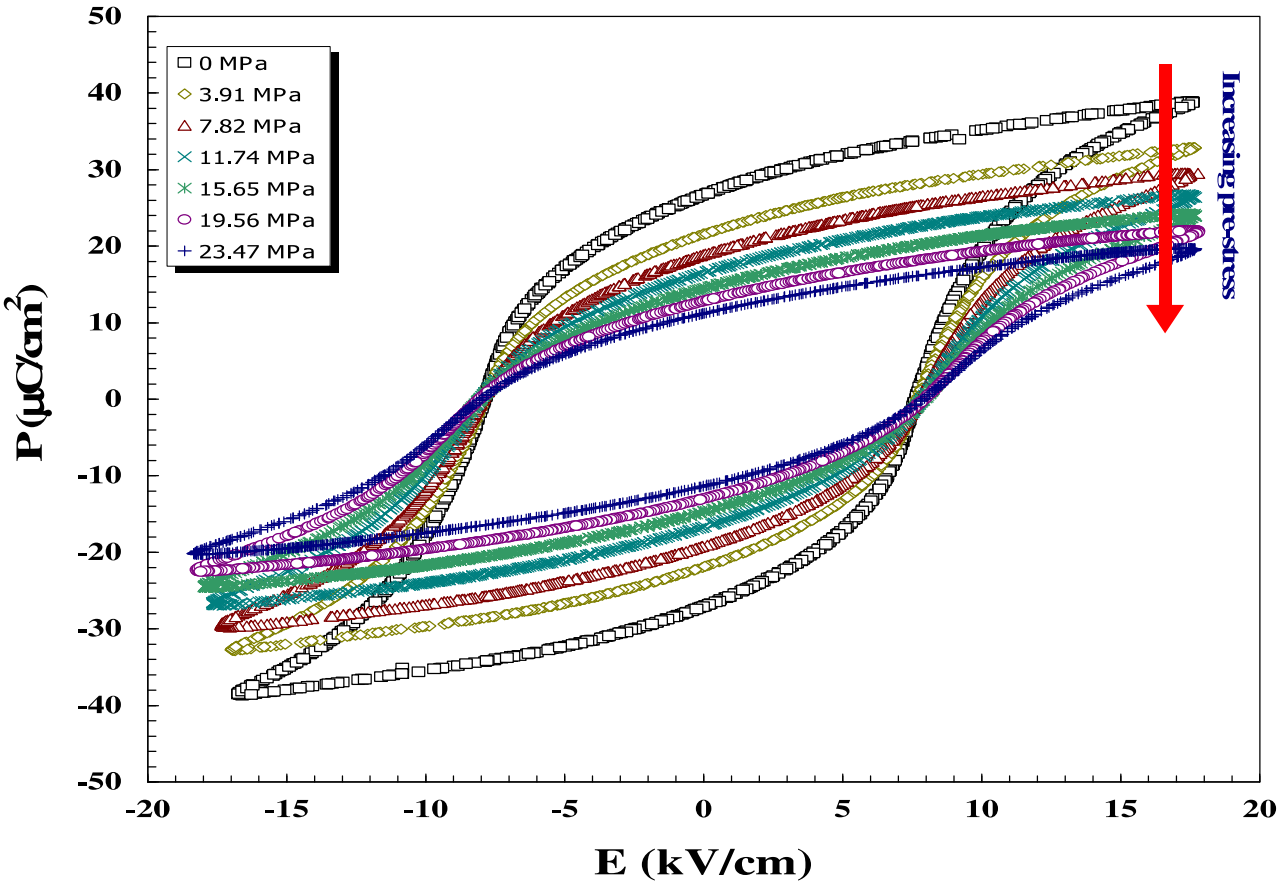

Figure 2. Polarization versus electric field (P–E) hysteresis loops as a function of compressive pre-stress for soft PZT ceramic during loading.

The changes in the saturation polarization (P_{sat}), the remanent polarization (P_r), and the coercive field (E_c) with the uniaxial compressive pre-stress are plotted in figures 5–7, respectively. Similarly to the trend observed in the dissipation energy, figures 5 and 6 clearly show that both the saturation and remanent polarizations decrease as the compressive pre-stress increases. The decrease is very pronounced with the polarization values at 24 MPa being approximately 50% of the stress-free values. In addition, a significant decrease in the polarization values of the ceramic is also observed after a mechanical stress cycle. The P_{sat} value before the stress cycle is recorded as 39 μC cm^{-2}, while the value is reduced to 23 μC cm^{-2} after the sample is exposed to a complete cycle of the mechanical stress. A similar drop is also observed for the P_r values, with the values before and after the stress cycle being 26.5 and 17, in the units of μC cm^{-2}, respectively. This suggests a significant stress-induced decrease in the switchable part of the spontaneous polarization of the soft PZT ceramic resulting in the observed decrease in the polarization values, as well as the dissipation energy, under high stress [17, 29]. In contrast, the applied pre-stress shows little or no influence on the coercive field (E_c), as demonstrated in figure 7. These results clearly indicate that soft PZT ceramics are not suitable for high stress applications. It should also be noted that previous investigations on other ceramic systems, such as BT, PLZT, PMN-PT and PMN-PZT, showed a similar tendency [13, 14, 21, 26–28, 30].

The ferroelectric characteristics of the soft PZT ceramic can also be assessed with the hysteresis loop squareness (R_{sq}), which can be calculated from the empirical expression

$$R_{sq} = (P_r/P_s) + (P_{1.1E_c}/P_r), \quad (1)$$

where P_r is the remanent polarization, P_s is the saturated polarization obtained at some finite field strength below the dielectric breakdown and $P_{1.1E_c}$ is the absolute value of the polarization at the field equal to 1.1 E_c [31]. For the ideal square loop, R_{sq} is equal to 2.00. As depicted in figure 8, the R_{sq} values generally decrease with increasing pre-stress and the values during the loading are slightly larger than those during the unloading. This observation is clearly a result of the decrease in the polarizations under the pre-stress. The observations in figures 2–8 clearly indicate that the ferroelectric characteristics of the soft PZT ceramic decrease considerably under the application of the compressive pre-stress.

To understand, at least qualitatively, these experimental results on the soft PZT ceramic, one can interpret the changes in terms of domain-reorientation processes [15–21]. When the uniaxial compressive stress is applied in the direction parallel to the poling direction, the applied stress tends to keep the ferroelectric domains aligned with their polar axes away from the stress direction through the non-180° ferroelectric domain switching processes. Therefore, it takes a larger than usual applied electric field to reorient the domains along the stress direction, resulting in a lower value of the saturated

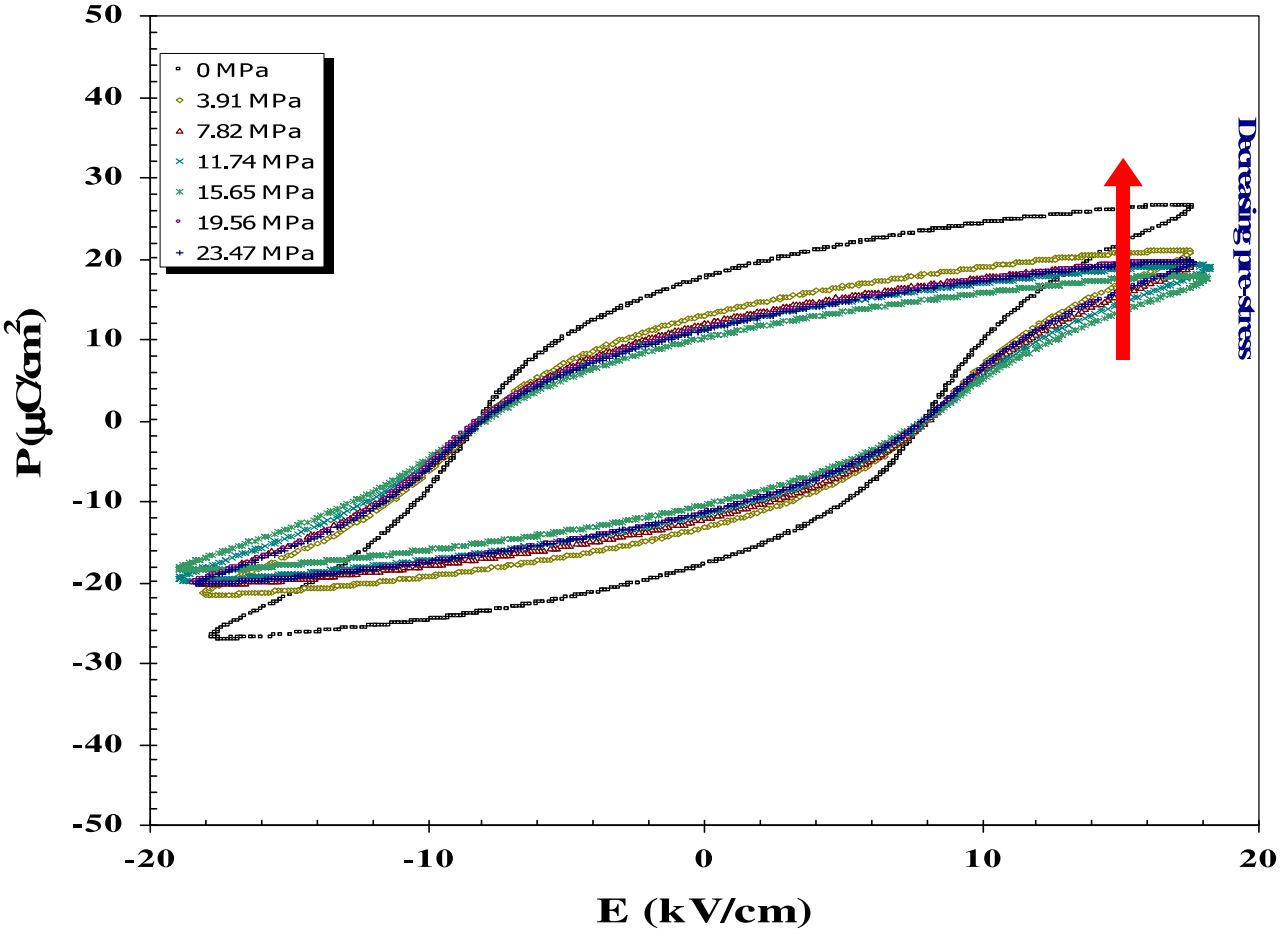

Figure 3. Polarization versus electric field (P–E) hysteresis loops as a function of compressive pre-stress for soft PZT ceramic during unloading.

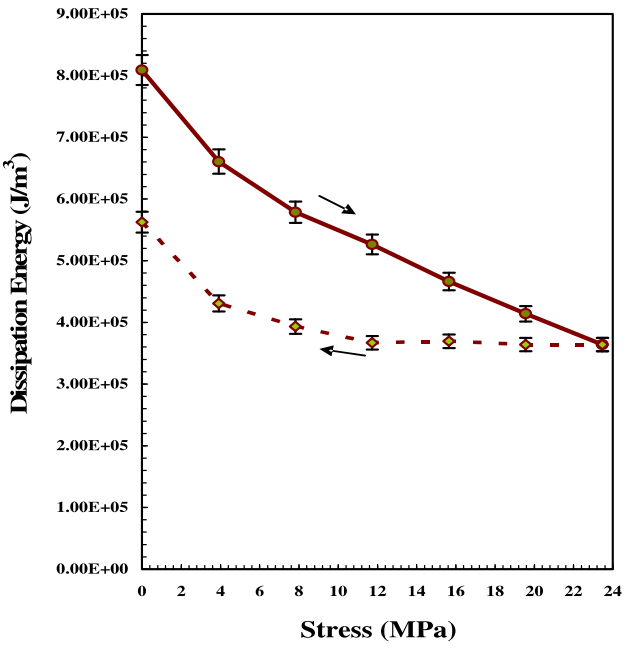

Figure 4. Changes in dissipation energy (hysteresis loop area) with compressive pre-stress for soft PZT ceramic.

polarization (P_{sat}), as shown in figure 5. When the electric field is reduced to zero the domains tend to rotate back away from the pre-stress direction, resulting in a lower than usual remanent polarization (P_r), as depicted in figure 6 [13, 21]. Furthermore, the decrease in the dissipation energy with increasing compressive pre-stress indicates that more and more ferroelectric domains are constrained by the pre-stress and cannot be re-oriented by the electric field so as to participate in the polarization reversal. Consequently, both the saturation and remanent polarizations become lower with increasing compressive pre-stress [21]. In addition, the decrease in the switchable part of spontaneous polarization at the high pre-stress causes the difference in the above-mentioned parameters during stress loading and unloading. The results of the changes in the ferroelectric characteristics of the soft PZT ceramic with increasing compressive pre-stress are in agreement with the previous investigations of many ferroelectric ceramics [13, 14, 20, 21, 26–28].

Furthermore, from the P–E loops the dielectric permittivity can be evaluated from the relation

$$\varepsilon = \frac{\Delta P}{\Delta E}, \tag{2}$$

where ΔP is the polarization difference between +1 and $-1\,\mathrm{kV\,cm^{-1}}$. The calculated dielectric permittivity can be called differential permittivity, which includes the reversible

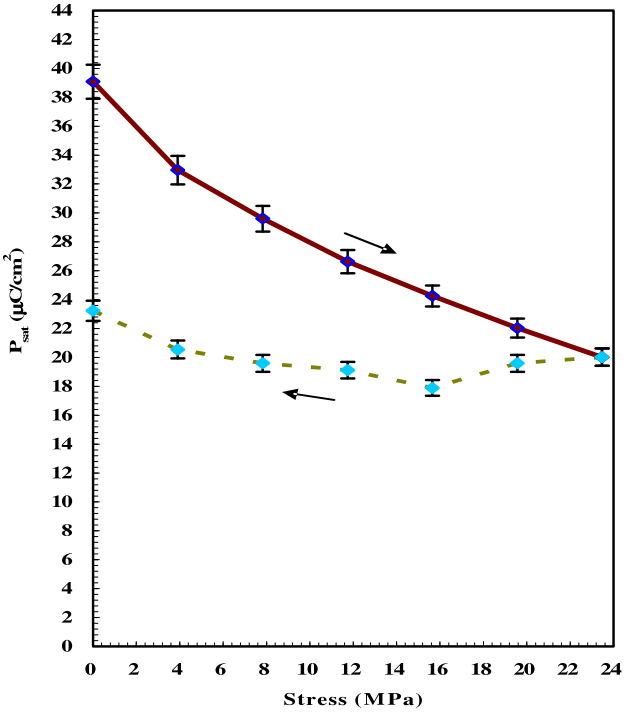

Figure 5. Changes in saturated polarization (P_{sat}) with compressive pre-stress for soft PZT ceramic.

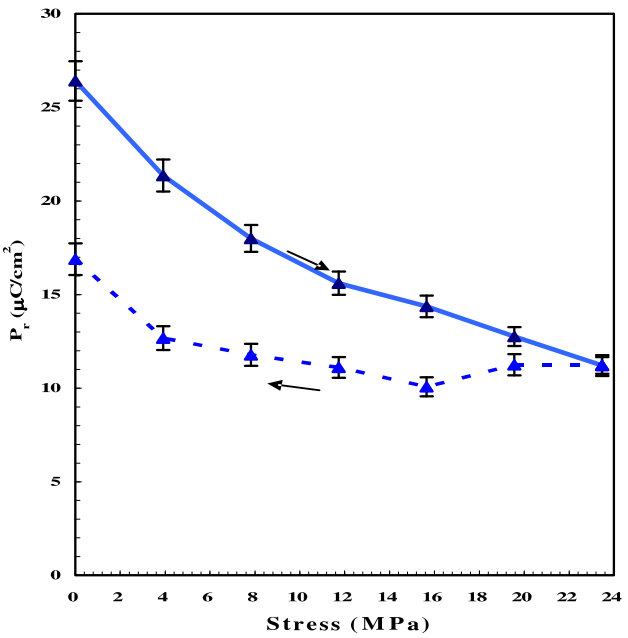

Figure 6. Changes in remanent polarization (P_r) with compressive pre-stress for soft PZT ceramic.

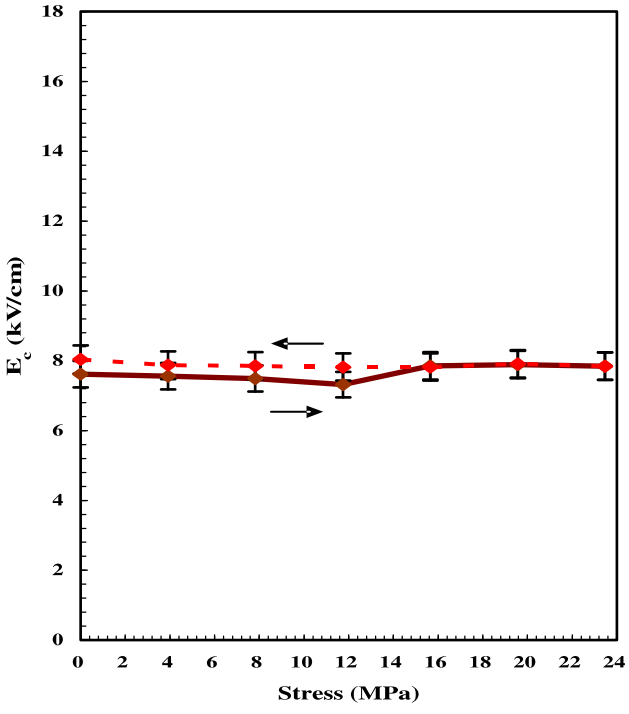

Figure 7. Changes in coercive field (E_c) with compressive pre-stress for soft PZT ceramic.

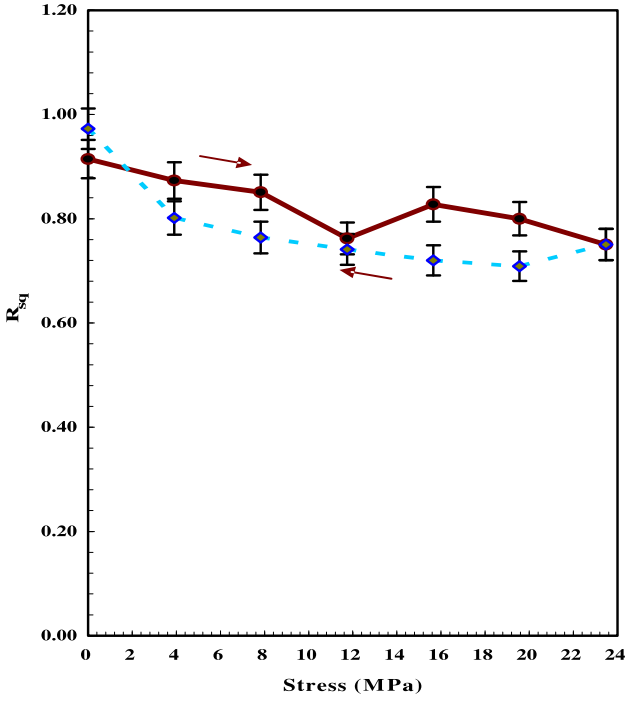

Figure 8. Changes in loop squareness (R_{sq}) with compressive pre-stress for soft PZT ceramic.

(intrinsic dielectric property) and irreversible (extrinsic domain switching related property) contributions of the materials [21]. Therefore, the stress-free value of the differential permittivity of ∼16 000 is significantly larger than that of the reported low-field permittivity of 3 400, which is largely governed by the reversible contributions [17, 21]. The study on another type of soft PZT reported the same order of dielectric permittivity enhancement under high-field measurement [26]. The change in the differential permittivity is illustrated in figure 9 as a function of the pre-stress. The differential permittivity of the soft PZT ceramic decreases with increasing applied pre-stress. This differs considerably from the results described in previous investigations [19, 29], in which the stress dependence of the dielectric properties was measured at a much lower field strength (1 V mm^{-1}). In those studies, the dielectric permittivity of the soft PZT was found

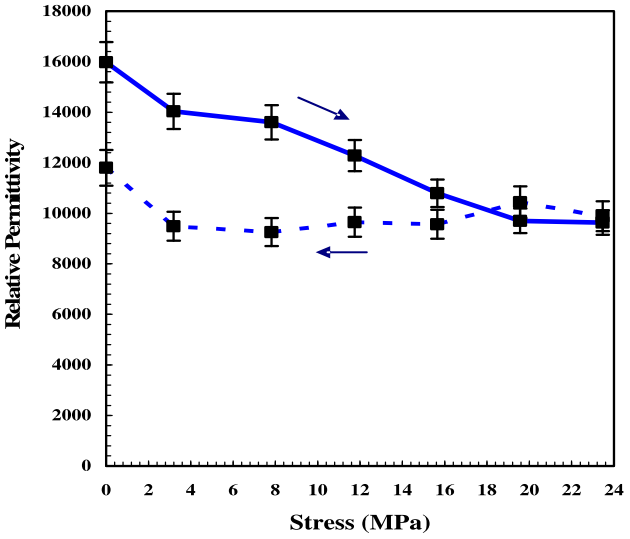

Figure 9. Changes in the differential permittivity (measured from the slope of P–E curves as the field passes through 0 kV cm^{-1}) with compressive pre-stress for soft PZT ceramic.

to increase slightly with the applied compressive stress up to 30 MPa.

4. Conclusions

In this study, the effects of uniaxial compressive pre-stress on the ferroelectric properties of soft PZT ceramics are investigated. The ferroelectric properties under the uniaxial compressive pre-stress of the ceramics are observed up to 24 MPa using a compressometer in conjunction with a modified Sawyer–Tower circuit. The results show that the ferroelectric characteristics, i.e. the area of the ferroelectric hysteresis (P–E) loops, which corresponds to the energy dissipation, the saturation polarization (P_{sat}), the remanent polarization (P_r) and the loop squareness (R_{sq}), decrease with increasing compressive pre-stress, while the coercive field (E_c) is virtually unaffected by the applied stress. The non-180° ferroelectric domain switching and stress-induced domain wall suppression processes are responsible for the changes observed. In addition, a significant decrease in these parameters after a full cycle of stress application has been observed and attributed to the stress induced decrease in the switchable part of spontaneous polarization. Furthermore, the permittivity calculated from the hysteresis loops is found to decrease with increasing applied pre-stress. This finding differs considerably from the results in the low-field experimental condition, which clearly signifies the importance of the experimental conditions used to determine the dielectric properties under the applied stress. Finally, this study undoubtedly shows that the applied stress has significant influences on the ferroelectric properties of the soft PZT ceramics.

Acknowledgment

Financial supports from the Thailand Research Fund (TRF) and Faculty of Science and Graduate School of Chiang Mai University are gratefully acknowledged.

References

[1] Jaffe B, Cook W R and Jaffe H 1971 *Piezoelectric Ceramics* (New York: Academic)
[2] Haertling G H 1999 *J. Am. Ceram. Soc.* **82** 797
[3] Cross L E 1996 *Mater. Chem. Phys.* **43** 108
[4] Moulson A J and Herbert J M 2003 *Electroceramics* 2nd edn (New York: Wiley-Interscience)
[5] Uchino K 2000 *Ferroelectric Devices* (New York: Dekker)
[6] Xu Y H 1991 *Ferroelectric Materials and Their Applications* (Amsterdam: North Holland)
[7] Cross L E 1987 *Ferroelectrics* **76** 241
[8] Cao W and Cross L E 1993 *Phys. Rev.* B **47** 4825
[9] Takahashi S 1982 *Ferroelectrics* **41** 143
[10] Chu S Y, Chen T Y and Tsai I T 2003 *Integr. Ferroelectr.* **58** 1293
[11] Chen X M and Yang J S 1998 *J. Eur. Ceram. Soc.* **18** 1059
[12] Kulcsar F 1959 *J. Am. Ceram. Soc.* **42** 49
[13] Fritz I J 1978 *J. Appl. Phys.* **49** 4922
[14] Lynch C S 1996 *Acta Mater.* **44** 4137
[15] Zhang Q M, Zhao J, Uchino K and Zheng J 1997 *J. Mater. Res.* **12** 226
[16] Zhao J, Glazounov A E and Zhang Q M 1999 *Appl. Phys. Lett.* **74** 436
[17] Yang G, Liu S F, Ren W and Mukherjee B K 2000 *Symp. on Smart Structures and Materials, Proc. SPIE* **3992** 103
[18] Viehland D and Powers J 2001 *J. Appl. Phys.* **89** 1820
[19] Yimnirun R, Ananta S, Meechoowas E and Wongsaenmai S 2003 *J. Phys. D: Appl. Phys.* **36** 1615
[20] Viehland D, Li J F, McLaughlin E, Powers J, Janus R and Robinson H 2004 *J. Appl. Phys.* **95** 1969
[21] Zhou D, Kamlah M and Munz D 2005 *J. Eur. Ceram. Soc.* **25** 425
[22] Jiang Q 1992 *PhD Thesis* Pennsylvania State University
[23] Park S E and Shrout T R 1997 *J. Appl. Phys.* **82** 1804
[24] Yimnirun R, Moses P J, Meyer R J and Newnham R E 2003 *Rev. Sci. Instrum.* **74** 3429
[25] Lines M E and Glass A M 1977 *Principles and Applications of Ferroelectrics and Related Materials* (Oxford: Clarendon Press)
[26] Fang D and Li C 1999 *J. Mater. Sci.* **34** 4001
[27] Guillon O, Delobelle P, Thiebaud F, Walter V and Perreux D 2004 *Ferroelectrics.* **308** 95
[28] Zhao J and Zhang Q M 1996 *Proc. IEEE Int. Symp. on Applications of Ferroelectrics (ISAF)* **2** 971
[29] Yang G, Ren W, Liu S F, Masys A J and Mukherjee B K 2000 *Proc. IEEE Ultrasonic Symp.* **2** 1005
[30] Yimnirun R, Ananta S, Ngamjarurojana A and Wongsaenmai S 2005 *Appl. Phys.* A—*Mater.* **81** 1227
[31] Jin B M, Kim J and Kim S C 1997 *Appl. Phys.* A—*Mater.* **65** 53

Available online at www.sciencedirect.com
SCIENCE DIRECT
Materials Letters 60 (2006) 1447–1452
materials letters
www.elsevier.com/locate/matlet

Effect of vibro-milling time on phase formation and particle size of lead titanate nanopowders

R. Wongmaneerung, R. Yimnirun, S. Ananta *

Department of Physics, Faculty of Science, Chiang Mai University, Chiang Mai 50200, Thailand

Received 5 August 2005; accepted 14 November 2005
Available online 1 December 2005

Abstract

A perovskite-like phase of lead titanate, $PbTiO_3$, nanopowder was synthesized by a solid-state reaction via a rapid vibro-milling technique. The effect of milling time on the phase formation and particle size of $PbTiO_3$ powder was investigated. Powder samples were characterized using TG-DTA, XRD, SEM and laser diffraction techniques. It was found that an average particle size of 17 nm was achieved at 25 h of vibro-milling after which a higher degree of particle agglomeration was observed on continuation of milling to 35 h. In addition, by employing an appropriate choice of the milling time, a narrow particle size distribution curve was also observed.

Keywords: Lead titanate; Milling; Nanopowders; Phase formation; Particle size

1. Introduction

Lead titanate, $PbTiO_3$ (PT), is one of the ferroelectric materials which exhibits a perovskite structure. It has a Curie temperature ~490 °C. The unique properties of the PT, i.e. the high transition temperature, pyroelectric coefficient and spontaneous polarization, make it useful for high frequency and high temperature applications in electronic devices [1,2]. When combined with other oxides, lead titanate can form a series of solid solutions such as $Pb(Zr_{1-x},Ti_x)O_3$ (PZT), $Pb(Mg_{1/3}Nb_{2/3})O_3$–$PbTiO_3$ (PMNT) and $Pb(Zn_{1/3}Nb_{2/3})O_3$–$PbTiO_3$ (PZN-PT) [2–4]. These ferroelectric alloys are widely used in ultrasonic transducers, nonvolatile memories, microactuators, multilayer capacitors and electro-optic devices [1,2]. To fabricate them, a fine powder of perovskite phase with a minimal degree of particle agglomeration is needed as the starting material in order to achieve a dense and uniform microstructure at a given sintering temperature. In order to improve the sintering behaviour of PT ceramics, a crucial focus of powder synthesis in recent years has been the formation of uniform-sized, single morphology particulates ranging in size from nanometer to micrometers [5–7].

The development of a method to produce nanopowders of precise stoichiometry and desired properties is complex, depending on a number of variables such as nature and purity of starting materials, processing history, temperature, etc. To obtain nanosized PT powders, many investigations have focused on several chemistry-based preparation routes, such as sol–gel [5], co-precipitation [6], hydrothermal reaction [7], besides the more conventional solid-state reaction of mixed oxides [8,9]. All these techniques are aimed at reducing the particle size and temperature of preparation of the compound even though they are more involved and complicated in approach than the solid-state reaction. Moreover, high-purity PT nanopowders are still not available in bulk quantity and also very expensive. The advantage of using mechanical milling for preparation of nanosized powders lies in its ability to produce mass quantities of powders in the solid state using simple equipment and low cost starting precursors [8,9]. Although some research has been done in the preparation of PT powders via a vibro-milling technique [10,11], to our knowledge a systematic study regarding the influence of milling time on the preparation of PT powders has not yet been reported.

* Corresponding author. Tel.: +66 53 943367; fax: +66 53 357512.
E-mail address: supon@chiangmai.ac.th (S. Ananta).

0167-577X/$ - see front matter © 2005 Elsevier B.V. All rights reserved.
doi:10.1016/j.matlet.2005.11.043

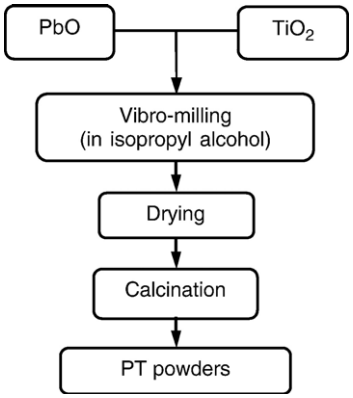

Fig. 1. Preparation route for PT powders.

Therefore, in this work, the effect of milling time on phase formation, and particle size of lead titanate powders was investigated in this connection. The potential of the vibro-milling technique as a simple and low-cost method to obtain usable quantities of single-phase lead titanate powders at low temperature and with nanosized particles was also examined.

2. Experimental procedure

Commercially available lead oxide, PbO (JCPDS file number 77-1971) and titanium oxide, TiO_2 (JCPDS file number 21-1272) (Fluka, >99% purity) were used in this study. The two oxide powders exhibited an average particle size in the range of 3 to 5 μm. $PbTiO_3$ powder was synthesized by the solid-state reaction of these raw materials. Powder-processing (Fig. 1) was carried out in a manner similar to that employed in the preparation of other materials, as described previously [12,13]. A vibratory laboratory mill (McCrone Micronizing Mill) powered by a 1/30 HP motor was employed for preparing the stoichiometric $PbTiO_3$ powders. The grinding vessel consists of a 125 ml capacity polypropylene jar fitted with a screw-capped, gasketless, polythene closure. The jar is packed with an ordered array of identical, cylindrical, grinding media of polycrystalline corundum. A total of 48 milling media cylinder with a powder weight of 20 g was kept constant in each batch. The milling operation was carried out in isopropanal inert to the polypropylene jar. Various milling times ranging from 0.5 to 35 h were selected in order to investigate the phase formation characteristic of lead titanate and the smallest particle size. After drying at 120 °C, the milled powders were calcined at 600 °C (inside a closed alumina crucible) for 1 h with heating/cooling rates of 20 °C min^{-1} [11].

Table 1
Effect of milling time on the variation of particle size of PT powders measured by different techniques

Milling time (h)	Per. phase (%)	XRD		SEM		Laser scattering	
		A (nm)	*c*/*a*	*D* (nm)	*P* (nm)	*D* (nm)	*P* (nm)
0.5	89.20	40	1.056	145	40–250	1090	140–2560
1	100	20.8	1.062	107	71–143	660	270–1090
5	100	22.5	1.059	101	67–135	690	290–1140
10	100	21.9	1.059	95	63–128	690	290–1140
15	100	22.0	1.061	78	43–114	4640	1640–7790
20	100	21.3	1.056	68	28–109	4800	1710–8060
25	100	21.5	1.057	63	17–109	180	70–310
30	100	21.5	1.052	93	43–143	170	70–290
35	100	21.4	1.053	92	56–128	3030	560–6180

Per. phase = Perovskite phase.
A = Crystallite size.
c/*a* = Tetragonality factor.
D = Average particle size.
P = Particle size distribution or range.

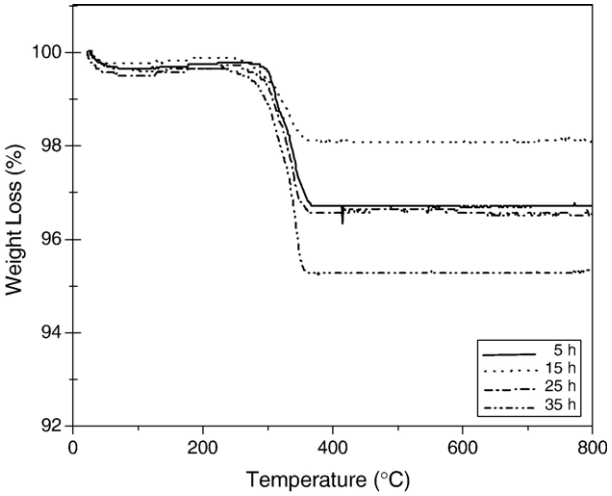

Fig. 2. TGA analysis of powder mixtures milled at different times.

The reactions of the uncalcined PT powders taking place during heat treatment were investigated by a combination of thermogravimetric and differential thermal analysis techniques (TG-DTA, Shimadzu) at a heating rate of 10 °C min^{-1} in air from room temperature up to 1000 °C. All powders were subsequently examined at room temperature by X-ray diffraction (XRD; Siemens-D500 diffractometer) using Ni-filtered CuK_α radiation to identify the phases formed and optimum milling time for the production of $PbTiO_3$ powders having the smallest particle size. The relative amount of perovskite and secondary phases was determined from XRD patterns of the samples by measuring the major characteristic peak intensities

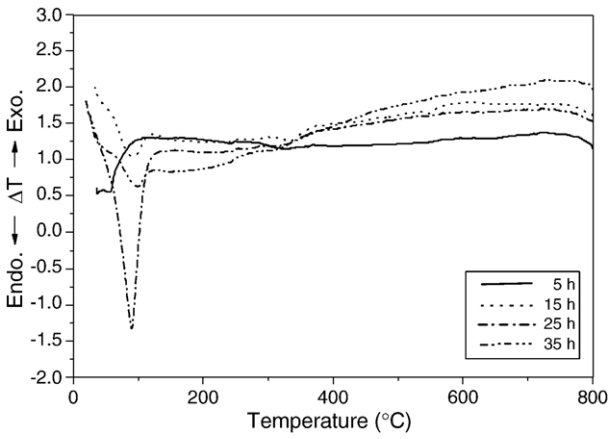

Fig. 3. DTA analysis of powder mixtures milled at different times.

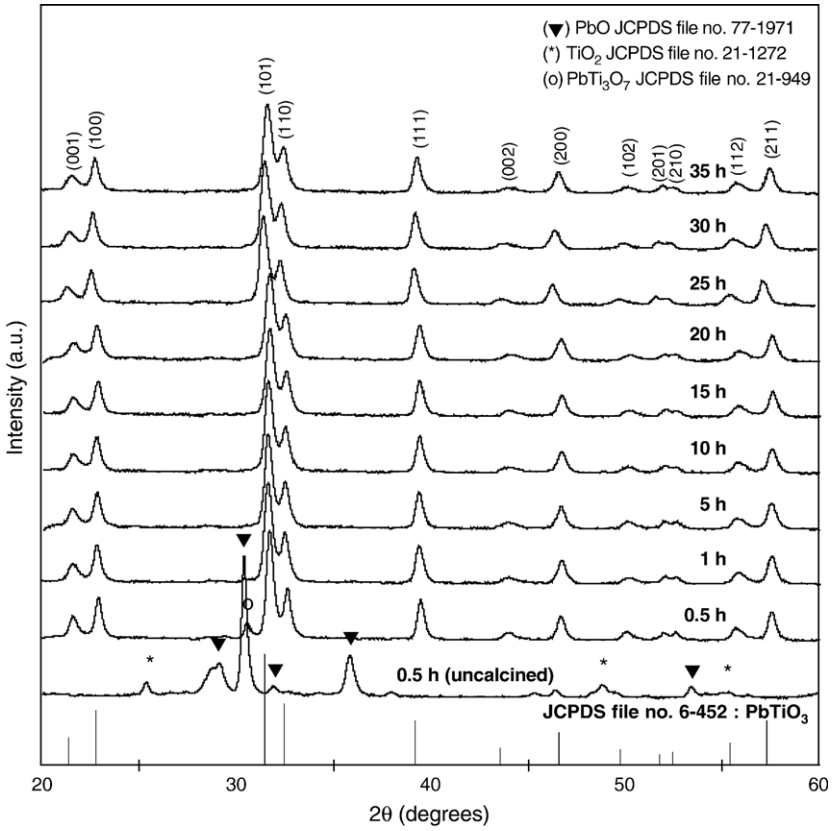

Fig. 4. XRD patterns of PT powders milled at different times (calcined at 600 °C for 1 h with heating/cooling rates of 20 °C min^{-1}).

for the perovskite (101) or I_P and secondary (o) phases or I_S. The following qualitative equation was used [14].

$$\text{perovskite phase(wt\%)} = \frac{I_P}{I_P + I_S} \times 100 \quad (1)$$

The crystalline lattice constants, lattice strain and average particle size were also estimated from XRD patterns [15]. The particle size distributions of the powders were determined by laser diffraction technique (DIAS 1640 laser diffraction spectrometer) with the particle sizes and morphologies of the powders observed by scanning electron microscopy (JEOL JSM-840 A SEM). The particle sizes of PT powders milled at different times obtained from different measuring techniques are provided in Table 1.

3. Results and discussion

TGA and DTA results for the powders milled at different times are compared and shown in Figs. 2 and 3, respectively. In general, similar thermal characteristics are observed in all cases. As shown in Fig. 2, all

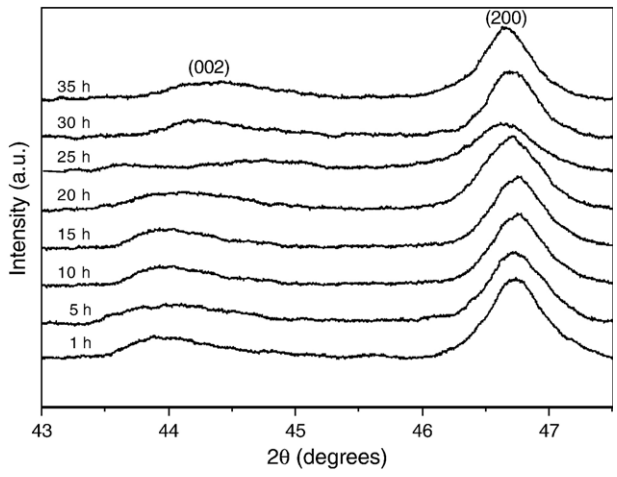

Fig. 5. Enlarged zone of XRD patterns showing (002) and (200) peaks broadening as a function of milling times.

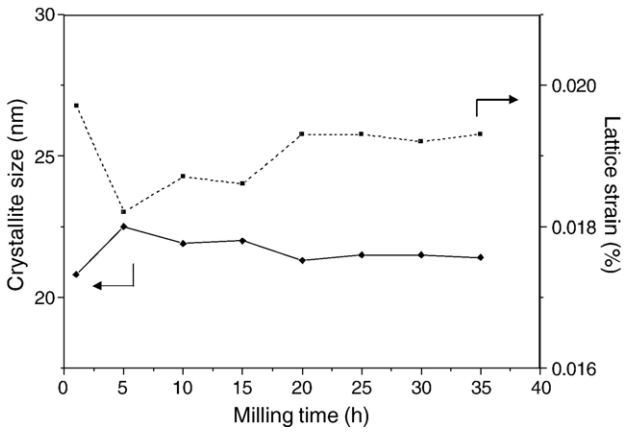

Fig. 6. Variation of crystalline size and lattice strain of PT powders as a function of milling times.

powders demonstrate two distinct weight losses below 400 °C. The first weight loss occurs below 100 °C and the second one above 200 °C. In the temperature range from room temperature to ~150 °C, all samples show exothermic peaks in the DTA curves at 120 °C (Fig. 3), which are related to the first weight loss. These DTA peaks can be attributed to the decomposition of the organic species originating from the milling process [11,16]. Corresponding to the second fall in specimen weight, by increasing the temperature up to ~800 °C, the solid-state reaction between lead oxide and titanium oxide occurs. The broad exothermic characteristic present in all the DTA curves represents that reaction, which has a maximum at ~600–750 °C. The slightly different temperature, intensities and shapes of the thermal peaks for the powders are probably related to the different sizes of the powders subjected to different milling times and, consequently, caused by the removal of organic species and rearrangement of differently bonded species in the network [16]. No further significant weight loss was observed for temperatures above 500 °C in the TGA curves, indicating that the minimum firing temperature to form PbO–TiO_2 compounds is in good agreement with XRD results (Fig. 4) and those of previous authors [17,18].

To further study the effect of milling time on phase formation, each of the powders milled for different times were calcined at 600 °C for 2 h in air, followed by phase analysis using XRD. For the purpose of estimating the concentrations of the phase present, Eq. (1) has been applied to the powder XRD patterns obtained, as given in Table 1. As shown in Fig. 4, for the uncalcined powder subjected to 0.5 h of vibro-

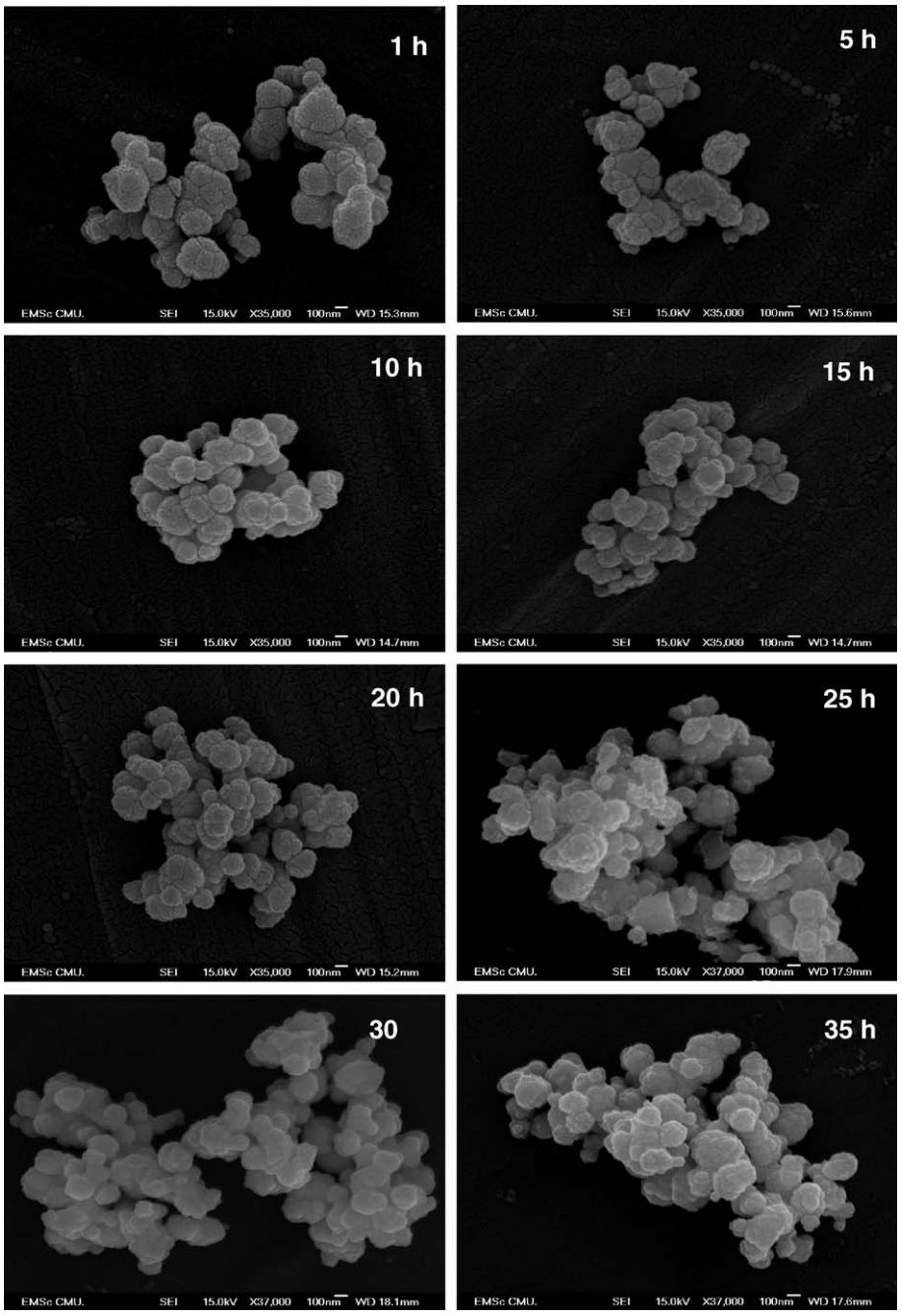

Fig. 7. SEM micrographs of PT powders milled at different times.

milling, only X-ray peaks of precursors PbO (▼) and TiO_2 (*) are present, indicating that no reaction had been initiated during the milling process. However, after calcinations at 600 °C, it is seen that the perovskite-type $PbTiO_3$ becomes the predominant phase in the powder milled for 0.5 h indicating that the reaction has occurred to a considerable extent. It is seen that ~11 wt.% of lead deficient phase, $PbTi_3O_7$ (o), reported by a number of workers [18,19] has been found only at a milling time of 0.5 h. This pyrochlore phase has a monoclinic structure with cell parameters a=107.32 pm, b=381.2 pm, c=657.8 pm and β=98.08° (JCPDS file number 21-949) [20]. This observation could be attributed mainly to the poor mixing capability under short milling time. With milling time of 1 h or more, it is apparent that a single phase perovskite PT (yield of 100% within the limitations of the XRD technique) was found to be possible after the same calcination process was applied.

In general, the strongest reflections found in the majority of these XRD patterns indicate the formation of the lead titanate, $PbTiO_3$. These can be matched with JCPDS file number 6-452 for the tetragonal phase, in space group $P4/mmm$ with cell parameters a=389.93 pm and c=415.32 pm [21], in consistent with other works [10,11]. It should be noted that no evidence for the introduction of impurity due to wear debris from the milling process was observed in any of the calcined powders (within the milling periods of 0.5–35 h), demonstrating the effectiveness of the vibro-milling technique for the production of high purity PT nanopowders.

Moreover, it has been observed that with increasing milling time, all diffraction lines broaden, e.g. (002) and (200) peaks, an indication of a continuous decrease in particle size and of the introduction of lattice strain, as shown in Fig. 5. These values indicate that the particle size affects the evolution of crystallinity of the phase formed by prolonged milling treatment (Fig. 6). For PT powders, the longer the milling time, the finer is the particle size, up to a certain level (Table 1). The results suggest that the steady state of the vibro-milling is attained at ~20 h of milling. Moreover, it is worthy to note that, in this condition, the mean crystalline size is close to ~21 nm. Also, the relative intensities of the Bragg peaks and the calculated tetragonality factor (c/a) for the powders tend to decrease with the increase of milling time. However, it is well documented that, as Scherer's analysis provides only a measurement of the extension of the coherently diffracting domains, the particle sizes estimated by this method can be significantly under

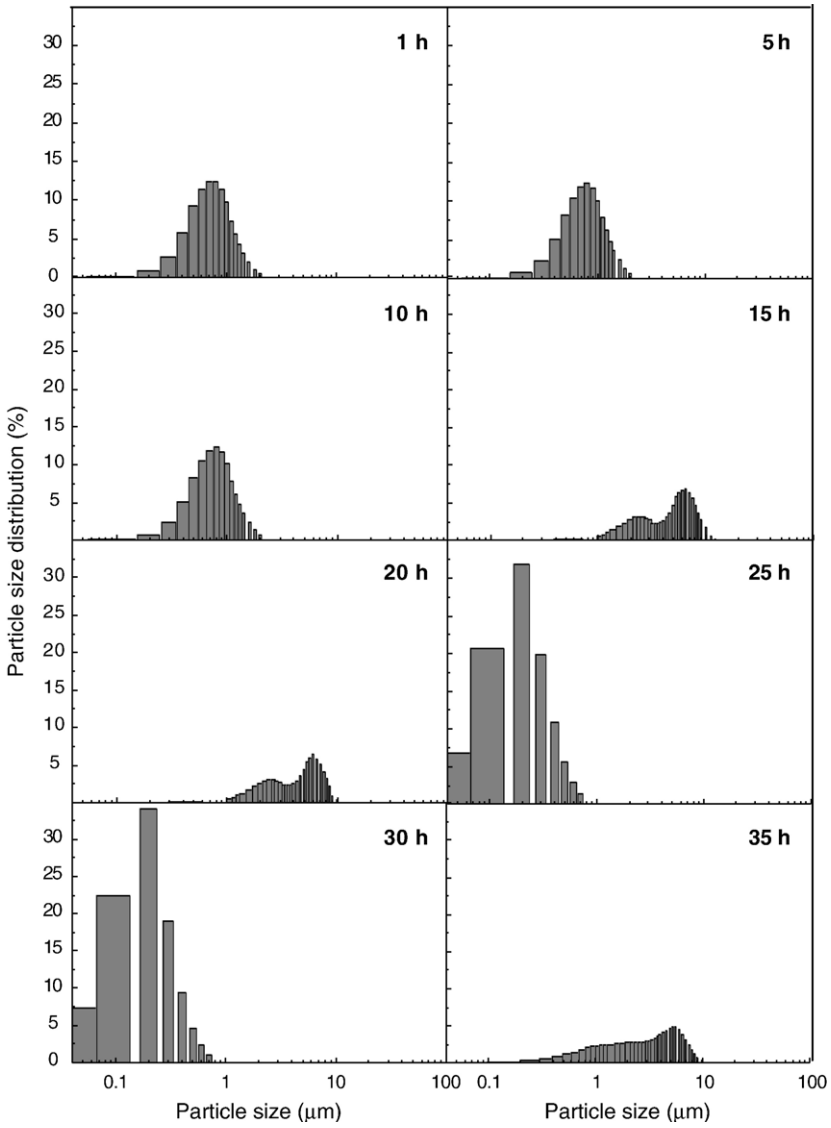

Fig. 8. Particle size distributions of PT powders milled at different times.

estimated [22]. In addition to strain, factors such as dislocations, stacking faults, heterogeneities in composition and instrumental broadening can contribute to peak broadening, making it almost impossible to extract a reliable particle size solely from XRD [15,23].

In this connection, scanning electron microcopy was also employed for particle size measurement (Table 1). The morphological evolution of the powders as a function of milling time was also revealed, as illustrated in the SEM micrographs (Fig. 7). At first sight, the morphological characteristic of PT powders with various milling times is similar for all cases. In general, the particles are agglomerated and basically irregular in shape, with a substantial variation in particle sizes. The powders consist of primary particles nanometers in size. Increasing the milling time over the range 0.5 to 35 h, the average size of the PT particle decreases significantly, until at 25 h, the smallest particle size (estimated from SEM micrographs to be ~17 nm) is obtained. However, it is also of interest to point out that a larger particle size was obtained for a milling time longer than 25 h. This may be attributed to the occurrence of hard agglomeration with strong inter-particle bonds within each aggregate resulting from dissipated heat energy of prolonged milling [24]. Fig. 7 also illustrates that vibro-milling has slightly changed the shape of the particles which become more equiaxed at long milling times. At the same time, the particle size is reduced. Fracture is considered to be the major mechanism at long milling times.

The effect of milling time on particle size distribution was found to be significant, as shown in Fig. 8. After milling times of 1, 5 and 10 h, the powders have a similar particle size distribution. They exhibit a single peak covering the size ranging from 0.2 to 1.1 μm. With increasing milling times to 15 and 20 h, the distribution curve of particle size separates into two groups. First is a monomodal distribution corresponding to the primary size of the $PbTiO_3$ particles. The second group (peak) is believed to arise mainly from particle agglomeration. By increasing the milling time to 25 and 30 h, a uniform particle size distribution with a much lower degree of particle agglomeration (<1 μm) is found. However, upon further increase of milling time up to 35 h, a bimodal distribution curve with peak broadening between 0.5 and 6.2 μm is observed again. Table 1 compares the results obtained for PT powders milled for different times via different techniques. Variations in these data may be attributed mainly to the formation of hard and large agglomerations found in the SEM results.

In this work, it is seen that the optimum milling time for the production of the smallest nanosized high purity PT powder was found to be at 25 h. The finding of this investigation indicates a strong relationship between the vibro-milling process and the yield of PT nanopowders. However, further investigation is required for the control and optimization of the PT formation. Studies on the effect of milling parameters and particle size distribution on phase formation kinetics would be useful for the particle size control. In case of the vibro-milling technique, other factors such as the milling speed, milling scale and type of milling media also need be taken into account.

4. Conclusion

The results infer that the milling time influences not only on the development of the solid-state reaction of lead titanate phase but also the particle size and morphology. The resulting PT powders have a range of particle size, depending on milling times. Production of a single-phase lead titanate nanopowder can be successfully achieved by employing a combination of 25 h milling time and calcination conditions of 600 °C for 2 h, with heating/cooling rates of 20 °C min^{-1}.

Acknowledgement

This work was supported by the Thailand Research Fund (TRF) and the Faculty of Science, Chiang Mai University. One of the authors (R.W.) wishes to acknowledge Maejo University for financial support during her study and also the Graduate School of Chiang Mai University.

References

[1] A.J. Moulson, J.M. Herbert, Electroceramics, 2nd ed.Wiley, Chichester, 2003.
[2] B. Jaffe, W.R. Cook, H. Jaffe, Piezoelectric Ceramics, Academic Press, New York, 1971.
[3] O. Bouquin, M. Lejeune, J.P. Boilot, J. Am. Ceram. Soc 74 (1991) 1152.
[4] T.R. Gururaja, A. Safari, A. Halliyal, Am. Ceram. Soc. Bull. 65 (1986) 1601.
[5] J.S. Wright, L.F. Francis, J. Mater. Res. 8 (1993) 1712.
[6] G.R. Fox, J.H. Adair, R.E. Newnham, J. Mater. Sci. 25 (1990) 3634.
[7] A. Rujiwatra, J. Jongphiphan, S. Ananta, Mater. Lett. 59 (2005) 1871.
[8] V.V. Dabhade, T.R. Rama Mohan, P. Ramakrishman, Appl. Surf. Sci. 182 (2001) 390.
[9] S. Ananta, Mater. Lett. 58 (2004) 2781.
[10] A. Udomporn, S. Ananta, Curr. Appl. Phys. 4 (2004) 186.
[11] A. Udomporn, S. Ananta, Mater. Lett. 58 (2003) 1154.
[12] S. Ananta, N.W. Thomas, J. Eur. Ceram. Soc. 19 (1999) 155.
[13] S. Ananta, R. Brydson, N.W. Thomas, J. Eur. Ceram. Soc. 20 (2000) 2315.
[14] S.L. Swartz, T.R. Shrout, Mater. Res. Bull. 17 (1982) 1245.
[15] H. Klug, L. Alexander, X-Ray Diffraction Procedures for Polycrystalline and Amorphous Materials, 2nd ed.Wiley, New York, 1974.
[16] S. Ananta, R. Tipakonitikul, T. Tunkasiri, Mater. Lett. 57 (2003) 2637.
[17] C.G. Pillai, P.V. Ravindran, Thermochim. Acta 66 (1996) 109.
[18] J. Tartaj, C. Moure, L. Lascano, P. Duran, Mater. Res. Bull. 36 (2001) 2301.
[19] M.L. Calzada, M. Alguero, L. Pardo, J. Sol–Gel Sci. Technol. 13 (1998) 837.
[20] Powder Diffraction File No. 21-949. International Centre for Diffraction Data, Newtown Square, PA, 2000.
[21] Powder Diffraction File No. 6-452. International Centre for Diffraction Data, Newtown Square, PA, 2000.
[22] C. Suryanarayana, Prog. Mater. Sci. 46 (2001) 1.
[23] A. Revesz, T. Ungar, A. Borbely, J. Lendvai, Nanostruct. Mater. 7 (1996) 779.
[24] P.C. Kang, Z.D. Yin, O. Celestine, Mater. Sci. Eng., A Struct. Mater.: Prop. Microstruct. Process. 395 (2005) 167.

Available online at www.sciencedirect.com
SCIENCE DIRECT
Current Applied Physics 6 (2006) 520–524
Current Applied Physics
An official journal of the KPS
www.elsevier.com/locate/cap
www.kps.or.kr

Effects of uniaxial stress on dielectric properties of ferroelectric ceramics

Rattikorn Yimnirun *, Supattra Wongsaenmai, Athipong Ngamjarurojana, Supon Ananta

Department of Physics, Faculty of Science, Chiang Mai University, Chiang Mai 50200, Thailand

Available online 27 December 2005

Abstract

The effects of uniaxial stress on the dielectric properties of ceramics in PMN–PZT system are investigated. Ceramics with the formula $(x)Pb(Mg_{1/3}Nb_{2/3})O_3$–$(1-x)Pb(Zr_{0.52}Ti_{0.48})O_3$ when $x = 0.0$, 0.1, 0.3, 0.5, 0.7, 0.9 and 1.0 are prepared by a conventional mixed-oxides method. The sintered ceramics are perovskite materials with their physical properties proportionally depending on the PMN and PZT contents. The dielectric properties under the uniaxial stress of the unpoled and poled PMN–PZT ceramics are observed at stress levels up to 5 MPa. For the unpoled ceramics, the dielectric properties do not change significantly with the applied stress and the changes are independent of the ceramic compositions. For the poled ceramics, on the other hand, the dielectric constant of the PZT-rich compositions increases slightly, while that of the PMN-rich compositions decreases with increasing applied stress. In addition, changes in the dielectric loss tangent with stress are found to be composition independent. This study clearly shows the influences of the domain re-orientation, domain wall motion, degradation and depoling mechanisms on the variation of the dielectric properties of PMN–PZT ceramics under the uniaxial stress.

PACS: 77.22.Ch; 77.84.Dy

Keywords: Uniaxial stress; Dielectric properties; Ferroelectric; PMN–PZT

1. Introduction

Ferroelectric ceramics have been established as good candidates for actuator and transducer applications. Widely used materials include barium titanate ($BaTiO_3$ or BT) and lead-based materials such as lead magnesium niobate ($Pb(Mg_{1/3}Nb_{2/3})O_3$ or PMN) and lead zirconate titanate ($Pb(Zr_{1-x}Ti_x)O_3$ or PZT) [1]. In many of these applications, ceramics are normally used under conditions where stresses are applied [2,3]. Despite this fact, materials constants used in any design calculations are often obtained from a stress-free measuring condition, which in turn may lead to incorrect or inappropriate actuator and transducer designs. It is therefore important to determine the properties of these materials as a function of applied stress. Previous investigations on the stress-dependence dielectric and electrical properties of many ceramic systems, such as PZT and PMN-PT have clearly emphasized the importance of this matter [4,5].

As a prototypic relaxor ferroelectric, PMN exhibits a high dielectric constant and a broad range transition of dielectric constant with temperature as a function of frequency [6]. In addition, PMN ceramics exhibit low loss and non-hysteretic characteristics. These make PMN a good candidate for a large number of applications, such as multilayer capacitors, sensors and actuators. However, PMN ceramics have relatively low electromechanical coupling coefficients, as compared to PZT. On the contrary to PMN, PZT ceramics have found several actuator and transducer applications due to their high electromechanical coupling coefficients and higher temperature of operation [7]. However, PZT ceramics are fairly lossy as a result of their highly hysteretic behavior, which makes them unsuited for applications that require high delicacy and reliability. Furthermore, PZT ceramics normally have a very high Curie temperature (T_C) in the vicinity of

* Corresponding author. Fax: +66 53 357 512.
E-mail address: rattikornyimnirun@yahoo.com (R. Yimnirun).

1567-1739/$ - see front matter © 2005 Elsevier B.V. All rights reserved.
doi:10.1016/j.cap.2005.11.053

400 °C. Usually many applications require that T_C is close to ambient temperature. Therefore, there is a general interest to reduce the T_C of PZT ceramics to optimize their uses. Forming a solid-solution of PZT and relaxor ferroelectrics has been one of the techniques employed to improve the properties of ferroelectric ceramics. With the complementary features of PMN and PZT, the solid solutions between PMN and PZT are expected to synergetically combine the properties of both ceramics, which could exhibit more desirable piezoelectric and dielectric properties for several technologically demanding applications than single-phase PMN and PZT [8,9]. Our previous investigation has emphasized synthesis and dielectric properties of ceramics in PMN–PZT system [10]. Since there has been no report on the stress-dependent properties of this ceramic system, this study is undertaken to investigate the influence of uniaxial stress on the dielectric properties of ceramics in PMN–PZT system.

2. Experimental methods

The $Pb(Mg_{1/3}Nb_{2/3})O_3$–$Pb(Zr_{0.52}Ti_{0.48})O_3$ ceramic composites were prepared from PMN and PZT powders by a mixed-oxide method. Perovskite-phase PMN powders were obtained via a well-known columbite method [11]. PZT powders, on the other hand, were prepared by a more conventional mixed-oxide method. The $(x)Pb(Mg_{1/3}Nb_{2/3})O_3$–$(1-x)Pb(Zr_{0.52}Ti_{0.48})O_3$ (when $x = 0.0$, 0.1, 0.3, 0.5, 0.7, 0.9, and 1.0) ceramic composites were then prepared from the starting PMN and PZT powders by a mixed-oxide method at various processing conditions. Detailed procedures of each method are described in earlier publication [10]. Various characterization techniques were employed to determine the physical and chemical characteristics of the sintered PMN–PZT ceramics. The densities of the sintered ceramics were measured by Archimedes method. The phase formations of the sintered specimens were studied by X-ray diffraction, while microstructure analyses were undertaken using a scanning electron microscopy. Grain size was determined from SEM micrographs by a linear intercept method. Results of these characterizations are described in our previous report and some important data are listed in Table 1.

Table 1
Characteristics of PMN–PZT ceramics with optimized processing conditions

Ceramic	Density (g/cm^3)	Grain size range (μm)	Average grain size (μm)
PZT	7.59 ± 0.11	2–7	5.23
0.1PMN–0.9PZT	6.09 ± 0.11	0.5–2	0.80
0.3PMN–0.7PZT	7.45 ± 0.10	0.5–3	1.65
0.5PMN–0.5PZT	7.86 ± 0.05	0.5–5	1.90
0.7PMN–0.3PZT	7.87 ± 0.07	1–4	1.40
0.9PMN–0.1PZT	7.90 ± 0.09	1–4	1.50
PMN	7.82 ± 0.06	2–4	3.25

For dielectric property characterizations, the sintered samples were lapped to obtain parallel faces, and the faces were then coated with silver paint as electrodes. The samples were heat-treated at 750 °C for 12 min to ensure the contact between the electrodes and the ceramic surfaces. The samples were subsequently poled in a silicone oil bath at a temperature of 120 °C by applying a dc field of 25 kV/cm for 30 min and field-cooled to room temperature. To study the effects of the uniaxial stress on the dielectric properties, a uniaxial compressometer was constructed. The details of the system are described elsewhere [12]. The dielectric properties were measured through spring-loaded pins connected to the LCZ-meter (Hewlett Packard, model 4276A). The capacitance and the dielectric loss tangent were determined at frequency of 1 kHz and room temperature (25 °C). The dielectric constant was then calculated from a parallel-plate capacitor equation, e.g. $\varepsilon_r = Cd/\varepsilon_0 A$, where C is the capacitance of the sample, d and A are the thickness and the area of the electrode, respectively, and ε_0 is the dielectric permittivity of vacuum (8.854×10^{-12} F/m).

3. Results and discussion

3.1. Physical properties

The optimized density of sintered xPMN–$(14-x)$PZT ceramics is listed in Table 1. It is observed that the compositions with $x = 0.1$ and 0.3 show relatively lower density than other compositions. This suggests that the addition of a small amount of PMN to the PMN–PZT compositions results in a significant decrease in the density of the ceramics. However, further addition of PMN into the compositions increased the density again. A similar result was reported in previous investigation [13]. In addition, the grain size of the PMN–PZT ceramics, as determined from the SEM micrographs, varied considerably from <1 to 7 μm, as tabulated in Table 1. It is of interest to see that the average grain size of all the mixed compositions is much smaller than that of the pure PZT and PMN materials. The reason for the changes of the density and the smaller grain sizes in the mixed compositions is not clearly understood, but this may be a result of PMN's role as a grain-growth inhibitor in the PMN–PZT composites. Results from XRD studies indicate that PZT ceramic is identified as a single-phase material with a perovskite structure having tetragonal symmetry, while PMN ceramic is a perovskite material with a cubic symmetry [14]. All PMN–PZT ceramic composites exhibit pseudo-cubic crystal structure, as reported in previous investigations [8,13,14].

3.2. Uniaxial stress dependence of the dielectric propertie of the unpoled ceramics

The experimental results of the uniaxial stress-dependence of the dielectric properties of the unpoled PMN–PZT ceramics are shown in Figs. 1 and 2. There is a trivial

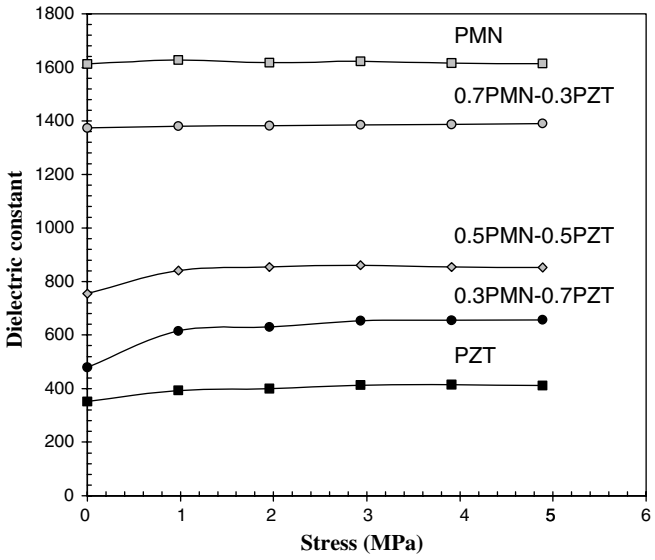

Fig. 1. Uniaxial stress dependence of dielectric constant of unpoled PMN–PZT ceramics.

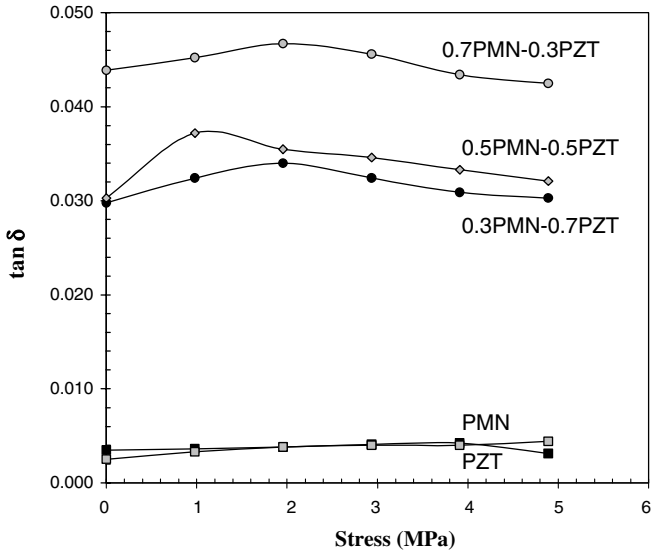

Fig. 2. Uniaxial stress dependence of dielectric loss tangent of unpoled PMN–PZT ceramics.

change of both the dielectric constant and the dielectric loss tangent of the ceramics when the applied stress increases from 0 to 1 MPa. However, these properties then become relatively constant when the applied stress increases further. This is a result of the randomness of the domain orientations in the unpoled ceramics. Since there is only a small portion of the domains that is aligned in the direction parallel or nearly parallel to the direction of the applied stress, the initial increase in the applied stress would then result in motion of these domains in favor of the applied stress, hence increasing dielectric constant and dielectric loss tangent. However, once all these domains are re-oriented, further increase in the applied stress would result in no change in the dielectric properties. The slight decrease in the dielectric loss tangent is probably an indication of the de-aging effect [15,16]. The non-180 °C domain re-orientations are the basic mechanism responsible for the changes in the dielectric properties with the applied stress. In addition, it was also found that the changes of the dielectric properties were composition independent.

3.3. Uniaxial stress dependence of the dielectric properties of the poled ceramics

The experimental results for the poled PMN–PZT ceramics are shown in Figs. 3 and 4. There is a significant change of both the dielectric constant and the dielectric loss tangent of the ceramics when the applied stress increases from 0 to 5 MPa. The changes of the dielectric constant with the applied stress can be divided into two different groups. For PMN-rich compositions (PMN, 0.9PMN–0.1PZT, and 0.7PMN–0.3PZT), the dielectric constant generally decreases with increasing applied stress. However, it should be noticed that only PMN and 0.9PMN–0.1PZT compositions show definite decreases in the dielectric constant, while the dielectric constant of the 0.7PMN–0.3PZT composition initially increases then decreases with very little difference in the dielectric constant between the 0 and 5 MPa. On the other hand, for PZT-rich compositions (PZT, 0.1PMN–0.9PZT, 0.3PMN–0.7PZT, and 0.5PMN–0.5PZT), the dielectric constant rises slightly when the applied stress increases from 0 to 1 MPa, and becomes relatively constant when the applied stress increases further. The dielectric loss tangent for most compositions, except for PMN and PZT, is found to first increase when the applied stress is raised from 0 to 1 MPa, and then decrease with further increasing stress. However, for PZT ceramic the dielectric loss tangent increases monotonously with the increasing stress, while PMN ceramic exhibits a slight

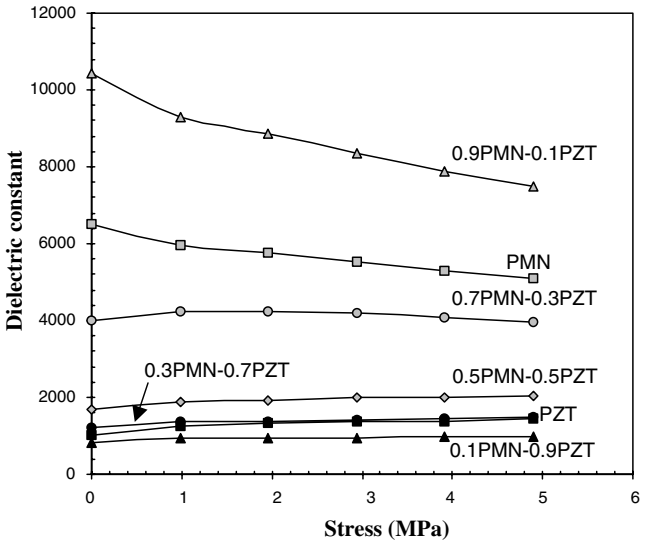

Fig. 3. Uniaxial stress dependence of dielectric constant of poled PMN–PZT ceramics.

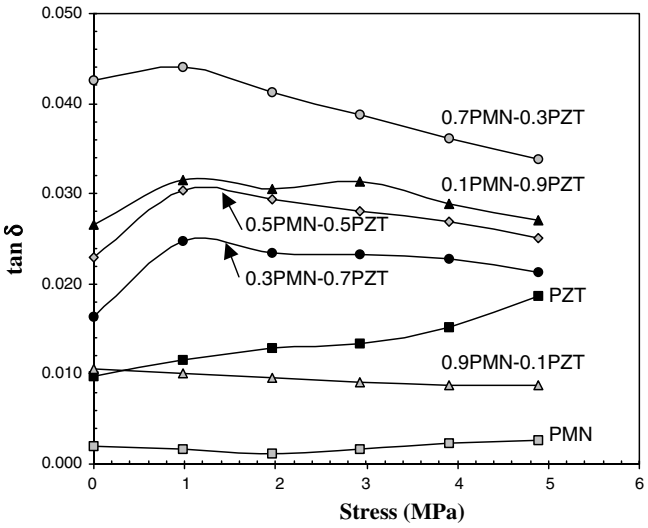

Fig. 4. Uniaxial stress dependence of dielectric loss tangent of poled PMN–PZT ceramics.

increase in the dielectric loss tangent followed by a drop, the turning point being around 2 MPa.

To understand these experimental results for the poled ceramics, various effects have to be considered. Normally, the properties of ferroelectric materials are derived from both the intrinsic contribution, which is the response from a single domain, and extrinsic contributions, which are from domain wall motions [15,16]. When a mechanical stress is applied to a ferroelectric material, the domain structure in the material will change to maintain the domain energy at a minimum; during this process some of the domains engulf other domains or change shape irreversibly. Under a uniaxial stress, the domain structure of ferroelectric ceramics may undergo domain switching, clamping of domain walls, de-aging, and de-poling [16].

In this study, the results for the case of PZT-rich compositions can easily be explained with the above statements. When the compressive uniaxial stress is applied in the direction parallel to the polar axis (poling) direction, the stress will move some of the polarization away from the poling direction resulting in a change in domain structures [15]. This change increases the non-180 °C domain wall density. Hence the increase of the dielectric constant is observed. The de-aging mechanism is also expected to play a role here. However, the stress clamping of domain walls and the de-poling mechanisms are not expected at this relative low stress level used in this study [15–17]. Therefore, a combination of the domain switching and the de-aging mechanisms is believed to be a reason for the slight increase of the dielectric constant with increasing applied stress in the PZT-rich compositions, as shown in Fig. 3. Since PMN is a relaxor ferroelectric material, the situation is very different for PMN-rich compositions. The stress dependence of the dielectric constant of the compositions is attributed to competing influences of the intrinsic contribution of non-polar matrix and the extrinsic contribution of re-polarization and growth of micro-polar regions [15,18]. Since the dielectric response of both contributions is affected by the applied stress in an opposite way, the behavior of the composites depends on the ratio between the micro-polar region and the non-polar matrix. Since the measurements are carried out at the room temperature, the micro-polar regions dominate the dielectric response of the composites [18]. Therefore, the dielectric constant of the PMN-rich compositions decreases with increasing applied stress, as seen in Fig. 3.

The cause of the stress dependence of the dielectric loss tangent is a little more straightforward than that of the dielectric constant. As depicted in Fig. 4, an increase in domain wall mobility clearly enhances the dielectric loss tangent in some compositions, while the de-aging in the materials normally causes the decrease of the dielectric loss tangent observed in some compositions [16,17]. More importantly, these results clearly demonstrate that the contribution of each mechanism to the dielectric responses of the PMN–PZT ceramic depends on the compositions and the stress level.

The results obtained for the poled ceramics are significantly different from those for the unpoled ones. In the poled ceramics, considerable changes of both the dielectric constant and dielectric loss tangent that depend upon the ceramic compositions are clearly observed. This distinct difference between the two ceramic groups can be intuitively attributed to the more active electrically re-oriented domains available in the poled ceramics. Clearly, these results demonstrate the contribution of the domain re-orientation procedure, e.g. poling, to the dielectric responses to external stresses in the PMN–PZT ceramics.

4. Conclusions

In this study, the $(x)Pb(Mg_{1/3}Nb_{2/3})O_3$–$(1-x)Pb(Zr_{0.52}Ti_{0.48})O_3$ (when $x = 0.0$, 0.1, 0.3, 0.5, 0.7, 0.9, and 1.0) ceramic composites were successfully prepared by a conventional mixed-oxide method at various processing conditions. The phase formation behavior, the microstructure features were studied using XRD and SEM techniques, respectively. The physical properties measurements revealed that the properties were relatively composition-dependent. The dielectric properties under the uniaxial stress of the unpoled and poled PMN–PZT ceramics were observed at stress levels up to 5 MPa using a calibrated uniaxial compressometer. For the unpoled PMN–PZT ceramics, the dielectric constant increased with increasing stress between 0 and 1 MPa and became relatively constant when the applied stress was further increased. On the other hand, the dielectric loss tangent first rises and then drops with increasing applied stress. Furthermore, the changes of the dielectric constant of these unpoled PMN–PZT ceramics are independent of the ceramic compositions. In the case of the poled ceramics, the results clearly show that the dielectric constant of the PMN-rich compositions decreases, while that of the PZT-rich compositions increases slightly, with increasing applied stress. However, the dielectric loss

tangent for most of the compositions first rises and then drops with increasing applied stress. It is very great interest to observe that the results for the unpoled PMN–PZT ceramics are significantly different from those for the poled PMN–PZT ceramics. This study shows that the applied stress has significant influences on the dielectric properties of the PMN–PZT ceramic composites.

Acknowledgement

This work is supported by the Thailand Research Fund (TRF), Faculty of Science and Graduate School of Chiang Mai University.

References

[1] L.E. Cross, Mater. Chem. Phys. 43 (1996) 108.
[2] K.V.R. Murty, S.N. Murty, K.C. Mouli, A. Bhanumathi, Proc. IEEE ISAF 1 (1992) 144.
[3] J.H. Yoo, H.S. Yoon, Y.H. Jeong, C.Y. Park, Proc. IEEE Ultra. Symp. 1 (1998) 981.
[4] D. Viehland, J. Powers, J. Appl. Phys. 89 (2001) 1820.
[5] J. Zhao, A.E. Glazounov, Q.M. Zhang, Appl. Phys. Lett. 74 (1999) 436.
[6] S.M. Gupta, A.R. Kulkarni, Mater. Chem. Phys. 39 (1994) 98.
[7] L.E. Cross, Ferroelectrics 76 (1987) 241.
[8] H. Ouchi, J. Am. Ceram. Soc. 51 (1968) 169.
[9] Y. Abe, Y. Yanagisawa, K. Kakagawa, Y. Sasaki, Solid State Commun. 113 (2000) 331.
[10] R. Yimnirun, S. Ananta, P. Laoratanakul, Mater. Sci. Eng. B 112 (2004) 79.
[11] S.L. Swartz, T.R. Shrout, Mater. Res. Bull. 17 (1982) 1245.
[12] R. Yimnirun, P.J. Moses, R.J. Meyer, R.E. Newnham, Rev. Sci. Instrum. 74 (2003) 3429.
[13] H. Ouchi, K. Nagano, S.J. Hayakawa, J. Am. Ceram. Soc. 48 (1965) 630.
[14] V. Koval, C. Alemany, J. Briancin, H. Brunckova, K. Saksl, J. Euro. Ceram. Soc. 23 (2003) 1157.
[15] Q.M. Zhang, J. Zhao, K. Uchino, J. Zheng, J. Mater. Res. 12 (1997) 226.
[16] G. Yang, S.F. Liu, W. Ren, B.K. Mukherjee, Proc. SPIE Symp. Smart Struct. Mater. 3992 (2000) 103.
[17] G. Yang, W. Ren, S.F. Liu, A.J. Masys, B.K. Mukherjee, Proc. IEEE Ultra. Symp. 1 (2000) 1005.
[18] J. Zhao, Q.M. Zhang, V. Mueller, Proc. IEEE ISAF 1 (1998) 361.

ELSEVIER

Materials Science and Engineering B 130 (2006) 246–253

MATERIALS SCIENCE & ENGINEERING B

www.elsevier.com/locate/mseb

Effects of milling method and calcination condition on phase and morphology characteristics of $Mg_4Nb_2O_9$ powders

R. Wongmaneerung [a], T. Sarakonsri [b], R. Yimnirun [a], S. Ananta [a,*]

[a] *Department of Physics, Faculty of Science, Chiang Mai University, Chiang Mai, 50200, Thailand*
[b] *Department of Chemistry, Faculty of Science, Chiang Mai University, Chiang Mai, 50200, Thailand*

Received 9 November 2005; received in revised form 23 February 2006; accepted 19 March 2006

Abstract

Magnesium niobate, $Mg_4Nb_2O_9$, powders has been synthesized by a solid-state reaction. Both conventional ball- and rapid vibro-milling have been investigated as milling methods, with the formation of the $Mg_4Nb_2O_9$ phase investigated as a function of calcination conditions by DTA and XRD. The particle size distribution of the calcined powders was determined by laser diffraction technique, while morphology, crystal structure and phase composition were determined via a combination of SEM, TEM and EDX techniques. The type of milling method together with the designed calcination condition was found to show a considerable effect on the phase and morphology evolution of the calcined $Mg_4Nb_2O_9$ powders. It is seen that optimization of calcination conditions can lead to a single-phase $Mg_4Nb_2O_9$ in both milling methods. However, the formation temperature and dwell time for single-phase $Mg_4Nb_2O_9$ powders were lower with the rapid vibro-milling technique.

Keywords: Magnesium niobate; Milling; Calcination; Phase formation; X-ray diffraction

1. Introduction

To date, magnesium niobate, $Mg_4Nb_2O_9$, is one of the four possible magnesium–niobium oxides which have been recognized [1]. It has an ordered corundum-type hexagonal structure and has been investigated as a potential candidate for the synthesis of low loss microwave dielectric materials [2] and as buffer layer materials for manufacturing ferroelectric memory devices [3]. It is also an important material which shows self activated photoluminescence at room temperature [4]. You et al. [5] reported that cerium-doped $Mg_4Nb_2O_9$ exhibited improved luminescence properties. Recent work on the preparation of relaxor ferroelectric $Pb(Mg_{1/3}Nb_{2/3})O_3$ [6,7], has also shown that $Mg_4Nb_2O_9$ is a better precursor than the columbite $MgNb_2O_6$ [8,9] for the successful preparation of single-phase perovskite PMN which is becoming increasingly important for electroceramic components such as multilayer ceramic capacitors and electrostrictive actuators [10–12].

The evolution of a method to produce particular powders of precise stoichiometry and desired properties is complex, depending on a number of variables such as raw materials, their purities, processing history, temperature, time, etc. For example, the synthesis of stoichiometric lead magnesium niobate (PMN) using $Mg_4Nb_2O_9$ as a key precursor by a conventional solid-state reaction [7] requires an additional amount of PbO to convert the pyrochlore phase to PMN. However, the effect of excess PbO on PMN preparation is still a matter of debate, and appears to depend critically on the amount of PbO added [13–15]. Determination of the appropriate excess of PbO is currently a matter of trial and error. Furthermore, it has been reported that residual MgO present in the sample after the reaction has to be removed by treating with dilute nitric acid. Interestingly, a two-stage mixed oxide route has also been employed with minor modifications in the synthesis of $Mg_4Nb_2O_9$ itself [16,17]. In general, production of single-phase $Mg_4Nb_2O_9$ is not straightforward, as minor concentrations of the $MgNb_2O_6$ phases and/or MgO inclusion are sometimes formed alongside the major phase of $Mg_4Nb_2O_9$ [15,17,18].

The development of $Mg_4Nb_2O_9$ powders, to date, has not been as extensive as that of $MgNb_2O_6$. Much of the work concerning the compound $Mg_4Nb_2O_9$ has been directed towards determining luminescent [4,5] or microwave dielectric [2] properties, and fabrication of $Mg_4Nb_2O_9$ single crystal [19] or PMN powders [6,7]. Only limited attempts have been made to improve

* Corresponding author. Tel.: +66 53 943367; fax: +66 53 943445.
E-mail address: suponananta@yahoo.com (S. Ananta).

0921-5107/$ – see front matter © 2006 Elsevier B.V. All rights reserved.
doi:10.1016/j.mseb.2006.03.027

the yield of $Mg_4Nb_2O_9$ powders derived from the solid-state reaction by optimizing milling method or calcination condition [13,20,21]. Moreover, the optimization of a combination between the milling method and the calcination condition in the mixed oxide process has not been studied. The purpose of this work was to explore a simple mixed oxide synthetic route for the production of $Mg_4Nb_2O_9$ powders and compare the characteristics of the resulting powders. Two milling techniques were employed as the mixing method. A conventional ball milling was compared against a rapid vibro-milling in terms of their phase formation, particle size, morphology and microchemical compositions of the powders calcined at various conditions.

2. Experimental procedure

The starting materials used in the present study were commercially available magnesium oxide, MgO and niobium oxide, Nb_2O_5 (Fluka, 98% purity). These two oxide powders exhibited an average particle size in the range of 5.0–10.0 μm. $Mg_4Nb_2O_9$ powders were synthesized by the solid-state reaction of appropriate amounts of MgO and Nb_2O_5 powders that were mixed using two wet-milling methods (Fig. 1). The ball-milling operation was carried out for 48 h [7,13,20,22] with zirconia balls [22] in isopropanal. For comparison, a McCrone vibro-milling technique [9] was carried out on another set of powders with corundum cylindrical media in isopropanal for 1 h [21]. After drying at 120 °C for 2 h, various calcination conditions, i.e. temperatures ranging from 550 to 1100 °C and dwell times ranging from 2 to 5 h with heating/cooling rates ranging from 10 to 30 °C/min. [22] were applied in order to investigate the formation of $Mg_4Nb_2O_9$ phase in powders from both milling methods. The reactions of the uncalcined powders taking place during heat treatment were investigated by thermal gravimetric and differential thermal analysis (TG-DTA, Shimadzu) using a heating rate of 10 °C/min. in air from room temperature up to 1100 °C. Calcined powders were subsequently examined by room temperature X-ray diffraction (XRD; Philips PW 1729 diffractometer) using Ni filtered Cu Kα radiation, to identify the phases formed and optimum calcination conditions for the manufacture of $Mg_4Nb_2O_9$ powder. The mean crystallite size was determined using the diffraction peak (1 0 4) of the corundum pattern by using Scherrer equation [23]. Particle size distributions of the powders were determined by laser diffraction technique (DIAS 1640 laser diffraction spectrometer), with the grain size and morphologies of the powders observed by scanning electron microscopy (SEM; JEOL JSM-840A). The chemical composition and structure of the phases formed were elucidated by transmission electron microscopy (CM 20 TEM/STEM) operated at 200 keV and fitted with an energy-dispersive X-ray (EDX) analyzer with an ultra-thin window. EDX spectra were quantified with the virtual standard peaks supplied with the Oxford Instruments eXL software. Powder samples were dispersed in solvent and deposited by pipette on to 3 mm holey copper grids for TEM observation. In addition, attempt was made to evaluate the crystal structures of the observed compositions/phases by correcting the XRD and TEM diffraction data.

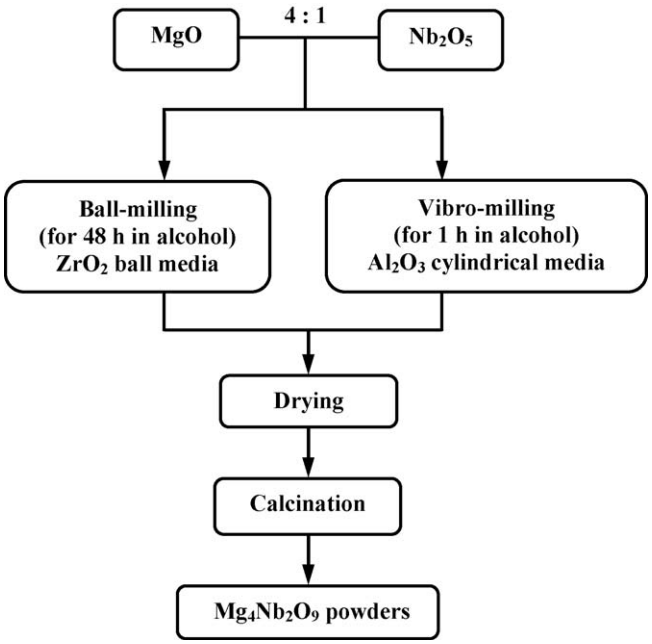

Fig. 1. Flow chart for preparing $Mg_4Nb_2O_9$ powders by ball- and vibro-milling methods.

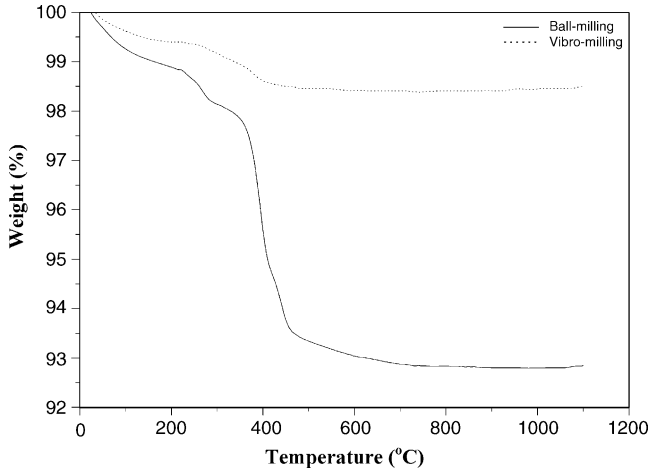

Fig. 2. TGA curves of the two MgO–Nb_2O_5 mixtures derived from (a) ball-milling and (b) vibro-milling methods.

3. Results and discussion

TGA and DTA results for the mixture of MgO and Nb_2O_5 milled by both methods are shown in Figs. 2 and 3, respectively. In general, similar trend of thermal characteristics is observed in both precursors. As shown in Fig. 2, the precursors prepared with both milling methods exhibit two distinct weight losses below 600 °C. The first weight loss occurs below 200 °C and the second one above 250 °C. In the temperature range from room temperature to ∼150 °C, both samples show small exothermic peaks in the DTA curves at ∼120 °C (Fig. 3), which are related to the first weight loss. These DTA peaks can be attributed to the decomposition of the organic species such as rubber lining from the milling process similar to those reported earlier [20]. In comparison between the two milling methods,

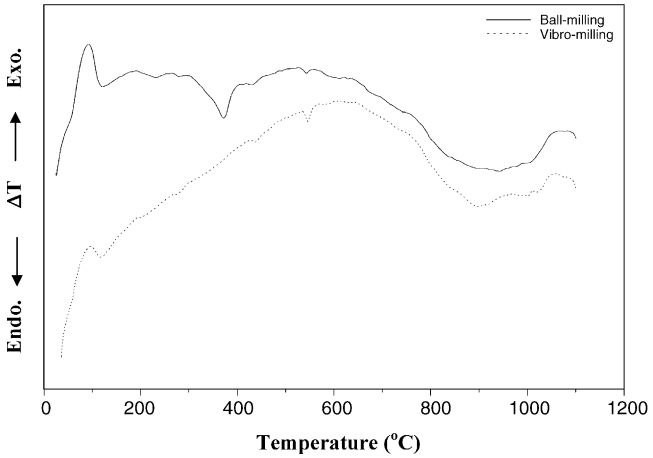

Fig. 3. DTA curves of the two MgO–Nb_2O_5 mixtures derived from (a) ball-milling and (b) vibro-milling methods.

after the first weight loss, the ball-milling precursor (solid line) shows a slightly less weight loss over the temperature range of ~150–250 °C, followed by a much more sharp fall in specimen weight with increasing temperature from ~250–500 °C. This precursor also exhibits a significantly larger overall weight loss (~7.25%) than that of the vibro milling (~1.50%). This may be accounted for by the fact that the vibro-milling method provides faster size reduction rate and is able to enhance mixing capability with lower contamination possibility due to shorter milling time applied as suggested by several authors [9,24,25].

Corresponding to the second fall in specimen weight, by increasing the temperature up to ~700 °C, the solid-state reaction occurs between magnesium oxide and niobium oxide. The broad exothermic characteristic in both DTA curves represents that reaction, which has a maximum at ~550 and 620 °C for ball- and vibro-milling precursors, respectively. No significant weight loss was observed for the temperatures above 800 °C in the TG curves (Fig. 2), indicating that the minimum firing temperature to obtain MgO–Nb_2O_5 compounds is in good agreement with XRD results (Figs. 4 and 5) and other workers [6,9,16]. However, the DTA curves show that there are other small peaks with maximum at ~1080 °C (for ball-milling) and 1050 °C (for vibro-milling). It is to be noted that there is no obvious interpretation of these peaks, although it is likely to correspond to a phase transition reported by a number of workers [14,17,22]. The different temperature, intensities, and shapes of the thermal peaks for the two precursors are probably related to the different milling conditions between the two methods, and consequently caused by the removal of organic species (such as rubber lining) and reactivity of species differently milled (difference in size and size distribution) and mixed in the powders. These data were used to define the range of temperatures for XRD investigation to between 550 and 1100 °C.

To further study the phase development with increasing calcination temperature in each of the two precursors, they were calcined for 2 h in air with a constant heating/cooling rates of 10 °C/min at various temperatures, up to 1100 °C, followed by phase analysis using XRD. As shown in Figs. 4 and 5, for the powders calcined at 550 °C, only X-ray peaks of MgO and

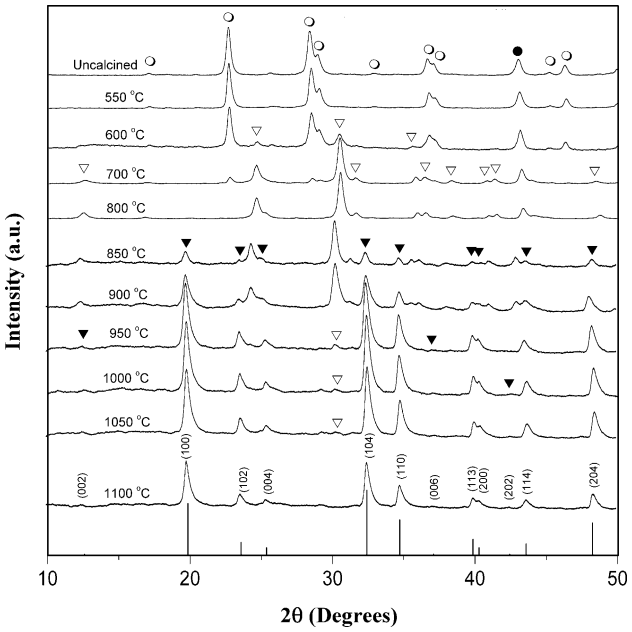

Fig. 4. Powder XRD patterns of the ball-milling powders calcined at various conditions for 2 h with constant heating/cooling rates of 10 °C/min (●, MgO; ◯, Nb_2O_5; ▽, $MgNb_2O_6$; ▼, $Mg_4Nb_2O_9$; ICDD file No. 38–1459: $Mg_4Nb_2O_9$).

Nb_2O_5 are present, indicating that the elimination of organic species occurs below 500 °C, which agrees with the TG-DTA results determined previously. The strongest reflections of the mixed phases of MgO (●) and Nb_2O_5 (◯) can be correlated with ICDD file Nos. 71–1176 [26] and 28–317 [27], respectively.

From Figs. 4 and 5, it is seen that little crystalline phase of $MgNb_2O_6$ (▽), earlier reported by many researchers [6,17,28] was found at 600 °C as separated phases in both calcined powders. This $MgNb_2O_6$ phase (ICDD file No. 33–0875 [29])

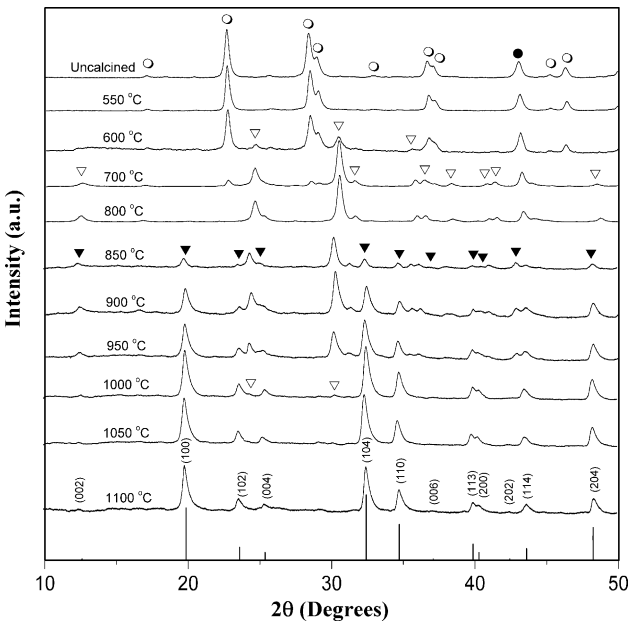

Fig. 5. Powder XRD patterns of the vibro-milling powders calcined at various conditions for 2 h with constant heating/cooling rates of 10 °C/min (●, MgO; ◯, Nb_2O_5; ▽, $MgNb_2O_6$; ▼, $Mg_4Nb_2O_9$; ICDD file No. 38–1459: $Mg_4Nb_2O_9$).

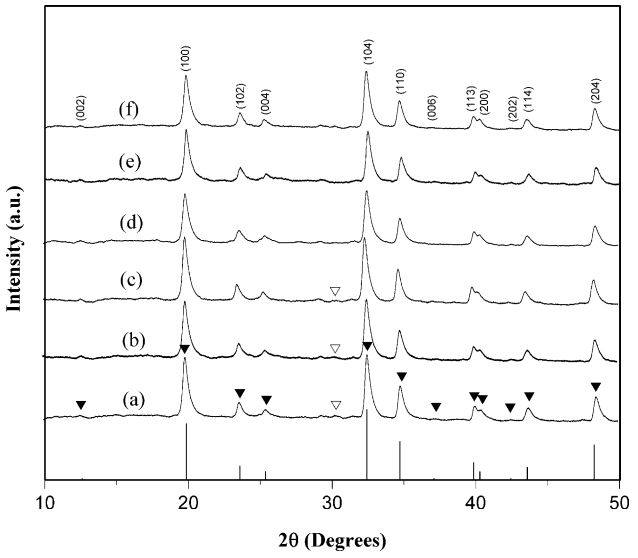

Fig. 6. Powder XRD patterns of the ball-milling powders calcined at 1050 °C with heating/cooling rates of 10 °C/min. for (a) 2 h, (b) 3 h, (c) 4 h and (d) 5 h, and at 1050 °C for 5 h with heating/cooling rates of (e) 20 °C/min and (f) 30 °C/min (▽, $MgNb_2O_6$; ▼, $Mg_4Nb_2O_9$; ICDD file No. 38–1459: $Mg_4Nb_2O_9$).

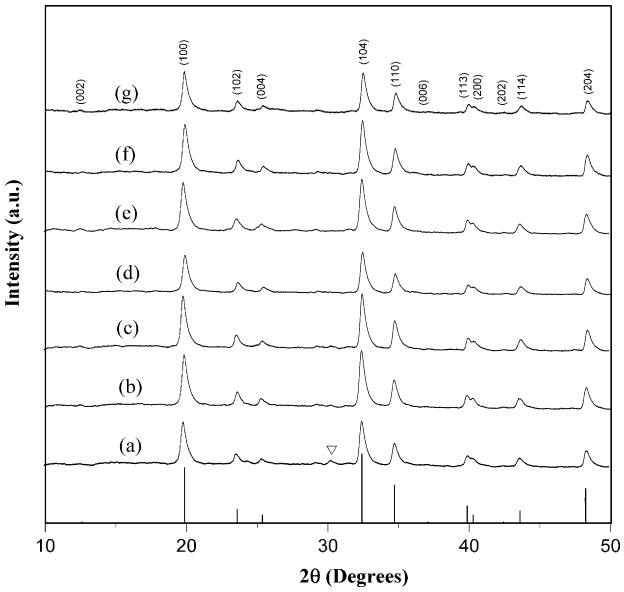

Fig. 7. Powder XRD patterns of the vibro-milling powders calcined at 1050 °C with heating/cooling rates of 10 °C/min. for (a) 1 h, (b) 2 h, (c) 3 h, (d) 4 h and (e) 5 h, and at 1050 °C for 5 h with heating/cooling rates of (f) 20 °C/min and (g) 30 °C/min (▽, $MgNb_2O_6$; ICDD file No. 38–1459: $Mg_4Nb_2O_9$).

has a columbite-type structure with an orthorhombic unit cell ($a = 5.70$ Å, $b = 14.19$ Å and $c = 5.032$ Å) with space group $I4_1/amd$ (No. 141), in agreement with literature [14,17,28]. As the temperature increased to 700 °C, the intensity of the $MgNb_2O_6$ peaks in both calcined powders was further enhanced and became the predominant phase, in consistent with the TG-DTA results. From Figs. 4 and 5, it is seen that the peaks corresponding to MgO and Nb_2O_5 phases were completely eliminated after calcination at 800 °C in both powders. These observations are associated to the DTA peaks found at the same temperature range within the broad exothermic effects (Fig. 3). After calcination at 850 °C, some new peaks (▼) of the desired $Mg_4Nb_2O_9$ started to appear, mixing with $MgNb_2O_6$ and MgO phases in both powders, in consistent with Ananta [20]. To a first approximation, this $Mg_4Nb_2O_9$ phase (ICDD file No. 38–1459 [30]) has a corundum-type structure with a hexagonal unit cell ($a = 5.162$ Å and $c = 14.024$ Å) with space group (no. 165), in consistent with other researchers [5,19,20].

Upon calcination at 1100 °C, the major phase of $Mg_4Nb_2O_9$ has been clearly identified in the ball-milling powders and most of second phases were eliminated. In particular, the peaks corresponding to $MgNb_2O_6$ disappeared. However, in comparison, a single phase of $Mg_4Nb_2O_9$ is already formed when the vibro-milling precursor was calcined at 1050 °C. Apart from calcination temperature, the effect of dwell time was also found to be significant (Figs. 6 and 7). It is seen that an essentially monophasic $Mg_4Nb_2O_9$ of corundum structure is obtainable in the ball-milling powders when the dwell time was extended to 5 h at 1050 °C (Fig. 6), which is 3 h longer than that of the vibro-milling precursor (Fig. 7). In this work, an attempt was also made to calcine these powders under various heating/cooling rates (Figs. 6(d–f) and 7(e–g)). In this connection, it is shown that the yield of $Mg_4Nb_2O_9$ phase did not vary significantly with different heating/cooling rates ranging from 10 to 30 °C/min, in good agreement with earlier results reported by Ananta et al. [20,31] for the mixture of the two kinds of refractory oxides.

The amount of corundum phase present in each of the powders was estimated using the following equation:

$$\text{corundum phase (wt.\%)} = \left[\frac{I_{\text{Cor}}}{(I_{\text{Cor}} + I_{\text{Col}})}\right] \times 100 \quad (1)$$

This equation is analogous to well-known equation [6,8] widely employed in connection with the fabrication of complex perovskite materials. It should be seen as a first approximation since its applicability requires comparable maximum intensities of the peaks of corundum and columbite phases. Here I_{Cor} refers to the intensity of the corundum (1 0 4) peak and I_{Col} the intensity of the columbite (1 3 1) peak [32]. For the purpose of estimating the concentration of the phase present, Eq. (1) has been applied to the powder XRD patterns obtained as given in Table 1.

It is well established that the columbite-type $MgNb_2O_6$ tends to form together with the corundum-type $Mg_4Nb_2O_9$, depending on calcination conditions [18,20,32]. In the work reported here, evidence for the formation of $MgNb_2O_6$ phase, which coexists with the $Mg_4Nb_2O_9$ phase, is found after calcination at temperature ~850–950 °C, similar to those reported by Ananta [20] and Yu et al. [22]. The formation temperature and dwell times for high purity $Mg_4Nb_2O_9$ observed in the powders derived from a combination of a mixed oxide synthetic route and a careful calcination condition (especially with a rapid vibro-milling technique) are slightly lower than those reported for the powders prepared via many other conventional mixed oxide methods [3–5,13].

Based on the DTA and XRD data, it may be concluded that, over a wide range of calcination conditions, single-phase $Mg_4Nb_2O_9$ cannot be straightforwardly formed via a solid-state mixed oxide synthetic route, as verified by a number of

Table 1
Calculated amount of $Mg_4Nb_2O_9$ phase as a function of calcination conditions and milling methods

Calcination conditions		Qualitative concentrations of phases[a]			
Temperature (°C)	Dwell time (h)	Ball-milling		Ball-milling	
		$Mg_4Nb_2O_9$ (wt.%)	$MgNb_2O_6$ (wt.%)	$Mg_4Nb_2O_9$ (wt.%)	$MgNb_2O_6$ (wt.%)
850	2	20.88	79.12	5.00	95.00
900	2	42.44	57.56	21.33	78.67
950	2	91.22	8.78	58.81	41.19
1000	2	93.69	6.31	93.44	6.56
1050	1	–	–	98.29	1.71
1050	2	93.96	6.04	100.00	0.00
1050	3	99.02	0.98	100.00	0.00
1050	4	99.13	0.87	100.00	0.00
1050	5	100.00	0.00	100.00	0.00
1100	2	100.00	0.00	100.00	0.00

[a] The estimated precision of the concentrations for the two phases is ±1%.

researchers [16,17,20]. The experimental work carried out here suggests that the optimal calcination conditions for single-phase $Mg_4Nb_2O_9$ are 1050 °C for 5 h or 1100 °C for 2 h (ball-milling) and 1050 °C for 2 h (vibro-milling), with heating/cooling rates as fast as 30 °C/min. The optimized formation temperature of single-phase $Mg_4Nb_2O_9$ was lower for the vibro-milling method probably due to the higher degree of mixing with more effective size reduction. Therefore, in general, the methodology presented in this work provides a simple method for preparing corundum $Mg_4Nb_2O_9$ powders via a solid-state mixed oxide synthetic route. It is interesting to note that, by using either ball-milling or vibro-milling methods with its respective optimized calcination condition, the reproducible, lower cost and flexible process involving simple synthetic route can produce high purity corundum $Mg_4Nb_2O_9$ (with impurities undetected by XRD technique) from relatively impure and inexpensive commercially available raw materials.

SEM micrographs of the calcined $Mg_4Nb_2O_9$ powders derived from ball- and vibro-milling methods are shown in Fig. 8(a) and (b), respectively. In general, the particles are agglomerated and basically irregular in shape, with a substantial variation in particle size. Observed diameters range from 0.5 to 1.6 and 0.1 to 1.8 μm for ball- and vibro-milling methods, respectively (Table 2). However, it is seen that higher degree of agglomeration with more rounded particle morphology is observed in the powders produced by vibro-milling. The strong inter-particle bond within each aggregate is evidenced by the formation of a well-established necking between neighbouring particles. This observation could be attributed to the mechanism of surface energy reduction of the ultrafine powders, i.e. the smaller the powder the higher the specific surface area [24,25]. In general, it is seen that higher and longer heat treatment of ball-milling powders leads to larger particle sizes with hard agglomeration. The averaged particle size of vibro-milling $Mg_4Nb_2O_9$ powders with finer particle size is regarded as

Table 2
Particle size range of $Mg_4Nb_2O_9$ particles measured by different techniques

Measurement techniques	Particle size range	
	Ball-milling	Vibro-milling
XRD (nm, ±2.0)	23.9	23.4
Laser diffraction (μm, ±0.2)	2.0–5.0	0.3–6.5
SEM (μm, ±0.1)	0.5–1.6	0.1–1.8
TEM (μm, ±0.01)	0.01–1.0	0.01–0.03

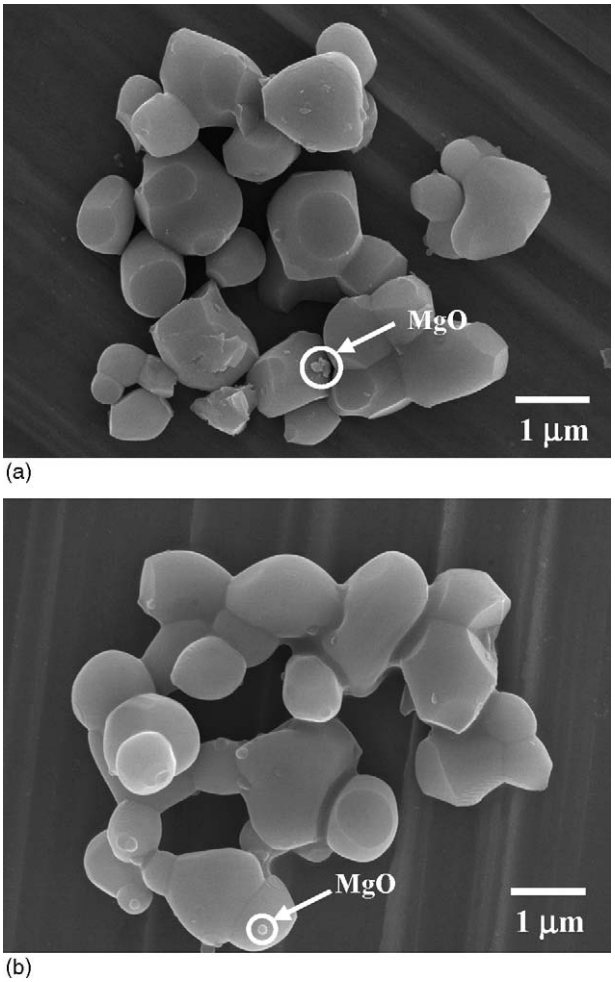

Fig. 8. SEM micrographs of the (a) ball-milling and (b) vibro-milling $Mg_4Nb_2O_9$ powders after calcined at their optimal conditions.

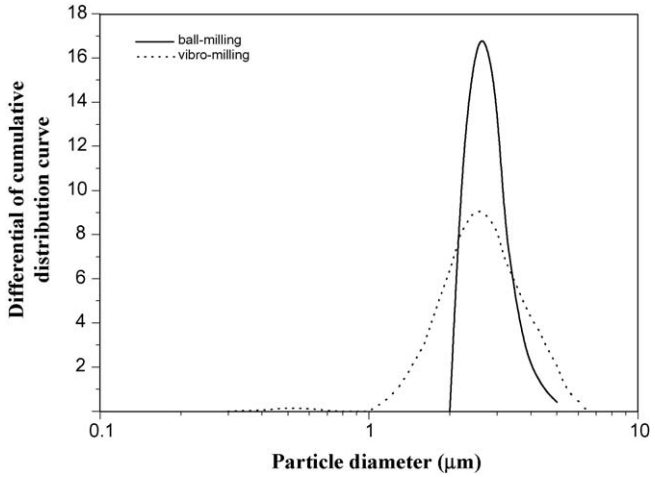

Fig. 9. The particle size curves of the ball- and vibro-milling $Mg_4Nb_2O_9$ powders after calcined at their optimal conditions.

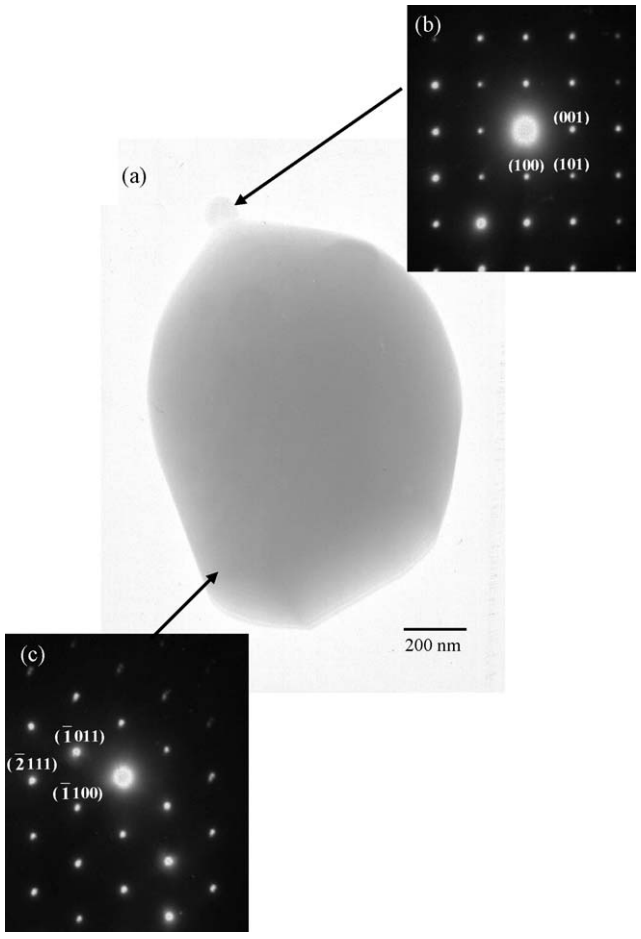

Fig. 10. (a) TEM micrograph of ball-milling $Mg_4Nb_2O_9$ particles and SAED patterns of (b) the major phase of hexagonal $Mg_4Nb_2O_9$ (zone axes [1 1 1]) and (c) the minor phase of orthorhombic $MgNb_2O_6$ (zone axes [0 1 0]).

advantage for better reactivity. A combination of SEM and EDX techniques has demonstrated that an MgO-rich phase (spherical particle with diameter of ~50–100 nm) exists neighbouring the $Mg_4Nb_2O_9$ parent phase, as circled in Figs. 8(a) and 9b). The existence of discrete nano-sized MgO phase points to the poor reactivity of MgO, although the concentration is too low for detection by XRD in consistent with earlier work by Ananta [20]. Fig. 9 shows the particle size distribution curves of calcined $Mg_4Nb_2O_9$ powders derived from both milling methods. As listed in Table 2, the particle size falls within the range of 2.0–5.0 and 0.3–6.5 μm for powders from ball- and vibro-milling methods, respectively. Even taking into account that the analysis does not reveal the real dimension of single particles (due to agglomeration effects as expected from the SEM results in Fig. 8), a uniform frequency distribution curve was observed for the ball-milling powders whilst broad distribution curve with tiny tail at front covering the range of 0.3–0.8 μm in sizes was found for the vibro-milling powders (dashed line), reflecting more of the size of agglomerates than the real size of particles, in good agreement with the SEM results previously determined.

Bright field TEM images of discrete particles of the calcined $Mg_4Nb_2O_9$ powders are shown in Fig. (ball-milling) and Fig. 11 (vibro-milling), indicating the particle sizes and shapes at higher magnifications. The observed morphology reveals the considerable difference in both size and shapes between the two particles. Primary particle in vibro-milling powders is clearly smaller in size than the ball-milling powders. As seen in Fig. 10(a), the ball-milling powders consist mainly of irregular round shape primary particles with a diameter of ~1 μm or less. In addition to the primary particles, the powders have another kind of very fine particle (brighter area)

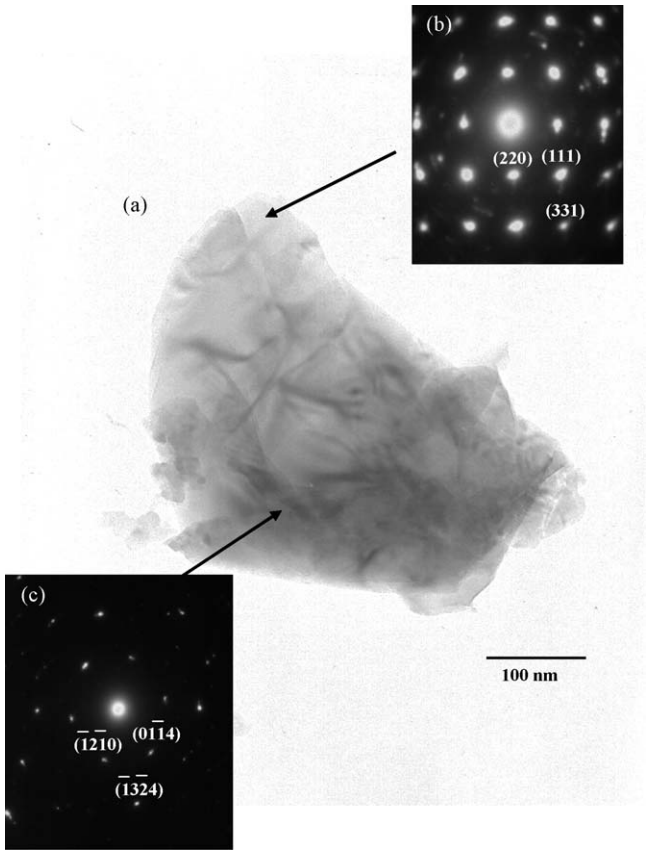

Fig. 11. (a) TEM micrograph of vibro-milling $Mg_4Nb_2O_9$ particles and SAED patterns of (b) the major phase of hexagonal $Mg_4Nb_2O_9$ (zone axes [$\bar{8}\,\bar{4}$ 1]) and (c) the minor phase of orthorhombic $MgNb_2O_6$ (zone axes [0 0 1]).

with diameter of about 93 nm (it is referred to as nanoparticle). Only single nanoparticle can be observed in this TEM micrograph. In contrast, the vibro-milling powders consist mainly of submicrometer-sized primary particles accompanying with several dark and bright areas (Fig. 11(a)). The particle diameters in these TEM micrographs are also given in Table 2. It is possible to observe in Table 2 that the particle sizes determined by XRD technique have almost the same value in nanometer range for different milling methods. It should be noted that the calculated values from the XRD technique were determined from the XRD peak-broadening and actually present the crystallite sizes [33], whereas the values from other methods as listed in Table 2 represent the particle sizes, which include polycrystalline, agglomerates, defects, etc. [23,33]. In addition, these other methods also provide information on particle morphology and powder quality, which is not available from the XRD technique alone. Thus the combination of the data listed in Table 2 provides better assessment of the powders produced from different milling techniques.

By employing a combination of both selected area electron diffraction (SAED) and crystallographic analysis, the major phase of hexagonal $Mg_4Nb_2O_9$ (Figs. 10(b) and 11(b)) and minor phase of $MgNb_2O_6$ nanoparticles in orthorhombic form were identified (Figs. 10(c) and 11(c)), in good agreement with the XRD results. In general, EDX analysis using a 20 nm probe from a large number of particles of the two calcined powders

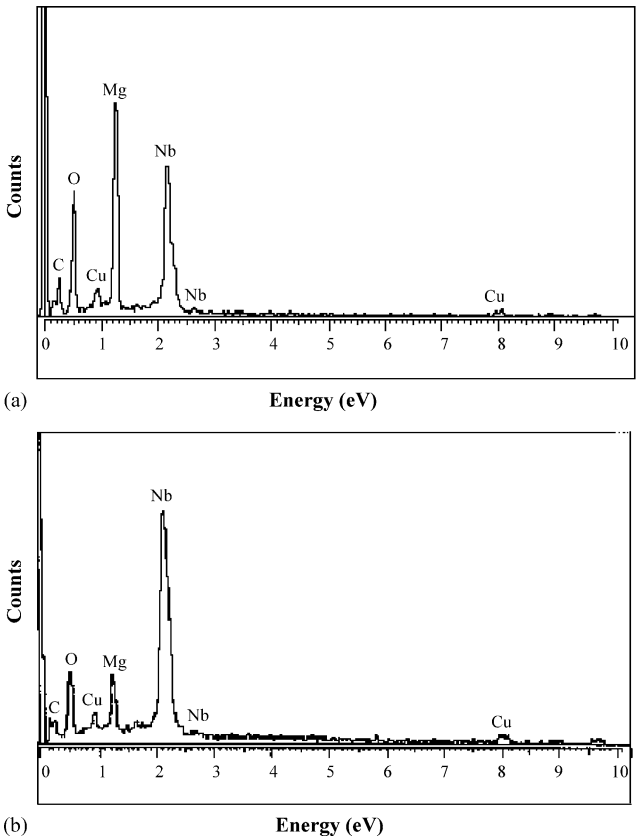

Fig. 12. EDX analysis of (a) the major phase $Mg_4Nb_2O_9$ and (b) the minor phase $MgNb_2O_6$ (some signals of C and Cu come from coated electrodes and sample stubs, respectively).

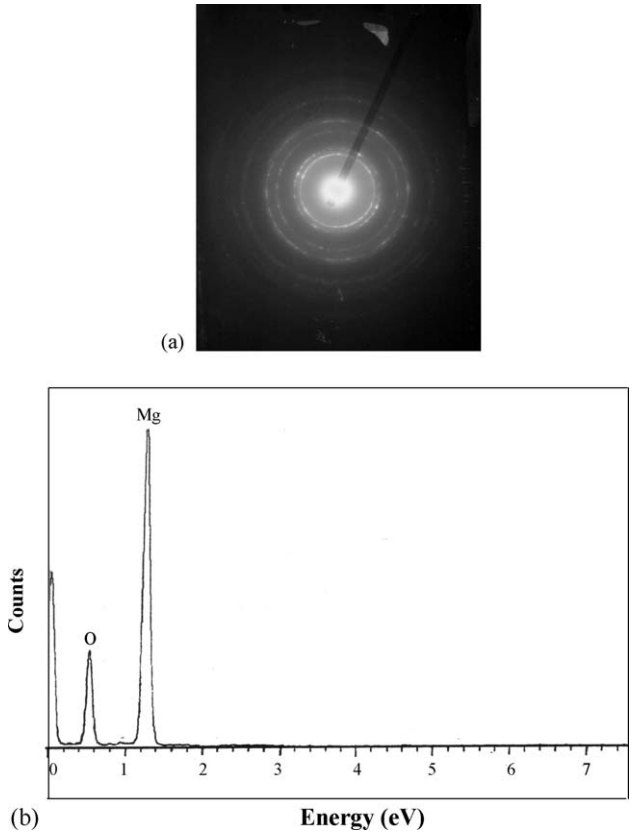

Fig. 13. (a) SAED pattern of the unreacted MgO phase and (b) EDX analysis of the MgO-rich phase.

confirmed the parent composition to be $Mg_4Nb_2O_9$ (Fig. 12(a)). Minor phase of $MgNb_2O_6$ was also confirmed by this technique, as illustrated in Fig. 12(b). It is interesting to noted that limited evidence for the presence of the unreacted starting precursor MgO (Fig. 13(a) the ring patterns indicating the polycrystalline nature and hence fine scale of this phase Fig. 13(b)) in good agreement with the SEM results, and nano-scale particle of $MgNb_2O_6$ was also found in the TEM–EDX investigation, even though this could not be detected by XRD. It is, therefore, intriguing to note the advantage of a combination between TEM and EDX techniques, which lies in its ability to reveal microstructural features often missed by the XRD diffraction method which requires at least 5 wt.% of the component [23].

4. Conclusions

It has been shown that pure corundum $Mg_4Nb_2O_9$ powders can be formed by the reaction of niobium oxide with magnesium oxide via either ball-milling or vibro-milling methods at about 1050–1100 °C. Evidence for the formation of a columbite $MgNb_2O_6$ minor phase, which coexists with the corundum $Mg_4Nb_2O_9$ parent phase, is found at calcination temperatures ranging from 800 to 1050 °C. Between the two methods, it is seen that lower optimized calcination temperature and dwell time for the production of pure $Mg_4Nb_2O_9$ powders can be obtained by using vibro-milling method. This technique was superior to ball-milling as measured by the required minimum firing temperature

and dwell time for the yield of single-phase $Mg_4Nb_2O_9$ in the powders together with the smallest particle size achieved.

Acknowledgments

The authors gratefully acknowledge the Thailand Research Fund (TRF), the Department of Physics, the Faculty of Science and the Graduate School, Chiang Mai University for all supports.

References

[1] S. Pagola, R.E. Carbonio, J.A. Alonso, M.T. Fernández-Díaz, J. Solid State Chem. 134 (1997) 76.
[2] A. Yokoi, H. Ogawa, A. Kan, H. Ohsato, Y. Higashida, J. Eur. Ceram. Soc. 25 (2005) 2871.
[3] C.W. Hwang, S.K. Lee, Japanese Patent No. JP97-293619 (1998).
[4] A. Wachtel, J. Electrochem. Soc. 111 (1964) 534.
[5] Y.C. You, N. Park, K.H. Jung, H.L. Park, K.C. Kim, S.I. Mho, T.W. Kim, J. Mater. Sci. Lett. 13 (1994) 1682.
[6] P.A. Joy, K. Sreedhar, J. Am. Ceram. Soc. 80 (1997) 770.
[7] C.H. Lu, H.S. Yang, Mater. Sci. Eng. B 84 (2001) 159.
[8] S.L. Swartz, T.R. Shrout, Mater. Res. Bull. 17 (1982) 1245.
[9] S. Ananta, N.W. Thomas, J. Eur. Ceram. Soc. 19 (1999) 155.
[10] G. Haertling, J. Am. Ceram. Soc. 82 (1999) 797.
[11] A.J. Moulson, J.M. Herbert, Electroceramics, 2nd ed., Wiley, Chichester, 2003.
[12] K. Uchino, Piezoelectrics and Ultrasonic Applications, Kluwer, 1998.
[13] E. Goo, T. Yamamoto, K. Okazaki, J. Am. Ceram. Soc. 69 (1986) C-188.
[14] D.H. Kang, K.H. Yoon, Ferroelectrics 87 (1988) 255.
[15] P.A. Joy, Mater. Lett. 32 (1997) 347.
[16] Y.C. You, H.L. Park, Y.G. Song, H.S. Moon, G.C. Kim, J. Mater. Sci. Lett. 13 (1994) 1487.
[17] K. Sreedhar, N.R. Pavaskar, Mater. Lett. 53 (2002) 452.
[18] N.K. Kim, Mater. Lett. 32 (1997) 127.
[19] N. Kumada, K. Taki, N. Kinomura, Mater. Res. Bull. 35 (2000) 1017.
[20] S. Ananta, Mater. Lett. 58 (2004) 2530.
[21] S. Ananta, Mater. Lett. 58 (2004) 2834.
[22] Y.H. Yu, C.D. Feng, W.L. Yao, Y. Yang, C.E. Li, H.X. Yan, J. Mater. Sci. Lett. 20 (2001) 2189.
[23] H.P. Klug, L.E. Alexander, X-ray Diffraction Procedures, 2nd ed., Wiley, New York, 1974.
[24] J.S. Reeds, Principles of Ceramics Processing, 2nd ed., Wiley, New York, 1995.
[25] D. Richerson, Modern Ceramic Engineering, 3rd ed., CRC Press, New York, 2005.
[26] Powder Diffraction File No. 71–1176, International Centre for Diffraction Data, Newton Square, PA, 2000.
[27] Powder Diffraction File No. 28–317, International Centre for Diffraction Data, Newton Square, PA, 2000.
[28] S. Ananta, Mater. Lett. 58 (2004) 2781.
[29] Powder Diffraction File No. 33–875, International Centre for Diffraction Data, Newton Square, PA, 2000.
[30] Powder Diffraction File No. 38–1459, International Centre for Diffraction Data, Newton Square, PA, 2000.
[31] S. Ananta, R. Tipakontitikul, T. Tunkasiri, Mater. Lett. 57 (2003) 2637.
[32] S. Ananta, R. Brydson, N.W. Thomas, J. Eur. Ceram. Soc. 19 (1999) 355.
[33] B.D. Cullity, Elements of X-Ray Diffraction, 2nd ed., Addison-Wesley Publishing Company Inc., Reading, 1978.

INSTITUTE OF PHYSICS PUBLISHING JOURNAL OF PHYSICS D: APPLIED PHYSICS
J. Phys. D: Appl. Phys. **39** (2006) 3097–3102 doi:10.1088/0022-3727/39/14/032

Change of dielectric properties of ceramics in lead magnesium niobate-lead titanate system with compressive stress

Rattikorn Yimnirun, Muangjai Unruan, Yongyut Laosiritaworn and Supon Ananta

Department of Physics, Faculty of Science, Chiang Mai University, Chiang Mai 50200, Thailand

Received 27 February 2006, in final form 12 June 2006
Published 30 June 2006
Online at stacks.iop.org/JPhysD/39/3097

Abstract
Effects of compressive stress on the dielectric properties of PMN–PT ceramics were investigated. The ceramics with the formula $(1-x)Pb(Mg_{1/3}Nb_{2/3})O_3$-$(x)PbTiO_3$ or $(1-x)$PMN–(x)PT ($x = 0.1$–0.5) were prepared by a conventional mixed-oxide method and then characterized with x-ray diffraction (XRD) and scanning electron microscopy. Dense perovskite-phase PMN–PT ceramics with uniform microstructure were successfully obtained. The dielectric properties under compressive stress were observed at stress up to 230 MPa using a home-built compressometer. The experimental results revealed that the superimposed compression stress significantly reduced both the dielectric constant and the dielectric loss tangent of 0.9PMN–0.1PT ceramic, while the changes were not as significant in the other PMN–PT ceramic compositions. In addition, the dielectric properties were considerably lowered after a stress cycle. Since change in the dielectric properties with applied stress was attributed to the competing influences of the intrinsic and the extrinsic contributions, the observations were mainly interpreted in terms of domain switching through non-180° domain walls, de-ageing, clamping of domain walls and the stress induced decrease in the switchable part of spontaneous polarization.

(Some figures in this article are in colour only in the electronic version)

1. Introduction

A family of materials which are of great interest due to their high polarizabilities is the lead-based relaxor ferroelectrics, particularly lead magnesium niobate, $Pb(Mg_{1/3}Nb_{2/3})O_3$ (PMN) and its solid solution with lead titanate, $PbTiO_3$ (PT), the so-called PMN–PT. These compounds have dielectric constants in excess of 20 000, making them potential candidates for capacitive applications. In addition, they also exhibit electrostrictive behaviour at temperatures above their phase transition temperatures. This behaviour extends their use to transducer and actuator applications [1–5]. $(1-x)Pb(Mg_{1/3}Nb_{2/3})O_3$-$(x)PbTiO_3$ or $(1-x)$PMN–(x)PT ceramic compositions with $x < 0.2$ have been studied for electrostrictive applications [4–7], while those with $x > 0.2$ can be utilized as piezoelectric materials [4, 6, 8, 9]. The differences between the electrostrictive and piezoelectric compositions of PMN–PT are due to differences in the degree of long-range polar order [4, 7, 10]. In the compositions with lower PT content, relaxor ferrfoelectric characteristics with polar clusters or nanodomains are observed [4, 11, 12]. On the other hand, long-range polar order with normal micrometre-sized ferroelectric domains exists in the compositions with higher PT content [4, 9, 10].

Practically, when used in specific applications PMN–PT ceramics are often subjected to mechanical loading, either deliberately in the design of the device itself or because the device is used to change shapes as in many smart structure applications or the device is used under environmental stresses [8, 13–17]. A prior knowledge of how the material properties change under different load conditions is crucial for the proper design of a device and for suitable selection of

materials for a specific application. Despite this fact, material constants used in any design calculations are often obtained from a stress-free measuring condition, which in turn may lead to incorrect or inappropriate actuator and transducer designs. It is therefore important to determine the properties of these materials as a function of applied stress. Previous investigations on the stress-dependence electrical properties of many ceramic systems have clearly emphasized the importance of this matter [7, 15, 18–23]. Recently, the uniaxial stress dependence of dielectric properties has been investigated in materials such as BT, PZT, PMN and PMN–PZT [19–22]. The results clearly showed that the effects of stress on the dielectric properties depended significantly on ceramic compositions and stress levels. Since PMN–PT ceramics are practically very important, there have been previous reports on the electromechanical properties of electrostrictive 0.9PMN–0.1PT and piezoelectric 0.7PMN–0.3PT ceramics under various mechanical and electrical loading conditions [7,15,23,24]. However, there has been no systematic study on the influence of an applied stress on the dielectric properties of ceramics in the PMN–PT system. Therefore, it is the aim of this study to determine the dielectric properties of the $(1-x)$PMN–(x)PT ceramics as a function of compressive stress.

2. Experimental method

PMN–PT ceramics were prepared from starting PMN and PT powders by a conventional mixed-oxide method. Perovskite-phase PMN powders were obtained from the columbite method, while PT powders were prepared by a simple mixed-oxide method [25]. To obtain the perovskite-phase PMN, the magnesium niobate powders were first prepared by mixing MgO (99.0%) and Nb_2O_5 (99.9%) powders and then calcining the mixed powders at 1100 °C for 3 h, to yield so called columbite powders ($MgNb_2O_6$). After that, the columbite powders were mixed with PbO (99.9%) by the ball-milling method and calcined at 800 °C for 1 h to form the perovskite-phase PMN powders. With a simple mixed-oxide route, PT powders were prepared from PbO (99.9%) and TiO_2 (99.9%) starting powders. These powders were ball-milled and calcined at 600 °C for 1 h.

The $(1-x)Pb(Mg_{1/3}Nb_{2/3})O_3$–$(x)PbTiO_3$ ceramics were then prepared from starting PMN and PT powders by the mixed-oxide method. After mixing the powders by the ball-milling method and drying process, the mixed powders were pressed hydraulically to form disc-shaped pellets 10 mm in diameter and 2 mm thick, with 3 wt% polyvinyl alcohol as a binder. The pellets were placed on the alumina powder-bed inside alumina crucible and surrounded with atmosphere powders of the same composition. Finally, for optimization purposes the pellets were sintered at temperatures between 1220 and 1240 °C for 2 h. Optimum sintering conditions for all ceramics were established by identifying the conditions for maximizing both the bulk density and the yield of perovskite. However since the PMN–PT compositions having high PT content in the range $0.6 \leqslant x \leqslant 0.9$ could not be fabricated in a bulk form of high density, these compositions could not be characterized any further for the rest of the study. Their comparatively large c/a values, which give rise to serious internal stress, are responsible for the frequent crack

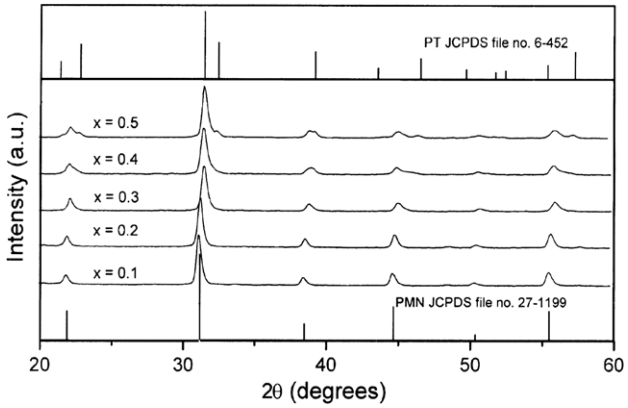

Figure 1. XRD diffraction patterns of the sintered $(1-x)$PMN–(x)PT ceramics.

developments around the phase transition temperature during the cooling of these sintered samples. In the present study, only compositions in the pseudo-binary system $(1-x)$PMN–xPT ($0.1 \leqslant x \leqslant 0.5$) have been successfully fabricated from the calcined $(1-x)$PMN–xPT powders, employing a normal sintering method, i.e. the pressureless sintering technique. Similar optimum sintering conditions of 1240 °C for 2 h with 15 °C min^{-1} were observed in samples at compositions of x between 0.1 to 0.3 while for compositions with PT content of $x = 0.4$ and 0.5 the optimum condition was found at 1220 °C for 2 h with 15 °C min^{-1} [25]. The phase-formation of the sintered ceramics was studied by the x-ray diffraction (XRD) technique. The densities of sintered specimens were measured by Archimedes method. The microstructure analyses were undertaken by scanning electron microscopy (SEM: JEOL Model JSM 840A). The grain size was determined from SEM micrographs by a linear intercept method.

Before studying the dielectric properties, the specimens were lapped to obtain parallel faces. After coating with silver paint as electrode at the faces, the specimens were heated at 750 °C for 12 min to ensure contact between the electrode and the surface of the ceramic. All the ceramics were then poled to a full remanent state prior to testing. A compressometer was constructed [19, 26, 27] to study the effects of the compressive stress on the dielectric properties of the ceramics. The dielectric properties were measured by LCR-meter (Instrek LCR-821). The room temperature (25 °C) capacitance and the dielectric loss tangent were obtained at a frequency of 1 kHz under compressive stress up to 230 MPa. The dielectric constant was then calculated from a parallel-plate capacitor equation, e.g. $\varepsilon_r = Cd/\varepsilon_0 A$, where C is the capacitance of the specimens, d and A are, respectively, the thickness and the area of the electrode and ε_0 is the dielectric permittivity of vacuum (8.854×10^{-12} F m^{-1}).

3. Results and discussion

The XRD patterns of sintered ceramics with maximum perovskite phase and bulk density are presented in figure 1, where complete crystalline solutions of perovskite structure are formed throughout the composition range between $x = 0.1$ and 0.5. In general, only a (pseudo) cubic symmetry is observed at low values of PT concentration, in good

Table 1. Characteristics of PMN–PT ceramics with optimized processing conditions.

Ceramic	Density[a] ($g\,cm^{-3}$)	Grain size range (μm)	Average grain size[b] (μm)	T_C (1 kHz) (°C)	Stress-free dielectric properties[c] ε_r	tan δ
0.9PMN–0.1PT	7.98	0.42–3.66	2.07	45	10 713	0.083
0.8PMN–0.2PT	7.94	0.44–3.02	2.02	100	2 883	0.079
0.7PMN–0.3PT	7.86	0.41–2.80	1.72	150	1 976	0.045
0.6PMN–0.4PT	7.83	0.41–3.45	1.93	210	1 909	0.031
0.5PMN–0.5PT	7.78	0.48–3.72	2.11	260	1 375	0.022

[a] The estimated precision of the density is ±1%.
[b] The estimated precision of the average grain size is ±1%.
[c] Measured at 1 V mm^{-1} (25 °C and 1 kHz).

agreement with other workers [28, 29]. By the influence of PT, however, several peaks split for $x \geqslant 0.4$, indicating the development of tetragonal symmetry, consistent with earlier work on PMN–PT ceramics [9, 30]. As listed in table 1, density values are found to decrease slightly with x (in units of grams per centimetre cube the value decreases gradually from 7.98 in 0.9PMN–0.1PT to 7.78 in 0.5PMN–0.5PT). SEM-micrographs of fractured surfaces of all compositions are shown in figure 2. In general, similar microstructure characteristics are observed in these samples, i.e. uniformly sized grains with a high degree of grain close-packing. Almost no abnormal grain growth is observed. All ceramic compositions display very similar grain size range between 0.4 and 3.7 μm. By applying the linear intercept method to SEM micrographs of polished and thermally etched specimens, mean grain sizes of about 1.72–2.11 μm are estimated for these samples as given in table 1. These characteristics indicate that dense perovskite-phase PMN–PT ceramics with uniform microstructure have been obtained. Since the physical and microstructure features of all ceramic compositions are not significantly different, these parameters should not play an important role in the composition-dependent dielectric properties under the compressive stress discussed in the following paragraphs.

The room temperature dielectric properties measured under stress-free condition are listed in table 1. It is clearly seen that the dielectric constant (ε_r) of $(1-x)$PMN–(x)PT ceramics decreases with increasing PT content. The dielectric constant decreases from 10713 in 0.9PMN–0.1PT to 1375 in 0.5PMN–0.5PT. In addition, a decreasing trend has been observed for the stress-free dielectric loss tangent (tan δ), which shows a decrease in value from 0.083 in 0.9PMN–0.1PT to 0.022 in 0.5PMN–0.5PT. This observation could be attributed to a high dielectric constant of PMN and a closer to ambient temperature T_C for PMN–PT compositions with higher PMN content [1, 4, 5]. Comparable stress-free dielectric properties have also been reported in earlier publications [2, 5, 29, 30].

The experimental results of the compressive stress dependence of the dielectric properties during loading and unloading for the ceramics in the PMN–PT system are displayed in figures 3 and 4. For better comparison, the dielectric properties of each composition under stress are normalized to the stress-free values. Clearly, there is a considerable change in both the dielectric constant and the dielectric loss tangent when the compressive stress increases from 0 to 230 MPa and returning to stress-free condition. As

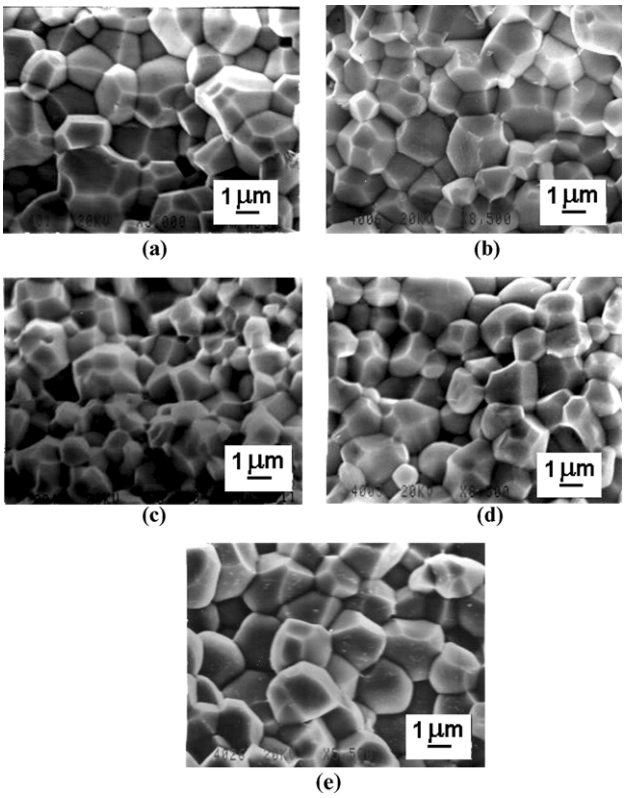

Figure 2. SEM micrographs of fracture surfaces of $(1-x)$PMN–(x)PT ceramics (*a*) 0.9PMN–0.1PT; (*b*) 0.8PMN–0.2PT; (*c*) 0.7PMN–0.3PT; (*d*) 0.6PMN–0.4PT and (*e*) 0.5PMN–0.5PT.

depicted in figure 3, the changes of the dielectric constant with the stress can be divided into two groups. For 0.9PMN–0.1PT ceramic, the dielectric constant decreases drastically with the stress. The dielectric constant decreases more than 70% when the stress reaches 230 MPa and only returns to slightly less than 50% of its original value when the stress is removed. The changing of the dielectric constant with increasing and decreasing stress does not follow the same path. On the other hand, for other PMN–PT ceramics, i.e. with x values of 0.2–0.5, the change is minimal. The dielectric constant is actually rather stable within this range of the stress. The dielectric constant of these compositions initially increases then decreases with very little difference in the dielectric constant between stress-free and maximum stress

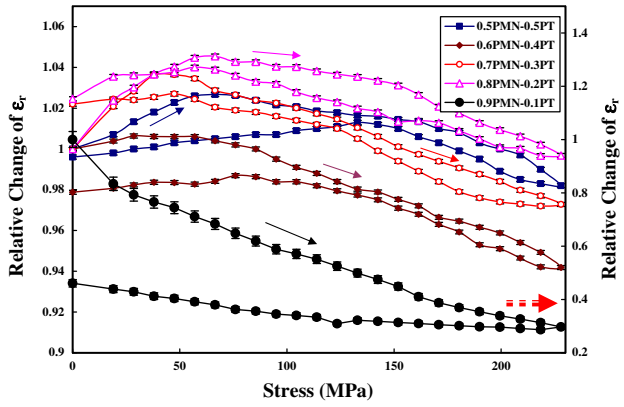

Figure 3. Relative changes of the dielectric constant (ε_r) with compressive stress for $(1-x)$PMN–(x)PT ceramics (measured at 25 °C and 1 kHz; secondary Y-axis is only for 0.9PMN–0.1PT and solid arrows indicate loading direction).

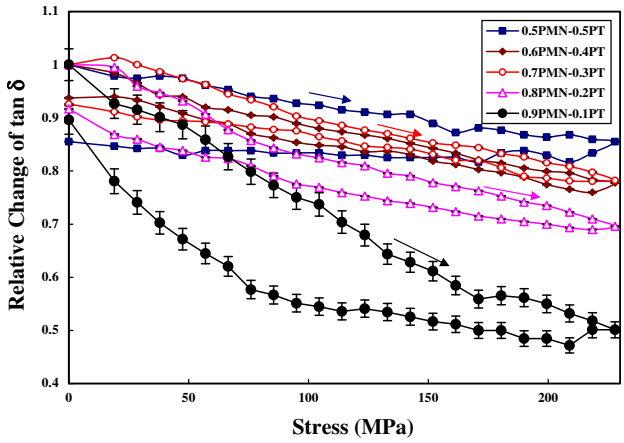

Figure 4. Relative changes of dielectric loss tangent (tan δ) with compressive stress for $(1-x)$PMN–(x)PT ceramics (measured at 25 °C and 1 kHz; solid arrows indicate loading direction).

conditions. In addition, the dielectric constants during loading and unloading are not significantly different.

Since the dielectric constant of the sample was measured through the capacitance, there is a change in sample capacitance due to the geometrical deformation under stress. The variation of the sample dielectric constant ($\Delta\varepsilon_r$) can be expressed as $\varepsilon_r^* X^*((1+2\upsilon)/E)$, where X is the applied stress, υ is the Poisson's ratio and E is the Young's modulus [26, 31]. By applying the estimated values of $\upsilon \sim 0.3$ and $E \sim 100$ GPa for PMN–PT ceramics [7, 23, 24, 32] and ε_r given in table 1, it can be estimated that at the maximum stress of 230 MPa, the variation in the sample dielectric constant due to the geometrical deformation is <0.5%. Therefore, this variation should not be an important factor in the variation of the dielectric constant under stress seen in figure 3.

Figure 4 shows the results of the compressive stress dependence of the dielectric loss tangent. The dielectric loss tangent decreases monotonously with increasing the stress and then increases slightly when stress is removed. The dielectric loss tangent is also found to decrease considerably after a stress cycle. This is clearly seen in 0.9PMN–0.1PT ceramics, where the change in the dielectric loss tangent value is very significant, as it decreases about 50% at the maximum stress and almost returns to its original value after a stress cycle. The changes in the other compositions are less significant with increasing PT content.

It is also noticed that the changes in the dielectric properties with the compressive stress obtained in this study are in parts similar to those for the $(1-x)$PMN–(x)PZT system in the earlier investigation [19]. By comparison, the 0.9PMN–0.1PT behaves more like PMN-rich compositions in that study, while the other PMN–PT compositions act more like the PZT-rich compositions. It should also be noted that the T_C range of 16–160 °C for the $(1-x)$PMN–(x)PZT system with $x = 0.1$–0.7 [33, 34] is nearly similar to that of the PMN–PT ceramics used in this study, as listed in table 1. More importantly, it is interesting to observe that a mixture of different normal and relaxor ferroelectrics responds to the applied stress in a similar manner.

To understand these experimental results, at least qualitatively, various effects have to be considered. Normally, the properties of ferroelectric materials are derived from both the intrinsic contribution of domains and extrinsic contributions of re-polarization and growth of micro-polar regions [19–23]. When a compressive stress is applied to the ferroelectric materials, the domain structure in the materials will change to maintain the domain energy at a minimum; during this process some of the domains engulf other domains or change shape irreversibly. Under the applied stress, the domain structure of ferroelectric ceramics may undergo domain switching through non-180° domain walls, de-ageing, clamping of domain walls and stress induced decrease in the switchable part of spontaneous polarization [21, 23, 35].

The situation for the PMN–PT system is quite complex because this system is a mixing between the relaxor ferroelectric PMN and the normal ferroelectric PT. Therefore, there is a competing mechanism between the two types of materials, depending upon temperature and composition. Since 0.9PMN–0.1PT is a relaxor ferroelectric with $T_C \sim 45$ °C and the experiment was carried out at room temperature (~25 °C) which is slightly below T_C, the experimental observations, which show decreases in both dielectric constant and dielectric loss tangent with increasing stress, can be attributed to competing influences of the intrinsic contribution of the non-polar matrix and the extrinsic contribution of re-polarization and growth of micro-polar regions. Since the dielectric response of both contributions is affected by the applied stress in an opposite way, the behaviour of 0.9PMN–0.1PT depends on the ratio between the micro-polar region and the non-polar matrix, in this case the non-polar matrix still dominates [21, 22]. Hence, the dielectric responses of the 0.9PMN–0.1PT ceramic are observed to decrease significantly with increasing compressive stress, as seen in figures 3 and 4. Earlier works on PMN and 0.9PMN–0.1PT ceramics also reported a similar observation [22, 23]. However, under stress as high as 230 MPa microcracks may develop, particularly in 0.9PMN–0.1PT, which in turn could lead to a significant change in the dielectric properties. Therefore, an additional experiment was carried out to investigate the existence of the microcracks. The stressed specimens were annealed at 300 °C for 3 h [36], then poled at the same condition used earlier. The dielectric properties were re-measured under a stress-free condition. The results showed a full recovery of the dielectric

properties, within experimental errors. This indicated that there were no microcracks in the stressed specimens.

For the other PMN–PT compositions with higher T_C, the extrinsic contribution of re-polarization and growth of micro-polar regions becomes dominant. When the compressive stress is applied in the direction parallel to the poling direction, the stress will move some of the polarization away from the poling direction resulting in a change in domain structures [20]. This change increases the non-180° domain wall density. Hence increase in the dielectric constant is observed. The de-ageing mechanism, which also increases the dielectric constant, is also expected to play a role here. After poling, ceramics undergo an ageing process during which some of the domain walls become pinned by impurities and structural imperfections. When a large enough stress is applied to the aged samples, it causes structural changes and redistribution of impurities [21]. As a result, the domain walls that were pinned during ageing can become active again. This de-ageing can increase dielectric responses [20, 23]. Therefore, a combination of the domain switching and the de-ageing mechanisms is believed to be a reason for the slight increase in the dielectric constant during low-stress application. With further increase in the stress, the stress clamping of domain walls, which results in a decrease of domain wall mobility, and the stress induced decrease in the switchable part of spontaneous polarization are expected to play a role in the decrease in the dielectric constant [21,23,35]. Therefore, the dielectric constant of these compositions is seen to be rather stable with the applied stress, as seen in figure 3. Similar observation has also been reported in soft PZT [20,23].

The cause of the stress dependence of the dielectric loss tangent is a little more straightforward than that of the dielectric constant. As depicted in figure 4, the clamping of the domain walls under the compressive stress results in a decrease of domain wall mobility and reduces the dielectric loss tangent [21]. This is a reversible effect with the domain wall mobility returning to near original values when the applied stress is removed, as seen in figure 4 that dielectric loss tangents return to near original values after a stress cycle. In addition, a significant decrease in the dielectric constant after a full cycle of stress application has been observed, particularly in 0.9PMN–0.1PT, and attributed to the stress induced decrease in the switchable part of the spontaneous polarization at high stress [23, 35].

4. Conclusions

In this study, the dielectric properties of $(1-x)\mathrm{Pb}(\mathrm{Mg}_{1/3}\mathrm{Nb}_{2/3})\mathrm{O}_3$–$(x)\mathrm{PbTiO}_3$ or $(1-x)$PMN–(x)PT ($x = 0.1$–0.5) ceramics prepared by a conventional mixed-oxide method are measured under compressive stress from 0 to 230 MPa. Phase formation behaviour and microstructure features of these ceramics are studied by an XRD and SEM methods, respectively. Perovskite-phase PMN–PT ceramics with homogeneous microstructure are obtained. The dielectric properties of 0.9PMN–0.1PT ceramic are found to decrease significantly with compressive stress, while the changes are not as significant in the other PMN–PT ceramic compositions. In addition, the dielectric properties are considerably lowered after a stress cycle. The change in dielectric properties with the applied stress is attributed to competing influences of intrinsic and extrinsic contributions. The observations are then mainly interpreted in terms of domain switching through non-180° domain walls, de-ageing, clamping of domain walls and the stress induced decrease in the switchable part of spontaneous polarization.

Acknowledgments

This work is supported by the Thailand Research Fund (TRF). Additional support from the Faculty of Science and Graduate School of Chiang Mai University are gratefully acknowledged. The authors would also like to express their gratitude to Aurawan Udomporn for help in sample preparation and characterization.

References

[1] Xu Y H 1991 *Ferroelectric Materials and Their Applications* (Amsterdam: North Holland)
[2] Moulson A J and Herbert J M 2003 *Electroceramics: Materials, Properties, Applications* (Chichester: Wiley)
[3] Haertling G H 1999 *J. Am. Ceram. Soc.* **82** 797
[4] Cross L E 1987 *Ferroelectrics* **76** 241
[5] Jang S 1979 *PhD Thesis* Pennsylvania State University
[6] Uchino K 1997 *Piezoelectric Actuators and Ultrasonic Motors* (Boston, MA: Kluwer)
[7] Viehland D, Li J, McLaughlin E, Powers J, Janus R and Robinson H 2004 *J. Appl. Phys.* **95** 1969
[8] Shrout T R, Chang Z, Kim N and Markgraf S 1990 *Ferroelectr. Lett. Sect.* **12** 63
[9] Viehland D, Kim M, Xu Z and Li J 1995 *Appl. Phys. Lett.* **67** 2471
[10] Smolenskii G and Agranovskaya A 1960 *Sov. Phys. Solid State* **1** 1429
[11] Randall C, Barber D and Whatmore R 1987 *J. Microsc.* **45** 275
[12] Dai X, Xu Z and Viehland D 1994 *Phil. Mag.* B **70** 33
[13] Kuwata J, Uchino K and Nomura S 1982 *Japan. J. Appl. Phys.* **21** 1298
[14] Park S and Shrout T R 1997 *J. Appl. Phys.* **82** 1804
[15] Viehland D and Powers J 2001 *Appl. Phys. Lett.* **78** 3112
[16] Stansfield D 1991 *Underwater Electroacoustic Transducers* (Bath, UK: Bath University Press)
[17] Mitrovic M, Carmen G P and Straub F K 2001 *Int. J. Solids Struct.* **38** 4357
[18] Zhou D, Kamlah M and Munz D 2005 *J. Euro. Ceram. Soc.* **25** 425
[19] Yimnirun R, Ananta S, Meechoowas E and Wongsaenmai S 2003 *J. Phys. D: Appl. Phys.* **36** 1615
[20] Zhang Q M, Zhao J, Uchino K and Zheng J 1997 *J. Mater. Res.* **12** 226
[21] Yang G, Liu S F, Ren W and Mukherjee B K 2000 *Proc. SPIE Symp. on Smart Struct. Mater.* **3992** 103
[22] Steiner O, Tagantsev A K, Colla E L and Setter N 1999 *J. Euro. Ceram. Soc.* **19** 1243
[23] Zhao J and Zhang Q M 1996 *Proc. IEEE Int. Symp. Appl. Ferroelectr.* **2** 971
[24] Zhao J, Glazounov A E and Zhang Q M 1999 *Appl. Phys. Lett.* **74** 436
[25] Udomporn A 2004 *PhD Thesis* Chiang Mai University
[26] Yimnirun R, Moses P J, Meyer R J and Newnham R E 2003 *Rev. Sci. Instrum.* **74** 3429
[27] Yimnirun R, Ananta S, Ngamjarurojana A and Wongsaenmai S 2005 *Appl. Phys.* A **81** 1227
[28] Kong L B, Ma J, Zhu W and Tan O K 2002 *Mater. Res. Bull.* **37** 23
[29] Liou Y C 2003 *Mater. Sci. Eng.* B **103** 281
[30] Brown L F, Carlson R L, Sempsrott J M, Standford G T and Fitzgerald J J 1997 *Proc. IEEE Ultrason. Symp.* **1** 561

[31] Preu P and Haussuhl S 1983 *Solid State Commun.* **45** 619
[32] Viehland D and Powers J 2001 *J. Appl. Phys.* **89** 1820
[33] Yimnirun R, Ananta S and Loaratanakul P 2004 *Mater. Sci. Eng.* B **112** 79
[34] Yimnirun R, Ananta S and Loaratanakul P 2005 *J. Euro. Ceram. Soc.* **25** 3225
[35] Yimnirun R, Loasiritaworn Y and Wongsaenmai S 2006 *J. Phys. D: Appl. Phys*. **39** 759
[36] Liao J, Jiang X P, Xu G S, Luo H S and Yin Q R 2000 *Mater. Charact.* **44** 453

Ferroelectrics, 331:9–18, 2006

ISSN: 0015-0193 print / 1563-5112 online
DOI: 10.1080/00150190600732850

Taylor & Francis
Taylor & Francis Group

Change in the Dielectric Properties of Normal and Relaxor Ferroelectric Ceramic Composites in BT-PZT and PMN-PZT Systems by an Uniaxial Compressive Stress

RATTIKORN YIMNIRUN*

Department of Physics, Faculty of Science, Chiang Mai University, Chiang Mai 50200, Thailand

Effects of an uniaxial compressive pre-stress on the dielectric properties of normal and relaxor ferroelectric ceramic composites in BT-PZT and PMN-PZT systems are investigated. The dielectric properties are observed under the compressive pre-stress levels up to 15 and 5 MPa for BT-PZT and PMN-PZT, respectively, using a uniaxial compressometer. Both the dielectric constant and the dielectric loss tangent of the BT-PZT ceramics increase significantly with increasing applied stress. Larger changes in the dielectric properties with the applied stress are observed in the PZT-rich compositions. For PMN-PZT ceramics, the dielectric constant of the PZT-rich compositions increases slightly, while that of the PMN-rich compositions decreases with increasing applied stress. On the other hand, changes in the dielectric loss tangent with stress are found to be compositional independent. The experimental results are explained with the domain wall motion and de-aging mechanisms from the application of the compressive pre-stress. More importantly, this study undoubtedly shows that the applied stress significantly influences the dielectric properties of both ceramic composite systems.

Keywords Dielectric properties; ferroelectrics; BT-PZT; PMN-PZT; uniaxial stress

Introduction

Among many smart systems, ceramic actuators and transducers are finding an increasingly wide range of applications. Ferroelectric ceramics have been established as good candidates for these applications. In many of these applications, ferroelectric ceramics are often subjected to mechanical loading, either deliberately in the design of the device itself or because the device is used to change shapes as in many smart structure applications or the device is used under environmental stresses [1–3]. Despite the fact, materials constants used in any design calculations are often obtained from a stress-free measuring condition, which in turn may lead to incorrect or inappropriate actuator and transducer designs. It is therefore important to determine the properties of these materials as a function of applied stress. Previous investigations on the stress-dependence dielectric and electrical properties of many ceramic systems, such as PZT and PMN-PT have clearly emphasized the importance of this matter [4, 5].

Received July 15, 2005; accepted October 31, 2005.
*Corresponding author. E-mail: rattikornyimnirun@yahoo.com

Among perovskite ferroelectric materials, barium titanate ($BaTiO_3$ or BT), lead zirconate titanate ($Pb(Zr_{1-x}Ti_x)O_3$ or PZT) and lead magnesium niobate ($Pb(Mg_{1/3}Nb_{2/3})O_3$ or PMN) ceramics have been investigated extensively and continuously since the late 1940s [6–9]. BT, PMN, and PZT are representative perovskite normal ferroelectric, relaxor ferroelectric, and piezoelectric prototypes, respectively, because of their excellent electrical properties. These three types of ceramics possess distinct characteristics that make each ceramic suitable for different applications. Forming a composite of these ferroelectrics has been one of the techniques employed to improve the properties of ferroelectric ceramics for specific requirements for each application.

One of the most studied piezoelectric compounds, $Pb(Zr_{0.52}Ti_{0.48})O_3$, a morphotropic phase boundary (MPB) compound of PZT, has great piezoelectric properties with a high Curie temperature (T_C) of $\sim$390°C. BT exhibits high dielectric constant and superior electrostrictive responses with a lower T_C ($\sim$120°C) [6–9]. In addition, BT is mechanically superior to PZT [10], whereas PZT ceramics can be easily sintered at temperature much lower than BT ceramics, which usually require high sintering temperatures even as high as 1400°C [10]. With their complementary features, the composites between PZT and BT are expected to exhibit better properties than those of the single-phase PZT and BT [6–9]. Furthermore, the properties can also be tailored over a wider range, by changing the compositions, to meet the strict requirements for specific applications [1, 6–9].

PMN exhibits a high dielectric constant and a broad range transition of dielectric constant, with temperature as a function of frequency [6]. In addition, PMN ceramics exhibit low loss and non-hysteretic characteristics. These make PMN a good candidate for a large number of applications, such as multilayer capacitors, sensors and actuators. However, PMN ceramics have relatively low electromechanical coupling coefficients, as compared to PZT. In contrast to PMN, PZT ceramics have found several actuator and transducer applications due to their high electromechanical coupling coefficients and higher temperature of operation [8, 9]. However, PZT ceramics also possess highly hysteretic behavior, which makes them unsuited for applications that require high delicacy and reliability. Furthermore, PZT ceramics normally have very high Curie temperature (T_C) in the vicinity of 400°C. Usually many applications require that T_C is close to ambient temperature. Therefore, there is a general interest to reduce the T_C of PZT ceramics to optimize their uses. With the complementary features of PMN and PZT, the composites between PMN and PZT are expected to synergetically combine the properties of both ceramics, which could exhibit more desirable piezoelectric and dielectric properties for several technologically demanding applications than single-phase PMN and PZT [11, 12].

Prior investigations have already revealed interesting results on the structure, and the dielectric and ferroelectric properties of the BT-PZT and PMN-PZT ceramics [10, 13–15]. However, there has been no report on the influences of the applied stress on the dielectric properties of ceramics in the BT-PZT and PMN-PZT systems. Therefore, this study is undertaken to investigate the influences of the uniaxial compressive pre-stress on the dielectric properties of ceramics in xBT-(1-x)PZT and xPMN-(1-x)PZT systems.

Experimental Procedure

The $BaTiO_3$–$Pb(Zr_{0.52}Ti_{0.48})O_3$ and $Pb(Mg_{1/3}Nb_{2/3})O_3$–$Pb(Zr_{0.52}Ti_{0.48})O_3$ ceramic composites are prepared from starting BT, PZT, and PMN powders by a mixed-oxide method. BT and PZT powders are first prepared by a conventional mixed-oxide method. On the other hand, perovskite-phase PMN powders are obtained via a well-known columbite

method [16]. Subsequently, the $(x)BaTiO_3$–$(1\text{-}x)Pb(Zr_{0.52}Ti_{0.48})O_3$ (when x = 0.0, 0.05, 0.15, 0.25, 0.35, 0.45, 0.55, 0.65, 0.75, 0.85, 0.95, and 1.0) and the $(x)Pb(Mg_{1/3}Nb_{2/3})O_3$–$(1\text{-}x)Pb(Zr_{0.52}Ti_{0.48})O_3$ (when x = 0.0, 0.1, 0.3, 0.5, 0.7, 0.9, and 1.0) ceramic composites are then prepared from the starting BT, PZT and PMN powders by the similar mixed-oxide method described above at various processing conditions. The detailed descriptions of powders and ceramics processing and characterizations are presented thoroughly in earlier publications [10, 14, 15].

For dielectric property characterizations, the sintered samples are lapped to obtain parallel faces, and the faces are then coated with silver paint as electrodes. The samples are heat-treated at 750°C for 12 min to ensure the contact between the electrodes and the ceramic surfaces. The samples are subsequently poled in a silicone oil bath at a temperature of 120°C by applying a dc field of 20 kV/cm for 30 min for BT-PZT ceramics, while for PMN-PZT ceramics the poling condition is 25 kV/cm for 30 min and field-cooled to room temperature. To study the effects of the uniaxial stress on the dielectric properties, the uniaxial compressometer is constructed. The uniaxial compressive stress applied parallel to the electric field direction is supplied by the servohydraulic load frame and the applied stress level is monitored with the pressure gage of the load frame. The details of the system are described elsewhere [17, 18]. The dielectric properties are measured through spring-loaded pins connected to the LCZ-meter (Hewlett Packard, model 4276A). The capacitance and the dielectric loss tangent are determined at a frequency of 1 kHz and room temperature (25°C). The dielectric constant is then calculated from a parallel-plate capacitor equation, e.g. $\varepsilon_r = Cd/\varepsilon_0 A$, where C is the capacitance of the sample, d and A are the thickness and the area of the electrode, respectively, and ε_0 is the dielectric permittivity of vacuum (8.854×10^{-12} F/m).

Experimental Results

The room temperature dielectric properties measured are under stress-free condition and are listed in Table 1. It is clearly seen that dielectric constant (ε_r) of xBT-(1-x)PZT ceramics increases with increasing BT content. The dielectric constant increases from 813 in PZT to 1429 in BT. For the PMN-PZT system, except for PZT, the dielectric constant increases steadily with increasing PMN content (ε_r increases from ~700 in 0.1PMN-0.9PZT to ~10300 in 0.9PMN-0.1PZT). The PMN is expected to show a larger value of the dielectric constant, but the lower value is attributed to the detrimental effect of the secondary pyrochlore phase. In addition, the stress-free dielectric loss tangent (tan δ) for BT-PZT system does not change significantly with compositions. Even though the dielectric loss tangent of PMN is very small, larger values of the dielectric loss tangent in PMN-PZT compositions is due mainly to lossy behavior of PZT. More details on the stress-free dielectric properties are available in other publications [14, 15].

The experimental results of the uniaxial compressive pre-stress dependence of the dielectric properties of the ceramics in BT-PZT system are shown in Figs. 1 and 2. There is a significant change of both the dielectric constant and the dielectric loss tangent of the ceramics when the applied stress increases from 0 to 15 MPa. The changes of the dielectric constant with the applied stress can be divided into three different groups. For PZT ceramic, the dielectric constant increases exponentially with applied stress. It can be seen that the dielectric constant is enhanced by approximately 8% at 15 MPa applied stress. For PZT-rich compositions (0.05BT-0.95PZT, 0.15BT-0.85PZT, 0.25BT-0.75PZT, 0.35BT-0.65PZT and 0.45BT-0.55PZT), the dielectric constant increases rather linearly with increasing applied

Table 1
Dielectric properties of xBT-(1-x)PZT and xPMN-(1-x)PZT ceramics measured at room temperature (25°C and 1 kHz) under stress-free condition

	xBT-(1-x)PZT											xPMN-(1-x)PZT							
x value	1	0.95	0.85	0.75	0.65	0.55	0.45	0.35	0.25	0.15	0.05	0	0	0.1	0.3	0.5	0.7	0.9	1
ε_r	1429	1288	1223	1077	1060	952	890	875	857	839	809	813	813	700	1400	2200	5600	10300	6000
$\tan\delta$	0.004	0.005	0.004	0.005	0.007	0.005	0.006	0.005	0.004	0.006	0.007	0.011	0.011	0.02	0.03	0.04	0.06	0.001	0.001

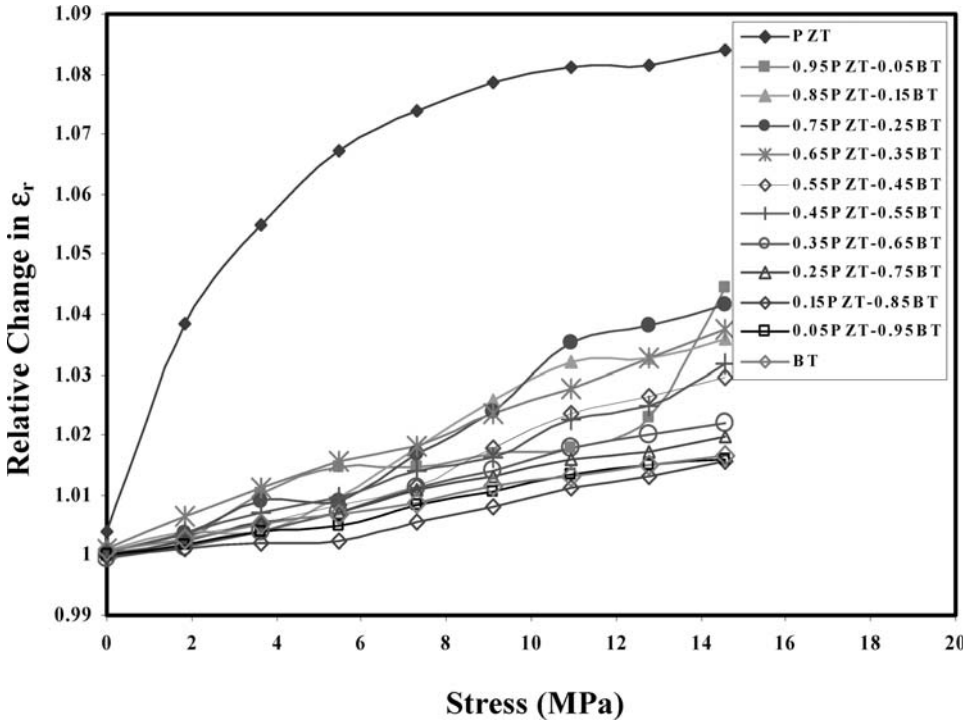

Figure 1. Relative changes of the dielectric constant (ε_r) as a function of compressive pre-stress for (x)BT-(1-x)PZT ceramics.

stress. The changes in the dielectric constant between 2 to 4% at 15 MPa applied stress are obviously smaller than that observed in PZT. For BT-rich compositions (BT, 0.95BT-0.05PZT, 0.85BT-0.15PZT, 0.75BT-0.25PZT and 0.65BT-0.35PZT), the dielectric constant only rises slightly (<2%) and in a linear manner when the applied stress increases to the maximum amplitude. The dielectric loss tangent for all compositions is found to increase significantly and non-linearly when the applied stress is raised from 0 to 15 MPa. The largest changes occur in PZT and 0.25BT-0.75PZT with the dielectric loss tangent enhancement of nearly 80% and 50%, respectively. For the other compositions, the increase in the dielectric loss tangent varies between 10 and 40% at 15 MPa applied stress. Again the changes of the dielectric loss tangent of BT-rich compositions are comparatively smaller than those of PZT-rich compositions, similar to what have been observed in the case of the dielectric constant. Similar experimental results have been reported previously for soft PZT [19, 20], un-doped PZT with various Zr/Ti ratio [21], and Ca-doped BT [22], in which the dielectric properties are found to increase with increasing magnitude of the compressive pre-stress.

The experimental results for the PMN-PZT ceramics are shown in Figs. 3 and 4. To prevent mechanical failures usually occurring in PMN-PZT, the experiments are carried out at the compressive pre-stress levels up to 5 MPa. However, there is a significant change of both the dielectric constant and the dielectric loss tangent of the ceramics even if the maximum applied stress is only 5 MPa. The changes of the dielectric constant

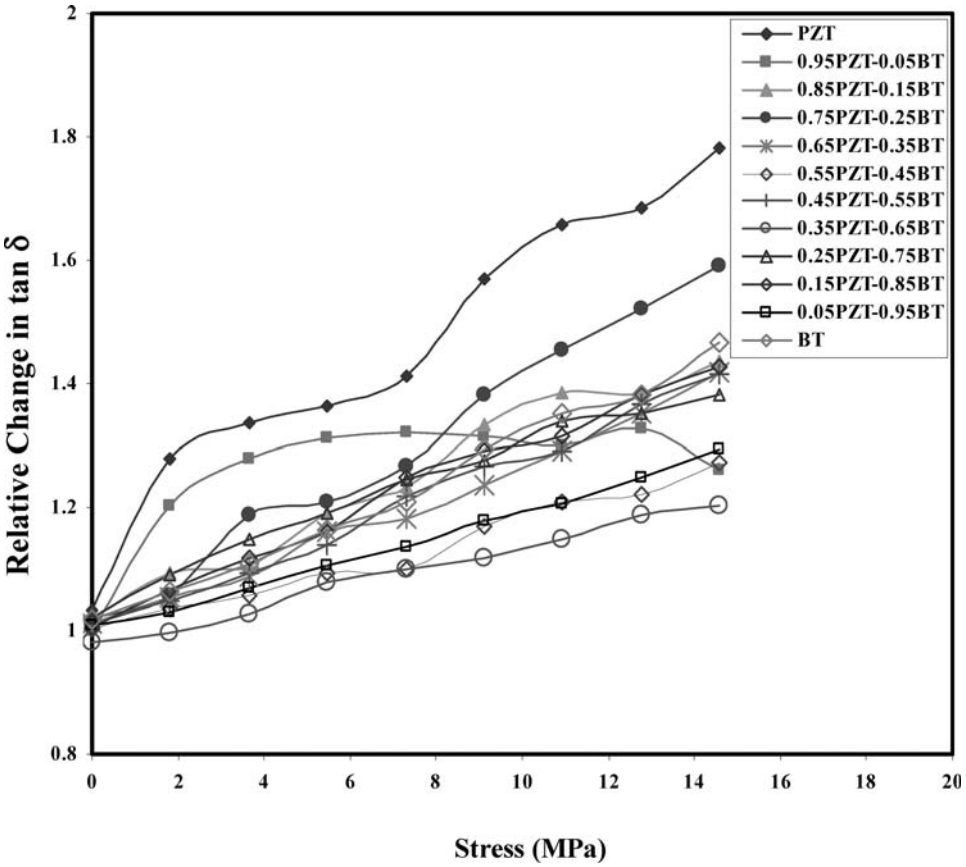

Figure 2. Relative changes of the dielectric loss tangent (tan δ) as a function of compressive pre-stress for (x)BT-(1-x)PZT ceramics.

with the compressive pre-stress can be divided into two different groups. For PMN-rich compositions (PMN, 0.9PMN-0.1PZT, and 0.7PMN-0.3PZT), the dielectric constant generally decreases with increasing applied stress. However, it should be noticed that only PMN and 0.9PMN-0.1PZT compositions show definite decreases in the dielectric constant, while the dielectric constant of the 0.7PMN-0.3PZT composition initially increases then decreases with very little difference in the dielectric constant between the 0 and 5 MPa. On the other hand, for PZT-rich compositions (PZT, 0.1PMN-0.9PZT, 0.3PMN-0.7PZT, and 0.5PMN-0.5PZT), the dielectric constant rises slightly when the compressive pre-stress increases from 0 to 1 MPa, and becomes relatively constant when the pre-stress level increases further. The dielectric loss tangent for most compositions, except for PMN and PZT, is found to first increase when the pre-stress is raised from 0 to 1 MPa, and then decrease with further increasing stress. However, for PZT ceramic the dielectric loss tangent increases monotonously with the increasing stress, while PMN ceramic exhibits a slight increase in the dielectric loss tangent followed by a drop, the turning point being around 2 MPa.

To understand these experimental results, various effects have to be considered. Normally, the properties of ferroelectric materials are derived from both the intrinsic

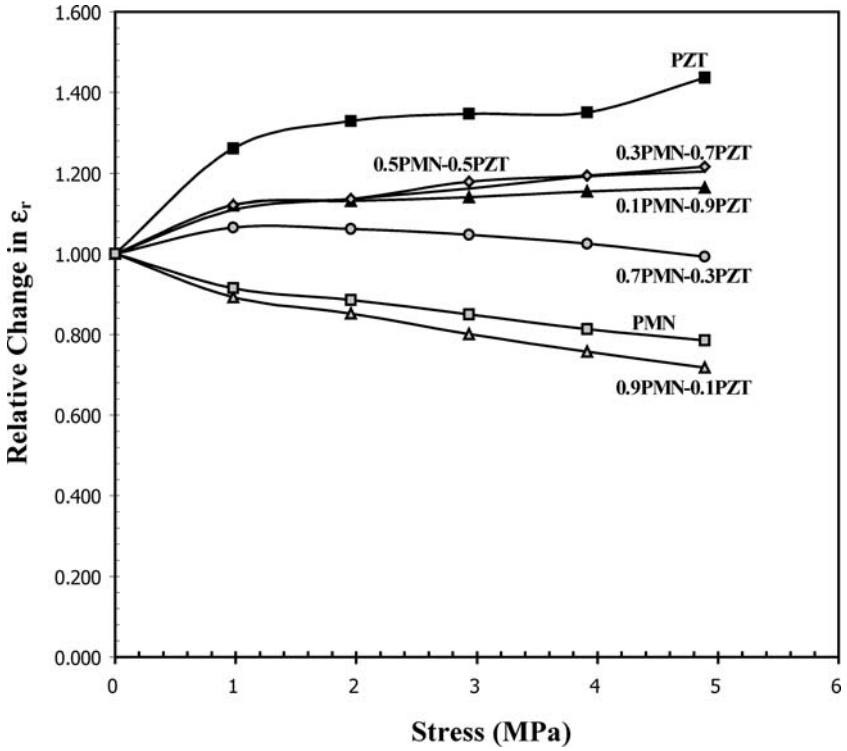

Figure 3. Relative changes of the dielectric constant (ε_r) as a function of compressive pre-stress for (x)PMN-(1-x)PZT ceramics.

contribution, which is the response from a single domain, and extrinsic contributions, which are from domain wall motions [5, 23, 24]. When a mechanical stress is applied to a ferroelectric material, the domain structure in the material will change to maintain the domain energy at a minimum; during this process some of the domains engulf other domains or change shape irreversibly. Under a uniaxial stress, the domain structure of ferroelectric ceramics may undergo domain switching, clamping of domain walls, de-aging, and de-poling [24].

For the case of BT-PZT system, the results on the uniaxial compressive pre-stress dependence of the dielectric properties can easily be explained with the above statements. When the uniaxial compressive pre-stress is applied in the direction parallel to the polar axis (poling) direction, the stress will move some of the polarization away from the poling direction resulting in a change in domain structures [4, 23, 24]. This change increases the non-180° domain wall density. Hence the increase of the dielectric constant with the applied stress is observed. The de-aging mechanism is also expected to play a role here. However, the stress clamping of domain walls and the de-poling mechanisms are not expected at this relatively low stress level used in this study [25]. Therefore, a combination of the domain switching and the de-aging mechanisms is believed to be a reason for the increase of the dielectric constant with increasing applied stress in the BT-PZT system, as shown in Fig. 1.

For the PMN-PZT system, the results for the case of PZT-rich compositions can easily be explained in the same way as in the BT-PZT system. Since PMN is a relaxor ferroelectric

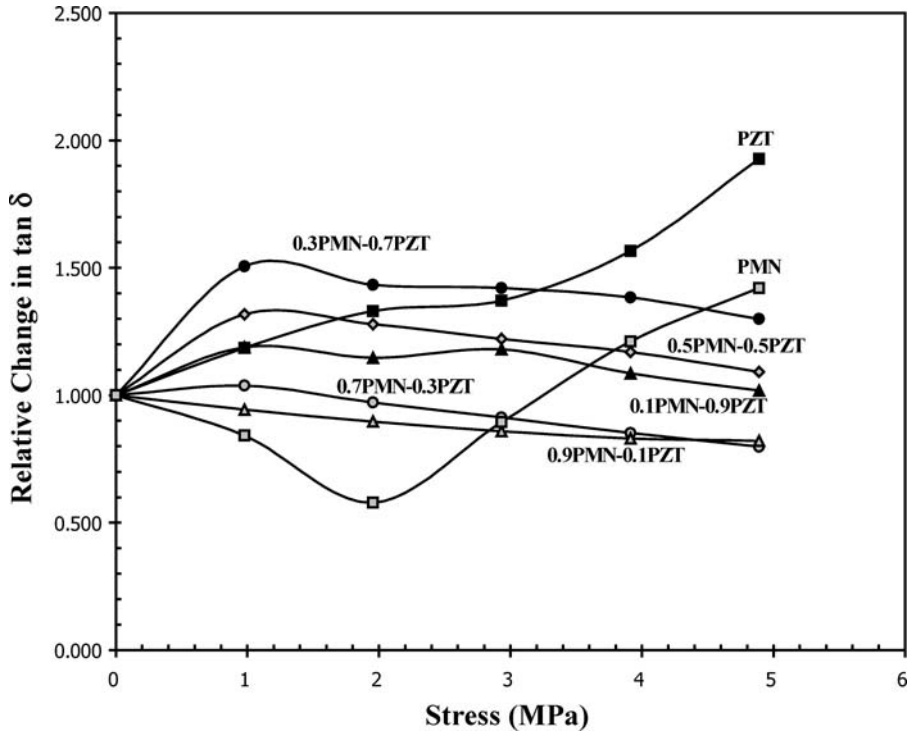

Figure 4. Relative changes of the dielectric loss tangent (tan δ) as a function of compressive pre-stress for (x)PMN-(1-x)PZT ceramics.

material, the situation is very different for PMN-rich compositions. The stress dependence of the dielectric constant of the compositions is attributed to competing influences of the intrinsic contribution of non-polar matrix and the extrinsic contribution of re-polarization and growth of micro-polar regions [4, 25]. Since the dielectric response of both contributions is affected by the applied stress in an opposite way, the behavior of the composites depends on the ratio between the micro-polar region and the non-polar matrix. Since the measurements are carried out at the room temperature, the micro-polar regions dominate the dielectric response of the composites [25]. Therefore, the dielectric constant of the PMN-rich compositions decreases with increasing applied stress, as seen in Figure 3.

The cause of the stress dependence of the dielectric loss tangent for both systems is a little more straightforward than that of the dielectric constant. Stress-induced depinning of the domain walls is expected to occur under the applied compressive pre-stress. As depicted in Figures 2 and 4, an increase in domain wall mobility clearly enhances the dielectric loss tangent in some compositions, while the de-aging in the materials normally causes the decrease of the dielectric loss tangent observed in some compositions [23, 24].

These results clearly demonstrate that the contribution of each mechanism to the dielectric responses of the BT-PZT and PMN-PZT ceramic composites depends on the compositions and the stress level. Finally, it should be noted here that the dielectric behaviors under the applied stress for BT-PZT system, which is a mixture of normal ferroelectrics, are significantly different from those observed in a mixture between normal and relaxor ferroelectrics, i.e. PMN-PZT system, in which the dielectric responses to the applied stress

depend more on the compositions and the stress level, and the dielectric properties of some compositions decrease with increasing applied stress.

Conclusions

In this study, the $(x)BaTiO_3–(1-x)Pb(Zr_{0.52}Ti_{0.48})O_3$ (when $x = 0.0$, 0.05, 0.15, 0.25, 0.35, 0.45, 0.55, 0.65, 0.75, 0.85, 0.95, and 1.0) and $(x)Pb(Mg_{1/3}Nb_{2/3})O_3–(1-x)Pb(Zr_{0.52}Ti_{0.48})O_3$ (when $x = 0.0$, 0.1, 0.3, 0.5, 0.7, 0.9, and 1.0) ceramic composites are successfully prepared by a conventional mixed-oxide method at various processing conditions. The dielectric properties under the uniaxial compressive pre-stress of the BT-PZT and PMN-PZT ceramics are observed at stress levels up to 15 and 5 MPa, respectively, using a uniaxial compressometer. The dielectric constant and the dielectric loss tangent of the BT-PZT ceramics increase significantly with increasing applied stress. Larger changes in the dielectric properties with the applied stress are observed in the PZT-rich compositions. For PMN-PZT system, the dielectric constant of the PMN-rich compositions decreases, while that of the PZT-rich compositions increases slightly, with increasing applied stress. On the other hand, the dielectric loss tangent for most of the compositions first rises and then drops with increasing applied stress. The experimental results are explained in terms of domain wall and de-aging mechanisms. More importantly, it is of interest to find that the results for the mixture normal ferroelectrics such as BT-PZT ceramics are significantly different from those for the mixture of normal and relaxor ferroelectrics such as PMN-PZT ceramics. Finally, this study undoubtedly shows that the applied stress has significant influence on the dielectric properties of both BT-PZT and PMN-PZT ceramic composites.

Acknowledgment

The author would like to express his sincerest and deepest gratitude for guidance and teaching by Prof. Robert E. Newnham throughout his career. Contributions from colleagues, S. Wongsaenmai, S. Chamunglap, and S. Ananta, are gratefully acknowledged. This work is supported by the Thailand Research Fund (TRF).

References

1. L. E. Cross, Relaxor ferroelectrics. *Ferroelectrics* **76**, 241–267 (1987).
2. Y. H. Xu, Ferroelectric Materials and Their Applications. Los Angeles: North Holland; (1991).
3. D. Viehland and J. Powers, Effects of uniaxial stress on the electromechanical properties of $0.7Pb(Mg_{1/3}Nb_{2/3})O_3$-$0.3PbTiO_3$ crystals and ceramics. *J. Appl. Phys*. **89**(3), 1820–1825 (2001).
4. J. Zhao and Q. M. Zhang, Effect of mechanical stress on the electromechanical performance of PZT and PMN-PT ceramics. *Proceedings of the IEEE International Symposium on Applications of Ferroelectrics* **2**, 971–974 (1996).
5. J. Zhao, A. E. Glazounov, and Q. M. Zhang, Change in electromechanical properties of 0.9PMN-0.1PZT relaxor ferroelectrics induced by uniaxial compressive stress directed perpendicular to the electric field. *Appl. Phys. Lett*. **74**, 436–438 (1999).
6. G. H. Haertling, Ferroelectric ceramics: history and technology. *J. Am. Ceram. Soc*. **82**(4), 797–818 (1999).
7. L. E. Cross, Review: ferroelectric materials for electromechanical transducer applications. *Mater. Chem. Phys*. **43**, 108–115 (1996).
8. A. J. Moulson and J. M. Herbert, Electroceramics: Materials, Properties, Applications, 2nd Ed., John Wiley & Sons Ltd (2003).

9. B. Jaffe and W. R. Cook, Piezoelectric Ceramics, R.A.N. Publishers (1971).
10. W. Chaisan, S. Ananta, and T. Tunkasiri, Synthesis of barium titanate-lead-zirconate titanate solid solutions by a modified mixed-oxide synthetic route. *Cur. Appl. Phys*. **4**, 182–185 (2004).
11. J. H. Yoo, H. S. Yoon, Y. H. Jeong, and C. Y. Park, Piezoelectric characteristics of PMN-PZT ceramics for piezoelectric transformer. *Proceedings of the IEEE Ultrasonic Symposium*. 981–984 (1998).
12. A. V. Shilnikov, A. V. Sopit, A. I. Burkhanov, and A. G. Luchaninov, The dielectric response of electrostrictive (1-x)PMN-xPZT ceramics. *J. Euro. Ceram. Soc*. **19**, 1295–1297 (1999).
13. B. K. Gan, J. M. Xue, D. M. Wan, and J. Wang, Lead zirconate titanate-barium titanate by mechanical activation of mixed oxides. *Appl. Phys. A*. **69**, 433–436 (1999).
14. R. Yimnirun, S. Ananta, and P. Laoratanakul, Effects of PMN-mixed-oxide modification on dielectric properties of PZT ceramics. *Mater. Sci. Eng. B*. **112**, 79–86 (2004).
15. R. Yimnirun, S. Ananta, and P. Laoratanakul, Dielectric and ferroelectric properties of PMN-PZT ceramics prepared by mixed-oxide method. *J. Euro. Ceram. Soc*. (2005) (in press).
16. S. L. Swartz and T. R. Shrout, Fabrication of perovskite lead magnesium niobate. *Mater. Res. Bull*. **17**, 1245–1250 (1982).
17. R. Yimnirun, P. Moses, R. J. Meyer, and R. E. Newnham, Dynamic compressometer for converse electrostriction measurements. *Rev. Sci. Instrum*. **74**, 3429–3432 (2003).
18. R. Yimnirun, S. Ananta, E. Meechoowas, and S. Wongsaenmai, Effects of uniaxial stress on dielectric properties of lead magnesium niobate-lead zirconate titanate ceramics. *J. Phys. D: Appl. Phys*. **36**, 1615–1619 (2003).
19. D. Zhou, M. Kamlah, and D. Munz, Effects of uniaxial prestress on the ferroelectric hysteretic response of soft PZT. *J. Euro. Ceram. Soc*. **25**, 425–432 (2005).
20. J. M. Calderon-Moreno, Stress induced domain switching of PZT in compression tests. *Mater. Sci. Eng. A*. **315**, 227–230 (2004).
21. D. Audigier, C. l. Richard, C. l. Descamps, M. Troccaz, and L. Eyraud, PZT uniaxial stress dependence: experimental results. *Ferroelectrics* **154**, 219–224 (1994).
22. I. J. Fritz, Ultrasonic, dilatometric, and dielectric study of uniaxial stress effects in a barium-calcium titanate ceramic. *J. Appl. Phys*. **49**, 788–794 (1978).
23. G. Yang, W. Ren, S. F. Liu, A. J. Masys, and B. K. Mukherjee, Effects of uniaxial stress and DC bias field on the piezoelectric, dielectric, and elastic properties of piezoelectric ceramics. *Proceedings of the IEEE Ultrasonic Symposium* 1005–1008 (2000).
24. G. Yang, S. F. Liu, E. Ren, and B. K. Mukherjee, Uniaxial stress dependence of the piezoelectric properties of lead zirconate titanate ceramics. *Proceedings of SPIE Symposium on Smart Structures and Materials* **3992**, 103–113 (2000).
25. Q. M. Zhang, J. Zhao, K. Uchino, and J. Zheng, Change of the weak-field properties of $Pb(ZrTi)O_3$ piezoceramics with compressive uniaxial stresses and its links to the effect of dopants on the stability of the polarizations in the materials. *J. Mater. Res*. **12**(1), 226–234 (1997).

Available online at www.sciencedirect.com
SCIENCE DIRECT®
Materials Letters 60 (2006) 2666–2671
materials letters
www.elsevier.com/locate/matlet

Effects of milling time and calcination condition on phase formation and particle size of lead titanate nanopowders prepared by vibro-milling

R. Wongmaneerung, R. Yimnirun, S. Ananta *

Department of Physics, Faculty of Science, Chiang Mai University, Chiang Mai 50200, Thailand

Received 10 August 2005; accepted 22 January 2006
Available online 13 February 2006

Abstract

Effect of calcination conditions on phase formation and particle size of lead titanate ($PbTiO_3$) powders synthesized by a solid-state reaction with different vibro-milling times was investigated. Powder samples were characterized using XRD, SEM, TEM and EDX techniques. A combination of the milling time and calcination conditions was found to have a pronounced effect on the phase formation and particle size of the calcined $PbTiO_3$ powders. The calcination temperature for the formation of single-phase perovskite lead titanate was lower when longer milling times were applied. More importantly, by employing an appropriate choice of the milling time and calcination conditions, perovskite lead titanate ($PbTiO_3$) nanopowders have been successfully prepared with a simple solid-state reaction method.

Keywords: Lead titanate; Perovskite; Nanopowders; Calcination; Phase formation

1. Introduction

Lead titanate, $PbTiO_3$ (PT), is one of the perovskite-type ferroelectric materials having unique properties such as high transition temperature (~490 °C), excellent pyroelectric coefficient and large spontaneous polarization [1,2]. These characteristics make it an interesting candidate for many applications e.g. ultrasonic transducers, microactuators and multilayer capacitors [3,4]. To fabricate them, a fine powder of perovskite phase with the minimized degree of particle agglomeration is needed as starting material in order to achieve a dense and uniform microstructure at the sintering temperature [5,6].

Recently, the studies of nanoparticles are also a very attractive field. The evolution of a method to produce nanopowders of precise stoichiometry and desired properties is complex, depending on a number of variables such as starting materials, processing history, temperature, etc. The advantage of using a solid-state reaction method via mechanical milling for preparation of nanosized powders lies in its ability to produce mass quantities of powder in the solid state using simple equipment and low cost starting precursors [7,8]. Although some research has been done in the preparation of PT powders via a vibro-milling technique [9,10], to our knowledge a detailed study considering the role of both milling times and firing conditions on the preparation of PT nanopowders has not been reported. Thus, in the present study, the primary attention was aimed towards the production of stoichiometric $PbTiO_3$ nanopowders by a mixed oxide method. The powder characteristics of the vibro-milling derived $PbTiO_3$ have also been thoroughly investigated.

2. Experimental procedure

The raw materials used were commercially available lead oxide, PbO and titanium oxide, TiO_2 (Fluka, >99% purity). The two oxide powders exhibited an average particle size in the range of 3.0 to 5.0 μm. $PbTiO_3$ powder was synthesized by the solid-state reaction of these raw materials. A McCrone Micronizing Mill was employed for preparing the stoichiometric $PbTiO_3$ powders as described in a previous work [11]. In order to improve the reactivity of the constituents, the milling process was carried out for various milling times ranging from 20 to 30 h (instead of 30 min [10]) with corundum media in

* Corresponding author. Tel.: +66 53 943367; fax: +66 53 357512.
E-mail address: supon@chiangmai.ac.th (S. Ananta).

0167-577X/$ - see front matter © 2006 Elsevier B.V. All rights reserved.
doi:10.1016/j.matlet.2006.01.062

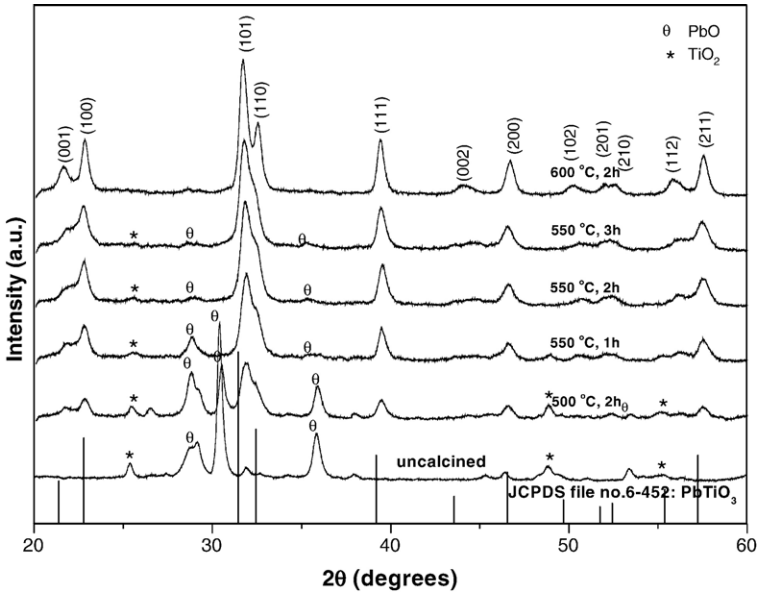

Fig. 1. XRD patterns of PT powders milled for 20 h and calcined at various conditions.

isopropyl alcohol (IPA). After drying at 120 °C for 2 h, various calcination conditions, i.e. temperature ranging from 500 to 600 °C, dwell times ranging from 1 to 4 h and heating/cooling rates ranging from 5 to 20 °C.min^{-1}, were applied (the powders were calcined inside a closed alumina crucible) in order to investigate the formation of $PbTiO_3$.

All powders were examined by room temperature X-ray diffraction (XRD; Siemens-D500 diffractometer) using Ni-filtered CuK_α radiation, to identify the phases formed, optimum milling time and firing conditions for the production of single-phase $PbTiO_3$ powders. The crystalline lattice constants, tetragonality factor (c/a), mean lattice strain and average particle size were also estimated from XRD patterns [12]. The particle size distributions of the powders were determined by laser diffraction technique (DIAS 1640 laser diffraction spectrometer) with the particle sizes and morphologies of the powders observed by scanning electron microscopy (JEOL JSM-840A SEM). The structures and chemical compositions of the phases formed were elucidated by transmission electron microscopy (CM 20 TEM/STEM operated at 200 keV) and an energy-dispersive X-ray (EDX) analyzer with an ultra-thin window.

3. Results and discussion

Powder XRD patterns of the calcined powders after different milling times are given in Figs. 1–3, with the corresponding JCPDS patterns. As shown in Fig. 1, for the uncalcined powder subjected to 20

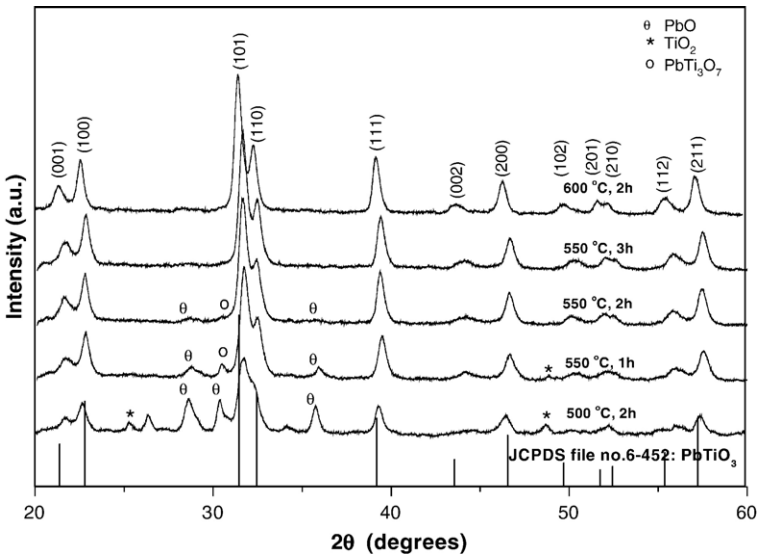

Fig. 2. XRD patterns of PT powders milled for 25h and calcined at various conditions.

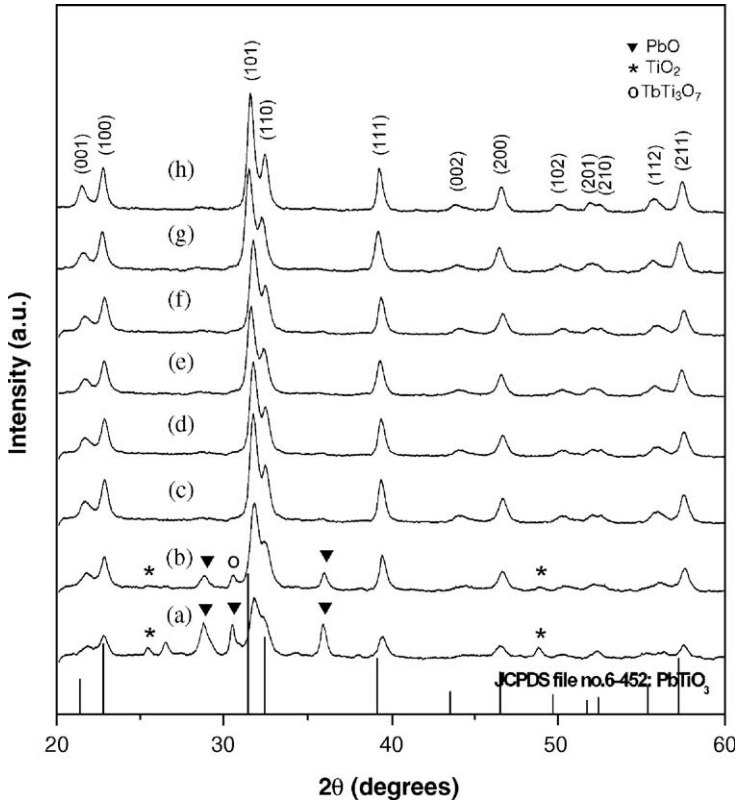

Fig. 3. XRD patterns of PT powders milled for 30 h and calcined at (a) 500 °C for 2 h, (b) 550 °C for 1 h, (c) 550 °C for 2 h, (d) 550 °C for 3 h, (e) 600 °C for 2 h, with heating/cooling rates of 5 °C/min and 550 °C for 3 h with heating/cooling rates of (f) 10 °C/min, (g) 20 °C/min and (h) 30 °C/min.

h of vibro-milling, only X-ray peaks of precursors PbO (▼) and TiO_2 (∗) are present, indicating that no reaction was yet triggered during the vibro-milling process. However, after calcination at 500 and 550 °C, it is seen that the perovskite-type $PbTiO_3$ becomes the predominant phase indicating that the reaction has occurred to a considerable extent. Further calcination at 550 °C with dwell time of 1 h or more does not result in a very much increase in the amount of $PbTiO_3$ whereas the traces of unreacted PbO and TiO_2 could not be completely eliminated. This could be attributed to the poor reactivity of lead and titanium species [9,10]. However, it should be noted that after calcination at 600 °C for 2 h, the single phase of perovskite PT (yield of 100% within the limitations of the XRD technique) was obtained.

In general, the strongest reflections apparent in the majority of these XRD patterns indicate the formation of $PbTiO_3$. These can be matched with JCPDS file number 6–452 for the tetragonal phase, in space group *P*4/*mmm* with cell parameters $a=389.93$ pm and $c=415.32$ pm [13], consistent with other works [9,10]. For 20 h of milling, the optimum calcination temperature for the formation of a high purity $PbTiO_3$ phase was found to be about 600 °C.

To further study the phase development with increasing milling times, an attempt was also made to calcine mixed powders milled at 25 h and 30 h under various conditions as shown in Figs. 2 and 3, respectively. In this connection, it is seen that by varying the calcination temperature, the minimum firing temperature for the single phase formation of each milling batch is gradually decreased with increasing milling time (Figs. 1–3). The main reason for this behavior is that a complete solid-state reaction probably takes place more easily when the particle size is milled down to accelerate an atomic diffusion mechanism resulting in the suitable level of homogeneous mixing. It is therefore believed that the solid-state reaction to form perovskite PT phase occurs at lower temperatures with decreasing the particle size of the oxide powders.

However, there is evidence that, even for a wide range of calcination conditions, single-phase $PbTiO_3$ cannot be produced easily, in agreement with literature [10,14]. A noticeable difference is noted when employing the milling time longer than 20 h (Figs. 2 and 3), since they lead to a considerable formation of lead deficient phase, $PbTi_3O_7$ (o), earlier reported by a number of workers [15,16]. This pyrochlore phase has a monoclinic structure with cell parameters $a=107.32$ pm, $b=381.2$ pm, $c=657.8$ pm and $\beta=98.08°$ (JCPDS file number 21–949) [17]. This observation could be attributed mainly to the poor reactivity of lead and titanium species [9,10] and also the limited mixing capability of the mechanical method [18].

From Figs. 2 and 3, it is clear that the intensity of the perovskite peaks was further enhanced when the dwell times of the calcinations process were extended up to 3 h at the expenses of PbO, TiO_2 and $PbTi_3O_7$ phases. An essentially monophasic $PbTiO_3$ of perovskite structure was obtained at 550 °C when the calcination time was increased to 3 h and 2 h for the milling time of 25 h and 30 h, respectively, as shown in Figs. 2 and 3(c). This was apparently a consequence of the enhancement in crystallinity of the perovskite phase with increasing degree of mixing and dwell time, in good agreement with other works [18,19].

In the present study, an attempt was also made to calcine the powders with 30 h of milling times under various heating/cooling rates (Fig. 3). In this connection, it is shown that the yield of $PbTiO_3$ phase did not vary significantly with different heating/cooling rates ranging from 5 to 30 °C min^{-1}, in good agreement with the early observation for the $PbTiO_3$ powders subjected to 0.5 h of vibro-milling times [10]. It should be noted that no evidence of the introduction of impurity due

Table 1
Effect of calcination conditions on the variation of crystalline size, tetragonality factor (c/a) and mean lattice strain of PT powders milled for different times

Calcination condition $T/D/R$ (°C/h/°C min^{-1})	Crystallite size (nm)	Lattice strain (%)	Tetragonality factor (c/a)
500/2/30	21.8	0.0188	1.038
550/1/30	19.4	0.0212	1.055
550/2/30	21.6	0.0190	1.052
550/3/30	20.9	0.0197	1.054
600/2/30	21.5	0.0193	1.057

T=calcination temperature.
D=dwell time.
R=heating/cooling rates.

to wear debris from the selected milling process was observed in all calcined powders, indicating the effectiveness of the vibro-milling technique for the production of high purity $PbTiO_3$ nanopowders.

The variation of calculated crystallite size, tetragonality factor (c/a) and lattice strain of the powders milled for different times with the calcination conditions is given in Table 1. In general, it is seen that the crystallite size of lead titanate decreases slightly with increasing calcination temperature for all different milling times, while the calculated values of the tetragonality factor and mean lattice strain progressively increase. However, it should be noted that by increasing the calcination time from 1 to 3 h, these calculated values decrease to the minimum at 2 h and then grow up further after longer dwell time was applied. There is no obvious interpretation of these observations, although it is likely to correspond to the competition between the major mechanisms leading to crystallization and agglomeration [19].

In this connection, a combination of SEM and TEM techniques was also employed for the particle size measurement. The morphological evolution during various calcination conditions of PT powders milled with different times was investigated by SEM technique as shown in Fig. 4. It is seen that all powders seem to have similar morphology. In general, the particles are agglomerated and basically irregular in shape, with a substantial variation in particle sizes, particularly in powders subjected to prolong milling times or high firing temperatures (Fig. 4(c) and (d)). The powders consist of primary particles of nanometers in size. The primary particles have sizes of ~17–57 nm, and the agglomerates measured ~109–157 nm. It is also of interest to point out that averaged particle size tends to increase with calcination temperatures (Fig. 4 and Table 1), in good agreement with other works [8,18]. This observation may be attributed to the occurrence of hard agglomeration with strong inter-particle bond within each aggregates resulting from firing process. The experimental work carried out here suggests that the optimal combination of the milling time and calcination condition for the production of single-phase $PbTiO_3$ powders with smallest particle size (~17 nm) is 25 h and 600 °C for 2 h with heating/cooling rates of 30 °C min^{-1}, respectively. Moreover, the employed heating/cooling rates for $PbTiO_3$ powders observed in this work are also faster than those reported earlier [9,10].

A TEM bright field image of an agglomerated or intergrown particle of the calcined PT powders derived from milling time of 25 h is shown in Fig. 5(a). By employing the selected area electron diffraction (SAED) technique, a perovskite-like phase of tetragonal *P4/mmm* $PbTiO_3$ is identified (Fig. 5(b)), in good agreement with the XRD analysis and the data in JCPDS file no. 6-452 [13]. The reciprocal lattice pattern of this PT phase was also simulated with the Carine Crytallography 3.0 software, as demonstrated in Fig. 5(c). In addition,

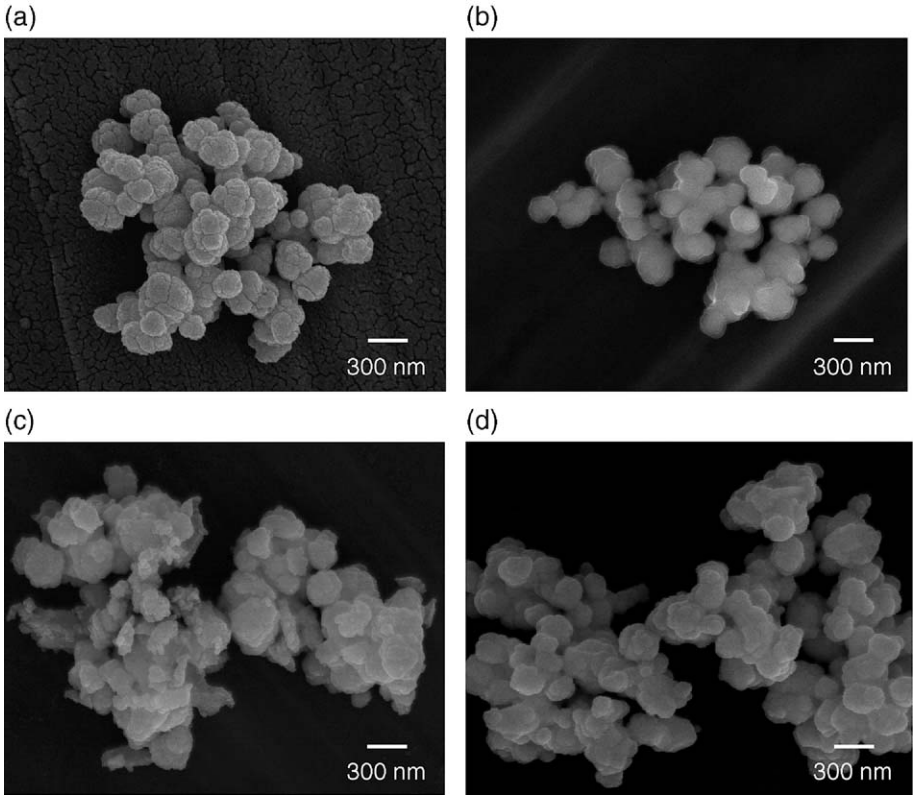

Fig. 4. SEM micrographs of PT powders milled for (a) 20 h and (b) 25 h, and calcined at 600 °C for 2h, (c) 25 h and (d) 30 h, and calcined at 550 °C for 3 h, with heating/cooling rates of 30 °C/min.

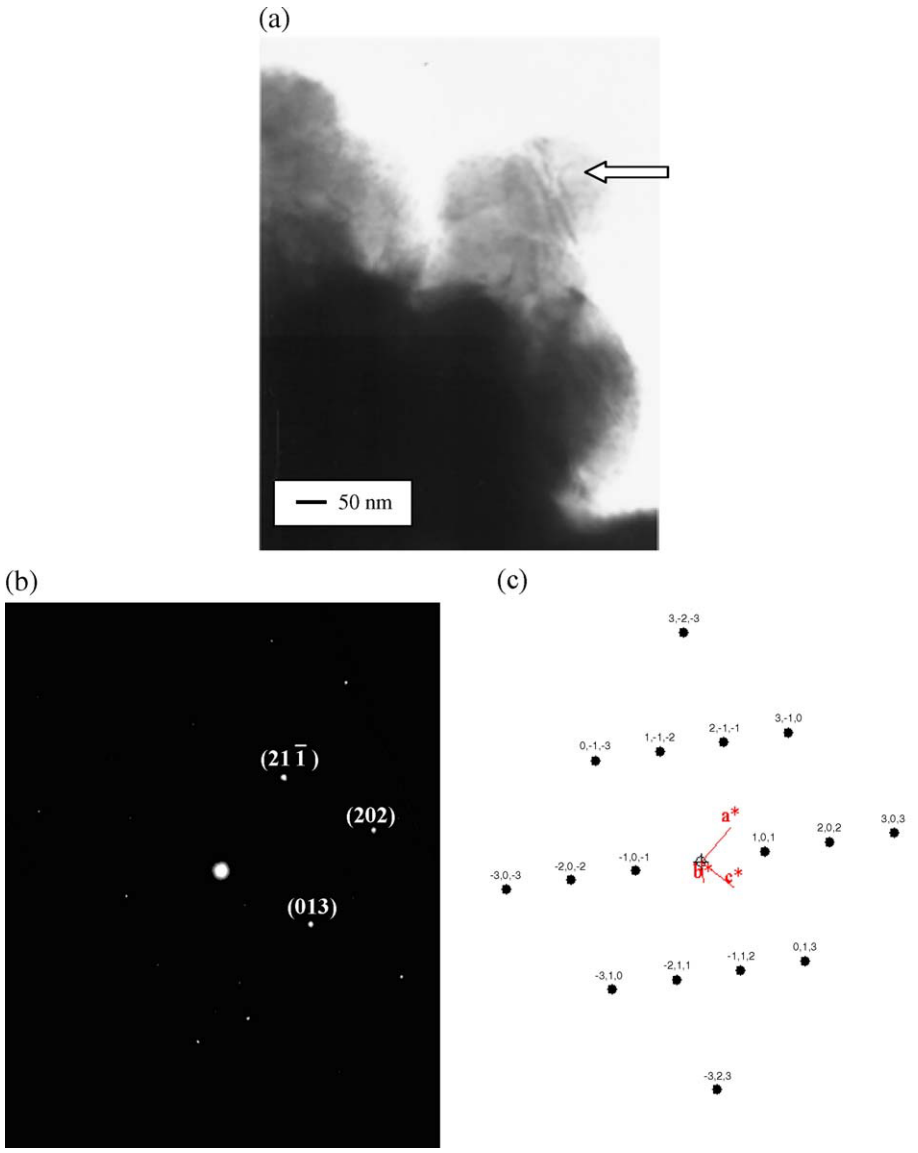

Fig. 5. (a) TEM micrograph, (b) SAED pattern ([13 $\bar{1}$] zone axis) and (c) reciprocal lattice pattern simulation of PT powders milled for 25 h and calcined at 600 °C for 2 h with heating/cooling rates of 30 °C/min.

EDX analysis using a 20 nm probe on a large number of particles of these calcined $PbTiO_3$ powders confirmed the existence of single phase perovskite, in good agreement with XRD results.

4. Conclusion

This work demonstrated that by applying an appropriate choice of the vibro-milling time, calcination temperature and dwell time, mass quantities of a high purity lead titanate nanopowders can be successfully produced by a simple solid-state mixed oxide synthetic route without the use of high purity starting precursors.

Acknowledgement

This work was supported by the Thailand Research Fund (TRF), the Faculty of Science and the Graduate School of Chiang Mai University.

References

[1] A.J. Moulson, J.M. Herbert, Electroceramics, 2nd ed., Wiley, Chichester, 2003.
[2] B. Jaffe, W.R. Cook, H. Jaffe, Piezoelectric Ceramics, Academic Press, New York, 1971.
[3] G.H. Haertling, J. Am. Ceram. Soc. 82 (1999) 797.
[4] K. Uchino, Piezoelectrics and Ultrasonic Applications, Kluwer, Deventer, 1998.
[5] J.S. Wright, L.F. Francis, J. Mater. Res. 8 (1993) 1712.
[6] G.R. Fox, J.H. Adair, R.E. Newnham, J. Mater. Sci. 25 (1990) 3634.
[7] V.V. Dabhade, T.R. Rama Mohan, P. Ramakrishman, Appl. Surf. Sci. 182 (2001) 390.
[8] S. Ananta, Mater. Lett. 58 (2004) 2781.
[9] A. Udomporn, S. Ananta, Curr. Appl. Phys. 4 (2004) 186.
[10] A. Udomporn, S. Ananta, Mater. Lett. 58 (2003) 1154.
[11] R. Wongmaneerung, R. Yimnirun, S. Ananta, Mater. Lett. (in press), doi:10.1016/j.matlet.2005.11.043.
[12] H. Klug, L. Alexander, X-ray Diffraction Procedures for Polycrystalline and Amorphous Materials, 2nd ed., Wiley, New York, 1974.

[13] JCPDS-ICDD Card no. 6-452, International Centre for Diffraction Data, Newtown Square, PA, 2000.
[14] C.G. Pillai, P.V. Ravindron, Thermochim. Acta 66 (1996) 109.
[15] J. Tartaj, C. Moure, L. Lascano, P. Duran, Mater. Res. Bull. 36 (2001) 2301.
[16] M.L. Calzada, M. Alguero, L. Pardo, J. Sol-Gel Sci. Technol. 13 (1998) 837.
[17] JCPDS-ICDD Card no. 6-452, International Centre for Diffraction Data, Newtown Square, PA, 2000.
[18] S. Ananta, R. Tipakontitikul, T. Tunkasiri, Mater. Lett. 57 (2003) 2637.
[19] S. Ananta, R. Brydson, N.W. Thomas, Mater. J. Eur. Ceram. Soc. 20 (2000) 2315.

International Journal of Modern Physics B
Vol. 20, No. 17 (2006) 2415–2424

World Scientific
www.worldscientific.com

EFFECT OF SINTERING TEMPERATURE ON DENSIFICATION AND DIELECTRIC PROPERTIES OF $Pb(Zr_{0.44}Ti_{0.56})O_3$ CERAMICS

R. YIMNIRUN*, R. TIPAKONTITIKUL and S. ANANTA

Department of Physics, Faculty of Science, Chiang Mai University, Chiang Mai, 50200, Thailand
**rattikornyimnirun@yahoo.com*

Received 31 October 2005

In this study, lead zirconate titanate ($Pb(Zr_{0.44}Ti_{0.56})O_3$) ceramics were fabricated with a mixed oxide synthetic route of lead oxide (PbO) and zirconium titanate ($ZrTiO_4$) precursors. The effects of sintering temperature on phase formation, densification and dielectric responses of the ceramics have been investigated using XRD, SEM, EDX and dielectric measurement techniques. The densification of the PZT ceramics with density of 97% theoretical density can be achieved with appropriate sintering condition without any sintering additives. The optimized sintering condition has been identified as 1225°C for 4 h. More importantly, the dielectric properties are found to improve with increasing sintering temperature and grain size. However, when sintered over 1250°C, the dielectric properties of the ceramics are seen to deteriorate as a result of PbO vaporization, ZrO_2 segregations and porosity.

Keywords: Lead zirconate titanate; PZT; sintering; densification; dielectric properties.

1. Introduction

Lead zirconate titanate ceramics, $Pb(Zr_xTi_{1-x})O_3$ or PZT, have been widely investigated on their electrical properties for several decades.[1] As a prototype of piezoelectrics, PZT ceramics exhibit good dielectric and piezoelectric properties, especially the compositions near the morphotropic phase boundary (MPB). Therefore, they have been exploited in several commercial applications such as ultrasonics, buzzers, actuators and transducers.[2,3] In addition, the compositions in the vicinity of MPB, generally identified as 52/48 for Zr/Ti ratio, have also been extensively investigated.[1,3,4] This is clearly a result of enhanced properties of the compositions, which have been attributed to the coexistence of tetragonal and rhombohedral phases.[4,5] More recently, the reports by Noheda *et al.* have also identified that the presence of the monoclinic distortion is the origin of the unusually high piezoelectric response of PZT compositions near the MPB.[6,7]

*Corresponding author.

The stoichiometry and densification behavior of the oxide ceramics, which are greatly influenced by sintering conditions, are known to be the key factors for ensuring good electrical properties.[4] PZT compositions are commonly sintered at high temperatures in the range 1100–1300°C. This creates problems with vaporization of PbO during sintering and possible lead deficiency which may cause segregation of a ZrO_2 phase or a formation of unwanted phases.[8] This may affect the electrical properties of the material. The B-site precursor method is one the techniques developed to counteract the problem.[9] In this method, the high temperature phase of $ZrTiO_4$ is first formed before reacting with PbO to form PZT at lower temperature. Furthermore, the microstructure features such as grain size, grain boundary, density, porosity, and homogeneity markedly influence the electrical characteristics of sintered piezoelectric ceramics.[10] Kakegawa *et al.*[11] reported that the dielectric constant of PZT ceramics depends on their chemical compositions. The room temperature dielectric constant of PZT ceramics was found to decrease with increasing grain size, while, on the other hand, the maximum dielectric constant of $Pb(Zr_{0.52}Ti_{0.48})O_3$ ceramics increased as the grain size decreased.[12] Generally, the grain size of PZT ceramics increases with the sintering temperature and dwell time.[13,14] Therefore, it could be intuitively expected that the electrical properties of the PZT ceramics would be greatly influenced by the sintering parameters. In this study, the effects of sintering temperature on the densification and the dielectric properties of the sintered PZT ceramics prepared by the B-site precursor method were investigated. In stead of the typical MPB composition of $Pb(Zr_{0.52}Ti_{0.48})O_3$, which have been extensively studied,[1,3,4,12] the tetragonal composition of $Pb(Zr_{0.44}Ti_{0.56})O_3$ was chosen in this study. This would extend an understanding on the processing-composition-properties relationships in PZT ceramics.

2. Materials and Methods

PZT powders were synthesized by a modified two-stage mixed oxide route. The $ZrTiO_4$ precursor powders were mixed with PbO for 24 h and calcined at 800°C for 2 h, as reported earlier.[9] Ceramic fabrication was achieved by adding 3 wt% polyvinyl alcohol (PVA) binder, then uniaxially pressed to form a green pellet of 10 mm diameter and 2 mm thick. The pellets were placed inside a closed alumina crucible covered with lead zirconate ($PbZrO_3$) powder to compensate the PbO volatilization and then sintered at various temperatures for 4 h with constant heating/cooling rates of 10°C/min. During the heating, the temperature was maintained at 500°C for 2 h to burn out the PVA binder. The pellets were subjected to bulk densities measurement with Archimedes method.

Finally, the XRD, SEM and dielectric properties measurement were carried out. X-ray diffraction analysis of the sintered samples was carried out at room temperature using CuKα radiation (40 kV) on X′ Pert X-ray diffractometer. Scanning electron microscopy (JEOL, JSM5910LV) was employed and the average grain size

(Φ_{av}) of samples was determined using the linear interception method. For electrical measurement, the as-sintered samples were polished to parallel surfaces. The major faces of the samples were coated with conductive Pt paint, and then heat cured at 700°C for 1 h to ensure that the electrodes were completely adhered to the ceramic. The dielectric properties were monitored as a function of temperatures (25–400°C) at a measuring frequency of 1 kHz using a computer controlled impedance analyzer (HP Model 4284A).

3. Results and Discussion

The densification of the PZT at various sintering temperatures is investigated. The change in density versus the sintering temperature (1100–1320°C) is shown in Fig. 1. In the sintering temperature range of 1100–1250°C, the density increases with increasing temperature. Further increase in the sintering temperature to 1320°C leads to the decrease of the density. This feature creates a maximum density value of about 97% of theoretical density which is comparable to the value reported by Wang *et al.*[15] where Li_2CO_3, Bi_2O_3 and CuO were used as sintering aids. The increasing density with rising sintering temperature up to 1250°C may be explained by the enhanced densification as the sintering of PZT is normally found at 1200°C.[16] Further increase in the sintering temperature causes a decrease in density values. This may be attributed to the loss of lead oxide at high sintering temperatures, which is similar to the results found in other Pb-based perovskite systems.[17,18]

XRD patterns of PZT ceramics sintered at various temperatures are plotted in Fig. 2. The strongest reflections in the majority of the XRD patterns can be identified as the perovskite phase of the composition $Pb(Zr_{0.44}Ti_{0.56})O_3$, which could be matched with JCPDS file 50-346. To a first approximation, this phase has a tetragonal perovskite-type structure in space group *P4mm* (No. 99), with cell

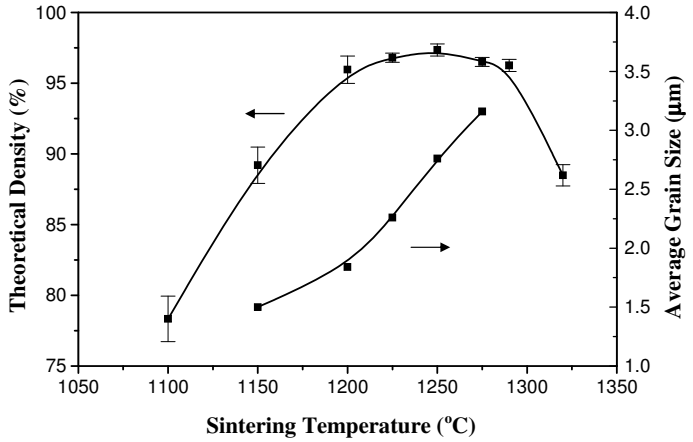

Fig. 1. Variation of density and grain size with sintering temperature for the PZT ceramics.

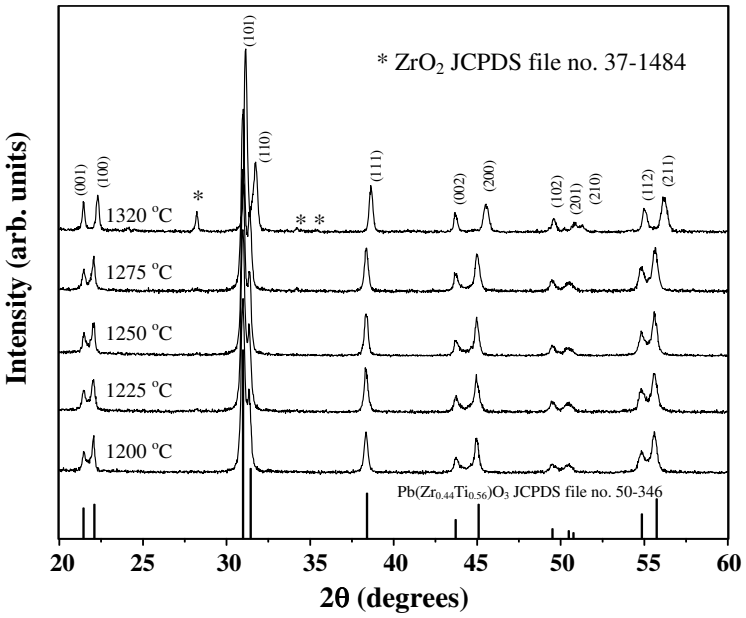

Fig. 2. XRD patterns of the PZT ceramics sintered at various temperatures.

parameters $a = 401$ pm and $c = 414$ pm, respectively.[19] However, for the sample sintered at 1320°C, some additional reflections (marked by $*$) are observed, and these can be identified as presence of ZrO_2 (JCPDS file 37-1484). This phase has a monoclinic structure with cell parameters $a = 531.2$, $b = 521.2$, $c = 514.7$ pm and $\beta = 99.218°$ in space group $P21/a$ (No. 14).[20] Due to no trace of ZrO_2 has been observed for the samples sintered at the temperatures below 1320°C, it is believed that the consequence of PbO evaporation is an apparently favorable factor in facilitating the occurrence of ZrO_2 at a higher sintering temperature.[21,22]

Microstructure development was investigated by scanning electron microscopy (SEM). Free surface micrographs of PZT ceramics sintered at various temperatures from 1150–1320°C are shown in Fig. 3. Also depicted in Fig. 1, the results indicate that grain size tends to increase with sintering temperatures in the temperature range 1150–1275°C that sees the grain size of the samples changed from 1.5 to 3.2 μm, in agreement with a previous work by Hong *et al.*[23] Similar findings were also reported in Nb-doped PZT and modified PT ceramics.[24,25] However, the average grain size of PZT sintered at 1320°C cannot be determined from SEM micrograph because of the ZrO_2 segregations that are confirmed by XRD results shown in Fig. 2, which also displays very high degree of porosity. In addition to the PbO evaporation, the presence of ZrO_2 segregations and a porous microstructure is believed to be another cause for the decrease in the ceramic density at high sintering temperature. As will be discussed later, these factors are also responsible for the dielectric behavior of the PZT ceramics.

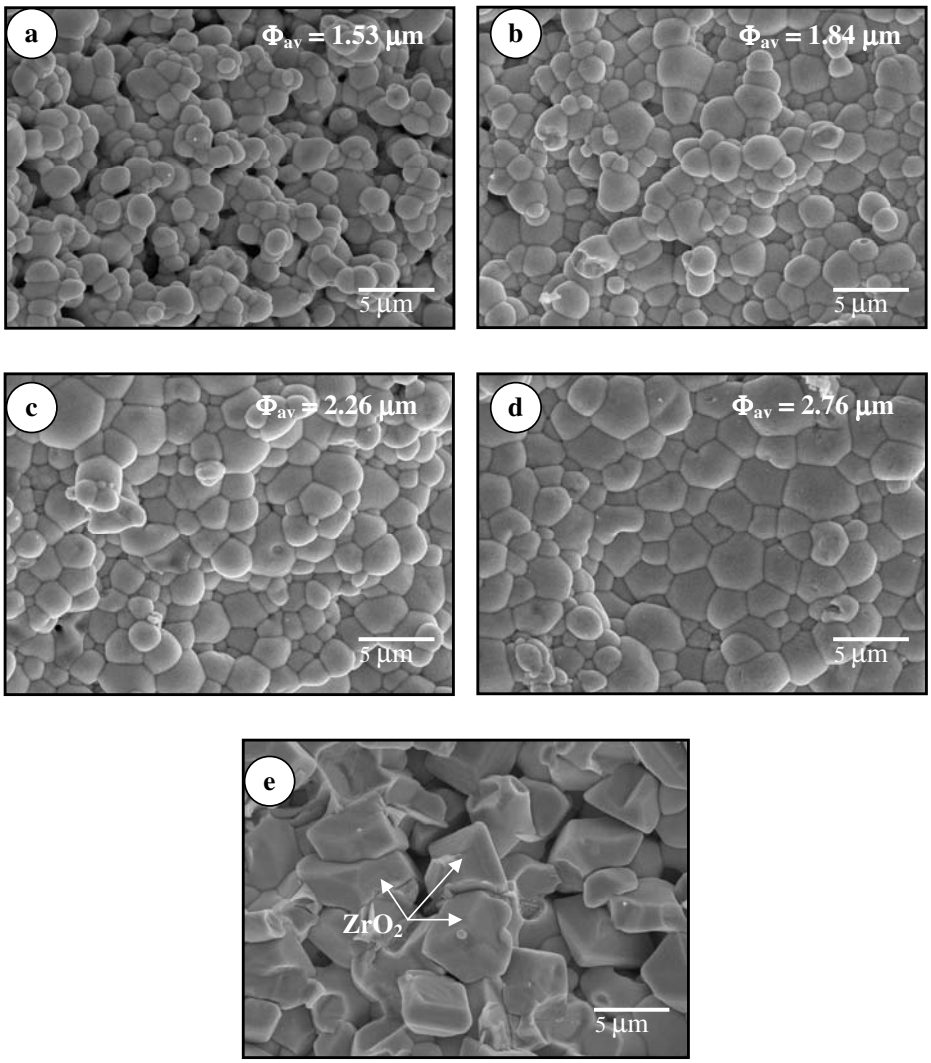

Fig. 3. SEM micrographs of the PZT ceramics sintered at (a) 1150°C, (b) 1200°C, (c) 1225°C, (d) 1250°C and (e) 1320°C.

The variations of dielectric constant (ε_r) and dissipation factor at 1 kHz with sintering temperature are shown in Fig. 4. For all samples in the present work, the Curie temperature is seen independent of the sintering temperature. Similar results have also been reported by other workers.[26,27] The results in Fig. 4 clearly indicate that the dielectric properties of the PZT ceramics depend on the sintering temperature. As listed in Table 1, the maximum value of dielectric constant ($\varepsilon_{r,\max}$) measured at T_C increases from 8250 to 18984 as the sintering temperature increases from 1150–1225°C. Further increase in the sintering temperature to 1275°C results

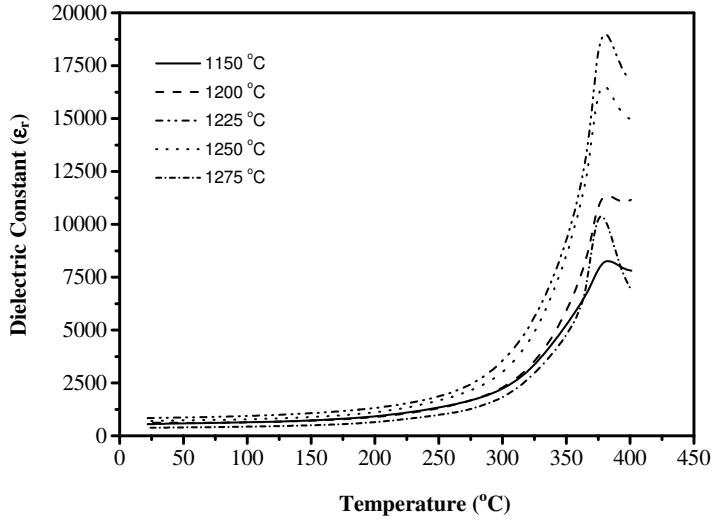

(a)

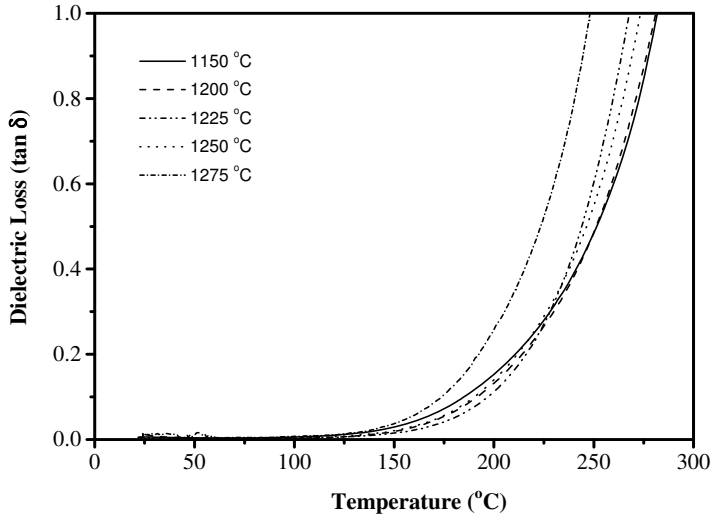

(b)

Fig. 4. Temperature dependence of (a) dielectric constant and (b) dissipation factors at 1 kHz for the PZT ceramics sintered at various temperatures.

in a drop in the values of $\varepsilon_{r,\max.}$ to 10378. The opposing trend is observed in the values of the high temperature dielectric loss (tan δ). It should also be noted here that since the dielectric loss in all ceramics increases significantly at high temperature as a result of thermally activated space charge conduction,[28] the values of the high temperature dielectric loss (tan δ) determined at 200°C are listed for comparison. As also listed in Table 1, the similar tendency is also observed for the

Table 1. Physical and dielectric properties of PZT ceramics sintered at various temperatures.

Sintering temperature (°C)	Average grain size (μm)	T_c (°C)	Dielectric Properties at 1 kHz			
			ε_r (25°C)	tan δ (25°C)	$\varepsilon_{r,\max}$ (T_C)	tan δ (200°C)
1150	1.53	381	564	0.0072	8250	0.160
1200	1.84	385	638	0.0039	11316	0.145
1225	2.26	380	697	0.0038	18984	0.120
1250	2.76	379	463	0.0042	16524	0.150
1275	3.16	377	397	0.0047	10378	0.265

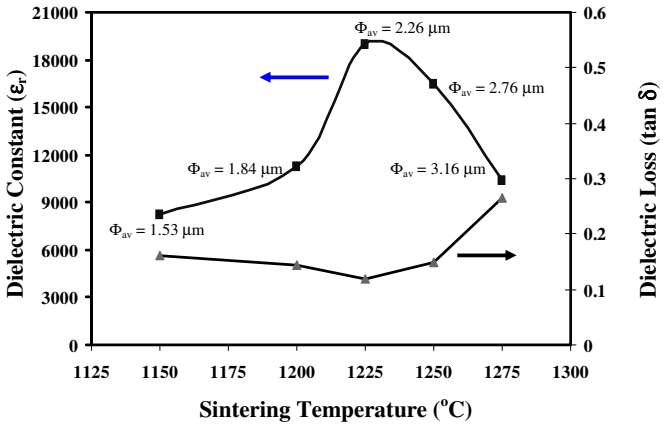

(a)

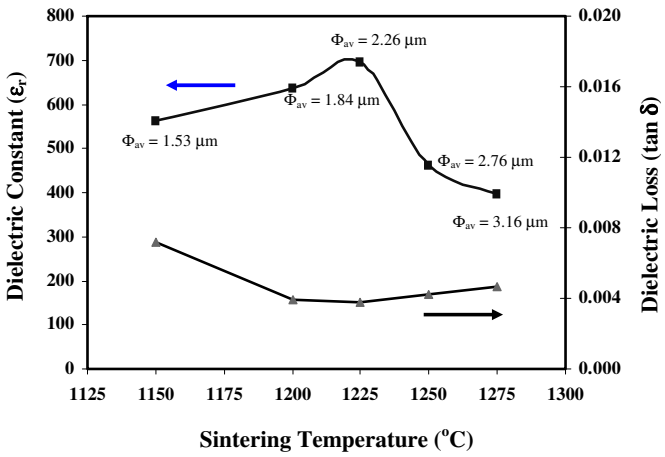

(b)

Fig. 5. Variation of (a) maximum dielectric properties and (b) room temperature dielectric properties with sintering temperature for the PZT ceramics.

room temperature dielectric properties. Figure 5 clearly depicts the relationship between the dielectric properties and the sintering temperature. In addition, it is worth noting that the measured values of the dielectric properties in the present work are in good agreement with the previous works on PZT ceramics prepared by different processing techniques.[12,29–31]

By comparing Figs. 1 and 5, the tendency of ε_r values with the sintering temperature is similar to that of density, in good agreement with the report by Kong and Ma,[31] while the average grain size also increases monotonically with sintering temperatures. Earlier report by Chu *et al.*[25] also showed similar observations in Nb-doped PZT ceramics. Clearly, the increasing dielectric constant (both at room and Curie temperatures) is due to the increasing density of the ceramics. However, the decreasing room temperature dielectric constant as sintering temperature above 1225°C can be related to the increasing grain size. Kang *et al.*[32] reported that the room temperature dielectric constant decreased with the increasing grain size. Similar results were also reported for $BaTiO_3$, modified PT and PLZT ceramics.[24,32,33] On the other hand, an earlier report by Okazaki *et al.*[34] showed that the maximum dielectric constant of PZT ceramics increased with increasing grain size. This is probably because increasing grain size results in reduction of the volume fraction of grain boundaries. The coupling effect between the grain boundaries and the domain wall, which makes domain reorientation more difficult and severely constrains the domain wall motion, is then decreased. This translates to an increase in the domain wall mobility corresponding to an increase in dielectric constant.[12,23,35] In this study, an initial increase of the maximum dielectric constant with the sintering temperature up to 1225°C, as shown in Fig. 5, can be related to the increasing grain size. However, the maximum dielectric constant values of the sintered samples then decrease from 18984 to 10378 as the sintering temperature is increased to 1275°C. This observation may be attributed to microstructure inhomogeneity of the PZT ceramics as a result of PbO deficiency, ZrO_2 precipitation, and porosity at higher sintering temperature. Thus, the higher sintering temperature and the presence of ZrO_2 impurity can significantly reduce the values of the dielectric constant of the PZT ceramics. Finally, it should be emphasized that even though many earlier studies have established a relationship between the dielectric properties and grain size in PZT as well as other perovskite ceramics, this study has shown that other factors such as the sintering conditions, the presence of pores, ZrO_2 and other secondary phases, chemical homogeneity, and Zr/Ti ratio clearly have strong influence on the dielectric properties of the PZT ceramics.

4. Conclusions

$Pb(Zr_{0.44}Ti_{0.56})O_3$ ceramics were successfully fabricated by employing the modified two-stage mixed oxide route and the effects of the sintering temperature on the densification and dielectric properties were investigated. High density PZT ceramics were obtained for the sintering temperatures about 1200–1250°C. The dielectric

properties of the PZT ceramics are dependent on sintering temperature. It is clear that the dielectric constant increases with increasing sintering temperature and grain size. However, the increasing trends between the density and dielectric properties and the sintering temperature are interrupted when the ceramics are sintered above 1250°C as a result of PbO vaporization, ZrO_2 segregation and porosity.

Acknowledgment

The authors would like to express their gratitude for financial support from the Thailand Research Fund (TRF) and Faculty of Science, Chiang Mai University.

References

1. G. H. Haertling, *J. Am. Ceram. Soc.* **82**(4), 797 (1999).
2. L. E. Cross, *Mater. Chem. Phys.* **43**, 108 (1996).
3. A. J. Moulson and J. M. Herbert, *Electroceramics*, 2nd edn. (Wiley-Interscience, New York, 2003).
4. B. Jaffe, W. R. Cook and H. Jaffe, *Piezoelectric Ceramics* (Academic Press, New York, 1971).
5. R. Guo, L. E. Cross, S.-E. Park, B. Noheda, D. E. Cox and G. Shirane, *Phys. Rev. Lett.* **84**(23), 5423 (2000).
6. B. Noheda, J. A. Gonzalo, L. E. Cross, R. Guo, S.-E. Park, D. E. Cox and G. Shirane, *Phys. Rev. B.* **61**(13), 8687 (2000).
7. B. Noheda, D. E. Cox, G. Shirane, J. A. Gonzalo, L. E. Cross and S.-E. Park, *Appl. Phys. Lett.* **74**(14), 2059 (1999).
8. B. V. Hiremath, A. I. Kingon and J. V. Biggers, *J. Am. Ceram. Soc.* **66**(11), 790 (1983).
9. R. Tipakontitikul and S. Ananta, *Mater. Lett.* **58**, 449 (2004).
10. Y. Xu, *Ferroelectric Materials and Their Applications* (Elsevier Science, Amsterdam, 1991).
11. K. Kakegawa, J. Mohri, T. Takahashi, H. Yamamura and S. Shirasaki, *Solid State Commun.* **24**, 769 (1977).
12. B. M. Jin, J. Kim and S. C. Kim, *Appl. Phys. A-Mater.* **65**, 53 (1997).
13. A. Garg and D. C. Agrawal, *Mat. Sci. Eng. B-Solid.* **56**, 46 (1999).
14. E. K. Goo, R. K. Mishra and G. Thomas, *J. Am. Ceram. Soc.* **64**(6), 517 (1981).
15. X. X. Wang, K. Murakami, O. Sugiyama and S. Kaneko, *J. Eur. Ceram. Soc.* **21**, 1367 (2001).
16. A. Megriche and M. Troccaz, *Mater. Res. Bull.* **33**, 569 (1998).
17. E. R. Nielsen, E. Ringgaard and M. Kosec, *J. Eur. Ceram. Soc.* **22**, 1847 (2002).
18. A. Boutarfaia, *Ceram. Inter.* **26**, 583 (2000).
19. Powder diffraction File no. 50-346. International Centre for Diffraction Data, Newton Square, PA, 2000.
20. Powder diffraction File no. 37-1484. International Centre for Diffraction Data, Newton Square, PA, 2000.
21. S. Fushimi and T. Ikeda, *J. Am. Ceram. Soc.* **50**, 129 (1967).
22. Z. Branković, G. Branković and J. A. Varela, *J. Mater. Sci.* **14**, 37 (2003).
23. Y.-S. Hong, H.-B. Park and S.-J. Kim, *J. Eur. Ceram. Soc.* **18**, 613 (1998).
24. T. Y. Chen, S. Y. Chu and Y. D. Juang, *Sensor. Actuat. A-Phys.* **102**, 6 (2002).
25. S. Y. Chu, T. Y. Chen and I. T. Tsai, *Integr. Ferroelectr.* **58**, 1293 (2003).

26. L. B. Kong, W. Zhu and O. K. Tan, *Mater. Lett.* **42**, 232 (2000).
27. G. Fantozzi, A. Bouzid, E. M. Bourim and M. Gabbay, *J. Eur. Ceram. Soc.* **25**(13), 3213 (2005).
28. R. Yimnirun, S. Ananta and P. Laoratanakul, *Mat. Sci. Eng. B-Solid.* **112**, 79 (2004).
29. H. Ouchi, M. Nishida and S. Hayakawa, *J. Am. Ceram. Soc.* **49**(11), 577 (1966).
30. E. R. Nielsen, E. Ringgaard and M. Kosec, *J. Eur. Ceram. Soc.* **22**, 1847 (2002).
31. L. B. Kong and J. Ma, *Mater. Lett.* **51**, 95 (2001).
32. B. S. Kang, G. C. Dong and S. K. Choi, *J. Mater. Sci. Lett.* **9**, 139 (1998).
33. K. Kinoshita and A. Yamaji, *J. Appl. Phys.* **47**(1), 371 (1976).
34. K. Okazaki and K. Nagata, *J. Electron. Commun. Soc. Jpn. C.* **53**, 815 (1970).
35. P. Ravindranathan, S. Komarneni, A. S. Bhalla and R. Roy, *J. Am. Ceram. Soc.* **74**, 2996 (1991).

ELSEVIER

Materials Science and Engineering B 132 (2006) 292–299

MATERIALS SCIENCE & ENGINEERING B

www.elsevier.com/locate/mseb

Effects of magnesium niobate precursor and calcination condition on phase formation and morphology of lead magnesium niobate powders

R. Wongmaneerung [a], T. Sarakonsri [b], R. Yimnirun [a], S. Ananta [a,*]

[a] *Department of Physics, Faculty of Science, Chiang Mai University, Chiang Mai 50200, Thailand*
[b] *Department of Chemistry, Faculty of Science, Chiang Mai University, Chiang Mai 50200, Thailand*

Received 1 March 2006; received in revised form 26 April 2006; accepted 28 April 2006

Abstract

A perovskite phase of lead magnesium niobate, $Pb(Mg_{1/3}Nb_{2/3})O_3$ or PMN, powders has been synthesized by a rapid vibro-milling technique. Both columbite $MgNb_2O_6$ and corundum $Mg_4Nb_2O_9$ have been employed as magnesium niobate precursors, with the formation of the PMN phase investigated as a function of calcination conditions by thermal gravimetric and differential thermal analysis (TG–DTA) and X-ray diffraction (XRD). The particle size distribution of the calcined powders was determined by laser diffraction technique. Morphology, crystal structure and phase composition have been determined via a combination of scanning electron microscopy (SEM), transmission electron microscopy (TEM) and energy-dispersive X-ray (EDX) techniques. The magnesium niobate precursor and calcination condition have been found to have a pronounced effect on the phase and morphology evolution of the calcined PMN powders. It is seen that optimisation of calcination conditions can lead to a single-phase PMN in both methods. However, the formation temperature and dwell time for single-phase PMN powders were lower for the synthetic method employing a columbite $MgNb_2O_6$ precursor.

Keywords: Lead magnesium niobate; Magnesium niobate; Perovskite; Powder synthesis; Calcination

1. Introduction

Lead magnesium niobate, $Pb(Mg_{1/3}Nb_{2/3})O_3$ or PMN, is one of the most widely investigated relaxor ferroelectric materials with a perovskite structure. The excellent dielectric broadening and electrostrictive properties make it a promising electroceramic material for capacitor, electrostrictive actuator, electromechanical transducer and electro-optic applications [1–3]. There has been a great deal of interest in the preparation of single-phase PMN powders as well as in the sintering and dielectric properties of PMN-based ceramics [4–6]. However, it is well documented that the formation of PMN perovskite via the solid-state reaction is often accompanied by the occurrence of unwanted pyrochlore-type phases because of the volatilisation of PbO, the low dispersion of MgO and the differences of the reactive temperature between Pb–Nb and Pb–Mg [7–9]. Hence, several innovation techniques [10–12] have been utilized to minimize the amount of pyrochlore phase formed.

The initial work of Lejeune and Boilot [10] considered the many parameters which influence the synthesis of PMN from PbO, MgO and Nb_2O_5 precursors, concluding that the formation of a pyrochlore phase could not be completely eliminated. Moreover, it was proposed that the reactivity of magnesium oxide with lead and niobium oxides was the definitive factor governing products of the reaction. These authors later proposed the use of $MgCO_3$ in place of MgO to increase the yield of perovskite PMN. Swartz and Shrout [7] developed an effective way of producing PMN powder in high yield by the introduction of a two-step process (the B-site precursor approach). In the method, an intermediate step to give columbite-type $MgNb_2O_6$ precursor is used to bypass the formation of the pyrochlore phases. Alternatively, Joy and Sreedhar [11] proposed the use of $Mg_4Nb_2O_9$ precursor in place of $MgNb_2O_6$ for the fabrication of pyrochlore-free PMN. More recently, Lu and Yang [12] adopted a two-stage synthesis method by precalcining the mixture of MgO and Nb_2O_5 at 1000 °C to form $Mg_4Nb_2O_9$. This compound was then quenched at 850–900 °C with PbO to form PMN without further soaking. This approach yielded perovskite PMN as the dominant phase, with pyrochlore impurities of less than 5% and some residual MgO. It was also claimed that the pyrochlore

* Corresponding author. Tel.: +66 53 943367; fax: +66 53 943445.
E-mail address: suponananta@yahoo.com (S. Ananta).

0921-5107/$ – see front matter © 2006 Elsevier B.V. All rights reserved.
doi:10.1016/j.mseb.2006.04.034

phases and the residual MgO could be eliminated completely with the introduction of excess PbO and nitric acid, respectively. However, the preparation of PMN using $Mg_4Nb_2O_9$ precursor, to date, has not been extensive as that of PMN using $MgNb_2O_6$ precursor. Moreover, its effect on the formation of perovskite PMN phase under various calcination conditions (especially the effects of applied dwell time and heating/cooling rates) has not been adequately characterized.

The purpose of this study was to compare the two B-site precursor synthetic routes of PMN formation and the characteristics of the resulting powders. The phase formation and morphology of the powders calcined at various conditions will be studied and discussed.

2. Experimental procedure

$Pb(Mg_{1/3}Nb_{2/3})O_3$ was synthesised by a similar methodology of B-site precursor mixed oxide synthetic route, as reported earlier [4]. Starting precursors were as follows: PbO (JCPDS file number 77-1971), MgO (periclase: JCPDS file number 71-1176) and Nb_2O_5 (JCPDS file number 80-2493) (Aldrich, 99% purity). These three oxide powders exhibited an average particle size in the range of 3.0–5.0 μm. First, two intermediate phases of magnesium niobate: $MgNb_2O_6$ and $Mg_4Nb_2O_9$ were separately prepared by the solid-state reaction method previously reported [13,14], employing an optimised calcination conditions of 1000 °C for 4 h with heating/cooling rates of 30 °C/min and 950 °C for 2 h with heating/cooling rates of 25 °C/min, respectively. The following reaction sequences were then proposed for the formation of PMN:

1. The columbite route:

$$3PbO(s) + MgNb_2O_6(s) \rightarrow 3Pb(Mg_{1/3}Nb_{2/3})O_3(s) \quad (1)$$

2. The corundum route:

$$12PbO(s) + Mg_4Nb_2O_9(s) + 3Nb_2O_5(s) \rightarrow 12Pb(Mg_{1/3}Nb_{2/3})O_3(s) \quad (2)$$

Instead of employing a ball-milling procedure (ZrO_2 media under acetone for 24 h [7]), a McCrone vibro-milling was used. In order to improve the reactivity of the constituents, the milling process was carried for 2 h (instead of 30 min [4]) with corundum media in isoproponal. After drying at 120 °C for 2 h, various calcination conditions were applied in order to investigate the formation of PMN phase in each calcined powders.

The reactions of the uncalcined powders taking place during heat treatment were investigated by thermal gravimetric and differential thermal analysis (TG–DTA, Shimadzu) using a heating rate of 10 °C/min in air from room temperature up to 900 °C. Calcined powders were subsequently examined by room temperature X-ray diffraction (XRD; Philips PW 1729 diffractometer) using Ni-filtered Cu Kα radiation, to identify the phases formed and optimum calcination conditions for the manufacture of PMN powders. The mean crystallite size was determined using the diffraction peak (1 1 0) of the perovskite pattern by using Scherrer equation [15]. Particle size distributions of powders were determined by laser diffraction technique (DIAS 1640 laser diffraction spectrometer), with the grain size and morphologies of powders observed by scanning electron microscopy (SEM; JEOL JSM-840A). The chemical composition and structure of the phases formed were elucidated by transmission electron microscopy (CM 20 TEM/STEM) operated at 200 keV and fitted with an energy-dispersive X-ray (EDX) analyser with an ultra-thin window. EDX spectra were quantified with the virtual standard peaks supplied with the Oxford Instruments eXL software. Powder samples were dispersed in solvent and deposited by pipette on to 3 mm holey copper grids for observation by TEM. In addition, attempt was made to evaluate the crystal structures of the observed compositions/phases by correcting the XRD and TEM diffraction data.

3. Results and discussion

TGA and DTA results for the mixtures synthesized by both B-site precursor methods are shown in Figs. 1 and 2, respectively. In general, similar trend of thermal characteristics is observed in both precursors. As shown in Fig. 1, the powders prepared via both B-site precursor mixed oxide methods demonstrate three distinct weight losses. The first weight loss occurs below 200 °C, the second one between 200–300 °C and the final one after 750 °C. In the temperature range from room temperature to ~150 °C, both samples show small thermal peaks in the DTA curves, Fig. 2, which are related to the first weight loss. These DTA peaks can be attributed to the decomposition of the organic species such as rubber lining from the milling process similar to our earlier reports [13,16]. In comparison between the two B-site precursor routes, after the first weight loss, the columbite route shows a slightly higher weight loss over the temperature range of ~50–220 °C, followed by a much sharper fall in specimen weight with increasing temperature from ~250 to 350 °C. This columbite-precursor method also exhibits larger overall weight loss (~1.25%) than that of the corundum route (~1.00%).

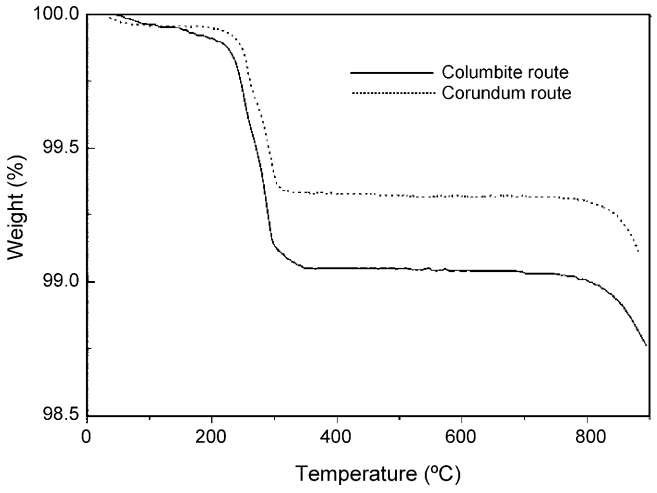

Fig. 1. TGA curves of the mixtures derived from columbite- and corundum-route.

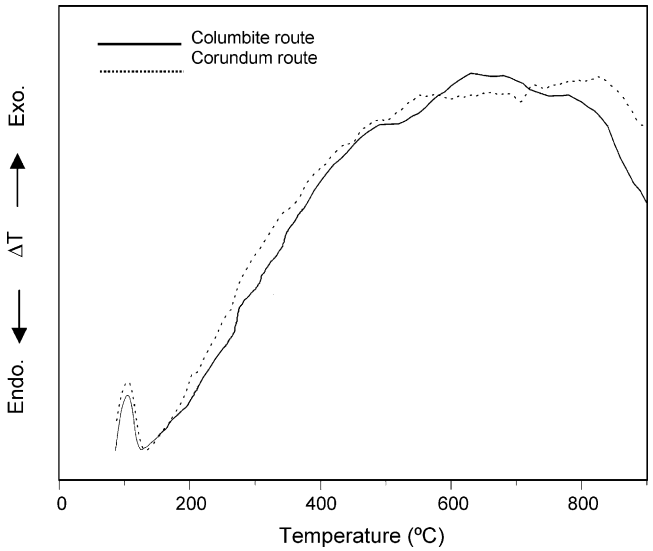

Fig. 2. DTA curves of the mixtures derived from columbite- and corundum-route.

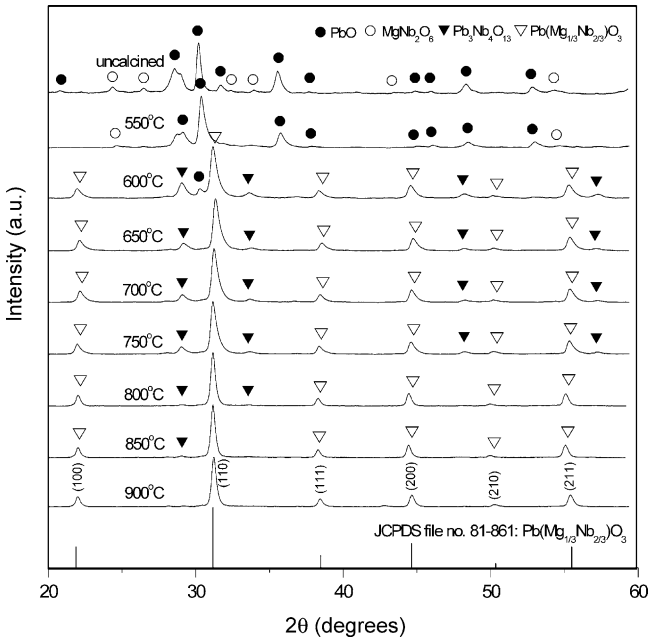

Fig. 3. XRD patterns of the columbite-route powders calcined at various conditions for 1 h with constant heating/cooling rates of 10 °C/min.

Corresponding to the second fall in specimen weight, by increasing the temperature up to ~700 °C, the solid-state reaction occurs between oxide precursors. The broad exothermic characteristic in both DTA curves represents that reaction, which has a maximum at ~600 and 800 °C for columbite- and corundum-routes, respectively. However, it is to be noted that there is no obvious interpretation of these peaks, although it is likely to correspond to a phase transition reported by a number of workers [4–8]. The different temperature, intensities and shapes of the thermal peaks for the two precursors here probably are related to the different starting materials especially magnesium niobate and consequently, caused by the removal of species differently bonded in the network, reactivity of different species (difference in type and dispersion of MgO) in the powders. These data were used to define the range of temperatures for XRD investigation between 550 and 1000 °C. It is to be noted that a significant weight loss in TG curves associated with large thermal change in DTA curves observed at temperatures above 750 °C (Figs. 1 and 2) may be attributed to the PbO volatilisation typically found in lead-based ferroelectrics, consistent with other investigators [17–19].

To study the phase development with increasing calcination temperature in each synthetic route, they were calcined at various temperatures for 1 h in air with constant heating/cooling rates of 10 °C/min, followed by phase analysis using XRD technique. As shown in Fig. 3, for the uncalcined powder and the powder calcined at 550 °C (columbite route), only X-ray peaks of PbO and $MgNb_2O_6$ precursors are present. Similarly, it is seen that unreacted precursors of PbO and $Mg_4Nb_2O_9$ are detected from the original mixture up to 650 °C for the corundum route (Fig. 4). These observations indicate that no reaction was yet triggered during the vibro-milling or low firing processes, in agreement with literature [4,13,16]. It is seen that PMN crystallites were developed in the powder at a calcination temperature as low as 600 and 650 °C for columbite- and corundum-routes, respectively. The results of X-ray diffraction measurement supported the DTA observation (Fig. 2) that PMN phase is formed at approximately 600–800 °C. In general, the strongest reflections apparent in the majority of these XRD patterns indicate the formation of the lead magnesium niobate, PMN (▽). These can be matched with JCPDS file number 81-0861 for the cubic phase, in space group $Pm\bar{3}m$ (no. 221) with cell parameters $a = 404$ pm [20] consistent with other workers [4,5]. According to Fig. 3, the formation of $Pb_3Nb_4O_{13}$ (▼) earlier reported by many researchers [4,21–23] has been found at 600 °C, which

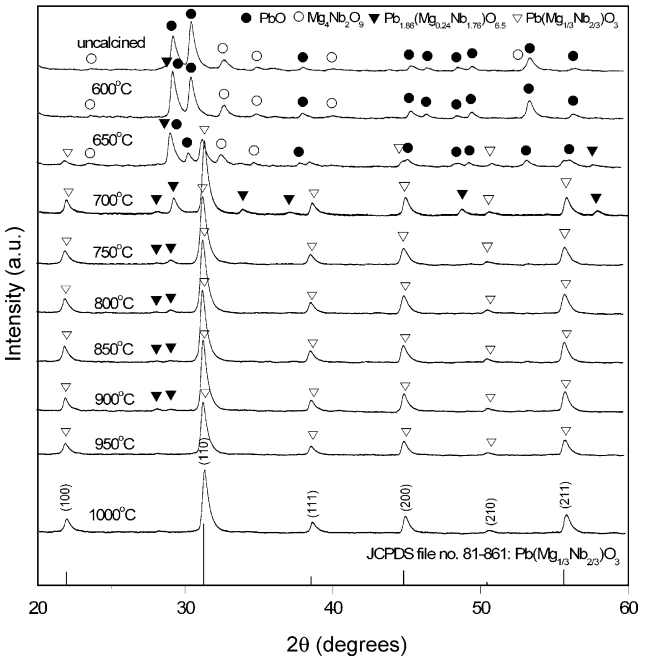

Fig. 4. XRD patterns of the corundum-route powders calcined at various conditions for 1 h with constant heating/cooling rates of 10 °C/min.

is associated to the second TG–DTA response in Figs. 1 and 2. This pyrochlore phase has a cubic structure with cell parameter $a = 1.056$ nm in space group *Fd3m* (no. 227) (JCPDS file number 25-0443) [24]. Upon calcination at 650 °C, the peak corresponding to PbO disappeared (not detectable by XRD). By increasing the calcination temperature from 650 to 850 °C, the yield of the cubic PMN phase increases significantly until at 900 °C, a single-phase of perovskite PMN is formed for the columbite route.

From Fig. 4, it is seen that calcination at 600 °C resulted in some new peak (▼) of the $Pb_{1.86}(Mg_{0.24}Nb_{1.76})O_{6.5}$ phase (JCPDS file number 82-0338) [25] mixing with the unreacted PbO and $Mg_4Nb_2O_9$ phases. To a first approximation, this $Pb_{1.86}(Mg_{0.24}Nb_{1.76})O_{6.5}$ phase earlier reported by many researchers [23,26,27] has a pyrochlore-type structure with a cubic unit cell $a = 1.060$ nm, space group *Fd3m* (no. 227). This pyrochlore phase was found at 600 °C and totally disappeared at 950 °C. As the temperature increased to 900 °C, the intensity of the PMN peaks was further enhanced and PMN becomes the predominant phase, in good agreement with the earlier TG–DTA results. This study also shows that PMN is the only detectable phase in the corundum-route powders after calcination in the range 950–1000 °C.

In the present study, an attempt was also made to calcine both precursors under various dwell times and heating/cooling rates (Figs. 5 and 6). In this connection, it is seen that the single-phase of PMN (yield of 100% within the limitation of the XRD technique) was also found to be possible in columbite-precursor powders calcined at 850 °C for 3 h with heating/cooling rates as fast as 30 °C/min (Fig. 5). The appearance of Nb_2O_5 and $Pb_3Nb_4O_{13}$ phases indicated that chemical decomposition probably caused by PbO volatilisation has occurred at relatively high firing temperatures (>850 °C) with long dwell times, consistent with other workers [4–8]. It is also interesting to note that in this

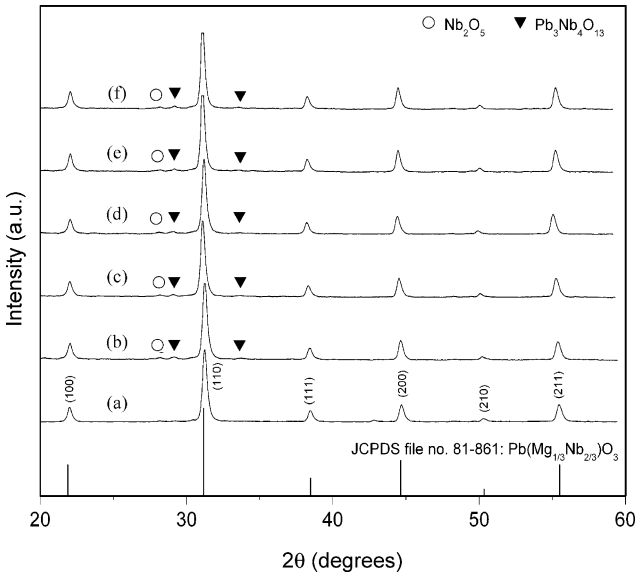

Fig. 5. XRD patterns of the columbite-route powders calcined at 850 °C, for 3 h with heating/cooling rates of (a) 30 °C/min, (b) 20 °C/min and (c) 10 °C/min, (d) for 2 h with heating/cooling rates of 10 °C/min and for 1 h with heating/cooling rates of (e) 30 °C/min and (f) 20 °C/min.

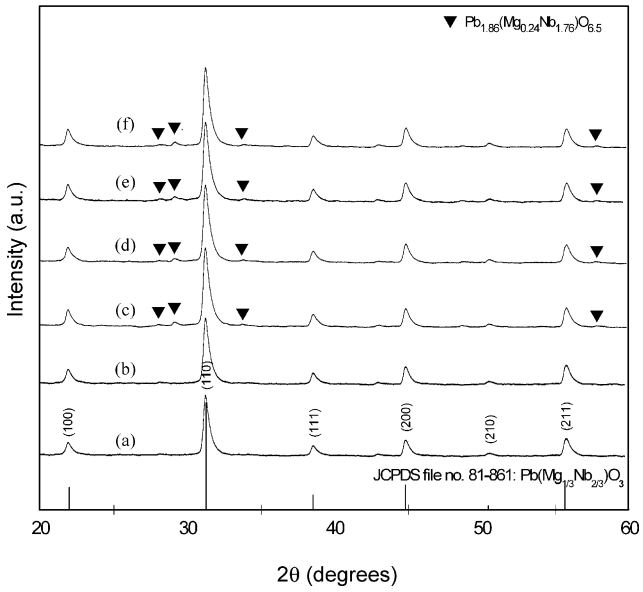

Fig. 6. XRD patterns of the corumdum-route powders calcined at 950 °C for 1 h with heating/cooling rates of (a) 30 °C/min and (b) 20 °C/min, at 900 °C for (c) 2 h (d) 3 h and (e) 4 h, with heating/cooling rates of 10 °C/min, and (f) at 950 °C, for 4 h with heating/cooling rates of 30 °C/min.

work the effects of both dwell time and heating/cooling rates were also found to be significant for the formation of perovskite PMN by using a corundum route (Fig. 6). It is seen that single-phase of PMN powders was also successfully obtained for a calcination temperature of 950 °C for 1 h with heating/cooling rates of 20 or 30 °C/min applied. The observation that the dwell time or heating/cooling rates may also play an important role in obtaining a single-phase of lead-based perovskite ferroelectrics is also consistent with other investigators [4,19,28]. However, some additional peaks at $2\theta \sim 43°$ are found in the Figs. 5(a) and 6(a). It is to be noted that there is no obvious interpretation of these peaks, although it is likely to correspond to a trace of MgO precursor. Nonetheless, with the limitation of X-ray technique and the inherent only single peak with very low intensity comparable to noise originated from the diffractometer, an accurate evaluation of the phase is not possible [15].

It is well established that the perovskite-type PMN tend to form together with the pyrochlore-type PbO–Nb_2O_5 compounds, depending on calcination conditions [7,8,23]. In the work reported here, evidence for the formation of PMN phase, which coexists with the cubic pyrochlore phase, is found after calcination at temperature ~650–900 °C, in agreement with literature [4,7,12,22]. No evidence of $Pb_{1.83}Mg_{0.29}Nb_{1.71}O_{6.39}$ was found, nor was there any indication of the pyrochlore phase of $Pb_3Nb_2O_8$ and $Pb_5Nb_4O_{15}$ [21–23] being present. In general, the formation temperature and dwell times for high purity PMN observed in the powders derived from a combination of a mixed oxide synthetic route and a carefully determined calcination condition (especially with a rapid vibro-milling technique) are slightly lower than those reported for the powders prepared via many other conventional mixed oxide methods [7–11].

Based on the TG–DTA and XRD data, it may be concluded that, over a wide range of calcination conditions, single-

phase perovskite PMN cannot be straightforwardly formed via a two-step B-site precursor method, as verified by a number of researchers [4,7,8]. The experimental work carried out here suggests that the optimal calcination conditions for single-phase PMN are 900 °C for 1 h or 850 °C for 3 h (columbite route) and 950 °C for 1 h (corundum route), with heating/cooling rates as fast as 30 °C/min. The optimised formation temperature of single-phase PMN was lower for the columbite route probably due to the higher degree of reactivity with less reacting species involved [7,8]. As suggested by several workers [8,17], the degree of cation mixing in precursors significantly affects the phase formation behavior in the B-site synthesis of PMN. This observation may be accounted for by the fact that the columbite route possibly provides faster chemical reaction rate (only the reaction between PbO and $MgNb_2O_6$) and is able to enhance the formation of perovskite PMN phase by increasing the reactivity of MgO [8]. However, the minimum firing temperature required for the manufacturing of single-phase corundum $Mg_4Nb_2O_9$ (∼950 °C [14]) is lower than that of columbite $MgNb_2O_6$ (∼1000 °C [13]).

Therefore, in general, the methodology presented in this work provides a simple method for preparing perovskite PMN powders via a solid-state mixed oxide synthetic route. It is interesting to note that, by using either columbite- or corundum-routes, with an optimal calcination condition, the reproducible, low cost and flexible process involving simple solid-state reaction synthetic route can produce high purity perovskite PMN (with impurities undetected by XRD technique) from relatively impure and inexpensive commercially available raw materials.

To further study the influence of precursor on the characteristics of the resulting PMN powders, a combination of particle size analysis, SEM, TEM and EDX is used to examine the powders obtained, as shown in Figs. 7–10 and Table 1. Fig. 7 compares the particle size distribution curves of calcined PMN powders derived from both B-site precursor methods, which indicate an appreciable size fractions at approximately 0.75–1.08 μm diameters, as also listed in Table 1 (averaged sizes). Even taking in account that the analysis does not reveal the real dimension of single particles (due to agglomeration effects as expected from the SEM results in Fig. 8), a uniform frequency distribution curve was observed for the columbite route whilst narrow distribution curve with tiny kink at front covering the range of 0.32–1.65 μm in sizes was found for the corundum route,

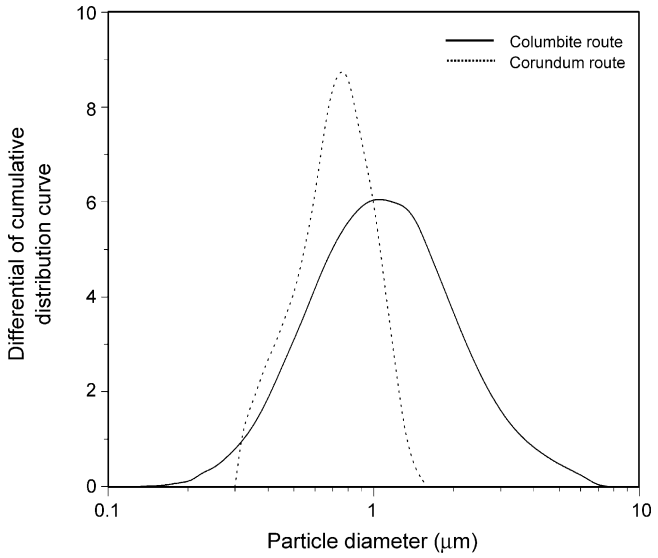

Fig. 7. The particle size curves of the columbite- and corundum-route PMN powders after calcined at their optimised conditions.

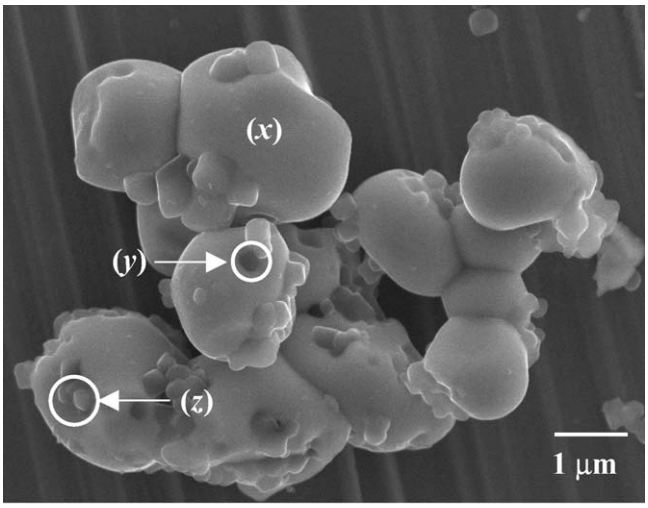

(a)

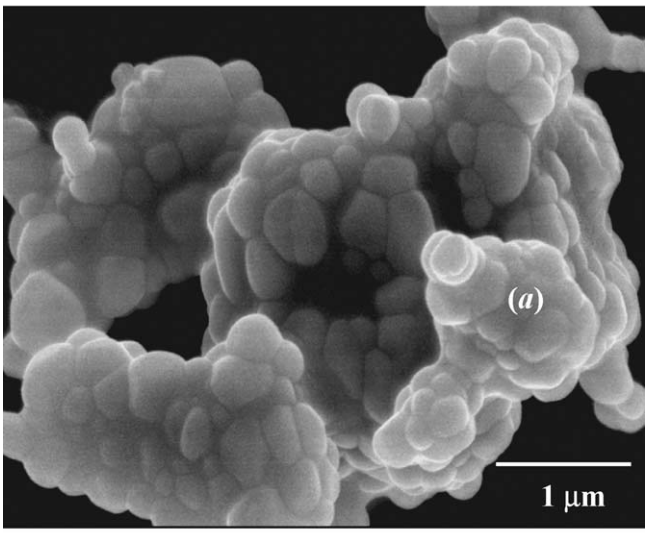

(b)

Fig. 8. SEM micrographs of the: (a) columbite- and (b) corundum-route PMN powders after calcined at their optimised conditions.

Table 1
Particle size data of both PMN powders measured by different techniques

Measurement techniques	Particle size range (average)	
	Columbite route	Corundum route
XRD[a] (nm, ±2.0)	26.60	22.50
Laser diffraction (μm, ±0.2)	0.15–7.50 (1.08)	0.32–1.65 (0.75)
SEM (μm, ±0.1)	0.25–3.00 (1.63)	0.20–1.25 (0.73)
TEM (μm, ±0.01)	0.25–0.65 (0.45)	0.10–0.55 (0.33)

[a] Crystallite size.

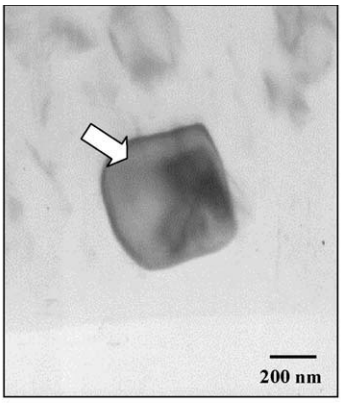

(a)

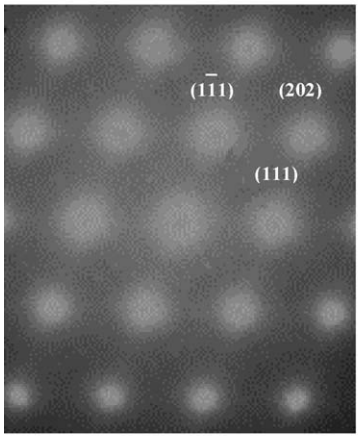

(b)

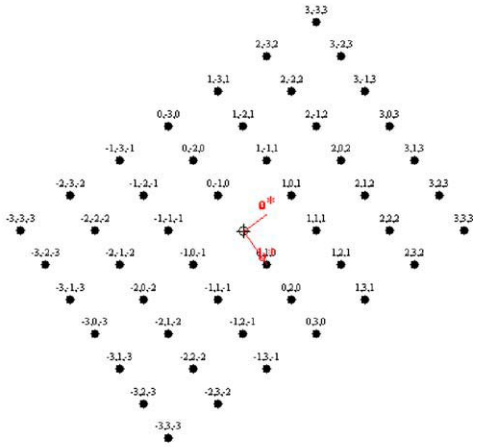

(c)

Fig. 9. (a) TEM micrograph with arrow indicates (b) SAED pattern ([$\bar{1}\,\bar{1}$ 0] zone axes) and (c) reciprocal lattice pattern simulation of the columbite-route PMN particles.

reflecting more the size of agglomerates than the real size of particles.

SEM micrographs of the calcined PMN powders derived from columbite- and corundum-precursor methods are shown in Fig. 8(a and b), respectively. In general, the particles are agglomerated and basically irregular in shape, with a substantial variation in particle size. Observed diameters range from 0.25 to 3.00 and 0.20 to 1.25 μm for columbite- and corundum-routes, respectively, in good agreement with the particle size distribution previously determined (Table 1). The primary particles in the agglomerates are, however, submicron in size. This is confirmed by TEM micrographs shown in Figs. 9 and 10. Additionally, the observed morphology reveals considerable difference in homogeneity, uniformity, size and shape between the two PMN powders. It is obviously evident that the columbite-route powders exhibit more heterogeneous morphology than the corundum-route powders. The columbite-route powders consist mainly of irregular round shape primary particles with a diameter of ∼1 μm or less (Fig. 8(a)). In addition to the primary particles, the powders have another kind of very fine particle (darker particles) with diameter of about 200 nm. A combination of SEM and EDX techniques has demonstrated that pyrochlore and unreacted precursor phases (marked as "*y*" and "*z*" in the micrograph in Fig. 8(a)) exist neighbouring the parent PMN phase (marked as "*x*") (see also Table 2). In general, EDX analysis using a 20 nm probe from a large number of particles of the two calcined powders confirmed the parent composition to be PMN. It is interesting to note that nano-scale MgO and PbO inclusions were also found in the SEM–EDX investigation for the columbite route, in agreement with earlier works [9,29], even though this could not be detected by XRD. It is, therefore, intriguing to note the advantage of a combination between SEM and EDX techniques, which lies in its ability to reveal microstructural features often missed by the XRD method which requires at least 5 wt% of the component [15].

However, it is seen that higher degree of agglomeration with more rounded particle morphology is observed in the powders produced by the corundum route (Fig. 8(b)). The strong inter-particle bond within each aggregate is evident by the formation of a well-established necking between neighbouring particles.

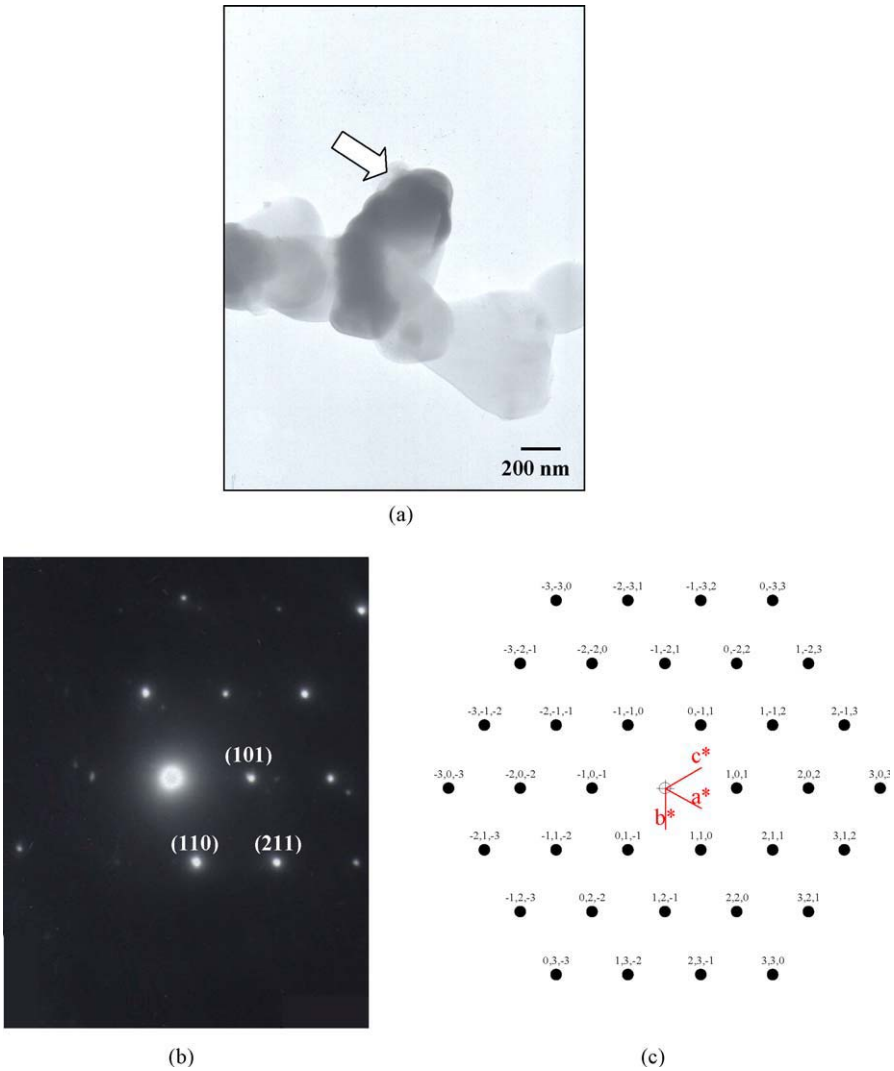

Fig. 10. (a) TEM micrograph with arrow indicates (b) SAED pattern ([$\bar{1}$ 1 1] zone axes) and (c) reciprocal lattice pattern simulation of the corundum-route PMN particles.

This observation could be attributed to the mechanism of surface energy reduction of the ultrafine powders, i.e. the smaller the powder the higher the specific surface area [30]. In general, it is seen that primary particle in corundum-route powders is clearly smaller in size than the columbite-route powders. The averaged particle size of corundum-precursor PMN powders with finer particle size is regarded as advantage for better reactivity.

Bright field TEM images of discrete particles of the calcined PMN powders are shown in Figs. 9(a) and 10(a) for the columbite- and corundum-routes, respectively, indicating the particle sizes and shapes at higher magnifications. The observed morphology reveals the considerable difference in both size and shapes between the two particles. Primary particle in the columbite-route PMN powders is clearly larger in size and also higher in angularity than the corundum-route powders. By employing a combination of both selected area electron diffraction (SAED) and crystallographic analysis, the perovskite phase of cubic PMN was identified for the columbite- and corundum-

Table 2
EDX analysis on PMN powders derived from columbite- and corundum-routes

EDX positions	Composition (at.%)			Possible phase(s)
	Pb (M)	Mg (K)	Nb (L)	
x	43.12	18.87	38.01	$Pb(Mg_{1/3}Nb_{2/3})O_3$
y	8.45	84.10	7.45	$Pb_{1.86}(Mg_{0.24}Nb_{1.76})O_{6.5}$ (M), $Pb_{1.83}(Mg_{0.29}Nb_{1.71})O_{6.39}$ (m), MgO (m)
z	5.75	89.85	4.40	$Pb_{1.86}(Mg_{0.24}Nb_{1.76})O_{6.5}$ (M), $Pb_{1.83}(Mg_{0.29}Nb_{1.71})O_{6.39}$ (m), MgO (m), PbO (m)
a	45.04	17.75	37.21	$Pb(Mg_{1/3}Nb_{2/3})O_3$

M, Majority; m, Minority.

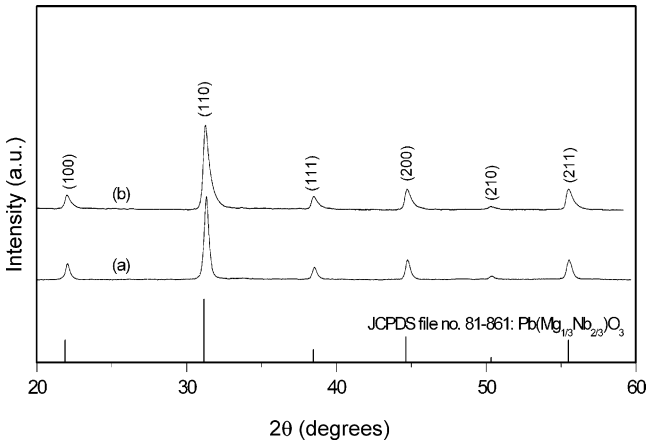

Fig. 11. XRD patterns of PMN ceramics derived from: (a) columbite- and (b) corundum-routes after sintering at 1225 °C for 2 h.

routes as shown in Figs. 9(b and c) and 10(b and c), respectively, in good agreement with the XRD results.

Preliminary study on the ceramic production from the powders prepared from both routes was also conducted. As shown in Fig. 11, it can be seen that the single-phase perovskite PMN ceramics can be prepared by sintering both PMN powders at 1225 °C for 2 h based upon the firing condition advocated by Ananta and Thomas [5].

4. Conclusions

It has been shown that single-phase perovskite PMN powders can be successfully formed by employing either columbite or corundum B-site precursor method via a rapid vibro-milling. Evidence for the formation of a cubic pyrochlore phase, which coexists with the perovskite PMN parent phase, is found at calcination temperture ranging from 800 to 1050 °C. Amongst the two B-site precursor methods, it is seen that lower optimised calcination temperature for the production of pure PMN powders can be obtained by using the columbite route, whereas the smallest obtainable particle size was found in the corundum-route PMN powders.

Acknowledgements

The authors gratefully acknowledge the Thailand Research Fund (TRF), the Faculty of Science and the Graduate School, Chiang Mai University for all support.

References

[1] A.J. Moulson, J.M. Herbert, Electroceramics, second ed., Wiley, Chichester, 2003.
[2] G. Haertling, J. Am. Ceram. Soc. 82 (1999) 797.
[3] K. Uchino, Piezoelectrics and Ultrasonic Applications, Kluwer, 1998.
[4] S. Ananta, N.W. Thomas, J. Eur. Ceram. Soc. 19 (1999) 155–163.
[5] S. Ananta, N.W. Thomas, J. Eur. Ceram. Soc. 19 (1999) 629–635.
[6] Y.-C. Liou, J.H. Chen, Ceram. Int. 30 (2004) 17–22.
[7] S.L. Swartz, T.R. Shrout, Mater. Res. Bull. 17 (1982) 1245–1250.
[8] T.R. Shrout, A. Halliyal, Am. Ceram. Soc. Bull. 66 (1987) 704–711.
[9] E. Goo, K. Okazaki, J. Am. Ceram. Soc. 69 (1986) C188–C190.
[10] M. Lejeune, J.P. Boilot, Mater. Res. Bull. 20 (1985) 493–499.
[11] P.A. Joy, K. Sreedhar, J. Am. Ceram. Soc. 80 (1997) 770.
[12] C.H. Lu, H.S. Yang, Mater. Sci. Eng. B84 (2001) 159.
[13] S. Ananta, Mater. Lett. 58 (2004) 2781–2786.
[14] S. Ananta, Mater. Lett. 58 (2004) 2530–2536.
[15] H.P. Klug, L.E. Alexander, X-ray Diffraction Procedures, second ed., Wiley, New York, 1974.
[16] R. Wongmaneerung, R. Yimnirun, S. Ananta, Mater. Lett. 60 (2006) 1447–1452.
[17] J.P. Guha, J. Mater. Sci. 36 (2001) 5219–5226.
[18] J. Ryu, J.J. Choi, H.E. Kim, J. Am. Ceram. Soc. 84 (2001) 902.
[19] A. Udomporn, S. Ananta, Mater. Lett. 58 (2004) 1154–1159.
[20] Powder Diffraction File No. 81-0861, International Centre for Diffraction Data, Newton Square, PA, 2000.
[21] M.M.A. Sekar, A. Halliyal, J. Am. Ceram. Soc. 81 (1998) 380–388.
[22] N.K. Kim, Mater. Lett. 32 (1997) 127–130.
[23] M. Dambekalne, I. Brante, A. Sternberg, Ferroelectrics 90 (1989) 1–14.
[24] Powder Diffraction File No. 25-0443, International Centre for Diffraction Data, Newton Square, PA, 2000.
[25] Powder Diffraction File No. 82-0338, International Centre for Diffraction Data, Newton Square, PA, 2000.
[26] J.P. Guha, J. Mater. Sci. 34 (1999) 4985–4994.
[27] L.P. Cruz, A.M. Segadães, J. Rocha, J.D. Pedrosa de Jesus, Mater. Res. Bull. 37 (2002) 1163–1173.
[28] R. Tipakontitikul, S. Ananta, Mater. Lett. 58 (2004) 449.
[29] A.L. Costa, G. Fabbri, E. Roncari, C. Capiani, C. Galassi, J. Eur. Ceram. Soc. 21 (2001) 1165–1170.
[30] J.S. Reeds, Principles of Ceramic Processing, second ed., Wiley, New York, 1995.

ELSEVIER

Materials Science and Engineering B 132 (2006) 300–306

MATERIALS SCIENCE & ENGINEERING B

www.elsevier.com/locate/mseb

Phase development and dielectric properties of $(1-x)Pb(Zr_{0.52}Ti_{0.48})O_3$–$xBaTiO_3$ ceramics

Wanwilai Chaisan [a,*], Rattikorn Yimnirun [a], Supon Ananta [a], David P. Cann [b]

[a] *Department of Physics, Faculty of Science, Chiang Mai University, Chiang Mai, Thailand*
[b] *Department of Mechanical Engineering, Oregon State University, Corvallis, OR, USA*

Received 8 February 2006; received in revised form 27 April 2006; accepted 28 April 2006

Abstract

$(1-x)Pb(Zr_{0.52}Ti_{0.48})O_3$–$xBaTiO_3$ ceramics were prepared by a modified mixed-oxide method. The phase formation was studied by XRD analysis. All compositions exhibit complete solid solutions of perovskite-like phase in the $(1-x)$PZT–xBT system. The (2 0 0)/(0 0 2) peak was found to split at the composition $x = 0.6$ and the co-existence of tetragonal–rhombohedral phases occurs with $x \leq 0.6$. The possible range of compositions which correspond to a phase transition is $0.6 < x < 0.7$. While pure BT ceramics exhibited a sharp phase transformation expected for normal ferroelectrics, phase transformation behavior of the $(1-x)$PZT–xBT solid solutions became more diffuse with increasing BT contents. This was primarily evidenced by an increased broadness in the dielectric peak, with a maximum peak width occurring at $x = 0.5$.

Keywords: Phase development; Dielectric properties; Barium titanate (BT); Lead zirconate titanate (PZT)

1. Introduction

Nowadays, many researches have been carried out on the phase development and dielectric behavior of various perovskite ferroelectric ceramics, which can be applied to several micro- and nano-electronic devices such as multilayer capacitors, microactuators and miniaturized transducers [1,2]. Among the many ferroelectric materials, barium titanate ($BaTiO_3$ or BT) and lead zirconate titanate ($Pb(Zr,Ti)O_3$ or PZT) are representative perovskite ferroelectric and piezoelectric prototypes because of their excellent electrical properties [3,4]. While, barium titanate is a normal ferroelectric with a high dielectric constant and a relatively low T_C (~120 °C), lead zirconate titanate has a higher T_C of 390 °C which allows PZT-based piezoelectric devices to be operated at relatively higher temperatures [2,5]. Although BT ceramic has better mechanical properties than PZT, the sintering temperature is also higher [1,3,5]. Thus, mixing PZT with BT is expected to decrease the sintering temperature of BT-based ceramics, a desirable move towards electrode of lower cost [6]. Moreover, since PZT–BT is not a pure-lead system, it is easier to prepare single phase ceramics with lower amount of undesirable pyrochlore phases [7,8]. With their complimentary characteristics, it is expected that excellent properties can be obtained from ceramics in PZT–BT system.

So far, there have been only a few studies on PZT–BT system [7–9]. These studies have focused mainly on powder preparation and some electrical properties. However, there have been no systematic studies on the phase development and dielectric properties of the whole series of PZT–BT compositions, which would help in identifying excellent electrical properties within this system. In the present study, PZT and BT were chosen as end components to prepare solid solutions via a modified mixed-oxide method. Phase development and lattice parameter changes of the whole series are investigated by XRD analysis. Finally, the dielectric properties of PZT–BT ceramics are determined as a function of temperature and frequency to establish structure–property relationships.

2. Experimental procedure

The $(1-x)$PZT–xBT compositions with $0.0 \leq x \leq 1.0$ were prepared by a modified mixed-oxide method [7]. The starting raw materials were reagent grade PbO, ZrO_2, TiO_2 and $BaCO_3$ powders (Fluka, >99% purity). For BT powder, $BaCO_3$ and TiO_2 were homogeneously mixed via ball-milling with zirconia media in ethanol for 24 h. The mixture was dried and

* Corresponding author. Tel.: +66 53 943 376; fax: +66 53 943 445.
E-mail address: wanwilai_chaisan@yahoo.com (W. Chaisan).

0921-5107/$ – see front matter © 2006 Elsevier B.V. All rights reserved.
doi:10.1016/j.mseb.2006.04.033

then calcined at 1300 °C for 2 h to form $BaTiO_3$. The PZT powders were synthesized through the modified mixed-oxide method, in which lead zirconate ($PbZrO_3$) was first prepared and then used as precursor in order to reduce the occurrence of undesirable pyrochlore phase, as well as very high melting temperature $ZrTiO_4$ phase, which is difficult to eliminate [7]. Pure $PbZrO_3$ phase was formed by reacting PbO with ZrO_2 at 800 °C for 2 h. $PbZrO_3$ powder was then mixed with PbO and TiO_2 and calcined at 900 °C for 2 h to form single phase PZT. The (1−*x*)PZT–*x*BT powders were then formulated from the BT and PZT components by employing the similar mixed-oxide procedure and calcining at various temperatures between 900 and 1300 °C for 2 h in order to obtain single phase (1−*x*)PZT–*x*BT powders. The phase formation process was followed by XRD analysis. The lattice parameters *a* and *c* were determined by using a non-linear least squares method [10]. The (1−*x*)PZT–*x*BT powders were then isostatically cold-pressed at 4 MPa into pellets, which were consequently sintered between 1050 to 1350 °C for 2 h in air. The grain morphology and size were directly imaged using scanning electron microscopy (SEM) and the average grain size was determined by using a mean linear intercept method [11]. For dielectric measurements, silver paste was fired on both sides of the polished samples at 550 °C for 30 min as the electrodes. Dielectric properties of the sintered ceramics were studied as a function of both temperature and frequency. The capacitance was measured with a HP4284A LCR meter in connection with a Delta Design 9023 temperature chamber and a sample holder (Norwegian Electroceramics) capable of high temperature measurement. Relative permittivity (ε_r) was calculated using the geometric area and thickness of discs.

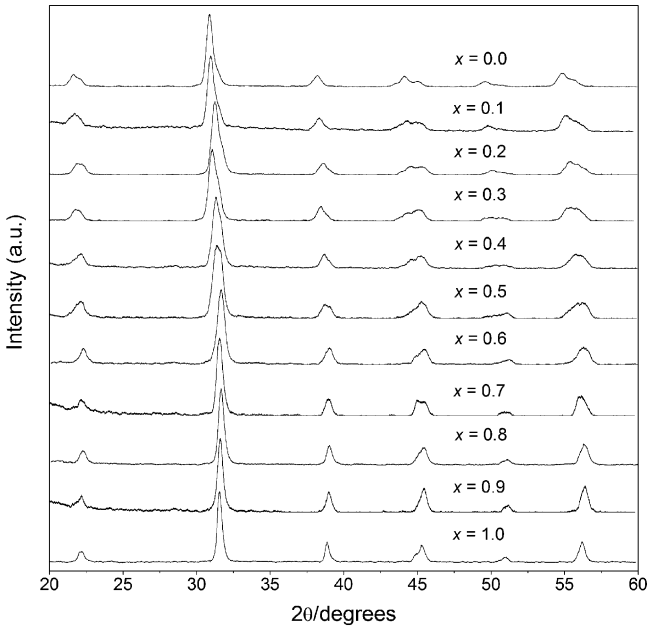

Fig. 1. XRD diffraction patterns of (1−*x*)PZT–*x*BT powders.

3. Results and discussion

The phase formation behavior of the (1−*x*)PZT–*x*BT powders is revealed by XRD as shown in Fig. 1. The diffraction pattern of powders with $x = 1.0$ match exactly that of perovskite $BaTiO_3$ (JCPDS no. 75-0460), whereas that of $x = 0.0$ is of a perovskite structure of $Pb(Zr_{0.52}Ti_{0.48})O_3$ with co-existence of both tetragonal and rhombohedral phases, matching with the

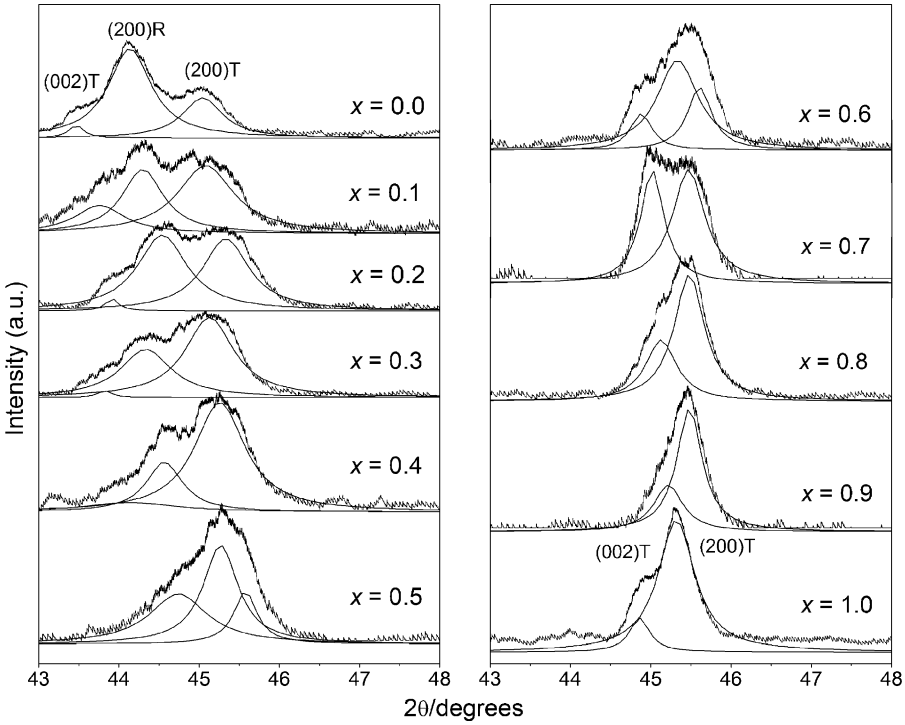

Fig. 2. XRD diffraction patterns for the (2 0 0) peaks of (1−*x*)PZT–*x*BT powders. Deconvolution of data shows the relative proportions of the rhombohedral and tetragonal phases.

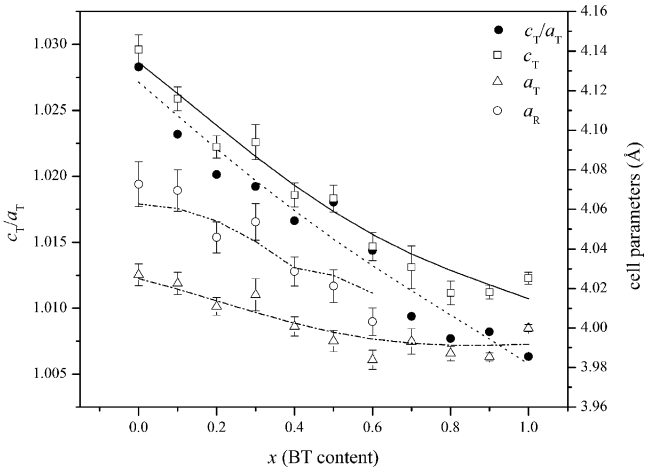

Fig. 3. Variation of cell parameters in the (1−x)PZT–xBT system. The solid and dashed lines are guides for the eyes.

JCPDS file no. 33-0784 and 73-2022, respectively. In the ladder pattern, a series of continuous solid solutions of PZT–BT with perovskite structure without any trace of pyrocholre phase normally forms. With increasing PZT content, the diffraction peaks shifted towards lower angle and the diffraction peak around 2θ of 43–46° was found to split at composition $x = 0.6$ (as shown in Fig. 2). This observation suggests that 0.4PZT–0.6BT composition may lead to a diffuse morphotropic phase boundary (MPB) between the tetragonal and rhombohedral PZT phases [12]. This is further evidenced in Fig. 2, which shows the evolution of the (2 0 0)/(0 0 2) peak as a function of composition over the range $2\theta = 43$–48. The data indicate the appearance of a triplet peak due to the superposition of the tetragonal and rhombohedral (2 0 0) peaks. With increasing PZT content, the intensity ratio of the (2 0 0)/(0 0 2) peak tends to decrease down to $x = 0.6$, where the rhombohedral peak is first observed. The XRD patterns with high degree of PZT content ($x \leq 0.6$) showed in all cases the co-existence of both tetragonal and rhombohedral phases as clearly shown in Fig. 2. The variation of these triplet-diffraction lines could be explained by microscopic compositional fluctuations occurring in these perovskite materials, which cannot provide real homogeneity in the solid solutions, and also by the different stresses induced in the particles, which determine the co-existence of tetragonal–rhombohedral phases [13,14].

The lattice parameters were then determined from the triplets (2 0 0) by using a non-linear least squares method [10]. The a-parameter, c-parameter and tetragonality (c/a) of (1−x)PZT–xBT ceramics are plotted as a function of BT content in Fig. 3. The results show that cell parameters of all compositions gradually decrease with increasing BT content as expected from the steady increase in 2θ of diffraction peaks (Fig. 2) and agreed with Vegard's law [15]. Thus, the perovskite PZT–BT system is confirmed to develop a complete solid solubility, as also observed in similar solid solutions [14]. However, the composition boundary between the real tetragonal and rhombohedral

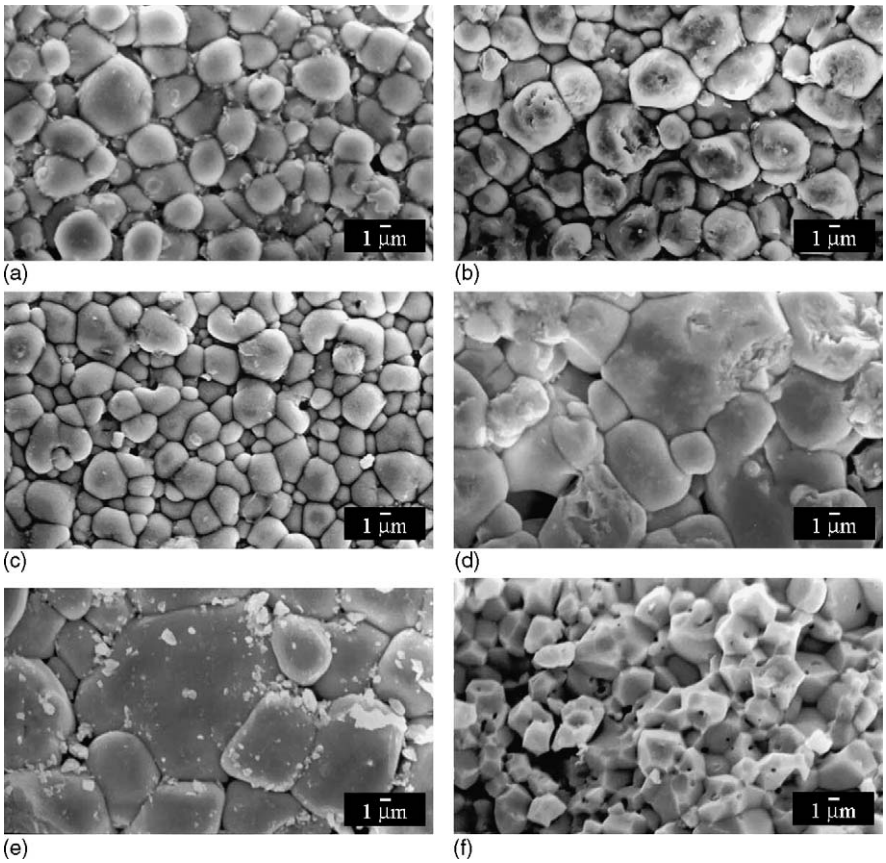

Fig. 4. The microstructure of (1−x)PZT–xBT ceramics: (a) $x = 0.0$, (b) $x = 0.1$, (c) $x = 0.3$, (d) $x = 0.7$, (e) $x = 0.9$ and (f) $x = 1.0$.

Table 1
Characteristics of (1−x)PZT–xBT ceramics with optimized processing conditions

Compositions	Sintering temperature (°C)	Density (g/cm^3)	Average grain size (μm)
PZT	1100	7.7	2.36
0.9PZT–0.1BT	1200	7.6	2.86
0.7PZT–0.3BT	1200	7.2	1.97
0.6PZT–0.4BT	1250	6.9	2.31
0.5PZT–0.5BT	1250	6.6	3.87
0.4PZT–0.6BT	1250	6.3	4.19
0.3PZT–0.7BT	1250	5.7	3.71
0.1PZT–0.9BT	1300	5.3	5.72
BT	1350	5.8	2.42

phases could not be delimited under the present experimental limit of accuracy. The possible range of compositions which corresponds to a phase transition is $0.6 < x < 0.7$ and high resolution XRD analysis is clearly necessary to detect the possible superposition of phases in further studies.

The optimized sintering temperatures, densities, and average grain sizes of the sintered (1−x)PZT–xBT ceramics are listed in Table 1. Higher firing temperatures were necessary for compositions containing a large fraction of BT. The microstructure of (1−x)PZT–xBT ceramics is shown in Fig. 4. Compositions with $x = 0.7$ and 0.9 could not be sintered to sufficient densities and the theoretical densities of ceramics in this range were about 86–89%. It is possible that volatilization of PbO during firing is the main reason for the failure in preparing dense ceramics over this composition range [16,17]. It should be noted that the grain size and density can influence dielectric properties [4] but in the present work average grain size varies between 2 and 5 μm, as shown in Table 1, which should not play significant role in variation of dielectric properties. The variation of the dielectric constant with temperature for ceramics with $x = 0.0$–0.6 is displayed in Fig. 5. The Curie temperatures and maximum dielectric constants of the pure PZT ceramics in this work was 390 °C and 14,900, respectively. With increasing BT content, the transition temperature shifts monotonously to lower temperatures and dielectric peak becomes broader, indicating the increasing of diffused phase transition. The frequency dependence of dielectric properties for $x = 0.0$ and 0.5 ceramics is shown in Fig. 6. For $x = 0.0$ (pure PZT) (Fig. 6a), the ε_r peak is sharp and approaches 15,000. A normal ferroelectric behavior is observed in PZT as evident by a relatively weak frequency dependence of dielectric properties, except at low frequencies as a result of high temperature space charge conduction. Similar observation is also found for pure BT. On the other hand, a diffuse phase transition and small frequency dispersion of the dielectric maxima are observed in $x = 0.5$ ceramic (Fig. 6b). Moreover, it should also be noted here that the dielectric constant rises and dielectric loss significantly increases at high temperature as a result of thermally activated space charge conduction [18]. For PZT ceramic (Fig. 6a), a dielectric constant at the lower frequencies seems to increase continuously. It can be assumed that polar defect pairs created under these conditions and may be related to such dielectric anomaly [19].

As described above, a combination of PZT with BT introduces dielectric peak broadening. For better understanding of the interesting dielectric behaviors of PZT–BT system, we look at these behaviors through Curie–Weiss law. For a normal ferroelectric such as PZT and BT, above the Curie temperature the

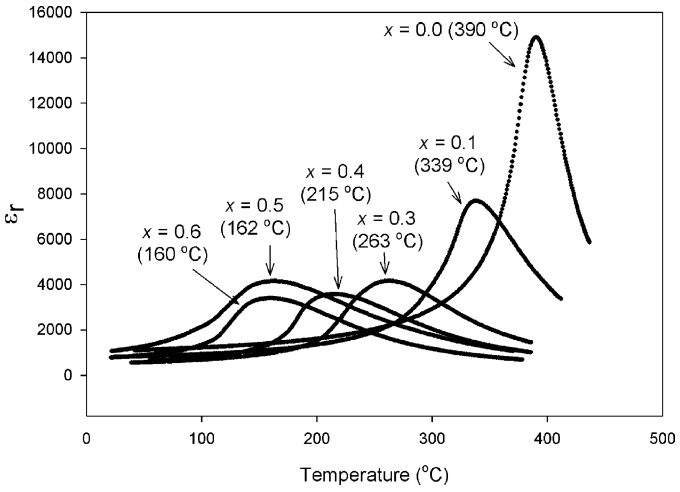

Fig. 5. Variation of dielectric constant (ε_r) with temperature for (1−x)PZT–xBT ceramics at 500 kHz (T_C of each composition is indicated in parenthesis).

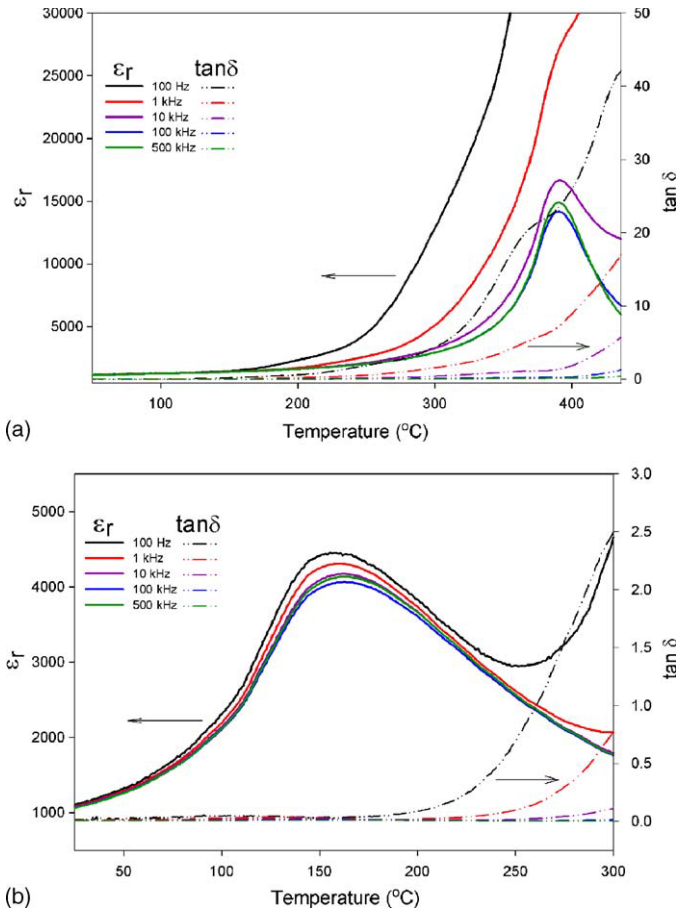

Fig. 6. Temperature and frequency dependence of the dielectric properties for: (a) $x = 0.0$ and (b) $x = 0.5$ ceramics.

dielectric constant follows the Curie–Weiss law:

$$\varepsilon = \frac{c}{T - T_0} \tag{1}$$

where c is the Curie constant and T_0 is the Curie–Weiss temperature [1,20,21]. For a ferroelectric with a diffuse phase transition (broad peak), the following equation:

$$\frac{1}{\varepsilon} = (T - T_m)^2 \tag{2}$$

has been shown to be valid over a wide temperature range instead of the normal Curie–Weiss law (Eq. (1)) [22,23]. In Eq. (2), T_m is the temperature at which the dielectric constant is maximum.

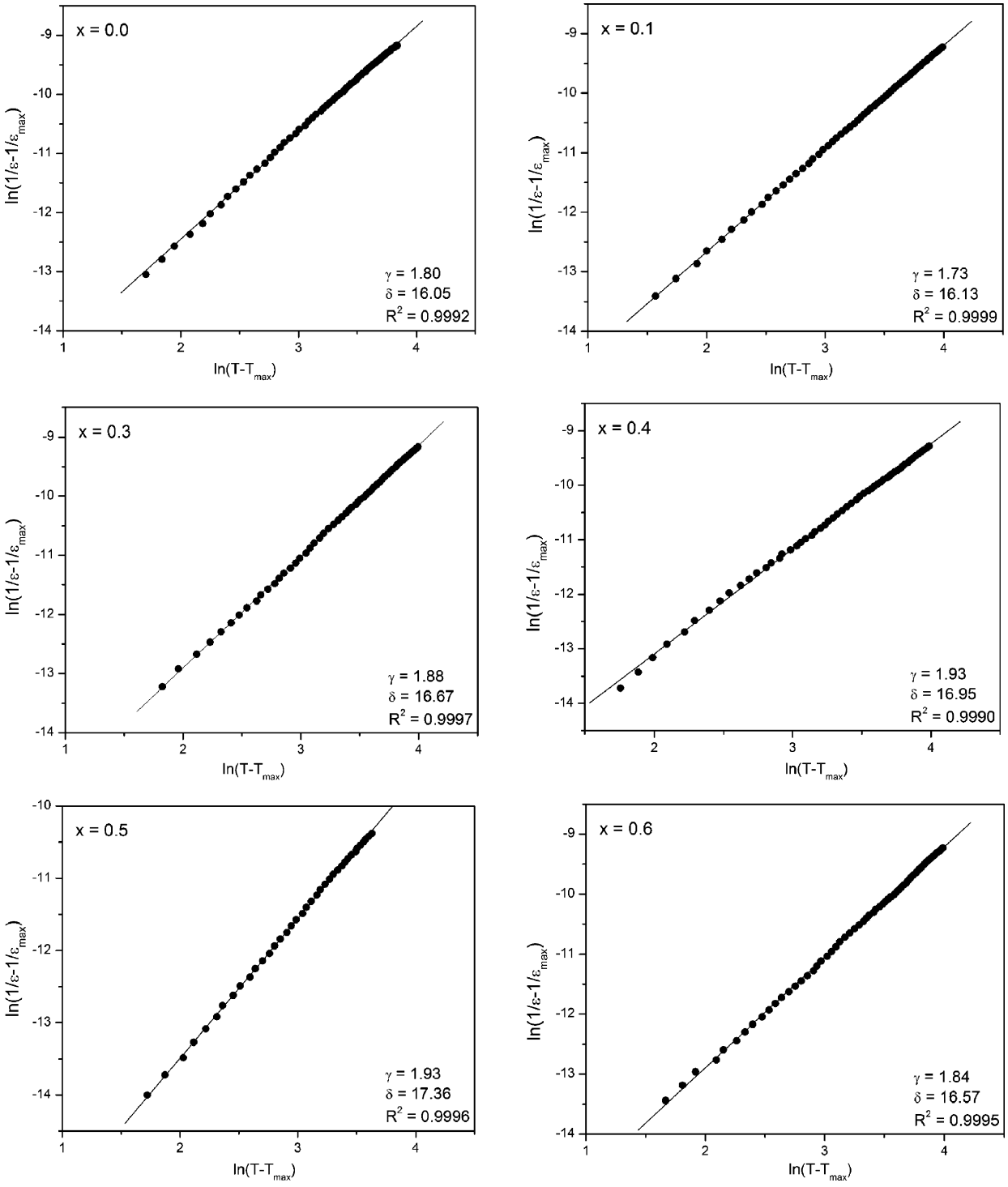

Fig. 7. Plots of $\ln((1/\varepsilon)-(1/\varepsilon_m))$ vs. $\ln(T-T_m)$ for $(1-x)$PZT–xBT ceramics. The solid lines are fits to Eq. (3). γ, δ and R^2 indicate fitting parameters (γ and δ) and correlation of the fit (R^2).

If the local Curie temperature distribution is Gaussian, the reciprocal permittivity can be written in the form [23,24]:

$$\frac{1}{\varepsilon} = \frac{1}{\varepsilon_m} + \frac{(T - T_m)^\gamma}{2\varepsilon_m \delta^2} \quad (3)$$

where ε_m is maximum permittivity, γ the diffusivity and δ is diffuseness parameter. For $(1-x)$PZT–xBT compositions, the diffusivity (γ) and diffuseness parameter (δ) can be estimated from the slope and intercept of the dielectric data shown in Fig. 7, which should be linear. The values of γ and δ are both materials constants depending on the composition and structure of materials [24]. The value of γ is the expression of the degree of dielectric relaxation, while the parameter δ is used to measure the degree of diffuseness of the phase transition. In a material with the "pure" diffuse phase transition described by the Smolenskii–Isutov relation (Eq. (2)), the value of γ is expected to be 2 [18]. The plots shown in Fig. 7 show that the variation is very linear with the correlation of all the fits $\geq$0.999. The mean value of the diffusivity (γ) is extracted from these plots by fitting a linear equation. The values of γ illustrated in Fig. 8 vary between 1.73 and 1.93, which confirms that diffuse phase transition occur in PZT–BT system. However, the phase transition in this system can be considered as "no purely" diffuse as the γ value is not equal to 2 [18]. Since for a perovskite ferroelectric it is established that the values of γ and δ could be caused by microstructure feature, density and grain size [18,25]. However, the relationship between these values, density and grain size in this work has not shown a very clear tendency. Nevertheless, this density and grain size effect can partly be the cause of increasing of the diffusivity when BT is added to PZT since the average grain size ranges from 2.4 μm in PZT to 4.2 μm in 0.4PZT–0.6BT, while the density decreases from 7.7 g/cm^3 in PZT to 6.3 g/cm^3 in 0.4PZT–0.6BT. With increasing BT content, the values of γ and δ seem to increase linearly over the wide composition range (as plotted in Fig. 8), which indicates more diffuse phase behavior in PZT–BT system with increasing BT content (up to $x = 0.5$). It should be noted the value of γ for PZT is nearly 2 (theoretical is 1 for normal ferroelectric with sharp phase transition). This is probably because the mixing of rhombohedral and tetragonal phases in PZT compound (verified by XRD in Fig. 2) and a formation of pyrochlore phase in pure PZT (though not detected by XRD) induced the occurrence of the chemical disorder and composition heterogeneity, which in turn lead to more diffuse phase transition behavior in PZT. As adding 10 mol% BT to PZT, the value of γ slightly drops from 1.78 to 1.73, it can be assumed that small amount of BT helps stabilize perovskite phase in PZT, as observed earlier by Halliyal et al. [23] in case of PZN. However, with further increase in BT content, γ value increases and reaches the highest value at $x = 0.5$. The appearance of diffuseness has been normally argued in terms of variations in local composition giving rise to distinct microregions, each of which has slightly different Curie point for its ferro-paraelectric phase transition resulting in a broad dielectric peak [18,26,27]. In this study, the variation in the diffuseness (Fig. 8) appears to coincide with the XRD results in Fig. 2, which indicate the co-existence of both tetragonal and rhombohedral phases and the microscopic composition fluctuations as a result of incomplete homogeneity in the PZT–BT solid solution. In addition, it is believed that there is an incomplete solubility of BT phase in PZT, little amount of BT (not detected by XRD) could remain as a secondary phase, leading to heterogeneous compositions. This composition heterogeneity also gives rise to random fields, which tend to make the phase transition "diffuse" instead of sharp as in normal ferroelectric [26,27]. For the compositions with $x > 0.5$, BT is now a dominant phase and the situation is reversed, hence the values of γ and δ then decrease with increasing BT content.

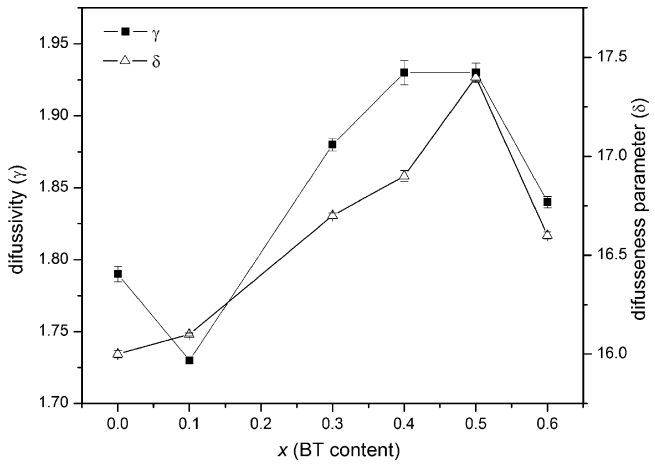

Fig. 8. Plots of diffusivity (γ) and diffuseness parameter (δ) for $(1-x)$PZT–xBT ceramics.

4. Conclusion

Phase formation characteristics of perovskite PZT–BT ceramics have been investigated for the whole series of compositions with XRD analysis. All compositions show complete solid solutions without unwanted phase. The crystal structure of $(1-x)$PZT–xBT system changes gradually from only tetragonal phase in BT to co-existence of tetragonal and rhombohedal phases with increasing PZT content. The (2 0 0)/(0 0 2) peak was found to split at $x = 0.6$ and the triplet peak appears with increasing PZT content. From XRD data, it can be seen that the possible range of compositions which corresponds to a phase transition is $0.6 < x < 0.7$. Lattice parameters and degree of tetragonality were found to vary with chemical composition and increase with decreasing PZT contents. The dielectric studies indicated that the phase transition behavior of the ceramic compositions becomes more diffuse with increasing BT content up to 50 mol%.

Acknowledgements

The authors would like to thank the financial support from the Thailand Research Fund (TRF), Faculty of Science and Graduate School of Chiang Mai University and the Ministry of University Affairs.

References

[1] G.H. Haertling, J. Am. Ceram. Soc. 82 (1999) 797–818.
[2] K. Uchino, Ferroelectric Devices, Marcel Dekker, New York, 2000, p. 308.
[3] B. Jaffe, W.R. Cook, Piezoelectric Ceramics, R.A.N. Publishers, 1971, p. 317.
[4] Y. Xu, Ferroelectric Materials and Their Applications, Elsevier Science Publishers B.V., 1991, p. 391.
[5] A.J. Moulson, J.M. Herbert, Electroceramics: Materials, Properties, Applications, John Wiley & Sons Ltd., Chichester, 2003, p. 500.
[6] J. Chen, Z. Shen, F. Liu, X. Liu, J. Yun, Scripta Mater. 49 (2003) 509–514.
[7] W. Chaisan, S. Ananta, T. Tunkasiri, Cur. Appl. Phys. 4 (2004) 182–185.
[8] B.K. Gan, J.M. Xue, D.M. Wan, J. Wang, Appl. Phys. A 69 (1999) 433–436.
[9] F. Xia, X. Yao, J. Mater. Sci. 34 (1999) 3341–3343.
[10] B.D. Cullity, Elements of X-ray Diffraction, Addison-Wesley Publishing Company, Inc., 1978, p. 32.
[11] D.G. Brandon, W.D. Kaplan, Microstructural Characterization of Materials, John Wiley & Sons, Ltd., 1999, p. 409.
[12] A.K. Arora, R.P. Tandon, A. Mansingh, Ferroelectrics 132 (1992) 9.
[13] P.G.R. Lucuta, F.L. Constantinescu, D. Barb, J. Am. Ceram. Soc. 68 (1985) 533–537.
[14] A. Boutarfaia, S.E. Bouaoud, Ceram. Int. 22 (1996) 281–286.
[15] L. Vegard, Z. Phys. 5 (1921) 17–26.
[16] A. Garg, D.C. Agrawal, Mater. Sci. Eng. B 56 (1999) 46–50.
[17] C.H. Wang, S.J. Chang, P.C. Chang, Mater. Sci. Eng. B 111 (2004) 124–130.
[18] J.-C. M'Peko, A.G. Peixoto, E. Jimenez, L.M. Gaggero-Sager, J. Electroceram. 15 (2005) 167–176.
[19] Z.R. Li, L.Y. Zhang, X. Yao, J. Mater. Res. 16 (2001) 834–836.
[20] L.E. Cross, Mater. Chem. Phys. 43 (1996) 108–115.
[21] R. Yimnirun, S. Ananta, P. Laoratanakul, Mater. Sci. Eng. B 112 (2004) 79–86.
[22] R.D. Shannon, C.T. Prewitt, Acta Crystallogr. B. Struct. Crystallogr. Cryst. Chem. 25 (1969) 925–945.
[23] A. Halliyal, U. Kumar, R.E. Newnham, L.E. Cross, Am. Ceram. Soc. Bull. 66 (1987) 671–676.
[24] N. Vittayakorn, G. Rujijanagul, X. Tan, M.A. Marquardt, D.P. Cann, J. Appl. Phys. 96 (2004) 5103–5109.
[25] R. Yimnirun, S. Ananta, P. Laoratanakul, J. Eur. Ceram. Soc. 25 (2005) 3235–3242.
[26] C.H. Tu, L.F. Chen, V.H. Schmidt, C.L. Tsai, Jpn. J. Appl. Phys. 40 (2001) 4118–4125.
[27] Z.Y. Cheng, R.S. Katiyar, X. Yao, A. Guo, Phys. Rev. B 55 (1997) 8165–8174.

Available online at www.sciencedirect.com
SCIENCE DIRECT®
Materials Letters 60 (2006) 2867–2872
materials letters
www.elsevier.com/locate/matlet

Effect of calcination conditions on phase formation and particle size of zinc niobate powders synthesized by solid-state reaction

A. Ngamjarurojana, O. Khamman, R. Yimnirun, S. Ananta *

Department of Physics, Faculty of Science, Chiang Mai University, Chiang Mai 50200, Thailand

Received 26 August 2005; accepted 2 February 2006
Available online 21 February 2006

Abstract

A columbite-like phase of zinc niobate, $ZnNb_2O_6$, has been synthesized by a solid-state reaction via a rapid vibro-milling technique. The formation of the $ZnNb_2O_6$ phase in the calcined powders has been investigated as a function of calcination conditions by TG–DTA and XRD techniques. Morphology, particle size and chemical composition have been determined via a combination of SEM and EDX techniques. It has been found that single-phase $ZnNb_2O_6$ powders were successfully obtained for calcination condition of 600 °C for 2 h or 550 °C for 6 h with heating/cooling rates of 30 °C/min. Clearly, this study has demonstrated the potentiality of a vibro-milling technique as a significant time-saving method to obtain single-phase $ZnNb_2O_6$ nanopowders (~50–300 nm) at low calcination temperature.

Keywords: Zinc niobate; $ZnNb_2O_6$; Columbite; Calcination; Phase formation; Powders; Solid-state reaction

1. Introduction

Zinc niobate ($ZnNb_2O_6$, ZN) is one of the binary niobate compounds with excellent dielectric properties at microwave frequencies [1–3]. It has very low loss and high dielectric constant and is a promising candidate for applications in microwave devices [4–6]. This compound with a columbite crystal structure is also a suitable reference material for investigating the defect induced in $LiNbO_3$ substrates for waveguide fabrication [6,7]. Moreover, recently, it is well established as the key precursor for the successful preparation of single-phase ferroelectric perovskite $Pb(Zn_{1/3}Nb_{2/3})O_3$ (PZN)-based ceramics, which is becoming increasingly important for actuator, transducer and ultrasonic motor applications [8,9].

There has been a great deal of interest in the preparation of single-phase PZN powders as well as in the sintering and piezoelectric properties of PZN-based ceramics [10–14]. In general, the constituents ZnO and Nb_2O_5 are first mixed and reacted together to form zinc niobate ($ZnNb_2O_6$), prior to mixing and reacting with PbO in the second step of calcination at elevated temperature. Interestingly, this mixed oxide route has been employed with minor modifications in the synthesis of $ZnNb_2O_6$ itself [10–12]. However, powders prepared by a mixed oxide route have spatial fluctuations in their compositions. The extent of the fluctuation depends on the characteristics of the starting powders as well as on the processing schedule. Generally, the mixed oxide method involves the heating of a mixture of zinc oxide and niobium oxide above 900 °C for long times i.e. 2 h [2,5,13], 4 h [12,14], 6 h [15] and 8 h [16]. The optimization of calcination conditions used in the mixed oxide process, however, has not received detailed attention, and the effects of applied dwell time and heating/cooling rates have not yet been studied extensively.

Therefore, the main purpose of this work was to explore a simple mixed oxide synthetic route for the production of $ZnNb_2O_6$ (ZN) powders via a rapid vibro-milling technique and to perform a systematic study of the reaction between the starting zinc oxide and niobium oxide precursors. The phase formation and morphology of the powder calcined at various conditions will be studied and discussed. The rapid vibro-milling technique was employed to explore the potentiality in obtaining nano-sized powders, which would in turn lead to lower required firing temperature.

* Corresponding author. Tel.: +66 53 943367; fax: +66 53 943445.
E-mail address: Supon@chiangmai.ac.th (S. Ananta).

0167-577X/$ - see front matter © 2006 Elsevier B.V. All rights reserved.
doi:10.1016/j.matlet.2006.02.004

2. Experimental procedure

The starting materials were commercially available zinc oxide, ZnO (Fluka Chemical, 99.9% purity) (JCPDS file number 89-1397) and niobium oxide, Nb_2O_5 (JCPDS file number 30-873) (Aldrich, 99.9% purity). The two oxide powders exhibited an average particle size in the range of 3.0–5.0 μm. $ZnNb_2O_6$ powders were synthesized by the solid-state reaction of thoroughly ground mixtures of ZnO and Nb_2O_5 powders that were milled in the required stoichiometric ratio. Instead of employing a ball-milling procedure [1,13–15], a McCrone vibro-milling technique was used [17]. In order to combine mixing capacity with a significant time saving, the milling operation was carried out for 0.5 h with corundum cylindrical media in isopropyl alcohol (IPA). After drying at 120 °C for 2 h, the reaction of the uncalcined powders taking place during heat treatment was investigated by themogravimetric and differential thermal analysis (TG–DTA, Shimadzu), using a heating rate of 10 °C/min in air from room temperature up to 1000 °C. Based on the TG–DTA results, the mixture was calcined at various conditions, i.e. temperatures ranging from 500 to 900 °C, dwell times ranging from 0.5 to 8 h and heating/cooling rates ranging from 5 to 30 °C /min, in closed alumina crucible, in order to investigate the formation of zinc niobate.

Calcined powders were subsequently examined by room temperature X-ray diffraction (XRD; Siemens-D500 diffractometer), using Ni-filtered CuK_α radiation to identify the phases formed and optimum calcination conditions for the formation of ZN powders. Powder morphologies and particle sizes were directly imaged, using scanning electron microscopy (SEM; JEOL JSM-840A). The chemical compositions of the phase formed were elucidated by an energy-dispersive X-ray (EDX) analyzer with an ultra-thin window. EDX spectra were quantified with the virtual standard peaks supplied with the Oxford Instruments eXL software.

3. Results and discussion

The TG–DTA simultaneous analysis of a powder mixed in the stoichiometric proportions of $ZnNb_2O_6$ is displayed in Fig. 1. In the temperature range from room temperature to ~200 °C, the sample shows both exothermic and endothermic peaks in the DTA curve, consistent with the first weight loss. These observations can be attributed to the decomposition of the organic species from the milling process [17,18]. Increasing the temperature up to ~1000 °C, the solid-state reaction occurred between ZnO and Nb_2O_5 [2,5,13]. The broad exotherm with several small peaks in the DTA curve represents that reaction, which has a maximum at ~550 and 800 °C. These are supported by a second fall in sample weight over the same temperature range. However, it is to be noted that there is no obvious interpretation of these peaks, although it is likely to correspond to a phase transition reported by a number of workers [13–16]. These data were used to define the range of calcination temperatures for XRD investigation between 500 and 900 °C.

To further study the phase development with increasing calcination temperature in the powders, they were calcined for 2 h in air at various temperatures, up to 900 °C, followed by phase analysis using XRD. As shown in Fig. 2, for the uncalcined powder, only X-ray peaks of precursors ZnO (○) and Nb_2O_5 (●), which could be matched with JCPDS file numbers 89-1397 [19] and 3-873 [20], respectively, are present, indicating that no reaction had yet been triggered during the milling process. It is seen that fine $ZnNb_2O_6$ crystallites (▽) were developed in the powder at a calcination temperature as low as 500 °C, accompanying with ZnO and Nb_2O_5 as separated phases. This observation agrees well with those derived from the TG–DTA results and other workers [13,16]. As the temperature increased to 550 °C, the intensity of the columbite-like $ZnNb_2O_6$ peaks was further enhanced and became the predominant phase. Upon calcination at 600 °C, an essentially monophasic of $ZnNb_2O_6$ phase is obtained. This ZN phase was indexable according to an orthorhombic columbite-type structure with lattice parameters a=1426 pm, b=572 pm and c=504 pm, space group *Pbcn* (no. 60), in consistent with JCPDS file numbers 76-1827 [21]. This study also shows that orthorhombic ZN crystallite is the only detectable phase in the powders, after calcination in the range of

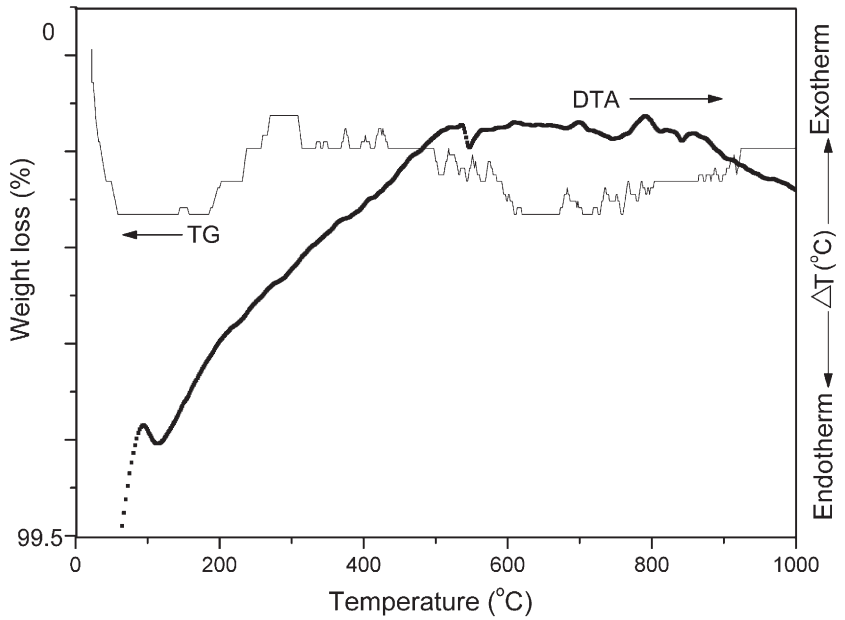

Fig. 1. TG–DTA curves for the mixture of ZnO–Nb_2O_5 powder.

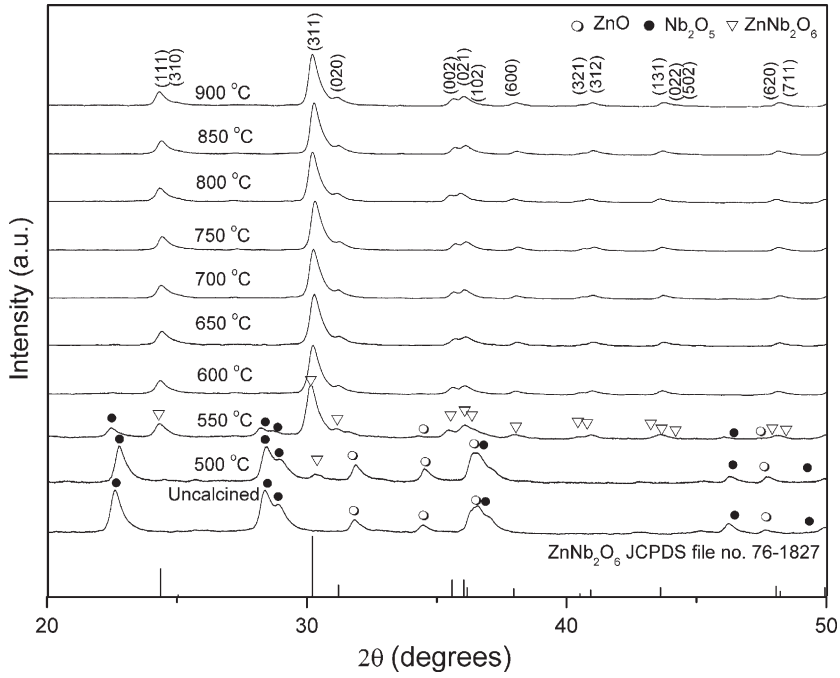

Fig. 2. XRD patterns of ZN powders calcined at various temperatures for 2 h with heating/cooling rates of 10 °C/min.

600–900 °C. In earlier works [12–16], long heat treatments at ~900–1000 °C for 2–8 h were proposed for the formation of $ZnNb_2O_6$ by a conventional mixed oxide synthetic route, although no details on phase formation were provided. However, in the present study, it was found that there are no significant differences between the powders calcined at 600 to 900 °C with dwell time of only 2 h, as shown in Fig. 2. This observation would clearly suggest the advantages of a rapid vibro-milling technique used in the present study.

Apart from the calcination temperature, the effect of dwell time was also found to be quite significant. From Fig. 3, it can be seen that the single phase of $ZnNb_2O_6$ (yield of 100% within the limitations of the XRD technique) was found to be possible in powders calcined at 600 °C with dwell time of 2 h or more. For the present work, there are no significant differences between the powders calcined at 600 °C with dwell times ranging from 2 to 8 h. This was apparently a consequence of the enhancement in crystallinity of the $ZnNb_2O_6$ phase with increasing dwell time. The appearance of ZnO and Nb_2O_5 phases indicated that full crystallization has not occurred at relatively short calcination times. However, in the work reported here, it is to be noted that single phase of $ZnNb_2O_6$ powder was also successfully obtained for a calcination temperature of 550 °C with dwell time of at least 6 h applied (Fig. 4). This is probably due to the effectiveness of vibro-milling and a carefully optimized reaction. The observation that the dwell time effect may also play an important role in obtaining a single-

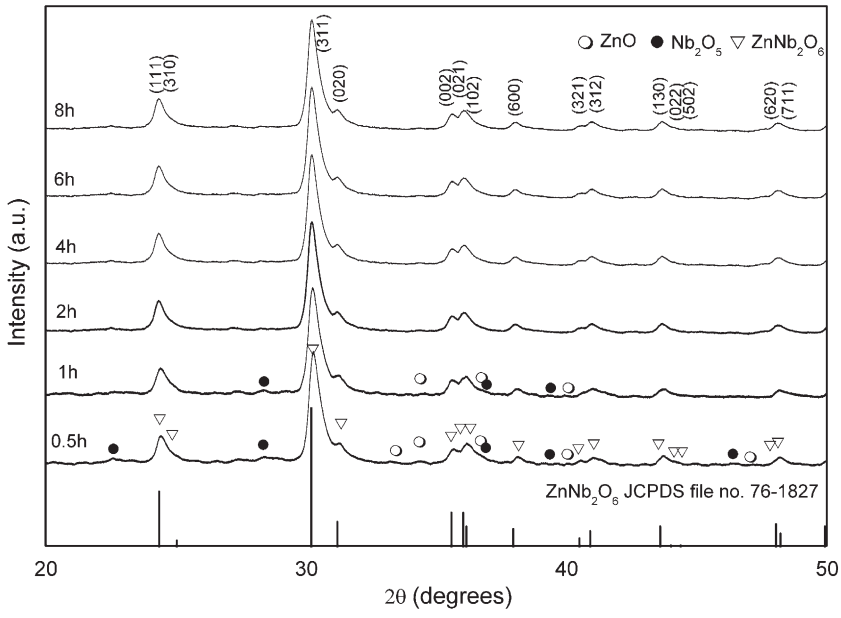

Fig. 3. XRD patterns of ZN powders calcined at 600 °C with heating/cooling rates of 10 °C/min for various dwell times.

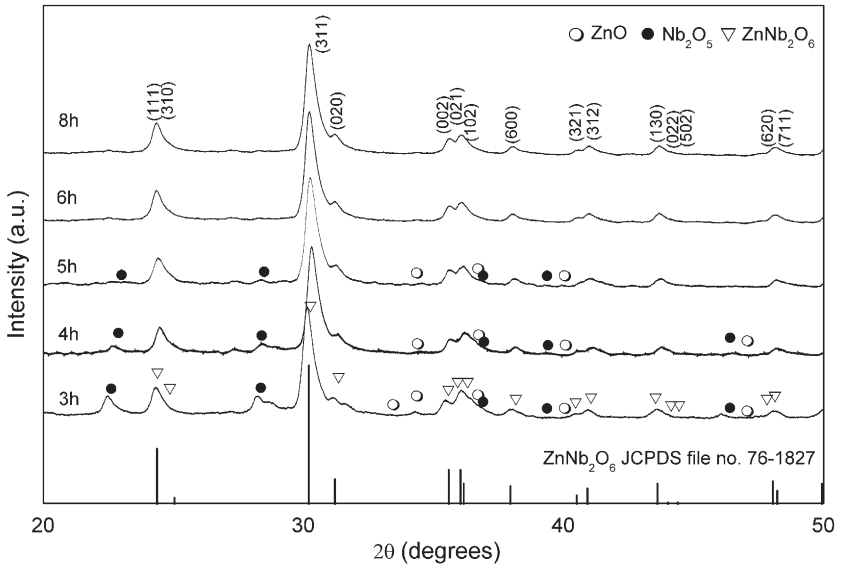

Fig. 4. XRD patterns of ZN powders calcined at 550 °C with heating/cooling rates of 10 °C/min for various dwell times.

phase columbite product is also consistent with other similar systems [22,23]. It is also very interesting to see that the on-set temperature is approximately 300–400 C lower than those reported earlier with a conventional ball-milling method [12–15]. The difference could be attributed to nano-sized mixed powders obtained from a rapid vibro-milling. Most importantly, this study suggests that a rapid vibro-milling method can significantly lower the optimum calcination temperature for formation of single-phase ZN powders.

In the present study, an attempt was also made to calcine ZN powders under various heating/cooling rates (Fig. 5). In this connection, it is shown that the yield of $ZnNb_2O_6$ phase did not vary significantly with different heating/cooling rates, ranging from 5 to 30 C/min, in good agreement with early results reported for the mixture of the two kinds of refractory oxides [17,23].

Based on the TG–DTA and XRD data, it may be concluded that, over a wide range of calcination conditions, single-phase $ZnNb_2O_6$ cannot be straightforwardly formed via a solid-state mixed oxide synthetic route, unless a careful design of calcination is performed. It is well documented that powders prepared by a conventional mixed oxide method have spatial fluctuations in their compositions. The extent of the fluctuation depends on the characteristics of the starting powders as well as the processing schedules [13,16,22]. The experimental work carried out here suggests that the optimal calcination conditions for single-phase $ZnNb_2O_6$ (with impurities undetected by XRD technique) is 600 °C for 2 h or 550 °C for 6 h, with heating/cooling rates as fast as 30 °C/min. Moreover, the formation temperature and dwell time for the production of $ZnNb_2O_6$ powders observed in this work are also much lower than those reported earlier [14–16]. This clearly emphasizes the advantages of a rapid vibro-milling technique.

Finally, the morphological changes in the $ZnNb_2O_6$ powders formed by a mixed oxide are illustrated in Fig. 6(a–f) as a function of calcination temperatures, dwell times and heating/cooling rates,

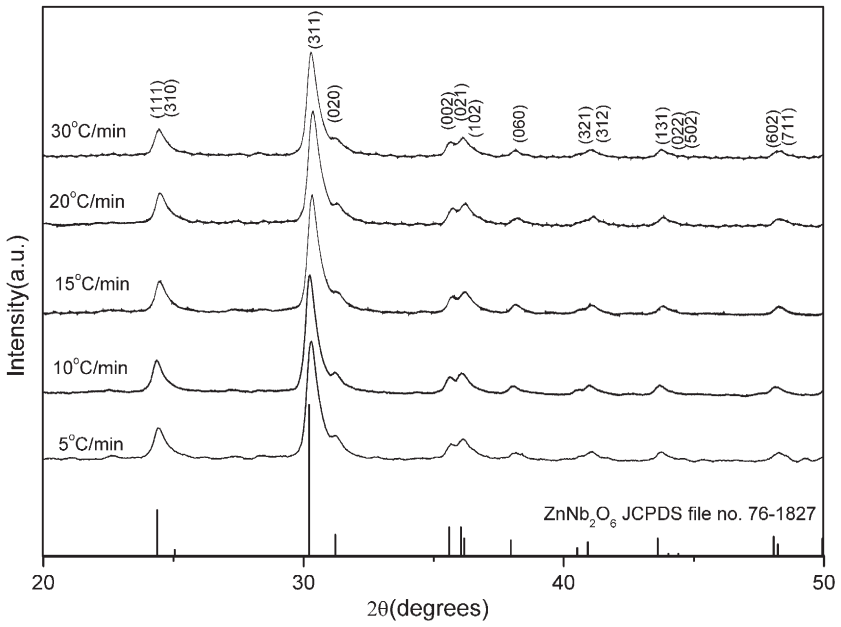

Fig. 5. XRD patterns of ZN powders calcined at 600 °C for 2 h with various heating/cooling rates.

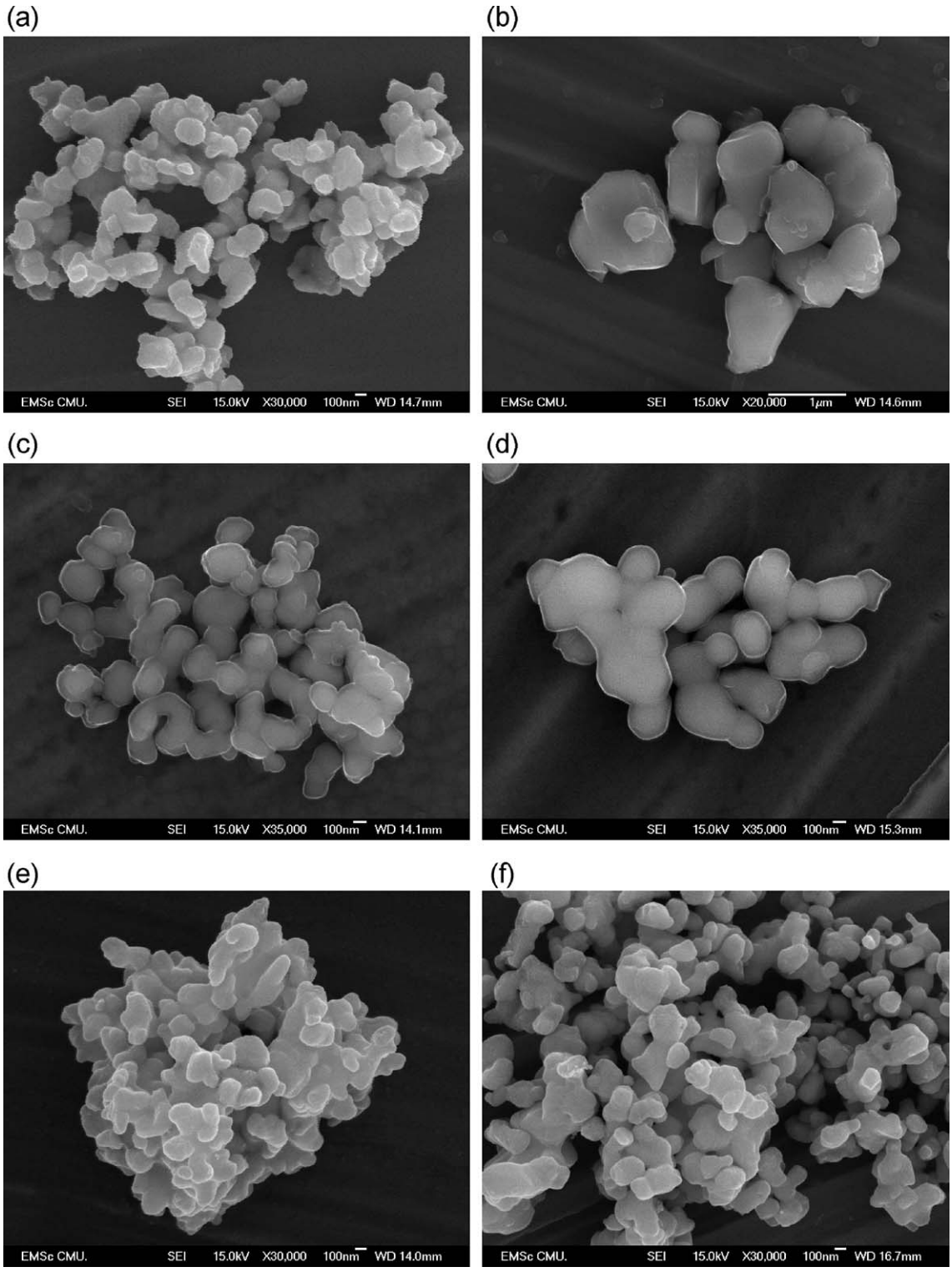

Fig. 6. SEM micrographs of the ZN powders calcined for 2 h with heating/cooling rates of 10 °C/min at (a) 600, (b) 900, and at 600 °C with heating/cooling rates of 10 °C/min for (c) 4, (d) 8 h, and at 600 °C for 2 h with heating/cooling rates of (e) 10 and (f) 30 °C/min.

respectively. The influence of calcination conditions on particle size is given in Table 1. In general, the particles are agglomerated and irregular in shape, with a substantial variation in particle size, particularly in samples calcined at high temperature (Fig. 6(b)) or with fast heating/cooling rates (Fig. 6(e,f)). This finding is also similar to that in $ZrTiO_4$ powders synthesized by Ananta et al. [17]. The results indicate that difference in particle size and degree of agglomeration tend to increase with calcination temperatures (Table 1). After calcinations at 900 °C (Fig. 6(b)), the powders seem to display a significant level of necking and bonding as if they were in the initial stages of sintering.

The effects of dwell time and heating/cooling rates on the morphology of the calcined powders were also found to be quite significant. As

Table 1
Particle size range of $ZnNb_2O_6$ powders calcined at various conditions

Calcination conditions			Particle size range (±10 nm)
Temperature (°C)	Dwell time (h)	Rates (°C/min)	
550	6	30	92–320
600	2	10	75–220
600	4	10	80–340
600	6	10	120–400
600	8	10	180–620
600	2	20	70–220
600	2	30	50–300
700	2	10	120–250
800	2	10	150–420
900	2	10	300–800

expected, it is seen that longer heat treatment leads to larger particle sizes and hard agglomeration (Fig. 6(c,d)). As shown in Fig. 6(e,f), by increasing the heating/cooling rates, averaged particle size tends to decrease whilst the degree of agglomeration tends to increase. This observation could be attributed to the mechanism of surface energy reduction of the ultrafine powders, i.e. the smaller the powder the higher the specific surface area [24]. To the author's knowledge, the present data are the first results for the morphology–calcination relationship of $ZnNb_2O_6$ powders prepared by the solid-state reaction. It is also of interest to point out that mass production of single-phase $ZnNb_2O_6$ nanopowders with the smallest particle size ~50 nm (estimated from SEM micrographs) can be achieved by employing a simple solid-state reaction combined with a rapid vibro-milling technique. In addition, EDX analysis using a 20 nm probe on a large number of particles of the calcined powders confirms that the parent composition is $ZnNb_2O_6$ powders, in good agreement with XRD results.

The results obtained in this study clearly suggest that a systematic study of the effect of milling parameters such as milling times and milling speed on the phase and morphology evolutions of the $ZnNb_2O_6$ powders are required for better understanding and verifying the attractiveness of the vibro-milling technique. Further investigation of this relationship is underway and will be reported in the future.

4. Conclusions

The solid-state mixed oxide method via a rapid vibro-milling technique is explored in the preparation of single phase ZN nanopowders. The calcination temperature and dwell time have been found to have a pronounced effect on phase formation and particle size of the calcined $ZnNb_2O_6$ powders. This work demonstrated that single-phase of zinc niobate powders with particle size ranging from 50–300 nm can be produced via this technique by using a calcination temperature of 600 °C for 2 h or 550 C for 6 h, with heating/cooling rates of 30 C/min. The resulting ZN powders consist of variety of agglomerated particle sizes, depending on calcination conditions.

Acknowledgements

We thank the Thailand Research Fund (TRF), Graduate School and Faculty of Science, Chiang Mai University, and Ministry of University Affairs of Thailand for all support.

References

[1] R.C. Pullar, J.D. Breeze, N.M. Alford, J. Am. Ceram. Soc. 88 (2005) 2466.
[2] H.J. Lee, S.J. Kim, I.T. Kim, Mater. Res. Bull. 32 (1997) 847.
[3] D.W. Kim, K.H. Ko, K.S. Hong, J. Am. Ceram. Soc. 84 (2001) 1286.
[4] Y.C. Zhang, Z.X. Yue, X. Qi, B. Li, Z.L. Gui, L.T. Li, Mater. Lett. 58 (2004) 1392.
[5] Y.C. Zhang, L.T. Li, Z.X. Yue, Z.L. Gui, Mater. Sci. Eng., B, Solid-State Mater. Adv. Technol. 99 (2003) 282.
[6] A.Z. Simoes, A.H.M. Gonzalez, A.A. Cavalheiro, M.A. Zaghete, B.D. Stojanovic, J.A. Varela, Ceram. Int. 28 (2002) 265.
[7] C. Zaldo, M.J. Martin, C. Coya, K. Polgar, A. Peter, J. Paitz, J. Phys., Condens. Matter 7 (1995) 2249.
[8] Y. Xu, Ferroelectric Materials and Their Applications, Elsevier Science, Amsterdam, The Netherlands, 1991.
[9] A.J. Moulson, J.M. Herbert, Electroceramics, 2nd ed.Wiley, New York, 2003.
[10] Y. Hou, M.K. Zhu, H. Wang, B. Wang, H. Yan, C.S. Tian, Mater. Lett. 58 (2004) 1508.
[11] W. Zhu, A.L. Kholkin, P.Q. Mantas, J.L. Baptista, J. Am. Ceram. Soc. 84 (2001) 1740.
[12] M. Villegas, A.C. Caballero, C. Moure, P. Durán, J.F. Fernández, R.E. Newnham, J. Am. Ceram. Soc. 83 (2000) 141.
[13] N. Vittayakorn, G. Rujijanagul, T. Tunkasiri, X. Tan, D.P. Cann, Mater. Sci. Eng., B, Solid-State Mater. Adv. Technol. 108 (2004) 258.
[14] X.J. Lu, X.M. Chen, J. Electroceram. 7 (2001) 127.
[15] C.L. Li, C.C. Chou, Int. Ferro. 55 (2003) 955.
[16] L.B. Kong, J. Ma, H. Huang, R.F. Zhang, T.S. Zhang, J. Alloys Compd. 347 (2002) 308.
[17] S. Ananta, R. Tipakontitikul, T. Tunkasiri, Mater. Lett. 57 (2003) 2637.
[18] S. Ananta, Mater. Lett. 58 (2004) 2834.
[19] Powder Diffraction File No. 89-1397. International Centre for Diffraction Data, Newton Square, PA, 2000.
[20] Powder Diffraction File No. 3-873. International Centre for Diffraction Data, Newton Square, PA, 2000.
[21] Powder Diffraction File No. 76-1827. International Centre for Diffraction Data, Newton Square, PA, 2000.
[22] S. Ananta, R. Brydson, N.W. Thomas, J. Eur. Ceram. Soc. 20 (2000) 2325.
[23] S. Ananta, Mater. Lett. 58 (2004) 2781.
[24] J.S. Reed, Principles of Ceramic Processing, 2nd ed.Wiley, New York, 1995.

International Journal of Modern Physics B
Vol. 20, No. 23 (2006) 3409–3417

World Scientific
www.worldscientific.com

CONTRIBUTIONS OF DOMAIN-RELATED PHENOMENA ON DIELECTRIC CONSTANT OF LEAD-BASED FERROELECTRIC CERAMICS UNDER UNIAXIAL COMPRESSIVE PRE-STRESS

RATTIKORN YIMNIRUN

Department of Physics, Faculty of Science, Chiang Mai University, Chiang Mai 50200, Thailand
rattikornyimnirun@yahoo.com

Received 15 February 2006

The dielectric constant of lead-based ferroelectric ceramics in three different systems, i.e. BT-PZT, PMN-PT and PMN-PZT, was measured under uniaxial compressive pre-stress to investigate the contributions of different domain-phenomena. The dielectric constant was observed at room temperature under the compressive pre-stress up to 15 MPa, 22 MPa and 5 MPa for BT-PZT, PMN-PT and PMN-PZT, respectively, using a homebuilt uniaxial compressometer. Dielectric constant of the BT-PZT ceramics increased significantly with increasing applied stress. Larger changes in the dielectric constant with the applied stress were observed in the PZT-rich compositions. However, for PMN-PT and PMN-PZT ceramic systems, changes in the dielectric constant with the stress were found to depend significantly on the ceramic compositions. The experimental results could be explained by both intrinsic and extrinsic domain-related mechanisms involving domain wall motions, as well as the de-aging phenomenon from the application of the compressive pre-stress. Roles of different types of domains, i.e. micro-domains and nano-domains, were also discussed.

Keywords: Domains; dielectric properties; ferroelectrics; uniaxial stress.

1. Introduction

Among perovskite ferroelectric materials, barium titanate ($BaTiO_3$ or BT), lead titanate ($PbTiO_3$ or PT), lead zirconate titanate ($Pb(Zr_{1-x}Ti_x)O_3$ or PZT) and lead magnesium niobate ($Pb(Mg_{1/3}Nb_{2/3})O_3$ or PMN) ceramics have been investigated extensively and continuously since the late 1940s.[1–4] BT and PT, PMN and PZT are representative perovskite normal ferroelectrics, relaxor ferroelectrics, and piezoelectric prototypes, respectively, because of their excellent electrical properties. These ceramics possess distinct characteristics that make each of them suitable for different applications. Forming a composite of these ferroelectrics has been one of the techniques employed to improve the properties of ferroelectric ceramics for specific requirements for each application.[2–4]

One of the most studied piezoelectric compounds, $Pb(Zr_{0.52}Ti_{0.48})O_3$, a morphotropic phase boundary (MPB) compound of PZT, has great piezoelectric properties with a high Curie temperature (T_C) of ∼390°C. BT exhibits high dielectric constant and superior electrostrictive responses with a lower T_C (∼120°C).[1–4] In addition, BT is mechanically superior to PZT, whereas PZT ceramics can be easily sintered at temperatures much lower than that in BT ceramics, which usually require as high sintering temperature as 1400°C.[5] With their complementary features, the composites between PZT and BT are expected to exhibit better properties than the single-phase PZT and BT.[1–3] Furthermore, the properties can also be tailored over a wider range by changing the compositions to meet the strict requirements for specific applications.[3–6]

PMN exhibits high dielectric constant and a broad range transition of dielectric constant, with temperature as a function of frequency.[3,6] In addition, PMN ceramics exhibit low loss and non-hysteretic characteristics. These make PMN a good candidate for a large number of applications, such as multilayer capacitors, sensors and actuators. However, it is difficult to form a single-phase PMN. It is widely accepted that forming a solid solution between PMN and PT results in ceramics with high dielectric constant and large electrostrictive coefficients.[7–9] In addition, PMN ceramics have relatively low electromechanical coupling coefficients, when compared with those of PZT, which are found in several actuator and transducer applications due to the latter's high electromechanical coupling coefficients and higher temperature of operation.[1,4] However, PZT ceramics also possess highly hysteretic behavior, which makes them unsuited for applications that require high delicacy and reliability. Furthermore, PZT ceramics normally have very high Curie temperature (T_C) in the vicinity of 400°C.[1,2] Usually many applications require that T_C be close to ambient temperature. Therefore, there is a general interest to reduce the T_C of PZT ceramics to optimize their uses. With the complementary features of PMN and PZT, the composites between PMN and PZT are expected to synergetically combine the properties of both ceramics, which could exhibit more desirable piezoelectric and dielectric properties for several technologically demanding applications than single-phase PMN and PZT.[10,11] With the reasons outlined above, it is therefore of interest to investigate the PMN-PT and PMN-PZT systems.

In many applications, these ferroelectric ceramics are often subjected to mechanical loading, either deliberately in the design of the device itself or because the device is used to change shapes as in many smart structure applications or when the device is used under environmental stresses.[6,12,13] Despite the fact, material constants used in any design calculations are often obtained from a stress-free measuring condition, which in turn, may lead to incorrect or inappropriate actuator and transducer designs. It is therefore important to determine the properties of these materials as a function of applied stress. Previous investigations on the stress-dependent dielectric and electrical properties of many ceramic systems have clearly emphasized the importance of the matter.[14,15] More importantly, since these

three ceramic systems possess very distinct dielectric characteristics, they display significantly different ranges of Curie temperature (T_C). BT-PZT has a range of T_C between 120°C and 400°C,[16] while the range extends from −10°C to 490°C for PMN-PT[7–9] and from −10°C to 400°C for PMN-PZT.[17,18] The experimental results of the uniaxial stress dependence of the room temperature dielectric properties of these ceramic systems will provide a tool in assessing the contributions of different domain-related mechanisms in these important ferroelectrics. Therefore, this study is undertaken to investigate the influences of the uniaxial compressive pre-stress on the dielectric properties of ceramics in BT-PZT, PMN-PT and PMN-PZT systems.

2. Materials and Methods

The ceramic composites with formula $BaTiO_3$–$Pb(Zr_{0.52}Ti_{0.48})O_3$ or BT-PZT, $Pb(Mg_{1/3}Nb_{2/3})O_3$–$PbTiO_3$ or PMN-PT and $Pb(Mg_{1/3}Nb_{2/3})O_3$–$Pb(Zr_{0.52}Ti_{0.48})O_3$ or PMN-PZT were prepared from the starting BT, PT, PZT and PMN powders by a mixed-oxide method. BT, PT and PZT powders were first prepared by a conventional mixed-oxide method. On the other hand, perovskite-phase PMN powders were obtained via a well-known columbite method.[19] Subsequently, the $(x)BaTiO_3$–$(1–x)Pb(Zr_{0.52}Ti_{0.48})O_3$ (when x = 0.0, 0.05, 0.15, 0.25, 0.35, 0.45, 0.55, 0.65, 0.75, 0.85, 0.95, and 1.0), the $(1-x)Pb(Mg_{1/3}Nb_{2/3})O_3$–$(x)Pb(Zr_{0.52}Ti_{0.48})O_3$ (when x = 0.1, 0.2, 0.3, 0.4, and 0.5) and the $(x)Pb(Mg_{1/3}Nb_{2/3})O_3$–$(1–x)Pb(Zr_{0.52}Ti_{0.48})O_3$ (when x = 0.0, 0.1, 0.3, 0.5, 0.7, 0.9, and 1.0) ceramic composites were then prepared from the starting BT, PT, PZT and PMN powders by the similar mixed-oxide method described above at various processing conditions. The detailed descriptions of powders and ceramics processing and characterizations were presented thoroughly in the earlier publications.[16–18]

For dielectric property characterizations, the sintered samples were lapped to obtain parallel faces, and the faces were then coated with silver paint as electrodes. The samples were heat-treated at 750°C for 12 min to ensure the contact between the electrodes and the ceramic surfaces. The samples were subsequently poled in a silicone oil bath at a temperature of 120°C by applying a dc field of 20 kV/cm for 30 min for BT-PZT ceramics, while for PMN-PT and PMN-PZT ceramics, the poling condition was 25 kV/cm for 30 min and field-cooled to room temperature. To study the effects of the uniaxial compressive pre-stress on the dielectric properties, the uniaxial compressometer was constructed. The uniaxial compressive pre-stress applied parallel to the electric field direction was supplied by the servohydraulic load frame and the applied stress was monitored with the pressure gauge of the load frame. The details of the system were described elsewhere.[20,21] The dielectric properties were measured through spring-loaded pins connected to the LCZ-meter (Hewlett Packard, Model 4276A). The capacitance was determined at a frequency of 1 kHz and room temperature (25°C). The dielectric constant was then calcu-

lated from a parallel-plate capacitor equation, e.g. $\varepsilon_r = Cd/\varepsilon_0 A$, where C is the capacitance of the sample, d and A are the thickness and the area of the electrode, respectively, and ε_0 is the dielectric permittivity of vacuum (8.854×10^{-12} F/m).

3. Results and Discussion

The experimental results of the uniaxial compressive pre-stress dependence of the dielectric constant of the ceramics in BT-PZT, PMN-PT and PMN-PZT systems are displayed in Figs. 1–3. For BT-PZT system (Fig. 1), there is a significant change of the dielectric constant of the ceramics when the applied stress increases from 0 MPa to 15 MPa. The changes of the dielectric constant with the applied stress can be divided into three different groups. For PZT ceramic, the dielectric constant increases exponentially with the applied stress. It can be seen that the dielectric constant is enhanced by approximately 8% at 15 MPa applied stress. For PZT-rich compositions (0.05BT-0.95PZT, 0.15BT-0.85PZT, 0.25BT-0.75PZT, 0.35BT-0.65PZT and 0.45BT-0.55PZT), the dielectric constant increases rather linearly with increasing applied stress. The changes in the dielectric constant between 2% to 4% at 15 MPa applied stress are obviously smaller than that observed in PZT. For BT-rich compositions (BT, 0.95BT-0.05PZT, 0.85BT-0.15PZT, 0.75BT-0.25PZT and 0.65BT-0.35PZT), the dielectric constant only rises slightly ($< 2\%$) and in

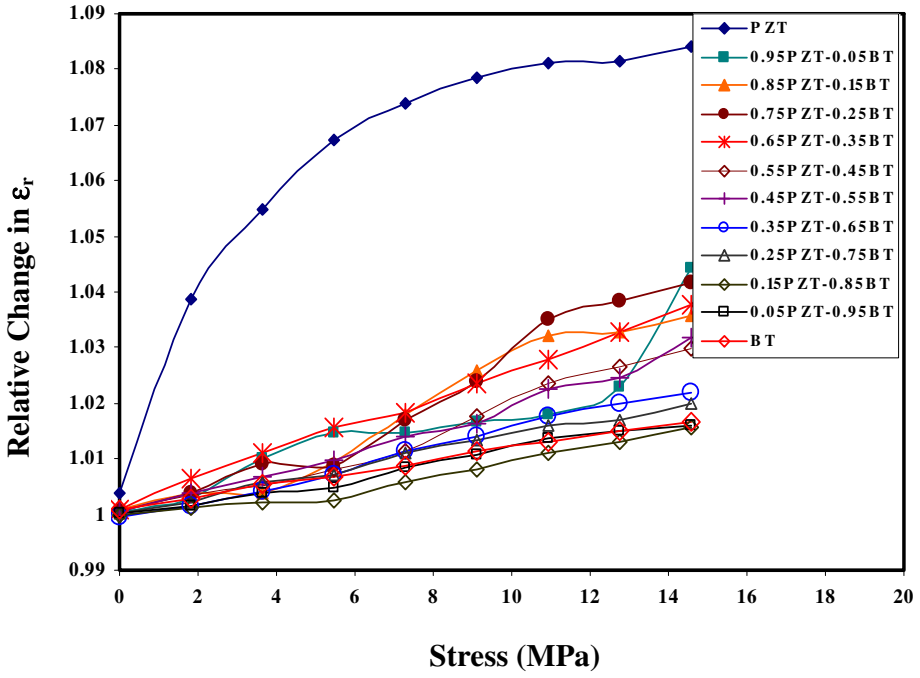

Fig. 1. Relative changes of dielectric constant (ε_r) as a function of compressive pre-stress for (x)BT–(1–x)PZT ceramics.

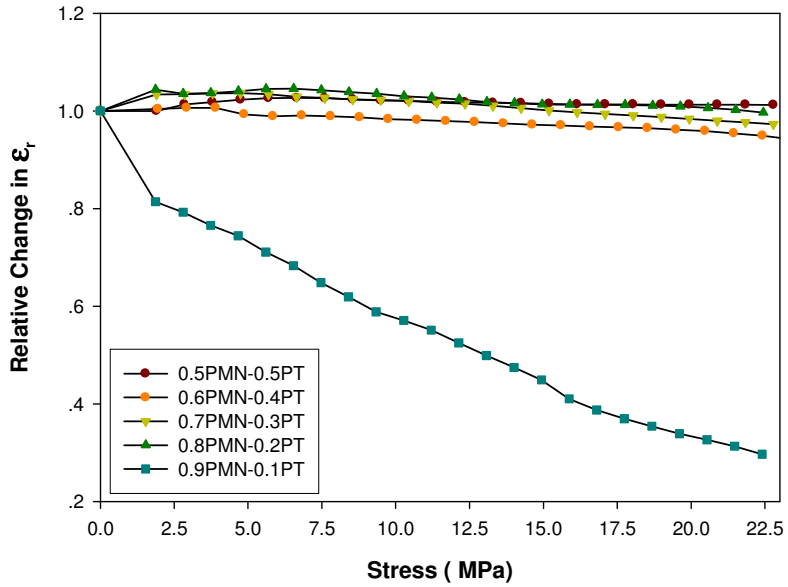

Fig. 2. Relative changes of dielectric constant (ε_r) as a function of compressive pre-stress for (x)PT–(1–x)PMN ceramics.

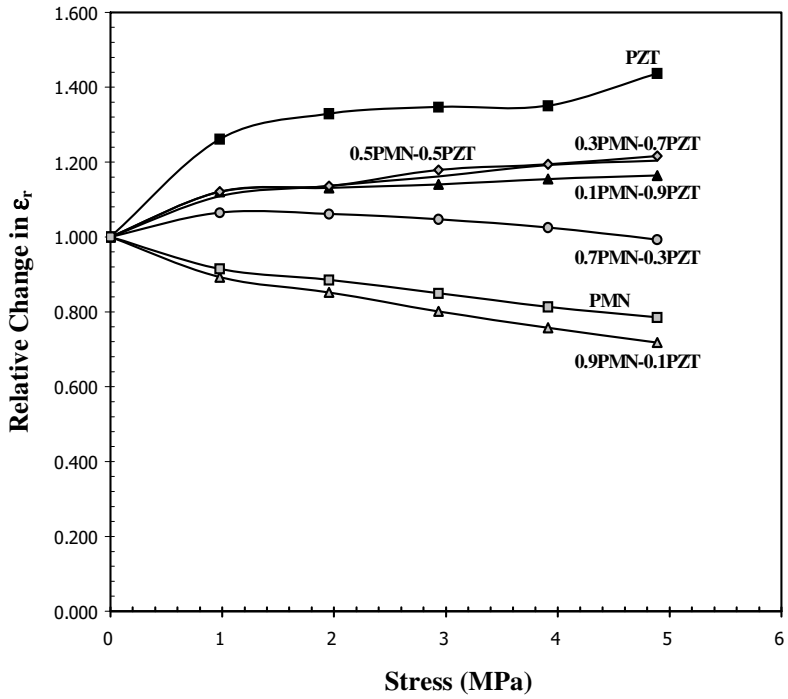

Fig. 3. Relative changes of dielectric constant (ε_r) as a function of compressive pre-stress for (x)PMN–(1–x)PZT ceramics.

a linear manner when the applied stress increases to the maximum amplitude. Similar experimental results have been reported previously for soft PZT[22,23] in which the dielectric properties are found to increase with increasing magnitude of the compressive pre-stress.

The experimental result for the PMN-PT ceramics is shown in Fig. 2. The changes of the dielectric constant with the applied stress can be divided into two groups. For 0.9PMN-0.1PT ceramic, the dielectric constant decreases drastically with the applied stress. The change is more than 70% decrease when the applied stress increases to 22 MPa. On the other hand, for other PMN-PT ceramics, i.e. with x values of 0.2–0.5, the change is minimal. The dielectric constant is actually rather stable within this range of the applied stress.

Figure 3 displays the experimental results for the PMN-PZT ceramics. To prevent mechanical failures usually occurring in PMN-PZT, the experiments are carried out at the compressive pre-stress only up to 5 MPa. However, there is already a significant change of the dielectric constant of the ceramics; even the maximum applied stress is only 5 MPa. The changes of the dielectric constant with the compressive pre-stress can be divided into two different groups. For PMN-rich compositions (PMN, 0.9PMN-0.1PZT, and 0.7PMN-0.3PZT), the dielectric constant generally decreases with increasing applied stress. However, it should be noticed that only PMN and 0.9PMN-0.1PZT compositions show definite decreases in the dielectric constant, while the dielectric constant of the 0.7PMN-0.3PZT composition initially increases, then decreases with very little difference in the dielectric constant between 0 MPa and 5 MPa. On the other hand, for PZT-rich compositions (PZT, 0.1PMN-0.9PZT, 0.3PMN-0.7PZT, and 0.5PMN-0.5PZT), the dielectric constant rises slightly when the compressive pre-stress increases from 0 MPa to 1 MPa, and becomes relatively constant when the pre-stress increases further.

To understand these experimental results, various effects will have to be considered. Normally, the properties of ferroelectric materials are derived from both the intrinsic contribution, which is the response from a single domain, and extrinsic contributions, which are from domain wall motions.[14,15,24–26] Intrinsically, these ferroelectric materials consist of different types of domains, depending upon composition and temperature. In normal ferroelectrics such as BT, PT and PZT, the domains called "micro-domain" are present when the temperature is below T_C, and the domains are non-existent above T_C. On the other hand, in a relaxor ferroelectric like PMN, the domain size gradually changes from nano-domain to micro-domain when the temperature decreases from far above temperature with maximum dielectric constant ($T_{\max}$) to below depolarization temperature (T_d).[6] Normally, the responses of nano-domains to the external compressive pre-stress result in the decrease in the dielectric constant with stress.[26] The extrinsic contribution is also very important. When a mechanical stress is applied to a ferroelectric material, the domain structure in the material will change to maintain the domain energy at a minimum; during this process some of the domains engulf other domains or change shape irreversibly. Under a uniaxial stress, the domain structure of ferroelectric

ceramics may undergo domain switching, clamping of domain walls, de-aging and de-poling.[25]

For the case of BT-PZT system, which exhibits normal ferroelectric behavior,[16] the results on the uniaxial compressive pre-stress dependence of the dielectric constant can easily be explained with the contribution from the extrinsic contribution because the range of T_C for these ceramics is far above the room temperature, at which the experiment was carried out. Therefore, the main contribution is from micro-domains and the domain walls. When the uniaxial compressive pre-stress is applied in the direction parallel to the poling direction, the stress will move some of the polarization away from the poling direction, resulting in a change in domain structures.[14,24,25] This change increases the non-180° domain wall density. Hence, the increase of the dielectric constant with the applied stress can be observed. The de-aging mechanism is also expected to play a role here. However, the stress clamping of domain walls and the de-poling mechanisms are not expected at this relatively-low stress level used in this study.[27] Therefore, a combination of the domain switching and the de-aging mechanism is believed to be a reason for the increase of the dielectric constant with increasing applied stress in the BT-PZT system, as shown in Fig. 1.

The situation for the PMN-PT system is a little more complex because this system is a mixing between the normal ferroelectric PT and the relaxor ferroelectric PMN. Therefore, there is a competing mechanism between the two types of materials, depending on temperature and composition. Since the $T_{\max}$ for 0.9PMN-0.1PT is ∼30°C[3,7−9] and the experiment was performed at ∼25°C, the nano-domains contribute greatly to the dielectric response; hence a significant decrease in dielectric constant with increasing stress is observed. For other compositions with higher $T_{\max}$ (110°C for 0.8PMN-0.2PT to 270°C for 0.5PMN-0.5PT),[7−9] since there are competing influences of the intrinsic contribution of domains, mainly micro-domains, and the extrinsic contribution of re-polarization and growth of micro-polar regions, with opposite responses, the dielectric constant of these compositions becomes rather stable with increasing applied stress, as seen in Fig. 2.

For the PMN-PZT system, the results for the case of PZT-rich compositions can easily be explained in the same way as in the BT-PZT system. Since PMN is a relaxor ferroelectric material, the situation is very different for PMN-rich compositions. The stress dependence of the dielectric constant of the compositions is attributed to competing influences of the domain contribution and the extrinsic contribution of re-polarization and growth of micro-polar regions.[14,27] Since the dielectric response of both contributions is affected by the applied stress in an opposite way, the behavior of the composites depends on the composition ratio between PMN and PZT. Since the measurements were carried out at room temperature (25°C), the nano-domains dominate the dielectric response of the composites.[27] Therefore, the dielectric constant of the PMN-rich compositions decreases with increasing applied stress, as seen in Fig. 3.

4. Conclusions

In this study, the dielectric constants under the uniaxial compressive pre-stress of the BT-PZT, PMN-PT and PMN-PZT ceramics are observed at stress up to 15 MPa, 22 MPa and 5 MPa, respectively, using a uniaxial compressometer. The dielectric constant of the BT-PZT ceramics increases significantly with increasing applied stress. Larger changes in the dielectric constant with the applied stress are observed in the PZT-rich compositions. For PMN-PT system, the dielectric constant of 0.9PMN-0.1PT decreases significantly with the applied stress, while that of other compositions is rather stable. For PMN-PZT system, the dielectric constant of the PMN-rich compositions decreases, while that of the PZT-rich compositions increases slightly with increasing applied stress. The experimental results are explained in terms of domains, domain walls and de-aging mechanisms. The contributions of different domain-related phenomena to the dielectric responses of these lead-based ferroelectric ceramics under the compressive pre-stress depend greatly on compositions and temperature. Finally, this study undoubtedly shows that the applied compressive pre-stress has significant influences on the dielectric properties of the lead-based ferroelectric ceramics.

Acknowledgments

The author would like to express his sincere gratitude for contributions from colleagues, S. Wongsaenmai, S. Chamunglap, M. Unruan and S. Ananta. This work was supported by the Thailand Research Fund (TRF).

References

1. B. Jaffe and W. R. Cook, *Piezoelectric Ceramics* (R.A.N. Inc., New York, 1971).
2. L. E. Cross, *Mater. Chem. Phys.* **43**, 108 (1996).
3. G. H. Haertling, *J. Am. Ceram. Soc.* **82**(4), 797 (1999).
4. A. J. Moulson and J. M. Herbert, *Electroceramics: Materials, Properties, Applications*, 2nd edn. (John Wiley, New York, 2003).
5. W. Chaisan, S. Ananta and T. Tunkasiri, *Cur. Appl. Phys.* **4**, 182 (2004).
6. L. E. Cross, *Ferroelectrics* **76**, 241 (1987).
7. M. Lejeune and J. P. Boilot, *Mater. Res. Bull.* **20**, 493 (1985).
8. S. W. Choi, T. R. Shrout, S. J. Jang and A. S. Bhalla, *Ferroelectrics* **100**, 29 (1989).
9. S. W. Choi, J. M. Tang and A. S. Bhalla, *Ferroelectrics* **189**, 27 (1996).
10. J. H. Yoo, H. S. Yoon, Y. H. Jeong and C. Y. Park, *Proc. IEEE Ultra. Symp.* **1**, 981 (1998).
11. A. V. Shilnikov, A. V. Sopit, A. I. Burkhanov and A. G. Luchaninov, *J. Eur. Ceram. Soc.* **19**, 1295 (1999).
12. Y. H. Xu, *Ferroelectric Materials and Their Applications* (North Holland, Los Angeles, 1991).
13. D. Viehland and J. Powers, *J. Appl. Phys.* **89**(3), 1820 (2001).
14. J. Zhao and Q. M. Zhang, *Proc. IEEE ISAF* **2**, 971 (1996).
15. J. Zhao, A. E. Glazounov and Q. M. Zhang, *Appl. Phys. Lett.* **74**, 436 (1999).
16. W. Chaisan, R. Yimnirun, S. Ananta and D. P. Cann, *Mater. Lett.* **59**, 3737 (2005).

17. R. Yimnirun, S. Ananta and P. Laoratanakul, *Mater. Sci. Eng. B* **112**, 79 (2004).
18. R. Yimnirun, S. Ananta and P. Laoratanakul, *J. Euro. Ceram. Soc.* **25**, 3225 (2005).
19. S. L. Swartz and T. R. Shrout, *Mater. Res. Bull.* **17**, 1245 (1982).
20. R. Yimnirun, P. Moses, R. J. Meyer and R. E. Newnham, *Rev. Sci. Instrum.* **74**, 3429 (2003).
21. R. Yimnirun, S. Ananta, E. Meechoowas and S. Wonsaenmai, *J. Phys. D: Appl. Phys.* **36**, 1615 (2003).
22. J. M. Calderon-Moreno, *Mater. Sci. Eng. A* **315**, 227 (2004).
23. D. Zhou, M. Kamlah and D. Munz, *J. Euro. Ceram. Soc.* **25**, 425 (2005).
24. G. Yang, W. Ren, S. F. Liu, A. J. Masys and B. K. Mukherjee, *Proc. IEEE Ultra. Symp.* **1**, 1005 (2000).
25. G. Yang, S. F. Liu, W. Ren and B. K. Mukherjee, *Proc. SPIE Symp. Smart Struct. Mats.* **3992**, 103 (2000).
26. O. Steiner, A. K. Tagantsev, E. L. Colla and N. Setter, *J. Euro. Ceram. Soc.* **19**, 1243 (1999).
27. Q. M. Zhang, J. Zhao, K. Uchino and J. Zheng, *J. Mater. Res.* **12**, 226 (1997).

Scaling behavior of dynamic hysteresis in soft lead zirconate titanate bulk ceramics

Rattikorn Yimnirun,[a] Yongyut Laosiritaworn, Supattra Wongsaenmai, and Supon Ananta
Department of Physics, Faculty of Science, Chiang Mai University, Chiang Mai 50200, Thailand

(Received 15 June 2006; accepted 2 September 2006; published online 16 October 2006)

The scaling behavior of the dynamic hysteresis of ferroelectric bulk system was investigated. The scaling relation of hysteresis area $\langle A\rangle$ against frequency f and field amplitude E_0 for the saturated loops of the soft lead zirconate titanate bulk ceramic takes the form of $\langle A\rangle \propto f^{-1/4}E_0$, which differs significantly from that of the theoretical prediction and that of the thin film. This indicates that the scaling relation is dimension dependent and that depolarizing effects in the interior must be taken into account to model bulk materials. Additionally, the scaling relation for the minor loops takes the form of $\langle A\rangle \propto f^{-1/3}E_0^3$, which is identical to that of the thin film as both cases contain similar 180° domain-reversal mechanism. © *2006 American Institute of Physics*. [DOI: 10.1063/1.2363143]

Lead zirconate titanate [$Pb(Zr_{1-x}Ti_x)O_3$ or PZT] ceramics have been employed extensively in sensors and actuators, particularly donor-doped PZT with "soft" piezoelectric behaviors.[1,2] In these applications, the dynamic hysteresis, i.e., hysteresis area $\langle A\rangle$ as a function of the field amplitude E_0 and frequency f, has become an important consideration.[1,3] Many theoretical studies have been focused on scaling law $\langle A\rangle \propto f^{\alpha}E_0^{\beta}$ (where α and β are exponents that depend on the dimensionality and symmetry of the system) of hysteresis curves in polarization systems.[4–7] The three-dimensional models [$(\Phi^2)^2$ and $(\Phi^2)^3$] by Rao *et al.*[4] and other investigators[7,8] proposed two scaling relations applicable to the low-f and high-f limits as follows:

$$\langle A\rangle \propto f^{1/3}E_0^{2/3} \quad \text{as } f\to 0, \tag{1}$$

$$\langle A\rangle \propto f^{-1}E_0^{2} \quad \text{as } f\to \infty. \tag{2}$$

Technologically, it is helpful to understand the scaling behavior so that the ultrahigh-frequency hysteresis can be predicted. Hence, there have been reports on the scaling behavior of the dynamic hysteresis in ferromagnetic and ferroelectric thin films, with some discrepancies between theoretical and experimental results.[6–13] In contrast to the theoretically predicted scaling relation at high-f limit in Eq. (2), the experimental investigation on PZT thin film[14] has resulted in a different relation, i.e.,

$$\langle A\rangle \propto f^{-1/3}E_0^{3} \quad \text{as } f\to \infty. \tag{3}$$

Interestingly, there has been no report on the scaling studies of ferroelectric hysteresis in bulk ceramics. Thus, we present in this letter the results on the scaling behavior of the dynamic hysteresis of soft PZT bulk ceramic.

The dynamic hysteresis (P-E) loops of commercial soft PZT ceramic disks (PKI-552, Piezo Kinetics Inc., USA) with diameter of 10 mm and thickness of 1 mm were characterized at room temperature (25 °C) by using a modified Sawyer-Tower circuit with f covering from 2 to 100 Hz and E_0 from 0 to 18 kV/cm. The electric field was applied to a sample by a high voltage ac amplifier (Trek 610D) with the input sinusoidal signal from a function generator (HP 3310A). The P-E loops were recorded by a digital oscilloscope (HP 54645A, 100 MHz). Each loop was obtained after 20 sampling cycles to average out the noise deformation. The details of the system were described elsewhere.[14] The hysteresis loop obtained was very consistent with that obtained by a standardized ferroelectric testing unit, RT66A (Radiant Technologies Inc., NM), which ensures the reliability of the measurements.

The hysteresis loops at different f but fixed E_0 (18 kV/cm) and at different E_0 but fixed f (100 Hz) are shown in Fig. 1. The loop area $\langle A\rangle$, remanent polarization (P_r), and coercive field (E_c) decrease with an increase of frequency, as shown in Fig. 1(a). The dependence of the hysteresis loop on E_0 is depicted in Fig. 1(b). For small fields (6 and 12 kV/cm), the loop does not saturate. With further increase in E_0, $\langle A\rangle$, P_r, and E_c increase until well saturated loop is achieved. Similar observations have been reported in thin films.[7,10,13]

To investigate the scaling behavior, we followed the theoretical predictions on the loop area[4,5,8] by plotting $\langle A\rangle$ against $f^{-1}E_0^2$. The data are shown in Fig. 2(a) and the dotted line represents a fitting in terms of $\langle A\rangle \propto f^{-1}E_0^2$. Clearly, the theoretically proposed scaling relation in Eq. (2) cannot be directly applied to the data obtained in this study. Moreover, earlier experimental work[13] on the PZT thin film showed a different relation, expressed in Eq. (3). To check the validity of the relation on the bulk ceramic, we plot $\langle A\rangle$ against $f^{-1/3}E_0^3$, as shown in Fig. 2(b) with the dotted line representing a fitting in terms of $\langle A\rangle \propto f^{-1/3}E_0^3$. Large deviation observed also implies that the experimentally obtained scaling relation for the thin film is not applicable to the bulk ceramic. However, a closer check shows that Eqs. (2) and (3) appear to yield reasonable fits to the low E-field data, as shown in Fig. 2. The discussion on this observation will be formulated later.

To obtain the suitable scaling relation for the bulk ceramic, one can fit the data with $\langle A\rangle \propto f^{m}E_0^{n}$, where m and n are exponents to be determined directly from the experimental data. By plotting $\langle A\rangle$ against f at fixed E_0, one obtains the exponent m. On the other hand, the exponent n can be obtained from plotting $\langle A\rangle$ against E_0 at fixed f. As plotted in

[a]Author to whom correspondence should addressed; electronic mail: rattikornyimnirun@yahoo.com

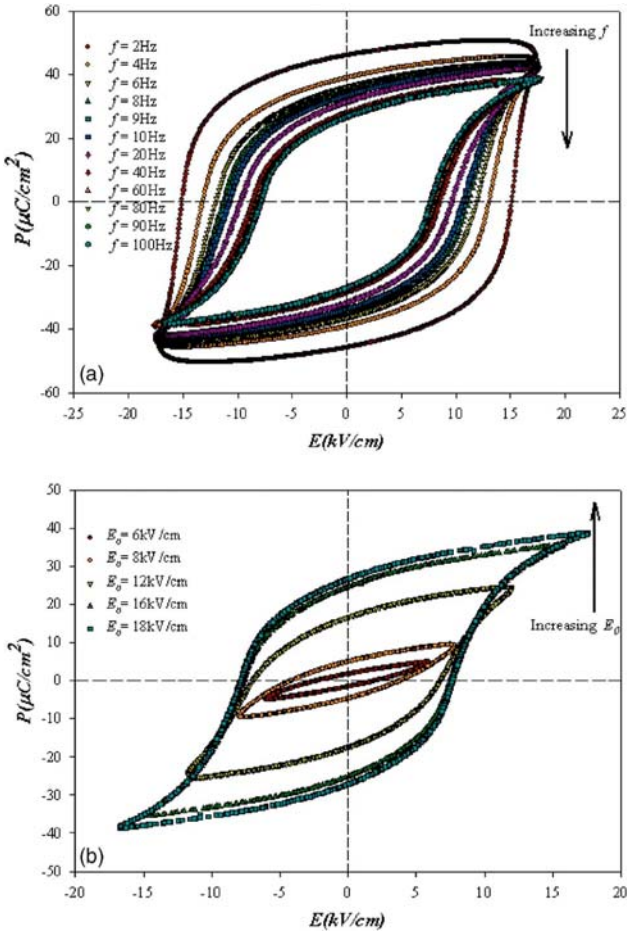

FIG. 1. (Color online) Hysteresis loops for soft PZT ceramic (a) at various f and $E_0=18$ kV/cm and (b) at various E_0 and $f=100$ Hz.

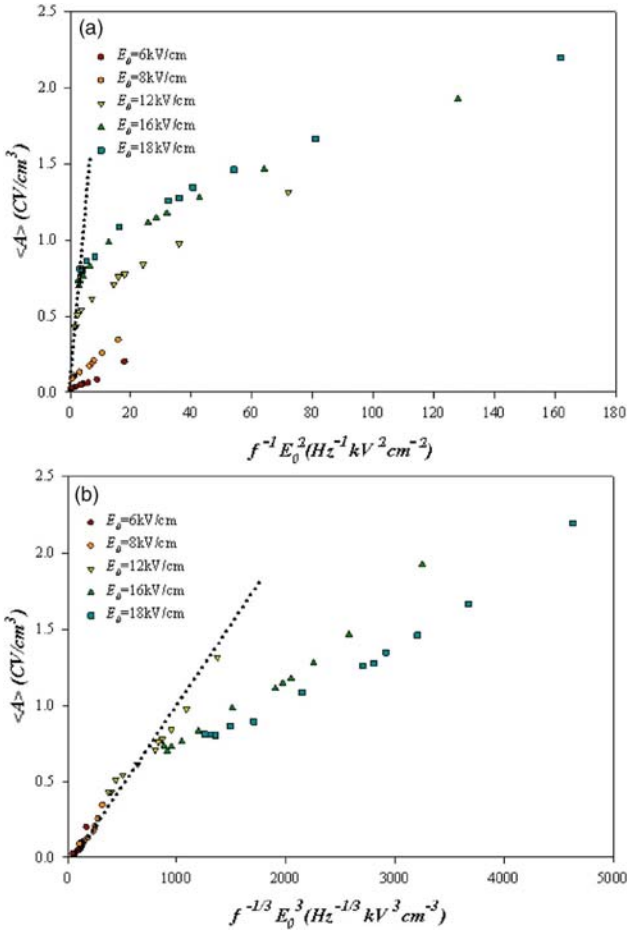

FIG. 2. (Color online) Scaling of hysteresis area $\langle A\rangle$ against (a) $f^{-1}E_0^2$ and (b) $f^{-1/3}E_0^3$ for soft PZT ceramic.

Fig. 3(a), it is revealed that the high E-field data can be much better fitted (with $R^2=0.97$), within the measured uncertainty, by

$$\langle A\rangle \propto f^{-1/4}E_0. \tag{4}$$

Though the minor loop data were excluded from the fitting reported in Eq. (4), it is possible that a different scaling behavior could be established for the low E-field region, as also reported in previous investigations.[11,12] More discussions on this will follow.

The scaling relation obtained in Eq. (4) indicates that $\langle A\rangle$ decays more slowly with f and grows more slowly with E_0 than the theoretical prediction, Eq. (2). $\langle A\rangle$ also decays slightly slower with f, but grows much more slowly with E than the PZT thin film, Eq. (3). An explanation for the difference may come from the polarization-interaction terms as considered in the $(\Phi^2)^2$ and $(\Phi^2)^3$ models, in which the polarization flip just has one contribution, i.e., polarization reversal.[4,5] This requires overcoming high energy barrier. The Potts model used by Liu *et al.*[13] also has the polarization orientation in various domains in directions not antiparallel to the direction of E, hence requires lower energy barrier for polarization flip to occur, which results in a higher exponent of 3 in the E_0 term, as compared to the exponent of 2 in the theoretical models. However, in ceramics, there are influences of many depolarizing effects, arisen from domain walls, grain boundaries, space charges, immobile defects, etc., which may retard the external field. Consequently, the energy barrier is very much higher, which leads to slower polarization-flip kinetics. Therefore, a low exponent for the E_0 term is expected from the ceramics.

In addition, the f term shows an exponent of $-1/4$, smaller in absolute value than that of PZT thin film (exponent is $-1/3$).[13] To explain the difference, one may need to consider not only the contribution from the domain switching and ionic type in thin films[13] but also additional contributions to hysteresis properties from space charges on grain boundaries, induced electric field from interface layers, immobile defects,[15] etc. Therefore, in a bulk-ceramic type these depolarizing effects, acting as a buffer to polarization-reversal mechanism, will be stronger than those in thin film structure. As a result, the hysteresis area must show a relatively weaker dependence on f than that observed in thin films.

Returning to the observation in Fig. 3(a), there are actually two slopes—one at low E fields (high frequencies) and a different slope at high E fields (low frequencies). Additionally, Eqs. (2) and (3) appear to yield reasonable fits to the low E-field data in Fig. 2. In contrast, Eq. (4) appears to fit the high E-field data to a reasonable extent. It is therefore important to explain the fundamental nature of the different slopes. Probable reasons lie in the complexities of the domain structure of PZT, which also depends on the dimensionality.[16,17] A number of recent studies have explored this behavior and reported that it is likely that different do-

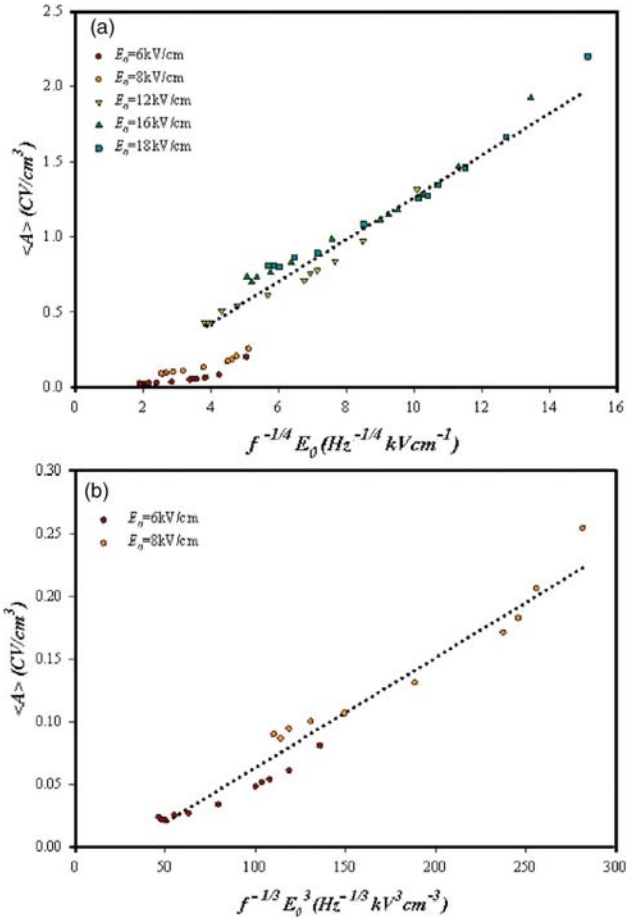

FIG. 3. (Color online) Scaling of hysteresis for soft PZT ceramic: (a) area $\langle A\rangle$ against $f^{-1/4}E_0$ for the saturated loops and (b) area $\langle A\rangle$ against $f^{-1/3}E_0^3$ for the minor loops.

main walls are being activated at different fields.[6,7,17–20] Generally, PZT ceramics have 180° and non-180° domain structures.[19,20] As the non-180° domain switching is normally accompanied with mechanical strain, it occurs at higher E field than the 180° domain reversal does.[18–20] Therefore, under low E fields, one would expect the 180° domain reversal to occur first. It is also well known that the non-180° domain wall motion is typically very heavily clamped in thin films.[17] Therefore, the main switching contribution in thin films would be from the 180° domain reversal. This explains why the scaling behavior of PZT bulk ceramics at low E fields is similar to that of thin films. This is further supported by the scaling relation of PZT bulk ceramics obtained for low E fields in the form of $\langle A\rangle \propto f^{-1/3}E_0^3$, as shown in Fig. 3(b). Considering the various domain types observed in PZT, it should be worthwhile to examine the scaling relation for a simpler ferroelectric with only one type of domain wall (e.g., $Bi_4Ti_3O_{12}$). Interestingly, a previous investigation[21] on Nd-doped $Bi_4Ti_3O_{12}$ yielded a scaling in the form of $\langle A\rangle \propto f^{-2/3}E_0^2$, which is closer to the theoretical prediction [Eq. (2)] and that for the $SrBi_2Ta_9O_4$ thick film.[12]

In summary, the scaling relation for the saturated hysteresis loops of the soft PZT ceramic takes the form of $\langle A\rangle \propto f^{-1/4}E_0$, which differs significantly from that of the theoretical prediction and that of the PZT thin film. Additionally, the scaling relation for the minor loops is identical to that of thin films, i.e., $\langle A\rangle \propto f^{-1/3}E_0^3$.

This work was supported by the Thailand Research Fund, Commission on Higher Education, Graduate School and Faculty of Science, Chiang Mai University.

[1]K. Uchino, *Ferroelectric Devices* (Dekker, New York, 2000), p. 145.
[2]B. Jaffe, W. R. Cook, and H. Jaffe, *Piezoelectric Ceramics* (Academic, New York, 1971), p. 271.
[3]J. F. Scott, Ferroelectr. Rev. **1**, 1 (1998).
[4]M. Rao, H. R. Krishnamurthy, and R. Pandit, Phys. Rev. B **42**, 856 (1990).
[5]M. Acharyya and B. K. Chakrabarti, Phys. Rev. B **52**, 6560 (1995).
[6]J.-M. Liu, H. L. W. Chan, C. L. Choy, and C. K. Ong, Phys. Rev. B **65**, 014416 (2001).
[7]J.-M. Liu, H. L. W. Chan, C. L. Choy, Y. Y. Zhu, S. N. Zhu, Z. G. Liu, and N. B. Ming, Appl. Phys. Lett. **79**, 236 (2001).
[8]M. Rao and R. Pandit, Phys. Rev. B **43**, 3373 (1991).
[9]Q. Jiang, H. N. Yang, and G. C. Wang, Phys. Rev. B **52**, 14911 (1995).
[10]B. Pan, H. Yu, D. Wu, X. H. Zhou, and J.-M. Liu, Appl. Phys. Lett. **83**, 1406 (2003).
[11]Y.-H. Kim and J.-J. Kim, Phys. Rev. B **55**, R11933 (1997).
[12]J.-H. Park, C.-S. Kim, B.-C. Choi, B. K. Moon, J. H. Jeong, and I. W. Kim, Appl. Phys. Lett. **83**, 536 (2003).
[13]J.-M. Liu, H. L. W. Chan, and C. L. Choy, Mater. Lett. **52**, 213 (2002).
[14]R. Yimnirun, Y. Laosiritaworn, and S. Wongsaenmai, J. Phys. D **39**, 759 (2006).
[15]D. Bolten, U. Böttger, and R. Waser, Appl. Phys. Lett. **84**, 2379 (2004).
[16]A. Gruverman, O. Auciello, and H. Tokumoto, Annu. Rev. Mater. Sci. **28**, 101 (1998).
[17]S. Trolier-McKinstry, N. B. Gharb, and D. Damjanovic, Appl. Phys. Lett. **88**, 202901 (2006).
[18]N. Uchida and T. Ikeda, Jpn. J. Appl. Phys. **4**, 867 (1965).
[19]T. Tsurumi, T. Sasaki, H. Kakemoto, T. Harigai, and S. Wada, Jpn. J. Appl. Phys., Part 1 **43**, 7618 (2004).
[20]K. Lee and S. Baik, Annu. Rev. Mater. Res. **36**, 81 (2006).
[21]J.-M. Liu, B. Pan, H. Yu, and S. T. Zhang, J. Phys.: Condens. Matter **16**, 1189 (2004).

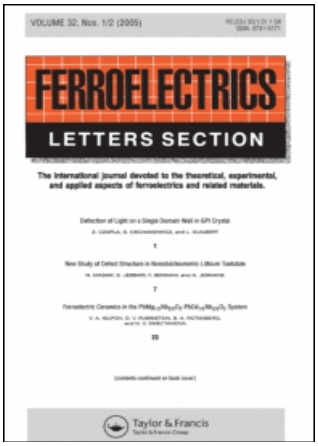

Ferroelectrics Letters Section
Publication details, including instructions for authors and subscription information:
http://www.informaworld.com/smpp/title~content=t713871498

Polarization Behavior in the Two Stage Sintered Lead Titanate Ceramics

R. Wongmaneerung [ab]; R. Yimnirun [a]; S. Ananta [a]; R. Guo [b]; A. S. Bhalla [b]
[a] Department of Physics, Faculty of Science, Chiang Mai University. Chiang Mai. Thailand
[b] Materials Research Laboratory, Pennsylvania State University. University Park, PA, 16802. USA

To cite this Article: R. Wongmaneerung, R. Yimnirun, S. Ananta, R. Guo and A. S. Bhalla , 'Polarization Behavior in the Two Stage Sintered Lead Titanate Ceramics', Ferroelectrics Letters Section, 33:5, 137 - 146
To link to this article: DOI: 10.1080/07315170601014984
URL: http://dx.doi.org/10.1080/07315170601014984

Ferroelectric Letters, 33:137–146, 2006

ISSN: 0731-5171 print / 1543-5288 online
DOI: 10.1080/07315170601014984

Taylor & Francis
Taylor & Francis Group

Polarization Behavior in the Two Stage Sintered Lead Titanate Ceramics

R. WONGMANEERUNG,[1,2] R. YIMNIRUN,[1] S. ANANTA,[1]
R. GUO,[2] and A. S. BHALLA[2]

[1]*Chiang Mai University, Department of Physics, Faculty of Science, Chiang Mai, Thailand*
[2]*Pennsylvania State University, Materials Research Laboratory, University Park, PA 16802, USA*

Communicated by Dr. George W. Taylor

(Received July 24, 2006)

Polarization behavior in lead titanate, prepared by the two stage sintering approach, is determined by using the dilatometer thermal expansion data. We report the temperature-dependent measurements of the strain, the magnitude of polarization, $\sqrt{\overline{P}_S^2}$, deduced from the sets of data gathered from the thermal expansion values. The calculated values of the electric polarization, P_S, on the two stage sintered lead titanate ceramics show the simple approach to determine the temperature dependence of the polarization below and around the transition temperature. Various aspects of our understanding of the polarization behavior and other effects in the ferroelectric are discussed.

Keywords: polarization behavior; thermal expansion; lead titanate

INTRODUCTION

The high Curie temperature of lead titanate, $PbTiO_3$, ceramics has long qualified these materials for potential high-temperature and high frequency applications [1–3]. For $PbTiO_3$, above the ferroelectric transition temperature, T_C, the structure is cubic and below T_C it becomes tetragonal with a spontaneous polarization P_S. In general, the value of P_S is difficult to measure due to its high coercive field and $T_C \approx 490^\circ C$ [1]. However, the change in polarization with temperature can be observed through thermal expansion (or strain) measurements and from the data, spontaneous polarization and

*Corresponding author. E-mail: asb2@psu.edu

its temperature dependence can be computed. Some authors [4, 5] suggest the value of P_S at room temperature to be greater than 50 μC/cm^2. Shirane [6] and Jona [7] give the value of $P_S = 80$ μC/cm^2.

It is always a challenge to measure the temperature-dependence of the polarization of the high T_C ferroelectric over the entire temperature range. In general with the increase in temperature and due to the increase in losses in the $PbTiO_3$ samples it hinders the real spontaneous polarization and its (P_S) temperature dependence measurements at higher temperature by using the hysteresis and pyroelectric techniques. Therefore, some alternate approaches have to be made in order to extract some useful data on $PbTiO_3$ for the polarization versus temperature behavior. From the phenomenological approach we know that the P_S values can be extracted by using the relation [8];

$$x_{ij} = \frac{\Delta l}{l} = Q_{ijkk} P_k^2 \tag{1}$$

where x_{ij} is the strain, $\Delta l/l$ is thermal expansion, Q_{ijkk} is the electrostrictive coefficient. Q coefficients are determined in paraelectric phase and considered constant. And P_k^2 is the polarization.

Also, by knowing the $\Delta l/l$ and its temperature dependence, P_k versus temperature as well as the transition temperature of $PbTiO_3$ and the nature of the transition can be studied.

In this paper, we report the P_S versus temperature behavior of $PbTiO_3$ samples prepared and sintered under various conditions. Thermal expansion versus temperature behavior has been measured and the values of polarization at various temperatures have been computed. Measurements have also been extended on the unpoled, poled and depoled samples and compared. As clear from the equation (1) that $\Delta l/l$ is directly related to the square of polarization and thus the measurements do not specifically require the poled samples.

EXPERIMENTAL PROCEDURE

Commercially available powders of PbO and TiO_2 (anatase form), (Fluka, >99% purity) were used as starting materials. $PbTiO_3$ powders were synthesized by a simple mixed oxide method. Ceramic fabrication was achieved by adding 3 wt% polyvinyl alcohol binder, prior to pressing as pellets in a pseudo-uniaxial die press at 100 MPa. Each pellet was placed in an alumina

crucible together with an atmosphere powder of identical chemical composition. Sintering was carried out with a dwell time of 2 h at each step, with constant heating/cooling rates of 1°C/min [9]. Three sets of the first sintering temperature were assigned for the two stage sintering [10] case: 700, 800 and 900°C. The second sintering temperature was set at 1200°C.

For thermal expansion measurement, the $PbTiO_3$ samples were cut in bar shapes (5 mm long and 1 mm thick). The sample was placed inside a fused silica holder and the thermal expansion was measured as a function of temperature using a linear voltage-differential transformer (LVDT) dilatometer. The samples were heated at a rate of 2°C/min from room temperature to 600°C. The LVDT has an advantage over the other transformer; it gives a linear output for every unit displacement.

RESULTS AND DISCUSSION

The thermal expansion behaviors of $PbTiO_3$ ceramics synthesized under various sintering condition and with unpoled, poled and depoled states were measured by a high-sensitivity dilatometer, Table I summarizes the various important features of these measurements. The results are shown in Figs. 1a, 1b and 1c, respectively. It should be noted that the thermal expansion measurements were made during the first heating from room temperature after poling. The results show the thermal expansion of $PbTiO_3$ ceramics sintered at 700/1200°C, 800/1200°C and 900/1200°C, respectively in Figs. 1a, b and c. The thermal expansion behaviors of these samples are linear at temperatures above 500°C, i.e., above Curie temperature.

The change of strain at the Curie point may be easily seen in the thermal contraction curves. The phase transition temperatures are in good agreement with the published values [11, 12]. The curves on the depoled samples are parallel to the curve for the unpoled sample, essentially restoring the sample

TABLE I Summary of the various important features of the thermal expansion measurements

	T_C (°C)			Calculates P_S at room temperature ($\mu C/cm^2$)		
Sample	Unpoled	Poled ll	Poled ⊥	Unpoled	Poled ll	Poled ⊥
1 $PbTiO_3$ 700/1200°C	489	482	489	74.99	75.76	69.47
2 $PbTiO_3$ 800/1200°C	481	478	482	75.49	72.28	72.06
3 $PbTiO_3$ 900/1200°C	478	477	476	76.85	74.62	75.81

dimension to the prepoled value. Effect of poling on thermal expansion properties was also determined. It can be noted that the strain values for both perpendicular and parallel (w.r.t. length direction) poled sampled can be reduced or changed by the surface charge. Moreover, it is indicated that the transition temperature is comparatively decreased from the Curie point of the unpoled ceramics.

The high temperature data in the cubic phase, above T_C, can be approximated by a straight line. The deviation from this linear high temperature behavior occurs at approximately the same temperature ($\sim$500°C). On analyzing the deviation of the strain from the high temperature linear behavior and by using Eq. (1) the P_S values can be obtained at various temperatures. Using the values of $Q_{11} = 8.9 \times 10^{-2}$ m^4/C^2 and $Q_{12} = -2.6 \times 10^{-2}$ m^4/C^2 [13], the P_S can be calculated. The results for various samples are plotted in

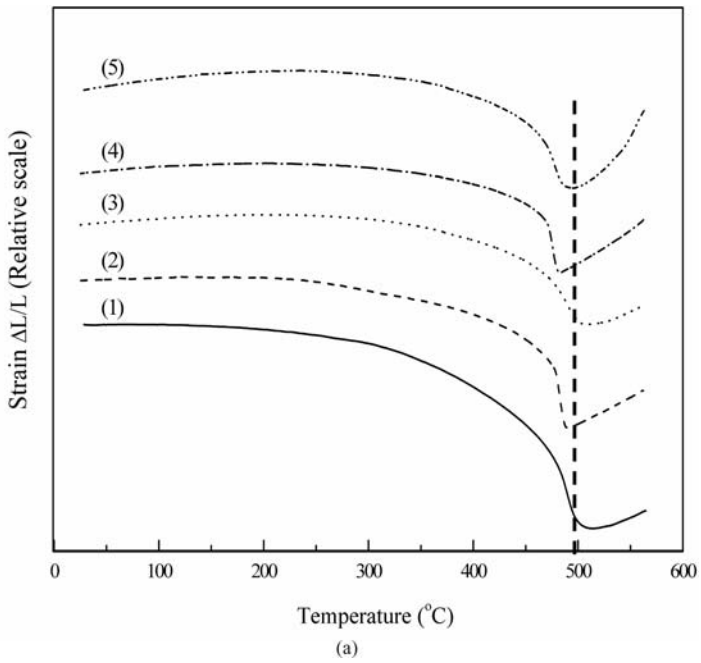

Figure 1. Strain as a function of temperature for $PbTiO_3$ ceramics and of different poling states: (1) unpoled, (2) poled parallel to the length direction, (3) poled perpendicular to the length direction, (4) depoled parallel to the length direction and (5) depoled perpendicular to the length direction (all measurements are in heating cycles and along the length direction); Figures a, b, c are for (a) sintered at 700/1200°C, (b) sintered at 800/1200°C and (c) sintered at 900/1200°C. *(Continued)*

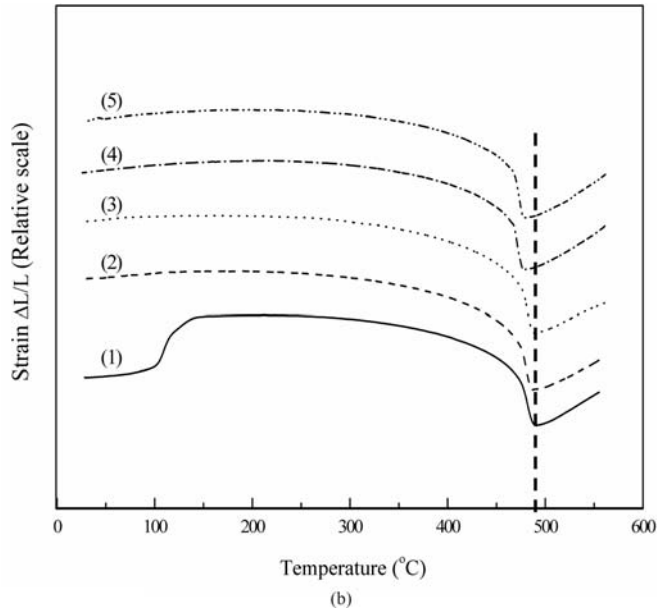

(b)

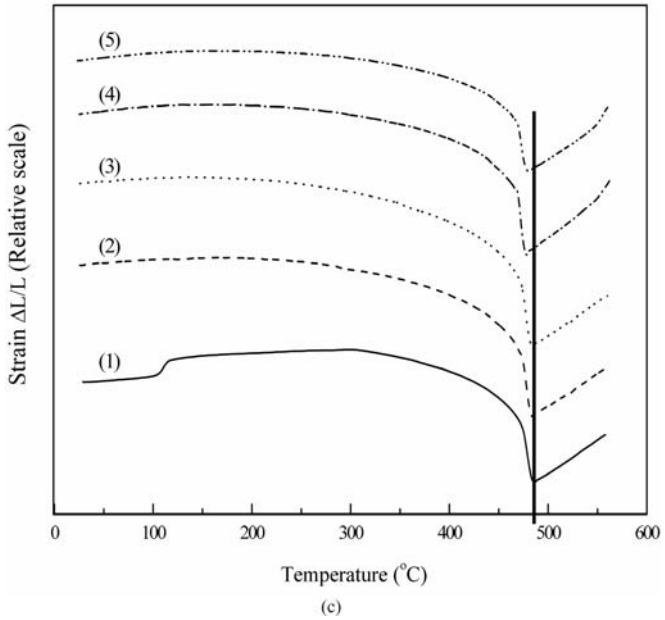

(c)

Figure 1. (Continued)

Figs. 2a, 2b and 2c, respectively. When calculating the spontaneous strains of the tetragonal at a particular temperature, the cubic cell constant should be extrapolated to that temperature accounting for the thermal expansion. A linear extrapolation from above the transition can be made over a narrow range with fairly good accuracy.

In Figures 2a, 2b and 2c are shown the $P_s = \sqrt{\bar{P}_S^2}$ values calculated from the thermal expansion data. The agreement in the P_S values is excellent. The values are also in good agreement not only in magnitude but also in the T_C values with the earlier reported results [6, 7]. Figure 2a, shows the P_S value versus temperature of $PbTiO_3$ ceramic sintered at 700/1200°C. The P_S value in the case of unpoled sample is slightly higher than those of both parallel and perpendicular poled samples in temperature range below Curie point, and is caused by the P_S of the poled ceramics. Also the P_S is smaller than the value in thermally depoled sample. Similar trends have

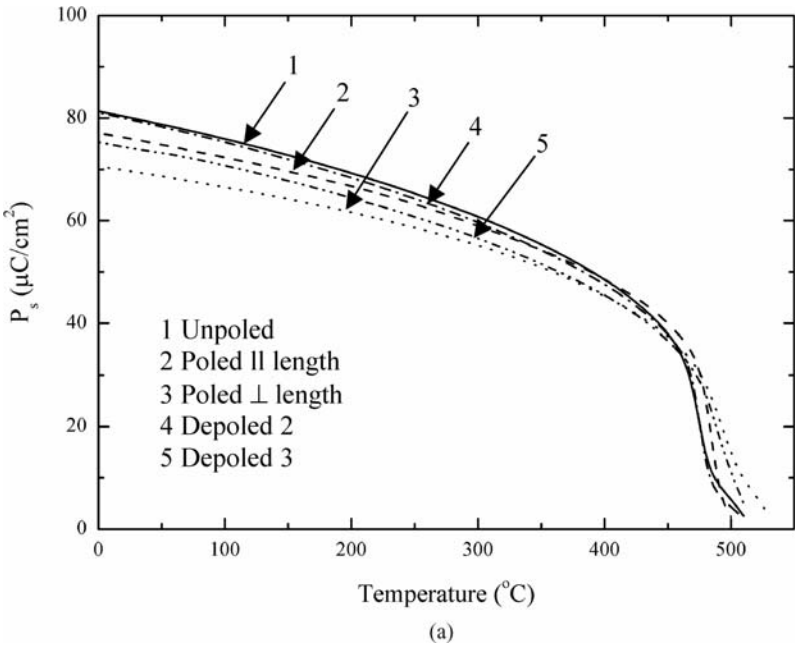

Figure 2. P_S as a function of temperature for $PbTiO_3$ ceramics with and without poling: (1) unpoled, (2) poled parallel to the length direction, (3) poled perpendicular to the length direction, (4) depoled parallel to the length direction and (5) depoled perpendicular to the length direction; figures a, b, c are for (a) sintered at 700/1200°C, (b) sintered at 800/1200°C and (c) sintered at 900/1200°C. *(Continued)*

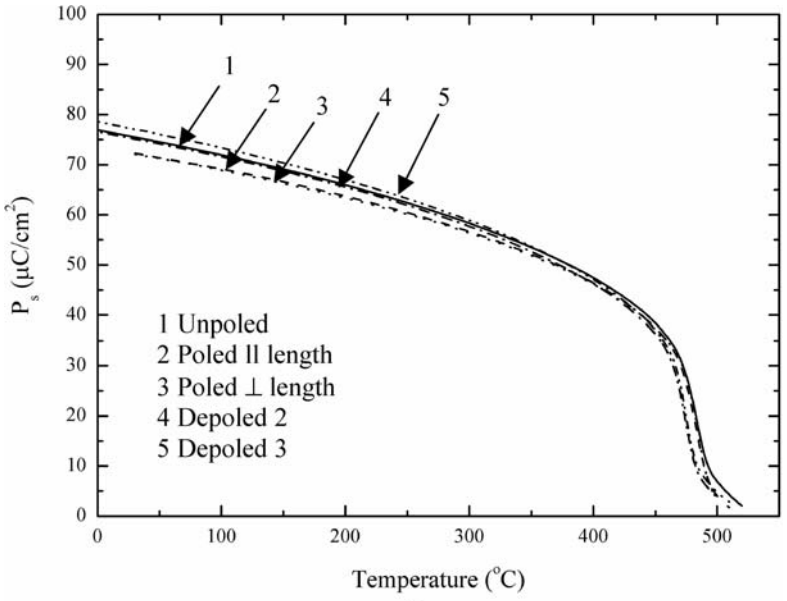

(b)

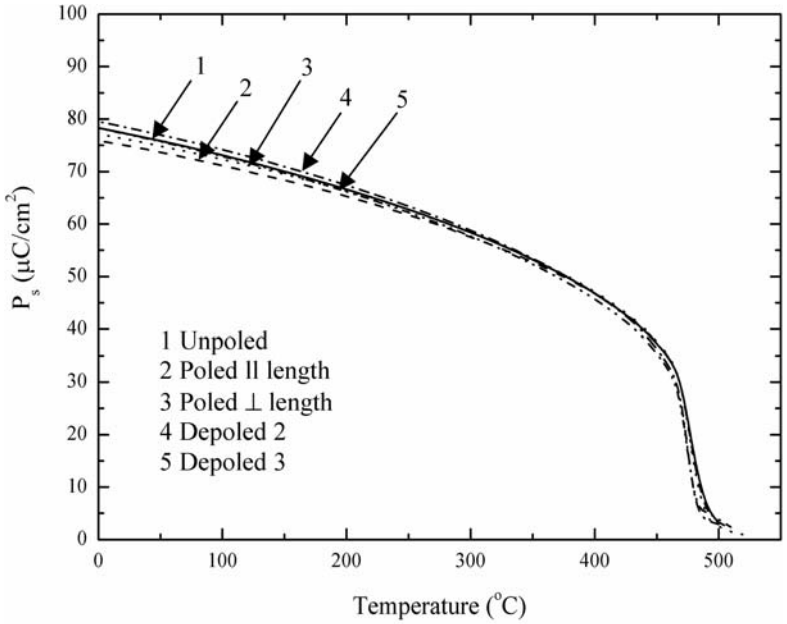

(c)

Figure 2. (Continued)

been noticed in the samples sintered under different processing conditions. There are a few factors which could be influencing the measurements. First, there are some sources of contributions to the strain in ferroelectrics, i.e., in addition to the structural component which is present at all temperatures, a component associated with the appearance of spontaneous polarization in the case of ferroelectric state is also present. The contribution of the spontaneous polarization to strain is due to electrostrictive coupling. Second, after poling it is also possible to have some residual surface charge on the surfaces which can affect the net strain. For perpendicular poling conditions, the net thermal strain might be more along the length due to the positive expansion of a-axis. Therefore, the strain along the length direction can be affected differently in the parallel and perpendicular poled samples. At temperature near T_C, it is seen that the P_S values of both poled samples are sharper compare to those of unpoled and depoled samples. For the other two samples sintered under different conditions, the polarization behaviors are slightly different, however, the magnitude of P_S and trend of polarization behavior are similar to that of 700/1200°C $PbTiO_3$ ceramic. The sharpness of the transition increases and the hyteresis space gradually decreases for the samples sintered at higher temperature in first step of the two stage sintering process.

CONCLUSIONS

We investigated the polarization behavior of $PbTiO_3$ ceramics in unpoled, poled and depoled states by using the thermal expansion data. The room temperature $P_S = 75\ \mu C/cm^2$ is in good agreement with the reported values and also suggesting that thermal strain data can be used for estimating the reliable polarization and its temperature dependence in the case of high T_C ferroelectrics or where the high conductivity of the samples interferes with the electrical measurements. Some important conclusions are made as follow:

(i) The temperature dependence of thermal strain of unpoled and poled ceramics showed nonlinearity and large anomalies resulting from polarization.
(ii) The unpoled and depoled samples synthesized under the different two stage sintering conditions exhibited similar behavior in strain versus temperature and the poled samples tend to increase the sharpness of the transition. The polarization behavior shows a sharp first-order phase transition.

(iii) Hysteresis of T_C in heating and cooling cycles is larger in the samples sintered at lower temperature (data not shown here).
(iv) On poling hysteresis of T_C (cooling and heating cycles) in general decreases.
(v) Transitions with parallel poled samples are sharper.
(vi) The polarization versus temperature and its decay, above T_C, is less dispersive for the high temperature sintered or the high density ceramics.
(vii) In the case of higher density samples, all the T_C (unpoled, poled and depoled) are approximately the same.

ACKNOWLEDGMENT

We thank the Thailand Research Fund (TRF), the Graduate School of Chiang Mai University and NSF Relaxor program, Materials Research Laboratory and MRI of Penn State University for all the support during this work.

REFERENCES

[1] B. Jaffe, W. R. Cook, and H. Jaffe, *Piezoelectric Ceramics* (New York, Academic Press, 1971).
[2] G. H. Haertling, Ferroelectric Ceramics: History and Ttechnology, *J. Am. Ceram. Soc*., **82**(4), 797–818 (1999).
[3] T. Takahashi, Lead Titanate Ceramics with Large Piezoelectric Anisotropy and Their Applications, *Am. Ceram. Soc. Bull.* **69**, 691–695 (1990).
[4] G. Burns and B.A. Scott, Lattice Modes in Ferroelectric Perovskite: $PbTiO_3$, *Phys. Rev. B* **7**, 3087–3101 (1973).
[5] F. G. Fesenko, V. G. Gavrilyachenko, and E. V. Zarochencev, *Izv, Akad. Nauk SSSR*, **34**, 2541 (1970).
[6] V. G. Gavrilyachenko, R. I. Spinko, M. A. Martynenko, and E. G. Fesenko, *Fiz. Tverd. Tela* **12**, 1532 (1970); *Sov. Phys. Solid State (English Transl.)* **12**, 1203 (1970).
[7] F. Jona and G. Shirane, *Ferroelectric Crystal* (Oxford, Pergamon Press, 1962).
[8] A. S. Bhalla, R. Guo, and L. E. Cross, Measurements of Strain and the Optical Indices in the Ferroelectric $Ba_{0.4}Sr_{0.6}Nb_2O_6$: Polarization Effects, *Phys. Rev. B.* **36**, 2030–2035 (1987).
[9] A. Udomporn, K. Pengpat, and S. Ananta, Highly Dense Lead Titanate Ceramics from Refined Processing, *J. Eur. Ceram. Soc.* **24**, 185–188 (2004).
[10] S. Ananta and N.W. Thomas, Fabrication of PMN and PFN Ceramics by a Two-Stage Sintering Technique, *J. Eur. Ceram. Soc.* **19**, 2917–2930 (1999).

[11] G. Shirane and S. Hoshino, On the Phase Transition in Lead Titanate, *J. Phys. Soc. Jpn*. **6**, 265–270 (1951).

[12] G. Shirane, R. Pepinsky, and B. C. Frazer, X-Ray and Neutron Diffraction Study of Ferroelectric $PbTiO_3$, *Acta Crystallogr*., **9**, 131–140 (1956).

[13] M. J. Huan, E. Furman, S. J. Jang, H. A. McKinstry and L. E. Cross, Thermodynamic Theory of $PbTiO_3$, *J. Appl. Phys.* **62**, 3331–3338 (1987).

Stress-dependent scaling behavior of dynamic hysteresis in bulk soft ferroelectric ceramic

Rattikorn Yimnirun,[a] Supattra Wongsaenmai, Supon Ananta, and Yongyut Laosiritaworn
Department of Physics, Faculty of Science, Chiang Mai University, Chiang Mai 50200, Thailand

(Received 12 September 2006; accepted 20 October 2006; published online 11 December 2006)

The effects of frequency f, field amplitude E_0, and mechanical stress σ on the hysteresis area $\langle A \rangle$ and their scaling relations were investigated on soft PZT bulk ceramics. The hysteresis area was found to depend on the frequency and field amplitude with a same set of exponents to the power-law scaling for both with and without stresses, indicating the universality. The inclusion of stresses into the power law was also obtained in the form of $\langle A - A_{\sigma=0} \rangle \propto f^{-0.25} E_0 \sigma^{0.44}$, which indicates the difference of the energy dissipation between the under stress and stress-free conditions and reveals how the hysteresis area decays with increasing stresses. © *2006 American Institute of Physics*. [DOI: 10.1063/1.2403182]

The dynamic hysteresis characteristics have become an important consideration since hysteresis area $\langle A \rangle$ as a function of the field amplitude E_0 and frequency f presents lots of information critical for many ferroelectric applications.[1,2] Theoretical studies have been carried out to understand the dynamic response of hysteresis curves in spin and polarization systems.[3–5] In particular, attention is focused on the scaling law $\langle A \rangle \propto f^m E_0^n$ (where m and n are exponents that depend on the dimensionality and symmetry of the system). Based on three-dimensional models, it has been suggested that $m=1/3$ and $n=2/3$ as $f \rightarrow 0$, whereas $m=-1$ and $n=2$ as $f \rightarrow \infty$.[3,5,6] Experimental investigations on a few thin-film systems have also been reported with variation in the scaling relations obtained.[5–11] On the contrary, there is only a single report on the scaling behavior studies of ferroelectric hysteresis loops of bulk ferroelectric ceramics.[12] More importantly, in many applications the ceramic specimens are often subjected to mechanical loading, either from the design of the device itself or from operating conditions which induce stresses.[1,13] Therefore, a prior knowledge of how the material properties change under different load conditions in materials is inevitably crucial for proper design of a device and for suitable selection of materials for a specific application. In many previous investigations the electrical properties of ceramics were found to depend strongly on stresses (σ).[14–18] Since f, E_0, and σ have been reported to impose significant influence on the dynamic hysteresis responses of ferroelectric ceramics, it is therefore the aim of this study to establish the scaling behavior of the dynamic hysteresis responses of bulk ceramics under the influence of the external stress.

Due to its commercial availability and many practical applications, a donor-doped or soft lead zirconate titanate (PZT) ceramic was used in this study. The disk-shaped samples of a commercially available soft PZT ceramic (PKI-552, Piezo Kinetics Inc., USA) with a diameter of 10 mm and a thickness of 1 mm were used in this study. Its basic properties are dielectric constant (1 kHz) $\varepsilon_r=3400$, Curie temperature $T_C=200\ ^\circ$C, piezoelectric strain constants $d_{33}=550$ pm/V and $d_{31}=-270$ pm/V, planar coupling factor $k_p=0.63$, mechanical quality factor $Q_m=75$, and coercive field (50 Hz) $E_c=7.5$ kV/cm. The dynamic hysteresis (P-E) loops were characterized at room temperature (25 °C) by using a modified Sawyer-Tower circuit with f covering from 2 to 100 Hz and E_0 from 0 to 18 kV/cm. The electric field was applied to a sample by a high voltage ac amplifier (Trek 610D) with the input sinusoidal signal from a function generator (HP 3310A). The P-E loops were recorded by a digital oscilloscope (HP 54645A, 100 MHz). The detailed descriptions of this system were explained elsewhere.[17] Effects of the external stress on the dynamic hysteresis were investigated with the compressometer, which was developed for simultaneous applications of the mechanical stress and the electric field.[18] The compressive stress, applying parallel to the electric field direction, was supplied by the servohydraulic load frame and monitored with the pressure gauge. The P-E loops were recorded as a function of mechanical stress applied discretely between 0 and 24 MPa for each applied field and frequency. At each constant stress, the loop was obtained after 20 sampling cycles to average out the noise deformation.

The hysteresis profiles for various frequencies f, field amplitude E_0, and stress σ are obtained. For a particular applied stress, as expected, the dependence of the loop pattern and area $\langle A \rangle$ on f and E is remarkable. At fixed E_0, the loop area $\langle A \rangle$, remnant polarization (P_r), and coercive field (E_c) decrease with an increase of frequency. For the dependence of the hysteresis loop on E_0, the loop does not saturate at small fields (6 and 8 kV/cm). With further increase in E_0, $\langle A \rangle$, P_r, and E_c increase until a well saturated loop is achieved. Similar stress-free observations have been reported in thin films and bulk ceramics.[5,9,12]

Figure 1 displays the hysteresis loops under different compressive stresses during loading at fixed f of 100 Hz and fixed E_0 of 18 kV/cm. The P-E loop area $\langle A \rangle$ is found to decrease steadily with increasing the stress. To investigate the scaling behavior under the effect of applied stresses, instead of including only the field amplitude E_0 and the frequency term f, the scaling relation should also include the stress (σ) term, i.e.,

$$\langle A \rangle \propto f^m E_0^n \sigma^p. \tag{1}$$

However, due to increasing number of exponents, to simplify the problem, the validity of the scaling law $\langle A \rangle(\sigma)$

[a]Author to whom correspondence should be addressed; electronic mail: rattikornyimnirun@yahoo.com

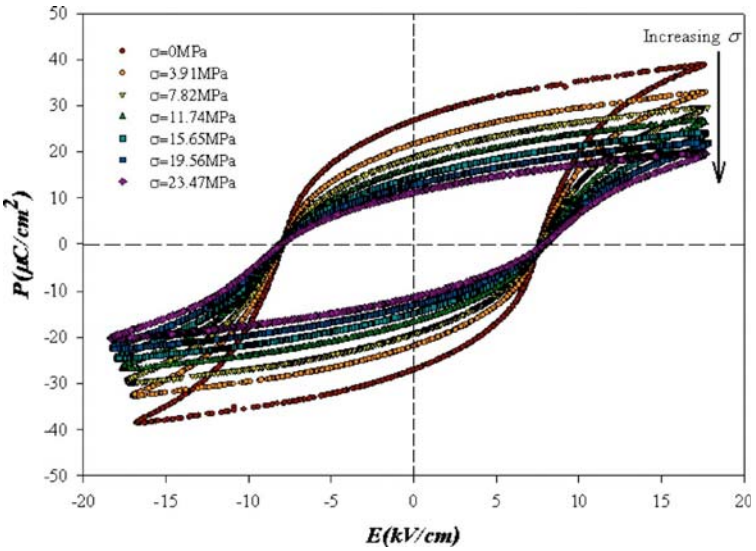

FIG. 1. (Color online) Hysteresis loops for soft PZT ceramic at various σ ($f=100$ Hz and $E_0=18$ kV/cm).

$\propto f^{-0.25}E_0$ is assumed, inspired by a stress-free investigation on bulk PZT,[12] for all applied stresses. Consequently, the area $\langle A\rangle$ for each stress is plotted against $f^{-0.25}E_0$, as shown in Fig. 2, and it can be seen from the least-squares linear fits that reasonably good linear relations can be found. As a result, the condition of universality having $m=-0.25$ and $n=1$ in soft PZT bulk ceramic systems is confirmed, whereas the proportional constant in Eq. (1) may still be a function of σ. Therefore, Eq. (1) is generalized by writing

$$\langle A\rangle = G(\sigma)f^{-0.25}E_0 + F(\sigma), \tag{2}$$

where both $G(\sigma)$ and $F(\sigma)$ are assumed to be a function of σ representing slope function and y-intercept function for a "linear relation" in Eq. (2), and their values are presented via linear-fit functions in Fig. 2. Next, to obtain the scaling form as indicated in Eq. (1), the slope function $G(\sigma)$ is assumed to take a form of power-law function, i.e., $G(\sigma)=a+b\sigma^c$, and a nonlinear fit for $G(\sigma)$ gives $a=0.136\pm0.021$, $b=-0.019\pm0.015$, and $c=0.439\pm0.173$ with $R^2\approx0.994$. However, for the y-intercept function $F(\sigma)$, the scattering data in $F(\sigma)$ do not follow a trivial power-law scaling form. Instead, the reasonably well-fitted function that suits $F(\sigma)$ in the current study is found to take a quadratic function. So $F(\sigma)=a_0+a_1\sigma+a_2\sigma^2$ is written and a least-squares fit is performed to give $a_0=-0.019\pm0.006$, $a_1=0.002\pm0.001$, and $a_2=-1.149\times10^{-4}\pm4.850\times10^{-4}$ with $R^2\approx0.878$. As a result, from Eq. (2), it is therefore possible to write the scaling area

$$\frac{\langle A\rangle - F(\sigma)}{G(\sigma)} = f^{-0.25}E_0, \tag{3}$$

and by plotting this scaling area $(\langle A\rangle - F(\sigma))/G(\sigma)$ against $f^{-0.25}E_0$ all the data should collapse onto a single linear line having a y intercept at zero. The data collapsing of the scaling area from all f, E_0, and σ was found to confirm Eq. (3) as evident in Fig. 3.

On the other hand, it is of interest if the scaling of $\langle A\rangle$ in a form given by Eq. (1) is allowed. Therefore, by discarding minor loops which usually occur at very low E_0, $F(\sigma)\equiv\langle A\rangle(E_0\to0)$ will be small in comparing to $\langle A\rangle$ and can be discarded in Eq. (3) at some intermediately high fields.[12] Consequently, $\langle A\rangle\propto(a+b\sigma^c)f^{-0.25}E_0$ may be written and by substituting the fitted parameters, it is found that

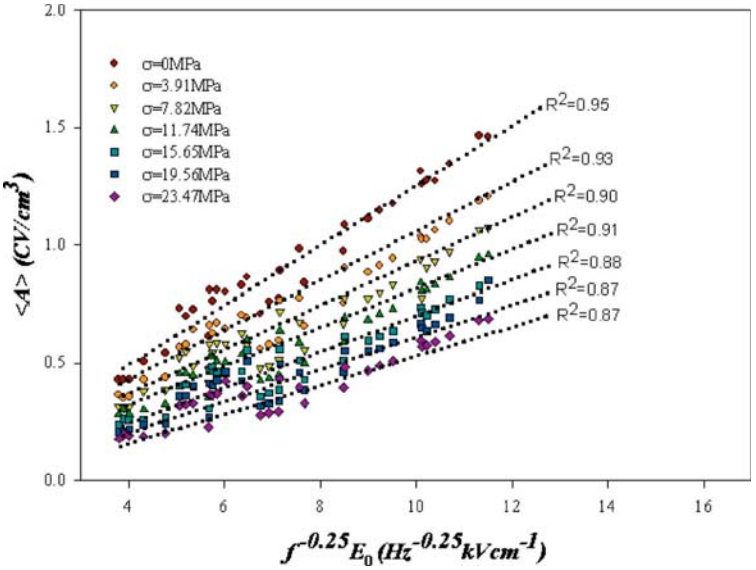

FIG. 2. (Color online) Scaling of hysteresis area $\langle A\rangle$ against $f^{-0.25}E_0$ for soft PZT ceramic at various σ.

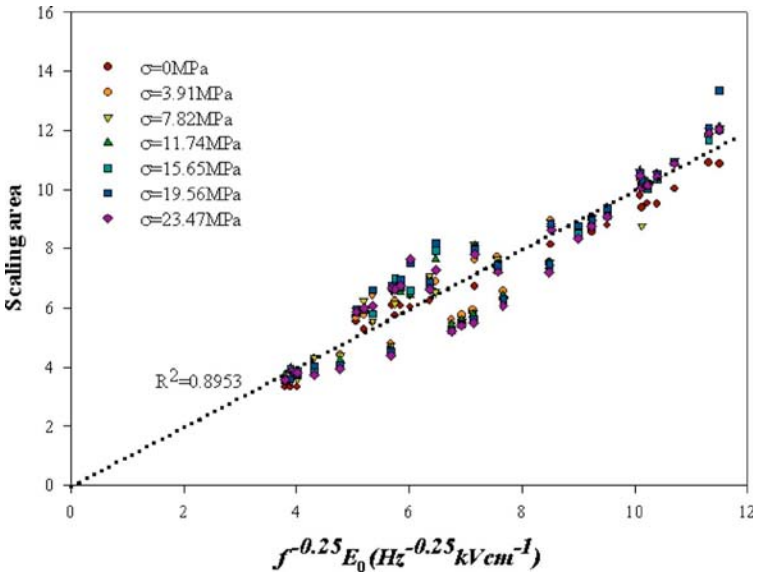

FIG. 3. (Color online) The collapse of the scaling area $(\langle A\rangle - F(\sigma))/(\sigma)$ against $f^{-0.25}E_0$ on a same linear line (with small fluctuation) for soft PZT ceramic.

$$\langle A\rangle - \langle A_{\sigma=0}\rangle = \langle A - A_{\sigma=0}\rangle \propto f^{-0.25}E_0\sigma^{0.44}, \tag{4}$$

where $\langle A_{\sigma=0}\rangle$ refers to the stress-free hysteresis area which will be a dominant term for zero stress. Note that from the appearance of stress σ, $\langle A - A_{\sigma=0}\rangle$, referring to the difference in energy dissipation between under stress and stress-free conditions, increases with increasing stress suggesting a decay of $\langle A\rangle$ with σ at a rate of $\sigma^{0.44}$ as observed in experiments. As a result, it can be concluded that the difference of the hysteresis area between under stress and stress-free conditions scales with frequency, field amplitude, and stress via exponents $m=-0.25$, $n=1$, and $p=0.44$. However, at a particular fixed stress, Eq. (4) gives $f^{-0.25}E_0$ which is the original form for how the area scales with the frequency and the field amplitude.[12]

To understand the scaling relation obtained, at least qualitatively, one needs to consider the following statements. Since the *P-E* loop area indicates the polarization dissipation energy subjected to one full cycle of electric field application, the loop area is therefore directly related to volume involved in the switching process during the application of electric field.[17–19] Hence, when the mechanical stress is applied, more and more ferroelectric domains are constrained by the applied stress and cannot be reoriented by the electric field so as to participate in the polarization reversal. Consequently, both the saturation and remnant polarizations become lower with increasing the compressive stress. The polarization dissipation energy is consequently found to decrease with increasing the applied stress, indicating that the sample volume contributing to polarization reversal decreases with the increasing stress. Similar observations have also been reported in other investigations.[14–18,20–22]

In summary, the scaling behavior of the dynamic hysteresis of the soft PZT bulk ceramics under the effect of mechanical stress has been investigated. With the presence of the external stress, the scaling law for the loop area yields the same set of exponents to frequency and field amplitude in stress-free condition which confirms the condition of universality in bulk system. Furthermore, the difference of the energy dissipation between the under stress and stress-free conditions is found to scale with $f^{-0.25}E_0\sigma^{0.44}$. As a result, the study provides a detailed understanding of how the energy dissipation of the hysteresis properties behaves in response to various conditions especially the mechanical stress.

Financial supports from the Thailand Research Fund (TRF), Commission on Higher Education (CHE), and Faculty of Science and Graduate School of Chiang Mai University are gratefully acknowledged.

[1] K. Uchino, *Ferroelectric Devices* (Dekker, New York, 2000), p. 145.
[2] O. Auciello, J. F. Scott, and R. Ramesh, Phys. Today **51**(7), 22 (1998).
[3] M. Rao, H. R. Krishnamurthy, and R. Pandit, Phys. Rev. B **42**, 856 (1990).
[4] M. Acharyya and B. K. Chakrabarti, Phys. Rev. B **52**, 6560 (1995).
[5] J.-M. Liu, H. L. W. Chan, C. L. Choy, Y. Y. Zhu, S. N. Zhu, Z. G. Liu, and N. B. Ming, Appl. Phys. Lett. **79**, 236 (2001).
[6] M. Rao and R. Pandit, Phys. Rev. B **43**, 3373 (1991).
[7] J.-M. Liu, H. L. W. Chan, C. L. Choy, and C. K. Ong, Phys. Rev. B **65**, 014416 (2001).
[8] Q. Jiang, H. N. Yang, and G. C. Wang, Phys. Rev. B **52**, 14911 (1995).
[9] B. Pan, H. Yu, D. Wu, X. H. Zhou, and J.-M. Liu, Appl. Phys. Lett. **83**, 1406 (2003).
[10] Y.-H. Kim and J.-J. Kim, Phys. Rev. B **55**, R11933 (1997).
[11] J.-H. Park, C.-S. Kim, B.-C. Choi, B. K. Moon, J. H. Jeong, and I. W. Kim, Appl. Phys. Lett. **83**, 536 (2003).
[12] R. Yimnirun, Y. Laosiritaworn, S. Wongsaenmai, and S. Ananta, Appl. Phys. Lett. **89**, 162901 (2006).
[13] K. Uchino, *Piezoelectric Actuators and Ultrasonic Motors* (Kluwer Academic, Boston, 1997), p. 129.
[14] J. Zhao, A. E. Glazounov, and Q. M. Zhang, Appl. Phys. Lett. **74**, 436 (1999).
[15] D. Viehland and J. Powers, J. Appl. Phys. **89**, 1820 (2001).
[16] D. Zhou, M. Kamlah, and D. Munz, J. Eur. Ceram. Soc. **25**, 425 (2005).
[17] R. Yimnirun, Y. Laosiritaworn, and S. Wongsaenmai, J. Phys. D **39**, 759 (2006).
[18] R. Yimnirun, S. Ananta, A. Ngamjarurojana, and S. Wongsaenmai, Appl. Phys. A: Mater. Sci. Process. **81**, 1227 (2005).
[19] M. E. Lines and A. M. Glass, *Principles and Applications of Ferroelectrics and Related Materials* (Clarendon, Oxford, 1977), p. 102.
[20] J. F. Shepard, Jr., F. Chu, B. Xu, and S. Trolier-McKinstry, Mater. Res. Soc. Symp. Proc. **493**, 81 (1997).
[21] T. Kumazawa, Y. Kumagai, H. Miura, M. Kitano, and K. Kushida, Appl. Phys. Lett. **72**, 608 (1998).
[22] X. Lu, J. Zhu, X. Li, Z. Zhang, X. Zhu, D. Wu, F. Yan, Y. Ding, and Y. Wang, Appl. Phys. Lett. **76**, 3103 (2000).

Appl. Phys. A 86, 249–255 (2007)
DOI: 10.1007/s00339-006-3753-3

Applied Physics A
Materials Science & Processing

R. WONGMANEERUNG
R. YIMNIRUN
S. ANANTA✉

Effects of sintering condition on phase formation, microstructure and dielectric properties of lead titanate ceramics

Department of Physics, Faculty of Science, Chiang Mai University, Chiang Mai 50200, Thailand

Received: 8 May 2006/Accepted: 4 October 2006
Published online: 17 November 2006 •

ABSTRACT Lead titanate ceramics have been prepared by two different processing methods: conventional (or single-stage) and two-stage sintering. Effects of designed sintering conditions on phase formation, densification, microstructure and dielectric properties of the ceramics were characterized via X-ray diffraction, Archimedes density measurement, scanning electron microscopy and dielectric measurement, respectively. The potentiality of a two-stage sintering technique as a simple ceramic fabrication method to obtain highly dense and pure lead titanate ceramics was demonstrated. It has been found that, under suitable two-stage sintering conditions, dense perovskite lead titanate ceramics can be successfully achieved with better dielectric properties than those of ceramics from a single-stage sintering technique.

PACS 77.22.-d; 77.84.-s; 77.84.Dy

1 Introduction

Being one of the lead-based perovskites, lead titanate ($PbTiO_3$ or PT) is of interest as a component in commercial electroceramic materials. In addition, PT when combined with other oxides can form a series of ferroelectric materials that exhibit many of the most desirable dielectric, piezoelectric and pyroelectric properties for use in electronic devices at high frequency and high temperature, such as infrared sensors, microactuators, capacitors and hydrophones [1–3]. The most important properties of perovskite PT ceramics are high Curie temperature ($\sim 490\,^{\circ}C$) and large mechanical-quality factor and pyroelectric coefficient [4, 5]. However, pure and dense PT ceramics are regarded to be one of the most difficult lead-based perovskite ferroelectric ceramics to produce [6]. PT ceramic is mechanically weak due to large distortion of the tetragonal phase at room temperature, which is characterized by the ratio between the lattice parameters (c/a, hereafter called tetragonality, ~ 1.06 [6, 7]). Apart from general problems of PbO volatilization and associated high porosity, the stress induced by cooling through the phase transition can create cracking in bulk ceramics. In addition, it is difficult to pole the ceramics with low resistivity (10^7–$10^8\ \Omega$ cm) [8].

✉ Fax: (6653) 943-445, E-mail: suponananta@yahoo.com

To overcome these problems, several techniques have been introduced, such as utilizing ultra-fine powders, using additives, employing spark-plasma sintering and carrying out appropriate milling and sintering conditions [8–13]. All these techniques are aimed at reducing the lattice tetragonality of the bulk ceramics, even though they inevitably affect the phase formation, structure and electrical properties of materials in different ways. Amongst all the approaches reported so far, most attention has been concentrated on the use of additives and powder processing, whereas investigations of modified sintering techniques have not been widely carried out [13, 14].

Therefore, in this work, a two-stage sintering method has been developed to resolve these problems. With this new scheme, instead of using a single, high firing temperature (of up to 1225 °C) [13] where the degree of PbO volatilization affects the stoichiometry of the product by forming a pyrochlore phase, in addition to a perovskite phase, two moderate temperatures (T_1 and T_2 with a constant dwell time of 2 h at each stage) were adopted. The aim of this study was to investigate the influence of these two ceramic processing methods (single- and two-stage sintering) on phase formation, densification, microstructure and dielectric properties of $PbTiO_3$ ceramics.

2 Materials and methods

Commercially available powders of PbO and TiO_2 (anatase form, Fluka, $> 99\%$ purity) were used as starting materials. A simple mixed oxide synthetic route was employed to synthesize $PbTiO_3$ powders. The mixing process was carried out by ball milling a mixture of raw materials for 24 h with corundum medium in isopropyl alcohol (IPA). After wet milling, the slurry was dried at 120 °C for 2 h, sieved and calcined in a closed alumina crucible, with the optimum calcination conditions determined by the X-ray diffraction (XRD) method (600 °C for 2 h with heating/cooling rates of 5 °C/min [15]). Ceramic fabrication was achieved by adding 3 wt % polyvinyl alcohol (PVA) binder, prior to pressing as pellets (15 mm in diameter and 1.0–1.3-mm thick) in a pseudo-uniaxial die press at 100 MPa. Each pellet was placed in an alumina crucible together with an atmosphere powder ($PbTiO_3$) of identical chemical composition. After the binder burn out at 500 °C for 1 h, sintering was carried out with a dwell time of 2 h at each step, with constant

heating/cooling rates of 1 °C/min [13] applied (Fig. 1). Variation of the firing temperature between 1150 and 1250 °C was carried out for the single-stage sintering samples. Three sets of the first sintering temperature (T_1) were assigned for the two-stage sintering case: 700, 800 and 900 °C. Variation of the second sintering temperature (T_2) between 1000 °C and 1250 °C was carried out for each case.

Densities of the final sintered products were determined by using the Archimedes principle. Sintered ceramics were examined by room-temperature X-ray diffraction (Siemens D500 diffractometer) using Cu K_α radiation to identify the phase formed. The lattice parameters and tetragonality factor (c/a) of the sintered ceramics were calculated from the XRD patterns [16]. The microstructural development was characterized using a JEOL JSM-840A scanning electron microscopy (SEM), equipped with an energy-dispersive X-ray (EDX) analyser. Mean grain sizes of the sintered ceramics were subsequently estimated by employing the linear intercept method [17]. In order to evaluate the dielectric properties, dense ceramics were polished to form flat, parallel faces (14 mm in diameter and 0.8-mm thick). The samples were then coated with silver-paste electrodes which were fired on both sides of the samples at 700 °C for 1 h. The dielectric properties were measured at a frequency of 1 MHz using a HIOKI 3532-50 LCR meter, on cooling through the transition range (500–25 °C) with a rate of 5 °C/min.

3 Results and discussion

X-ray diffraction patterns of the PT ceramics sintered at various conditions are displayed in Figs. 2 and 3, indicating the formation of both perovskite and impurity phases in each case. The strongest reflections in the majority of all XRD traces indicate the formation of the $PbTiO_3$ perovskite phase of lead titanate, which could be matched with JCPDS file no. 6-452, in agreement with other works [11–13]. To a first approximation, this major phase has a tetragonal perovskite-type structure in space group P4/mmm (no. 123) with cell parameters $a = 389.93$ pm and $c = 415.32$ pm [18]. For the singly sintered PT ceramics, additional weak reflections are found in the samples sintered above 1175 °C (marked by θ in Fig. 2), which correlate to the starting precursor PbO (JCPDS file no. 77-1971) [19]. This observation could be attributed mainly to the poor mixing of the employed powders derived from the ball-milling technique. The relative amounts of perovskite and minor phase present in each sintered ceramic were calculated from the intensities of the major X-ray reflections from the respective phases. In this connection, the following approximation was adopted, as in the earlier PMN ($Pb(Mg_{1/3}Nb_{2/3})O_3$) and PFN ($Pb(Fe_{1/2}Nb_{1/2})O_3$) studies [14]:

$$\text{perovskite phase (wt\%)} = I_P/(I_P + I_M) \times 100\,. \qquad (1)$$

Here I_P and I_M refer to the intensities of the {110} perovskite and {111} minor phase peaks, respectively, these being the most intense reflections in the XRD patterns of both phases. For the purposes of estimating the concentration of minor phase present, (1) has been applied to the diffraction patterns obtained (numerical data are presented in Tables 1 and 2).

More interestingly, a single phase of perovskite PT is found in all the doubly sintered samples (Fig. 3), in contrast to the observations for the singly sintered samples. No evidence of pyrochlore phase of $PbTi_3O_7$ composition earlier reported by Udomporn, Ananta and Tartaj et al. [15, 20] was found, nor was there any evidence of other second phases [21] being present. This could be due to the lower firing temperature of the doubly sintered samples as compared to the singly sintered ceramics, leading to a smaller degree of lead losses and consequently avoiding the pyrochlore formation, while a sufficient amount of energy required for ceramic densification still to be reached was provided by the longer holding time, in agreement with other works [14, 22, 23]. However, many other factors come into play, e.g. homogeneity of materials, reactivity of starting powders and processing variables. These XRD results clearly show that, in general, the different processing methods used for preparing PT ceramics gave rise to a different phase formation in the sintered materials. The absence of minor phase in doubly sintered samples was related to the more reactive process used [14].

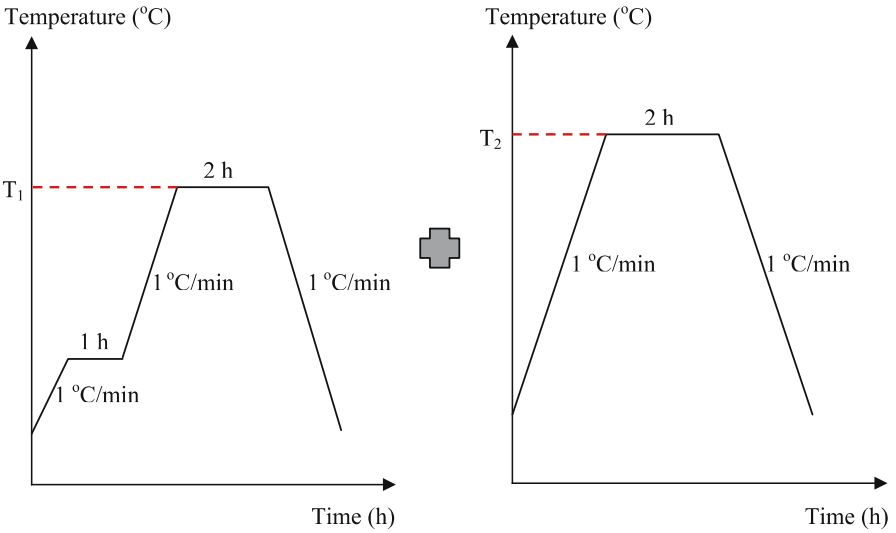

FIGURE 1 A two-stage method sintering profile

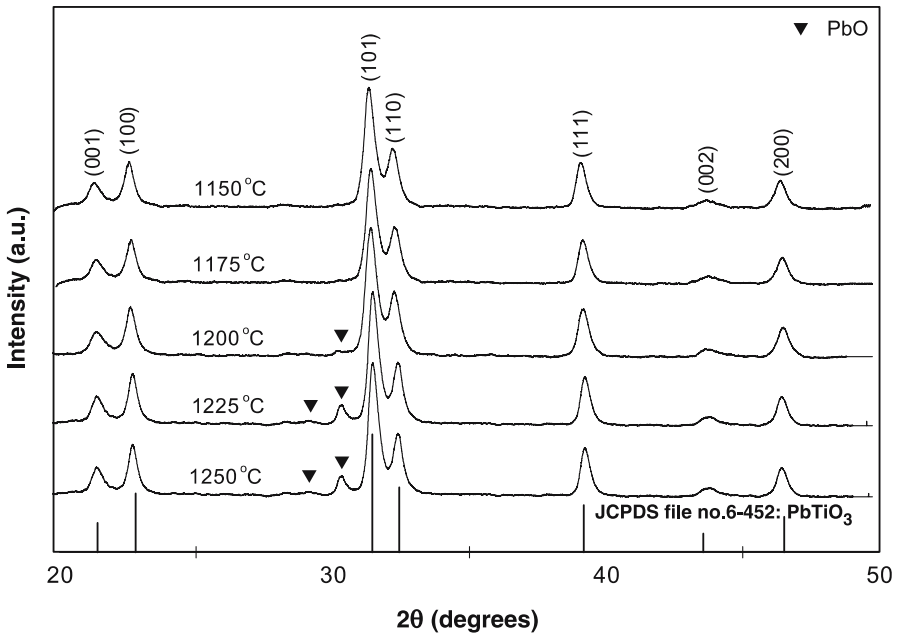

FIGURE 2 XRD patterns of PT ceramics singly sintered at various temperatures

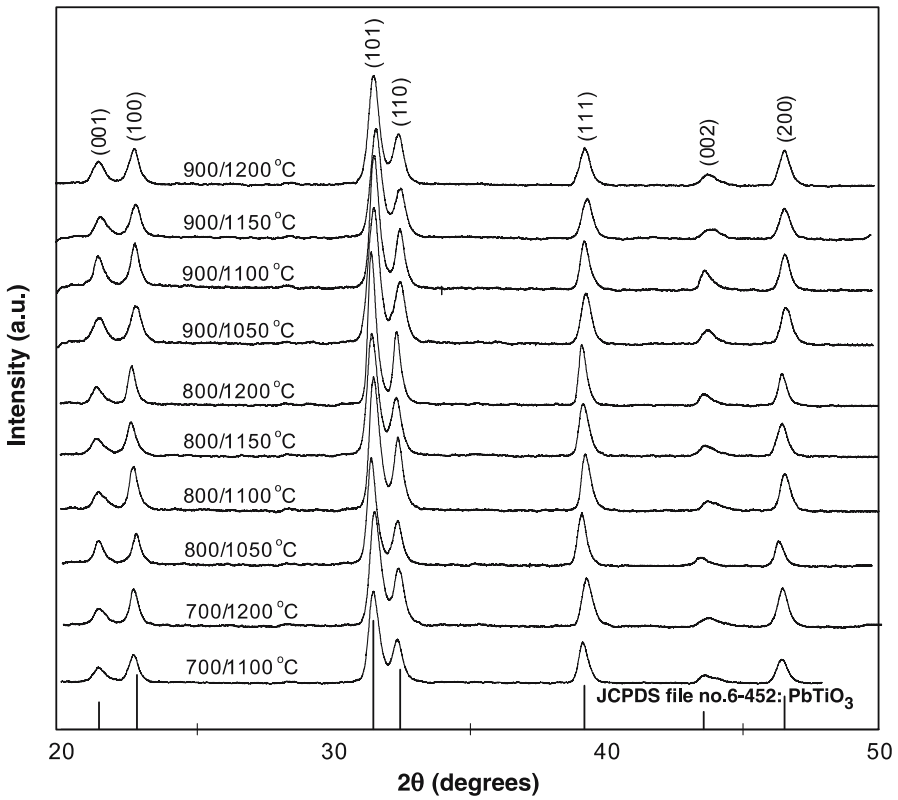

FIGURE 3 XRD patterns of PT ceramics doubly sintered at various conditions, with the first sintering temperature (T_1) at 700, 800 and 900 °C

Tables 1 and 2 also present the tetragonality factor (c/a), relative density and average grain size of singly and doubly sintered samples, respectively. Generally, it is evident that as the sintering temperature increases, the density of almost all the samples increases. However, it can be seen that the sintering behaviour of singly and doubly sintered PT ceramics was dissimilar. Doubly sintered ceramics reached a maximum density of $\sim 97\%$ at 900/1150 °C or 900/1200 °C. On the other hand, singly sintered samples exhibit less densification, and a temperature of 1225 °C was required to reach a densification level of $\sim 94\%$. The densification of all materials slightly decreased at temperatures higher than those of the maximum density, accompanied by a significant increase of weight loss ($\sim 2\%$–5%). By comparison with singly sintered PT ceramics, lower values of tetragonality (c/a) are found in all doubly sintered cases, indicating lower internal stress in these sintered samples.

Microstructural features of PT samples singly sintered at different temperatures for 2 h with heating/cooling rates of 1 °C/min are shown in Fig. 4. It was found that the samples

Sintering temperature (°C)	Perovskite phase (%)	Tetragonality (c/a)	Relative density (%)	Grain size range (mean)* (μm)
1150	100	1.064	87	2.5–15.0 (6.5)
1175	100	1.064	89	8.0–26.5 (13)
1200	99.3	1.063	92	12.0–40.0 (29)
1225	90.1	1.063	94	20.0–65.0 (36)
1250	89.2	1.063	93	41.0–83.0 (52)

* The estimated precision of the grain size is ±10%

TABLE 1 Physical properties of singly sintered PT ceramics

T_1 (°C)	T_2 (°C)	Perovskite phase (%)	Tetragonality (c/a)	Relative density (%)	Grain size range (mean)* (μm)
700	1000	–	–	–	–
700	1050	–	–	–	–
700	1100	100	1.058	96	0.3–0.5 (0.3)
700	1150	100	1.060	96	0.3–1.2 (0.8)
700	1200	100	1.062	96	0.4–1.7 (1.3)
700	1250	–	–	–	–
800	1000	–	–	–	–
800	1050	100	1.064	95	1.0–2.2 (1.6)
800	1100	100	1.061	96	0.5–3.3 (1.9)
800	1150	100	1.060	96	1.0–2.7 (1.8)
800	1200	100	1.062	96	0.6–1.7 (1.2)
800	1250	–	–	–	–
900	1000	–	–	–	–
900	1050	100	1.060	96	0.4–2.2 (1.2)
900	1100	100	1.060	96	0.7–1.5 (1.1)
900	1150	100	1.057	96	0.6–1.9 (0.8)
900	1200	100	1.061	97	1.0–2.2 (1.5)
900	1250	100	–	–	–

* The estimated precision of the grain size is ±10%
– Data are not available because the samples were too fragile for the measurements

TABLE 2 Physical properties of doubly sintered PT ceramics

subjected to low sintering temperature, e.g. 1150 °C, eventually burst into pieces because of the internal anisotropic stress caused by the phase transition in the ceramics, as can be confirmed by the SEM images showing a loose formation of large grains (Fig. 4a and b), in agreement with high values of c/a given in Table 1. Additionally, average grain sizes were found to increase with the sintering temperature. For higher-temperature treatments, a pronounced second phase is segregated at the grain boundaries. The EDX spectra indicated that there was more Pb and less Ti in the bright region ([Pb] : [Ti] ∼ 4 : 1 at. %) than in the dark region ([Pb] : [Ti] ∼ 1 : 1 at. %), as shown in Fig. 4b–d. The observation of these (second-phase) layers could be attributed to a liquid-phase formation during the sintering process as proposed by many researchers [24, 25].

In addition, a combination of SEM and EDX techniques has demonstrated that small amounts of nanosized ($\varphi \sim 1.7$–2.5 nm) spherical TiO_2 inclusions (brighter phase) exist on the surface of perovskite PT grains in some samples, as shown in Fig. 4b and c, similar to those found by Takeuchi et al. [26]. The existence of a discrete TiO_2 phase points to the expected problem of poor homogeneity of the samples arising from PbO volatilization after being subjected to prolonged heating, although the concentration is too low for XRD detection.

Representative microstructures for doubly sintered PT ceramics are given in Fig. 5. The first sintering temperature was designed at 700, 800 and 900 °C, for constant dwell time and

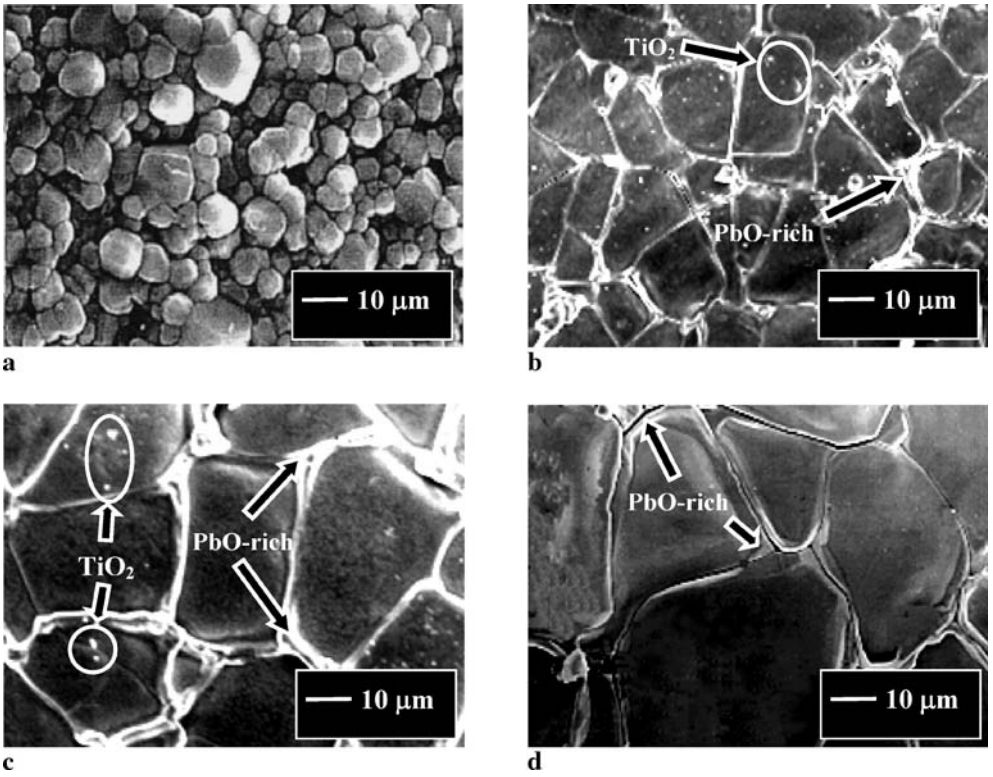

FIGURE 4 SEM micrographs of PT ceramics singly sintered at (**a**) 1150 (**b**) 1175 (**c**) 1200 and (**d**) 1225 °C

heating/cooling rates of 2 h and 1 °C/min at each stage, while the second sintering temperature was varied from 1100 °C to 1200 °C. It is seen that a uniform grain shape of typical perovskite ceramics [9, 22, 23] is observed, with sizes in the range of 0.4–2.0 μm. It should be noted that the average grain size of the doubly sintered PT ceramics is < 2.0 μm, which is less than the critical value of 3 μm reported by several workers [11, 26, 27]. Here, it is believed that smaller grains with random orientations result in lower internal stress in sintered samples because they compensate the anisotropy of thermal expansion coefficients.

By comparison with singly sintered PT ceramics, almost clean microstructures with high uniformity, denser angular grain packing and more homogeneity are generally observed in doubly sintered PT samples. These microstructures are typical of a solid-state sintering mechanism. In the present study (Fig. 5 and Table 2), the microstructural features of the doubly sintered PT ceramics with various second sintering temperatures ranging from 1050 to 1200 °C are not significantly different. However, it should be noted that higher angular grains were evidenced for higher second sintering temperature (see Fig. 5b, d and f). The observation that the sintering temperature effect may also play an important role in obtaining a high angularity in the grains of perovskite ceramics is also consistent with other similar systems [22, 23]. Moreover, an abnormal grain growth probably due to the inhibition of the normal grain growth mechanism during the double sintering process [14] was also found in some samples, as shown in Fig. 5c. It is also of interest to point out that evidence has been found for the existence of microcracks (arrowed) along the grain boundaries of the samples sintered at lower second sintering temperatures (Fig. 5c and e), in agreement with other works [9, 26, 28].

Interestingly, only the samples sintered at 700/1100–1200 °C, 800/1050–1200 °C or 900/1050–1200 °C with the highest relative density and smallest average grain size of about 95%–97% and 0.3–1.9 μm, respectively, remained unbroken. It may be simply assumed that the ceramics consisting of very fine grains have less elastic strain energy than the ceramics with significantly large grains (Tables 1 and 2). Consequently, the experimental work carried out here suggests that the optimum conditions for forming the highly dense PT ceramics in this work are double sintering temperatures at 700–900/1100–1200 °C, 2 h dwell time and 1 °C/min

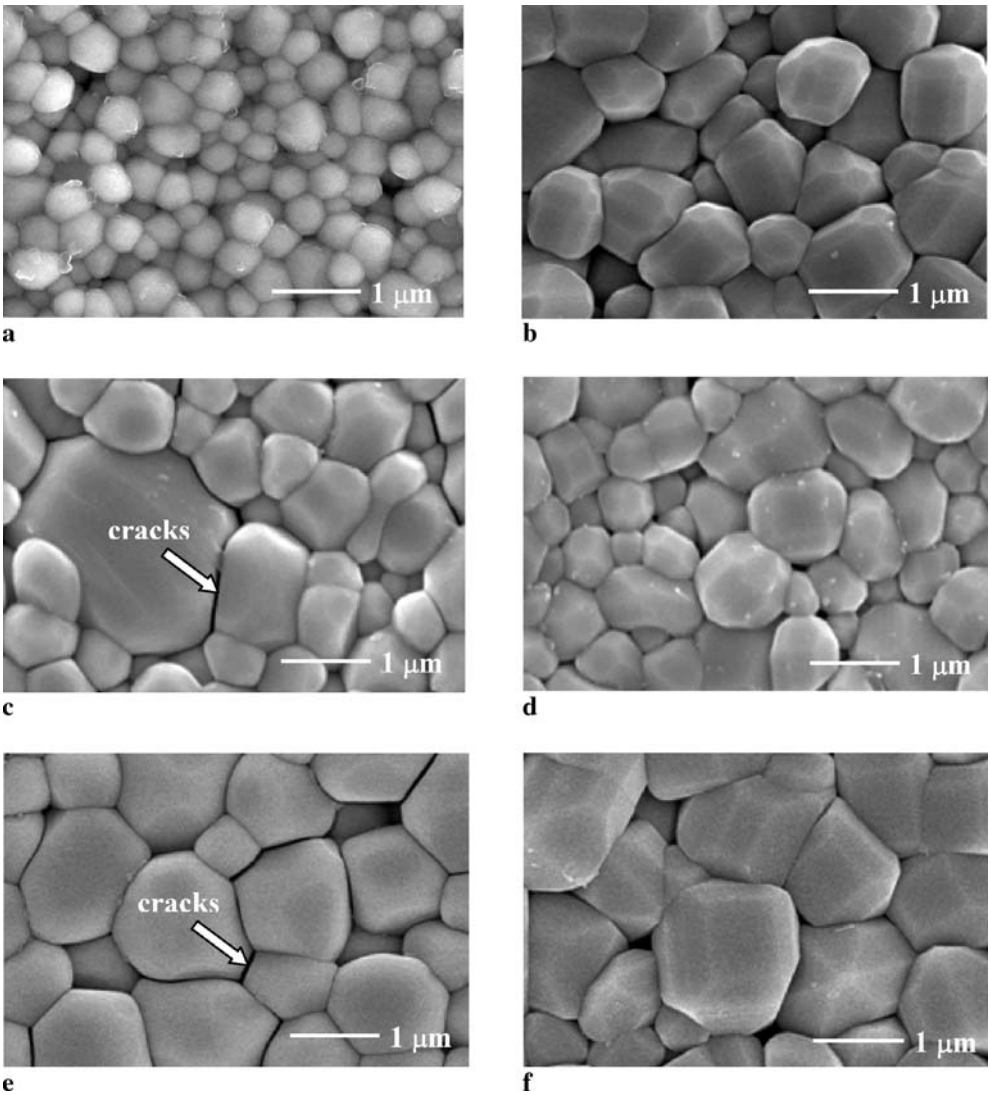

FIGURE 5 SEM micrographs of PT ceramics doubly sintered at (**a**) 700/1100 (**b**) 700/1200 (**c**) 800/1100 (**d**) 800/1200 (**e**) 900/1100 and (**f**) 900/1200 °C

heating/cooling rates. The different microstructure evolution of PT ceramics confirms the importance of the processing method. More importantly, considered from the perovskite content and microstructure of PT ceramics sintered by two different methods, the doubly sintered method was clearly preferable for obtaining dense perovskite PT ceramics. The following discussion of the dielectric properties of the PT ceramics obtained in this study would further support the advantage of the double sintering method.

The dielectric properties of the PT samples sintered with different techniques are also compared in Table 3, as well as in Fig. 6. The Curie temperatures are about the same for all samples measured, whilst the dielectric properties of both sets of the sintered PT ceramics seem to be different. As listed in Table 3, the room-temperature dielectric properties of the two sets of ceramics are not significantly different. The values of dielectric constant in the order of 200 are slightly higher than those reported earlier [9, 29]. However, the high-temperature dielectric properties of the doubly sintered PT samples are noticeably higher than those of the singly sintered PT samples, as seen in the inset of Fig. 6. As mentioned earlier, the reason for this is the high amount of secondary phase present in the singly sintered PT ceramics. In addition, a PbO-rich phase (as observed in Fig. 4b–d), with low dielectric constant, might be forming a continuous layer between grains and hence decreasing the dielectric constant of the singly sintered PT ceramics [13, 24, 30]. The secondary phases in singly sintered PT are interconnected at grain boundaries and, as suggested by Wang and Schulze [24], exert more influence on the dielectric properties than when they are isolated. It should also be noted that in singly sintered specimens the grain boundaries are mostly PbO-rich, while in doubly sintered specimens the grain boundaries are mainly PT with Pb/Ti ratio very close to 1. Although the number of grain boundaries increases in the doubly sintered ceramic, the improved properties are a result of a more chemical homogeneity of the microstructure in the doubly sintered ceramics. Therefore, in this study, it could be stated that the number of grain boundaries is not the main controlling factor for the properties in the doubly sintered ceramics, but the properties are rather dictated by the chemical composition of the grain boundaries.

Grain sizes also play a role in the difference in the dielectric properties, especially the dielectric constant. As clearly seen in Tables 1 and 2 (as well as Figs. 4 and 5), the larger grain size in the singly sintered ceramics would lead to lower dielectric constant than that of the doubly sintered ceramics. This relation is well established in several ceramic perovskite systems, e.g. $BaTiO_3$ [31], PZT ($Pb(Zr_{1/2}Ti_{1/2})O_3$) [32, 33], PMN [22, 34] and PFN [23].

The different microstructure and the different amount of secondary phases present in singly and doubly sintered PT ceramics strongly influence the dielectric properties of these materials, leading to superior electrical behaviour in doubly sintered PT ceramics. Moreover, this study demonstrated that the dielectric properties of PT ceramics are also influenced by microstructural features, especially the phase compositions at grain boundaries, microcracks and the densification mechanism rather than by only pyrochlore phase or by grain size itself.

Although a disadvantage of the proposed two-stage sintering method is a greater time requirement, the significant reduction in firing temperature is a positive development, par-

Dielectric Properties (1 MHz)	Sintering Condition (°C for 2 h) Single 1225	Single 700/1200	Double (T_1/T_2) 800/1200	Double (T_1/T_2) 900/1200
ε_r (25 °C)	243	209	255	209
tanδ(25 °C)	0.01	0.05	0.03	0.03
$\varepsilon_{r,max}$	7680	8993	8322	8198
tanδ_{max}	1.07	1.00	1.10	0.95
T_C	482	484	484	484

TABLE 3 Dielectric properties (at 1 MHz) of PT ceramics sintered at various conditions

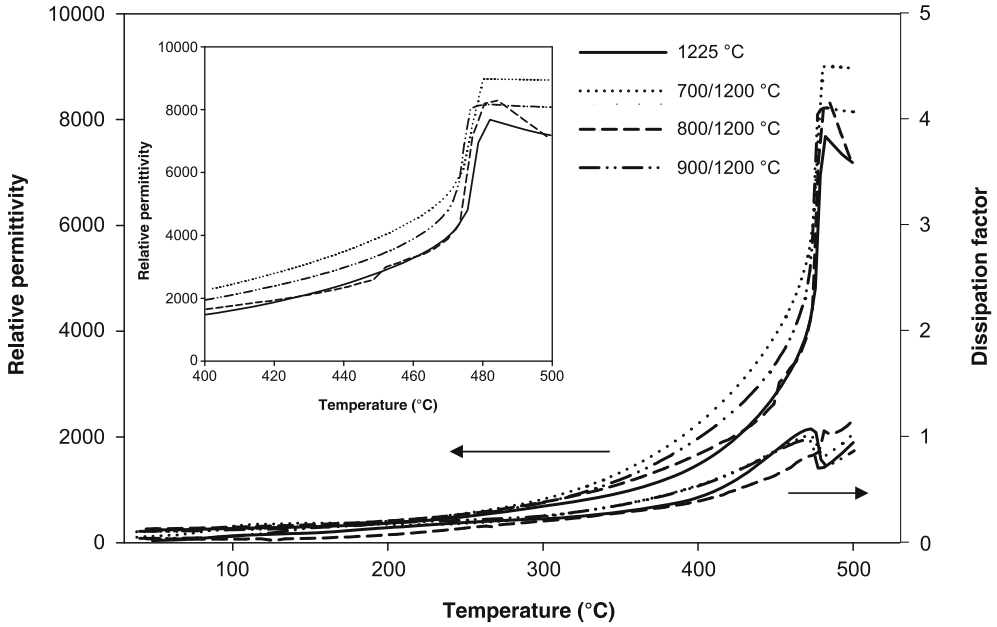

FIGURE 6 Variation with temperature of (**a**) relative permittivity (ε_r) and (**b**) dissipation factor (tanδ) at 1 MHz for PT ceramics sintered at various conditions (*inset*: relative permittivity vs temperature from 400 °C to 500 °C)

ticularly with regard to the drive towards electrodes of lower cost [1–3]. In general, these PT ceramics exhibit complex microstructures which are a result of variation in grain size and orientation, variation in chemical homogeneity, and the presence and distribution of additional minor phase, pores and (micro)cracks. These factors, which are strongly influenced by the sintering conditions, have an important effect on the dielectric properties of materials and their reproducibility.

4 Conclusion

The processing method used for preparing PT ceramics greatly influences the final properties of the ceramics. Even though the simple mixed oxide method employing conventional ball milling was used, this work demonstrated that it was possible to obtain rather dense PT ceramics with homogeneous microstructure by the two-stage sintering technique. It has been shown that, under suitable sintering conditions, the phase formation and densification of the ceramics are better than those obtained from the single-stage sintering. Reductions in the maximum required sintering temperature are possible as compared to the single-stage sintering.

ACKNOWLEDGEMENTS This work was supported by the National Nanotechnology Center (NANOTEC), the Faculty of Science and the Graduate School of Chiang Mai University.

REFERENCES

1 B. Jaffe, W.R. Cook, H. Jaffe, *Piezoelectric Ceramics* (Academic, New York, 1971)
2 G.H. Haertling, J. Am. Ceram. Soc. **82**, 797 (1999)
3 A.J. Moulson, J.M. Herbert, *Electroceramics*, 2nd edn. (Wiley, Chichester, 2003)
4 T. Takahashi, Am. Ceram. Soc. Bull. **69**, 691 (1990)
5 L.E. Cross, Mater. Chem. Phys. **43**, 108 (1996)
6 G. Shirane, S. Hoshino, J. Phys. Soc. Japan **6**, 265 (1951)
7 G. Shirane, R. Pepinsky, B.C. Frazer, Acta Crystallogr. **9**, 131 (1956)
8 H. Takeuchi, S. Jyomura, E. Yamamoto, Y. Ito, J. Acoust. Soc. Am. **72**, 1114 (1982)
9 L.B. Kong, W. Zhu, O.K. Tan, J. Mater. Sci. Lett. **19**, 1963 (2000)
10 T. Suwannasiri, A. Safari, J. Am. Ceram. Soc. **76**, 3155 (1993)
11 T. Takeuchi, M. Tabuchi, I. Kondoh, N. Tamari, H. Kageyama, J. Am. Ceram. Soc. **83**, 541 (2000)
12 J.S. Forrester, J.S. Zobec, D. Phelan, E.H. Kisi, J. Solid State Chem. **177**, 3553 (2004)
13 A. Udomporn, K. Pengpat, S. Ananta, J. Eur. Ceram. Soc. **24**, 185 (2004)
14 S. Ananta, N.W. Thomas, J. Eur. Ceram. Soc. **19**, 2917 (1999)
15 A. Udomporn, S. Ananta, Mater. Lett. **58**, 1154 (2004)
16 H. Klug, L.E. Alexander, *X-ray Diffraction Procedures for Polycrystalline and Amorphous Materials*, 2nd edn. (Wiley, New York, 1974)
17 R.L. Fullman, Trans. AIME **197**, 447 (1953)
18 JCPDS-ICDD card no. 6-452, International Centre for Diffraction Data, Newtown Square, PA, 2000
19 JCPDS-ICDD card no. 77-1971, International Centre for Diffraction Data, Newtown Square, PA, 2000
20 J. Tartaj, C. Moure, L. Lascano, P. Durán, Mater. Res. Bull. **36**, 2301 (2001)
21 M.L. Calzada, M. Alguero, L. Pardo, J. Sol-Gel Sci. Technol. **13**, 837 (1998)
22 S. Ananta, N.W. Thomas, J. Eur. Ceram. Soc. **19**, 629 (1999)
23 S. Ananta, N.W. Thomas, J. Eur. Ceram. Soc. **19**, 1873 (1999)
24 H.C. Wang, W.A. Schulze, J. Am. Ceram. Soc. **73**, 825 (1990)
25 S.M. Gupta, A.R. Kulkarni, J. Mater. Res. **10**, 953 (1995)
26 T. Takeuchi, M. Takahashi, K. Ado, N. Tamari, K. Ichikawa, S. Miyamoto, M. Kawahara, M. Tabuchi, H. Kageyama, J. Am. Ceram. Soc. **84**, 2521 (2001)
27 Y. Matsuo, H. Sasaki, J. Am. Ceram. Soc. **49**, 229 (1966)
28 S.R. Dhage, Y.B. Khollam, H.S. Potdar, S.B. Deshpande, B.D. Sarwade, D.K. Date, Mater. Lett. **56**, 564 (2002)
29 S. Chattopadhyay, P. Ayyub, V.R. Palkar, M. Multani, Phys. Rev. B **52**, 13177 (1995)
30 M. Villegas, A.C. Caballero, M. Kosec, C. Moure, P. Duran, J.F. Fernandez, J. Mater. Res. **14**, 891 (1999)
31 A. Yamaji, Y. Enomoto, K. Kinoshita, T. Murakami, J. Am. Ceram. Soc. **60**, 97 (1977)
32 B.M. Jin, J. Kim, S.C. Kim, Appl. Phys. A **65**, 53 (1997)
33 W. Cao, C.A. Randall, J. Phys. Chem. Solids **57**, 1499 (1996)
34 S.L. Swartz, T.R. Shrout, W.A. Schulze, L.E. Cross, J. Am. Ceram. Soc. **67**, 311 (1984)

Available online at www.sciencedirect.com
ScienceDirect
Materials Chemistry and Physics 102 (2007) 165–170
MATERIALS CHEMISTRY AND PHYSICS
www.elsevier.com/locate/matchemphys

Dielectric properties of $(1-x)Pb(Zr_{0.52}Ti_{0.48})O_3$–$(x)BaTiO_3$ ceramics under uniaxial compressive pre-stress

Rattikorn Yimnirun*, Supon Ananta, Sawarin Chamunglap

Department of Physics, Faculty of Science, Chiang Mai University, Chiang Mai 50200, Thailand

Received 30 May 2005; received in revised form 26 August 2006; accepted 29 November 2006

Abstract

Effects of uniaxial compressive pre-stress on the dielectric properties of ceramics in PZT–BT solid-solution system are investigated. The physical properties measurements reveal that the addition of BT into PZT results in the increase of grain size and microstructural heterogeneity, except for the density which sees the opposite trend. The dielectric properties measured under stress-free condition show a gradual increase of the dielectric constant with increasing BT content, while the dielectric loss tangent is not considerably different. The dielectric properties under the uniaxial compressive pre-stress of the PZT–BT ceramics are observed at stress levels up to 15 MPa using a uniaxial compressometer. The results clearly show that both the dielectric constant and the dielectric loss tangent of the PZT–BT ceramics increase significantly with increasing applied stress. Larger changes in the dielectric properties with the applied stress are observed in the PZT-rich compositions. The experimental observations have been attributed to the increase of the domain wall motions from the application of the compressive pre-stress.

Keywords: Uniaxial stress; Dielectric properties; PZT–BT

1. Introduction

Along with nanotechnology, smart materials and systems have recently been identified as the next generation technology [1–3]. Among many smart systems, piezoelectric ceramic actuators and transducers are finding an increasingly wide range of applications. In most applications, ceramics are often subjected to mechanical loading, either deliberately in the design of the device itself or because the device is used to change shapes as in many smart structure applications or the device is used under environmental stresses. In some cases, due to the piezoelectric nature of a material used within, the devices are also subjected to the self-induced internal stress [2–4]. A prior knowledge of how the materials behave under different load conditions is therefore very crucial for proper design of a device and for suitable selection of materials for a specific application. Therefore, it is very important to determine the properties of these materials as a function of applied stress. Previous investigations on the stress-dependence dielectric and electrical properties of many ceramic systems, such as PZT, PMN–PZT and PMN–PT have clearly emphasized the importance of the subject [4–11].

Among perovskite ferroelectric materials, lead zirconate titanate ($Pb(Zr_{1-x}Ti_x)O_3$ or PZT) and barium titanate ($BaTiO_3$ or BT) ceramics have been investigated extensively and continuously since the late 1940s [12–15]. PZT and BT are representative perovskite piezoelectric and ferroelectric prototypes, respectively, because of their excellent electrical properties. These two ceramics possess distinct characteristics that make each ceramic suitable for different applications. One of the most studied piezoelectric compounds, $Pb(Zr_{0.52}Ti_{0.48})O_3$, a morphotropic phase boundary (MPB) compound of PZT, has great piezoelectric properties with a high Curie temperature (T_C) of ~390 °C. BT exhibits high dielectric constant and superior electrostrictive responses with a lower T_C (~120 °C) [12–15]. In addition, BT is mechanically superior than PZT [16], whereas PZT ceramics can be easily sintered at temperature much lower than BT ceramics, which usually require as high sintering temperature as 1400 °C [16]. With their complementary features, the solid solutions between PZT and BT are expected to exhibit better properties than those of the single-phase PZT and BT [12–15]. Furthermore, the properties can also be tailored over a wider range by changing the compositions to meet the strict

* Corresponding author. Tel.: +66 53943367; fax: +66 53943445.
E-mail address: rattikornyimnirun@yahoo.com (R. Yimnirun).

0254-0584/$ – see front matter © 2006 Elsevier B.V. All rights reserved.
doi:10.1016/j.matchemphys.2006.11.021

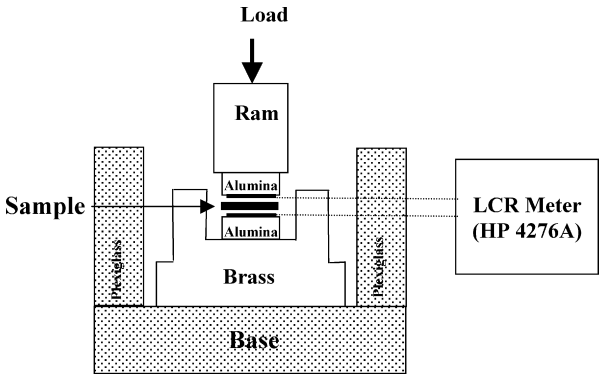

Fig. 1. A schematic of the experimental set-up.

requirements for specific applications [3,12–15]. Prior investigations have already revealed interesting results on the structure, and the dielectric and ferroelectric properties of the PZT–BT solid solutions [16–18]. However, there has been no report on the influences of the applied stress on the electrical properties of the PZT–BT systems. Therefore, this study is undertaken to investigate the influences of the uniaxial compressive pre-stress on the dielectric properties of $(1-x)$PZT–xBT ceramic systems.

2. Experimental

The $(1-x)Pb(Zr_{0.52}Ti_{0.48})O_3$–$(x)BaTiO_3$ ceramic systems used in this study are prepared from the PZT and BT starting powders by a mixed-oxide method. The precursor PZT and BT powders are first prepared from reagent-grade PbO (99%), ZrO_2 (99%) and TiO_2 (99%), and $BaCO_3$ (99%) and TiO_2 (99%) starting powders, respectively. These powders are ball-milled for 24 h and later calcined for 2 h at 900 °C for PZT and at 1300 °C for BT. Subsequently, the $(1-x)Pb(Zr_{0.52}Ti_{0.48})O_3$–$(x)BaTiO_3$ (when $x = 0.0, 0.05, 0.15, 0.25, 0.35, 0.45, 0.55, 0.65, 0.75, 0.85, 0.95$ and 1.0) ceramics are prepared from the starting PZT and BT powders by a mixed-oxide method at various processing conditions. Initially, the PZT and BT powders for a given composition are weighed and then ball-milled in ethanol for 24 h. After drying process, the mixed powders are pressed hydraulically to form disc-shaped pellets 10 mm in diameter and 2 mm thick, with 5 wt.% polyvinyl alcohol (PVA) as a binder. The pellets are stacked in a covered alumina crucible filled with PZ powders to prevent lead loss. Finally, the sintering is carried out at a sintering temperature for 2 h with 5 min °C^{-1} heating and cooling rates. The firing profile includes a 1-h dwell time at 500 °C for binder burnout process to complete. For optimization purpose, the sintering temperature is varied between 1050 and 1400 °C depending upon the compositions. The densities of the sintered ceramics are measured by Archimedes method. The phase formations of the sintered specimens are studied by an X-ray diffractometer (Philips Analytical). The microstructure analyses are undertaken by a scanning electron microscopy (SEM: JEOL Model JSM 840A). Grain size is determined from SEM micrographs by a linear intercept method. The detailed descriptions of powders and ceramics processing and characterizations are presented thoroughly in the earlier publication [16].

For dielectric property characterizations under a uniaxial compressive pre-stress, the sintered samples are lapped to obtain parallel faces disc-shaped specimens with diameter of 10 mm and thickness of 2 mm, and the faces are then coated with silver paint as electrodes. The samples are then heat-treated at 750 °C for 12 min to ensure the contact between the electrodes and the ceramic surfaces. The samples are subsequently poled in a silicone oil bath at a temperature of 120 °C by applying a dc field of 20 kV cm^{-1} for 30 min. To study the effects of the uniaxial compressive pre-stress on the dielectric properties, the uniaxial compressometer is constructed [10,11]. As shown in Fig. 1, the compressometer is developed for simultaneous applications of the mechanical stress and the electric field. The compressometer cell consisting of a cylindrical brass cell with a heavy brass base, a brass ram and a precisely guided loading platform provides true uniaxial stress during mechanical loading. The prepared specimen is carefully placed between the two alumina blocks and the electric field is applied to the specimen via the copper shims attached to the alumina blocks. With this setting, the uniaxial compressive stress is applied parallel to the electric field direction. The uniaxial compressive stress is supplied by the servohydraulic load frame and the applied stress level is monitored with the pressure gage of the load frame. Measurements are performed as a function of mechanical pre-stress applied discretely between 0 and 15 MPa. The measurements are carried out on the samples for loading and unloading conditions. Each measurement is repeated two to three times to ensure the reliability of the experimental results. During the measurements, a desired pre-stress is first applied to the sample and the dielectric properties are then recorded. The dielectric properties are measured through the LCZ-meter (Hewlett Packard, model 4276A). The capacitance and the dielectric loss tangent are determined at frequency of 1 kHz and room temperature (25 °C). The dielectric constant is then calculated from a parallel-plate capacitor equation, e.g. $\varepsilon_r = Cd/\varepsilon_0 A$, where C is the capacitance of the sample, d and A the thickness and the area of the electrode, respectively, and ε_0 is the dielectric permittivity of vacuum (8.854×10^{-12} F m^{-1}).

3. Experimental results

The phase formation behavior of the sintered ceramics is revealed by an XRD method. The XRD patterns, shown in Fig. 2, show that the sintered ceramics are clearly in perovskite phase. From the XRD patterns, PZT and BT ceramics are both identified as a single-phase material with a perovskite structure having tetragonal symmetry [16]. The patterns can be matched with JCPDF files no 33-0784 and 79-2264 for PZT and BT, respectively. For other PZT–BT compositions, the diffraction peaks move gradually towards higher angles with increasing BT contents, indication of smaller cell parameters. It should also be noticed that compositions with $0.45 \leq x \leq 0.75$ exhibit evidence of a possible rhombohedral structure with no clear splitting of peaks around 2θ of 43–46°. However, it is still clearly seen from the XRD patterns that PZT–BT forms a series of continuous solid solutions [16].

The optimized density of sintered $(1-x)$PZT–xBT ceramics is listed in Table 1. It is observed that an addition of BT to the PZT–BT compositions results in a continual decrease in the density of the ceramics from, in the units of gram per centimeter

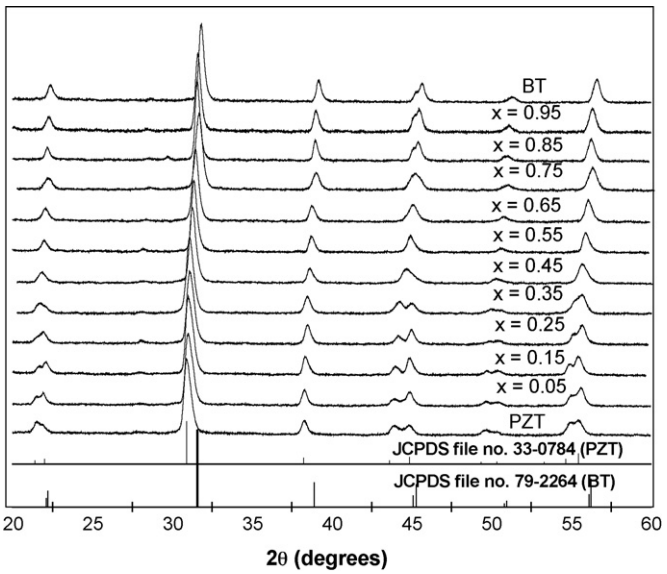

Fig. 2. XRD diffraction patterns of the sintered $(1-x)$PZT–(x)BT ceramics.

Table 1
Microstructural and dielectric features of $(1-x)$PZT–xBT ceramics

Ceramic	Density (g cm^{-3})	Grain size range (μm)	Average grain size (μm)	Stress-free ε_r (25 °C/1 kHz)	Stress-free tan δ (25 °C/1 kHz)
PZT	7.75	1–5	1.89 ± 0.52	813	0.011
0.95PZT–0.05BT	7.67	1–4	1.66 ± 0.32	809	0.007
0.85PZT–0.15BT	7.42	1–5	2.40 ± 0.58	839	0.006
0.75PZT–0.25BT	7.30	1–3	1.91 ± 0.47	857	0.004
0.65PZT–0.35BT	6.99	1–4	2.36 ± 0.71	875	0.005
0.55PZT–0.45BT	6.78	1–6	2.93 ± 0.53	890	0.006
0.45PZT–0.55BT	6.63	1–7	3.17 ± 0.72	952	0.005
0.35PZT–0.65BT	6.38	1–10	4.42 ± 0.79	1060	0.007
0.25PZT–0.75BT	6.28	1–10	3.28 ± 0.53	1077	0.005
0.15PZT–0.85BT	6.07	1.5–9	3.52 ± 0.77	1223	0.004
0.05PZT–0.95BT	5.95	2–10	4.86 ± 0.88	1288	0.005
BT	5.35	7–12	10.82 ± 0.53	1429	0.004

cube, 7.75 for PZT to 5.35 for BT. This is clearly due to the fact that BT has lower density than PZT. Except for BT which has a density of 89% of the theoretical density, all other ceramics are well sintered with high density (as high as 96% of the theoretical density in PZT ceramic). Relatively low density observed in BT ceramic is a result of porous and non-uniform microstructure, as seen from SEM micrograph in Fig. 3(f). For BT-rich compositions, SEM micrographs also show porous microstructure which

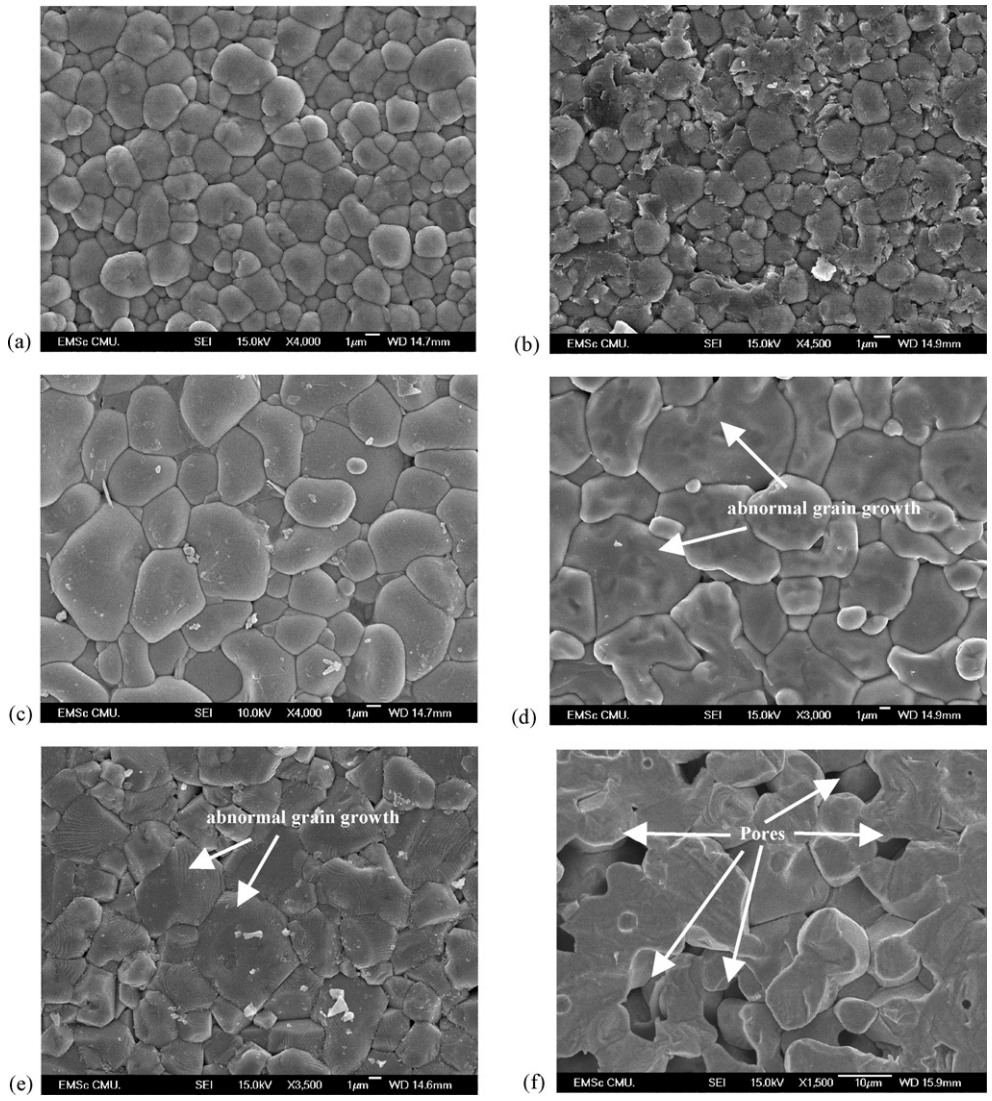

Fig. 3. SEM micrographs of $(1-x)$PZT–xBT ceramics: (a) PZT; (b) 0.75PZT–0.25BT; (c) 0.55PZT–0.45BT; (d) 0.35PZT–0.65BT; (e) 0.15PZT–0.85BT; (f) BT.

could be attributed to PbO loss during high sintering temperatures required for these compositions. In addition, an abnormal grain growth observed in the BT-rich compositions is probably due to the fact that the sintering temperatures required for highest densification for PZT and BT ceramics are very different, which could lead to distinctive grain growth behaviors between two phases [16]. Hence, the heterogeneous microstructure with a large grain size range is observed for BT-rich ceramic compositions, as seen in Fig. 3(d and e) and as listed in Table 1. On the other hand, PZT-rich compositions exhibit more uniform microstructure with the average grain size in the range of 1–3 μm. Moreover, the average grain size of the whole compositional range increases significantly from <2 μm in PZT to >10 μm in BT, as tabulated in Table 1.

The room temperature dielectric properties measured under stress-free condition are also listed in Table 1. It is clearly seen that dielectric constant (ε_r) of $(1-x)$PZT–xBT ceramics increases with increasing BT content. The dielectric constant increases from 813 in PZT to 1429 in BT. The increase of the dielectric constant within the compositional range is due to the high dielectric constant of BT [12–15]. When compared to PZT, higher dielectric constant observed in BT at room temperature is a result of its two ferroelectric transition temperatures at 0 and 120 °C [13–15]. However, the stress-free dielectric loss tangent ($\tan\delta$) does not change significantly with compositions. The relatively higher value of dielectric loss tangent of 0.011 for PZT is probably due to more domain wall motions expected in piezoelectric PZT as compared to piezoelectrically less active BT [6,19,20]. Similar dielectric behaviors have been reported in other solid-solution systems, such as PZN–BT [21], PMN–PZT [22] and PNN–PZT [23].

The experimental results of the uniaxial compressive pre-stress dependence of the dielectric properties of the ceramics in PZT–BT system are shown in Figs. 4 and 5. There is a significant change of both the dielectric constant and the dielectric loss tangent of the ceramics when the applied stress increases from 0 to 15 MPa. The changes of the dielectric constant with the applied stress can be divided into three different groups.

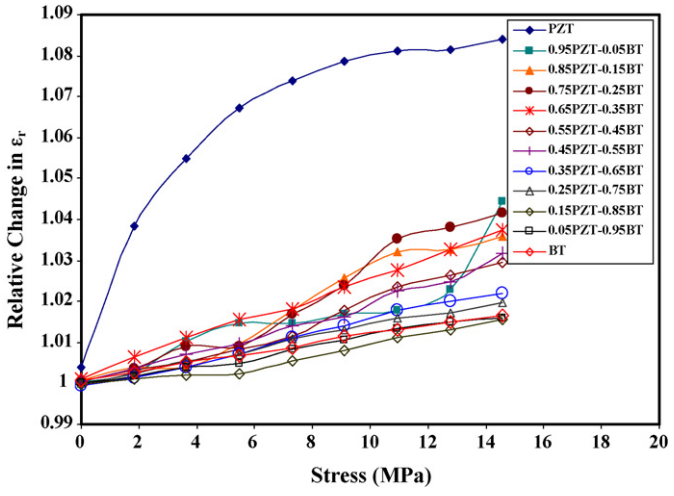

Fig. 4. Relative changes of dielectric constant (ε_r) as a function of compressive pre-stress for $(1-x)$PZT–(x)BT ceramics.

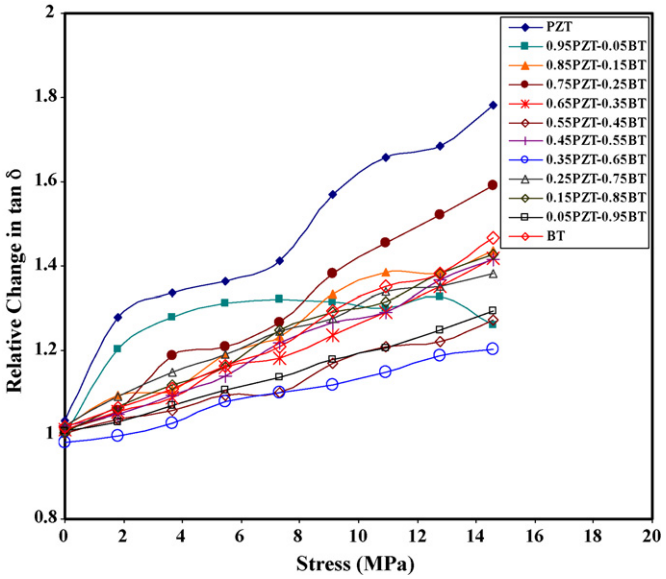

Fig. 5. Relative changes of dielectric loss tangent ($\tan\delta$) as a function of compressive pre-stress for $(1-x)$PZT–(x)BT ceramics.

For PZT ceramic, the dielectric constant increases exponentially with applied stress. It can be seen that dielectric constant is enhanced by approximately 8% at 15 MPa applied stress. For PZT-rich compositions (0.95PZT–0.05BT, 0.85PZT–0.15BT, 0.75PZT–0.25BT, 0.65PZT–0.35BT and 0.55PZT–0.45BT), the dielectric constant increases rather linearly with increasing applied stress. The changes in the dielectric constant between 2 and 4% at 15 MPa applied stress are obviously smaller than that observed in PZT. For BT-rich compositions (BT, 0.05PZT–0.95BT, 0.15PZT–0.85BT, 0.25PZT–0.75BT and 0.35PZT–0.65BT), the dielectric constant only rises slightly (<2%) and in a linear manner when the applied stress increases to the maximum amplitude. The dielectric loss tangent for all compositions is found to increase significantly and non-linearly when the applied stress is raised from 0 to 15 MPa. The largest changes occur in PZT and 0.75PZT–0.25BT with the dielectric loss tangent enhancement of nearly 80 and 50%, respectively. For other compositions, the increase in the dielectric loss tangent varies between 10 and 40% at 15 MPa applied stress. Again the changes of the dielectric loss tangent of BT-rich compositions are comparatively smaller than those of PZT-rich compositions, similar to what have been observed in the case of the dielectric constant. Similar experimental results have been reported previously for soft PZT [9,24], un-doped PZT with various Zr/Ti ratio [25], and Ca-doped BT [26], in which the dielectric properties are found to increase with increasing magnitude of the compressive pre-stress.

To understand these experimental results, various effects have to be considered. Normally, the properties of ferroelectric materials are derived from both the intrinsic contribution, which is the response from a single domain, and extrinsic contributions, which are from domain wall motions [19,25–27]. When a mechanical stress is applied to a ferroelectric material, the domain structure in the material will change to maintain the domain energy at a minimum; during this process, some of

the domains engulf other domains or change shape irreversibly. Under a uniaxial stress, the domain structure of ferroelectric ceramics may undergo domain switching, clamping of domain walls, de-aging and de-poling [20,27]. In this study, the results on the uniaxial compressive pre-stress dependence of the dielectric properties can easily be explained with the above statements. When the compressive uniaxial stress is applied in the direction parallel to the polar axis (poling) direction, the stress will move some of the polarization away from the poling direction resulting in a change in domain structures [6,25–27]. This change increases the non-180° domain wall density. Hence, the increase of the dielectric constant with the applied stress is observed. The de-aging mechanism is also expected to play a role here. However, the stress clamping of domain walls and the de-poling mechanisms are not expected at this relatively low stress level used in this study [6,27]. Therefore, a combination of the domain switching and the de-aging mechanisms is believed to be a reason for the increase of the dielectric constant with increasing applied stress in the PZT–BT system, as shown in Fig. 4. The cause of the stress dependence of the dielectric loss tangent is a little more straightforward than that of the dielectric constant. Stress-induced de-pinning of the domain walls is expected to occur under the applied compressive pre-stress. As depicted in Fig. 5, an increase in domain wall mobility clearly enhances the dielectric loss tangent in all compositions [19,20,27]. Additionally, it should also be noticed that pure PZT obtained from this study has a tetragonal structure and is supposed to be hard to switch its polarization. In comparison, as described earlier the compositions $x = 0.45$ and 0.75 seem to be MPB compositions between tetragonal and rhombohedral PZT phases, thus high response to external stress is expected in these two compositions. However, the experimental results did not show the high dielectric response to stress, as seen in Figs. 4 and 5. This interesting observation could be explained as follows. Since the two compositions are seen to exhibit the co-existence of both tetragonal and rhombohedral PZT phases, one would expect to observe enhanced properties, as observed in PZT [3,15]. However, the dielectric properties observed in this PZT–BT system are not seen to enhance at the two MPB compositions, as listed in Table 1. This is probably because the dielectric properties are not entirely controlled by the chemical composition, but also dictated by other factors, such as microstructure and chemical homogeneity [14,15]. Since BT requires significantly higher sintering temperature than does PZT, very different microstructures are observed in pure PZT and PZT–BT compositions, as evident from grain size variation listed Table 1, and abnormal grain-growth behavior and porous microstructure displayed in Fig. 3. These features clearly suppress the dielectric properties of the MPB compositions [28,29]. This observation also suggests that the dielectric responses to the external stress are not controlled exclusively by the intrinsic contribution from single domain, but the main contribution may arise from the extrinsic contributions from domain wall motions, which could be heavily clamped by inhomogeneous microstructures [19,27]. Therefore, this explains relatively low dielectric responses to the stress in the two MPB compositions. Similar observations have been reported in the MPB compositions in PZT–PMN [30,31] and PMN–PT [32]. Finally, it should be noted here that the dielectric behaviors under the applied stress for PZT–BT system are significantly different from those observed in a solid solution between normal and relaxor ferroelectrics, i.e. PZT–PMN systems, in which the dielectric responses to the applied stress depend more on the compositions and the stress level, and the dielectric properties of some compositions decrease with increasing applied stress [10].

4. Conclusions

In this study, effects of uniaxial compressive pre-stress on the dielectric properties of ceramics in PZT–BT system are investigated. The $(1-x)Pb(Zr_{0.52}Ti_{0.48})O_3$–$(x)BaTiO_3$ (when $x = 0.0$, 0.05, 0.15, 0.25, 0.35, 0.45, 0.55, 0.65, 0.75, 0.85, 0.95 and 1.0) ceramics used are prepared by a conventional mixed-oxide method from starting PZT and BT powders at various processing conditions. The phase formation behavior studied using the XRD indicates that PZT–BT forms a series of continuous solid solutions. The physical properties measurements reveal that the properties are relatively composition-dependent. Except for the density which sees the opposite trend, the addition of BT into PZT results in the increase of grain size and microstructural heterogeneity. The dielectric properties measured under stress-free conditions show a gradual increase of the dielectric constant with increasing BT content, while the dielectric loss tangent is not significantly different. The dielectric properties under the uniaxial compressive pre-stress of the PZT–BT ceramics are observed at stress levels up to 15 MPa using a uniaxial compressometer. The results clearly show that both the dielectric constant and the dielectric loss tangent of the PZT–BT ceramics increase significantly with increasing applied stress. Larger changes in the dielectric properties with the applied stress are observed in the PZT-rich compositions. The experimental observations have been attributed to the increase of the domain wall motions from the application of the compressive pre-stress.

Acknowledgment

Financial support from the Thailand Research Fund (TRF) is gratefully acknowledged.

References

[1] N. Setter, R. Waser, Acta Mater. 48 (2000) 151.
[2] N. Setter, J. Eur. Ceram. Soc. 21 (2001) 1279.
[3] L.E. Cross, Ferroelectrics 76 (1987) 241.
[4] D. Viehland, J. Powers, J. Appl. Phys. 89 (2001) 1820.
[5] J. Zhao, A.E. Glazounov, Q.M. Zhang, Appl. Phys. Lett. 74 (1999) 436.
[6] Q.M. Zhang, J. Zhao, K. Uchino, J. Zheng, J. Mater. Res. 12 (1997) 226.
[7] D. Viehland, J. Powers, Appl. Phys. Lett. 78 (2001) 3112.
[8] D. Viehland, J.F. Li, E. McLaughlin, J. Powers, R. Janus, H. Robinson, J. Appl. Phys. 95 (2004) 1969.
[9] D. Zhou, M. Kamlah, D. Munz, J. Eur. Ceram. Soc. 25 (2005) 425.
[10] R. Yimnirun, S. Ananta, E. Meechoowas, S. Wongsaenmai, J. Phys. D: Appl. Phys. 36 (2003) 1615.
[11] R. Yimnirun, S. Ananta, A. Ngnamjarurojana, S. Wongsaenmai, Appl. Phys. A 81 (2005) 1227.
[12] G.H. Haertling, J. Am. Ceram. Soc. 82 (1999) 797.

[13] L.E. Cross, Mater. Chem. Phys. 43 (1996) 108.
[14] A.J. Moulson, J.M. Herbert, Electroceramics: Materials, Properties, Applications, second ed., John Wiley & Sons Ltd., 2003.
[15] B. Jaffe, W.R. Cook, Piezoelectric Ceramics, R.A.N. Publishers, 1971.
[16] W. Chaisan, R. Yimnirun, S. Ananta, D.P. Cann, Mater. Lett. 59 (2005) 3732.
[17] B.K. Gan, J.M. Xue, D.M. Wan, J. Wang, Appl. Phys. A 69 (1999) 433.
[18] F. Xia, X. Yao, J. Mater. Sci. 34 (1999) 3341.
[19] G. Yang, W. Ren, S.F. Liu, A.J. Masys, B.K. Mukherjee, Proc. IEEE Ultrason. Symp. (2000) 1005.
[20] O. Steiner, A.K. Tagantsev, E.L. Colla, N. Setter, J. Eur. Ceram. Soc. 19 (1999) 1243.
[21] A. Halliya, U. Kumar, R.E. Newnham, L.E. Cross, Am. Ceram. Soc. Bull. 68 (1987) 671.
[22] R. Yimnirun, S. Ananta, P. Laoratanakul, J. Eur. Ceram. Soc. 25 (2005) 3225.
[23] N. Vittayakorn, G. Rujijanagul, X. Tan, M.A. Marquadrt, D.P. Cann, J. Appl. Phys. 96 (2004) 5103.
[24] J.M. Calderon-Moreno, Mater. Sci. Eng. A 315 (2004) 227.
[25] D. Audigier, Cl. Richard, Cl. Descamps, M. Troccaz, L. Eyraud, Ferroelectrics 154 (1994) 219.
[26] I.J. Fritz, J. Appl. Phys. 49 (1978) 4922.
[27] G. Yang, S.F. Liu, W. Ren, B.K. Mukherjee, Proc. SPIE Symp. Smart Struct. Mater. 3992 (2000) 103.
[28] W. Chaisan, R. Yimnirun, S. Ananta, D.P. Cann, Mater. Sci. Eng. B 132 (2006) 300.
[29] S. Wongsaenmai, Y. Laosiritaworn, S. Ananta, R. Yimnirun, Mater. Sci. Eng. B 128 (2006) 83.
[30] R. Yimnirun, S. Ananta, A. Ngamjarurojana, S. Wongsaenmai, Curr. Appl. Phys. 6 (2006) 520.
[31] R. Yimnirun, Ferroelectrics 331 (2006) 9.
[32] R. Yimnirun, M. Unruan, Y. Laosiritaworn, S. Ananta, J. Phys D: Appl. Phys. 39 (2006) 3097.

Temperature scaling of dynamic hysteresis in soft lead zirconate titanate bulk ceramic

R. Yimnirun,[a] R. Wongmaneerung, S. Wongsaenmai, A. Ngamjarurojana, S. Ananta, and Y. Laosiritaworn
Department of Physics, Faculty of Science, Chiang Mai University, Chiang Mai 50200, Thailand

(Received 15 November 2006; accepted 8 February 2007; published online 13 March 2007)

The temperature scaling of the dynamic hysteresis was investigated in soft ferroelectric bulk ceramic. The power-law temperature scaling relations were obtained for hystersis area $\langle A\rangle$ and remnant polarization P_r, while the coercivity E_C was found to scale linearly with temperature T. The three temperature scaling relations were also field dependent. At fixed field amplitude E_0, the scaling relations take the forms of $\langle A\rangle \propto T^{-1.1024}$, $P_r \propto T^{-1.2322}$, and $(E_{C0}-E_C)\propto T$. Furthermore, the product of P_r and E_C also provides the same scaling law on the T dependence in comparison with $\langle A\rangle$.
 [DOI: 10.1063/1.2713336]

Soft lead zirconate titanate [$Pb(Zr_{1-x}Ti_x)O_3$ or PZT] ceramics have been employed extensively in sensors and actuators. In these applications, the dynamic hysteresis characteristics have become an important consideration.[1] Theoretical studies have been carried out to understand the dynamic response of hysteresis curves in spin and polarization systems.[2–5] In particular, attention is focused on scaling law $\langle A\rangle \propto f^m E_0^n$ (where $\langle A\rangle$ is hysteresis area, E_0 is field amplitude, f is frequency, and m and n are exponents that depend on the dimensionality and symmetry of the system). Experimental investigations on a few thin-film systems have also been reported.[6–12] Recently, the scaling relation for soft PZT bulk ceramic was reported in the form of $\langle A\rangle \propto f^{-0.25}E_0$.[13] We also reported the stress-dependent scaling relation in the form of $\langle A-A_{\sigma=0}\rangle \propto f^{-0.25}E_0\sigma^{0.44}$, which indicates the difference of the energy dissipation between the under stress and stress-free conditions.[14] More importantly, it is well known that the size and shape of the hysteresis loop in the ferroelectric state depend strongly on temperature T.[1,15] The temperature dependence of ferroelectric properties is of interest in view not only of technological applications, but also in a fundamental sense.[16–22] The theoretical investigation by Rao *et al.*[2] has already proposed a temperature scaling for ferromagnetic materials, which indicates that the hysteresis area decreases with increasing temperature. Experimental results on ferromagnetic thin films have revealed various temperature scaling relations.[2,3,6,8] Interestingly, there has been no report on the temperature scaling of dynamic hysteresis in ferroelectrics, both theoretically and experimentally. It is therefore the aim of this study to experimentally establish the temperature scaling of the ferroelectric hysteresis for soft PZT bulk ceramic.

The polarization–electric field (P-E) hysteresis loops of commercial soft PZT ceramic disks (APC-855, APC International, Ltd., USA) with diameter of 8 mm and thickness of 1 mm were obtained by a standardized ferroelectric testing unit, RT66A (Radiant Technologies Inc., NM), over the temperature range 298–453 K with E_0 up to 40 kV/cm (f was fixed at 4 Hz). The measurements were performed on three ceramic disks. The Curie temperature (T_C) of the soft PZT used was experimentally determined from dielectric measurement to be 523 K. Other basic properties provided by the supplier are dielectric constant (1 kHz) $\varepsilon_r=3400$, piezoelectric strain constants $d_{33}=600$ pm/V and $d_{31}=-276$ pm/V, planar coupling factor $k_p=0.68$, and mechanical quality factor $Q_m=65$. It should also be noted that after being subjected to the hysteresis measurements, the samples showed a reduction of 10% in ε_r value and of 30% in d_{33} value.

Figure 1 displays the hysteresis loop profile for various electric field amplitudes E_0 at a fixed $T=373$ K [Fig. 1(a)] and for various temperatures at a fixed $E_0=40$ kV/cm [Fig. 1(b)]. From the P-E loops, it is obvious that both E_0 and T play a crucial role on the hysteresis area $\langle A\rangle$. Similar observations have been reported in many other ferroelectric systems.[12,18,20,22] More interestingly, the observed temperature dependence of these hysteresis parameters prompts a question of whether there exist temperature scaling relations for these parameters.

Figure 2 shows the relation between $\langle A\rangle$ and T in a double logarithmic form, where good linear fits are apparent (R^2 close to 1). This implies a power-law relation between the hysteresis area and temperature, i.e., $\langle A\rangle \propto T^{\gamma}$, and for each E_0, the exponent γ can be extracted from the slope, i.e., $\gamma = d\ln\langle A\rangle / d\ln T$. However, both the slope γ and the y intercept seem to vary with E_0. Thus, to prove this E_0 dependence, both the slope γ and the y intercept are plotted as a function of E_0 (insets in Fig. 2), and the linear dependences on E_0 are noticeable. The linear least square fits of both slopes and y intercepts with E_0 give $y=-0.0332x-1.1024$ with $R^2=0.9983$ for the slope (lower inset) and $y=0.0769x+6.0137$ with $R^2=0.9966$ for the y intercept (upper inset). However, the y intercept refers to the value of $\ln\langle A\rangle$ at the limit $\ln T$ approaching zero, and from the fitting, $\ln\langle A\rangle$ is not ceased at this limit, which is not really sound because at low temperatures the dynamics of the dipoles or domain walls is frozen. This could be due to the fact that the domain wall motion at high temperature is very different from those at very low temperature.[23,24] Consequently, this study does not imply if there is a finite hysteresis area at T approaching zero (i.e., in this case $\ln T=0$ or $T=1$), but the quantity $\ln\langle A\rangle$ at $\ln T=0$ here comes from an empirical fit to fulfill the validity of the linear fit. Therefore, based on the proposed assump-

[a]Author to whom correspondence should be addressed; electronic mail: rattikornyimnirun@yahoo.com

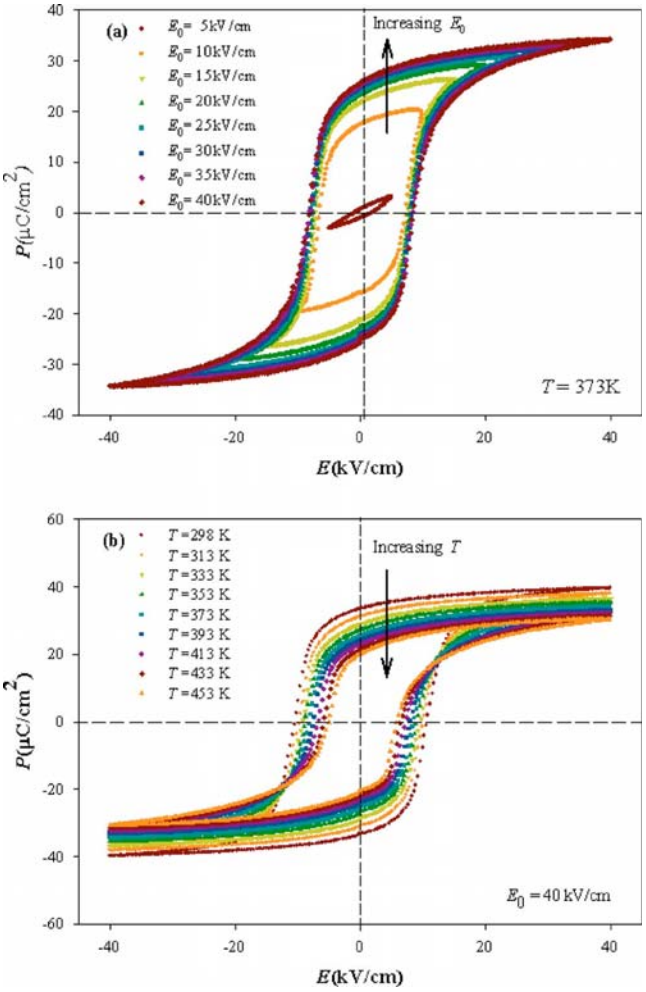

FIG. 1. Hysteresis loops for soft PZT ceramic (a) at T=373 K with varying E_0, and (b) at E_0=40 kV/cm with varying T.

tions and fitting techniques, and by integrating all the relevant fits, it is found that

$$\langle A\rangle = \exp(0.0769E_0 + 6.0137)T^{-(0.0332E_0+1.1024)}. \quad (1)$$

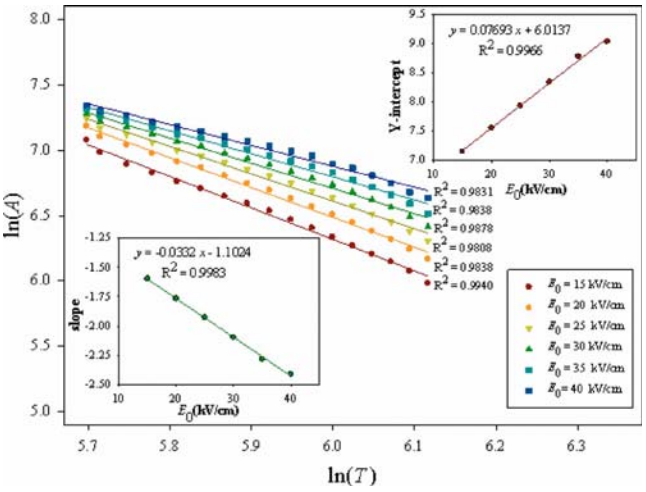

FIG. 2. Double logarithmic plot between ln(A) and ln(T) for various E_0, where the linear relations are found but the y intercepts and slopes seem to be E_0 dependent. The insets show those linear relations with E_0.

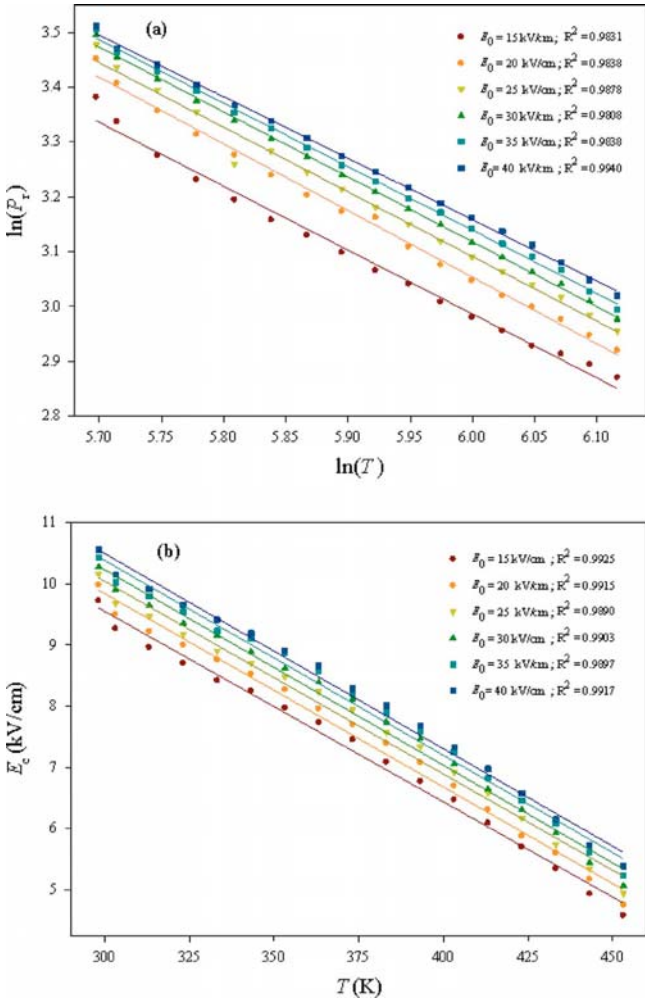

FIG. 3. (a) Double logarithmic plot between ln(P_r) and ln(T), and (b) linear plot between E_C and T.

Through similar mathematical treatment performed on $\langle A\rangle$, temperature-dependent relations for remnant polarization (P_r) and coercivity (E_C) are also obtained. Figure 3(a) shows the relation between P_r and T in a double logarithmic plot. As being evident, the power-law relation seems suitable for the fit since good R^2 are attained. It is found that

$$P_r = \exp(-0.0068E_0 + 10.305)T^{(0.0022E_0-1.2322)}. \quad (2)$$

The relation between E_C and T is shown in Fig. 3(b). Surprisingly, linear relations are apparent so an approximation on $y=ax+b$ could be used to fit the data. Nonlinear fits between E_C and T are also performed (not shown) and the linear dependence of E_C and T is confirmed. Therefore, it could be estimated that

$$E_C = (-0.000\,03E_0 - 0.030\,85)T + (0.0459E_0 + 18.319). \quad (3)$$

The temperature dependences of $\langle A\rangle$, P_r, and E_C shown in Eqs. (1)–(3) are also slightly E_0 dependent. Obviously, small coefficients to E_0 (for the whole range of E_0 used in this study) suggests that at fixed E_0

$$\langle A\rangle \propto T^{-1.1024}, \quad (4)$$

$$P_r \propto T^{-1.2322}, \quad (5)$$

$$(E_{C0} - E_C) \propto T. \tag{6}$$

E_{C0} in Eq. (6) can be viewed as the coercivity at $T \sim 0$ K. However, as $T \rightarrow 0$, thermal energy is low, causing a nonsymmetric hysteresis loop; hence, E_{C0} cannot be meaningfully defined. Here E_{C0} is used for proposing the fit, which is valid for the experimental range in this study.

More importantly, Eqs. (4)–(6) present simple relations for the temperature scaling of ferroelectric hysteresis parameters. It should be noted that there have only been few theoretical treatments to include a temperature term in the dynamic hysteresis scaling of ferromagnetics.[2,3,25] Considering relatively successful applications of the treatments to E- and f-dependent ferroelectric hysteresis,[2–5] it would be worthwhile to compare our experimental results with the theoretically derived scaling. Theoretical scaling relations have been proposed as $\langle A \rangle \propto T^{-\gamma}$, with γ being 0.7, 1.18, and 1.98 for continuum three-dimensional (3D) $((\Phi^2)^2$, two-dimensional, and 3D Ising models, respectively.[2,3,25] An explanation for the variation may come from the different polarization-interaction terms as considered in these models. It could be seen that our experimentally obtained temperature scaling of $\langle A \rangle$ (with $\gamma \sim 1.1$) falls between the values obtained from the models. The difference could be attributed to additional contributions from depolarizing effects within the ceramics (arisen from domain walls, grain boundaries, space charges, immobile defects, etc.),[13,14] as compared to physically oversimplified polarization interaction proposed in the theoretical models.[2,3,25]

Furthermore, the relation $E_C \propto (T - T_C)^{-0.35}$ drawn from the 3D $((\Phi^2)^2$ model[2] is significantly different from the linear relation obtained from our study, which further clarifies that the theoretical models cannot be applied to ferroelectric bulk ceramics. This study clearly serves as a survey to show that more improvement of the theoretical approach is needed to predict the scaling behavior in bulk ferroelectric ceramics. Interestingly, different forms of temperature scaling of E_C extracted from the previous experimental data on PZT thin films also indicate dimensional dependence of the coercivity, as reported in previous investigations.[8,26,27]

In approaching the saturation, the hysteresis area can be roughly estimated with $(2P_r)(2E_C)$.[9,18] It is also interesting to check if the product of P_r and E_C would provide the same scaling law on the T dependence in comparison with $\langle A \rangle$. So, by substituting the E_0 dependence on both E_C and P_r [Eqs. (2) and (3)], it is found that

$$\begin{aligned}(2E_C)(2P_r) = 4[&(-0.000\,03E_0 - 0.030\,85)T + (0.0459E_0 \\ &+ 18.319)] \times [\exp(-0.0068E_0 \\ &+ 10.305)T^{(0.0022E_0 - 1.2322)}].\end{aligned} \tag{7}$$

Since all coefficients to E_0 are small, by taking an approximation that E_0 is fixed (or not very high), the $(2P_r) \times (2E_C)$ reduces to

$$(2E_C)(2P_r) \approx 4(9.2 \times 10^2 T^{-0.2322} + 5.5 \times 10^5 T^{-1.2322}). \tag{8}$$

As can be seen, the term $T^{-1.2322}$ strongly decays in temperature than the term $T^{-0.2322}$, but $T^{-1.2322}$ has a much larger coefficient. However, by substituting all temperatures used in this study, it is found that $T^{-1.2322}$ should be a principal term. Therefore, the scaling of "area" in this way on the temperature should have the exponent γ closer to -1.2322. In comparison with those extracted from the $\ln\langle A \rangle$ and $\ln T$ plot (in which the exponent γ has a value of -1.1024), these two scaling methods seem to agree. So once the scaling of area to the temperature is found, it is possible to guess how the E_C would scale with T if the scaling relation between P_r and T is known or vice versa. Similarly, a scaling of area to frequency has also been reported in a previous investigation.[28]

In summary, the power-law temperature scaling relations have been found for hystersis area $\langle A \rangle$ and remnant polarization P_r, while the coercivity E_C scales linearly with temperature. The three temperature scaling relations are also field dependent. At fixed E_0, the scaling relations take the forms of $\langle A \rangle \propto T^{-1.1024}$, $P_r \propto T^{-1.2322}$, and $(E_{C0} - E_C) \propto T$. Furthermore, the product of P_r and E_C also provides the same scaling law on the T dependence in comparison with $\langle A \rangle$.

Financial support from the Thailand Research Fund (TRF) and the Commission on Higher Education (CHE) are gratefully acknowledged.

[1] K. Uchino, *Ferroelectric Devices* (Dekker, New York, 2000).
[2] M. Rao, H. R. Krishnamurthy, and R. Pandit, Phys. Rev. B **42**, 856 (1990).
[3] M. Acharyya and B. K. Chakrabarti, Phys. Rev. B **52**, 6560 (1995).
[4] L.-F. Wang and J.-M. Liu, J. Appl. Phys. **98**, 064106 (2005).
[5] J.-M. Liu, H. L. W. Chan, C. L. Choy, and C. K. Ong, Phys. Rev. B **65**, 014416 (2001).
[6] Q. Jiang, H. N. Yang, and G. C. Wang, Phys. Rev. B **52**, 14911 (1995).
[7] Y.-H. Kim and J.-J. Kim, Phys. Rev. B **55**, R11933 (1997).
[8] J. S. Suen and J. L. Erskine, Phys. Rev. Lett. **78**, 3567 (1997).
[9] J.-M. Liu, H. P. Li, C. K. Ong, and L. C. Lim, J. Appl. Phys. **86**, 5198 (1999).
[10] B. Pan, H. Yu, D. Wu, X. H. Zhou, and J.-M. Liu, Appl. Phys. Lett. **83**, 1406 (2003).
[11] J.-H. Park, C.-S. Kim, B.-C. Choi, B. K. Moon, J. H. Jeong, and I. W. Kim, Appl. Phys. Lett. **83**, 536 (2003).
[12] J.-M. Liu, B. Pan, H. Yu, and S. T. Zhang, J. Phys.: Condens. Matter **16**, 1189 (2004).
[13] R. Yimnirun, Y. Laosiritaworn, S. Wongsaenmai, and S. Ananta, Appl. Phys. Lett. **89**, 162901 (2006).
[14] R. Yimnirun, S. Wongsaenmai, S. Ananta, and Y. Laosiritaworn, Appl. Phys. Lett. **89**, 242901 (2006).
[15] M. E. Lines and A. M. Glass, *Principles and Applications of Ferroelectrics and Related Materials* (Clarendon, Oxford, 1977).
[16] T. Mihara, H. Watanabe, and C. A. Araujo, Jpn. J. Appl. Phys., Part 1 **33**, 3996 (1994).
[17] Q. Tan, J. Li, and D. Viehland, Appl. Phys. Lett. **75**, 418 (1999).
[18] G. L. Yuan, J.-M. Liu, S. T. Zhang, D. Wu, Y. P. Wang, Z. G. Liu, H. L. W. Chan, and C. L. Choy, Appl. Phys. Lett. **84**, 954 (2004).
[19] B. S. Li, G. R. Li, Q. R. Yin, Z. G. Zhu, A. L. Ding, and W. W. Cao, J. Phys. D **38**, 1107 (2005).
[20] D. Lin, D. Xiao, J. Zhu, and P. Yu, Appl. Phys. Lett. **88**, 062901 (2006).
[21] W. Chang, A. H. King, and K. Bowman, Appl. Phys. Lett. **88**, 242901 (2006).
[22] S. K. Pandey, O. P. Thakur, A. Kumar, C. Prakash, R. Chatterjee, and T. C. Goel, J. Appl. Phys. **100**, 014104 (2006).
[23] A. Gruverman, O. Auciello, and H. Tokumoto, Annu. Rev. Mater. Sci. **28**, 101 (1998).
[24] K. Lee and S. Baik, Annu. Rev. Mater. Res. **36**, 81 (2006).
[25] M. Rao and R. Pandit, Phys. Rev. B **43**, 3373 (1991).
[26] O. Lohse, D. Bolten, S. Tiedke, T. Schneller, and R. Waser, Proceedings of the IEEE-ISAF 98 (IEEE, Piscataway, NJ, 1998), Vol. 1, p. 27.
[27] H. Maiwa and N. Ichinose, Ferroelectrics **293**, 89 (2003).
[28] J.-M. Liu, W. M. Wang, Z. G. Liu, H. L. Chan, and C. L. Choy, Appl. Phys. A: Mater. Sci. Process. **75**, 507 (2002).

Dynamic hysteresis and scaling behavior of hard lead zirconate titanate bulk ceramics

R. Yimnirun,[a] R. Wongmaneerung, S. Wongsaenmai, A. Ngamjarurojana, S. Ananta, and Y. Laosiritaworn
Department of Physics, Faculty of Science, Chiang Mai University, Chiang Mai 50200, Thailand

(Received 20 November 2006; accepted 9 February 2007; published online 14 March 2007)

The scaling relation of ferroelectric hysteresis area $\langle A \rangle$ against frequency f and field amplitude E_0 for the saturated loops of the hard lead zirconate titanate bulk ceramic takes the form of $\langle A \rangle \propto f^{-0.28} E_0^{0.89}$, while that for the minor loops takes the form of $\langle A \rangle \propto f^{-0.43} E_0^{3.19}$. In both cases, the scaling relations are similar to those of its soft counterpart. This indicates that the dynamic behaviors and scaling relations in bulk ceramics are mainly governed by the domain states and structures, while the distinct types of complex defects contribute mainly to the difference in the coercive field observed in hard and soft ceramics. © *2007 American Institute of Physics*.
[DOI: 10.1063/1.2713769]

Lead zirconate titanate [$Pb(Zr_{1-x}Ti_x)O_3$ or (PZT)] ceramics are among the lead-based complex perovskites that have been investigated extensively both from academic and commercial viewpoints with various applications.[1,2] However, PZT ceramics are usually modified with dopants.[3,4] Generally, donor (higher-valency) additives induce "soft" piezoelectric behaviors with higher dielectric and piezoelectric activities, while acceptor (lower-valency) additives result in "hard" piezoelectric behaviors.[1–4]

In many applications, the dynamic hysteresis, i.e., hysteresis area $\langle A \rangle$ as a function of the field amplitude E_0 and frequency f, has become an important consideration.[1–5] Hence, there have been reports on the scaling behavior of the dynamic hysteresis in ferromagnetic and ferroelectric thin films.[6–13] Many theoretical studies have been focused on the scaling law,

$$\langle A \rangle \propto f^{\alpha} E_0^{\beta} \tag{1}$$

(where α and β are exponents that depend on the dimensionality and symmetry of the system), of hysteresis curves in polarization systems.[6–8] Earlier investigations[6–8,13] have reported the scaling relations for the high-f region with α and β values, respectively, of −1 and 2 for $(\Phi^2)^2$ and $(\Phi^2)^3$ models and of −0.33 and 3 for a PZT thin film. We also reported the scaling relation for soft PZT bulk ceramics with α and β values, respectively, of −0.25 and 1 for saturated loops.[14] Interestingly, the scaling form for the minor loops is identical to that of the PZT thin film. The difference in the scaling relations has been attributed to the different domain dynamics.[14] Generally, the domain dynamics differs depending on the composition and the doping type.[15,16] In this point of view, the domain dynamics in hard and soft PZT ceramics, which contain distinct types of complex defects, should be very different.[16] Since our earlier work has already shown unique scaling relations for the soft PZT bulk ceramics,[14] it will be of interest to investigate the scaling behavior of the hard PZT bulk ceramic, as the direct comparison will help extracting roles of complex defects to the dynamic hysteresis behavior. Thus, we present in this letter the results on the scaling behaviors of the dynamic hysteresis of a hard PZT bulk ceramic. As will be seen, the dynamic hysteresis and scaling behaviors of the hard ceramic are surprisingly very similar to those of the soft one.

The dynamic hysteresis (P-E) loops of commercial hard PZT ceramic disks (APC-840, APC International, Ltd., USA) with a diameter of 8 mm and a thickness of 1 mm were characterized at room temperature (298 K) by using a modified Sawyer-Tower circuit with f covering from 1 to 100 Hz and E_0 from 0 to 40 kV/cm. The electric field was applied to a sample by a high voltage ac amplifier (Trek 610D) with the input sinusoidal signal from a function generator (HP 3310A). The P-E loops were recorded by a digital oscilloscope (HP 54645A, 100 MHz). Each loop was obtained after 20 sampling cycles to average out the noise deformation. The hysteresis loop obtained was very consistent with that obtained by a standardized ferroelectric testing unit, RT66A (Radiant Technologies Inc., NM), which ensures the reliability of the measurements. It should be noted that the exact compositional formulation for APC-840 is proprietary to APC International, Ltd., but our elemental analysis showed multiple lower valent substituents, such as Na, Ni, Co, and Ga, which are known to produce hard properties through the formation of complex defects.[1,2,4,15,16]

The hysteresis loops of unpoled samples at different f but fixed E_0 (40 kV/cm) and at different E_0 but fixed f (20 Hz) are shown in Fig. 1. The loop area $\langle A \rangle$, remanent polarization (P_r), and coercive field (E_c) decrease with an increase of frequency, as shown in Fig. 1(a). The dependence of the hysteresis loop on E_0 is depicted in Fig. 1(b). For small fields (10 and 15 kV/cm), the loops do not saturate. With further increase in E_0, $\langle A \rangle$, P_r, and E_c increase until a well saturated loop is achieved. Similar observations have been reported in thin films and ceramics.[8,10,13,14]

To investigate the scaling behavior for unpoled hard PZT bulk ceramics, we followed the scaling relation reported earlier for soft PZT bulk ceramics in the form of $\langle A \rangle \propto f^{-0.25} E_0$.[14] The data are shown in Fig. 2 and the solid line represents the fitting. Surprisingly, it is revealed that the high E-field (saturated loops) data can be fitted reasonably well ($R^2 \sim 0.97$) with the scaling relation obtained experimentally for the soft PZT bulk ceramics. However, some deviation is still ob-

[a]Author to whom correspondence should be addressed; electronic mail: rattikornyimnirun@yahoo.com

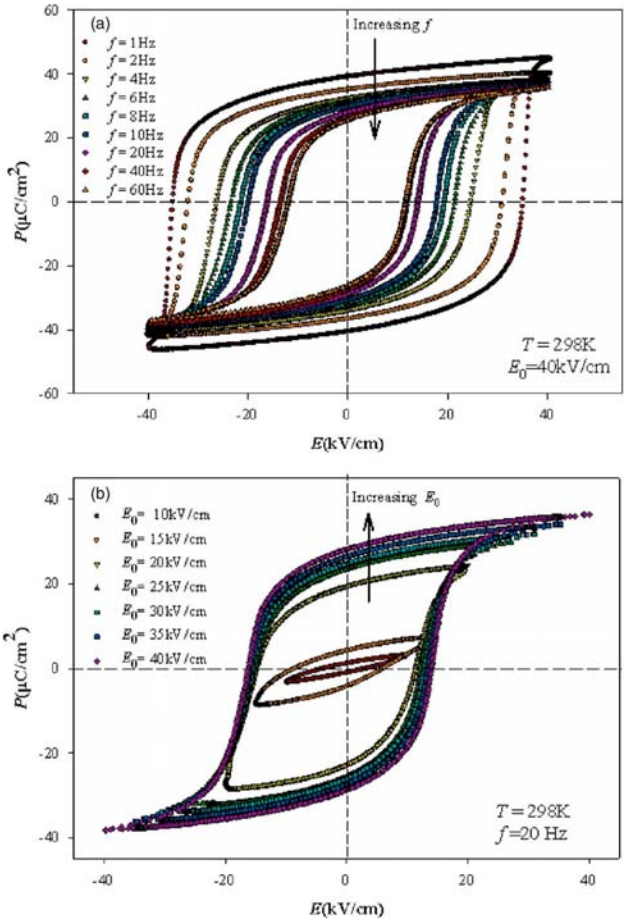

FIG. 1. (Color online) Hysteresis loops for hard PZT bulk ceramic (a) at various f and E_0=40 kV/cm and (b) at various E_0 and f=20 Hz.

served, particularly for low E-field (minor loops) data. This was also the case for the soft PZT bulk ceramics, as reported earlier,[14] in which the different scaling relations were obtained for the saturated and minor loops. Apparently, a similar situation is also observed in the hard PZT bulk ceramics.

Attempt to obtain better scaling can be done by fitting the data with $\langle A\rangle \propto f^m E_0^n$, where m and n are exponents to be determined directly from the experimental data. By plotting $\langle A\rangle$ against f at fixed E_0, one obtains the exponent m. On the

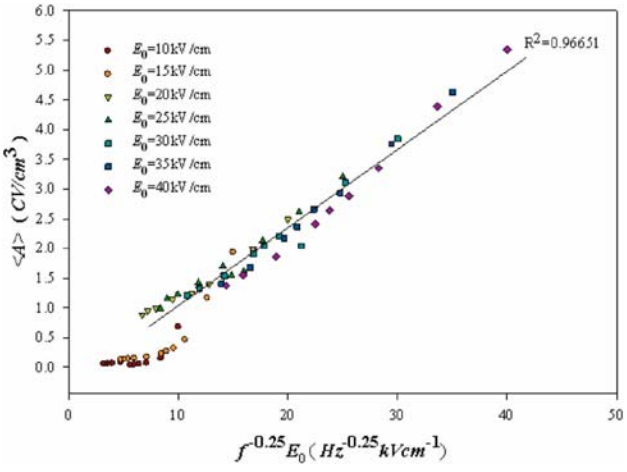

FIG. 2. (Color online) Scaling of hysteresis area $\langle A\rangle$ against $f^{-0.25}E_0$ for hard PZT bulk ceramic.

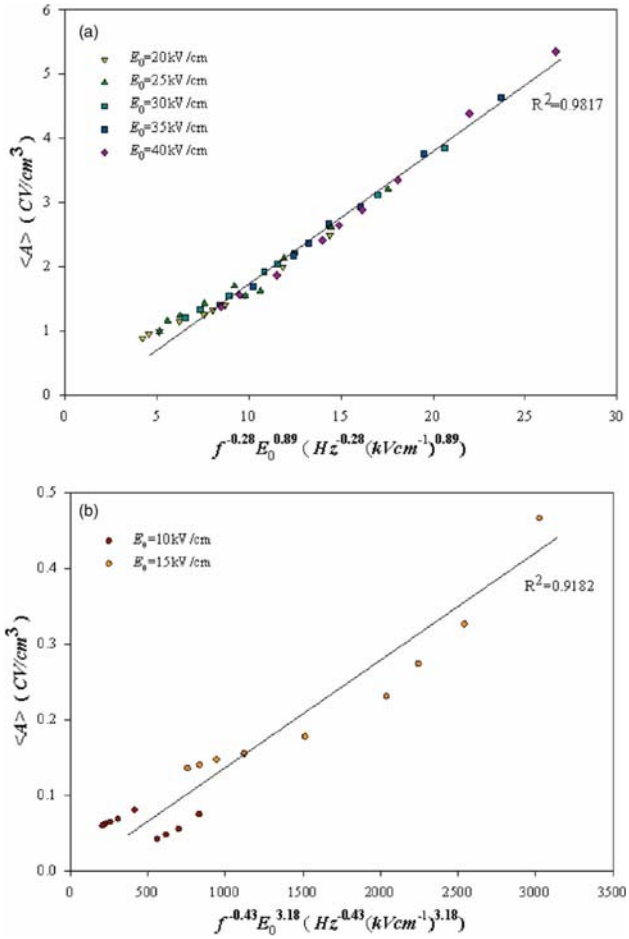

FIG. 3. (Color online) Scaling of hysteresis for hard PZT bulk ceramic. (a) Area $\langle A\rangle$ against $f^{-0.28}E_0^{0.89}$ for the saturated loops; (b) area $\langle A\rangle$ against $f^{-0.43}E_0^{3.19}$ for the minor loops.

other hand, the exponent n can be obtained from plotting $\langle A\rangle$ against E_0 at fixed f. By least-squares-fitting method, for the high E-field data (saturated loops) the exponents $m=-0.28\pm0.01$ and $n=0.89\pm0.05$ were obtained. As plotted in Fig. 3(a), it is revealed that the high E-field data can be fitted only slightly better ($R^2\sim0.98$), within the measured uncertainty, by

$$\langle A\rangle \propto f^{-0.28}E_0^{0.89}. \tag{2}$$

Furthermore, the exponents $m=-0.43\pm0.08$ and $n=3.19\pm0.56$ were obtained and fitted reasonably well ($R^2\sim0.92$) for the minor loop data, as plotted in Fig. 3(b). Therefore, the scaling relation for minor loops of hard PZT bulk ceramic takes the form of

$$\langle A\rangle \propto f^{-0.43}E_0^{3.19}. \tag{3}$$

The scaling relation obtained in Eq. (2) for the saturated loops of the hard PZT bulk ceramic indicates that $\langle A\rangle$ decays more slowly with f and grows more slowly with E_0 than that theoretically predicted and that observed in the PZT thin film, as listed in Table I and discussed in an earlier publication.[14]

As listed in Table I, it is even more interesting to observe that the scaling behaviors for the hard PZT bulk ceramic are to some extent similar to those of the soft counterpart. By a direct comparison, the exponents m and n for the two ceram-

TABLE I. Dynamic scaling exponents for different systems [refer to Eq. (1)].

System	α	β	References
$(\Phi^2)^2$ and $(\Phi^2)^3$ model	−1	2	6 and 7
1–3 composite	−1	2	17
Nd-doped $Bi_4Ti_3O_{12}$ thin film	−0.66	2	18
SBT thin film	−0.33	2	19
PZT thin film	−0.33	3	13
Soft PZT bulk ceramic			
-Saturated loops	−0.25	1	14
-Minor loops	−0.33	3	14
Hard PZT bulk ceramic			
-Saturated loops	−0.28±0.01	0.89±0.05	This work
-Minor loops	−0.43±0.08	3.19±0.56	This work

ics are not significantly different. As well known, the major difference between the two types of ceramic is the complex defects.[1,3,4,15,16] In the hard PZT, the oxygen vacancies are introduced, are trapped at the domain walls, and then form electric dipoles with the acceptor atoms. These dipoles called complex defects act as pinning points for the domain wall, and the domain wall motion is reduced. The complex defects are absent in the soft PZT ceramics; hence the domain walls can move more easily. Therefore, hard PZT ceramics typically show higher E_C than soft ones. Other dielectric and piezoelectric properties of the two types of ceramics are also significantly different.[1–4,15,16] However, the similar scaling behaviors for the two types of ceramics suggest that though the complex defects contribute greatly to the difference on the electrical properties, they contribute only slightly to the dynamic behaviors. At high fields (saturated loops), one can picture that beyond the critical field, i.e., E_C which is different between the hard and soft ceramics, the dynamic hysteresis behavior of the PZT bulk ceramics is mainly governed by the available domain states for polarization switching, while the contribution the complex defects is very minimal; hence the scaling behavior is nearly similar between the hard and soft PZT ceramics. However, at lower fields (minor loops), the complex defects still play limited roles in controlling the dynamic behavior, as can be observed from the relatively larger differences in the values of m and n between the soft and hard PZT ceramics.

More importantly, all these observations suggest that bulk PZT ceramics with similar domain structures should have very comparable dynamic hysteresis and scaling behavior. As also listed in Table I, it is interesting to observe that models and thin films of different materials, which contain similar domain structures, show comparable scaling behaviors (with only a slight difference in exponents m and n). It could be stated that the dynamic hysteresis (hence the scaling behavior) is mainly controlled by available domain states and polarization switching mechanism. Therefore, the scaling relations obtained theoretically and experimentally from models, thin films, and bulks with distinct types of domain structures and mechanisms should be noticeably different (hence different universality classes among them), as shown in Table I. Our opinion on the contribution of the domain states in controlling the dynamic hysteresis behavior may be strengthened by a further study of the domain states in different materials, particularly in soft and hard PZT ceramics. Previous transmission electron microscopy studies have already shown fine "wavy" domains in hard PZT, while irregular domain morphologies have been reported in soft PZT.[20–22] Thus, giving the complexity of the dopant types and concentrations in the commercial hard and soft PZT ceramics, it may be too complicated to evaluate the domain state contribution to the dynamic behavior in these ceramics. It is more suitable to compare the domain states in undoped PZT and single-element soft- and hard-doped PZT ceramics.[15,23]

In summary, the scaling relation for the saturated hysteresis loops of the hard PZT ceramic takes the form of $\langle A\rangle \propto f^{-0.28}E_0^{0.89}$, while that for the minor loops takes the form of $\langle A\rangle \propto f^{-0.43}E_0^{3.19}$. The two scaling relations are very similar to those of soft PZT bulk ceramics, suggesting that the scaling behaviors of the two types of bulk ceramics are in the same universality class.

This work was supported by the Thailand Research Fund (TRF), Commission on Higher Education (CHE), and Faculty of Science and Graduate School of Chiang Mai University.

[1] B. Jaffe, W. R. Cook, and H. Jaffe, *Piezoelectric Ceramics* (Academic, New York, 1971), p. 271.
[2] Y. H. Xu, *Ferroelectric Materials and Their Applications* (North Holland, Los Angeles, 1991), p. 121.
[3] K. Uchino, *Ferroelectric Devices* (Dekker, New York, 2000), p. 145.
[4] A. J. Moulson and J. M. Herbert, *Electroceramics* (Wiley-Interscience, New York, 2003), p. 358.
[5] J. F. Scott, Ferroelectr. Rev. **1**, 1 (1998).
[6] M. Rao, H. R. Krishnamurthy, and R. Pandit, Phys. Rev. B **42**, 856 (1990).
[7] M. Acharyya and B. K. Chakrabarti, Phys. Rev. B **52**, 6560 (1995).
[8] J.-M. Liu, H. L. W. Chan, C. L. Choy, Y. Y. Zhu, S. N. Zhu, Z. G. Liu, and N. B. Ming, Appl. Phys. Lett. **79**, 236 (2001).
[9] Q. Jiang, H. N. Yang, and G. C. Wang, Phys. Rev. B **52**, 14911 (1995).
[10] B. Pan, H. Yu, D. Wu, X. H. Zhou, and J.-M. Liu, Appl. Phys. Lett. **83**, 1406 (2003).
[11] Y.-H. Kim and J.-J. Kim, Phys. Rev. B **55**, R11933 (1997).
[12] J.-H. Park, C.-S. Kim, B.-C. Choi, B. K. Moon, J. H. Jeong, and I. W. Kim, Appl. Phys. Lett. **83**, 536 (2003).
[13] J.-M. Liu, H. L. W. Chan, and C. L. Choy, Mater. Lett. **52**, 213 (2002).
[14] R. Yimnirun, Y. Laosiritaworn, S. Wongsaenmai, and S. Ananta, Appl. Phys. Lett. **89**, 162901 (2006).
[15] Q. Tan, J. Li, and D. Viehland, Appl. Phys. Lett. **75**, 418 (1999).
[16] W. Chang, A. H. King, and K. J. Bowman, Appl. Phys. Lett. **88**, 242901 (2006).
[17] B. Pan, Y. Yang, L. C. Yu, J. M. Liu, K. Li, Z. G. Liu, and H. L. W. Chan, Mater. Sci. Eng., B **B99**, 179 (2005).
[18] J.-M. Liu, B. Pan, H. Yu, and S. T. Zhang, J. Phys.: Condens. Matter **16**, 1189 (2004).
[19] J.-M. Liu, B. Pan, K. F. Wang, and H. Yu, Ceram. Int. **30**, 1471 (2004).
[20] Q. Tan, Z. Xu, J. F. Li, and D. Viehland, J. Appl. Phys. **80**, 5866 (1996).
[21] J. F. Li, X. H. Dai, A. Chow, and D. Viehland, J. Mater. Res. **10**, 926 (1995).
[22] W. Cao and C. A. Randall, J. Phys. Chem. Solids **37**, 1499 (1996).
[23] T. Granzow, E. Suvaci, H. Kungl, and M. J. Hoffmann, Appl. Phys. Lett. **89**, 262908 (2006).

Available online at www.sciencedirect.com
ScienceDirect
Materials Letters 61 (2007) 2426–2429
materials letters
www.elsevier.com/locate/matlet

Effects of calcination conditions on phase formation and particle size of indium niobate nanopowders synthesized by the solid-state reaction

S. Wongsaenmai, R. Yimnirun, S. Ananta *

Department of Physics, Faculty of Science, Chiang Mai University, Chiang Mai 50200, Thailand

Received 17 March 2006; accepted 13 September 2006
Available online 2 October 2006

Abstract

A wolframite-type phase of indium niobate, $InNbO_4$, has been synthesized by a solid-state reaction via a rapid vibro-milling technique. The formation of the $InNbO_4$ phase in the calcined powders has been investigated as a function of calcination conditions by TG–DTA and XRD techniques. Morphology, particle size and chemical composition have been determined via a combination of SEM and EDX techniques. It has been found that single-phase $InNbO_4$ powders have been obtained successfully at the calcination condition of 950 °C for 2 h with heating/cooling rates of 30 °C/min. Higher temperatures and longer dwell times clearly favoured particle growth and the formation of large and hard agglomerates.

Keywords: Indium niobate; $InNbO_4$; Calcination; Phase formation; Powders–solid-state reaction

1. Introduction

Earlier works concerning the wolframite-type indium niobate ($InNbO_4$, IN) have been directed towards determining low-temperature dielectric, luminescent and photocatalytic properties [1–3]. Recently, this compound is also a potential material for the development of photocatalytic systems capable of splitting water into H_2 and O_2 under visible light irradiation [4,5]. Moreover, it is well established as a key precursor for the partially successful preparation of single-phase ferroelectric perovskite lead indium niobate $Pb(In_{1/2}Nb_{1/2})O_3$ (PIN)-based ceramics, which is becoming increasingly important for actuator, transducer and ultrasonic motor applications [6].

There has been a great deal of interest in the preparation of single-phase perovskite PIN powders as well as in the phase transition, ordering behaviour and electrical properties of PIN-based ceramics [7–11]. In general, the constituents In_2O_3 and Nb_2O_5 are first mixed and reacted together to form indium niobate ($InNbO_4$), prior to mixing and reacting with PbO in the second step of calcination at elevated temperature. Interestingly, this mixed oxide route has been employed with minor modifications in the synthesis of $InNbO_4$ itself [8–11]. However, powders prepared by a mixed oxide route have spatial fluctuations in their compositions. The extent of the fluctuations depends on the characteristics of the starting powders as well as on the processing schedule. Generally, the mixed oxide method involves the heating of a mixture of indium oxide and niobium oxide above 1000 °C for long times *i.e.* 4 h [7,8], 12 h [4], 24 h [9–11] and 48 h [3,5]. The optimization of calcination conditions used in the mixed oxide process, however, has not received detailed attention, and the effects of applied dwell time and heating/cooling rates have not yet been studied extensively.

Therefore, the main purpose of this work is to explore a simple mixed oxide synthetic route for the production of $InNbO_4$ powders via a rapid vibro-milling technique and to perform a systematic study of the reaction between the starting indium oxide and niobium oxide precursors. The phase formation and morphology of the powders calcined at various conditions will be studied and discussed.

2. Experimental procedure

The starting materials were commercially available indium oxide, In_2O_3 (JCPDS file number 71-2195) and niobium oxide, Nb_2O_5 (JCPDS file number 30-873) (Aldrich, 99.9% purity). The two oxide powders exhibited an average particle size in the range of 1.0–3.0 μm. $InNbO_4$ powders were synthesized by the

* Corresponding author. Tel.: +66 53 943367; fax: +66 53 943445.
E-mail address: Supon@chiangmai.ac.th (S. Ananta).

0167-577X/$ - see front matter © 2006 Elsevier B.V. All rights reserved.
doi:10.1016/j.matlet.2006.09.028

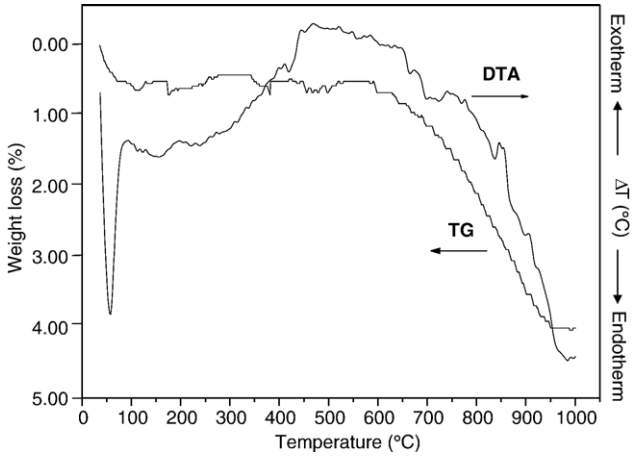

Fig. 1. TG–DTA curves for the mixture of In_2O_3–Nb_2O_5 powder.

solid-state reaction of thoroughly ground mixtures of In_2O_3 and Nb_2O_5 powders that were milled in the required stoichiometric ratio. Instead of employing a ball-milling procedure [7,11], a McCrone vibro-milling technique was used [12]. In order to combine mixing capacity with a significant time saving, the milling operation was carried out for 0.5 h with corundum cylindrical media in isopropyl alcohol (IPA). After drying at 120 °C for 2 h, the reaction of the uncalcined powders taking place during heat treatment was investigated by themogravimetric and differential thermal analysis (TG–DTA, Shimadzu), using a heating rate of 10 °C/min in air from room temperature up to 1000 °C. Based on the TG–DTA results, the mixture was calcined in air at various conditions in a closed alumina crucible, in order to investigate the formation of indium niobate.

Calcined powders were subsequently examined by room temperature X-ray diffraction (XRD; Siemens-D500 diffractometer), using Ni-filtered CuK_α radiation to identify the phases formed and optimum calcination conditions for the formation of $InNbO_4$ powders. Powder morphologies and particle sizes were

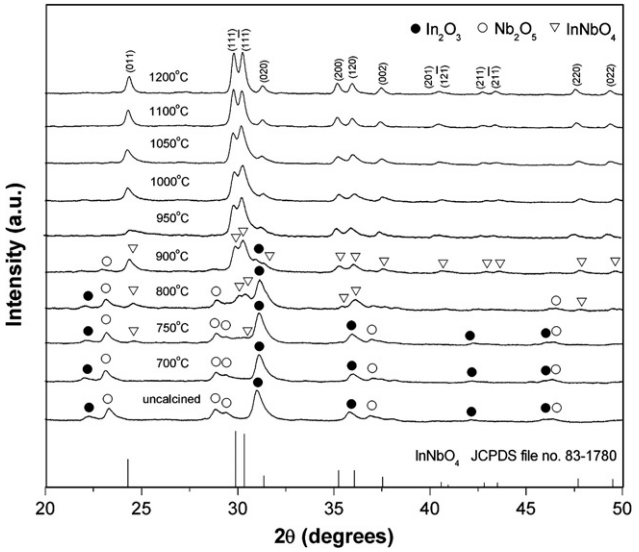

Fig. 2. XRD patterns of IN powders calcined at various temperatures for 2 h with heating/cooling rates of 10 °C/min.

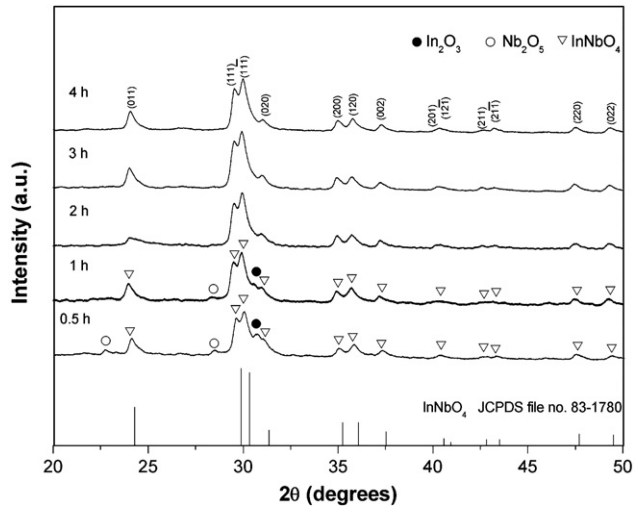

Fig. 3. XRD patterns of IN powders calcined at 950 °C with heating/cooling rates of 10 °C/min for various dwell times.

directly imaged, using scanning electron microscopy (SEM; JEOL JSM-840A). The chemical compositions of the phase formed were elucidated by an energy-dispersive X-ray (EDX) analyzer with an ultra-thin window. EDX spectra were quantified with the virtual standard peaks supplied with the Oxford Instruments eXL software.

3. Results and discussion

The TG–DTA simultaneous analysis of a powder mixed in the stoichiometric proportion of $InNbO_4$ is displayed in Fig. 1. The TG curve shows two distinct weight losses. In the temperature range from room temperature to ~150 °C, both exothermic and endothermic peaks are observed in the DTA curve, in consistent with the first weight loss. These observations can be attributed to the decomposition of the organic species (*i.e.* polyethylene milling jar, rubber gloves, skin, etc.) from the milling process [12]. Increasing the temperature up to ~1000 °C, the solid-state reaction occurred between In_2O_3 and Nb_2O_5 [7,11]. The broad exotherm in the DTA curve represents that reaction, which has a

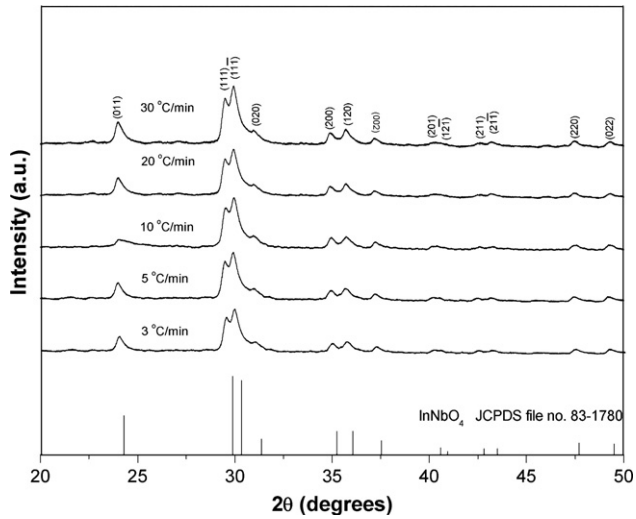

Fig. 4. XRD patterns of IN powders calcined at 950 °C for 2 h with various heating/cooling rates.

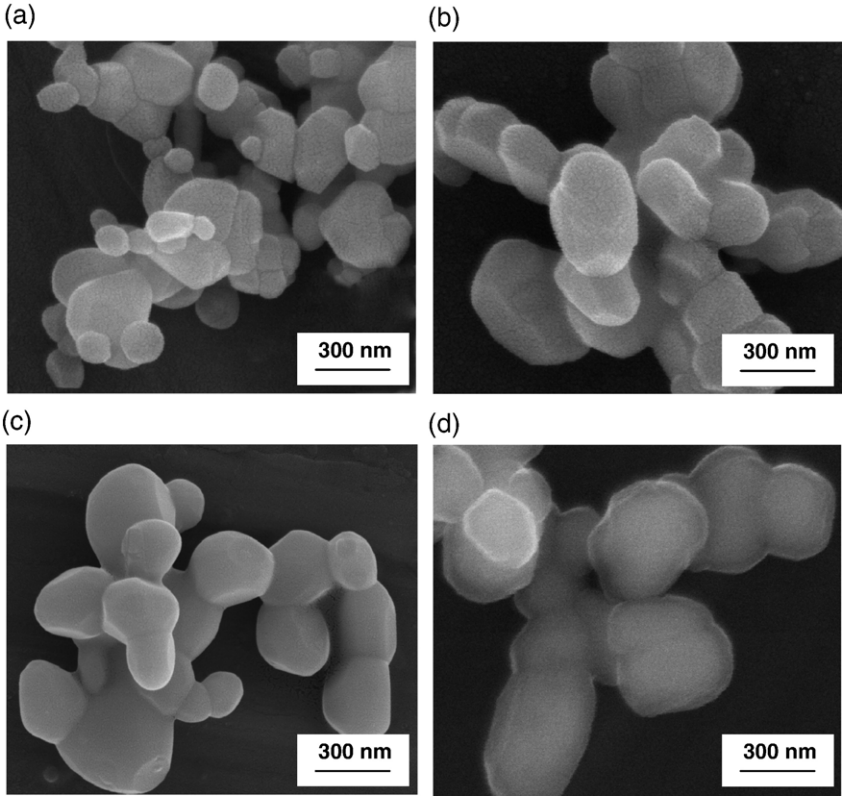

Fig. 5. SEM micrographs of the IN powders calcined at (a) 950 °C for 2 h, (b) 950 °C for 4 h, (c) 1200 °C for 2 h with heating/cooling rates of 10 °C/min, and at (d) 950 °C for 2 h with heating/cooling rates of 30 °C/min.

maximum at ~500 °C. This is supported by a large fall in sample weight over the same temperature range. Although the DTA curve shows that there are other small peaks at ~750, 850 and 900 °C, however, it is to be noted that there is no obvious interpretation of these peaks. These data were used to define the range of calcination temperatures for XRD investigation between 700 and 1200 °C.

To further study the phase development with increasing calcination temperature in the powders, they were calcined for 2 h in air at various temperatures, up to 1200 °C, followed by phase analysis using XRD. As shown in Fig. 2, for the uncalcined powders and the powders calcined at 700 °C, only X-ray peaks of precursors In_2O_3 (●) and Nb_2O_5 (○), which could be matched with JCPDS file numbers 71-2195 [13] and 30-0873 [14], respectively, are present, indicating that no reaction had yet been triggered during the milling or low firing processes. It is seen that fine $InNbO_4$ crystallites (▽) were developed in the powders at a calcination temperature as low as 750 °C, accompanied with In_2O_3 and Nb_2O_5 as separated phases. This observation agrees well with those derived from the TG–DTA results. As the temperature increased to 900 °C, the intensity of the $InNbO_4$ peaks was further enhanced and became the predominant phase. Upon calcination at 950 °C, an essentially monophasic of $InNbO_4$ phase is obtained. This $InNbO_4$ phase was indexable according to a monoclinic wolframite-type structure with lattice parameters a=514.40 pm, b=577.09 pm, c=483.55 pm and β=91.13°, space group *P2/a* (no. 13), in consistent with JCPDS file numbers 83-1780 [15] and literature [2,4]. This study also shows that monoclinic $InNbO_4$ is the only detectable phase in the powders, after calcination in the range of 950–1200 °C. The variation of the intensity ratio between the two major peaks (111) and ($11\bar{1}$) at $2\theta \sim 29$–31° could be attributed mainly to the expansion of the NbO_6 volume similar with those observed in other ABO_4 systems [2,4]. In the structure of $InNbO_4$, there are two kinds of octahedron, InO_6 and NbO_6. The InO_6 octahedron connects to each other to form a zigzag chain by sharing edges. These chains are connected through NbO_6 octahedron to form the three-dimensional network [5,16]. It is believed that the InO_6 chains are highly distorted because they must accommodate the strain of the defect, which probably leads to lattice rotation [5].

In earlier works [3,7,9], long heat treatments at ~1000–1200 °C for at least 4 h were proposed for the formation of $InNbO_4$ by a conventional mixed oxide synthetic route, although no details on phase formation were provided. However, in the present study, it was found that, except the fluctuation of the intensity ratio between the (111) and ($11\bar{1}$) peaks, there are no significant differences between the powders calcined at 950 to 1200 °C with dwell time of only 2 h, as shown in Fig. 2. This observation would clearly suggest the advantages of a rapid vibro-milling technique used in the present study.

Apart from the calcination temperature, the effect of dwell time was also found to be quite significant. From Fig. 3, it can be seen that the single-phase of $InNbO_4$ (yield of 100% within the limitations of the

Table 1
Particle size range of $InNbO_4$ powders calcined at various conditions

Calcination conditions			Estimated particle size range (±10 nm)
Temperature (°C)	Dwell time (h)	Rates (°C/min)	
950	2	3	150–550
950	2	10	150–350
950	2	30	100–350
950	3	10	300–450
950	4	10	300–700
1000	2	10	200–500
1100	2	10	250–600
1200	2	10	350–700

XRD technique) was found to be possible in powders calcined at 950 °C with dwell time of 2 h or more. The appearance of In_2O_3 and Nb_2O_5 phases indicated that full crystallization has not occurred at relatively short calcination times. The observation that the dwell time effect may also play an important role in obtaining a single-phase wolframite product is also consistent with other similar systems [12,17]. It is also very interesting to see that the on-set firing time is approximately 2–22 h shorter than those reported earlier with a conventional ball-milling method [7–11]. The difference could be attributed to the effectiveness of vibro-milling and a carefully optimized reaction. Most importantly, this study suggests that a rapid vibro-milling method can significantly lower the optimum calcination temperature and dwell time for the formation of single-phase $InNbO_4$ powders.

In the present study, an attempt was also made to calcine $InNbO_4$ powders under various heating/cooling rates. In this connection, it is shown that for the powders calcined at 950 °C for 2 h, the yield of $InNbO_4$ phase did not vary significantly with different heating/cooling rates, ranging from 3 to 30 °C/min (Fig. 4). The observation that faster heating/cooling rates are required for the mixtures containing low-melting point oxide constituent (In_2O_3), is in good agreement with early results reported in other similar systems [18,19].

Based on the TG–DTA and XRD data, it may be concluded that, over a wide range of calcination conditions, single-phase $InNbO_4$ cannot be straightforwardly formed via a solid-state mixed oxide synthetic route, unless a careful design of calcination condition is performed. It is well documented that powders prepared by a conventional mixed oxide method have spatial fluctuations in their compositions. The extent of the fluctuation depends on the characteristics of the starting powders as well as the processing schedules [12,17]. It is rather surprising that no evidence of the monoclinic *P2/c* (13) of $InNbO_4$ [20] was found in this study, nor was there any indication of the one with *P2/a* (13) reported by Brixner and Chen [2] being present. The experimental work carried out here suggests that the optimal calcination conditions for single-phase $InNbO_4$ (with impurities undetected by XRD technique) is 950 °C for 2 h with heating/cooling rates as fast as 30 °C/min. Moreover, the formation temperature and dwell time for the production of $InNbO_4$ powders observed in this work are also lower than those reported earlier [8–11]. This clearly emphasizes the advantages of a combination between a rapid vibro-milling technique and a carefully optimized reaction.

The morphological evolution during calcination was investigated by scanning electron microscopy (SEM). Micrographs of $InNbO_4$ powders calcined at various temperatures, dwell times and heating/cooling rates are illustrated in Fig. 5. The influence of calcination conditions on particle size is also given in Table 1. After calcinations at 950 to 1200 °C, the powders have similar morphology. In general, the particles are agglomerated and irregular in shape, with a substantial variation in particle size, particularly in samples calcined at high temperature (Fig. 5(c)). The results indicate that averaged particle size tends to increase with calcination temperatures and dwell times but seems to decrease with faster heating/cooling rates (Table 1).

The effects of dwell time and heating/cooling rates on the morphology of the calcined powders were also found to be quite significant. As expected, it is seen that longer heat treatment leads to larger particle sizes and hard agglomeration (Fig. 5(a) and (b)). As shown in Fig. 5(a) and (d), as well as in Table 1, by increasing the heating/cooling rates, averaged particle size tends to decrease whilst the degree of agglomeration tends to increase. This observation could be attributed to the mechanism of surface energy reduction of the ultrafine powders, *i.e.* the smaller the powder the higher the specific surface area [21]. This finding is also similar to that in $Mg_4Nb_2O_9$ powders synthesized by Ananta [22]. To the author's knowledge, the present data are the first results for the morphology–calcination relationship of $InNbO_4$ powders prepared by the solid-state reaction. It is also of interest to point out that mass production of single-phase $InNbO_4$ nanopowders with the smallest particle size ~100 nm (estimated from SEM micrographs) can be achieved by employing a simple solid-state reaction combined with a rapid vibro-milling technique. In addition, EDX analysis using a 20 nm probe on a large number of particles of the calcined powders confirms that the chemical composition is $InNbO_4$ powders, in good agreement with the XRD results.

4. Conclusions

The solid-state mixed oxide method via a rapid vibro-milling technique is explored in the preparation of single-phase $InNbO_4$ nanopowders. The calcination temperature, dwell time and heating/cooling rates have been found to show a pronounced effect on phase formation and particle size of the calcined $InNbO_4$ powders. This work demonstrated that the single-phase of indium niobate powders with particle size ranging from 100 to 350 nm can be produced via this technique by using a calcination temperature of 950 °C for 2 h, with heating/cooling rates of 30 °C/min. The resulting $InNbO_4$ powders exhibit similar morphology and variety of agglomerated particle sizes, depending on the calcination conditions.

Acknowledgments

We thank the Thailand Research Fund (TRF), Commission on Higher Education (CHE), Graduate School and Faculty of Science, Chiang Mai University for all the support.

References

[1] J.K. Hulme, Phys. Res. 92 (1953) 504.
[2] L.H. Brixner, H.-Y. Chen, Mater. Res. Bull. 15 (1980) 607.
[3] Z. Zou, J. Ye, H. Arakawa, Chem. Phys. Lett. 332 (2000) 271.
[4] Z. Zou, J. Ye, K. Sayama, H. Arakawa, Nature 414 (2001) 625.
[5] Z. Zou, H. Arakawa, J. Photochem. Photobiol., A Chem. 158 (2003) 145.
[6] A.J. Moulson, J.M. Herbert, Electroceramics, 2nd ed.,Wiley, New York, 2003.
[7] E.F. Alberta, A.S. Bhalla, Ferroelectrics 188 (1996) 95.
[8] E.F. Alberta, A.S. Bhalla, J. Phys. Chem. Solids 63 (2002) 1759.
[9] C. Elissalde, F. Weill, J. Ravez, Mater. Sci. Eng., B, Solid-State Mater. Adv. Technol. 25 (1994) 85.
[10] N. Yasuda, T. Mizuno, Appl. Phys. Lett. 66 (1995) 571.
[11] K.H. Lee, S.B. Lee, H. Kim, Ceram. Int. 30 (2004) 1035.
[12] S. Ananta, Mater. Lett. 58 (2004) 2834.
[13] Powder Diffraction File No. 71-2195. International Centre for Diffraction Data, Newton Square, PA, 2000.
[14] Powder Diffraction File No. 30-873. International Centre for Diffraction Data, Newton Square, PA, 2000.
[15] Powder Diffraction File No. 83-1780. International Centre for Diffraction Data, Newton Square, PA, 2000.
[16] Z. Zou, J. Ye, H. Arakawa, Chem. Phys. Lett. 332 (2000) 271.
[17] S. Ananta, R. Brydson, N.W. Thomas, J. Eur. Ceram. Soc. 19 (1999) 489.
[18] R. Tipakontitikul, S. Ananta, Mater. Lett. 58 (2004) 449.
[19] B.C. Kim, J.H. Lee, J.J. Kim, T. Ikegami, Mater. Lett. 52 (2002) 114.
[20] Liebertz, Acta Crystallogr., B 28 (1972) 3100.
[21] J.S. Reed, Principles of Ceramics Processing, 2nd ed.,Wiley, New York, 1995.
[22] S. Ananta, Mater. Lett. 58 (2004) 2530.

Available online at www.sciencedirect.com
ScienceDirect
Materials Letters 61 (2007) 2822–2826
materials letters
www.elsevier.com/locate/matlet

Effect of vibro-milling time on phase formation and particle size of lead zirconate nanopowders

O. Khamman, W. Chaisan, R. Yimnirun, S. Ananta *

Department of Physics, Faculty of Science, Chiang Mai University, Chiang Mai 50200, Thailand

Received 24 March 2006; accepted 17 October 2006
Available online 13 November 2006

Abstract

A perovskite phase of lead zirconate, $PbZrO_3$, nanopowder was synthesized by a solid-state reaction via a rapid vibro-milling technique. The effect of milling time on the phase formation and particle size of $PbZrO_3$ powder was investigated. Powder samples were characterized using TG–DTA, XRD, SEM and laser diffraction techniques. It was found that an average particle size of 50 nm was achieved at 25 h of vibro-milling after which a higher degree of particle agglomeration was observed upon continuation of milling to 35 h. In addition, by employing an appropriate choice of milling time, a narrow particle size distribution curve was also observed.

Keywords: Lead zirconate; Milling; Nanopowders; Phase formation; Particle size

1. Introduction

Lead zirconate, $PbZrO_3$ (PZ), is one of the antiferroelectric materials which exhibit a perovskite structure. It shows antiferroelectric phase with cubic symmetry at high temperature and undergoes two phase transitions which are close in temperature (~230 °C and 220 °C) upon cooling [1]. The low temperature phase has orthorhombic symmetry with antiparallel shift of Pb ions along the pseudocubic <110>, which results in antiferroelectricity [2]. When combined with other oxides, lead zirconate can form a series of solid solutions such as $Pb(Zr_{1-x},Ti_x)O_3$ (PZT), $(Pb,La)(Zr,Ti)O_3$ (PLZT), $Pb(Fe_{1/3}W_{2/3})O_3$–$PbZrO_3$ (PFW–PZ) and $Pb(Zn_{1/3}Nb_{2/3})O_3$–$PbZrO_3$ (PZN–PZ) [2–4]. These compositions are widely used in ultrasonic transducers, electro-optic devices, nonvolatile memories, microactuators and multilayer capacitors [1–4]. To fabricate them, a fine powder of perovskite phase with a minimal degree of particle agglomeration is needed as the starting material in order to achieve a dense and uniform microstructure at a given sintering temperature. Thus, a crucial focus of powder synthesis in recent years has been the formation of uniform-sized, single morphology particulates ranging in size from nanometer to micrometers [5–8].

The development of a method to produce nanopowders of precise stoichiometry and desired properties is complex, depending on a number of variables such as nature and purity of starting materials, processing history, temperature, etc. To obtain nanosized PZ powders, many investigations have focused on several chemistry-based preparation routes, such as sol–gel [5], homogeneous precipitation [6], hydrothermal reaction [7], oxidant-peroxo method [8], besides the more conventional solid-state reaction of mixed oxides [9]. All these techniques are aimed at reducing the particle size and temperature of preparation of the compound even though they are more involved and complicated in approach than the solid-state reaction. Moreover, high-purity PZ nanopowders are still not available in bulk quantity. The advantage of using mechanical milling for preparation of nanosized powders lies in its ability to produce mass quantities of powders in the solid state using simple equipment and low-cost starting precursors [10]. Although some research has been done in the preparation of PZ powders via a vibro-milling technique [9], to our knowledge a systematic study regarding the influence of milling time on the preparation of PZ powders has not yet been reported.

* Corresponding author. Tel.: +66 53 943367; fax: +66 53 943445.
E-mail address: suponananta@yahoo.com (S. Ananta).

0167-577X/$ - see front matter © 2006 Elsevier B.V. All rights reserved.
doi:10.1016/j.matlet.2006.10.063

Thus, in the present study, the effect of milling time on phase formation, and particle size of lead zirconate powders was investigated in this connection. The potential of the vibro-milling technique as a simple and low-cost method to obtain usable quantities of single-phase lead zirconate powders at low temperature and with nanosized particles was also examined.

2. Experimental procedure

The starting materials were commercially available lead oxide, PbO (JCPDS file number 77-1971) and zirconium oxide, ZrO_2 (JCPDS file number 37-1484) (Fluka, >99% purity). The two oxide powders exhibited an average particle size in the range of 3 to 5 μm. $PbZrO_3$ powder was synthesized by the solid-state reaction of these raw materials. Powder-processing was carried out in a manner similar to that employed in the preparation of other materials, as described previously [10,11]. A vibratory laboratory mill (McCrone Micronizing Mill) powered by a 1/30 HP motor was employed for preparing the stoichiometric $PbZrO_3$ powders. The grinding vessel consists of a 125 ml capacity polypropylene jar fitted with a screw-capped, gasketless, polythene closure. The jar is packed with an ordered array of identical, cylindrical, grinding media of polycrystalline corundum (instead of employing zirconia media under alcohol for 8 h [9]). A total of 48 milling media cylinder with a powder weight of 20 g was kept constant in each batch. The milling operation was carried out in isopropanol inert to the polypropylene jar. Various milling times ranging from 0.5 to 35 h were selected in order to investigate the phase formation characteristic of lead zirconate and the smallest particle size. After drying at 120 °C for 2 h, the reaction of the uncalcined powders taking place during heat treatment was investigated by thermogravimetric and differential thermal analysis techniques (TG–DTA, Shimadzu) at a heating rate of 10 °C/min in air from room temperature up to 1000 °C. Based on the TG–DTA results and literature [9,12], the mixture was calcined at 800 °C (in closed alumina crucible) for 2 h with heating/cooling rates of 10 °C/min.

All powders were subsequently examined by room temperature X-ray diffraction (XRD; Siemens-D500 diffractometer), using Ni-filtered CuK_α radiation to identify the phases formed and optimum milling time for the production of $PbZrO_3$ powders having the smallest particle size. The relative amount of perovskite and secondary phases was determined from XRD patterns of the samples by measuring the major characteristic peak intensities for the perovskite (221) or I_P and secondary (o) phases or I_S. The following qualitative equation was used [10].

$$\text{perovskite phase (wt.\%)} = \frac{I_P}{I_P + I_S} \times 100 \quad (1)$$

The crystalline lattice constants, lattice strain and average particle size were also estimated from XRD patterns [13]. The particle size distributions of the powders were determined by laser diffraction technique (DIAS 1640 laser diffraction spectrometer) with the particle sizes and morphologies of the powders observed by scanning electron microscopy (JEOL JSM-840A SEM). The particle sizes of PZ powders milled at different times obtained from different measuring techniques are provided in Table 1.

3. Results and discussion

The TGA and DTA results for the powders milled at different times are compared and displayed in Fig. 1(a) and (b), respectively. In general, similar thermal characteristics are observed in all cases. In the temperature range from room temperature to ~150 °C, all samples show both exothermic and endothermic peaks in the DTA curves (Fig. 1(b)), which are related to a slight drop in weight loss at the same temperature range. These observations can be attributed to the decomposition of the organic species originating from the milling process [10,11]. Corresponding to the large fall in specimen weight, (~8–9%), the other DTA peaks are detected within ~300 to 450 °C temperature range. However, it is to be noted that there is no obvious interpretation of these peaks, although it is likely to correspond to a phase transformation of ZrO_2 precursor alloyed with PbO precursor suggested by Aoyama et al. [14]. Increasing the temperature up to ~800 °C, the solid-state reaction between lead oxide and zirconium oxide occurs. The broad exothermic characteristics from ~500 to 700 °C in all DTA curves represent that reaction, which is supported by a gradual decrease in sample weight over the same temperature range. The slightly different temperature, intensities and shapes of the thermal peaks of the powders are probably related to the different sizes of the

Table 1
Effect of milling time on the particle size of PZ powders measured by different techniques

Milling time (h)	Perovskite phase (%)	XRD				SEM		Laser scattering	
		A (nm)	*a* (nm)	*b* (nm)	*c* (nm)	*D* (nm)	*P* (nm)	*D* (nm)	*P* (nm)
0.5	93.34	57.39	0.8162	1.1624	0.5814	3800	2410–5000	5280	2840–7650
2	100	42.51	0.8161	1.1611	0.5816	1800	970–2520	1380	1340–5600
5	100	30.73	0.8184	1.1679	0.5846	880	740–950	1380	580–3000
15	100	18.17	0.8238	1.1712	0.5872	300	70–700	720	290–2210
25	100	18.19	0.8241	1.1720	0.5879	180	50–400	180	35–750
35	100	19.34	0.8238	1.1712	0.5872	250	50–420	1540	240–6200

A = Crystallite size.
a, *b*, *c* = Lattice parameters.
D = Average particle size.
P = Particle size distribution or range.

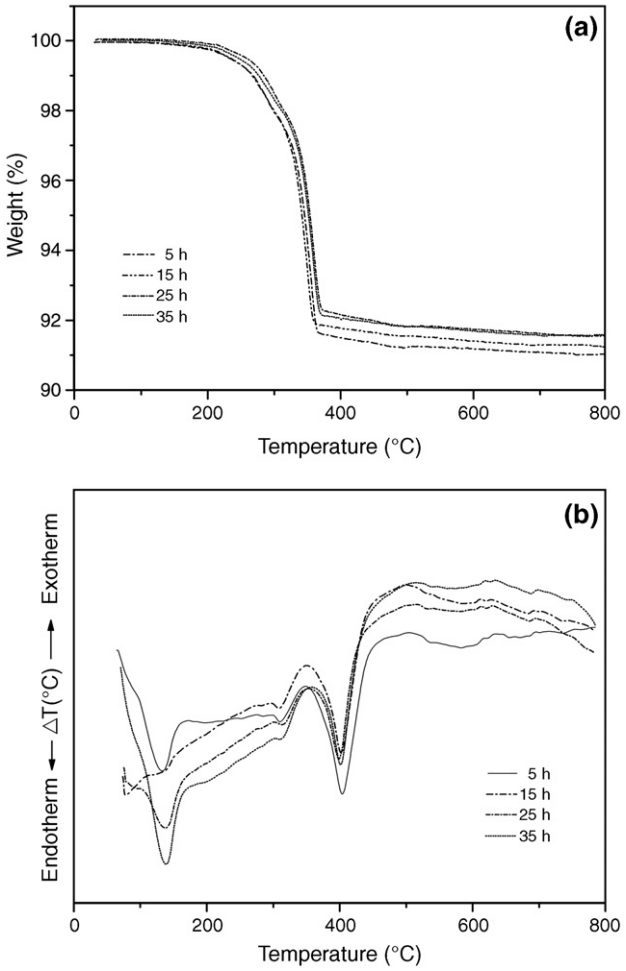

Fig. 1. (a) TGA and (b) DTA analysis of powder mixtures milled at different times.

powders subjected to different milling times and, consequently, caused by the removal of organic species and rearrangement of differently bonded species in the network [2,15].

To further study the effect of milling time on phase formation, each of the powders milled for different times were calcined at 800 °C for 2 h in air, followed by phase analysis using XRD. For the purpose of estimating the concentrations of the phase present, Eq. (1) has been applied to the powder XRD patterns obtained, as given in Table 1. As shown in Fig. 2, for the uncalcined powder subjected to 0.5 h of vibro-milling, only X-ray peaks of precursors PbO (●) and ZrO_2 (○) are present, indicating that no reaction had been initiated during the milling process. However, after calcination, it is seen that the perovskite-type $PbZrO_3$ becomes the predominant phase in the powder milled for 0.5 h, indicating that the reaction has occurred to a considerable extent. It is seen that only traces of unreacted PbO and ZrO_2 precursors have been found along with the PZ parent phase at a milling time of 1.5 h or less. This observation could be attributed mainly to the poor mixing capability under short milling time, similar with another work [10]. With milling time of 2 h or more, it is apparent that a single-phase perovskite PZ (yield of 100% within the limitations of the XRD technique) was found to be possible after the same calcination process was applied.

In general, the strongest reflections found in the majority of these XRD patterns indicate the formation of the lead zirconate, $PbZrO_3$. These can be matched with JCPDS file number 35-0739 for the orthorhombic phase, in space group *P2cb* (no. 32) with cell parameters $a=823.1$ pm, $b=1177.0$ pm and $c=588.1$ pm [16], consistent with other works [6,7]. It should be noted that no evidence for the introduction of impurity due to wear debris from the milling process was observed in any of the calcined powders (within the milling periods of 0.5–35 h), demonstrating the effectiveness of the vibro-milling technique for the production of high-purity PZ nanopowders, without any introduction of excess ZrO_2 [9].

Moreover, it has been observed that with increasing milling time, all diffraction lines broaden, e.g. (261) and (402) peaks, as shown in Fig. 2, an indication of a continuous decrease in particle size and of the introduction of lattice strain. These observations indicate that the prolonged milling treatment affects the particle size and evolution of crystallinity of the phase formed (Table 1), in good agreement with other similar system [10]. For PZ powders, the longer the milling time, the finer the particle size, up to a certain level. The results suggest that the steady state of the vibro-milling is attained at ~25 h of milling. Moreover, it is worthy to note that, in this condition, the mean crystalline size is close to ~50 nm. Also, the relative intensities of the Bragg peaks and the calculated lattice parameters (*b* and *c*) for the powders tend to decrease with the increase of milling time. However, it is well documented that, as Scherrer's analysis provides only a measurement of the extension of the coherently diffracting domains, the particle sizes estimated by this method can be significantly under estimated [17]. In addition to strain, factors such as dislocations, stacking faults, heterogeneities in composition and instrumental broadening can contribute to peak broadening, making it almost impossible to extract a reliable particle size solely from XRD [12,18].

In this connection, scanning electron microcopy was also employed for particle size measurement (Table 1). The morphological evolution of the powders and their corresponding particle size distributions as a function of milling time were also revealed, as illustrated in Fig. 3. At first sight, the morphological characteristic of PZ powders with various milling times is similar for all cases. In general, the particles are agglomerated and basically irregular in shape, with a substantial variation in particle sizes. The powders consist of primary particles nanometers in size. Increasing the milling time over the range 5 to 35 h, the average size of the PZ particles decreases significantly, until at 25 h, the smallest particle size (estimated from SEM micrographs to be

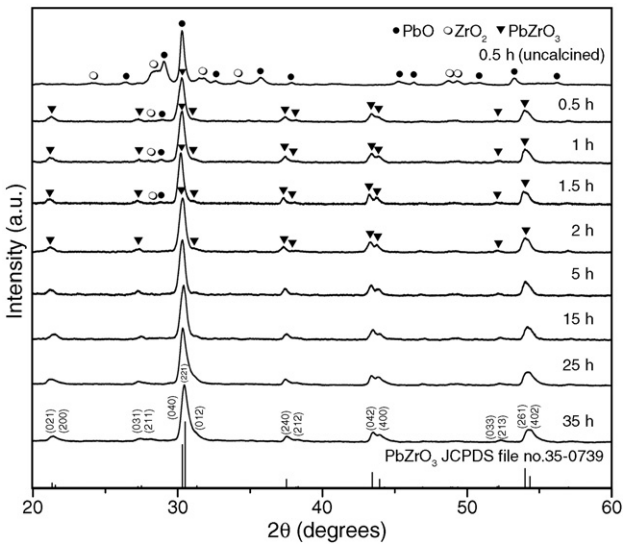

Fig. 2. XRD patterns of PZ powders milled at different times (calcined at 800 °C for 2 h with heating/cooling rates of 10 °C/min).

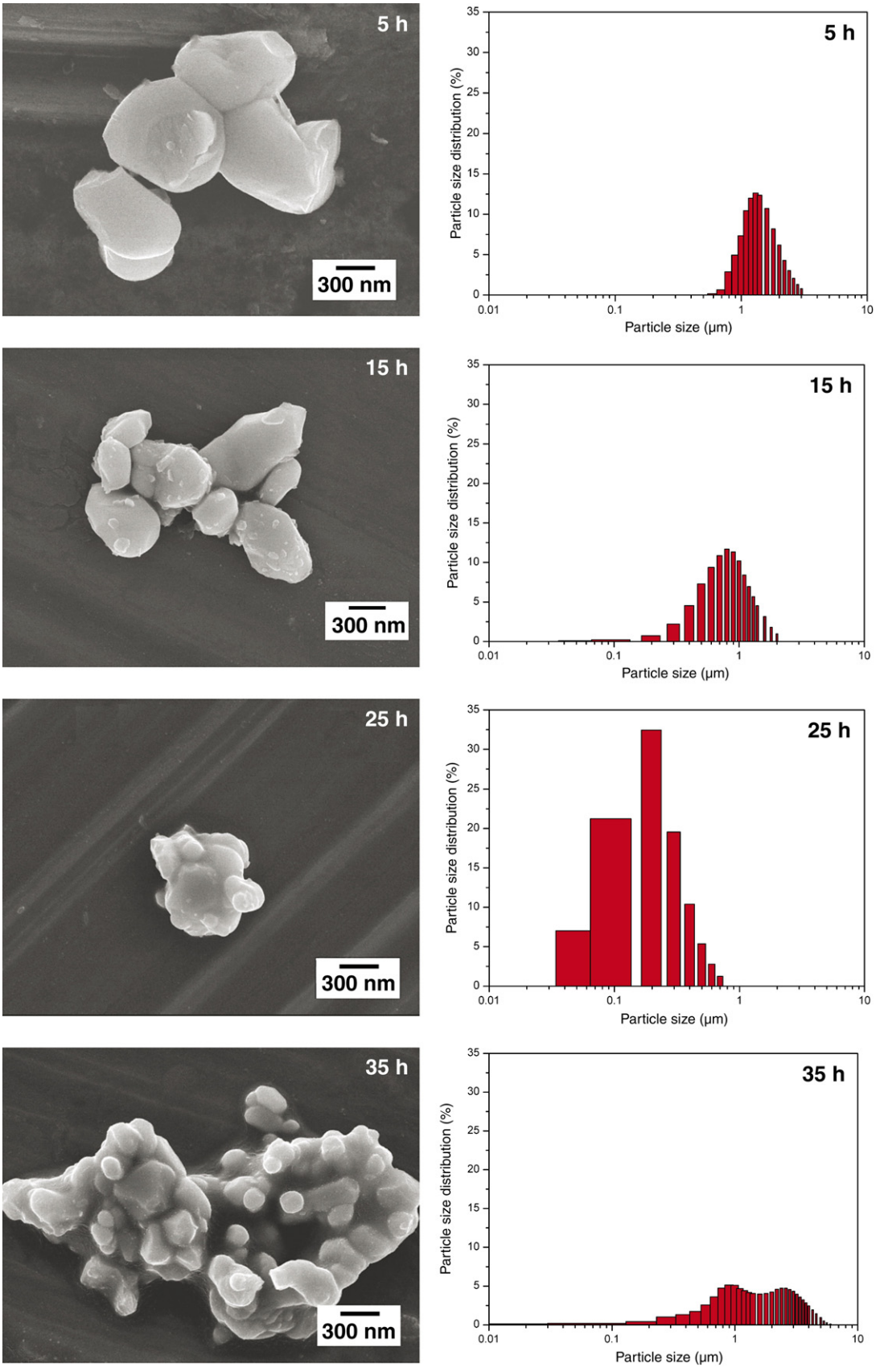

Fig. 3. SEM micrographs and particle size distribution of PZ powders milled at different times.

~50 nm) is obtained. However, it is also of interest to point out that a larger particle size was obtained for a milling time longer than 25 h. This may be attributed to the occurrence of hard agglomeration with strong inter-particle bonds within each aggregate resulting from dissipated heat energy of prolong milling [19]. Fig. 3 also illustrates that vibro-milling has slightly changed the shape of the particles which become more rounded at long milling times. At the same time, the particle size is reduced. Fracture is considered to be the major mechanism at long milling times.

As shown in Fig. 3, after milling times of 5 and 15 h, the powders have a similar particle size distribution. They exhibit a single peak covering the size ranging from 0.29 to 3.00 μm. With increasing milling times to 25 h, a uniform particle size distribution with a much lower degree of particle agglomeration (<1 μm) is found. However, upon further increase of milling time up to 35 h, a bimodal distribution curve with peak broadening between 0.24 and 6.20 μm is observed. First is a monomodal distribution corresponding to the primary size of the $PbZrO_3$ particles. The second group (peak) is believed to arise mainly from particle agglomeration. Table 1 compares the results obtained for PZ powders milled for different times via different techniques. Variations in these data may be attributed mainly to the formation of hard and large agglomerations found in the SEM results.

In this work, it is seen that the optimum milling time for the production of the smallest nanosized high-purity PZ powder was found to be at 25 h. The finding of this investigation indicates a strong relationship between the vibro-milling process and the yield of PZ nanopowders. However, in the case of the vibro-milling technique, other factors such as the milling speed, milling scale and type of milling media also need to be taken into account.

4. Conclusion

The results infer that the milling time influences not only the development of the solid-state reaction of lead zirconate phase but also the particle size and morphology. The resulting PZ powders have a range of particle size, depending on milling times. Production of a single-phase lead zirconate nanopowder can be successfully achieved by employing a combination of 25 h milling time and calcination condition of 800 °C for 2 h, with heating/cooling rates of 10 °C min^{-1}.

Acknowledgements

This work was supported by the National Nanotechnology Center (NANOTEC), the Royal Golden Jubilee Ph.D. Program, the Faculty of Science and the Graduate School of Chiang Mai University.

References

[1] B. Jaffe, W.R. Cook, H. Jaffe, Piezoelectric Ceramics, Academic Press, New York, 1971.
[2] F. Jona, G. Shirane, F. Mazzi, R. Pepinsky, Phys. Rev. 105 (1957) 849.
[3] T.R. Shrout, A. Halliyal, Am. Ceram. Soc. Bull. 66 (1987) 704.
[4] A.J. Moulson, J.M. Herbert, Electroceramics, 2nd ed.Wiley, Chichester, 2003.
[5] D.M. Ibrahim, H.W. Hennicke, Trans. J. Br. Ceram. Soc. 80 (1981) 18.
[6] E.E. Oren, E. Taspinar, A.C. Tas, J. Am. Ceram. Soc. 80 (1997) 2714.
[7] A. Rujiwatra, S. Tapala, S. Luachan, O. Khamman, S. Ananta, Mater. Lett. 60 (2006) 2893.
[8] E.R. Camargo, M. Popa, J. Frantti, M. Kakihana, Chem. Mater. 13 (2001) 3943.
[9] M.T. Lanagan, J.H. Kim, S. Jang, R.E. Newnham, J. Am. Ceram. Soc. 71 (1988) 311.
[10] R. Wongmaneerung, R. Yimnirun, S. Ananta, Mater. Lett. 60 (2006) 1447–1452.
[11] A. Udomporn, S. Ananta, Mater. Lett. 58 (2004) 1154.
[12] C. Puchmark, G. Rujijanagul, S. Jiansirisomboon, T. Tunkasiri, Ferroelectr. Lett. 31 (2004) 1.
[13] H. Klug, L. Alexander, X-Ray Diffraction Procedures for Polycrystalline and Amorphous Materials, 2nd ed.Wiley, New York, 1974.
[14] T. Aoyama, N. Kurata, K. Hiroto, O. Yamaguchi, J. Am. Ceram. Soc. 78 (1995) 3163.
[15] M.D. Johannes, D.J. Singh, Phys. Rev., B 71 (2005) 212101.
[16] Powder Diffraction File No. 35-0739. International Centre for Diffraction Data, Newtown Square, PA, 2000.
[17] C. Suryanarayana, Prog. Mater. Sci. 46 (2001) 1.
[18] A. Revesz, T. Ungar, A. Borbely, J. Lendvai, Nanostruct. Mater. 7 (1996) 779.
[19] P.C. Kang, Z.D. Yin, O. Celestine, Mater. Sci. Eng., A Struct. Mater.: Prop. Microstruct. Process. 395 (2005) 167.

ELSEVIER

Journal of Alloys and Compounds xxx (2007) xxx–xxx

Journal of ALLOYS AND COMPOUNDS

www.elsevier.com/locate/jallcom

Dielectric and ferroelectric properties of fine grains $Pb(In_{1/2}Nb_{1/2})O_3$–$PbTiO_3$ ceramics

Supattra Wongsaenmai [a], Xiaoli Tan [b], Supon Ananta [a], Rattikorn Yimnirun [a,*]

[a] *Department of Physics, Faculty of Science, Chiang Mai University, Chiang Mai 50200, Thailand*
[b] *Department of Materials Science and Engineering, Iowa State University, Ames, IA 50011, USA*

Received 3 October 2006; accepted 10 December 2006

Abstract

The dielectric and ferroelectric properties of $(1-x)Pb(In_{1/2}Nb_{1/2})O_3$–$xPbTiO_3$ (when $x = 0.1$, 0.2, 0.3, 0.4, and 0.5) ceramics prepared by an oxide-mixing method via a vibro-milling technique were investigated. Fine grains ceramics were achieved with average grain size of 1–2 μm, indicating advantage of the vibro-milling technique used. While PIN ceramic exhibited relaxor behavior, the dielectric properties of PIN–PT ceramics showed a mixed relaxor and normal ferroelectric behavior, with more normal ferroelectric behavior observed with increasing PT content. In addition, the ferroelectric properties of the ceramics in PIN–PT system changed from the relaxor ferroelectric behavior in PIN ceramic to the normal ferroelectric behavior in PIN–PT ceramics. These results clearly show the significance of the added PT in reducing the relaxor ferroelectric behavior in PIN ceramic. Finally, the existence of the MPB composition between $x = 0.3$ and 0.4 has been confirmed from the XRD analysis, and dielectric and ferroelectric properties measurements.

Keywords: Dielectric properties; Ferroelectric properties; Mixed-oxide; PIN–PT

1. Introduction

Lead-based perovskite-type solid solutions consisting of the ferroelectric and relaxor materials have attracted a growing fundamental and practical interest because of their excellent dielectric, piezoelectric and electrostrictive properties which are useful in actuating and sensing applications [1–3]. Among the lead-based complex perovskites, lead magnesium niobate–lead titanate ($(1-x)Pb(Mg_{1/3}Nb_{2/3})O_3$–$xPbTiO_3$ or PMN-PT) and lead zinc niobate–lead titanate ($(1-x)Pb(Zn_{1/3}Nb_{2/3})O_3$–$xPbTiO_3$ or PZN-PT) have attracted much attention due to their superior electrical properties [4–7]. However, the major disadvantage of the two ceramic systems is relatively low Curie temperatures (T_C) of the morphotropic phase boundary (MPB) compositions, i.e. lower than 200 °C for the two systems [5–8]. This low T_C comes with the expenses of more temperature dependent properties and less polarization stability, which in turn restrict the operating temperature range to less than 100 °C [7,8]. Interestingly, the MPB composition of the lead indium niobate–lead titanate ($(1-x)Pb(In_{1/2}Nb_{1/2})O_3$–$xPbTiO_3$ or PIN–PT) solid solution system has been reported to possess T_C higher than 250 °C [8–13], and therefore potential for high temperature applications. Many previous studies have focused on the processing and properties of PIN–PT single crystals, particularly the MPB composition [9,12,14,15], while the information on PIN–PT ceramics is still limited [8,10,13]. In addition, most of the PIN–PT ceramics studied were prepared by the mixed-oxide method with a conventional ball-milling technique, which resulted in coarse grains ceramics [11,13], even though it is well known that fine grains ceramics usually show superior electrical properties [16,17]. Recently, a vibro-milling technique has been employed to produce nano-sized powders which can be used to fabricate ceramics with fine grain microstructure [18–20]. Therefore, as an extension to the research on the PIN–PT ceramics, the overall purpose of this study was to systematically determine the dielectric and ferroelectric properties of ceramics in the $(1-x)Pb(In_{1/2}Nb_{1/2})O_3$–$xPbTiO_3$ (when $x = 0.0$, 0.1, 0.2, 0.3, 0.4, and 0.5) system prepared by the mixed-oxide method via the vibro-milling technique. The vibro-milling technique

* Corresponding author. Tel.: +66 53 943 367; fax: +66 53 943 445.
E-mail addresses: rattikor@chiangmai.ac.th, rattikornyimnirun@yahoo.com (R. Yimnirun).

0925-8388/$ – see front matter © 2006 Elsevier B.V. All rights reserved.
doi:10.1016/j.jallcom.2006.12.053

was employed to explore the potential in obtaining fine grains ceramics, which would in turn lead to superior electrical properties.

2. Experimental

The $Pb(In_{1/2}Nb_{1/2})O_3$–$PbTiO_3$ ceramics used in this study were prepared from $Pb(In_{1/2}Nb_{1/2})O_3$ and $PbTiO_3$ starting powders obtained via the vibro-milling technique. In this technique, a vibratory laboratory mill (McCrone Micronizing Mill) was employed. A total of 48 polycrystalline corundum milling media with a powder weight of 20 g was kept constant in each batch. The milling operation was carried out in isopropanal inert to the polypropylene jar [18–20]. Initially, pure-phase PIN powders were obtained via a well-known wolframite method [21,22], while PT powders were prepared by a mixed-oxide method [23]. With the wolframite method, the single-phase indium niobate ($InNbO_4$) powders were first prepared by mixing starting indium oxide (In_2O_3) and niobium oxide (Nb_2O_5) (Aldrich, 99.9% purity) powders by employing the vibro-milling technique for 0.5 h and then calcining the mixed powders at 900 °C for 4 h with heating/cooling rates of 30 °C/min [24]. This yielded a so-called wolframite ($InNbO_4$) powder. The wolframite precursor powders were subsequently vibro-milled with lead oxide (PbO) (Fluka, 99% purity) for 0.5 h. The mixed powders were calcined at 1100 °C for 2 h with heating/cooling rates of 10 °C/min to form a single-phase PIN [25]. It should, however, be noted that to obtain the pure-phase PIN powders 2 mol% excess of In_2O_3 and PbO had to be added to compensate the loss during calcination [25]. With a more conventional oxide-mixing route, PT powders were prepared from PbO and titanium oxide (TiO_2) (Riedel-de Haën, 99% purity) starting powders. These powders were vibro-milled for 0.5 h and later calcined at 600 °C for 2 h with heating/cooling rates of 5 °C/min [23]. The $(1-x)Pb(In_{1/2}Nb_{1/2})O_3$–$xPbTiO_3$ (when $x = 0.0, 0.1, 0.2, 0.3, 0.4$, and 0.5) ceramics were then prepared from the PIN and PT powders by the same mixed-oxide method. The PIN and PT powders were weighed in the required stoichiometric ratio and vibro-milled for 0.5. The thoroughly mixed powders were then pressed hydraulically to form disc-shaped pellets 10 mm in diameter and 2 mm thick, with 3 wt.% polyvinyl alcohol as a binder. The pellets were placed on the alumina powder-bed inside alumina crucible and surrounded with atmosphere powders of the same composition. Finally, the pellets were sintered at 1175 °C (1050 °C for PIN) for 2 h with heating/cooling rates of 10 °C/min.

The densities of the sintered ceramics were measured by Archimedes method. The phase formations of the sintered specimens were studied by an X-ray diffractometer (XRD; Siemen-D500 diffractometer). The microstructure analyses were undertaken by a scanning electron microscopy (SEM: JEOL Model JSM 840A). Grain size was determined from SEM micrographs by a linear intercept method. The dielectric properties were evaluated with a computer-controlled dielectric measurement system consisted of a precision LCR-meter (Hewlett Packard, model 4284A), a temperature chamber (Delta Design, model 9023), and a sample holder (Norwegian Electroceramics) capable of high temperature measurement. The room temperature ferroelectric polarization versus electric field (*P–E*) measurements was made using a standardized ferroelectric test system (RT-66A, Radiant Technologies) with an applied field of 30–60 kV/cm.

3. Results and discussion

The XRD patterns of $(1-x)$PIN–xPT ceramics with various x values are shown in Fig. 1(a). It can be seen that a complete crystalline solution of perovskite structure is formed throughout the composition range without the presence of pyrochlore or unwanted phases. From the patterns, PIN ceramic is identified as a single-phase material with a perovskite structure having cubic symmetry which could be matched with JCPDS file no. 87-0304. The XRD patterns of the PIN–PT compositions show a combination between PIN and PT patterns, showing a perovskite structure having the symmetry varying between pseudo-cubic and tetragonal types. For better comparison, the

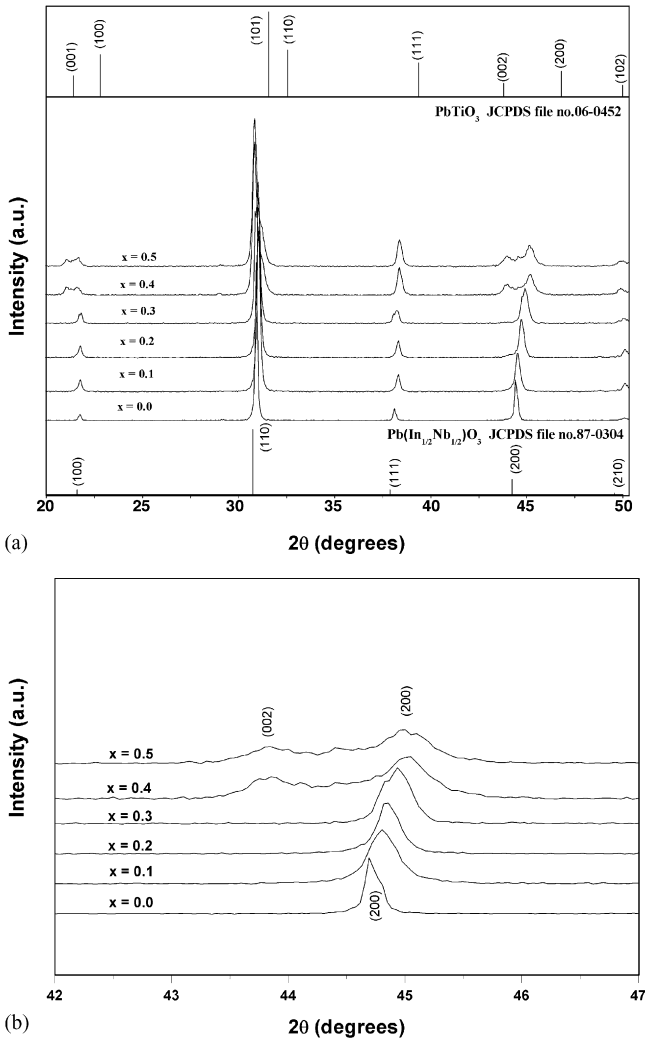

Fig. 1. (a) XRD patterns of $(1-x)$PIN–xPT ceramics and (b) selected region of the diffraction patterns.

JCPDS file no. 06-0452 for PT with a tetragonal structural symmetry is also displayed in Fig. 1(a). More interestingly, the composition with $x = 0.3$ began to exhibit broadening of peaks at $2\theta \approx 21.5°$, 30.5°, and 44.5° for (1 0 0)/(0 0 1), (1 1 0)/(1 0 1), and (2 0 0)/(0 0 2), respectively. Fig. 1(b) shows the broadened peaks at $2\theta \sim 44.5$–45°, indicating the structural transformation from the pseudo-cubic phase to the tetragonal phase, characterized by (2 0 0)/(0 0 2) peaks. This observation is obviously associated with the composition with coexistence of two symmetries, which in this case are tetragonal and pseudo-cubic phases. To a first approximation, it could be said that the composition between $x = 0.3$ and 0.4 is close to the morphotropic phase boundary (MPB) of the $Pb(In_{1/2}Nb_{1/2})O_3$–$PbTiO_3$ system, where the structure of the PIN–PT compositions is gradually changing from pseudo-cubic to tetragonal. Earlier studies have reported the MPB composition for PIN–PT system at $x \sim 0.37$ [9–12]. Electrical data described later further support this observation.

SEM micrographs in Fig. 2 reveal fine grains microstructure in all PIN–PT ceramics with little variation of the average grain

Please cite this article in press as: S. Wongsaenmai et al., J. Alloys Compd. (2007), doi:10.1016/j.jallcom.2006.12.053

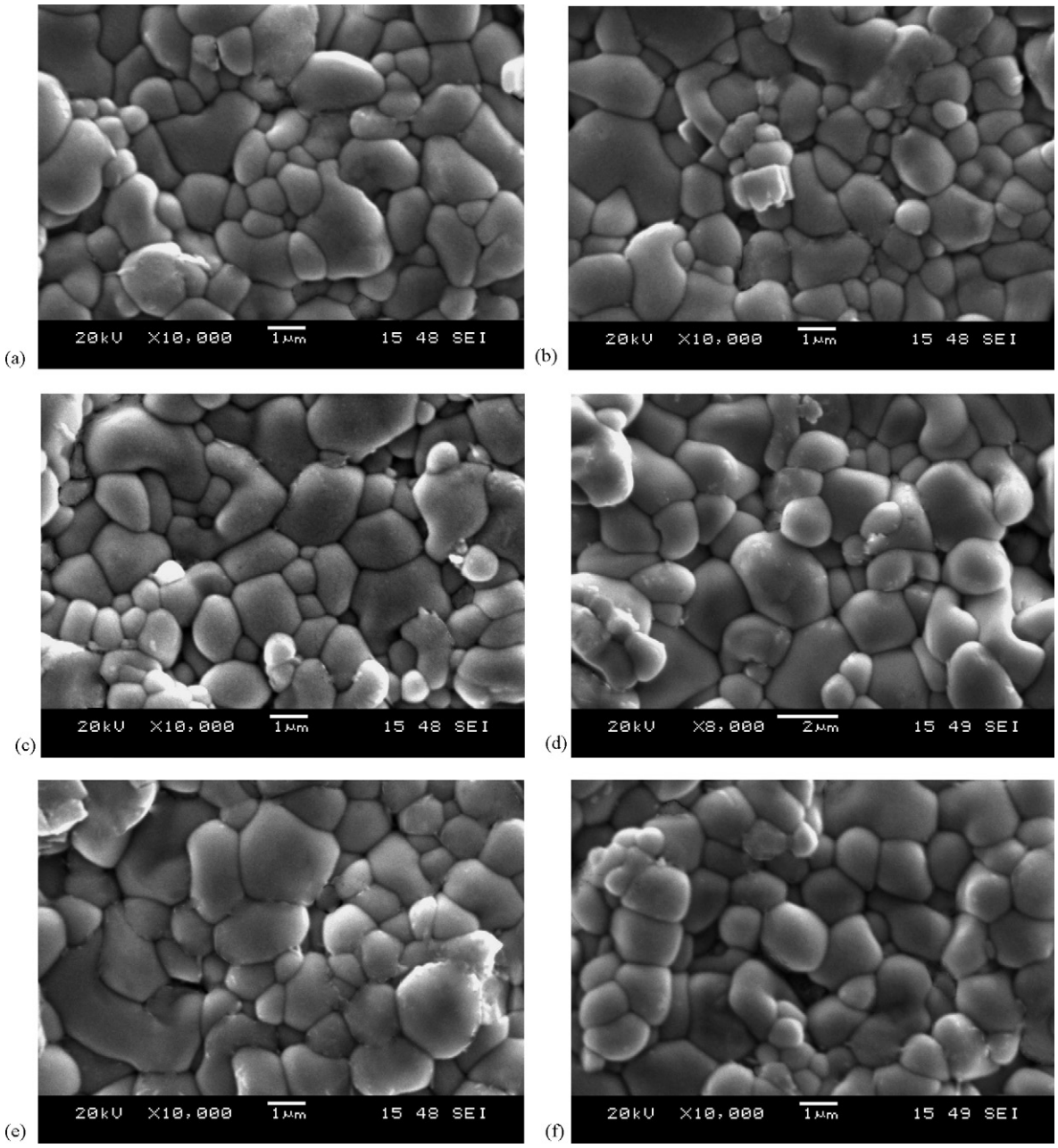

Fig. 2. SEM micrographs of $(1-x)$PIN–xPT with various compositions: (a) $x=0.0$, (b) $x=0.1$, (c) $x=0.2$, (d) $x=0.3$, (e) $x=0.4$, and (f) $x=0.5$.

size between 1 and 2 μm. The average grain size, as well as the density, does not vary significantly with the ceramic compositions, as listed in Table 1. However, it should be noticed that the microstructure of all the compositions also represents two distinct grain sizes, i.e. large grains (∼2 μm) and submicron grains. Earlier study on PIN–PT ceramics prepared with the conventional ball-milling method has also reported bimodal grain sizes but with large grains over 10 μm and fine grains about 1–2 μm [10]. Clearly, this shows the advantage of the vibro-milling technique in producing fine grains PIN–PT ceramics.

The dielectric properties, e.g. dielectric constant (ε_r) and $\tan\delta$, are measured as functions of both temperature and frequency, as shown in Fig. 3(a)–(f). As listed in Table 1 and plotted separately in Fig. 4, the maximum dielectric constant increases steadily with increasing PT content up to 30 mol% (ε_r increases from 4310 in PIN to 16028 in 0.7PIN–0.3PT). Then a drop in the dielectric constant is observed with further increase in PT content to 40 mol%. This supports the XRD observation that the MPB composition should lie between compositions $x=0.3$ and 0.4. It should also be noted that a rise in the dielectric constant with more PT content (50 mol%) is possibly caused by large thermal conduction at high temperature [26]. Furthermore, as listed in Table 1, since the transition temperature of PT is very high (490 °C) [27], it is expected to observe that the transition temperature increases with increasing amount of PT in the PIN–PT system. This is clearly evident in Fig. 4. Again, it should also be noted here that, as shown in Fig. 3, the dielectric properties of most compositions increase significantly at high temperature

Please cite this article in press as: S. Wongsaenmai et al., J. Alloys Compd. (2007), doi:10.1016/j.jallcom.2006.12.053

Table 1
Physical features and dielectric properties of $(1-x)$PIN–xPT ceramics (measured at 1 kHz)

x	Density (g/cm^3)	Grain size (μm)	T_{max} (°C)	ε_r at		$\Delta T = T_{m,100\,kHz} - T_{m,100\,Hz}$ (°C)	Diffusivity (γ)
				T_{max}	25 °C		
0.0	7.83	1.22 ± 0.08	71	4310	3345	26.2	1.89
0.1	7.51	1.29 ± 0.10	175	7120	2336	8.0	1.83
0.2	7.95	1.41 ± 0.12	210	10,733	1659	5.4	1.75
0.3	8.09	1.84 ± 0.16	267	16,028	1056	1.6	1.70
0.4	7.98	1.51 ± 0.16	327	11,867	1291	1.0	1.65
0.5	7.95	1.33 ± 0.10	375	15,038	573	0.4	1.62

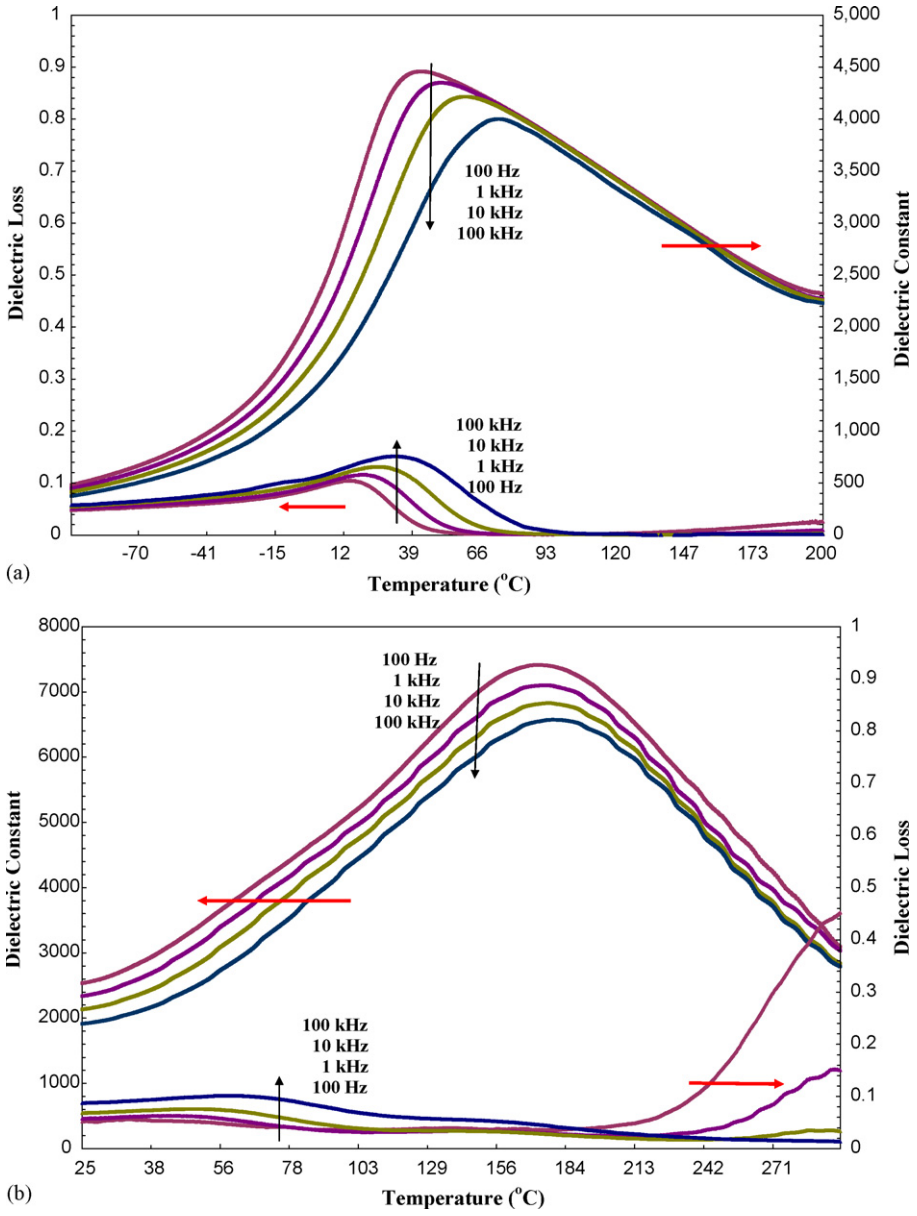

Fig. 3. (a) Temperature and frequency dependences of dielectric properties of PIN ceramic. (b) Temperature and frequency dependences of dielectric properties of 0.9PIN–0.1PT ceramic. (c) Temperature and frequency dependences of dielectric properties of 0.8PIN–0.2PT ceramic. (d) Temperature and frequency dependences of dielectric properties of 0.7PIN–0.3PT ceramic. (e) Temperature and frequency dependences of dielectric properties of 0.6PIN–0.4PT ceramic. (f) Temperature and frequency dependences of dielectric properties of 0.5PIN–0.5PT ceramic.

Please cite this article in press as: S. Wongsaenmai et al., J. Alloys Compd. (2007), doi:10.1016/j.jallcom.2006.12.053

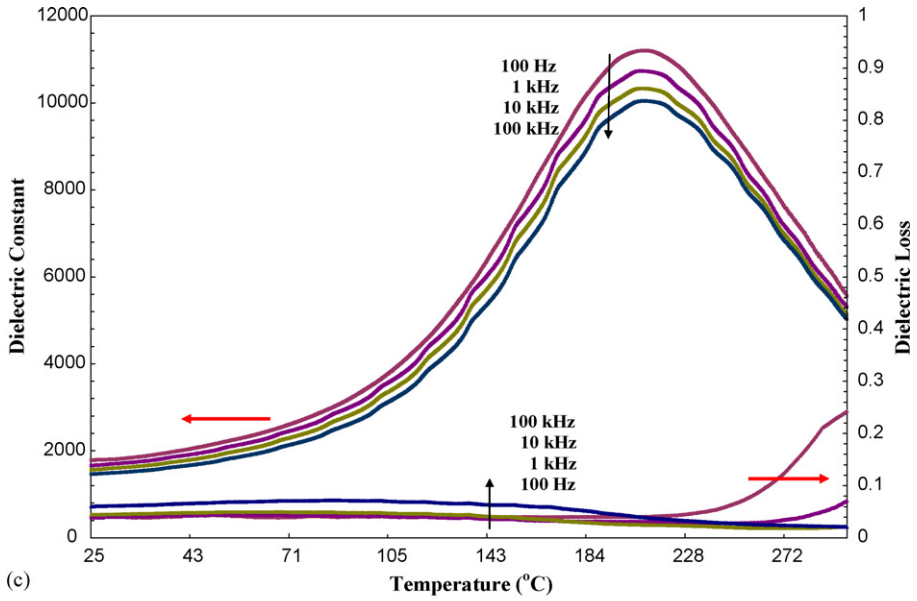

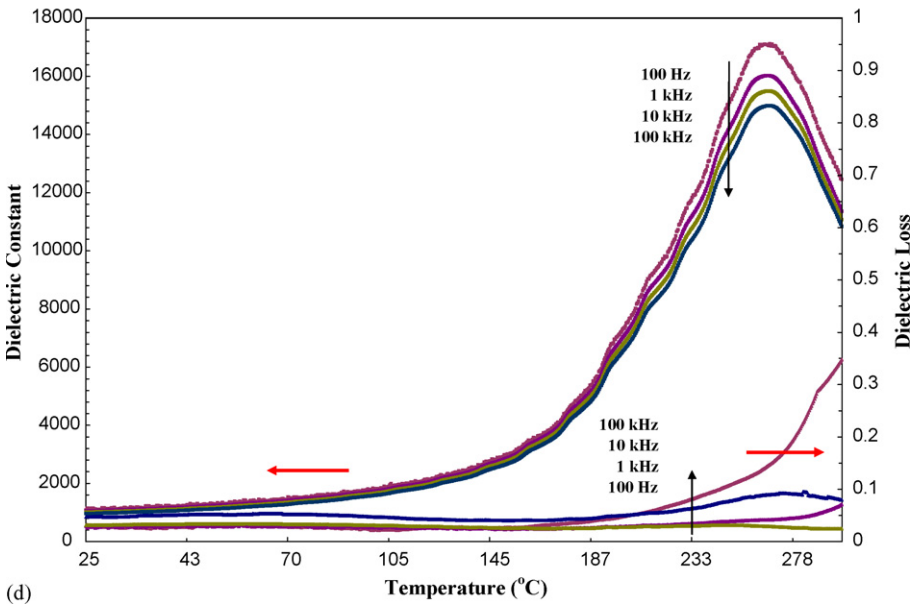

Fig. 3. (*Continued*)

as a result of thermally activated space charge conduction [26].

The dielectric properties of PIN ceramic, as plotted in Fig. 3(a), change significantly with temperature and frequency. Both dielectric constant (ε_r) and dielectric loss tangent ($\tan\delta$) exhibit strong temperature-frequency dependence below the transition temperature, indication of a typical relaxor ferroelectric behavior. In this case, the temperatures of maximum dielectric constant and dielectric loss tangent are shifted to higher temperature with increasing frequency. The maximum value of the dielectric constant decreases with increasing frequency, while that of the dielectric loss tangent increases. The dielectric properties then become frequency independence above the transition temperature [2,26]. While PIN exhibits a relaxor ferroelectric behavior, PT is a normal ferroelectric with nearly frequency-independent dielectric properties [27]. When PT is added to form the binary system with PIN, the dielectric behavior of PIN–PT should shift towards that of normal ferroelectric materials. As seen in Fig. 3(b)–(f), the dielectric properties exhibit a mixture of both normal and relaxor characteristics, in which the transition temperature is not shifted with frequency as much as for the PIN ceramic and the dielectric properties exhibit weaker temperature-frequency dependence below the transition temperature. This frequency dispersion in the dielectric properties can be quantified with $\Delta T = T_{m,100\,kHz} - T_{m,100\,Hz}$, which can be used as a rough estimate for more relaxor behavior with higher ΔT. As listed in Table 1, an addition of PT results in smaller ΔT. These results indicate the decreasing of relaxor behavior with increasing PT content [28]. Consequently, the dielectric peaks have become sharper with increasing PT content. Similar tendency has also been observed in several prior investigations [4–7,9,11].

Please cite this article in press as: S. Wongsaenmai et al., J. Alloys Compd. (2007), doi:10.1016/j.jallcom.2006.12.053

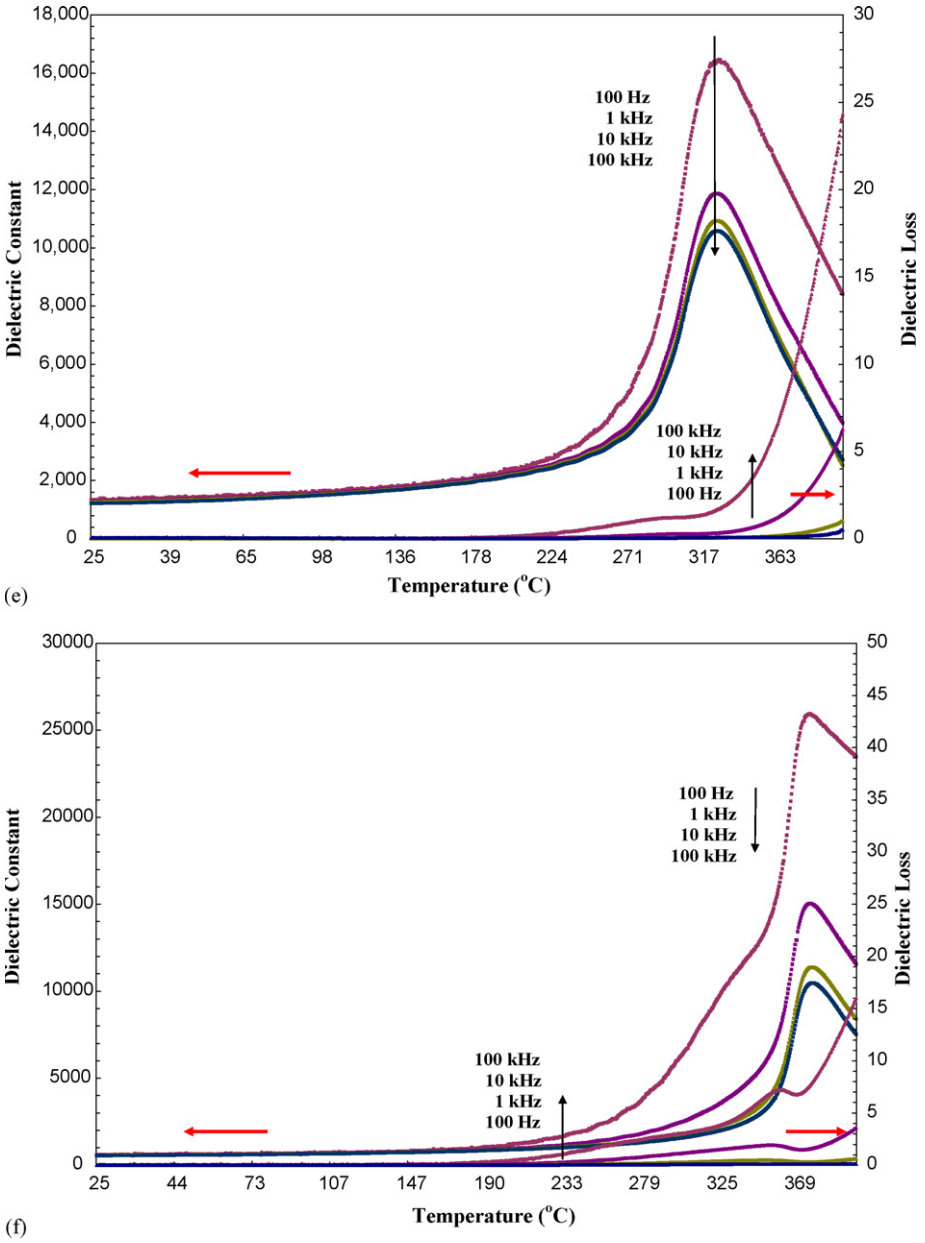

Fig. 3. (*Continued*).

The degree of broadening or diffuseness in the observed dielectric variation could also be estimated with the diffusivity (γ) using the expression $\ln(1/\varepsilon_r - 1/\varepsilon_{max})$ versus $(T - T_{max})^{\gamma}$. The value of γ can vary from 1, for normal ferroelectrics with a normal Curie–Weiss behavior, to 2, for completely disordered relaxor ferroelectrics [6,26]. The values of γ listed in Table 1 vary between 1.89 and 1.62, which confirms that diffuse phase transitions (DPT) occur in PIN–PT ceramics with a high degree of disorder. This observation clearly quantifies the decreasing of relaxor behavior with increasing PT content, as discussed earlier. Decreasing trend of γ value with increasing of PT content observed in PIN–PT system agrees with the previous study [29].

The dependence of temperature of maximum dielectric constant (T_m) on frequency of PIN–PT system can be explained with Vogel–Fulcher equation:

$$\varpi = f_0 \exp\left[\frac{-E_a}{k(T_m - T_f)}\right] \quad (1)$$

where f_0, E_a and T_f are the Debye frequency, the activation energy and the static freezing temperature, respectively [30]. The Debye frequency, the activation energy and the static freezing temperature obtained by fitting the experimental data with Eq. (1) are listed in Table 2. From Eq. (1), it is known that the activation energy is an internal energy of the cluster, which concerns with an anisotropy energy, K_{anis} and the cluster volume, V [31]. The fitting results show that the activation energy increases with increasing PT content for PIN–PT system, indicating that PT induces the increasing of the anisotropy energy and the cluster

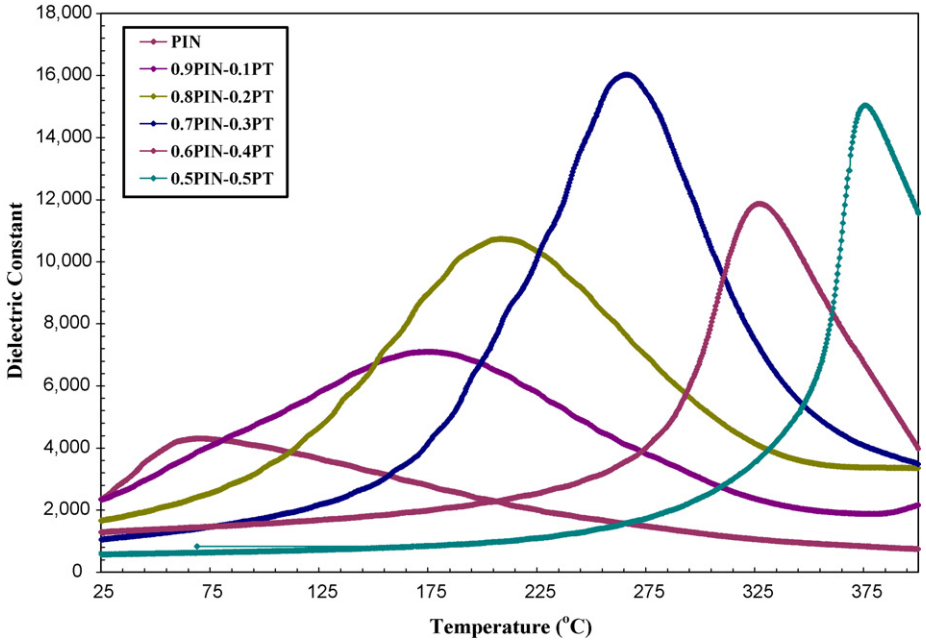

Fig. 4. Temperature dependence of dielectric constant of $(1-x)$PIN–xPT ceramics (measured at 1 kHz).

volume. It can be implied that size of isolated cluster or ordering increase with increasing PT contents [30,31]. For relaxor ferroelectrics, the value of Debye frequency concerns with size of polar nano-region and interaction between polar nano-regions [30]. In general, the stronger interaction and larger size show the smaller of the Debye frequency value [31]. Therefore, it can be implied that the increasing PT content shows marked effect in decreasing relaxor behavior by increasing size of and interaction between polar nano-regions, in good agreement with the observations discussed earlier. Similar observation has also been reported in other relaxor-based systems [32].

Fig. 5 illustrates a series of polarization (P–E) hysteresis loops for the PIN–PT ceramics. It is clearly evident that the shape of P–E loops varies greatly with the ceramic compositions. The hysteresis curve of PIN ceramic is of a "slim" loop type, a characteristic of the suppressed ferroelectric interaction [2,26]. This is typically found in the relaxor ferroelectrics with polar nano-regions. The hysteresis loops of PIN–PT ceramics become more developed showing large remnant polarization (P_r: remaining polarization when electric field is decreased to zero) and large saturated polarization (P_s) with increasing PT content up to 30 mol%. The hysteresis loops are of a typical "square" form as a result of domain switching in an applied field. This is a typical characteristic of a phase that contains long-range interaction between dipoles in the ferroelectric micro-domain state [26]. From the loops, the polarizations (P_r and P_s) and the coercive field E_C (indicating an electric field required to zero the polarization) are determined and listed in Table 3. In addition, the ferroelectric characteristic of the ceramics can be assessed with the hysteresis loop squareness (R_{sq}) which is typically understood to be the ratio of P_r/P_s where P_r is the remnant polarization at zero electric field and P_s is the saturated polarization obtained at some finite field strength below the dielectric breakdown. Jin et al. [33] used the loop squareness to measure not only the deviation in the polarization axis but also that in the electric field axis with the empirical expression $R_{sq} = (P_r/P_s) + (P_{1.1E_c}/P_r)$, where $P_{1.1E_c}$ is the polarization at the field equal to $1.1E_c$. For the ideal square loop, R_{sq} is equal to 2.00. As listed in Table 3, the value of R_{sq} increases with increasing PT content up to 30 mol%.

These results clearly indicate that an addition of PT induces the normal ferroelectric behaviors of PT into the PIN–PT ceramic system. More interestingly, it should also be noticed that a conclusion drawn from the XRD analysis and dielectric properties measurements discussed earlier that the MPB composition should exist between $x = 0.3$ and 0.4 is supported further

Table 2
The parameters obtained from fitting Vogel–Fulcher equation for $(1-x)$PIN–xPT ceramics

x	T_f (K)	f_0 (Hz)	E_a (eV)
0.0	310	3.9×10^{10}	0.042
0.1	434	3.0×10^{10}	0.015
0.2	471	2.8×10^{10}	0.010
0.3	535	2.6×10^{10}	0.004
0.4	599	2.3×10^{10}	0.002
0.5	649	1.4×10^{10}	0.001

Table 3
Ferroelectric properties of $(1-x)$PIN–xPT ceramics

x	Ferroelectric properties (at 25 °C)			Loop squareness (R_{sq})
	P_r (μC/cm^2)	P_s (μC/cm^2)	E_C (kV/cm)	
0.0	–	–	–	–
0.1	6.46	14.25	6.57	0.73
0.2	15.52	19.63	9.47	1.31
0.3	20.43	27.05	8.58	0.97
0.4	5.65	11.99	11.68	0.59
0.5	1.28	3.75	8.70	0.46

Please cite this article in press as: S. Wongsaenmai et al., J. Alloys Compd. (2007), doi:10.1016/j.jallcom.2006.12.053

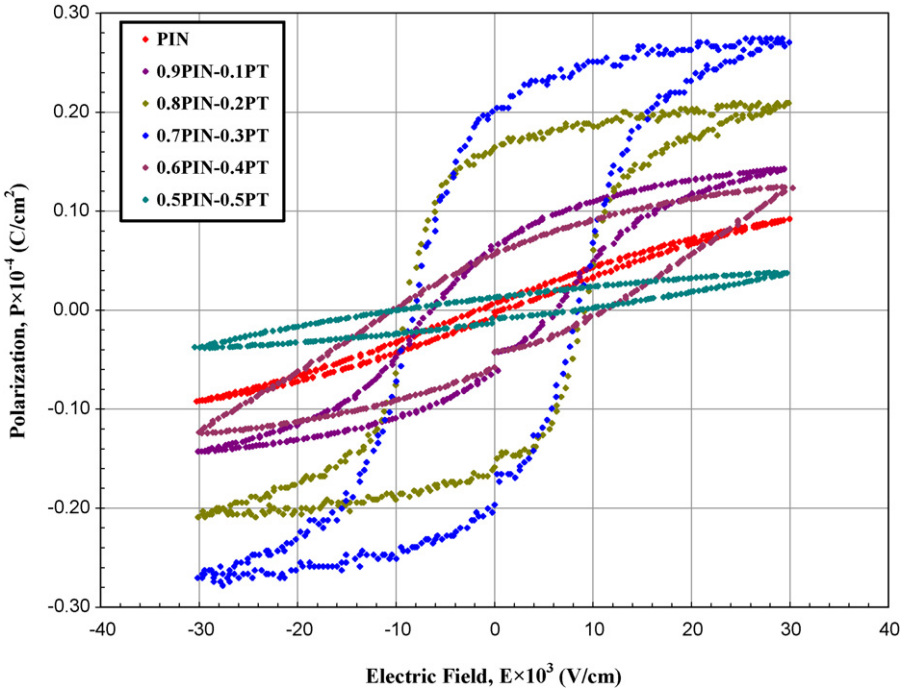

Fig. 5. *P–E* hysteresis loops of $(1-x)$PIN–xPT ceramics.

by the ferroelectric properties, as seen from a strong enhancement of polarization values with increasing PT content up to $x=0.3$, then a sudden drop of the polarization values with further increase in PT content. Finally, it is worthy noting that the fine grains PIN–PT ceramics obtained via the vibro-milling technique used in this study yield slightly better dielectric properties than the coarse grains PIN–PT ceramics in previous investigations [10–13]. However, as only very few investigations have been performed on PIN–PT ceramics, further investigations are still needed for more thoroughly and better comparison.

4. Conclusion

The $(1-x)Pb(In_{1/2}Nb_{1/2})O_3$–$xPbTiO_3$ (when $x=0.1$, 0.2, 0.3, 0.4, and 0.5) ceramics were prepared by an oxide-mixing method via a vibro-milling technique. The dielectric properties of the ceramics were determined as functions of both temperature and frequency with an automated dielectric measurement system, while the room temperature ferroelectric properties were measured by means of a standardized ferroelectric test system. The dielectric measurement took place over the temperature range of 25 and 400 °C with measuring frequency between 100 Hz and 100 kHz. Fine grains ceramics were achieved with average grain size of 1–2 μm, indicating advantage of the vibro-milling technique used. The results indicated that the dielectric properties of PIN ceramic were of relaxor ferroelectric behavior. The dielectric properties of PIN–PT ceramics showed a mixed relaxor and normal ferroelectric behavior, with more normal ferroelectric behavior observed with increasing PT content. The *P–E* hysteresis loop measurements demonstrated that the ferroelectric properties of the ceramics in PIN–PT system changed from the relaxor ferroelectric behavior in PIN ceramic to the normal ferroelectric behavior in PIN–PT ceramics. These results clearly show the significance of the added PT in reducing the relaxor ferroelectric behavior in PIN ceramic. More interestingly, XRD analysis, and dielectric and ferroelectric properties measurements also indicated the existence of the MPB composition between $x=0.3$ and 0.4. Finally, the fine grains PIN–PT ceramics showed slightly better dielectric properties than the coarse grains ceramics in previous investigations.

Acknowledgments

The authors would like to express their gratitude for financial supports from the Thailand Research Fund (TRF), Commission on Higher Education (CHE), Graduate School and Faculty of Science of Chiang Mai University, and Ministry of University Affairs in Thailand.

References

[1] K. Uchino, Ferroelectric Devices, Marcel Dekker, New York, 2000.
[2] G.H. Haertling, J. Am. Ceram. Soc. 82 (1999) 797–818.
[3] L.E. Cross, Mater. Chem. Phys. 43 (1996) 108–115.
[4] S.E. Park, T.R. Shrout, J. Appl. Phys. 82 (1997) 1804–1811.
[5] J. Kuwata, K. Uchino, S. Nomura, Jpn. J. Appl. Phys. 21 (1982) 1298–1302.
[6] R. Yimnirun, Int. J. Mod. Phys. B, in press.
[7] G. Xu, H. Luo, Y. Guo, Y. Gao, H. Xu, Z. Qi, W. Zhong, Z. Yin, Solid State Commun. 120 (2001) 321–324.
[8] N. Yasuda, H. Ohwa, M. Kume, Y. Yamashita, Jpn. J. Appl. Phys. 39 (2000) 5586–5588.
[9] N. Yasuda, H. Ohwa, D. Hasegawa, H. Hosono, Y. Yamashita, M. Iwata, Y. Ishibashi, Ferroelectrics 270 (2002) 247–252.
[10] M. Pham-Thi, C. Augier, H. Dammak, P. Gaucher, Ultrasonics 44 (2006) e627–e631.
[11] C. Augier, M. Pham-Thi, H. Dammak, P. Gaucher, J. Eur. Ceram. Soc. 25 (2005) 2429–2432.

[12] Y. Guo, H. Luo, T. He, Z. Yin, Solid State Commun. 123 (2002) 417–420.
[13] E.F. Alberta, A.S. Bhalla, J. Phys. Korea 32 (1998) s1265–s1269.
[14] N. Yasuda, M. Sakaguchi, Y. Itoh, H. Ohwa, Y. Yamashita, M. Iwata, Y. Ishibashi, Jpn. J. Appl. Phys. 42 (2003) 6205–6208.
[15] N. Yasuda, H. Ohwa, M. Kume, K. Hayashi, Y. Hosono, Y. Yamashita, J. Cryst. Growth 229 (2001) 299–304.
[16] B. Jaffe, W.R. Cook, H. Jaffe, Piezoelectric Ceramics, Academic Press, New York, 1971.
[17] Y.H. Xu, Ferroelectric Materials and their Applications, North Holland, Los Angeles, 1991.
[18] R. Wongmaneerung, R. Yimnirun, S. Ananta, Mater. Lett. 60 (2006) 2666–2671.
[19] R. Wongmaneerung, T. Sarnkonsri, R. Yimnirun, S. Ananta, Mater. Sci. Eng. B 130 (2006) 246–253.
[20] A. Ngamjarurojana, O. Khamman, R. Yimnirun, S. Ananta, Mater. Lett. 60 (2006) 2867–2872.
[21] S. Wongsaenmai, R. Yimnirun, S. Ananta, Mater. Lett., in press.
[22] E.F. Alberta, A.S. Bhalla, Mater. Lett. 29 (1996) 127–129.
[23] R. Wongmaneerung, R. Yimnirun, S. Ananta, Mater. Lett. 60 (2006) 1447–1452.
[24] S. Wongsaenmai, R. Yimnirun, S. Ananta, J. Mater. Sci., in press.
[25] S. Wongsaenmai, O. Khamman, S. Ananta, R. Yimnirun, J. Electroceram., in press.
[26] L.E. Cross, Ferroelectrics 76 (1987) 241–267.
[27] R. Wongmaneerung, R. Yimnirun, S. Ananta, Appl. Phys. A 86 (2007) 249–255.
[28] C. Lei, K. Chen, X. Zhang, J. Wang, Solid State Commun. 123 (2002) 445–450.
[29] M. Kuwabara, S. Takahashi, K. Goda, K. Oshima, K. Watanabe, Jpn. J. Appl. Phys. 31 (1992) 3241–3244.
[30] D. Viehland, S.-J. Jang, L.E. Cross, J. Appl. Phys. 68 (1990) 2916–2921.
[31] D. Viehland, S.-J. Jang, L.E. Cross, M. Wutting, Phys. Rev. B 46 (1992) 8003–8006.
[32] G. Singh, V.S. Triwari, V.K. Waghawan, Solid State Commun. 129 (2004) 665–670.
[33] B.M. Jin, J. Kim, S.C. Kim, Appl. Phys. A 65 (1997) 53–56.

Please cite this article in press as: S. Wongsaenmai et al., J. Alloys Compd. (2007), doi:10.1016/j.jallcom.2006.12.053

Available online at www.sciencedirect.com
ScienceDirect
Materials Letters xx (2007) xxx–xxx
materials letters
www.elsevier.com/locate/matlet

Effect of calcination conditions on phase formation and particle size of $Zn_3Nb_2O_8$ powders synthesized by solid-state reaction

A. Prasatkhetragarn, R. Yimnirun, S. Ananta *

Department of Physics, Faculty of Science, Chiang Mai University, Chiang Mai 50200, Thailand

Received 19 October 2006; accepted 21 December 2006

Abstract

The solid-state mixed oxide method via a rapid vibro-milling technique is explored in the preparation of single-phase $Zn_3Nb_2O_8$ powders. The formation of the $Zn_3Nb_2O_8$ phase in the calcined powders has been investigated as a function of calcination conditions by TG–DTA and XRD techniques. Morphology, particle size and chemical composition have been determined via a combination of SEM and EDX techniques. It has been found that the minor phases of unreacted ZnO and Nb_2O_5 precursors and the columbite $ZnNb_2O_6$ phase tend to form together with the $Zn_3Nb_2O_8$ phase, depending on calcination conditions. It is seen that optimization of calcination conditions can lead to a single-phase $Zn_3Nb_2O_8$ in a monoclinic phase.

Keywords: $Zn_3Nb_2O_8$; Calcination; Phase formation; Particle size; Nanopowders

1. Introduction

The quest for optimal powder characteristics (controlled chemical composition, homogeneity, reactivity, particle size and shape) in the fabrication of materials has directed attention particularly towards powder production techniques. It is known that various compositions are possible in the Zn–Nb–O system [1,2]. To date, three possible zinc niobium oxides have been identified: $ZnNb_2O_6$, $Zn_2Nb_{34}O_{87}$ and $Zn_3Nb_2O_8$ [1,2]. Amongst these compounds, zinc niobate ($ZnNb_2O_6$) is one of the most well-known materials, which has recently gained considerable attention [3,4]. This compound is very well known as the key precursor for the successful preparation of single-phase perovskite lead zinc niobate, $Pb(Zn_{1/3}Nb_{2/3})O_3$, or PZN-based materials, which are becoming increasingly important for multilayer ceramic capacitor, electrostrictor and actuator applications [5,6]. In general, production of single-phase $ZnNb_2O_6$ is not straightforward, as a minor concentration of the ZnO is sometimes formed alongside the major phase of $ZnNb_2O_6$ [7,8].

In contrast, very little is known about $Zn_3Nb_2O_8$, since no work has been dedicated to the synthesis of this compound.

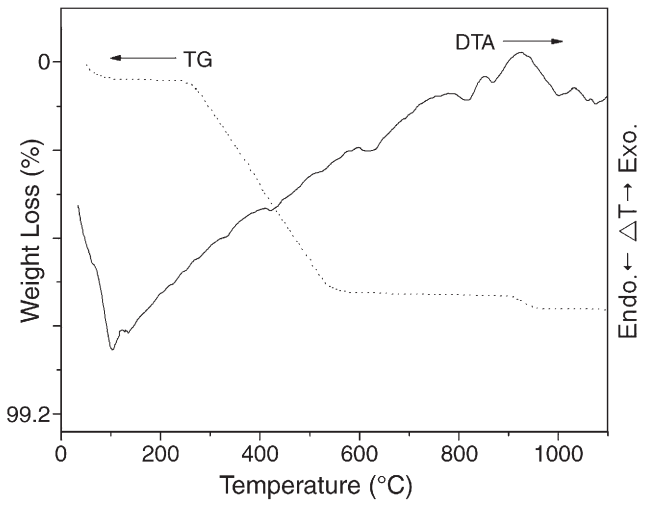

Fig. 1. TG–DTA curves for the mixture of $3ZnO–Nb_2O_5$ powder.

* Corresponding author. Tel.: +66 53 943367; fax: +66 53 943445.
E-mail address: Suponananta@yahoo.com (S. Ananta).

0167-577X/$ - see front matter © 2007 Published by Elsevier B.V.
doi:10.1016/j.matlet.2006.12.050

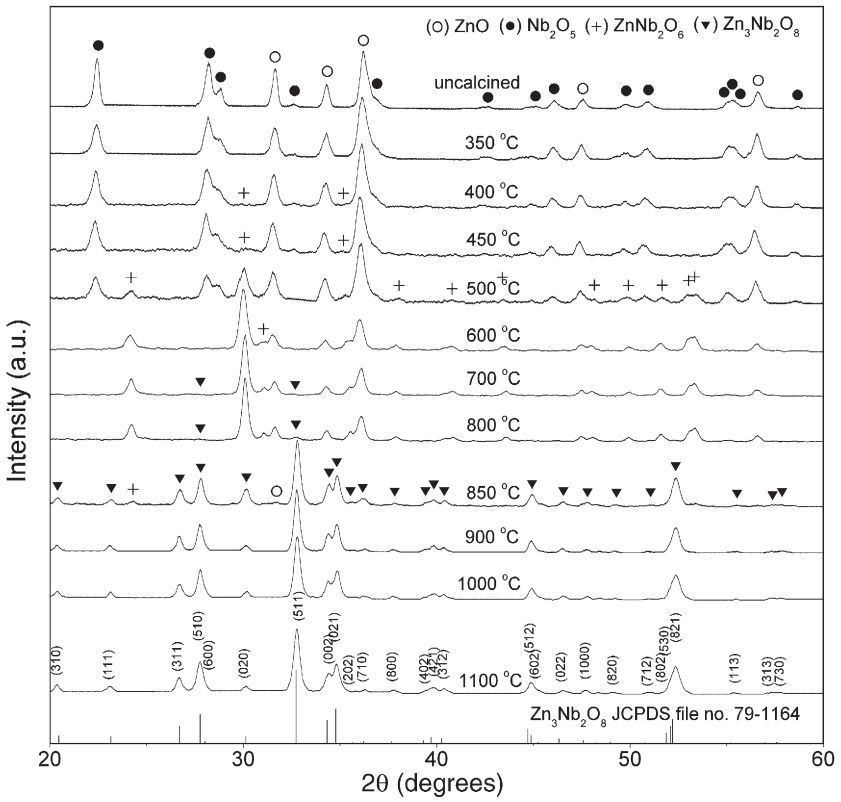

Fig. 2. XRD patterns of ZN powders calcined at various temperatures for 5 h with heating/cooling rates of 10 °C/min.

Much of the work concerning the $Zn_3Nb_2O_8$ compound has been directed towards determining crystal structure and microwave dielectric properties [9–11]. Kasper [10] and Isobe et al. [11] reported that the structure of $Zn_3Nb_2O_8$ is closely related to the columbite structure of $ZnNb_2O_6$. Its crystal structure can be represented as an order super-structure of α-PbO_2 [12]. Moreover, to date, the potential of $Zn_3Nb_2O_8$ as a possible alternative precursor for the preparation of PZN has not yet been reported. Interestingly, the mixed oxide route for the production of $Zn_3Nb_2O_8$ powders has not received detailed attention, and the effects of calcination conditions (*i.e.* applied firing temperature, dwell time and heating/cooling rates) have not yet been studied extensively. Therefore, the main purpose of this work was to explore a simple mixed oxide synthetic route

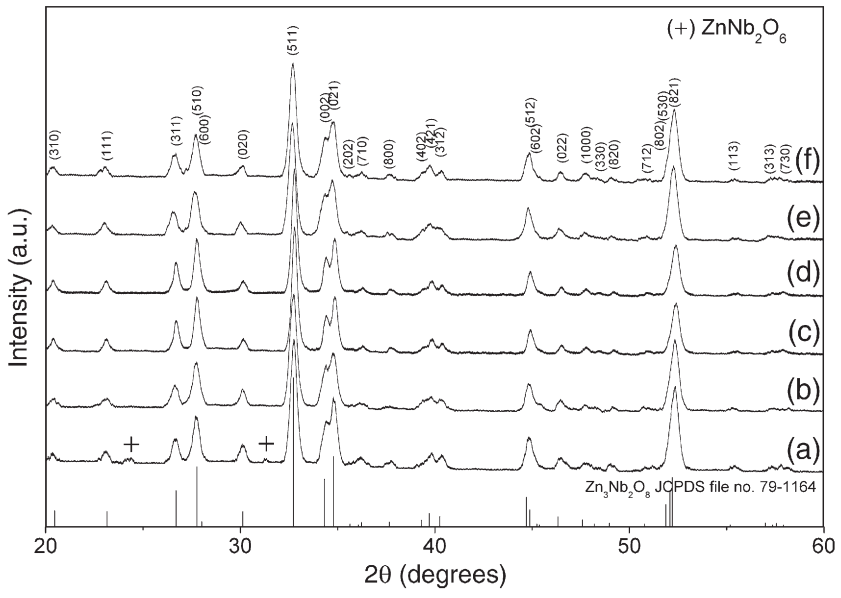

Fig. 3. XRD patterns of ZN powders calcined at 900 °C for (a) 0.5, (b) 1, (c) 2 and (d) 3 h, with heating/cooling rates of 10 °C/min and for 1 h with heating/cooling rates of (e) 20 and (f) 30 °C/min.

Please cite this article as: A. Prasatkhetragarn et al., Effect of calcination conditions on phase formation and particle size of $Zn_3Nb_2O_8$ powders synthesized by solid-state reaction, Mater. Lett. (2007), doi:10.1016/j.matlet.2006.12.050

for the production of $Zn_3Nb_2O_8$ powders via a rapid vibro-milling technique and to perform a systematic study of the reaction between the starting zinc oxide and niobium oxide precursors. The phase formation and morphology of the powder calcined at various conditions will be studied and discussed. The study also forms a possible basis for a further survey on PZN preparation.

2. Experimental procedure

The starting materials were commercially available zinc oxide, ZnO (JCPDS file number 89-1397) and niobium oxide, Nb_2O_5 (JCPDS file number 30-0873) (Aldrich, 99.9% purity). The two oxide powders exhibited an average particle size in the range 3.0–5.0 μm. $Zn_3Nb_2O_8$ powders were synthesized by the solid-state reaction of thoroughly ground mixtures of ZnO and Nb_2O_5 powders that were milled in the required stoichiometric ratio. In order to combine mixing capacity with a significant time saving, a McCrone vibro-milling technique [8,13] was carried out for 0.5 h with corundum cylindrical media in isopropyl alcohol (IPA). After drying at 120 °C for 2 h, the reaction of the uncalcined powders taking place during heat treatment was investigated by thermogravimetric and differential thermal analyses (TG–DTA, Shimadzu), using a heating rate of 10 °C/min in air from room temperature up to 1100 °C. Based on the TG–DTA results, the mixture was calcined at

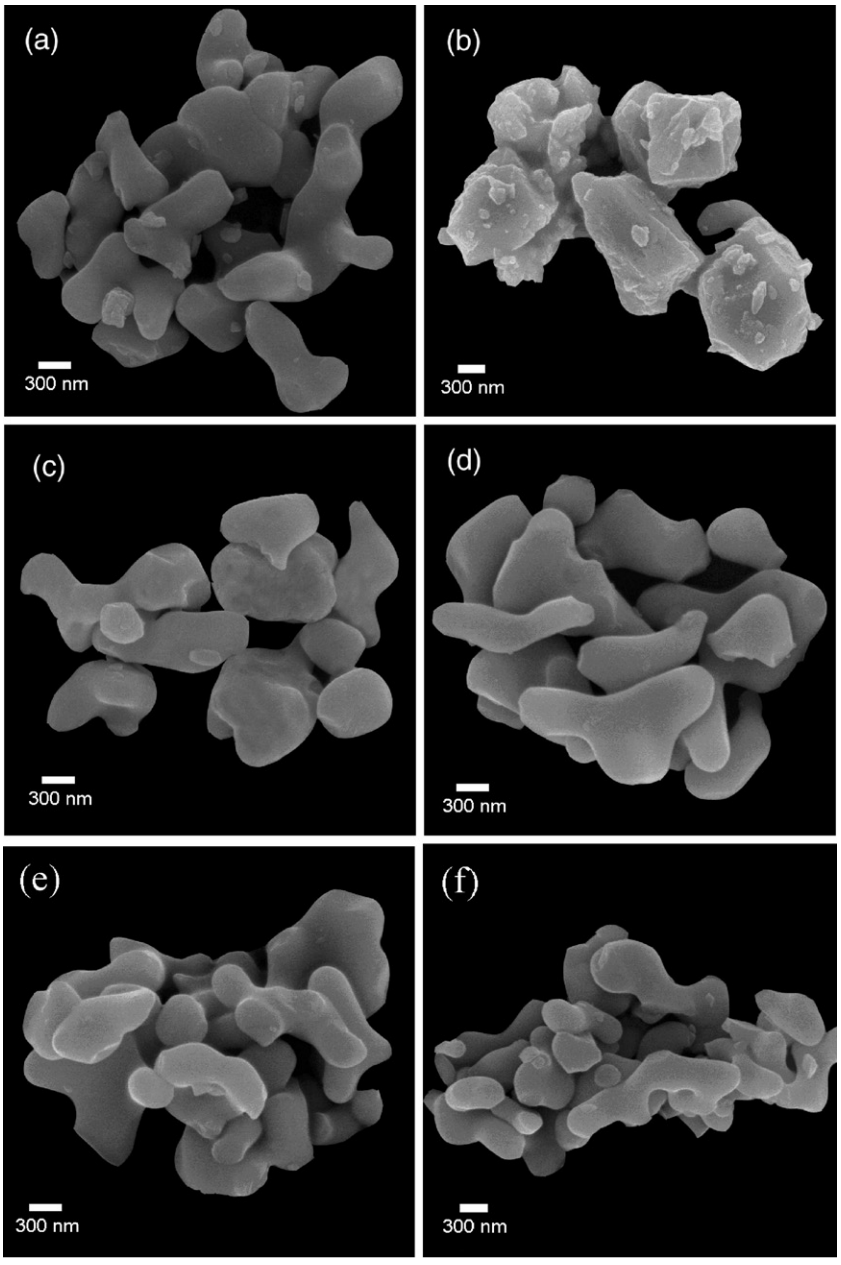

Fig. 4. SEM micrographs of ZN powders calcined for 1 h with heating/cooling rates of 10 °C/min at (a) 900 and (b) 1050 °C, and at 900 °C for (c) 3 and (d) 5 h; and at 900 °C for 1 h with heating/cooling rates of (e) 20 and (f) 30 °C/min.

Please cite this article as: A. Prasatkhetragarn et al., Effect of calcination conditions on phase formation and particle size of $Zn_3Nb_2O_8$ powders synthesized by solid-state reaction, Mater. Lett. (2007), doi:10.1016/j.matlet.2006.12.050

Table 1
Particle size range of $Zn_3Nb_2O_8$ powders calcined at various conditions

Calcination conditions			Particle size range	
Temperature (°C)	Dwell times (h)	Heating/cooling rates (°C/min)	SEM (±5 nm)	XRD (±0.05 nm)
900	1	10	60–1950	30.18
900	1	20	80–2130	31.11
900	1	30	110–2740	37.00
900	3	10	283–1988	35.31
900	5	10	313–2400	35.87
1050	1	10	80–2110	40.73

various conditions, in closed alumina crucible, in order to investigate the formation of $Zn_3Nb_2O_8$.

All powders were subsequently examined by room temperature X-ray diffraction (XRD; Siemens-D500 diffractometer), using Ni-filtered CuK_α radiation to identify the phases formed and optimum calcination conditions for the formation of $Zn_3Nb_2O_8$ powders. Powder morphologies and particle sizes were directly imaged, using scanning electron microscopy (SEM; JEOL JSM-840A). The chemical compositions of the phase formed were elucidated by an energy-dispersive X-ray (EDX) analyzer with an ultra-thin window. EDX spectra were quantified with the virtual standard peaks supplied with the Oxford Instruments eXL software.

3. Results and discussion

The TG–DTA simultaneous analysis of a powder mixed in the stoichiometric proportions of $Zn_3Nb_2O_8$ is displayed in Fig. 1. In the temperature range from room temperature to ~150 °C, the sample shows both exothermic and endothermic peaks in the DTA curve, consistent with the first weight loss. These observations can be attributed to the decomposition of the organic species such as rubber lining from the milling process similar to our earlier reports [8,13]. Corresponding to the second fall in sample weight, by increasing the temperature further to ~400 °C, a slight thermal fluctuation in the DTA curve is observed. This may be attributed to the crystallization of $ZnNb_2O_6$ as reported earlier [8]. Increasing the temperature up to ~1100 °C, the solid-state reaction occurred between ZnO and Nb_2O_5 [8,14]. The broad exotherm with several peaks in the DTA curve represents that reaction, which has maxima at ~830 °C and 900 °C. These are supported by the third falls in sample weight over the same temperature ranges. However, it is to be noted that there is no obvious interpretation of these peaks, although it is likely to correspond to a phase transition reported earlier [1,8,14]. These data were used to define the range of calcination temperatures for XRD investigation between 350 and 1100 °C.

To further study the phase development with increasing calcination temperature in the powders, they were calcined for 5 h in air at various temperatures, up to 1100 °C, followed by phase analysis using XRD. As shown in Fig. 2, for the uncalcined powders and the powders calcined at 350 °C, only X-ray peaks of precursors ZnO (○) and Nb_2O_5 (●), which could be matched with JCPDS file numbers 89-1397 [15] and 30-0873 [16], respectively, are present, indicating that no reaction had yet been triggered during the vibro-milling and low firing processes. However, it is seen that a small portion of the crystalline phase of the $ZnNb_2O_6$ crystallites (+) as reported by Ngamjarurojana et al. [8] was found as separated phases in the powders calcined at 400 °C, and became the predominant phase in the powder calcined above 450 °C. As the temperature increased to 800 °C, the intensity of the $ZnNb_2O_6$ peaks was further enhanced whereas some new peaks (▼) of the desired $Zn_3Nb_2O_8$ phase, started to appear, mixing with the $ZnNb_2O_6$ and ZnO phases after calcinations above 600 °C. These observations are associated with the DTA peaks found at the same temperature range within the broad exothermic effects in Fig. 1. In a first approximation, this $ZnNb_2O_6$ phase has a columbite-type structure with an orthorhombic unit cell (a=1420.8 pm, b=572.6 pm and c=504.0 pm, space group *Pbcn* (no. 60)), consistent with JCPDS file number 76-1827 [17]. This observation could be attributed mainly to the poor reactivity of zinc and niobium species [8]. Upon calcination at 900 °C, a single phase of $Zn_3Nb_2O_8$ is already formed. For the present work, there are no significant differences between the powders calcined at temperatures ranging from 900 to 1100 °C. This $Zn_3Nb_2O_8$ phase (JCPDS file number 79-1164 [18]) has a corundum structure with a monoclinic unit cell (a=1909.3 pm, b=592.7 pm and c=522.0 pm, space group *C2/c* (no. 15)), in agreement with the literature [11].

Apart from the calcination temperature, the effect of dwell time was also found to be quite significant. From Fig. 3, it can be seen that the single phase of $Zn_3Nb_2O_8$ (yield of 100% within the limitations of the XRD technique) was found to be possible in powders calcined at 900 °C with dwell time of at least 1 h (Fig. 3(a–d)) applied. This is probably due to the effectiveness of vibro-milling and a carefully optimized reaction. The observation that the dwell time may also play an important role in obtaining a single-phase corundum product is also consistent with other similar systems [8,19]. It is also very interesting to see that the on-set temperature is approximately 200–250 °C lower than that reported earlier with a conventional ball-milling method [9,14]. The difference could be attributed to nano-sized mixed powders obtained from a rapid vibro-milling. Most importantly, this study suggests that a rapid vibro-milling method can significantly lower the optimum calcination temperature for formation of single-phase $Zn_3Nb_2O_8$ powders.

In the present study, an attempt was also made to calcine $Zn_3Nb_2O_8$ powders under various heating/cooling rates (Fig. 3(b, e and f)). In this connection, it is shown that faster heating/cooling rates can also lead to crystallization of the $Zn_3Nb_2O_8$ phase. Based on the TG–DTA and XRD data, it may be concluded that, over a wide range of calcination conditions, a single phase of $Zn_3Nb_2O_8$ cannot be straightforwardly formed via a solid-state mixed oxide synthetic route, unless a careful design of calcination is performed. The experimental work carried out here suggests that the optimal calcination conditions for single-phase $Zn_3Nb_2O_8$ (with impurities undetected by XRD technique) are 900 °C for 1 h with heating/cooling rates as fast as 30 °C/min. Moreover, the formation temperature and dwell time for the production of $Zn_3Nb_2O_8$ powders observed in this work are also much lower than those reported

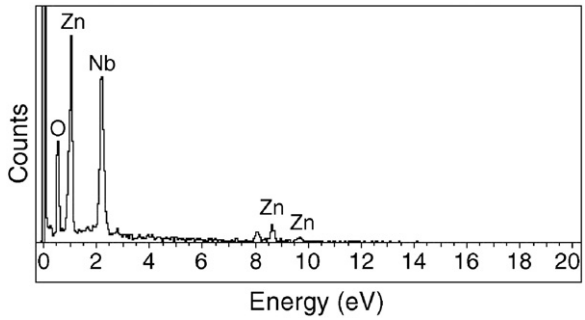

Fig. 5. EDX analysis of the $Zn_3Nb_2O_8$ powders.

Please cite this article as: A. Prasatkhetragarn et al., Effect of calcination conditions on phase formation and particle size of $Zn_3Nb_2O_8$ powders synthesized by solid-state reaction, Mater. Lett. (2007), doi:10.1016/j.matlet.2006.12.050

earlier [9,14]. This clearly emphasizes the advantages of a rapid vibro-milling technique.

Finally, the morphological changes in the $Zn_3Nb_2O_8$ powders formed by a mixed oxide are illustrated in Fig. 4(a–f) as a function of calcination temperatures, dwell times and heating/cooling rates, respectively. The influence of calcination conditions on particle size is given in Table 1. In general, the particles are agglomerated and irregular in shape, with a substantial variation in particle size, particularly in samples calcined at high temperature (Fig. 4(b)) or with fast heating/cooling rates (Fig. 4(e, f)). This finding is also similar to that in $ZnNb_2O_6$ and $ZrTiO_4$ powders [8,20]. The results indicate that calculated crystalline size and degree of agglomeration tend to increase with calcination temperatures or heating/cooling rates (Table 1). All powders seem to display a significant level of necking and bonding as if they were in the initial stages of sintering. This observation could be attributed to the mechanism of surface energy reduction of the ultrafine powders, *i.e.* the smaller the powder the higher the specific surface area [21]. To the authors' knowledge, the present data are the first results for the morphology–calcination relationship of $Zn_3Nb_2O_8$ powders prepared by the solid-state reaction. It is also of interest to point out that mass production of single-phase $Zn_3Nb_2O_8$ nanopowders with the smallest particle size of ~60 nm (estimated from SEM micrographs) can be achieved by employing a simple solid-state reaction combined with a rapid vibro-milling technique. In addition, EDX analysis using a 20 nm probe on a large number of particles of the calcined powders confirms that the parent composition is $Zn_3Nb_2O_8$ (Fig. 5), in good agreement with XRD results.

4. Conclusions

The potential of a rapid vibro-milling technique as a significant time saving method to obtain single-phase $Zn_3Nb_2O_8$ nanopowders at low calcination temperatures has been demonstrated. The calcination conditions have been found to have a pronounced effect on both phase formation and particle size of the calcined $Zn_3Nb_2O_8$ powders. The resulting $Zn_3Nb_2O_8$ powders consist of a variety of agglomerated particle sizes, depending on the calcination conditions.

Acknowledgements

This work was supported by the Thailand Research Fund (TRF), the Commission on Higher Education (CHE), the Faculty of Science and the Graduate School, Chiang Mai University.

References

[1] A.J. Pollard, J. Am. Ceram. Soc. 44 (1961) 630.
[2] R.R. Dayal, J. Less-Common Met. 26 (1972) 381.
[3] R.C. Pullar, J.D. Breeze, N.M. Alford, J. Am. Ceram. Soc. 88 (2005) 2466.
[4] Y.C. Zhang, Z.X. Yue, Z.L. Gui, L.T. Li, Ceram. Int. 29 (2003) 555.
[5] J. Wang, W. Dongmei, X. Junmin, N.W. Beng, J. Am. Ceram. Soc. 82 (1999) 477.
[6] A.J. Moulson, J.M. Herbert, Electroceramics, 2nd ed.Wiley, Chichester, 2003.
[7] C.L. Li, C.C. Chou, Int. Ferro., vol. 55, 2003, p. 955.
[8] A. Ngamjarurojana, O. Khamman, R. Yimnirun, S. Ananta, Mater. Lett. 60 (2006) 2867.
[9] D.W. Kim, J.H. Kim, J.R. Kim, K.S. Hong, Jpn. J. Appl. Phys. 40 (2001) 5994.
[10] H. Kasper, Z. Anorg, Allg. Chem. 355 (1967) 1.
[11] M. Isobe, F. Marumo, S.I. Iwai, Y. Kondo, Bull. Tokyo Inst. Technol. 120 (1974) 1.
[12] F. Laves, G. Bayer, A. Panagos, Schweiz. Mineral. Petrogr. Mitt. 43 (1963) 217.
[13] R. Wongmaneerung, R. Yimnirun, S. Ananta, Mater. Lett. 60 (2006) 1447.
[14] Y.C. Lee, C.H. Lin, I.N. Lin, Mater. Chem. Phys. 79 (2003) 124.
[15] Powder Diffraction File No. 89-1397, International Centre for Diffraction Data, Newton Square, PA, 2000.
[16] Powder Diffraction File No. 30-0873, International Centre for Diffraction Data, Newton Square, PA, 2000.
[17] Powder Diffraction File No. 76-1827, International Centre for Diffraction Data, Newton Square, PA, 2000.
[18] Powder Diffraction File No. 79-1164, International Centre for Diffraction Data, Newton Square, PA, 2000.
[19] S. Ananta, Mater. Lett. 58 (2004) 2530.
[20] S. Ananta, R. Tipakontitikul, T. Tunkasiri, Mater. Lett. 57 (2003) 2637.
[21] J.S. Reed, Principles of Ceramic Processing, 2nd ed.Wiley, New York, 1995.

Please cite this article as: A. Prasatkhetragarn et al., Effect of calcination conditions on phase formation and particle size of $Zn_3Nb_2O_8$ powders synthesized by solid-state reaction, Mater. Lett. (2007), doi:10.1016/j.matlet.2006.12.050

J Mater Sci
DOI 10.1007/s10853-006-0404-1

Influence of calcination conditions on phase formation and particle size of indium niobate powders synthesized by the solid-state reaction

S. Wongsaenmai · R. Yimnirun · S. Ananta

Received: 4 November 2005 / Accepted: 2 May 2006

Abstract A wolframite-type phase of indium niobate, $InNbO_4$, has been synthesized by a solid-state reaction via a rapid vibro-milling technique. The formation of the $InNbO_4$ phase in the calcined powders has been investigated as a function of calcination conditions by TG-DTA and XRD techniques. Morphology, particle size and chemical composition have been determined via a combination of SEM and EDX techniques. Single-phase $InNbO_4$ powders have been obtained successfully for calcination condition of 900 °C for 4 h or 950 °C for 2 h with heating/cooling rates of 30 °C/min. Higher temperatures and longer dwell times clearly favoured particle growth and the formation of large and hard agglomerates.

Introduction

Indium niobate ($InNbO_4$, IN) is one of the binary niobate compounds with a wolframite crystal structure [1]. Earlier works concerning the $InNbO_4$ have been directed towards determining low-temperature dielectric [2], luminescent [3] and photocatalytic [4] properties. Recently, this compound is also a potential material for the development of photocatalytic systems capable of splitting water into H_2 and O_2 under visible light irradiation [5–7]. Moreover, it is well established as a key precursor for the partially successful preparation of single-phase ferroelectric perovskite lead indium niobate $Pb(In_{1/2}Nb_{1/2})O_3$ (PIN)-based ceramics, which is becoming increasingly important for actuator, transducer and ultrasonic motor applications [8, 9].

There has been a great deal of interest in the preparation of single-phase PIN powders as well as in the phase transition, ordering behaviour and electrical properties of PIN-based ceramics [10–18]. In general, the constituents In_2O_3 and Nb_2O_5 are first mixed and reacted together to form indium niobate ($InNbO_4$), prior to mixing and reacting with PbO in the second step of calcination at elevated temperature. Interestingly, this mixed oxide route has been employed with minor modifications in the synthesis of $InNbO_4$ itself [13–16]. However, powders prepared by a mixed oxide route have spatial fluctuations in their compositions. The extent of the fluctuations depends on the characteristics of the starting powders as well as on the processing schedule. Generally, the mixed oxide method involves the heating of a mixture of indium oxide and niobium oxide above 1,000 °C for long times i.e. 4 h [10, 13], 12 h [6], 24 h [14–17] and 48 h [4, 7]. The optimization of calcination conditions used in the mixed oxide process, however, has not received detailed attention, and the effects of applied dwell time and heating/cooling rates have not yet been studied extensively.

Therefore, the main purpose of this work is to explore a simple mixed oxide synthetic route for the production of $InNbO_4$ powders via a rapid vibro-milling technique and to perform a systematic study of the reaction between the starting indium oxide and niobium oxide precursors. The phase formation and morphology of the powders calcined at various conditions will be studied and discussed. The rapid vibro-milling technique is

S. Wongsaenmai · R. Yimnirun · S. Ananta (✉)
Department of Physics, Faculty of Science, Chiang Mai University, Chiang Mai 50200, Thailand
e-mail: Supon@chiangmai.ac.th

employed to explore the potentiality in obtaining nano-sized powders, which would in turn lead to lower required firing temperature.

Experimental procedure

The starting materials were commercially available indium oxide, In_2O_3 (JCPDS file number 71-2195) and niobium oxide, Nb_2O_5 (JCPDS file number 30-873) (Aldrich, 99.9% purity). The two oxide powders exhibited an average particle size in the range of 1.0–3.0 μm. $InNbO_4$ powders were synthesized by the solid-state reaction of thoroughly ground mixtures of In_2O_3 and Nb_2O_5 powders that were milled in the required stoichiometric ratio. Instead of employing a ball-milling procedure [10, 16], a McCrone vibro-milling technique was used [19, 20]. In this technique, a vibratory laboratory mill (McCrone Micronizing Mill) powered by a 1/30 HP motor was employed. The grinding vessel consists of a 125 mL capacity polypropylene jar fitted with a screw-capped, gasketless, polythene closure. The jar is packed with an ordered array of identical, cylindrical, grinding media of polycrystalline corundum. A total of 48 milling media with a powder weight of 20 g was kept constant in each batch. The milling operation was carried out in isopropanal inert to the polypropylene jar. In order to combine mixing capacity with a significant time saving, the milling operation was carried out for 0.5 h with corundum cylindrical media in isopropyl alcohol (IPA). After drying at 120 °C for 2 h, the reaction of the uncalcined powders taking place during heat treatment was investigated by themogravimetric and differential thermal analysis (TG-DTA, Shimadzu), using a heating rate of 10 °C/min in air from room temperature up to 1,000 °C. Based on the TG-DTA results, the mixture (~10 g for each batch) was calcined at various conditions, i.e. temperatures ranging from 700 °C to 1,200 °C, dwell times ranging from 0.5 h to 4 h and heating/cooling rates ranging from 3 °C/min to 30 °C/min, in closed alumina crucible [cylindrical shape with 25 mL capacity (3 cm in diameter and 3.5 cm in height)], in order to investigate the formation of indium niobate.

Calcined powders were subsequently examined by room temperature X-ray diffraction (XRD; Siemens-D500 diffractometer), using Ni-filtered CuK_α radiation to identify the phases formed and optimum calcination conditions for the formation of $InNbO_4$ powders. Powder morphologies and particle sizes were directly imaged, using scanning electron microscopy (SEM; JEOL JSM-840A). The chemical compositions of the phase formed were elucidated by an energy-dispersive X-ray (EDX) analyzer with an ultra-thin window. EDX spectra were quantified with the virtual standard peaks supplied with the Oxford Instruments eXL software.

Results and discussion

The TG-DTA simultaneous analysis of a powder mixed in the stoichiometric proportion of $InNbO_4$ is displayed in Fig. 1. The TG curve shows two distinct weight losses. In the temperature range from room temperature to ~150 °C, both exothermic and endothermic peaks are observed in the DTA curve, in consistent with the first weight loss. These observations can be attributed to the decomposition of the organic species (i.e. polyethylene milling jar, rubber gloves, skin, etc.) from the milling process [19, 20]. Increasing the temperature up to ~1,000 °C, the solid-state reaction occurred between In_2O_3 and Nb_2O_5 [10, 16]. The broad exotherm in the DTA curve represents that reaction, which has a maximum at ~500 °C. This is supported by a large fall in sample weight over the same temperature range. The causes for these observations are not well documented, but could probably be related to (i) the partial formation of InO_6 and NbO_6 octahedra prior to $InNbO_4$ formation [6, 7] and (ii) the possible formation of $InNbO_4$ in a very small container containing only 0.5 g of powder in TG-DTA apparatus. It should be noted, however, that in the calcination process, a much larger crucible containing ~10 g of powder was used, hence, higher calcination temperature than that observed from TG-DTA is expected. Although the DTA curve shows that there are other small peaks at ~750, 850 and 900 °C, however, it is to be noted that there is no obvious interpretation of these peaks. These data were used to

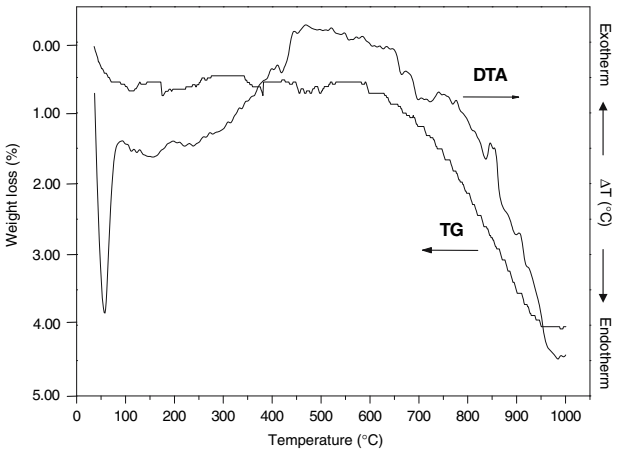

Fig. 1 TG-DTA curves for the mixture of In_2O_3–Nb_2O_5 powder

define the range of calcination temperatures for XRD investigation to between 700 °C and 1,200 °C.

To further study the phase development with increasing calcination temperature in the powders, they were calcined for 2 h in air at various temperatures, up to 1,200 °C, followed by phase analysis using XRD. As shown in Fig. 2, for the uncalcined powders and the powders calcined at 700 °C, only X-ray peaks of precursors In_2O_3 (•) and Nb_2O_5 (○), which could be matched with JCPDS file numbers 71-2195 [21] and 30-873 [22], respectively, are present, indicating that no reaction had yet been triggered during the milling or low firing processes. It is seen that fine $InNbO_4$ crystallites (∇) were developed in the powders at a calcination temperature as low as 750 °C, accompanying with In_2O_3 and Nb_2O_5 as separated phases. This observation agrees well with those derived from the TG-DTA results. As the temperature increased to 900 °C, the intensity of the wolframite-like $InNbO_4$ peaks was further enhanced and became the predominant phase. Upon calcination at 950 °C, an essentially monophasic of $InNbO_4$ phase is obtained. This $InNbO_4$ phase was indexable according to a monoclinic wolframite-type structure with lattice parameters $a = 514.40$ pm, $b = 577.09$ pm, $c = 483.55$ pm and $\beta = 91.13°$, space group $P2/a$ (no. 13), in consistent with JCPDS file numbers 83-1780 [23] and literature [3, 6]. This study also shows that monoclinic $InNbO_4$ is the only detectable phase in the powders, after calcination in the range of 950–1,200 °C. The variation of the intensity ratio between the two major peaks $(11\bar{1})$ and (111) at 2θ~29–31° could be attributed mainly to the expansion of the NbO_6 volume similar with those observed in other ABO_4 systems [3, 6]. In the structure of $InNbO_4$, there are two kinds of octahedron, InO_6 and NbO_6. The InO_6 octahedron connects to each other to form zigzag chain by sharing edges. These chains are connected through NbO_6 octahedron to form the three-dimensional network [6, 7, 24]. It is believed that the InO_6 chains are highly distorted because they must accommodate the strain of the defect, which probably leads to lattice rotation [11].

In earlier works [4, 6, 10, 14], long heat treatments at ~1,000–1,200 °C for 4, 12, 24 and 48 h were proposed for the formation of $InNbO_4$ by a conventional mixed oxide synthetic route, although no details on phase formation were provided. However, in the present study, it was found that, except the fluctuation of the intensity ratio between the $(11\bar{1})$ and (111) peaks, there are no significant differences between the powders calcined at 950 °C to 1,200 °C with dwell time of only 2 h, as shown in Fig. 2. This observation would clearly suggest the advantages of a rapid vibro-milling technique used in the present study.

Apart from the calcination temperature, the effect of dwell time was also found to be quite significant. From Fig. 3, it can be seen that the single phase of $InNbO_4$ (yield of 100% within the limitations of the XRD technique) was found to be possible in powders calcined at 950 °C with dwell time of 2 h or more. The appearance of In_2O_3 and Nb_2O_5 phases indicated that full crystallization has not occurred at relatively short calcination times. However, in the work reported here, it is to be noted that single phase of $InNbO_4$ powders was also successfully obtained for a calcination temperature of 900 °C with dwell time of at least 4 h

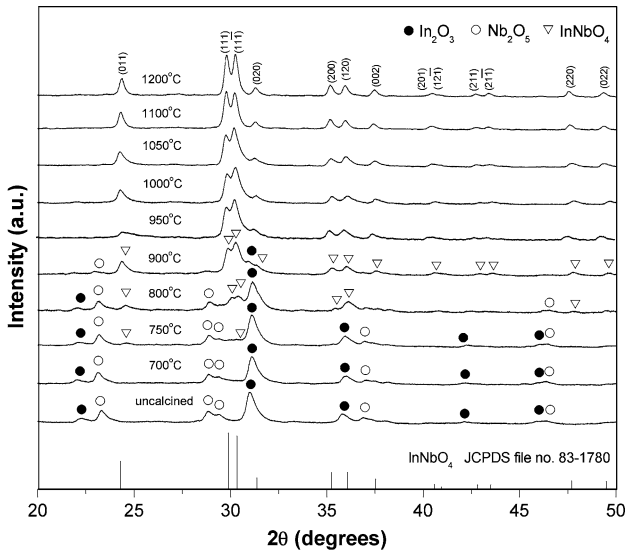

Fig. 2 XRD patterns of IN powders calcined at various temperatures for 2 h with heating/cooling rates of 10 °C/min

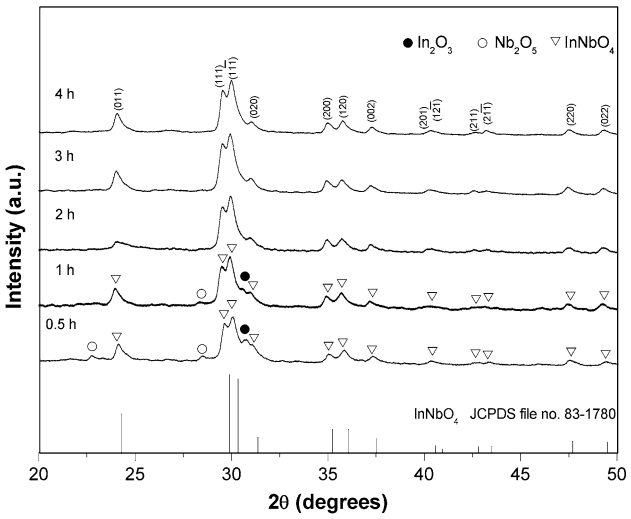

Fig. 3 XRD patterns of IN powders calcined at 950 °C with heating/cooling rates of 10 °C/min for various dwell times

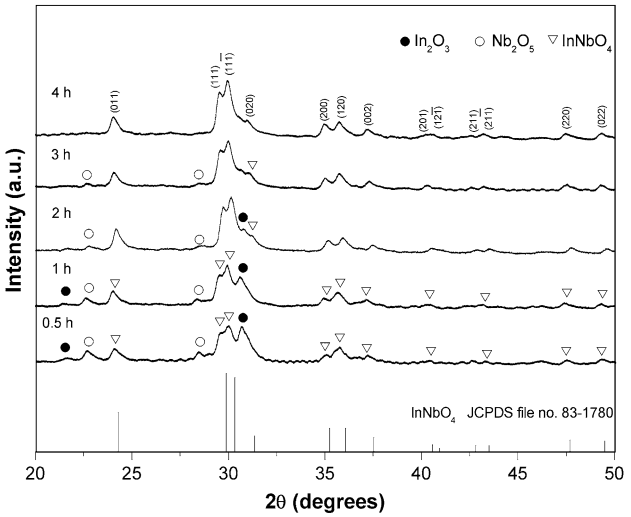

Fig. 4 XRD patterns of IN powders calcined at 900 °C with heating/cooling rates of 10 °C/min for various dwell times

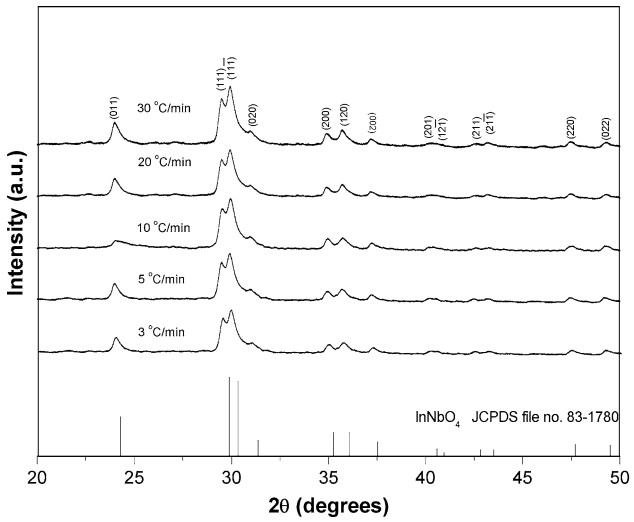

Fig. 5 XRD patterns of IN powders calcined at 950 °C for 2 h with various heating/cooling rates

applied (Fig. 4). This was apparently a consequence of the enhancement in crystallinity of the $InNbO_4$ phase with increasing dwell time. The observation that the dwell time effect may also play an important role in obtaining a single-phase wolframite product is also consistent with other similar systems [19, 25, 26]. It is also very interesting to see that the on-set firing time is approximately 2–22 h shorter than those reported earlier with a conventional ball-milling method [10–17]. The difference could be attributed to the effectiveness of vibro-milling and a carefully optimized reaction. Most importantly, this study suggests that a rapid vibro-milling method can significantly lower the optimum calcination temperature and dwell time for formation of single-phase $InNbO_4$ powders.

In the present study, an attempt was also made to calcine $InNbO_4$ powders under various heating/cooling rates. In this connection, it is shown that for the powders calcined at 950 °C for 2 h, the yield of $InNbO_4$ phase did not vary significantly with different heating/cooling rates, ranging from 3 °C/min to 30 °C/min (Fig. 5). However, for the powders calcined at 900 °C for 4 h, different result was observed. It is seen that single-phase $InNbO_4$ can be detected only in the powders where heating/cooling rates of 10 °C/min or faster were applied (Fig. 6). These results indicated that faster heating/cooling rates can probably lead to better crystallization of $InNbO_4$ phase without time for the indium vaporization (due to the volatilization of In_2O_3). The observation that faster heating/cooling rates are required for the mixtures containing *volatile* oxide constituent (In_2O_3), is in good agreement with early results reported in other similar systems [27, 28].

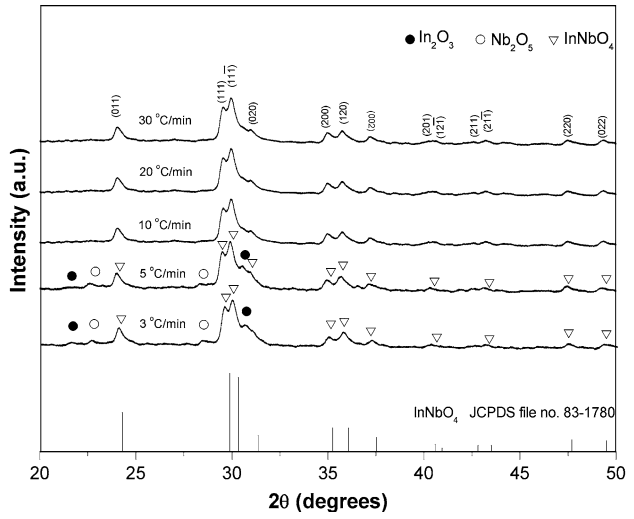

Fig. 6 XRD patterns of IN powders calcined at 900 °C for 4 h with various heating/cooling rates

Based on the TG-DTA and XRD data, it may be concluded that, over a wide range of calcination conditions, single-phase $InNbO_4$ cannot be straightforwardly formed via a solid-state mixed oxide synthetic route, unless a careful design of calcination condition is performed. It is well documented that powders prepared by a conventional mixed oxide method have spatial fluctuations in their compositions. The extent of the fluctuation depends on the characteristics of the starting powders as well as the processing schedules [20, 26]. It is rather surprising that no evidence of the monoclinic *P*2/*c* (13) of $InNbO_4$ [29, 30] was found in this study, nor was there any indication of the one with *P*2/*a* (13) reported by Brixner and Chen [3, 31] being

present. The experimental work carried out here suggests that the optimal calcination conditions for single-phase $InNbO_4$ (with impurities undetected by XRD technique) is 950 °C for 2 h or 900 °C for 4 h, with heating/cooling rates as fast as 30 °C/min. Moreover, the formation temperature and dwell time for the production of $InNbO_4$ powders observed in this work are also lower than those reported earlier [13–17]. This clearly emphasizes the advantages of a combination between a rapid vibro-milling technique and a carefully optimized reaction.

The morphological evolution during calcination was investigated by scanning electron microscopy (SEM). Micrographs of $InNbO_4$ powders calcined at various temperatures, dwell times and heating/cooling rates are illustrated in Figs. 7 and 8. The influence of calcination conditions on particle size is also given in Table 1. After calcinations at 950–1,200 °C, the powders have similar morphology (Fig. 7). In general, the particles are agglomerated and irregular in shape, with a substantial variation in particle size, particularly in samples calcined at high temperature (Fig. 7d). The results indicate that averaged particle size tends to increase with calcination temperatures and dwell times but seems to decrease with faster heating/cooling rates (Table 1). After calcinations above 950 °C (Fig. 7b–d), the powders seem to display a significant level of necking and bonding as if they were in the initial stages of sintering.

The effects of dwell time and heating/cooling rates on the morphology of the calcined powders were also found to be quite significant. As expected, it is seen that longer heat treatment leads to larger particle sizes and hard agglomeration (Figs. 7a, 8a, b). As shown in Figs. 7a, 8c, d, and also Table 1, by increasing the heating/cooling rates, averaged particle size tends to decrease whilst the degree of agglomeration tends to increase. This observation could be attributed to the mechanism of surface energy reduction of the ultrafine powders, i.e. the smaller the powder the higher the specific surface area [32]. This finding is also similar to that in $Mg_4Nb_2O_9$ powders synthesized by Ananta [33]. To the author's knowledge, the present data are the first results for the morphology–calcination relationship of $InNbO_4$ powders prepared by the solid-state reaction. It is also of interest to point out that mass production of single-phase $InNbO_4$ nanopowders with the smallest particle size ~100 nm (estimated from SEM micrographs) can be achieved by employing a simple solid-state reaction combined with a rapid vibro-milling technique. In addition, EDX analysis using a 20 nm probe on a large number of particles of the calcined powders confirms that the chemical composition is $InNbO_4$ powders, in good agreement with XRD results. For example, a chemical composition of $In_{0.95}Nb_{1.03}O_4$ can be approximated through a chemical analysis of EDX spectra in Fig. 9, which were obtained from one measurement point.

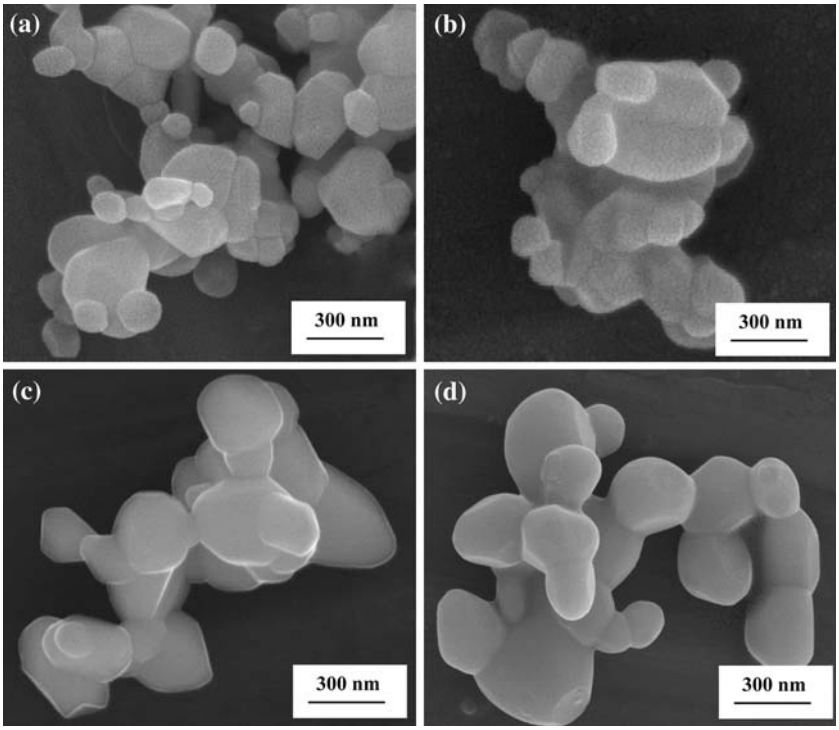

Fig. 7 SEM micrographs of the IN powders calcined for 2 h with heating/cooling rates of 10 °C/min at (**a**) 950, (**b**) 1,000, (**c**) 1,100 and (**d**) 1,200 °C

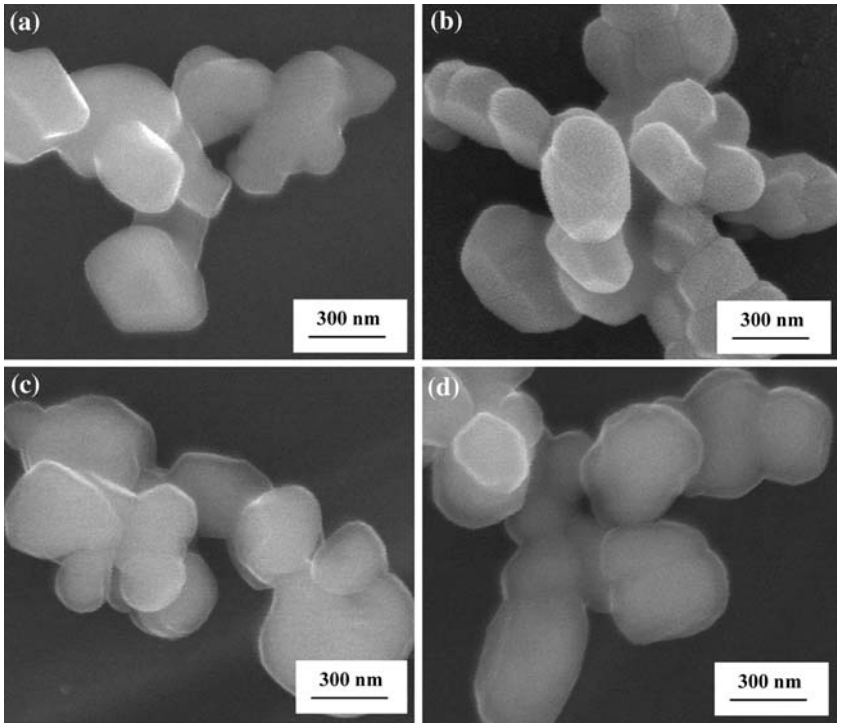

Fig. 8 SEM micrographs of the IN powders calcined at 950 °C with heating/cooling rates of 10 °C/min for (**a**) 3 h, (**b**) 4 h, and at 950 °C for 2 h with heating/cooling rates of (**c**) 3 and (**d**) 30 °C/min

Table 1 Particle size range of $InNbO_4$ powders calcined at various conditions

Calcination conditions			Estimated particle size range (±10 nm)
Temperature (°C)	Dwell time (h)	Rates (°C/min)	
900	4	10	250–600
900	4	30	200–450
950	2	3	150–550
950	2	10	150–350
950	2	30	100–350
950	3	10	300–450
950	4	10	300–700
1000	2	10	200–500
1100	2	10	250–600
1200	2	10	350–700

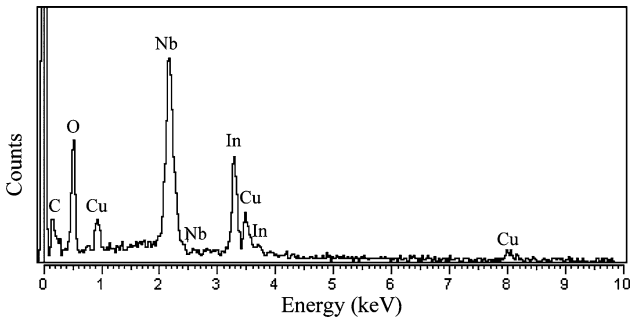

Fig. 9 EDX analysis of IN powders calcined at 950 °C for 2 h with heating/cooling rates of 30 °C/min (some spectra indexed as C and Cu come from coated electrode and sample stub, respectively)

The results obtained in this study clearly suggest that a systematic study of the effect of milling parameters such as milling times and milling speed on the phase and morphology evolutions of the $InNbO_4$ powders is required for better understanding and verifying the attractiveness of the vibro-milling technique. Further investigation of this relationship is underway and will be reported in the future.

Conclusions

The solid-state mixed oxide method via a rapid vibro-milling technique is explored in the preparation of single-phase $InNbO_4$ nanopowders. The calcination temperature, dwell time and heating/cooling rates have been found to show a pronounced effect on phase formation and particle size of the calcined $InNbO_4$ powders. This work demonstrated that single phase of indium niobate powders with particle size ranging from 100 nm to 450 nm can be produced via this technique by using a calcination temperature of 900 °C for 4 h or 950 °C for 2 h, with heating/cooling rates of 30 °C/min. The resulting $InNbO_4$ powders exhibit similar morphology and variety of agglomerated particle sizes, depending on calcination conditions.

Acknowledgements We thank the Thailand Research Fund (TRF) and the Commission on Higher Education (CHE), Graduate School and Faculty of Science, Chiang Mai University for all supports.

References

1. Keller C, Anorg Z (1962) Chem 318:89
2. Hulme JK (1953) Phys Res 92:504
3. Brixner LH, Chen H-Y (1980) Mater Res Bull 15:607
4. Zou Z, Ye J, Arakawa H (2000) Chem Phys Lett 332:271
5. Zou Z, Ye J, Sayama K, Arakawa H (2001) Nature 414:625
6. Ye J, Zou Z, Arakwa H, Oshikiri M, Shimoda M, Matsushita A, Shishido T (2002) J Photochem Photobiol A 148:79
7. Zou Z, Arakawa H (2003) J Photochem Photobiol A 158:145
8. Xu Y (1991) Ferroelectric materials and their applications. Elsevier Science, Amsterdam, The Netherlands
9. Moulson AJ, Herbert JM (2003) Electroceramics, 2nd edn. Wiley, New York
10. Alberta EF, Bhalla AS (1996) Ferroelectrics 188:95
11. Nomura K, Shingai T, Ishino S-I, Terauchi H, Yasuda N, Ohwa H (1999) J Phys Soc Jpn 68:39
12. Park SS, Choo WK (1991) Ferroelectrics 118:117
13. Alberta EF, Bhalla AS (2002) J Phys Chem Solids 63:1759
14. Elissalde C, Weill F, Ravez J (1994) Mater Sci Eng B 25:85
15. Yasuda N, Mizuno T (1995) Appl Phys Lett 66:571
16. Lee KH, Lee SB, Kim H (2004) Ceram Int 30:1035
17. Yasuda N, Inaguki H, Imamura S (1992) Jpn J Appl Phys 31:L574
18. Iwata M, Katagiri S, Orihara H, Maeda M, Suzuki I, Ohwa H, Yasuda N, Ishibashi Y (2004) Ferroelectrics 301:179
19. Ananta S, Tipakontitikul R, Tunkasiri T (2003) Mater Lett 57:2637
20. Ananta S (2004) Mater Lett 58:2834
21. Powder Diffraction File No. 71-2195 (2000) International Centre for Diffraction Data, Newton Square, PA
22. Powder Diffraction File No. 30-873 (2000) International Centre for Diffraction Data, Newton Square, PA
23. Powder Diffraction File No. 83-1780 (2000) International Centre for Diffraction Data, Newton Square, PA
24. Zou Z, Ye J, Arakawa H (2000) Chem Phys Lett 332:271
25. Youmee P, Phanichphant S, Ananta S, Heimann RB (2001) Ceram Forum Int DKG 78:E48
26. Ananta S, Brydson R, Thomas NW (1999) J Eur Ceram Soc 19:489
27. Tipakontitikul R, Ananta S (2004) Mater Lett 58:449
28. Kim BC, Lee JH, Kim JJ, Ikegami T (2002) Mater Lett 52:114
29. Powder Diffraction File No. 25-384 (2000) International Centre for Diffraction Data, Newton Square, PA
30. von Liebertz J (1972) Acta Crystallogr B 28:3100
31. Powder Diffraction File No. 33-619 (2000) International Centre for Diffraction Data, Newton Square, PA
32. Reed JS (1995) Principles of ceramics processing, 2nd edn. Wiley, New York
33. Ananta S (2004) Mater Lett 58:2530

Ferroelectrics
Publication details, including instructions for authors and subscription information:
http://www.informaworld.com/smpp/title~content=t713617887

Two-Stage Sintering of Barium Titanate Ceramic and Resulting Characteristics

To cite this Article: , 'Two-Stage Sintering of Barium Titanate Ceramic and Resulting Characteristics', Ferroelectrics, 346:1, 84 - 92
To link to this article: DOI: 10.1080/00150190601180380
URL: http://dx.doi.org/10.1080/00150190601180380

Ferroelectrics, 346:84–92, 2007

ISSN: 0015-0193 print / 1563-5112 online
DOI: 10.1080/00150190601180380

Taylor & Francis
Taylor & Francis Group

Two-Stage Sintering of Barium Titanate Ceramic and Resulting Characteristics

W. CHAISAN,* R. YIMNIRUN, AND S. ANANTA

Department of Physics, Faculty of Science, Chiang Mai University, Chiang Mai 50200, Thailand

The potential of a two-stage sintering technique as a low-cost and simple ceramic fabrication to obtain highly dense and pure barium titanate ceramics with small grain size was demonstrated in this study. Effects of designed sintering conditions on phase formation, densification, microstructure, and electrical properties of the $BaTiO_3$ ceramics were examined via X-ray diffraction (XRD), Archimedes method, scanning electron microscopy (SEM), dielectric and hysteresis measurements, respectively. It has been found that, under suitable two-stage sintering conditions, the dense perovskite BT ceramics with fine grain can be successfully achieved with good electrical properties.

Keywords Barium titanate; sintering; microstructure; dielectric properties; ferroelectric properties

1. Introduction

Barium titanate ($BaTiO_3$ or BT), which exhibits a perovskite structure and a Curie temperature $\sim$120°C, is a classical ferroelectric material that has been extensively exploited both for academic and for technological utilizations over the past decades [1, 2]. Owing to its high dielectric constant, large mechanical-quality factor, large pyroelectric coefficient, nontoxic handling and low cost of manufacturing, compared to several lead-based perovskite ferroelectrics, ceramics based on BT have been strong candidates for several electronic applications, including ultrasonic transducers, multilayer capacitors, pyroelectric detectors, semiconductors with positive temperature coefficient of resistance (PTCR) and electro-optic devices [3–7]. Because of these important technological applications, there has been a great deal of interest in the preparation process of pure BT ceramic as well as in the electrical properties of BT-based ceramics [8, 9].

Electrical properties of $BaTiO_3$ depend strongly on microstructure as well as chemical compositions [1, 6]. It was reported earlier that the high value of dielectric constant can be revealed if polycrystalline BT of fine grain size (<1 μm) is achieved [10, 11]. Thus, a fine grain is essential to achieve optimum dielectric properties. The microstructure of BT can be controlled by two approaches. Utilizing additives to prohibit the grain growth is one approach. Some additives such as Dy, Nb and Ca have been reported to be effective grain growth inhibitors [12–14]. Another approach uses novel processing technique to modify the microstructure. Numerous studies on the sintering of barium titanate have been reported

Received May 15, 2006.
*Corresponding author. E-mail: wanwilai_chaisan@yahoo.com

in the literature [11, 15, 16]. Recently, a two-stage sintering method has been proposed by Chen and Wang to achieve the densification of ceramic bodies without significant grain growth [17]. Moreover, Kim and Han [11] found that intermediate dense and fine grain size BT ceramic was achieved from the two-stage sintering technique and showed much greater dielectric constant than that of the normal sintering technique. Since the two-stage sintering process is a low-cost technique and simple ceramic fabrication to obtain highly dense ceramics with pure phase, therefore, in this work a two-stage sintering method has been adopted to produce the fine grain BT ceramic. The influence of two-stage sintering on densification, microstructure, dielectric and ferroelectric properties of the ceramics is investigated with comparison to the normal sintering scheme.

2. Experimental Procedure

$BaTiO_3$ powders used in this study were prepared by a simple mixed oxide synthetic route. Commercially available powders of $BaCO_3$ and TiO_2 (anatase form), (Fluka, >99% purity) were used as starting materials. The mixing process was carried out by ball-milling a mixture of raw materials for 24 h with corundum media in isopropyl alcohol (IPA). After wet-milling, the slurry was dried at 120°C for 2 h and calcined in a closed alumina crucible, with the optimum calcination condition determined by the XRD method (1300°C for 2 h with heating/cooling rates of 5°C/min) [18]. Ceramic fabrication was achieved by adding 1 wt% polyvinyl alcohol (PVA) binder, prior to pressing as pellets (15 mm in diameter and 1.0 to 1.3 mm thick) in a pseudo-uniaxial die press at 100 MPa. Each pellet was placed in an alumina crucible together with atmosphere powders of identical chemical composition. In the so-called two-stage sintering process, the first sintering temperature (T_1) was assigned for 1100°C and variation of the second sintering temperature (T_2) between 1200°C and 1400°C was carried out (Fig. 1). For comparison, normal sintering process was also carried out at the firing temperature between 1250 and 1450°C for 2 h with constant heating/cooling rates of 5°C/min. The two sintering schemes also included the binder burn out process at 500°C for 1 h.

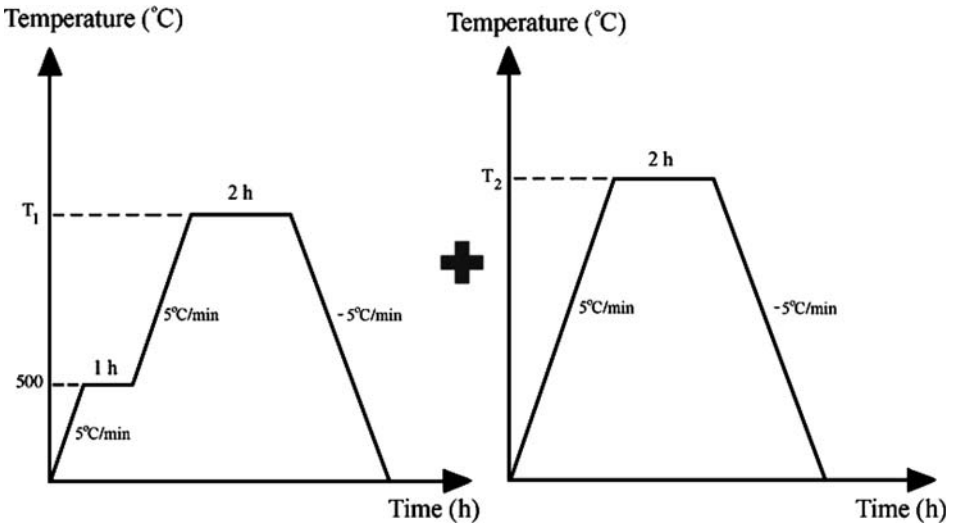

Figure 1. A two-stage method sintering profile.

Densities of the final sintered products were determined by using the Archimedes principle. Microstructural development was characterized using a JEOL JSM-840A scanning electron microscopy (SEM). Mean grain sizes of the sintered ceramics were subsequently estimated by employing the linear intercept method [19]. In order to evaluate the electrical properties, dense ceramics were polished to form flat, parallel faces (14 mm in diameter and 0.8 mm thick). Silver electrodes were then fired on both sides of the samples at 750°C for 12 min. The dielectric properties were measured at frequency of 10 kHz using a HIOKI 3532-50 LCR meter, on cooling through the transition range (200 to 25°C) with a rate of 3°C/min. For ferroelectric hysteresis characteristics, the polarization (P) was measured as a function of electric field (E), using a modified Sawyer-Tower circuit [20].

3. Results and Discussion

The XRD patterns of two stage sintered BT ceramic compared with normal sintered ceramic were illustrated in Fig. 2. The results indicated that the single phase of perovskite $BaTiO_3$ (yield of 100% within the limitations of the XRD technique) was found in both samples with no evidence of the second phase of Ba_2TiO_4, $BaTi_2O_5$ and $BaTi_3O_7$ compositions [16, 21, 22]. The strongest reflections in the majority of XRD trace indicate the formation of the perovskite phase of barium titanate ($BaTiO_3$) which could be matched with JCPDS file no. 5-0626, in agreement with other works [18, 23]. To a first approximation, this phase has a tetragonal perovskite structure in space group *P4/mm* (no. 99) with cell parameters $a =$ 399.4 pm and $c = 403.8$ pm [24]. Moreover, the XRD profiles around diffraction angles

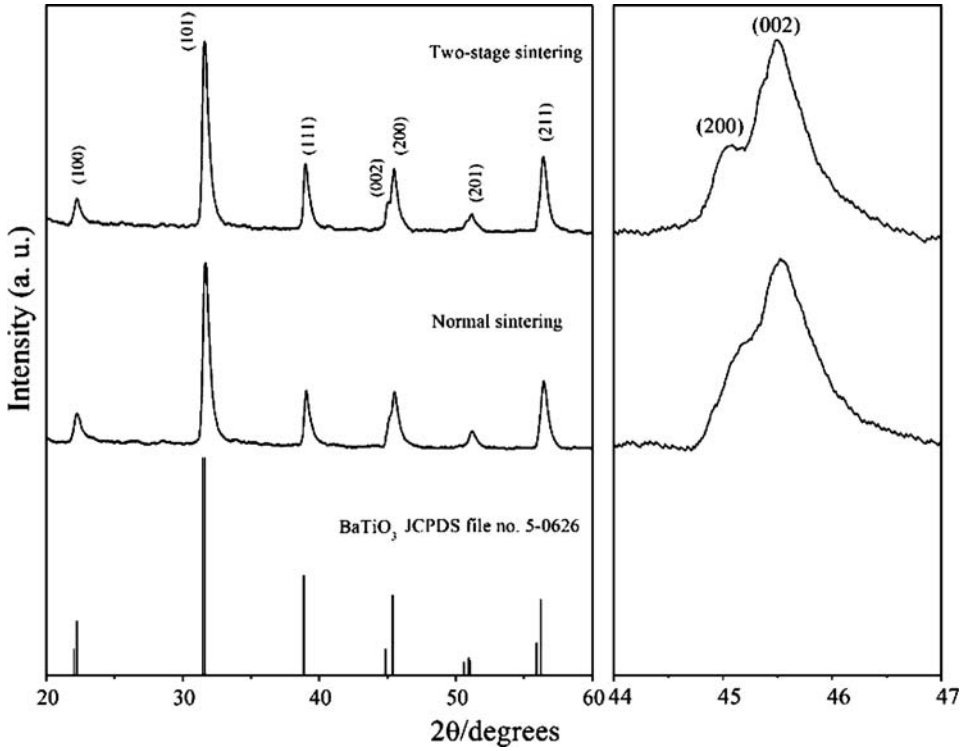

Figure 2. XRD patterns for BT ceramics.

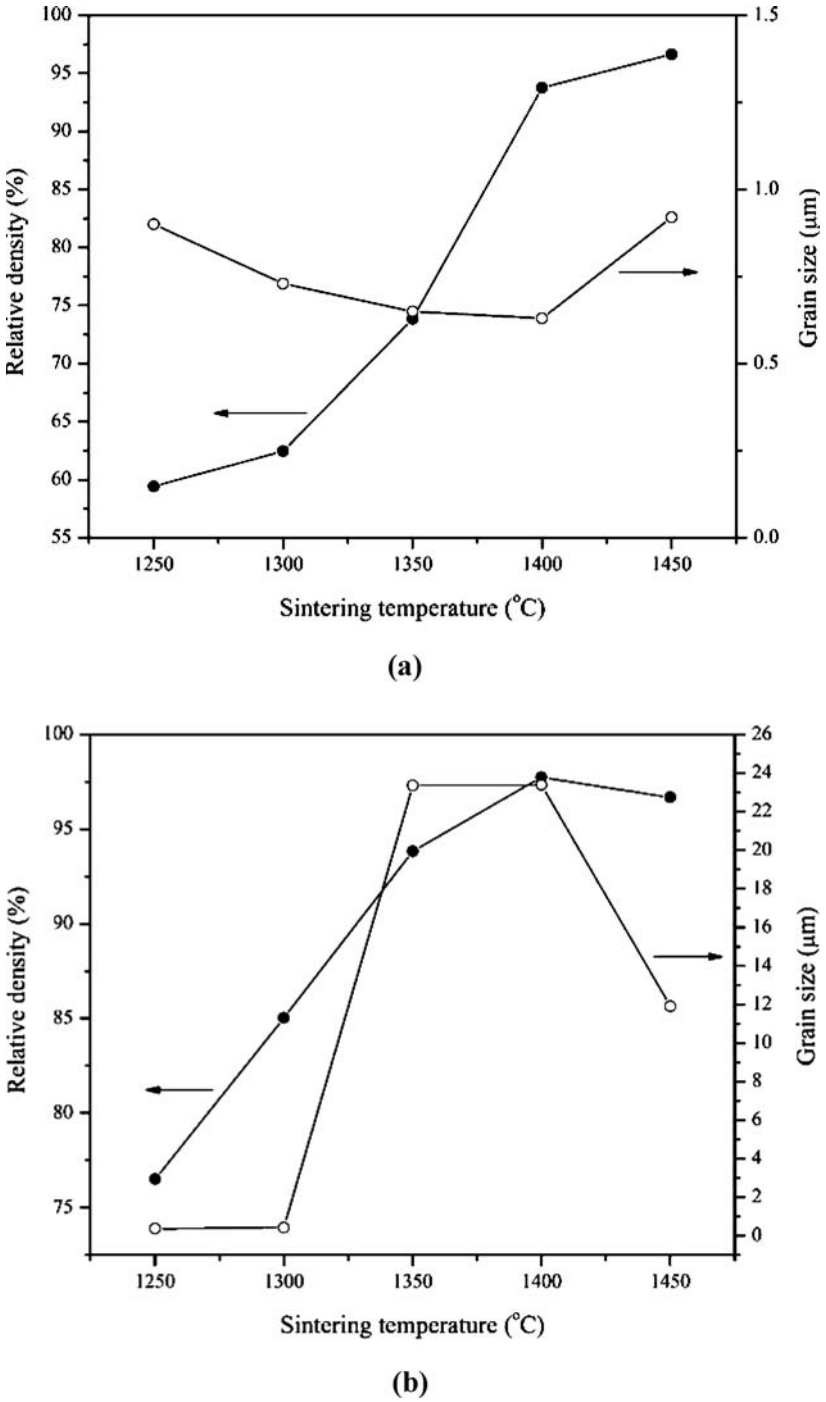

Figure 3. The relative density of sintered BT ceramics and grain size as a function of sintering temperatures: (a) two-stage sintering, with the first sintering temperature (T_1) at 1100°C and (b) normal sintering.

$2\theta \sim 44$–47° were also shown in Fig. 2. The expected positions of tetragonal (002) and (200) peaks are also indicated. The XRD data of two-stage sintered BT ceramic show a larger splitting of the tetragonal (002)/(200) peaks, as compared to the normal sintering peaks. The lattice parameters estimated from the peak position are $a = 398.3$ pm and $c = 401.6$ pm ($c/a = 1.008$), which are close to those reported previously [24].

Figure 3 shows the sintered density and average grain size of $BaTiO_3$ samples as a function of sintering temperature. In the two-stage sintering process (Figure 3a), the first sintering temperature was fixed at 1100°C, for constant dwell time of 2 h and heating/cooling rates of 5°C/min, while the second sintering temperature was varied from 1200°C to 1400°C. It can be seen that the relative density of the two-stage sintered ceramics increased significantly from 60 to 97% with increasing sintering temperature, while grain size changed only slightly (about 0.6–0.9 μm). However, in normal sintering process, while the relative density changed from 77 to 98%, similar to that of the two-stage sintering, but the average grain size increased significantly from 1 to 23 μm as the sintering temperature increased from 1250 to 1400°C. Further increase in the sintering temperature to 1450°C, the observed fall-off in density is probably due to the dominant effect of grain coarsening mechanism at high sintering temperature as suggested by other workers [25, 26]. The observation clearly signifies the advantage of the two-stage sintering technique in producing fine-grained BT ceramics.

The microstructure of BT ceramics with the highest density was revealed by SEM. Micrographs of BT samples sintered with different schemes are shown in Fig. 4. Clearly, the microstructure of the two-stage sintered ceramics (Fig. 4a) is significantly different from that of the normal sintered BT samples (Fig. 4b) which exhibit highly dense microstructure with abnormal grains of size around $\sim$50 μm due to the recrystallization during firing and variation of stoichiometric compositions [27, 28]. The two-stage sintered ceramic contains small grain size consisted with many pores. The average grain size is about 0.92 μm. Moreover, with careful observation, it can be found that BT grains in two-stage sintered ceramics also exhibit whisker-like shape. With sizes of $\sim$300–500 nm in length and $\sim$10 nm in width, these whiskers are seen to distribute and coat on the grain. Even though exact mechanism of the microstructure observed here is not well established, but it should be noted that the various features of microstructure in BT ceramics are dependent on the grain growth rate in the different planes [29]. However, the sintering process and growth environment also play an important role in the formation [30]. More importantly, it can be assumed that the two-stage sintering process could suppress the grain growth mechanism efficiently whereas the highest density of both normal- and two-stage sintered ceramics is similar in value. This can be explained that the feasibility of densification without grain growth, which is believed to occur in two-stage sintered ceramic, relies on the suppression of grain boundary migration while keeping grain boundary diffusion active. The kinetic and the driving force for grain growth behavior in the second-step sintering were previously discussed by Chen and Wang [17]. Their work suggested that the suppression of the final stage grain growth was achieved by exploiting the difference in kinetics between grain-boundary diffusion and grain-boundary migration.

The dielectric properties of sintered $BaTiO_3$, in fact, exhibit a strong dependence on grain size [10, 11, 31]. For the grain size <1 μm, anomalously high room-temperature permittivity values were obtained along with a general broadening and flattening of the permittivity peak at Curie temperature [15]. Therefore, grain size control of the sintered bodies is very important. Figure 5 shows a comparison of the dielectric properties of maximum density BT ceramics sintered by the two different schemes. It is very interesting to observe that though the average grain size of the two-stage sintered ceramic is lower than 1 μm, the Curie temperatures and the dielectric constants of the two ceramics are about the same.

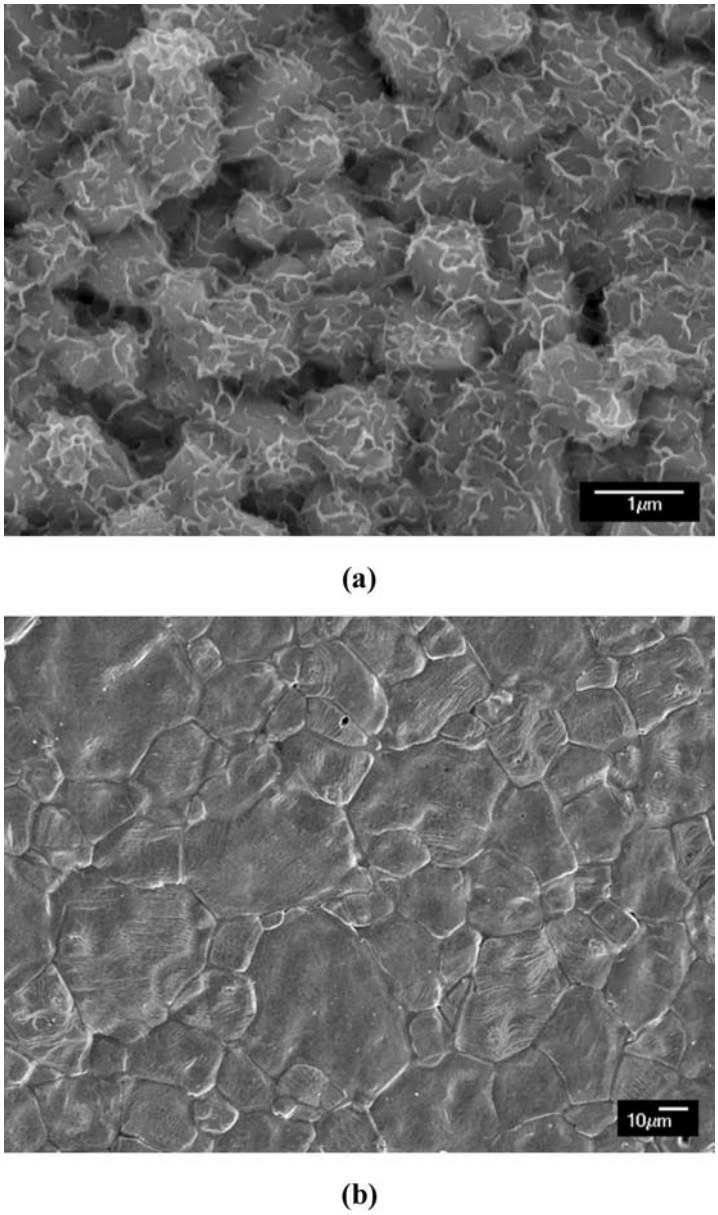

Figure 4. SEM micrographs of BT ceramics (a) two-stage sintered at 1100/1400°C, and (b) normal sintered at 1400°C.

Since the densities of the two ceramics are very similar in value (97–98%), this indicated that density could not be the controlling factor. It can be assumed that the employed sintering temperature in the two-stage sintering process is not enough for driving densification mechanism to achieve dense BT ceramics, as evidenced in Fig. 4(a). The highly porous microstructure was induced which could be the main reasons for low dielectric constant in fine grain case. However, the scope for improving two-stage sintering by raising the temperature is limited by the capability of the furnace. Nevertheless, the room temperature

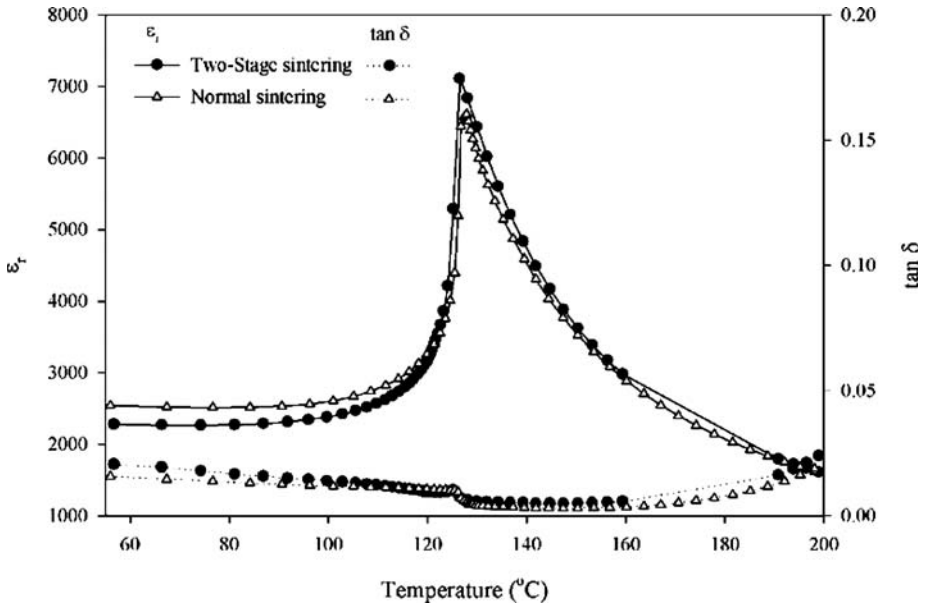

Figure 5. Variation with temperature of relative permittivity (ε_r) and dissipation factor ($\tan\delta$) at 10 kHz for two-stage sintered BT ceramics.

dielectric values in the order of 2000 for both ceramics are higher than those reported earlier [11, 23]. In the same way with the dielectric properties, the ferroelectric properties of the two-stage sintered BT ceramic were similar to those of the normal sintered ceramic, as shown in Fig. 6.

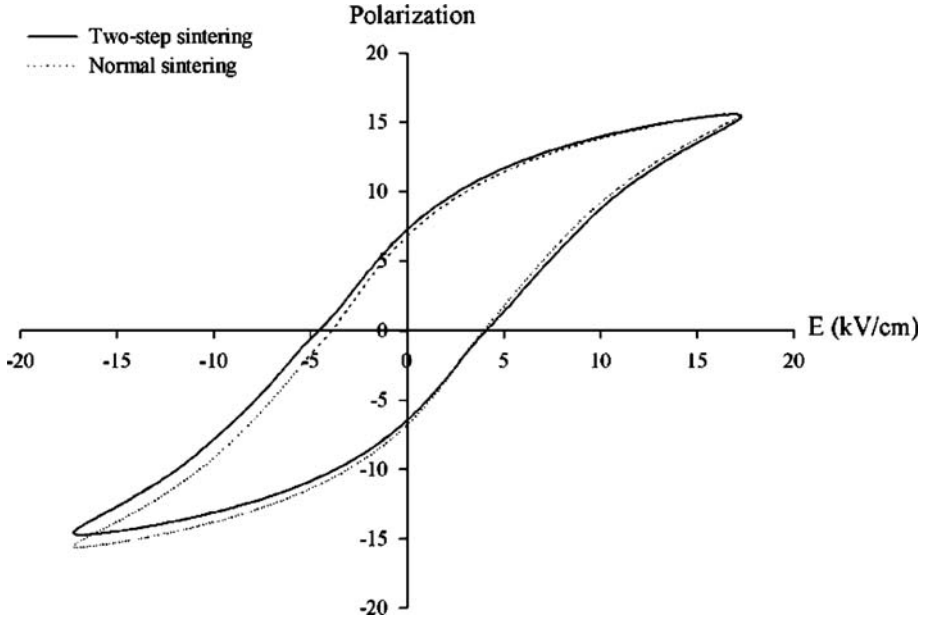

Figure 6. Hysteresis graphs of normal and two-stage sintered BT ceramics.

4. Conclusion

Even though the simple mixed-oxide method employing a conventional ball-milling was used, this work demonstrated that it was possible to obtain smaller grain size BT ceramics with high densification by the two-stage sintering technique. It has been shown that, under suitable condition, two-stage sintering can effectively suppress the grain growth in BT, leading to fine-grained microstructure ($\sim$1 μm). Moreover, whisker morphology is also found in all two-stage sintered ceramics. More importantly, the dielectric properties of BT ceramics in this work are interestingly independent of the grain size, as it is evident that dielectric constant of the small grained ceramic prepared by the two-stage sintering is of the same value with large grained ceramic prepared by the normal sintering.

Acknowledgment

We thank the Thailand Research Fund (TRF), Commission on Higher Education (CHE) the Faculty of Science, Chiang Mai University for all support.

References

1. A. J. Moulson and J. M. Herbert, Electroceramics: Materials, Properties, Applications (John Wiley & Sons Ltd., Chichester, 2003), pp. 500.
2. G. H. Haertling, *J. Am. Ceram. Soc*. **82**, 797–818 (1999).
3. K. Uchino, Piezoelectrics Actuators and Ultrasonic Motors (Kluwer, Boston, 1997), pp. 349.
4. S. L. Swartz, *IEEE Trans. Electr*. Insul. **25**, 935–987 (1990).
5. T. R. Shrout and J. P. Dougherty, *Ceramic Transactions*. **8**, 3–19 (1990).
6. Y. Xu, Ferroelectric Materials and Their Applications (Elsevier Science Publishers B. V., 1991), pp. 391.
7. K. Uchino, Ferroelectric Devices (Marcel Dekker, New York, 2000), pp. 308.
8. N. Halder, D. Chattopadhyay, A. D. Sharma, D. Saha, A. Sen, and H. S. Maiti, *Mat. Res. Bull*. **36**, 905–913 (2001).
9. B. D. Stojanovic, C. R. Foschini, M. A. Zaghete, F. O. S. Veira, K. A. Peron, M. Cilense, and J. A. Varela, *J. Mater. Process. Technol*. **113–114**, 802–806 (2003).
10. K. Kinoshita and A. Yamaji, *J. Appl. Phys*. **47**, 371–373 (1976).
11. H. T. Kim and Y. H. Han, *Ceram. Int*. **30**, 1719–1723 (2004).
12. A. Yamaji, Y. Enomoto, K. Kinoshita, and T. Murakami, *J. Am. Ceram. Soc*. **60**, 97–101 (1977).
13. M. Kahn, *J. Am. Ceram. Soc*. **54**, 452–454 (1971).
14. V. S. Tiwari, N. Singh, and D. Pandey, *J. Am. Ceram. Soc*. **77**, 1813–1818 (1994).
15. J. S. Choi and H. G. Kim, *J. Mater. Sci*. **27**, 1285–1290 (1992).
16. J. K. Lee, K. S. Hong, and J. W. Jang, *J. Am. Ceram. Soc*. **84**, 2001–2006 (2001).
17. I. W. Chen and X. H. Wang, *Nature*. **404**, 168–171 (2000).
18. W. Chaisan, S. Ananta, and T. Tunkasiri, *Cur. Appl. Phys*. **4**, 182–185 (2004).
19. R. L. Fullman, *Trans. AIME*. **197**, 447–452 (1953).
20. R. Yimnirun, S. Ananta, A. Ngamjarurojana, and S. Wongsaenmai, *Appl. Phys. A: Mat. Sci. Proc*. **81**, 1227–1231 (2005).
21. W. Maison, R. Kleeberg, R. Heimann, and S. Phanichphant, *J. Eur. Ceram. Soc*. **23**, 127–132 (2003).
22. V. Berbenni, A. Marini, and G. Bruni, *Thermochimica Acta*. **374**, 151–158 (2001).
23. W. Chaisan, R. Yimnirun, S. Ananta, and D. P. Cann, *Mater. Lett*. **59**, 3732–3737 (2005).
24. JCPDS-ICDD card no. 5-0626. International Centre for Diffraction Data, Newtown, PA, 2002.
25. F. Valdivieso, M. Pijolat, C. Magnier, and M. Soustelle, *Solid State Ionics*. **83**, 283–292 (1996).
26. G. S. Rohrer, *Annu. Rev. Mater. Res*. **35**, 99–126 (2005).

27. B. Jaffe, W. R. Cook, and H. Jaffe, Piezoelectric Ceramics (Academic Press, London, 1971), pp. 317.
28. S. H. Hur, J. K. Lee, K. W. Park, K. S. Hong, and S. J. Park, *Mater. Lett*. **35**, 78–84 (1998).
29. M. H. Lin, J. F. Chou, and H. Y. Lu, *J. Eur. Ceram. Soc*. **20**, 517–526 (2000).
30. R. M. German, Sintering Theory and Practice (Wiley, New York, 1996), pp. 550.
31. G. Arlt, D. Hennings, and G. d. With, *J. Appl. Phys*. **58**, 1619–1625 (1985).

J Mater Sci
DOI 10.1007/s10853-006-0569-7

Effects of calcination conditions on phase and morphology evolution of lead zirconate powders synthesized by solid-state reaction

W. Chaisan · O. Khamman · R. Yimnirun · S. Ananta

Received: 9 December 2005 / Accepted: 13 June 2006

Abstract Lead zirconate ($PbZrO_3$) powder has been synthesized by a solid-state reaction via a rapid vibro-milling technique. The effects of calcination temperature, dwell time and heating/cooling rates on phase formation, morphology, particle size and chemical composition of the powders have been investigated by TG-DTA, XRD, SEM and EDX techniques. The results indicated that at calcination temperature lower than 800 °C minor phases of unreacted PbO and ZrO_2 were found to form together with the perovskite $PbZrO_3$ phase. However, single-phase $PbZrO_3$ powders were successfully obtained at calcination conditions of 800 °C for 3 h or 850 °C for 1 h, with heating/cooling rates of 20 °C/min. Higher temperatures and longer dwell times clearly favored the particle growth and formation of large and hard agglomerates.

Introduction

Lead zirconate, $PbZrO_3$ (PZ), which is a typical antiferroelectric (AFE) material at room temperature with a Curie temperature of ~230 °C, has an orthorhombic symmetry with a structure similar to that of classical ferroelectric of orthorhombic barium titanate ($BaTiO_3$) [1–5]. Practically, this material is a potential candidate for energy storage applications for DC fields and low loss linear capacitor, owing to its AFE nature [6–12]. Recently, the double hysteresis behavior of this material makes it attractive for the microelectronic, microelectromechanical systems (MEMs) as well as for actuator applications [12–14].

Lead zirconate when combined with other oxides can form a series of solid solution materials such as $Pb(Zr_x,Ti_{1-x})O_3$, $PbZrO_3$–$Pb(Mg_{1/3}Nb_{2/3})O_3$, $PbZrO_3$–$PbTiO_3$–$Pb(Fe_{1/5}Nb_{1/5}Sb_{3/5})O_3$, and $PbZrO_3$–$Pb(Mg_{1/3}Nb_{2/3})O_3$, which find tremendous applications in the electroceramic industries [13–15]. In all these applications, the stoichiometry and homogeneity of materials are known to be the important factor for ensuring the performance of devices [14, 15]. This is especially important in PZT compositions in which the useful properties depend significantly on Zr/Ti ratio [1, 14, 16]. Over decades, tremendous amount of work has been dedicated to the processing of PZT with various preparation routes, one of which is a modified mixed oxide route [1, 17, 18]. In this route, the PZT is prepared by mixing precursor PZ with $PbTiO_3$ or PbO and TiO_2 powders [1, 19, 20]. This preparation route, as well as the B-site cations route, offers advantages in producing PZT with more controllable Zr/Ti ratio and desirable properties at lower sintering temperature without using excess PbO typically practiced in a more conventional mixed-oxide method [17, 21, 22]. The resulting PZT is, however, found to show variation in properties, probably caused in part by the stoichiometry of PZ precursor powders. In addition, earlier work by Reaney et al. [23] reported that impure PZ specimen showed significantly inferior electrical properties as well as unclear TEM results in the antiferroelectric–ferroelectric (AFE-FE) phase boundary as a result of unreacted ZrO_2 phases. These reasons outlined have

W. Chaisan · O. Khamman · R. Yimnirun · S. Ananta (✉)
Department of Physics, Faculty of Science, Chiang Mai University, Chiang Mai 50200, Thailand
e-mail: Supon@chiangmai.ac.th

clearly indicated from both practical and fundamental viewpoints needs to obtain stoichiometric and better homogeneity PZ. To do such, different preparative methods have been introduced, such as chemical co-precipitation [24], sol–gel [25], precipitation of molecular precursors [26], citrate combustion [27], hydrothermal [28] and microemulsion method [29]. All these techniques are aimed at reducing the temperature of preparation of the compound even though they are more involved and complicated in approach than the solid-state reaction method. Moreover, high purity PZ powders are still not available in mass quantity and also expensive. So far, only limited attempts have been made to improve the yield of $PbZrO_3$ by optimizing calcination conditions [30–32]. The effects of applied dwell time and heating/cooling rates have not yet been studied extensively. Therefore, it is our interest to explore a simple mixed oxide synthetic route for the production of PZ powders. The effect of calcination conditions on the development of phase, morphology and particle size of lead zirconate powders is investigated in this connection. The potential of a vibro-milling technique as a significant time-saving method to obtain single-phase lead zirconate powders, at low temperature and with small particles is also examined.

Experimental procedure

The starting materials were commercially available lead oxide, PbO (JCPDS file number 77-1971) and zirconium oxide, ZrO_2 (JCPDS file number 37-1484) (Fluka, >99% purity). The two oxide powders exhibited an average particle size in the range of 3.0–5.0 μm. $PbZrO_3$ powders were synthesized by the solid-state reaction of thoroughly ground mixtures of PbO and ZrO_2 powders that were milled in the required stoichiometric ratio. Instead of employing a ball-milling procedure (ZrO_2 media under ethanol for 24 h [30] or under a mixture of cyclohexane and deionized water for 12 h [31]), use was made of a McCrone vibro-milling technique [22, 32, 33]. In order to combine mixing capacity with a significant time saving, the milling operation was carried out for 0.5 h with corundum cylindrical media in isopropyl alcohol (instead of 8 h with zirconia media [32]). After drying at 120 °C for 2 h, the reaction of the uncalcined powders taking place during heat treatment was investigated by themogravimetric and differential thermal analysis (TG-DTA, Shimadzu), using a heating rate of 10°C/min in air from room temperature up to 1000 °C. Based on the TG-DTA results, the mixture was calcined at various conditions, i.e. temperatures ranging from 700 to 900 °C, dwell times ranging from 1 to 5 h and heating/cooling rates ranging from 1 to 20 °C/min, in closed alumina crucible, in order to investigate the formation of lead zirconate.

Calcined powders were subsequently examined by room temperature X-ray diffraction (XRD; Siemens-D500 diffractometer), using Ni-filtered CuK_α radiation to identify the phases formed and optimum calcination conditions for the formation of $PbZrO_3$ powders. Crystallite sizes and lattice parameters in the calcined powders were estimated from XRD data [34, 35]. Powder morphologies and particle sizes were directly imaged, using scanning electron microscopy (SEM; JEOL JSM-840A).

Results and discussion

The TG-DTA simultaneous analysis of a powder mixed in the stoichiometric proportions of $PbZrO_3$ is displayed in Fig. 1. In the temperature range from room temperature to ~150 °C, the sample shows both exothermic and endothermic peaks in the DTA curve, in consistent with a slight drop in weight loss at the same temperature range. These observations can be attributed to the decomposition of the organic species (most likely polyethylene from the milling jar) from the milling process. [22, 33]. Corresponding to a large fall in sample weight (~4.5%), the other exotherm and endotherm are observed within 300–450 °C temperature range in the DTA curve. However, it is to be noted that there is no obvious interpretation of these peaks, although it is likely to correspond to a phase transformation of ZrO_2 precursor alloyed with PbO precursor reported by a number of workers [35–38]. In general, it is well established that there are a number of polymorphic forms of PbO and ZrO_2 stable at different temperatures and pressures [35, 37]. However, in this

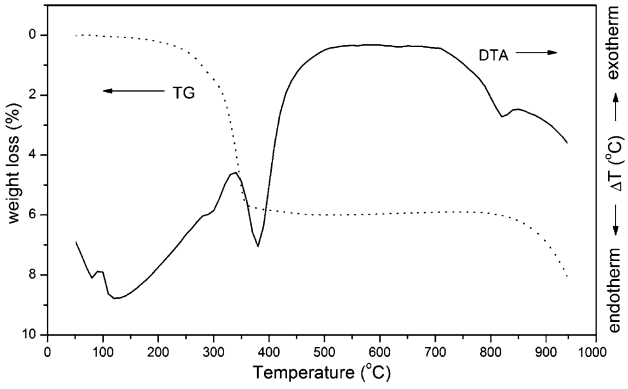

Fig. 1 TG-DTA curves for the mixture of PbO–ZrO_2 powders

work, the possibility of these phase transformations has not been investigated, since the overriding objective is to synthesize single phase $PbZrO_3$, irrespective of the polymorph in which it is stabilized.

Increasing the temperature up to ~1000 °C, the solid-state reaction occurred between PbO and ZrO_2 [29–32]. The broad exotherm from 500 to 700 °C in the DTA curve represents that reaction, which is supported by a gradual decrease in sample weight over the same temperature range. Finally, a significantly drop in weight loss is also observed above 800 °C, that is associated with the DTA peaks at the same temperature range and may be attributed to the PbO volatilization commonly found in the lead-based perovskite systems [22, 33, 39]. These data were used together with those from literature [30–32] to assign the range of calcination temperatures for XRD investigation between 700 and 900 °C.

Therefore, to investigate the effect of calcination temperature on the phase development, the mixed powders were calcined for 2 h in air at various temperatures, up to 900 °C, followed by phase analysis using XRD. As shown in Fig. 2, for the uncalcined powder, only X-ray peaks of precursors PbO (▼) and ZrO_2 (●), which could be matched with JCPDS file numbers 77-1971 [40] and 37-1484 [41], respectively, are present, indicating that no reaction had yet been triggered during the milling process. It is seen that fine $PbZrO_3$ crystallites (*) were developed in the powder at a calcination temperature as low as 750°C, accompanying with PbO and ZrO_2 as separated phases. This observation agrees well with those derived from the TG-DTA results and other workers [31, 38]. As the temperature increased to 800 °C, the intensity of the perovskite-like $PbZrO_3$ peaks was further enhanced and became the predominant phase. Upon calcination at 850 °C, an essentially monophasic of $PbZrO_3$ phase is obtained. This PZ phase was indexable according to an orthorhombic perovskite-type structure with lattice parameters a = 823.1 pm, b = 1177 pm and c = 588.1 pm, space group *P2cb* (no. 32), in consistent with JCPDS file numbers 35-739 [42] and other investigators [24, 30, 43]. This study also shows that crystalline orthorhombic PZ is the only detectable phase in the powder, after calcination in the range 850–900 °C.

Having established the optimum calcination temperature, dwell times ranging from 1 to 5 h with constant heating/cooling rates of 5°C/min were applied at 850 and 800 °C, as shown in Figs. 3 and 4, respectively. From Fig. 3, it can be seen that the single phase of $PbZrO_3$ (yield of 100% within the limitations of the XRD technique) was found to be possible in all powders calcined at 850 °C with dwell time ranging from 1 to 5 h. This is probably due to the effectiveness of vibro-milling and a carefully optimized reaction. However, in the work reported here, it is to be noted that single-phase of $PbZrO_3$ powders was also successfully obtained for a calcination temperature of 800 °C with dwell time of 3 h or more applied (Fig. 4). This was apparently a consequence of the enhancement in crystallinity of the $PbZrO_3$ phase with increasing dwell time. The appearance of PbO phase indicated that full crystallization has not occurred at relatively shorter calcination times. The observation

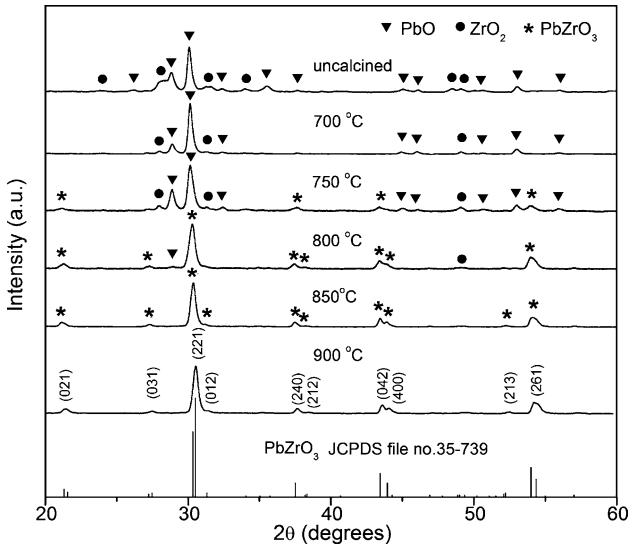

Fig. 2 XRD patterns of PZ powder calcined at various temperatures for 1 h with heating/cooling rates of 10°C/min

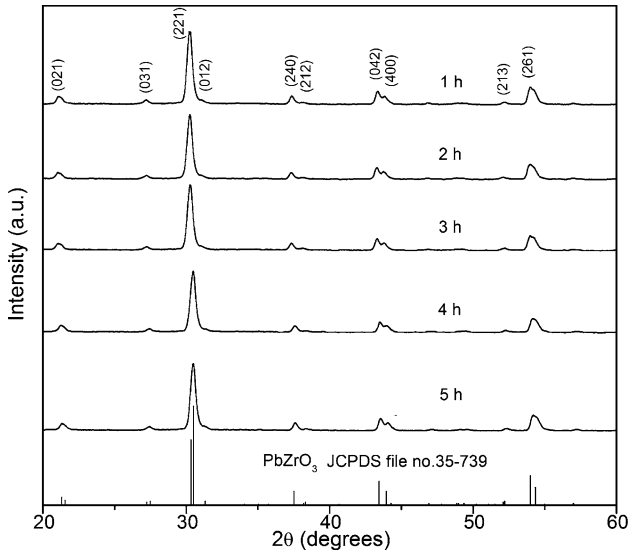

Fig. 3 XRD patterns of PZ powder calcined at 850 °C with heating/cooling ratesof 10 °C/min for various dwell times

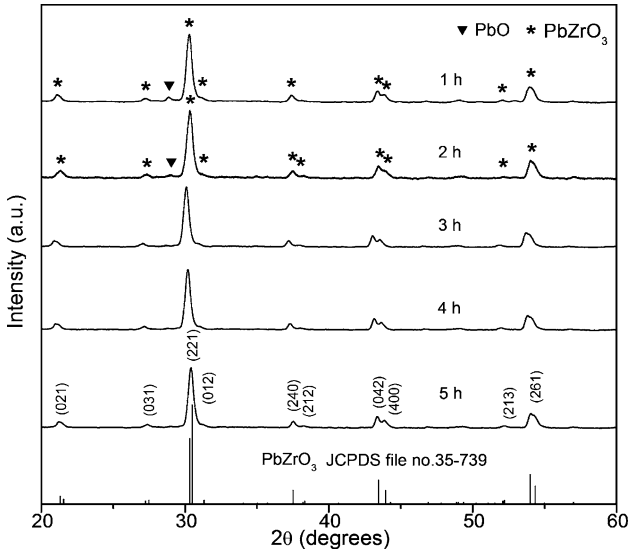

Fig. 4 XRD patterns of PZ powder calcined at 800 °C with heating/cooling rates of 10 °C/min for various dwell times

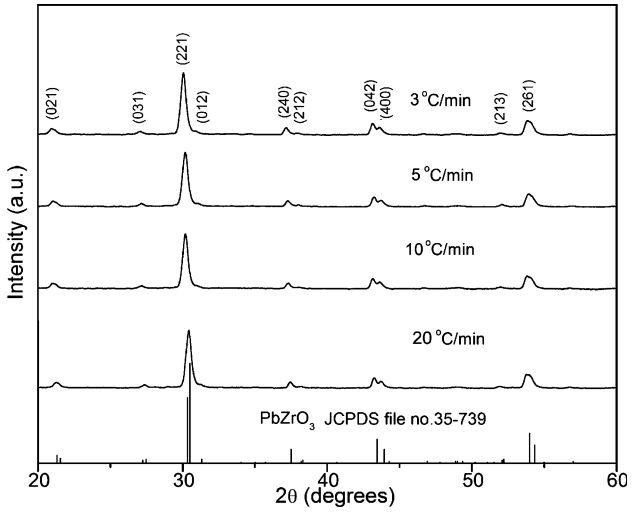

Fig. 6 XRD patterns of PZ powder calcined at 850 °C for 1 h with various heating/cooling rates

that the dwell time effect may also play an important role in obtaining a single-phase perovskite product is also consistent with other similar systems [33, 39, 44].

Apart from the calcination temperature and dwell time, the effect of heating/cooling rates on the formation behavior of $PbZrO_3$ was also investigated. Various heating/cooling rates ranging from 1 to 20 °C/min were selected for calcination conditions of 800 °C for 3 h (Fig. 5) and 850 °C for 1 h (Fig. 6). In this connection, it is shown that the yield of $PbZrO_3$ phase was not depending on heating/cooling rates, indicating that fast heating/cooling rates can lead to full crystallization of $PbZrO_3$ phase without time for the formation of minor

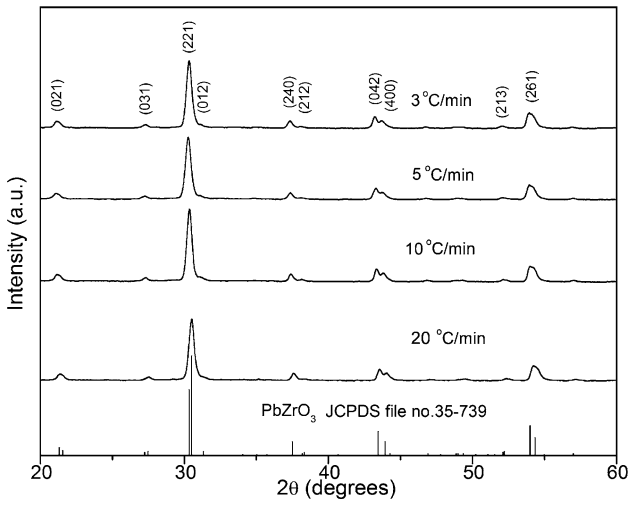

Fig. 5 XRD patterns of PZ powder calcined at 800 °C for 3 h with various heating/cooling rates

phase or lead vaporization. The observation that faster heating/cooling rates are required for lead-based ferroelectrics is also consistent with other researchers [39, 45, 46]. It should be once again emphasized that these results clearly indicate effects of heating/cooling rates on the phase formation behavior of PZ powders. These parameters are very crucial for Pb-based compounds [22, 47]. Usually, heating/cooling rates and dwell time show marked influences on phase formation behavior of other Pb-based compounds, such as PZT. It is of interest to observe that in PZ powders the heating/cooling rates do not show any effects on the behavior, while the dwell time only shows the effects on the particle agglomeration.

Based on the TG-DTA and XRD data, it may be concluded that, over a wide range of calcination conditions, single phase $PbZrO_3$ cannot be straightforwardly formed via a solid-state mixed oxide synthetic route, unless carefully designed calcination condition was performed. It is well documented that powders prepared by a conventional mixed oxide method have spatial fluctuations in their compositions. The extent of the fluctuation depends on the characteristics of the starting powders as well as the processing schedules [22, 33, 39]. The experimental work carried out here suggests that the optimal calcination conditions for single-phase $PbZrO_3$ (with impurities undetected by XRD technique) is 800 °C for 3 h or 850 °C for 1 h, with heating/cooling rates of 20 °C/min, which is closed to that of Puchmark et al. [30] (775 °C for 3 h with heating/cooling rates of 5 °C/min) but with significantly faster heating/cooling rates. Moreover, the formation temperature and/or dwell time for the production of

$PbZrO_3$ powders observed in this work are also lower than those reported by Fang et al. [31] (900 °C for 1 h) and Lanagan et al. [32] (900 °C for 8 h).

Finally, the morphological changes in the $PbZrO_3$ powders formed by a mixed oxide are illustrated in Fig. 7 as a function of calcination temperatures, dwell times and heating/cooling rates, respectively. The influence of calcination conditions on particle size is given in Table 1. These particle size data were directly estimated from SEM micrographs. Even though these data are not precisely determined, they were shown to provide estimated comparison between different calcination conditions and to form a basis for other more detailed studies with use of a combination between TEM and particle size distribution analyzer. After calcinations at 800 to 900°C, the powders seem to have similar morphology. In general, the particles are agglomerated and irregular in shape, with a substantial variation in particle size, particularly in samples calcined at higher temperatures or for longer dwell times. This observation is also similar to that of $Mg_4Nb_2O_9$ powders synthesized by Ananta [48]. The results indicate that averaged particle size and degree of agglomeration tend to increase with calcination temperature and dwell time (Table 1). However, the smallest particle size (estimated from SEM micrographs to be ~250 nm) and the morphology of the calcined powders are about the same. It is also of interest to point out that no evidence has been obtained for the existence of the cubic or spherical shape morphology as that of the hydrothermally derived $PbZrO_3$ powders [28, 49].

Conclusions

The methodology presented in this work provides a simple method for preparing perovskite $PbZrO_3$ powders via a solid-state mixed oxide synthetic route. By using optimal calcination conditions of 800 °C for 3 h or 850 °C for 1 h, with heating/cooling rates of 20 °C/min, the reproducible, low cost and fast process involving vibro-milling can provide high-purity perovskite $PbZrO_3$ powders with particle size ranging from 200–500 nm from inexpensive commercially available raw materials. The resulting $PbZrO_3$ powders consist of variety of agglomerated particle sizes, depending on calcination conditions. Finally, it should be emphasized that this work presents for the first time the effects of calcination conditions on the phase formation behavior of the PZ powders. These parameters clearly show significant influences on the processing of even simple binary system as PZ, and there is no doubt that they will show even more effects on other complicated materials such as PZT, PMN, PZN, PIN, and PMN-PT. The results on those systems are being produced and will be presented in future publications.

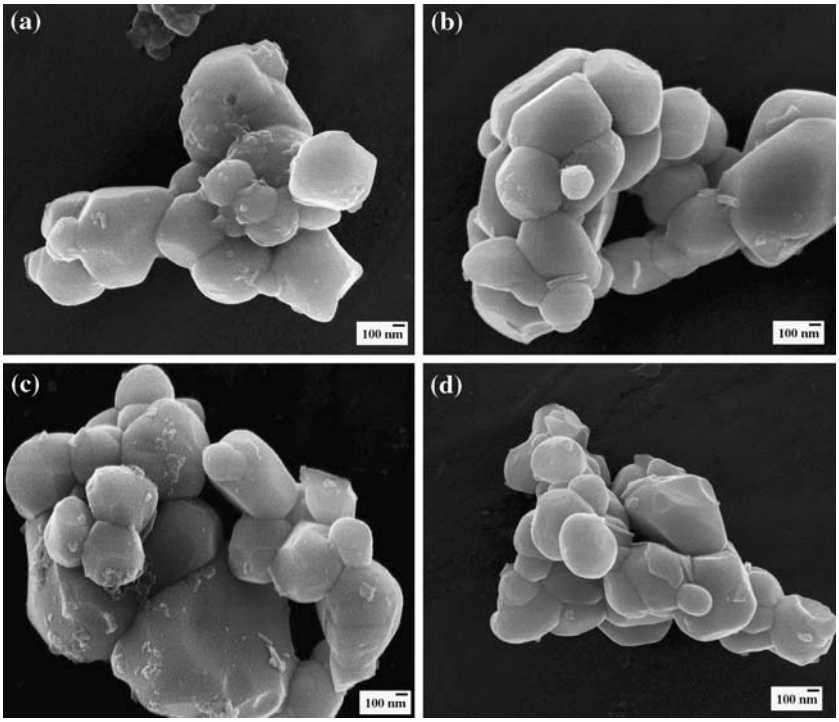

Fig. 7 SEM micrographs of the PZ powders calcined at (**a**) 850 °C/1h, (**b**) 850 °C/2 h, (**c**) 900 °C/2 h, with heating/cooling rates of 10 °C/min and (**d**) 850 °C/1 h with heating/cooling rates of 20 °C/min

Table 1 Particle size range of $PbZrO_3$ powders calcined at various conditions

Temperature (°C)	Dwell time(h)	Heating/cooling rates(°C/min)	Particle size range (mean)*(μm)
800	3	3	0.35–0.60 (0.41)
800	3	5	0.15–1.00 (0.52)
850	1	3	0.30–1.00 (0.44)
850	1	5	0.30–0.80 (0.59)
850	1	10	0.25–0.70 (0.54)
850	1	20	0.30–0.80 (0.51)
850	2	10	0.25–1.20 (0.64)
900	2	10	0.35–1.50 (0.77)

*The estimated precision of the particle size is ±10%

Acknowledgements We thank the Thailand Research Fund (TRF), the Comission on Higher Education (CHE), Graduate School, Faculty of Science, and Center of Excellence in Functional Nanomaterials, Chiang Mai University for all supports.

References

1. Jaffe B, Cook WJ, Jaffe H (1971) Piezoelectric ceramics. Academic Press, London
2. Jona F, Shirane G (1993) Ferroelectric crystals. Dover Publications, New York
3. Sawaguchi E, Maniwa H,Hoshino S (1951) Phys Rev 83:1078
4. Shirane G, Sawaguchi E, Takagi Y (1951) Phys Rev 84:476
5. Sawaguchi E, Kittaka K (1952) J Phys Soc Jpn 7:336
6. Tennery VJ (1966) J Am Ceram Soc 49:483
7. Scott BA, Burns G (1972) J Am Ceram Soc 55:331
8. Shirane G, Hoshino S (1954) Acta Crystallogr **7**:203
9. Pokharel BP, Pandey D (1999) J Appl Phys 86:3327
10. Bongarn T, Rujijanagul G, Milne SJ (2005) Mater Lett 59:1200
11. Whatmore RW (1976) Ph.D. Thesis, Genville and Cauis College, Cambridge
12. Singh K (1989) Ferroelectrics 94:433
13. Haertling GH (1999) J Am Ceram Soc 82:797
14. Moulson AJ, Herbert JM (2003) Electroceramics, 2nd edn. Wiley, New York
15. Uchino K (1998) Piezoelectrics and ultrasonic applications. Kluwer, Deventer
16. Kakegawa K, Mohri J, Takahashi T, Yamamura H, Shirasaki S (1977) Solid State Commun 24:769
17. Kingon AI, Clark JB (1983) J Am Ceram Soc 66:253
18. Matsuo Y, Sasaki H (1965) J Am Ceram Soc 48:289
19. Babushkin O, Lindback T, Lue JC, Leblais JYM (1996) J Eur Ceram Soc 16:1293
20. Hanky DL, Biggers JV (1951) J Am Ceram Soc 12:172
21. Garg A, Agrawal DC (1999) Mat Sci Eng B 56:46
22. Tipakontitikul R, Ananta S (2004) Mater Lett 58:449
23. Reaney IM, Glazounov A, Chu F, Bell A, Setter N (1997) Brit Ceram Trans 96:217
24. Oren EE, Taspinar E, Tas AC (1997) J Am Ceram Soc 80:2714
25. Ibrahim DM, Hennicke HW (1981) Trans J Br Ceram Soc 80:18
26. Deshpande AS, Khollam YB, Patil AJ, Deshpande SB, Potdar HS, Date SK (2001) Mater Lett 51:161
27. Rao YS, Sunandana CS (1992) J Mater Sci Lett 11:595
28. Choi JY, Kim CH, Kim DK (1998) J Am Ceram Soc 81:1353
29. Fang J, Wang J, Ng SC, Gan LM, Quek CH, Chew CH (1998) Mater Lett 36:179
30. Puchmark C, Rujijanagul G, Jiansirisomboon S, Tunkasiri T (2004) Ferroelectric Lett 31:1
31. Fang J, Wang J, Ng SC, Gan LM, Chew CH (1998) Ceram Inter 24:507
32. Lanagan MT, Kim JH, Jang S, Newnham RE (1988) J Am Ceram Soc 71:311
33. Ananta S, Thomas NW (1999) J Eur Ceram Soc 19:155
34. Klug H, Alexander LE (1974) X-ray diffraction procedures for polycrystalline and amorphous materials, 2nd edn. Wiley, New York
35. Aoyama T, Kurata N, Hirota K, Yamaguchi O (1995) J Am Ceram Soc 78:3163
36. Fushimi S, Ikeda T (1967) J Am Ceram Soc 50:129
37. Lee WE, Rainforth WM (1994) Ceramic microstructures: Property control by processing. Chapman & Hall, London
38. Deyneka TG, Vouk EA, Ishchuk VM, Ramakaeva RF, Volkova GK, Konstantinova TE (2004) Funct Mater 11:44
39. Udomporn A, Ananta S (2004) Mater Lett 58:1154
40. JCPDS-ICDD Card No. 77-1971 (2002) International Centre for Diffraction Data, Newtown Square, PA
41. JCPDS-ICDD Card No. 37-1484 (2002) International Centre for Diffraction Data, Newtown Square, PA
42. JCPDS-ICDD Card No. 35-739 (2002) International Centre for Diffraction Data, Newtown Square, PA, 2002
43. Tani T, Li JF, Viehland D, Payne DA (1994) J Appl Phys 75:3017
44. Ananta S, Brydson R, Thomas NW (2000) J Eur Ceram Soc 20:2315
45. Ryu J, Choi JJ, Kim HE (2001) J Am Ceram Soc 84:902
46. Baumgartner CE (1988) J Am Ceram Soc 71:C-350
47. Udomporn A, Pengpat K, Ananta S (2004) J Eur Ceram Soc 24:185
48. Ananta S (2004) Mater Lett 58:2530
49. Kim HK (1993) Thesis MS, Seoul National University, Seoul, Korea

Appl. Phys. A (2007)
DOI: 10.1007/s00339-007-3932-x

Applied Physics A
Materials Science & Processing

R. YIMNIRUN[1,✉]
X. TAN[2]
S. ANANTA[1]
S. WONGSAENMAI[1]

Preparation of fine-grain lead indium niobate ceramics with wolframite precursor method and resulting electrical properties

[1] Department of Physics, Faculty of Science, Chiang Mai University, Chiang Mai 50200, Thailand
[2] Department of Materials Science and Engineering, Iowa State University, Ames, IA 50011, USA

Received: 5 October 2006/Accepted: 30 January 2007

ABSTRACT In this study, lead indium niobate ($Pb(In_{1/2}Nb_{1/2})O_3$ or PIN) ceramics were prepared by a wolframite precursor method via a vibro-milling technique. Fine-grain ceramics were achieved with average grain size of 1–2 μm, indicating advantage of the vibro-milling technique used. The dielectric and ferroelectric properties were measured by means of an automated dielectric measurement set-up and a standardized ferroelectric tester, respectively. The dielectric properties of PIN ceramic were measured as functions of both temperature and frequency. The results indicated that the dielectric properties of the PIN ceramic were of relaxor ferroelectric behavior with temperature of dielectric maximum (T_m) ∼ 53 °C and dielectric constant (ε_r) ∼ 4300 (at 1 kHz). The P–E hysteresis loop measurements at various temperatures showed that the ferroelectric properties of the PIN ceramic changed from the paraelectric behavior at temperature above T_m to slim-loop type relaxor behavior at temperature slightly below T_m. Moreover, the P–E loop became more open at temperatures much lower than T_m.

PACS 77.22.Ch; 77.84.Dy

1 Introduction

Lead indium niobate $Pb(In_{1/2}Nb_{1/2})O_3$ (PIN) compounds are of interest for the kinetics of compositional ordering investigation [1]. It has been reported that the degrees of ordering on the B-site can be varied by thermal annealing and by forming solid solutions with perovskite compounds that exhibit normal dielectric behavior, such as $Pb(Fe_{1/2}Nb_{1/2})O_3$ (PFN), $PbZrO_3$ (PZ) and $PbTiO_3$ (PT) [2]. With different thermal treatments, the degrees of the In/Nb cation ordering on the B-site in a perovskite structure can be manipulated from a structurally disordered state into various degrees of ordering. The disorder PIN is a relaxor ferroelectric with a pseudocubic perovskite structure exhibiting the relaxor behavior with a broad dielectric maximum near 66 °C, when measured at 1 kHz [3, 4]. On the other hand, the ordered PIN has the antiferroelectric orthorhombic phase [5–9] with a sharp peak in the dielectric constant at 168 °C [4, 10]. However, phase-pure perovskite PIN ceramics free of the pyrochlore phase are very difficult to prepare using a conventional mixed oxide method [7, 11]. This is because the tolerance and the electronegativity difference of PIN are very low compared with other perovskite compounds such as PMN [2, 12]. The wolframite method, as used by Groves [13] for the preparation of perovskite PIN ceramic, is not effective in suppressing pyrochlore phase formation. The addition of excess In_2O_3 was shown to yield higher amount of perovskite phase (up to 98%) [13]. Recently, Alberta and Bhalla [7] were able to produce 100% phase-pure perovskite PIN ceramic with the addition of excess indium and/or lithium with wolframite method under oxygen atmosphere. Interestingly, these previous studied employed a mixed-oxide method with a conventional ball-milling technique. The powders prepared by the conventional mixed oxide route usually have spatial fluctuations in their compositions, which may lead to formation of unwanted phases. The extent of the fluctuation depends on the characteristics of the starting powders as well as on the processing schedule. Many recent studies have paid attention to processing schedule in details to yield phase-pure powders in many perovskite systems [14–20]. In addition, a vibro-milling technique has recently been employed to produce nano-sized powders which can also be used to fabricate ceramics with fine-grain microstructure that may lead to better resulting properties [14, 16, 20]. Therefore, the main purpose of this work is to prepare PIN powders and ceramics with the wolframite method via the vibro-milling technique. The vibro-milling technique is employed in this study to explore the potential in obtaining fine-grain ceramics, which would in turn lead to superior electrical properties. The effects of processing conditions on the phase formation behavior are also investigated. More importantly, the dielectric and ferroelectric properties of the resulting ceramics are also studied.

2 Experimental

The $Pb(In_{1/2}Nb_{1/2})O_3$ ceramics were prepared from $Pb(In_{1/2}Nb_{1/2})O_3$ powders obtained with the wolframite method via the vibro-milling technique. In this technique, a vibratory laboratory mill (McCrone micronizing mill) was employed. A total of 48 polycrystalline corundum milling media with a powder weight of 20 g was kept constant in each batch. The milling operation was carried out in isopropanal inert to the polypropylene jar [14, 16, 20]. Initially,

✉ Fax: +6653-943-445, E-mail: rattikornyimnirun@yahoo.com

phase-pure PIN powders were obtained via a well-known wolframite method [7, 19]. With the wolframite method, the single-phase indium niobate ($InNbO_4$) powders were first prepared by mixing starting indium oxide (In_2O_3) and niobium oxide (Nb_2O_5) (Aldrich, 99.9% purity) powders by employing the vibro-milling technique for 0.5 h and then calcining the mixed powders at 900 °C for 4 h with heating/cooling rates of 30 °C/min [21]. This yielded a so-called wolframite ($InNbO_4$) powder. The wolframite precursor powders were subsequently vibro-milled with lead oxide (PbO) (Fluka, 99% purity) for 0.5 h. After drying at 120 °C for 2 h, the reaction of the uncalcined powders taking place during heat treatment was investigated by themogravimetric and differential thermal analysis (TG-DTA, Shimadzu), using a heating rate of 5 °C/min in air from room temperature up to 1000 °C. Based on the TG-DTA results, the mixture was calcined at various conditions, in closed alumina crucible, in order to investigate the formation of $Pb(In_{1/2}Nb_{1/2})O_3$. Calcined powders were subsequently examined by room temperature X-ray diffraction (XRD; Siemen-D500 diffractometer), using Ni-filtered Cu K_α radiation to identify the phases formed and optimum calcination conditions for the formation of $Pb(In_{1/2}Nb_{1/2})O_3$ powders. It should, however, be noted that to obtain the phase-pure PIN powders 2 mol. % excess of In_2O_3 and PbO had to be added to compensate the loss during calcination [22]. The PIN powders obtained were vibro-milled for 0.5, then pressed hydraulically to form disc-shaped pellets 10 mm in diameter and 2 mm thick, with 3 wt. % polyvinyl alcohol as a binder. The pellets were placed on the alumina powder-bed inside alumina crucible and surrounded with atmosphere powders of the same composition. Finally, the pellets were sintered at 1050 °C for 2 h with heating/cooling rates of 5 °C/min. The phase formations of the sintered specimens were again studied by the X-ray diffractometer.

The densities of the sintered ceramics were measured by Archimedes method. The microstructure analyses were undertaken by a scanning electron microscopy (SEM: JEOL Model JSM 840A). Grain size was determined from SEM micrographs by a linear intercept method. The dielectric properties were evaluated with a computer-controlled dielectric measurement system consisted of a precision LCR-meter (Hewlett-Packard, model 4284A), a temperature chamber (Delta Design, model 9023), and a sample holder (Norwegian Electroceramics) capable of high temperature measurement. The ferroelectric polarization versus electric field (P–E) measurements were made using a standardized ferroelectric test system (RT-66A, Radiant Technologies) with an applied field of 30 kV/cm. More importantly, the temperature dependent ferroelectric properties were also examined.

3 Results and discussion

Initially, the DTA-TG analysis was performed on uncalcined powders to obtain thermal behavior to define the range of calcination temperature for the XRD investigation. The results from DTA-TG studies shown in Fig. 1 indicate that the suitable range of the calcination temperature is between 700 and 1000 °C. To study the phase development with increasing calcination temperature in the powders, they were calcined for 2 h in air at various temperatures, between

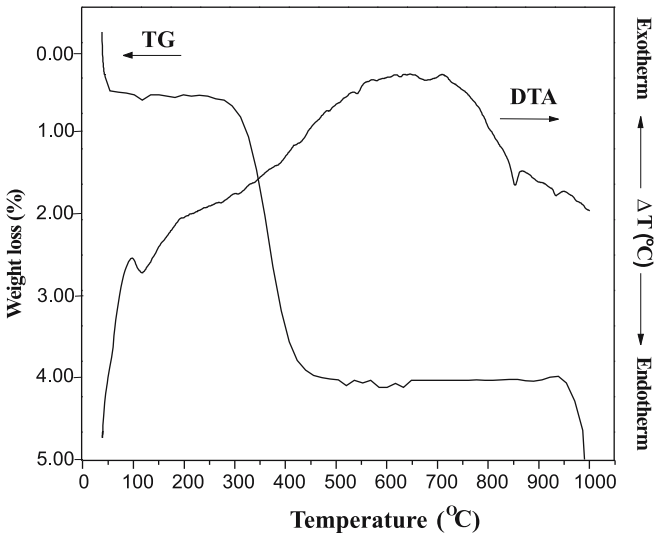

FIGURE 1 TG-DTA curves for the mixture of PbO-$InNbO_4$ powders

700 and 1000 °C, followed by phase analysis using XRD. As shown in Fig. 2, for the uncalcined powders, only X-ray peaks of starting precursors are present, indicating that no reaction had yet been triggered during the milling or low firing processes. It is seen that fine $Pb(In_{1/2}Nb_{1/2})O_3$ crystallites (∇) were developed in the powders at a calcination temperature as low as 700 °C, accompanying with separated pyrochlore phase (▼). This observation agrees well with those derived from the TG-DTA results. As the temperature increased to 800 °C, the intensity of the $Pb(In_{1/2}Nb_{1/2})O_3$ peaks was further enhanced and became the predominant phase. Upon calcination at 950 °C, an essentially monophasic of $Pb(In_{1/2}Nb_{1/2})O_3$ phase is obtained. This $Pb(In_{1/2}Nb_{1/2})O_3$ phase was indexable according to a cubic structure with lattice parameter $a = 4.110$ Å, in consistent with JCPDS file numbers 87-0304. This study also shows that the cubic

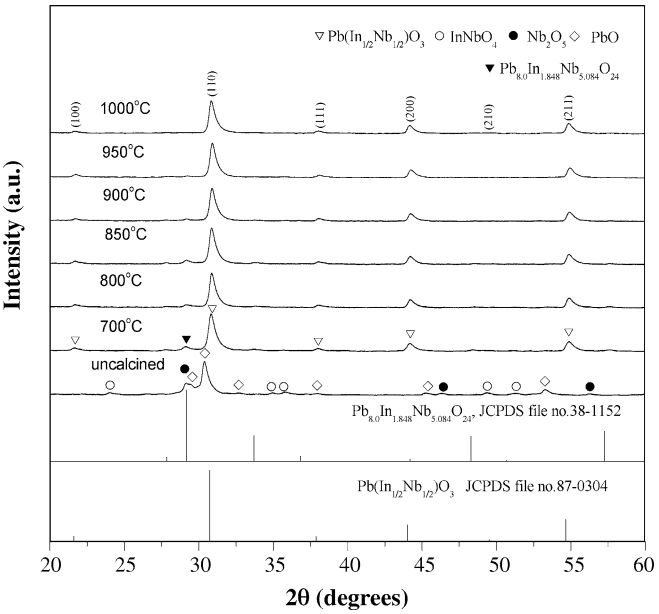

FIGURE 2 XRD patterns of PIN powders calcined at various temperatures for 2 h with heating/cooling rates of 5 °C/min

$Pb(In_{1/2}Nb_{1/2})O_3$ is the only detectable phase in the powders after calcination in the range of 950–1000 °C. Apart from the calcination temperature, the effect of dwell time was also studied. It was found that the single phase of $Pb(In_{1/2}Nb_{1/2})O_3$ (yield of 100% within the limitations of the XRD technique) was found to be possible in powders calcined at 950 °C with dwell time of 2 h or more, and in the powders calcined at 1000 °C with dwell time of 1 h or more. It should be noted that in earlier works [3, 7, 9], long heat treatments at ∼ 1000–1200 °C for at least 4 h were proposed for the formation of $Pb(In_{1/2}Nb_{1/2})O_3$ by a conventional mixed oxide synthetic route, although no details on phase formation were provided. However, in the present study phase-pure $Pb(In_{1/2}Nb_{1/2})O_3$ powders were obtained at 950 °C with dwell time of only 2 h or even shorter dwell time of 1 h at 1000 °C. This observation would clearly suggest the advantage of a rapid vibro-milling technique to significantly lower the optimum calcination temperature and dwell time for formation of single-phase $Pb(In_{1/2}Nb_{1/2})O_3$ powders.

Figure 3 shows the XRD pattern of PIN ceramics sintered at 1050 °C for 2 h with heating/cooling rate of 5 °C/min, which indicates $Pb(In_{1/2}Nb_{1/2})O_3$ along with very small amount of pyrochlore phase. The amount of perovskite PIN phase was calculated to be 98.5%, as compared to 90%–98% reported in previous investigations [13, 23]. The density of the sintered specimen was also determined to be 91% of the theoretical density, similar to that reported earlier [7, 24]. SEM micrographs in Fig. 4 reveal fine-grain microstructure (< 3 μm) in PIN ceramics with the average grain size of 1.22 μm. However, it should be noticed that the microstructure also represents two distinct grain sizes, i.e., large grains (∼ 2 μm) and submicron grains. Earlier study on PIN-based ceramics prepared with the conventional ball-milling method has also reported bimodal grain sizes but with large grains

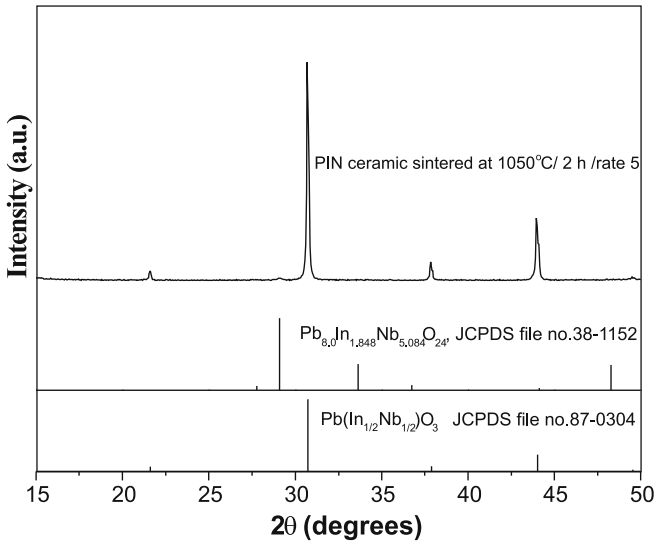

FIGURE 3 XRD pattern for PIN ceramic

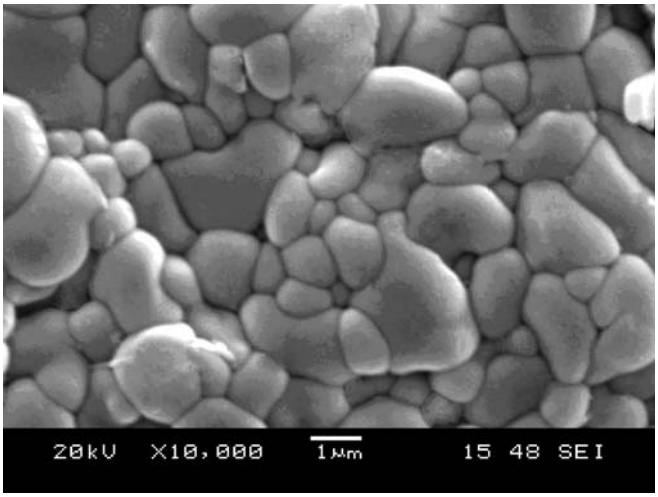

FIGURE 4 SEM micrographs of fine-grain PIN ceramic

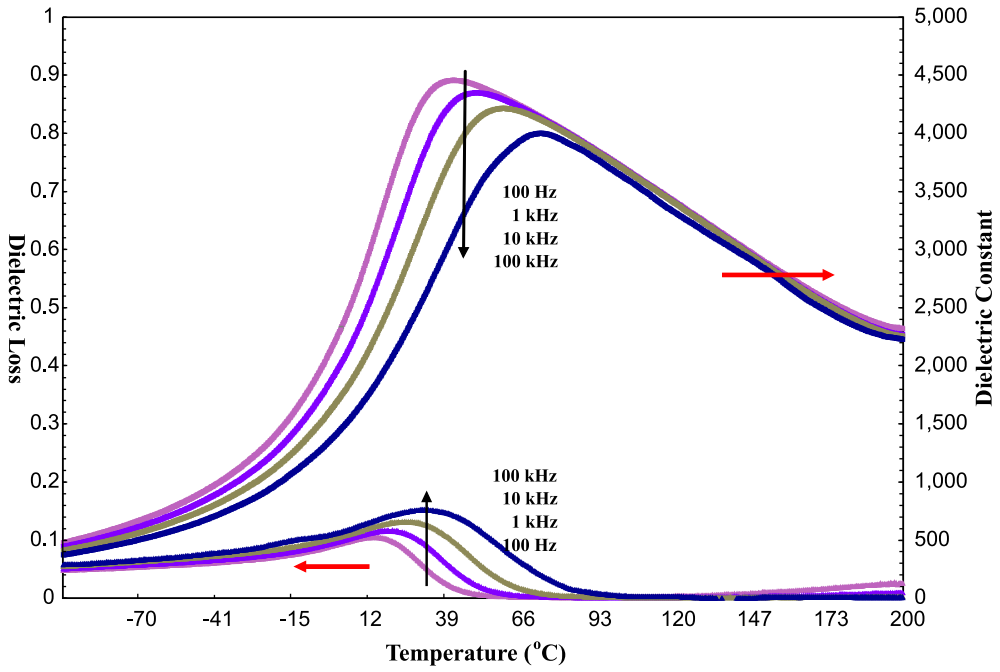

FIGURE 5 Temperature and frequency dependences of dielectric properties (dielectric constant (ε_r) and dielectric loss ($\tan\delta$)) of PIN ceramic

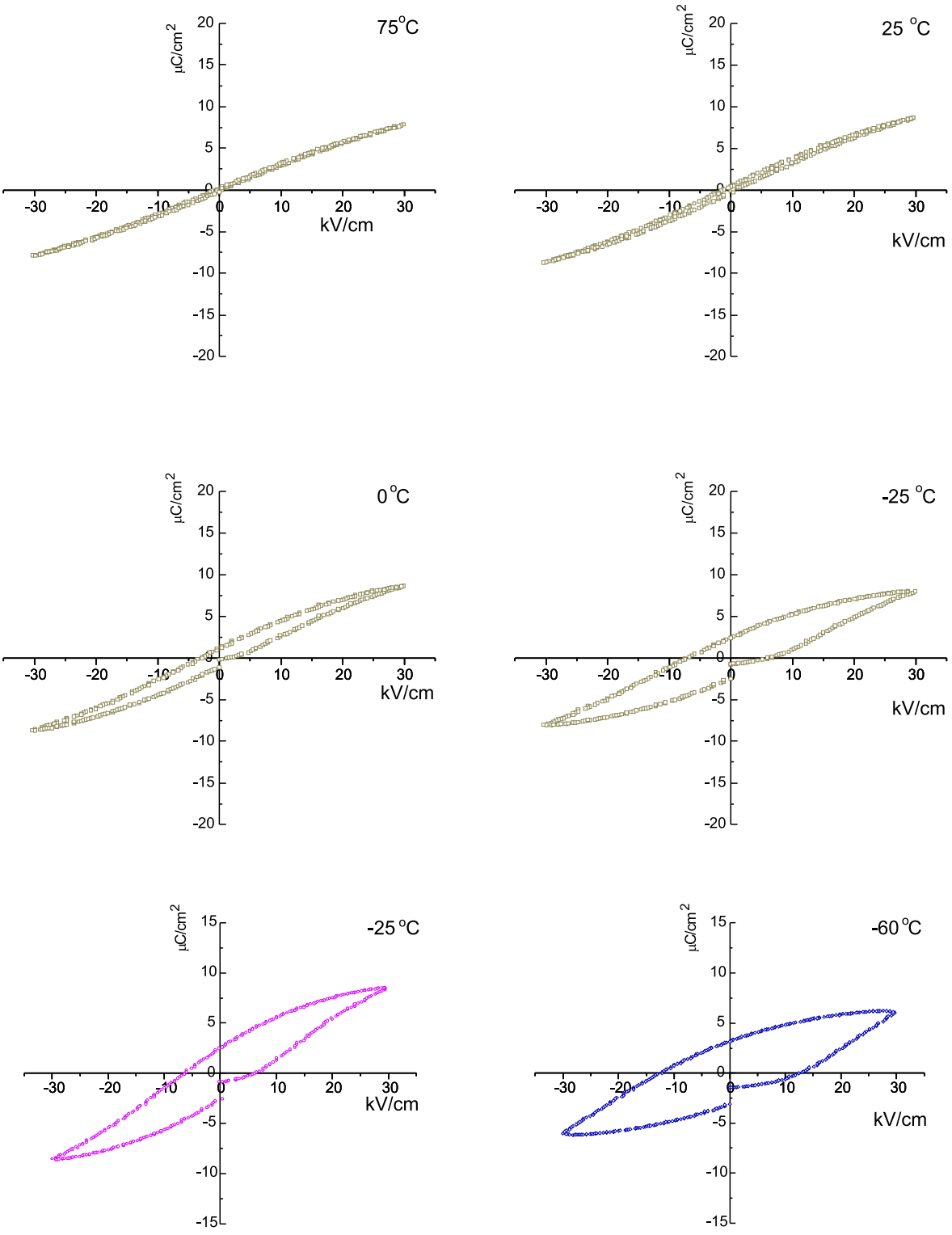

FIGURE 6 Temperature dependence of the P–E hysteresis loops of PIN ceramics

over 10 μm and fine grains about 1–2 μm [25]. Clearly, this shows the advantage of the vibro-milling technique in producing fine-grain PIN ceramics.

The dielectric properties, e.g., dielectric constant (ε_r) and tan δ, are measured as functions of both temperature and frequency, as shown in Fig. 5. At 1 kHz, the dielectric constant shows a maximum value of 4300 at 53 °C. The value of dielectric constant is higher than those reported earlier by Groves [13] and Park and Choo [23] with similar amount of perovskite phase. This suggests that the fine-grain PIN ceramics obtained exhibit better dielect ric properties. However, the dielectric constant is still lower in value than that of phase-pure PIN ceramic reported earlier by Alberta and Bhalla [7]. The lower value is attributed to the detrimen-

tal effect of the secondary pyrochlore phase. The dielectric properties of PIN ceramic change significantly with temperature and frequency. Both dielectric constant (ε_r) and dielectric loss tangent ($\tan\delta$) exhibit strong temperature-frequency dependence below the transition temperature, indication of a typical relaxor ferroelectric behavior. In this case, the temperatures of maximum dielectric constant and dielectric loss tangent are shifted to higher temperature with increasing frequency. The maximum value of the dielectric constant decreases with increasing frequency, while that of the dielectric loss tangent increases. The dielectric properties then become frequency independence above the transition temperature [26]. Interestingly, 98% porovskite PIN ceramic reported earlier [7] showed strong frequency-dependent dielectric properties even above the transition temperature. The degree of broadening or diffuseness in the observed dielectric variation could also be estimated with the diffusivity (γ) using the expression $\ln(1/\varepsilon_r - 1/\varepsilon_{max})$ vs. $(T - T_{max})^{\gamma}$. The value of γ can vary from 1, for normal ferroelectrics with a normal Curie–Weiss behavior, to 2, for completely disordered relaxor ferroelectrics [26]. The value of γ of the PIN ceramic is calculated to be 1.89, which confirms that diffuse phase transitions (DPT) occur in the PIN ceramics with a high degree of disorder. It is also observed that the degree of broadening for fine-grain PIN ceramics in this study is larger than that of coarse grains PIN reported earlier [7], a result of decreased grain size, as reported earlier in other perovskite systems [27, 28].

Figure 6 illustrates a series of polarization (P–E) hysteresis loops for the PIN ceramics as a function of temperature from −60 to 75 °C. It is clearly evident that the shape of P–E loops and the polarization values vary greatly with the temperature. At 75 °C, which is above the temperature of maximum dielectric constant ($T_m \sim 53$ °C), the P–E loop shows a paraelectric behavior. When the temperature was lowered to 25 °C, the P–E loop is of a "slim" loop type, a characteristic of the suppressed ferroelectric interaction typically found in the relaxor ferroelectrics with polar nano-regions [26, 27]. As temperature decreases further, the hysteresis loops of PIN ceramics become more developed and open with increasing remnant polarization (P_r), spontaneous polarization (P_s) and coercive field (E_c). It could be said that the hysteresis loops become more of a typical "square" form, a typical characteristic of a phase that contains long-range interaction between dipoles in the ferroelectric micro-domain state [26]. Similar observations have been reported earlier [24, 27, 28]. At −425 °C, the maximum polarization is found to be 8 $\mu C/cm^2$ at a field of 30 kV/cm, with P_r value of 2.5 $\mu C/cm^2$ and E_c of 7.5 kV/cm, in the same range as reported earlier [24]. For better comparison, Table 1 summarizes properties of PIN ceramic prepared with different experimental conditions, which show the advantage of the method used in this present study.

4 Conclusions

The $Pb(In_{1/2}Nb_{1/2})O_3$ ceramics were prepared by a wolframite precursor method via a vibro-milling technique. The phase-pure $Pb(In_{1/2}Nb_{1/2})O_3$ powders were obtained at 950 °C with dwell time of 2 h or at 1000 °C with dwell time of 1 h. The 98.5% perovskite fine-grain PIN ceramics with average grain size of 1–2 μm were obtained by sintering at 1050 °C for 2 h. This study suggested the advantage of the vibro-milling technique to lower the optimum calcination temperature and dwell time for formation of single-phase PIN powders and for obtaining fine-grain ceramics. The dielectric and ferroelectric properties of the ceramics were determined. The results indicated that the dielectric properties of PIN ceramics were of relaxor ferroelectric behavior with the maximum dielectric constant of 4300 at 53 °C. Interestingly, the fine-grain PIN ceramics showed slightly better dielectric properties than the coarse grains ceramics in previous investigations. The P–E hysteresis loop measurements also demonstrated strong temperature dependent ferroelectric properties. At −25 °C, the maximum polarization is found to be 8 $\mu C/cm^2$ at a field of 30 kV/cm, with P_r value of

Processing conditions	% Perovskite	Average Grain size (μm)	T_m (°C)	$\varepsilon_{r,max}$ (1 kHz)	$\tan\delta_{max}$ (1 kHz)	P_r ($\mu C/cm^2$)	P_{max} ($\mu C/cm^2$)	E_c (kV/cm)	Ref.
Vibro-milled with Wolframite route Excess 2 mol. % PbO and In_2O_3 950 °C/2 h (calcine) and 1050 °C/2 h (sinter)	98.5	1.22	53	4300	0.08	2.5 (−25 °C)	8 (at 30 kV/cm)	7.5	This work
Ball-milled with Wolframite route Sintered in O_2-atm 1050 °C/4 h (calcine) and 1100 °C/2 h (sinter)	100	–	66	5500	0.12	1.5	22 (at 60 kV/cm)	6	[7]
Ball-milled with Wolframite route Excess 3 mol. % Li_2CO_3 and In_2O_3 1050 °C/4 h (calcine) and 1050 °C/2 h (sinter)	95	–	25	3200	0.07	–	–	–	[13]
Ball-milled with Wolframite route Excess 2 wt. % In_2O_3 1000 °C/1 h (calcine) and 1050 °C/4 h (sinter)	98	–	63	4700	0.11	1.1	–	–	[23]
Ball-milled with Wolframite route Fast-firing 900 °C/1 h (sinter)	100	1.5	56	3100	0.02	6.6 (at 20 kV/cm)	11	16	[24]
Ball-milled with Wolframite route Fast-firing 900 °C/0.5 h (sinter)	95	1	62	3850	0.08	–	–	–	[29]

TABLE 1 Comparison of preparation conditions and properties for PIN ceramics

$2.5\,\mu C/cm^2$ and E_c of $7.5\,kV/cm$, in the same range as reported earlier.

ACKNOWLEDGEMENTS The authors would like to express their gratitude for financial support from the Thailand Research Fund (TRF) and Graduate School and Faculty of Science, Chiang Mai University, and Ministry of University Affairs of Thailand.

REFERENCES

1 A.A. Bokov, I.P. Rayevskii, V.G. Smotrakov, O.I. Prokopalo, Phys. Stat. Solidi A **93**, 411 (1986)
2 T.R. Shrout, A. Halliyal, Am. Ceram. Soc. Bull. **66**, 704 (1987)
3 E.F. Alberta, A.S. Bhalla, Mater. Lett. **40**, 114 (1999)
4 E.F. Alberta, A.S. Bhalla, J. Phys. Chem. Solids **63**, 1759 (2002)
5 C.A. Randall, D.J. Barber, P. Groves, R.W. Whatmore, J. Mater. Sci. **23**, 3678 (1988)
6 N. Yasuda, T. Mizuno, Appl. Phys. Lett. **66**, 571 (1995)
7 E.F. Alberta, A.S. Bhalla, Mater. Lett. **29**, 127 (1996)
8 E.F. Alberta, A.S. Bhalla, Ferroelectrics **188**, 96 (1996)
9 N. Yasuda, H. Ohwa, T. Mizunao, M. Iwata, Y. Ishibashi, Appl. Phys. Lett. **68**, 3404 (1996)
10 M. Iwata, S. Katagiri, H. Orihara, M. Maeda, I. Zusuki, H. Ohwa, N. Yasuda, Y. Ishibashi, Ferroelectrics **301**, 179 (2004)
11 Y. Yoshikawa, J. Eur. Ceram. Soc. **21**, 2041 (2001)
12 Y. Guo, H. Luo, T. He, Z. Yin, Solid State Commun. **123**, 417 (2002)
13 P. Groves, Ferroelectrics **65**, 67 (1985)
14 R. Wongmaneerung, R. Yimnirun, S. Ananta, Mater. Lett. **60**, 2666 (2006)
15 A. Ngamjarurojana, O. Khamman, R. Yimnirun, S. Ananta, Mater. Lett. **60**, 2867 (2006)
16 R. Wongmaneerung, T. Sarnkonsri, R. Yimnirun, S. Ananta, Mater. Sci. Eng. B **130**, 246 (2006)
17 R. Wongmaneerung, T. Sarnkonsri, R. Yimnirun, S. Ananta, Mater. Sci. Eng. B **132**, 292 (2006)
18 O. Khamman, R. Yimnirun, S. Ananta, Mater. Lett. **61**, 639 (2007)
19 S. Wongsaenmai, R. Yimnirun, S. Ananta, Mater. Lett. (2007), in press, DOI: 10.1016/j.matlet.2006.09.028
20 R. Wongmaneerung, R. Yimnirun, S. Ananta, Mater. Lett. **60**, 1447 (2006)
21 S. Wongsaenmai, R. Yimnirun, S. Ananta, J. Mater. Sci. (2007), in press, DOI: 10.1007/s10853-006-0404-1
22 S. Wongsaenmai, O. Khamman, S. Ananta, R. Yimnirun, J. Electroceram. (2007), in press
23 S.S. Park, W.K. Choo, Ferroelectrics **118**, 117 (1991)
24 N. Yasuda, S. Shibuya, J. Phys.: Condens. Matter **1**, 10613 (1989)
25 M. Pham-Thi, C. Augier, H. Dammak, P. Gaucher, Ultrasonics **44**, e627 (2006)
26 L.E. Cross, Ferroelectrics **76**, 241 (1987)
27 R. Yimnirun, S. Ananta, P. Laoratanakul, J. Eur. Ceram. Soc. **25**, 3225 (2005)
28 V. Koval, C. Alemany, J. Briancin, H. Brunckova, J. Electroceram. **10**, 19 (2003)
29 C. Elissalde, F. Weill, J. Ravez, Mater. Sci. Eng. B **25**, 85 (1994)

ELSEVIER

Journal of Alloys and Compounds xxx (2007) xxx–xxx

Journal of ALLOYS AND COMPOUNDS

www.elsevier.com/locate/jallcom

Preparation of perovskite nanopowders by vibro-milling technique

Orawan Khamman, Rewadee Wongmaneerung, Wanwilai Chaisan, Rattikorn Yimnirun, Supon Ananta *

Department of Physics, Faculty of Science, Chiang Mai University, Chiang Mai 50200, Thailand

Received 24 December 2006; received in revised form 27 January 2007; accepted 20 February 2007

Abstract

The potential of the vibro-milling technique as a simple method to obtain usable quantities of single-phase perovskite powders with nanosized particles was examined. A detailed study considering the role of both milling time and firing condition on phase formation and particle size of the final product was performed. Powder samples were mainly characterized using XRD, SEM and laser diffraction techniques. The calcination temperature for the formation of the desired phase was lower when longer milling times applied. More importantly, by employing an appropriate choice of the milling time and calcination condition, high purity perovskite nanopowders have been successfully prepared with a simple solid-state reaction method.

Keywords: Powders; Solid-state reaction; Milling; Perovskite

1. Introduction

Electroceramic materials with perovskite structure, such as $BaTiO_3$, $PbTiO_3$, $PbZrO_3$, $Pb(Zr,Ti)O_3$, etc. have attracted interest for several decades, with tremendous applications including multilayer ceramic capacitors, transducers, sensors and actuators [1–3]. The major challenge in manufacturing these materials is in the processing of the materials with reliable and reproducible properties [3,4].

Recently, the studies of nanoparticles are also very attractive field [5,6]. The evolution of a method to produce nanopowders of precise stoichiometry and desired properties is complex, depending on a number of variables, such as starting materials, processing history, temperature, etc. It is known that electroceramic nanopowders with very good mixing on an atomic scale have normally been synthesized by a number of processing techniques, such as sol–gel [7], co-precipitation [8] and hydrothermal [9]. All of these techniques are aimed at reducing temperature of preparation of the compound even though they are more involved and complicated than the mixed oxide route. Generally, the mixed oxide method involves the heating of a mixture of oxide constituents at high temperature for long times and has been employed intensively in the last decade [10–12]. The optimization of calcination conditions used in the mixed oxide process, however, has not received much detailed attention, and the effects of applied dwell time and heating/cooling rates have not been studied extensively.

More recently, it has been reported that many nanoparticles can be successfully synthesized by using several mechanical milling method [6,12–14]. From the point of view of energy efficiency, the vibro-mill (or vibratory mill or vibro-energy mill which is a machine for vibrating vessel filled with grinding media at amplitudes up to a approximately 5 cm) seems to be more attractive than the ball mill [12]. Relative to ball-milling, vibro-milling produces finer particles and a narrower size distribution at a faster rate [12–14]. This implies that mills, especially, fine grinders like a vibro-mill are recognized as a tool for producing nanopowders, and the milling time is a key operation for such materials processing as well as the nanopowder preparation. Moreover, the advantage of using a solid-state reaction method via mechanical milling for preparation of nanopowders lies in its ability to produce mass quantities of powder in the solid-state using simple equipment and low cost starting precursors. Although some research has been done in the

* Corresponding author.
E-mail address: suponananta@yahoo.com (S. Ananta).

0925-8388/$ – see front matter © 2007 Elsevier B.V. All rights reserved.
doi:10.1016/j.jallcom.2007.02.109

preparation of perovskite powders via a vibro-milling technique [12–14], to our knowledge a detailed study considering the role of both milling times and firing conditions on the preparation of perovskite nanopowders has not been widely reported yet.

In the present study, we have demonstrated the potential of a rapid vibro-milling technique in the production of several important perovskite nanopowders, such as $PbZrO_3$ or PZ, $PbTiO_3$ or PT and $BaTiO_3$ or BT.

2. Experimental

The raw materials used were commercially available lead oxide, zirconium oxide, titanium oxide and barium carbonate (Fluka, >99% purity). These oxide powders exhibited an average particle size in the range of 3.0–5.0 μm. $PbZrO_3$, $PbTiO_3$ and $BaTiO_3$ powders were synthesized by the solid-state reaction of these raw materials. A vibratory laboratory mill (McCrone Micronizing Mill) powered by a 1/30 HP motor was employed for preparing the stoichiometric powders [13]. The grinding vessel consists of a 125 ml capacity polypropylene jar fitted with a screw-capped, gasketless, polythene closure. The jar is packed with an ordered array of identical, cylindrical, grinding media of polycrystalline corundum. A total of 48 milling media cylindrical with a powder weight of 20 g was kept constant in each batch. The milling operation was carried out in isopropanal inert to the polypropylene jar. Various milling times ranging from 0.5 to 35 h were selected in order to investigate the phase formation characteristic of all desired powders and the smallest particle size. After drying at 120 °C for 2 h, various calcination conditions, i.e. temperature ranging from 500 to 1200 °C, dwell times ranging from 1 to 6 h and heating/cooling rates ranging from 10 to 30 °C/min, were applied (the powders were calcined inside a closed alumina crucible) in order to investigate the formation of the desired phases.

All powders were examined by room temperature X-ray diffraction (XRD; Siemens-D500 diffractometer) using Ni-filtered Cu Kα radiation, to identify the phases formed, optimum milling time and firing conditions for the production of single-phase powders. The average crystallite size is also estimated from XRD patterns [15]. The particle size distributions of the powders were determined by laser diffraction technique (DIAS 1640 laser diffraction spectrometer) with the particle sizes and morphologies of the powders observed by scanning electron microscopy (JEOL JSM-840A SEM). The chemical compositions of the phases formed were elucidated by an energy-dispersive X-ray (EDX) analyzer with an ultra-thin window. EDX spectra were quantified with the virtual standard peaks supplied with the Oxford Instruments eXL software.

3. Results and discussion

XRD patterns of the calcined $PbZrO_3$ powders after different combination of milling time and calcination condition are given in Fig. 1. For the uncalcined powder subjected to 15 h of vibro-milling, only X-ray peaks of precursors PbO (●) and ZrO_2 (◯) are present, indicating that no reaction was yet triggered during the vibro-milling process. However, after calcination at 800 °C for 1 h, it is seen that the perovskite $PbZrO_3$ becomes the predominant phase, indicating that the reaction has occurred to a considerable extent. It should be noted that when the dwell time of the calcination at 800 °C was extended up to 2 h, the single-phase of perovskite PZ (yield of 100% within the limitations of the XRD technique) was obtained. This was apparently a consequence of the enhancement in crystallinity of the perovskite phase with increasing degree of mixing and dwell time, in good

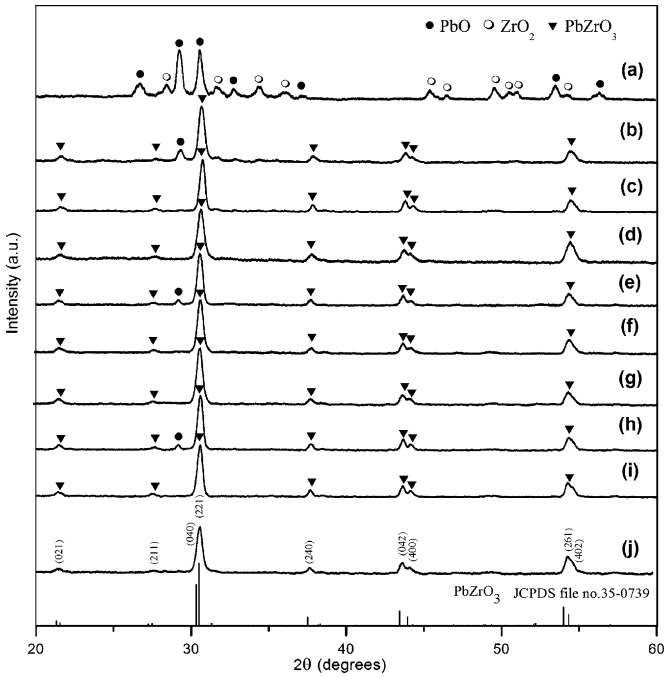

Fig. 1. XRD patterns of PZ powders milled for 15 h (a) uncalcined, and calcined at 800 °C for (b) 1 h and (c) 2 h with heating/cooling rates of 10 °C/min and (d) 30 °C/min; milled for 25 h and calcined at (e) 750 °C for 5 h (f) 800 °C for 1 h with heating/cooling rates of 10 °C/min and (g) 30 °C/min.; and milled for 35 h and calcined at 750 °C for (h) 3 h and (i) 4 h with heating/cooling rates of 10 °C/min and (j) 30 °C/min.

Table 1
Effect of milling time on the variation of particle size of perovskite powders calcined at their optimum conditions with heating/cooling rates of 30 °C/min and measured by different techniques

Powders	Milling time (h)	Calcination condition (°C/h)	XRD	SEM		Laser scattering	
			A (nm)	*D* (nm)	*P* (nm)	*D* (nm)	*P* (nm)
PZ	15	800/2	60.41	280	53–692	700	35–2000
	25	800/1	35.11	223	31–400	170	35–750
	35	750/4	27.50	121	31–228	1570	10–6000
PT	5	600/1	22.50	101	67–135	690	290–1140
	15	600/1	22.00	78	43–114	4640	1640–7790
	25	600/1	21.50	63	17–109	180	70–310
BT	0.5	1300/2	38.32	610	250–1400	1000	400–1500
	25	1200/2	31.60	390	250–700	400	60–700
	30	1200/2	31.56	250	100–400	600	120–1000

A: Crystallite size; *D*: average particle size; *P*: particle size distribution or range.

Please cite this article in press as: O. Khamman et al., J. Alloys Compd. (2007), doi:10.1016/j.jallcom.2007.02.109

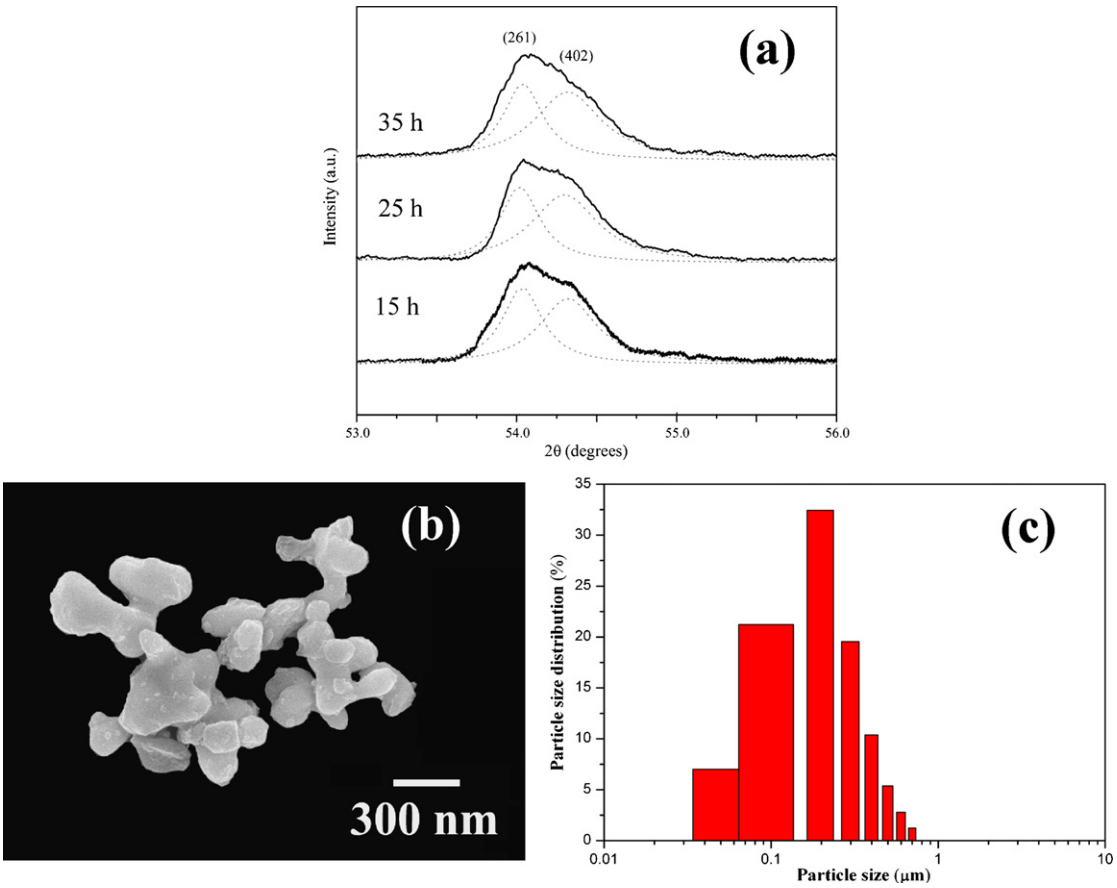

Fig. 2. (a) Enlarged zone of XRD patterns showing peaks broadening as a function of milling times of PZ powders, (b) SEM micrograph and (c) particle size distribution of PZ powders milled for 25 h and calcined at 800 °C for 1 h with heating/cooling rates of 30 °C/min.

agreement with other works [13,14]. In general, the strongest reflections apparent in the majority of these XRD patterns indicate the formation of the lead zirconate, $PbZrO_3$. These can be matched with JCPDS file number 35-0739 for the orthorhombic phase, in space group *P*2*cb* (no. 32) with cell parameters $a = 823$ pm, $b = 1177$ pm and $c = 588$ pm [16], consistent with other works [17,18]. For 15 h of milling, the optimum calcination condition for the formation of a high purity $PbZrO_3$ phase was found to be about 800 °C for 2 h with heating/cooling rates of 30 °C/min.

To further study the phase development with increasing milling times, an attempt was also made to calcine mixed powders milled at 25 and 35 h under various conditions as shown in Fig. 1(e–j). In this connection, it is seen that by varying the calcination condition, the minimum firing temperature for the single-phase formation of each milling batch is gradually decreased with increasing milling time. The main reason for this behavior is that a complete solid-state reaction probably takes place more easily when the particle size is milled down by accelerating an atomic diffusion mechanism to meet the suitable level of homogeneity mixing. It is thought that reducing the particle size significantly reduces heat diffusion limitations. It is therefore, believed that the solid-state reaction to form perovskite PZ phase occurs at lower temperatures with decreasing the particle size of the oxide powders.

In the work reported here, evidence for the minor phase of PbO which coexists with the parent phase of $PbZrO_3$ is found after calcination at temperature 750–800 °C, in agreement with literature [11,19]. This second phase has an orthorhombic structure with cell parameters $a = 589.3$ pm, $b = 549.0$ pm and $c = 475.2$ pm (JCPDS file number 77-1971) [20]. This observation could be attributed mainly to the poor reactivity of lead and zirconium species [19] and also the limited mixing capability of the mechanical method [13,14]. A noticeable difference is noted when employing the milling time longer than 15 h, Fig. 1(e–j), since an essentially monophasic $PbZrO_3$ of perovskite structure was obtained at 800 °C for 1 h (or 750 °C for 4 h) for the milling time of 25 h (or 35 h). This was apparently a consequence of the enhancement in crystallinity of the perovskite phase with increasing degree of mixing and dwell time, in good agreement with other works [13,14].

In the present study, an attempt was also made to calcine the powders under various heating/cooling rates (Fig. 1). In this connection, it is shown that the yield of $PbZrO_3$ phase did not vary significantly with different heating/cooling rates ranging from 10 to 30 °C/min, in good agreement with the early observation for the $PbZrO_3$ powders subjected to 0.5 h of vibro-milling time [19].

After establishing the optimum combination between vibro-milling time and calcination condition, similar investigation was

Please cite this article in press as: O. Khamman et al., J. Alloys Compd. (2007), doi:10.1016/j.jallcom.2007.02.109

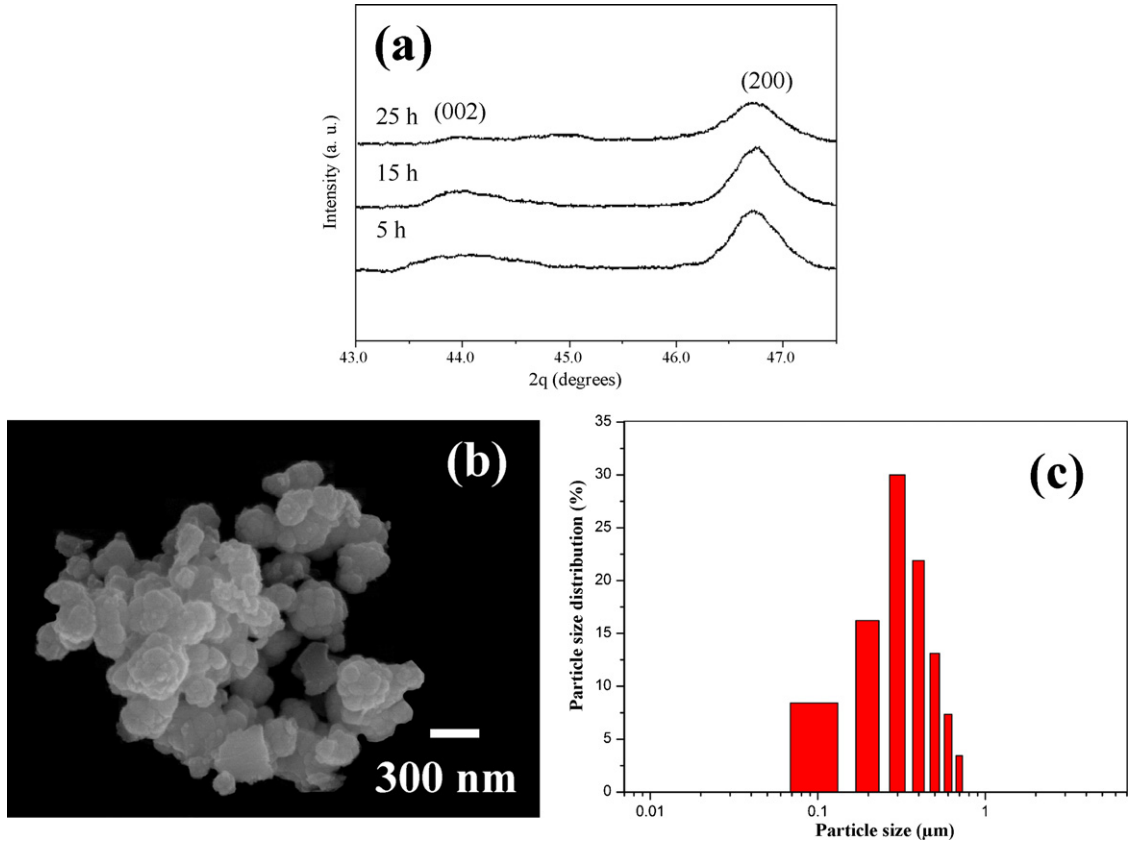

Fig. 3. (a) Enlarged zone of XRD patterns showing peaks broadening as a function of milling times of PT powders, (b) SEM micrograph and (c) particle size distribution of PT powders milled for 25 h and calcined at 600 °C for 1 h with heating/cooling rates of 30 °C/min.

also performed on the preparation of $PbTiO_3$ and $BaTiO_3$ powders as shown in Figs. 3 and 4, respectively. It should be noted that no evidences of the introduction of impurity due to wear debris from the selected milling process was observed in all calcined powders, indicating the effectiveness of the vibro-milling technique for the production of high purity nanopowders. Our previous investigations on related systems also indicated that no evidence of contamination from milling media was detected by XRD, EDX–SEM and TEM techniques [12,14,19,21,22]. As expected, there is evidence that, even for a wide range of calcination conditions, single-phase of all selected electroceramic powders cannot easily be produced, in agreement with literature [11–14]. This could be attributed mainly to the poor reactivity of starting species [13,14] and also the limited mixing capability of the mechanical method [23].

The variation of calculated crystallite size of all single-phase perovskite powders milled for different times and calcined at their optimum conditions is given in Table 1. In general, it is seen that the crystalline size of all powders decreases with increasing milling times. These observations indicate that the particle size affects the evolution of crystallinity of the phase formed by prolong milling treatment. Moreover, it has been observed that with increasing milling time, all diffraction lines broaden, as shown in Figs. 2(a), 3(a) and 4(a), which are an indication of a continuous decrease in particle size and of the introduction of lattice strain [15].

For all powders, the longer the milling time, the finer is the particle size. Also the relative intensities of the Bragg peaks and the calculated crystallite size for all powders tend to decrease with the increase of milling time. However, it is well documented that, as Scherer's analysis provides only a measurement of the extension of the coherently diffracting domains, the particle sizes estimated by this method can be significantly under estimated [14,15]. In addition to strain, factors, such as dislocations, stacking faults, heterogeneities in composition and instrumental broadening can contribute to peak broadening, making it almost impossible to extract a reliable particle size solely from XRD [15,23]. However, it should be noted that by increasing the calcination time from 1 to 4 h, these calculated values decrease to the minimum at 2 h and then grow up further after more dwell time applied. There is no obvious interpretation of these observations, although it is likely to correspond to the competition between the major mechanisms leading to crystallization and agglomeration [19].

In this connection, a combination of SEM and laser diffraction techniques was also employed for the morphology and particle size distribution measurement, as some examples shown in Figs. 2(b,c), 3(b,c) and 4(b,c). In general, all powders are agglomerated and basically irregular in shape, with a substantial variation in particle sizes, particularly in powders subjected to high firing temperatures (Fig. 4(b)). The powders consist of primary particles of nanometers in size. The primary particles have

Please cite this article in press as: O. Khamman et al., J. Alloys Compd. (2007), doi:10.1016/j.jallcom.2007.02.109

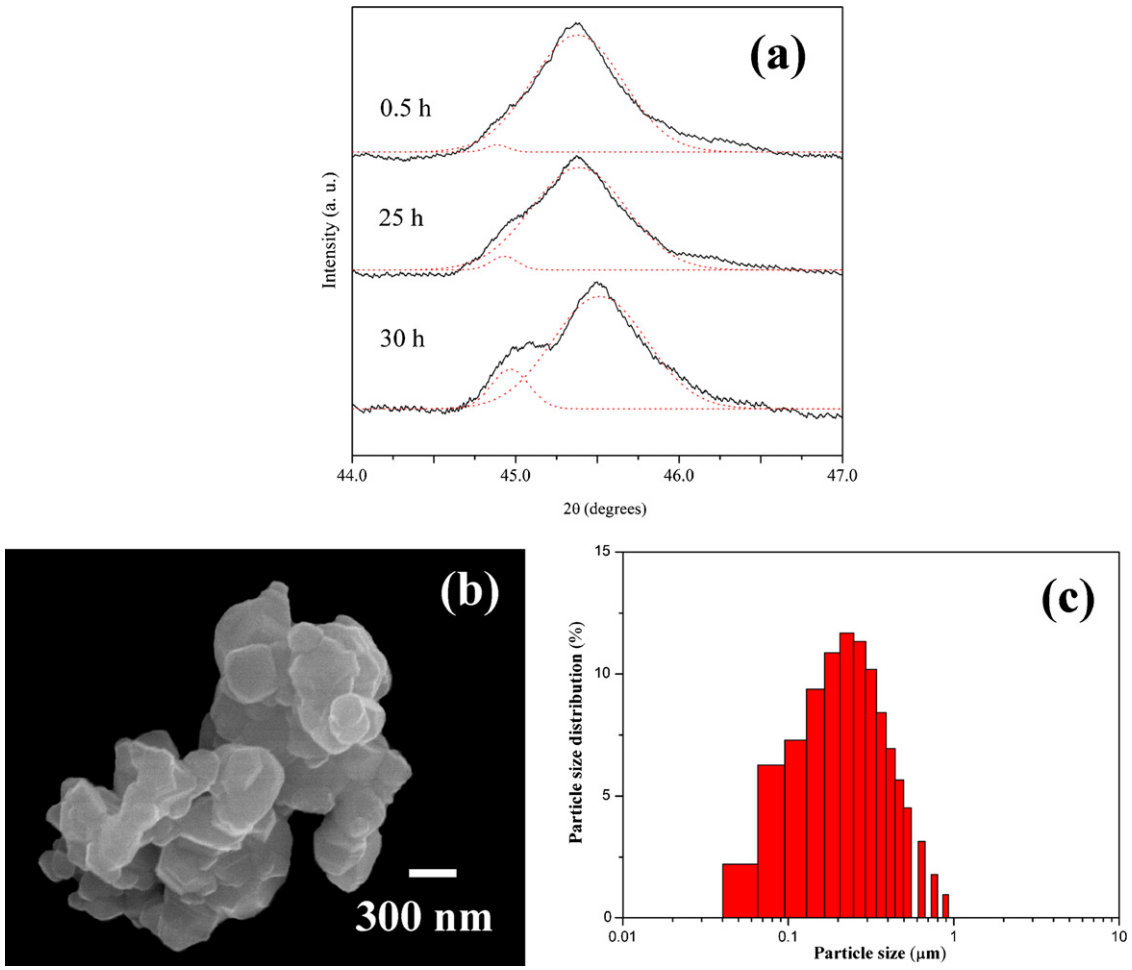

Fig. 4. (a) Enlarged zone of XRD patterns showing peaks broadening as a function of milling times of BT powders, (b) SEM micrograph and (c) particle size distribution of BT powders milled for 25 h and calcined at 1200 °C for 2 h with heating/cooling rates of 30 °C/min.

sizes of ~31–400, 17–109 and 250–700 nm, and the agglomerates measured ~35–750, 70–310 and 60–700 nm, for PZ, PT and BT powders, respectively. It is also of interest to point out that degree of agglomeration tends to increase with milling time and calcination temperatures (Fig. 4(b and c)), in good agreement with other works [12–14]. This observation may be attributed to the occurrence of hard agglomeration with strong inter-particle bond within each aggregates resulting from firing process. Any milling parameter, such as milling time, milling media or milling frequency, that influences the grain size within the particles has a corresponding effect on the resulting particle size.

The experimental work carried out here, suggests that mass production of single-phase PZ, PT and BT nanopowders with the smallest particle size ~31, 17 and 100 nm, respectively (estimated from SEM micrographs), can be achieved by employing a combination of suitable vibro-milling time and calcination condition. Moreover, the employed heating/cooling rates for all selected powders observed in this work are also faster than those reported earlier [23–25]. In general, EDX analysis using a 20 nm probe on a large number of particles of these calcined electroceramic powders confirmed the existence of single (perovskite)-phase, in good agreement with XRD results.

4. Conclusions

Using commercially available oxide powders as the starting materials, this work demonstrated that a rapid vibro-milling technique has considerable potential for the low cost, large scale production of several high purity perovskite nanopowders. Through the suitable selection of milling time and calcination condition, the vibro-milling technique may be extended to the preparation of a very wide range of nanopowders.

Acknowledgements

This work was supported by the Thailand Research Fund (TRF), the Commission on Higher Education (CHE), National Nanotechnology Center (Nanotec), the Faculty of Science and the Graduate School of Chiang Mai University.

References

[1] A.J. Moulson, J.M. Herbert, Electroceramics, second ed., Wiley, Chichester, 2003.
[2] Y. Xu, Ferroelectric Materials and their Applications, North-Holland, New York, 1991.

[3] G.H. Haertling, J. Am. Ceram. Soc. 82 (1999) 797–818.
[4] D. Segal, Processing of ceramics, Part 1, in: R.J. Brook (Ed.), Materials Science and Technology, Verlagsgesellscaft mbH, Weinheim, 1996.
[5] N. Setter, J. Eur. Ceram. Soc. 21 (2001) 1279–1293.
[6] P.G. McCormick, T. Tsuzuki, J.S. Robinson, J. Ding, Adv. Mater. 13 (2001) 1008–1010.
[7] D.D.E. Lakeman, D.A. Payne, Mater. Chem. Phys. 38 (1994) 305–324.
[8] W.E. Rhine, K. Saegusa, R.B. Hallock, M.J. Cima, Ceram. Trans. 12 (1990) 107–118.
[9] A. Dias, V.T.L. Buono, V.S.T. Ciminelli, R.L. Moreira, J. Eur. Ceram. Soc. 19 (1999) 1027–1031.
[10] M. Dambekalne, I. Brante, A. Sternberg, Ferroelectrics 90 (1989) 1–14.
[11] S. Ananta, N.W. Thomas, J. Eur. Ceram. Soc. 19 (1999) 155–163.
[12] R. Wongmaneerung, T. Sarakonsri, R. Yimnirun, S. Ananta, Mater. Sci. Eng. B 130 (2006) 246–253.
[13] R. Wongmaneerung, R. Yimnirun, S. Ananta, Mater. Lett. 60 (2006) 1447–1452.
[14] R. Wongmaneerung, R. Yimnirun, S. Ananta, Mater. Lett. 60 (2006) 2666–2671.
[15] H. Klug, L. Alexander, X-ray Diffraction Procedures for Polycrystalline and Amorphous Materials, second ed., Wiley, New York, 1974.
[16] JCPDS-ICDD Card no. 35-0739, International Centre for Diffraction Data, Newtown Square, PA, 2000.
[17] S.D. Pradhan, S.D. Sathaye, K.R. Patil, A. Mitra, Mater. Lett. 48 (2001) 351–355.
[18] E.E. Oren, E. Taspinar, A.C. Tas, J. Am. Ceram. Soc. 80 (1997) 2714–2716.
[19] W. Chaisan, O. Khamman, R. Yimnirun, S. Ananta, J. Mater. Sci., in press.
[20] JCPDS-ICDD Card no. 77-1971, International Centre for Diffraction Data, Newtown Square, PA, 2000.
[21] R. Wongmaneerung, T. Sarnkonsri, R. Yimnirun, S. Ananta, Mater. Sci. Eng. B132 (2006) 292–299.
[22] A. Prasatkhetragarn, R. Yimnirun, S. Ananta, Mater. Lett., in press.
[23] A. Revesz, T. Ungar, A. Borbely, J. Lendvai, Nanostruct. Mater. 7 (1996) 779–788.
[24] A. Udomporn, S. Ananta, Mater. Lett. 58 (2004) 1154–1159.
[25] W. Chaisan, S. Ananta, T. Tunkasiri, Curr. Appl. Phys. 4 (2004) 182–185.

Please cite this article in press as: O. Khamman et al., J. Alloys Compd. (2007), doi:10.1016/j.jallcom.2007.02.109

Available online at www.sciencedirect.com
ScienceDirect
Materials Chemistry and Physics xxx (2007) xxx–xxx
MATERIALS CHEMISTRY AND PHYSICS
www.elsevier.com/locate/matchemphys

Dielectric and ferroelectric properties of lead zirconate titanate-barium titanate ceramics prepared by a modified mixed-oxide method

Wanwilai Chaisan [a,*], Rattikorn Yimnirun [a], Supon Ananta [a], David P. Cann [b]

[a] *Department of Physics, Faculty of Science, Chiang Mai University, Chiang Mai, Thailand*
[b] *Department of Mechanical Engineering, Oregon State University, Corvallis, OR, USA*

Received 14 June 2005; received in revised form 5 February 2007; accepted 27 February 2007

Abstract

Ceramic solid solutions within the system $(1-x)Pb(Zr_{0.52}Ti_{0.48})O_3$–$xBaTiO_3$, where x ranged from 0.0 to 1.0, were prepared by a modified mixed-oxide method. The crystal structure, microstructure, dielectric and ferroelectric properties of the ceramics were investigated as a function of composition via X-ray diffraction (XRD), scanning electron microscopy (SEM), dielectric spectroscopy and hysteresis measurement. The $(1-x)$PZT–xBT solid solutions showed that with increasing solute concentration (BT or PZT), the phase transformation became diffuse. This was primarily evidenced by an increased broadness in the dielectric peak, with a maximum peak width occurring at $x=0.5$. The *P–E* hysteresis loop measurements showed that while BT showed a well-formed hysteresis loop, PZT and 0.1PZT–0.9BT ceramics exhibited pinched-shape hysteresis loops due to abnormal domain switching mechanism. In addition, other compositions exhibited very slim-loop hysteresis occurred in materials with mixed phase or with diffuse phase transition. This observation was believed to be caused by nano-scaled chemical heterogeneity in these compositions.

Keywords: Dielectric properties; Ferroelectric properties; Barium titanate (BT); Lead zirconate titanate (PZT)

1. Introduction

Currently lead-based perovskite ferroelectric ceramics are widely applied in multilayer capacitors and sensors because of their excellent electrical properties [1]. Many of these applications require materials with superior dielectric and piezoelectric properties. Both $BaTiO_3$ (BT) and $Pb(Zr,Ti)O_3$ (PZT) are among the most common ferroelectric materials and have been studied extensively since the late 1940s [2,3]. These two ceramics have distinct characteristics that make each ceramic suitable for different applications. The compound $Pb(Zr_{0.52}Ti_{0.48})O_3$ (PZT) has great piezoelectric properties which can be applied in transducer applications. Furthermore, it has a high T_C of 390 °C which allows piezoelectric devices to be operated at relatively high temperatures. Barium titanate (BT) is a normal ferroelectric material which exhibits a high dielectric constant, a lower T_C (∼120 °C) and better mechanical properties [1–3]. However, sintering temperature of BT is higher than PZT. With their complimentary characteristics, it is expected that excellent properties can be obtained from ceramic in PZT–BT system. In addition, the Curie temperature of PZT–BT system can be engineered over a wide range of temperature by varying the composition in this system.

BT has been mixed into solid solutions with $SrTiO_3$ (BST) and with $PbTiO_3$ (BPT) to adjust the Curie temperature and to optimize the dielectric and piezoelectric response [1,2,4,5]. PZT ceramics are always modified with other chemical constituents, such as Nb and La, to improve the physical properties for specific applications [2,3,6]. Moreover, solid solutions between normal and relaxor ferroelectric materials such as PZN–BT [7], PMN–PZT [8] and PZT–PNN [9] have been widely studied for dielectric applications and to examine the order-disorder behavior. However, even though there have been extensive work on PZT-based and BT-based solid solutions, there are only a few studies on PZT–BT solid solutions [10–12]. Chaisan et al. [10] prepared perovskite powders in the whole series of the solid solutions in PZT–BT system. The phase formation characteristics, cell parameters and the degree of tetragonality were examined as a function of composition. Moreover, pseudo-binary system of PZN–BT–PZT was studied

* Corresponding author. Tel.: +66 53943376; fax: +66 53892271.
E-mail address: wanwilai_chaisan@yahoo.com (W. Chaisan).

0254-0584/$ – see front matter © 2007 Elsevier B.V. All rights reserved.
doi:10.1016/j.matchemphys.2007.02.094

and the effect of processing conditions on the piezoelectric and dielectric properties of this system was also discussed [12].

Thus far, there have been no systematic studies on the dielectric and ferroelectric properties of the whole series of PZT–BT compositions. Therefore, as an extension of our earlier work on structural studies of PZT–BT system [10], the overall purpose of this study is to investigate the dielectric properties of the PZT–BT system and the ferroelectric behavior of the solid solution between two normal ferroelectrics with the aim of identifying excellent electrical properties within this system. This paper presents the dielectric and ferroelectric properties of compositions in the PZT–BT binary system prepared via a modified mixed-oxide method.

2. Experimental procedures

The compositions $(1-x)Pb(Zr_{0.52}Ti_{0.48})O_3$–$xBaTiO_3$ or $(1-x)$PZT–xBT, where $x = 0.0$, 0.1, 0.3, 0.4, 0.5, 0.7, 0.9 and 1.0, were prepared by a modified mixed-oxide method [10]. Reagent grade PbO, ZrO_2, TiO_2 and $BaCO_3$ powders (Fluka, >99% purity) were used as starting materials. For the preparation of BT, $BaCO_3$ and TiO_2 powders were homogeneously mixed via ball-milling for 24 h with zirconia media in ethanol. The well-mixed powder was calcined at 1300 °C for 2 h in an alumina crucible. The PZT powders were prepared by using a lead zirconate ($PbZrO_3$) as precursor in order to reduce the occurrence of undesirable phase. Pure $PbZrO_3$ phase was first formed by reacting PbO with ZrO_2 at 800 °C for 2 h. $PbZrO_3$ powder was then mixed with PbO and TiO_2 and milled, dried and calcined at 900 °C for 2 h to form single phase PZT. The $(1-x)$PZT–xBT powders were then formulated from the BT and PZT components by employing the similar mixed-oxide procedure and calcining at various temperatures between 900 and 1300 °C for 2 h in order to obtain single phase $(1-x)$PZT–xBT powders [10].

The calcined $(1-x)$PZT–xBT powders were then isostatically cold-pressed into pellets with a diameter of 15 mm and a thickness of 1 mm at a pressure of 4 MPa and sintered for 2 h over a range of temperatures between 1050 and 1350 °C depending upon the composition. Densities of sintered ceramics were measured by Archimedes method and X-ray diffraction (XRD using Cu Kα radiation) was employed to identify the phases formed. The grain morphology and size were directly imaged using scanning electron microscopy (SEM) and the average grain size was determined by using a mean linear intercept method. For electrical measurements, silver paste was fired on both sides of the polished samples at 550 °C for 30 min as the electrodes. Dielectric properties of the sintered ceramics were studied as a function of both temperature and frequency. The capacitance was measured with a HP4284A LCR meter in connection with a Delta Design 9023 temperature chamber and a sample holder (Norwegian Electroceramics) capable of high temperature measurement. Dielectric constant (ε_r) was calculated using the geometric area and thickness of the discs. The polarization (P) was measured as a function of electric field (E), using a ferroelectric tester system (Radiant Technologies, Inc., RT66A).

3. Results and discussion

The phase formation behavior of the sintered $(1-x)$PZT–xBT ceramics is revealed by XRD as shown in Fig. 1. The $BaTiO_3$ ceramic sintered at 1350 °C was identified as single phase perovskite having tetragonal symmetry. With increasing PZT content, the diffraction peaks shifted towards lower angle and the diffraction peak around 2θ of 43–46° was found to split at composition $x = 0.5$. This observation suggests that this composition may lead to a diffuse MPB between the tetragonal and rhombohedral PZT phases [13]. In this case, the peak of tetragonal phase is much stronger than that of rhombohedral phase. However, the (2 0 0) peak

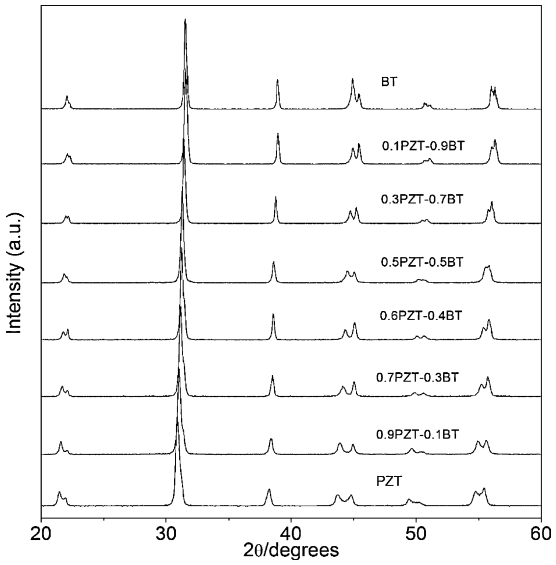

Fig. 1. XRD diffraction patterns of sintered $(1-x)$PZT–xBT ceramics.

splitting for the PZT–BT system exhibited more clearly in powders as reported in our earlier work [10]. Additionally, the PZT–BT ceramics showed single diffraction peaks which indicate good homogeneity and complete solid solution within the $(1-x)$PZT–xBT system [14]. The pure $Pb(Zr_{0.52}Ti_{0.48})O_3$ ceramic sintered at 1100 °C showed a co-existence of both tetragonal and rhombohedral phases which can be matched with the JCPDS file no. 33-0784 and 73-2022, respectively.

The optimized sintering temperatures, relative densities, and average grain sizes of the sintered $(1-x)$PZT–xBT ceramics are listed in Table 1. Higher firing temperatures were necessary for compositions containing a large fraction of BT. Compositions with $x = 0.7$ and $x = 0.9$ could not be sintered to sufficient densities and the theoretical densities of ceramics in this range were about 86–89%. It is possible that volatilization of PbO during firing is the main reason for the failure in preparing dense ceramics over this composition range [15,16]. As shown in Fig. 2, SEM micrographs reveal that the compositions with $0.0 \le x \le 0.4$ exhibit good densification and homogenous grain size. For the compositions with $0.5 \le x \le 0.9$, the grain size varies greatly from 1 to 15 μm and defective grains and some degree of porosity are clearly seen, matched with the density data. The reason for the variation of grain sizes in this com-

Table 1
Characteristics of $(1-x)$PZT–xBT ceramics with optimized processing conditions

Compositions	Sintering temperature (°C)	Relative density (%)	Average grain size (μm)
PZT	1100	96.1	2.36
0.9PZT–0.1BT	1200	96.8	2.86
0.7PZT–0.3BT	1200	97.0	1.97
0.6PZT–0.4BT	1250	96.5	2.31
0.5PZT–0.5BT	1250	94.4	3.87
0.3PZT–0.7BT	1250	86.1	3.71
0.1PZT–0.9BT	1300	86.0	5.72
BT	1350	95.9	2.42

Please cite this article in press as: W. Chaisan et al., Dielectric and ferroelectric properties of lead zirconate titanate-barium titanate ceramics prepared by a modified mixed-oxide method, Mater. Chem. Phys. (2007), doi:10.1016/j.matchemphys.2007.02.094

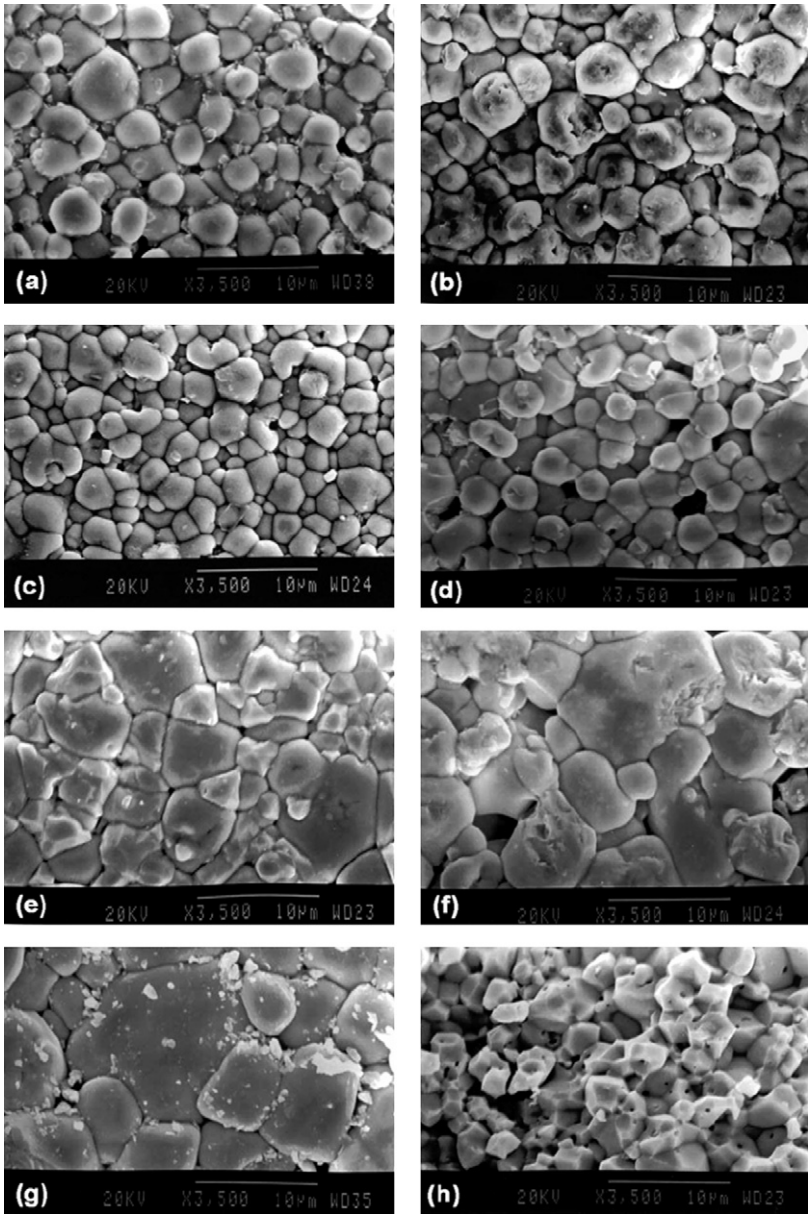

Fig. 2. SEM micrographs of $(1-x)$PZT–xBT ceramics: (a) PZT, (b) 0.9PZT–0.1BT, (c) 0.7PZT–0.3BT, (d) 0.6PZT–0.4BT, (e) 0.5PZT–0.5BT, (f) 0.3PZT–0.7BT, (g) 0.1PZT–0.9BT and (h) BT.

position range is not clearly understood. However, it can be assumed that since sintering temperatures for highest densification of PZT and BT ceramics are very different (900 and 1300 °C, respectively), this could lead to different grain growth behaviors between two phases, hence heterogeneous microstructure [17].

Fig. 3 shows the temperature dependence of dielectric constant (ε_r) and dissipation factor ($\tan\delta$) at various frequencies for compositions with $x = 0.1$, 0.3, 0.7 and 0.9. All compositions show broad peaks of dielectric constant, which indicate the diffuse phase transition, and the weak frequency dependence of all dielectric peaks are observed. The diffuse phase transition can be caused by chemical composition inhomogeniety in nano-scaled region of the $(1-x)$PZT–xBT solid solutions [18]. In addition, Curie temperatures (T_C) are also noticeably frequency independent [19]. It should be noted that the dielectric loss tangent of all ceramics increases rapidly at high temperature as a result of thermally activated space charge conduction [8]. The temperature dependence of the dielectric constant (ε_r) measured at 100 kHz for $(1-x)$PZT–xBT samples with $0.0 \le x \le 1.0$ is shown in Fig. 4. The Curie temperatures and maximum dielectric constants of the pure PZT and BT ceramics in this work were, respectively, 390 and 14,200 °C for PZT, and 129 and 7800 °C for BT. Therefore, a solid solution between PZT and BT is expected to show a transition temperature between 390 and 129 °C. The variation of T_C with compositions and dielectric data are listed in Table 2. The Curie temperature significantly decreases with increasing BT content up to 50 mol%. However, for the compositions $0.5 \le x \le 0.9$, T_C is not clearly depending on composition and remains at a nearly constant value between 140 and 160 °C. Even though the presence of Pb is known to

Please cite this article in press as: W. Chaisan et al., Dielectric and ferroelectric properties of lead zirconate titanate-barium titanate ceramics prepared by a modified mixed-oxide method, Mater. Chem. Phys. (2007), doi:10.1016/j.matchemphys.2007.02.094

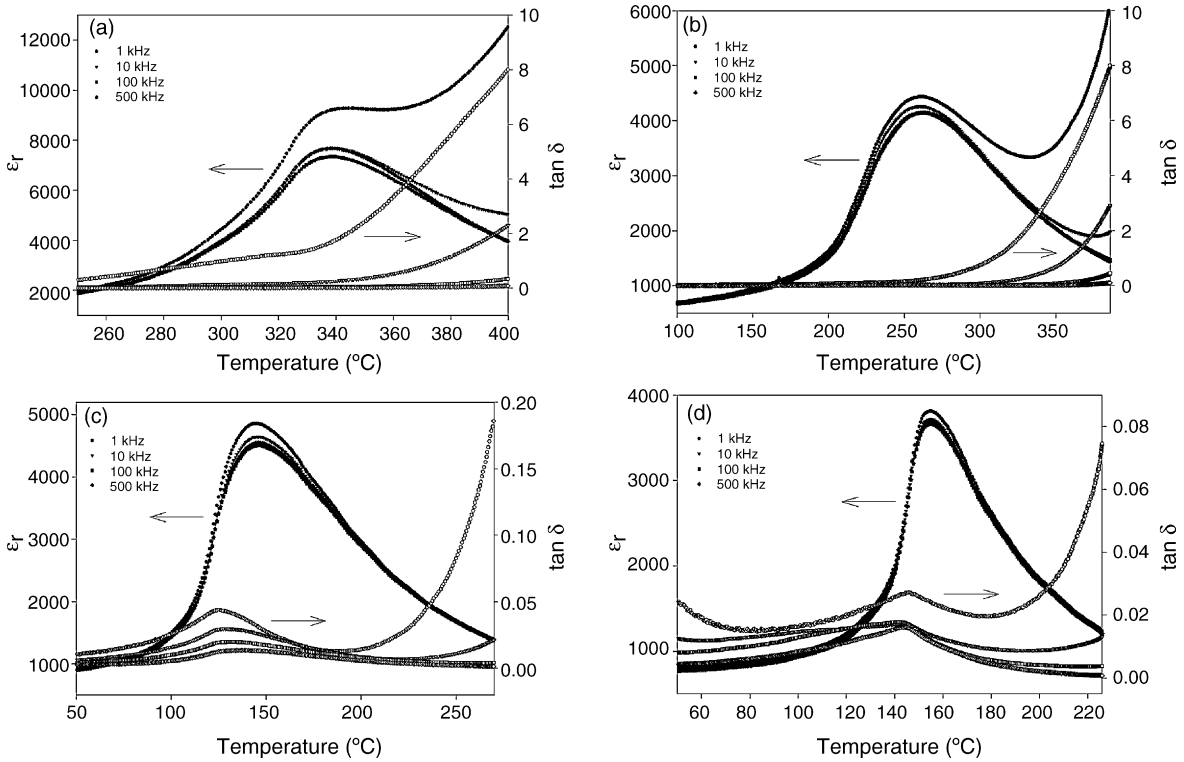

Fig. 3. Temperature and frequency dependences of dielectric properties of (a) 0.9PZT–0.1BT, (b) 0.7PZT–0.3BT, (c) 0.3PZT–0.7BT and (d) 0.1PZT–0.9BT ceramics.

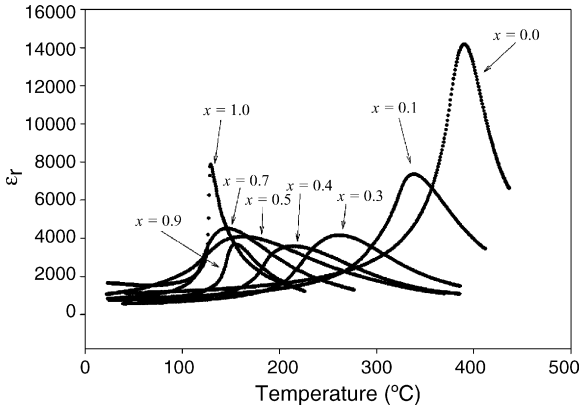

Fig. 4. Temperature dependence of dielectric constant (ε_r) of $(1-x)$PZT–xBT ceramics at 100 kHz.

Table 2
Dielectric properties of $(1-x)$PZT–xBT ceramics

Compositions	T_C (°C)	ε_m	γ	δ
PZT	390	14200	1.74	16.1
0.9PZT–0.1BT	338	7300	1.76	16.2
0.7PZT–0.3BT	262	4100	1.86	16.6
0.6PZT–0.4BT	214	3600	1.97	17.1
0.5PZT–0.5BT	162	4100	1.91	17.3
0.3PZT–0.7BT	146	4500	1.74	15.9
0.1PZT–0.9BT	155	3700	1.63	14.4
BT	129	7800	1.16	12.5

shift T_C to higher temperatures [2,3], the nearly constant T_C with increasing Pb content in the composition with $0.5 \leq x \leq 0.9$ is likely caused by PbO loss due to the high sintering temperatures required for these compositions [15,16]. For pure PZT, the ε_r peak is sharp and approaches 15,000. However, the ε_r peaks become broader with increasing BT content, and the broadest peak occurs at the $x = 0.4$ composition. It is very interesting to observe that the ε_r peak becomes more sharp as the BT content further increases.

To understand the interesting dielectric behavior of PZT–BT system, we look at the different ferroelectric behaviors through the Curie–Weiss relation. For a normal ferroelectric such as PZT and BT, above the Curie temperature the dielectric constant follows the equation:

$$\varepsilon = \frac{c}{T - T_0} \tag{1}$$

where c is the Curie constant and T_0 is the Curie–Weiss temperature [2,8,20]. For a ferroelectric with a diffuse phase transition such as the PZT–BT solid solutions, the following equation:

$$\frac{1}{\varepsilon} \approx (T - T_m)^2 \tag{2}$$

has been shown to be valid over a wide temperature range instead of the normal Curie–Weiss law (Eq. (1)) [7,21]. In Eq. (2), T_m is the temperature at which the dielectric constant is maximum. If the local Curie temperature distribution is Gaussian, the reciprocal permittivity can be written in the form [7,9]:

$$\frac{1}{\varepsilon} = \frac{1}{\varepsilon_m} + \frac{(T - T_m)^\gamma}{2\varepsilon_m \delta^2} \tag{3}$$

Please cite this article in press as: W. Chaisan et al., Dielectric and ferroelectric properties of lead zirconate titanate-barium titanate ceramics prepared by a modified mixed-oxide method, Mater. Chem. Phys. (2007), doi:10.1016/j.matchemphys.2007.02.094

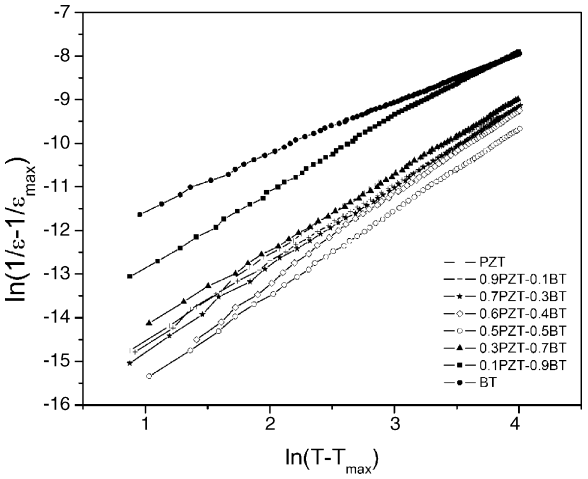

Fig. 5. Plots of $\ln(1/\varepsilon - 1/\varepsilon_m)$ vs. $\ln(T - T_m)$ for $(1-x)$PZT–xBT ceramics.

where ε_m is maximum permittivity, γ is diffusivity, and δ is diffuseness parameter. For $(1-x)$PZT–xBT compositions, the diffusivity (γ) and diffuseness parameter (δ) can be estimated from the slope and intercept of the dielectric data shown in Fig. 5, and tabulated in Table 2.

The values of γ and δ are both materials constants depending on the composition and structure of materials [9]. The value of γ is the expression of the degree of dielectric relaxation, while the parameter δ is used to measure the degree of diffuseness of the phase transition. In a material with the "pure" diffuse phase transition described by the Smolenskii–Isutov relation (Eq. (2)), the value of γ is expected to be 2 [17]. The mean value of the diffusivity (γ) is extracted from these plots by fitting a linear equation. The values of γ vary between 1.74 and 1.97, which confirms that diffuse phase transition occur in PZT–BT system. However, the phase transition in this system can be considered as no purely diffuse as the γ value is not equal to 2 [17]. Since for a perovskite ferroelectric it is established that the values of γ and δ could be caused by microstructure feature, density and grain size [22], it should be noted the value of γ for PZT is nearly 2 (theoretical is 1 for normal ferroelectric with sharp phase transition). This is probably because the mixing of rhombohedral and tetragonal phases in PZT compound and a formation of pyrochlore phase in pure PZT (though not detected by XRD) induced the occurrence of the chemical disorder and composition heterogeneity, which in turn lead to more diffuse phase transition behavior in PZT [18,23]. For the PZT-rich ceramics, the values of γ and δ increase with increasing BT content, confirming the diffuse phase transitions in PZT–BT solid solutions. It is clear that the addition of BT raises the degree of disorder in $(1-x)$PZT–xBT over the compositional range $0.1 \le x \le 0.5$. The highest degree of diffuseness is exhibited in the 0.5PZT–0.5BT ceramic. Similarly, from the BT end member, the values of both γ and δ exhibits the same trend with increasing PZT content. This observation indicates that PZT addition also induces disorder in BT-rich compositions. It should also be mentioned here that different dielectric behaviors could also be caused by grain size variation [8]. However, the grain size, as shown in Table 1, in this study does not differ significantly enough to cause such a variation in the dielectric properties.

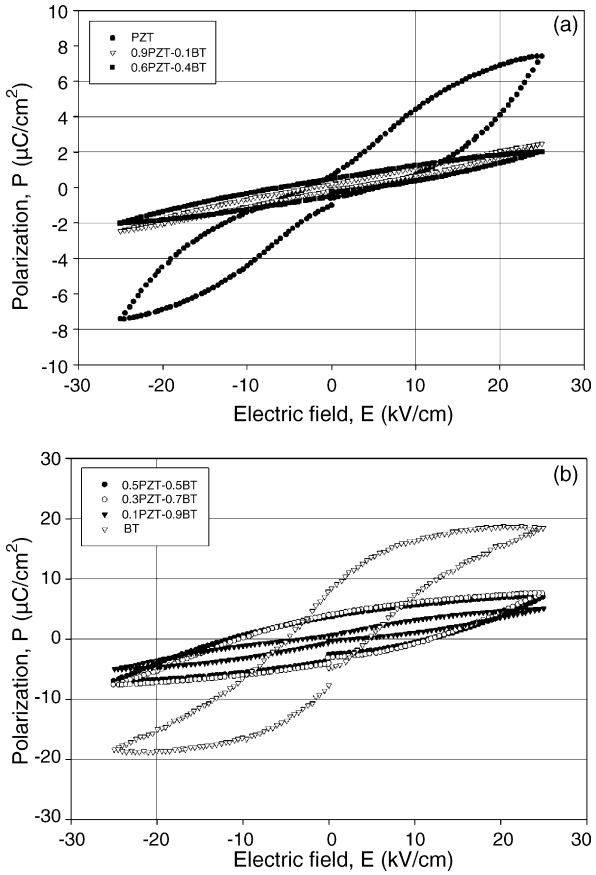

Fig. 6. P–E hysteresis loops of $(1-x)$PZT–xBT ceramics: (a) $0 \le x \le 0.4$ and (b) $0.5 \le x \le 1.0$.

Fig. 6(a and b) illustrates the polarization (P–E) hysteresis loops of $(1-x)$PZT–xBT ceramics. It should be noted that these measurements were carried out on unpoled ceramics. The shape of P–E loops varies greatly with the ceramic compositions. PZT ceramic exhibits a type of pinched or propeller-shaped polarization-field hysteresis loop as shown in Fig. 6a, similar to but not to be confused with that of an antiferroelectric [24]. This behavior is more likely observed in conventionally sintered sample and was found to be stronger in the tetragonal composition than in the rhombohedral one. This phenomenon may reveal abnormal domain switching mechanism and is believed to be related with the strong interaction between point defect and domain walls [25,26]. However, this kind of pinched loop is found to diminish under severe electrical excitation [3]. Similarly, this pinched effect is also found in 0.1PZT–0.9BT ceramic (Fig. 6b). As also shown in Fig. 6b, BT ceramic shows a well-developed ferroelectric loop with 4.626 kV cm^{-1} of coercive field (E_C), 7.775 μC cm^{-2} of remnant polarization (P_r) and 0.491 of loop squareness (R_{sq}), a typical hysteresis loop of barium titanate ceramic [1]. Whereas, the other compositions ($x = 0.1$ and 0.4) show very small degree of loop opening with large E_C but small P_r. These very slim loops can be explained by the "mixed" phases of solid solutions between PZT and BT (with diffuse phase transition) which need much larger field to

Please cite this article in press as: W. Chaisan et al., Dielectric and ferroelectric properties of lead zirconate titanate-barium titanate ceramics prepared by a modified mixed-oxide method, Mater. Chem. Phys. (2007), doi:10.1016/j.matchemphys.2007.02.094

Table 3
Ferroelectric properties of $(1-x)$PZT–xBT ceramics

Compositions	Ferroelectric properties			Loop squareness (R_{sq})
	P_r ($\mu C\,cm^{-2}$)	P_s ($\mu C\,cm^{-2}$)	E_C ($kV\,cm^{-1}$)	
0.5PZT–0.5BT	3.673	6.996	11.68	0.839
0.3PZT–0.7BT	3.988	7.597	11.79	0.654
BT	7.775	18.41	4.626	0.491

open up loops [27,28]. However, the insufficient electric field was applied to the samples due to the limitation of measurement set-up. Additionally, arguments could also be made that an addition of PZT into BT results in narrower loops, a characteristic of suppressed normal ferroelectric behavior in this system, in good agreement with dielectric and diffusivity data in Table 2. This clearly confirms the occurrence of the diffuse phase transition when BT or PZT is added to the PZT–BT system.

The ferroelectric data of $(1-x)$PZT–xBT ceramics is listed in Table 3. An empirical relationship between remanent polarization (P_r), saturation polarization (P_s) and polarization at the fields above the coercive field was derived by Haertling et al. [29]. This permits the quantification of changes in the hysteresis behavior for $(1-x)$PZT–xBT samples through the following equation:

$$R_{sq} = \frac{P_r}{P_s} + \frac{P_{1.1E_C}}{P_r} \quad (4)$$

where R_{sq} is the squareness of hysteresis loop and $P_{1.1Ec}$ is the polarization at an electric field equal to 1.1 times the coercive field (E_C). For an ideal hysteresis loop, R_{sq} is equal to 2.0. Since for fully saturated hysteresis loops some compositions could not be obtained due to the limited capability of the measuring set-up, the data are unavailable. From the ferroelectric data in Table 3, R_{sq} seems to increase with increasing of PZT content, a characteristic of the enhanced ferroelectric interaction for ceramics in this system [22]. The highest degree of loop squareness is found in 0.5PZT–0.5BT ceramic. This is a result of better homogeneity and uniformity of grain size [2], agreed with SEM investigation. It should be noticed that it is possible to receive higher E_C value in some compositions of PZT–BT solid solutions than in pure PZT and BT. These compositions could lead to hard switching of domain.

4. Conclusions

The dielectric properties of solid solutions in the $(1-x)$PZT–xBT system prepared via the mixed-oxide method are reported. All compositions in this study were single phase perovskite with tetragonal symmetry. The results indicated that solid solutions of $(1-x)$PZT–xBT ($0.1 \le x \le 0.9$) exhibited a diffuse phase transition behavior with a Curie temperature ranging between 390 and 129 °C. In $(1-x)$PZT–xBT solid solutions, the degree of diffuseness increased with increased solute content up to a maximum at $x = 0.5$. From P–E hysteresis loops, it was observed that PZT and 0.1PZT–0.9BT ceramics exhibited pinched-shape hysteresis loops. This phenomenon may be caused by abnormal domain switching mechanism related to the strong interaction between point defect and domain walls. Additionally, while BT showed a well-developed hysteresis loop, other composition exhibited very slim-loop hysteresis, a characteristic of mixed-phase or diffuse phase transition materials.

Acknowledgements

This work was supported by the Thailand Research Fund (TRF), Graduate School of Chiang Mai University and the Ministry of University Affairs.

References

[1] A.J. Moulson, J.M. Herbert, Electroceramics: Materials, Properties, Applications, John Wiley & Sons Ltd., Chichester, 2003, p. 500.
[2] G.H. Haertling, J. Am. Ceram. Soc. 82 (1999) 797–818.
[3] B. Jaffe, W.R. Cook, H. Jaffe, Piezoelectric Ceramics, Academic Press, London, 1971, p. 317.
[4] K. Uchino, Acta Mater. 46 (1998) 3745–3753.
[5] A.D. Polli, F.F. Lange, C.G. Levi, J. Am. Ceram. Soc. 83 (2000) 873–881.
[6] H. Jaffe, D.A. Berlincourt, Proc. IEEE 53 (1965) 1372–1386.
[7] A. Halliyal, U. Kumar, R.E. Newnham, L.E. Cross, Am. Ceram. Soc. Bull. 66 (1987) 671–676.
[8] R. Yimnirun, S. Ananta, P. Laoratanakul, Mater. Sci. Eng. B 112 (2004) 79–86.
[9] N. Vittayakorn, G. Rujijanagul, X. Tan, M.A. Marquardt, D.P. Cann, J. Appl. Phys. 96 (2004) 5103–5109.
[10] W. Chaisan, S. Ananta, T. Tunkasiri, Curr. Appl. Phys. 4 (2004) 182–185.
[11] B.K. Gan, J.M. Xue, D.M. Wan, J. Wang, Appl. Phys. A 69 (1999) 433–436.
[12] F. Xia, X. Yao, J. Mater. Sci. 34 (1999) 3341–3343.
[13] A.K. Arora, R.P. Tandon, A. Mansingh, Ferroelectrics 132 (1992) 9–25.
[14] B.D. Cullity, Elements of X-ray diffraction, Addison-Wesley Publishing Company, Inc., 1978, p. 32.
[15] A. Garg, D.C. Agrawal, Mater. Sci. Eng. B 56 (1999) 46–50.
[16] C.H. Wang, S.J. Chang, P.C. Chang, Mater. Sci. Eng. B 111 (2004) 124–130.
[17] Y.-M. Chiang, D.P. Birnie, W.D. Kingery, Physical Ceramics, John Wisley & Sons. Inc., 1997, p. 522.
[18] I.W. Chen, P. Li, Y. Wang, J. Phys. Chem. Solids 57 (1996) 1525–1536.
[19] T.R. Shrout, J. Fielding, Proc. IEEE Ultrason. Symp. (1990) 711–720.
[20] L.E. Cross, Mater. Chem. Phys. 43 (1996) 108–115.
[21] R.D. Shannon, C.T. Prewitt, Acta Crystallogr. Sect. B. Struct. Crystallogr. Cryst. Chem. 25 (1969) 925–945.
[22] R. Yimnirun, S. Ananta, P. Laoratanakul, J. Eur. Ceram. Soc. 25 (2005) 3235–3242.
[23] K.V. Im, J.H. Kim, W.K. Choo, Proc. IEEE Int. Symp. Appl. Ferroelectr. 11th (1998) 467–470.
[24] M. Takahashi, Jpn. J. Appl. Phys. 9 (1970) 1236–1246.
[25] K. Carl, K.H. Hardtl, Ferroelectrics 17 (1978) 473–486.
[26] X. Wei, Y. Feng, L. Hang, S. Xia, L. Jin, X. Yao, Mater. Sci. Eng. B 120 (2005) 64–67.
[27] S. Sharma, R. Singh, T.C. Goel, S. Chandra, Compos. Mater. Sci. 37 (2006) 86–89.
[28] M.E. Lines, A.M. Glass, Principles and Applications of Ferroelectrics and Related Materials, Clarendon Press, Oxford, 1977, p. 541.
[29] G.H. Haertling, W.J. Zimmer, Am. Ceram. Soc. Bull. 45 (1966) 1084–1089.

Please cite this article in press as: W. Chaisan et al., Dielectric and ferroelectric properties of lead zirconate titanate-barium titanate ceramics prepared by a modified mixed-oxide method, Mater. Chem. Phys. (2007), doi:10.1016/j.matchemphys.2007.02.094

Effects of Uniaxial Stress on Dielectric Properties of 0.9PMN-0.1PT Ceramics

N. Triamnak, M. Unruan, S. Ananta, and R. Yimnirun

Department of Physics, Faculty of Science, Chiang Mai University,

Chiang Mai 50200, Thailand

*Corresponding Author E-mail:rattikornyimnirun@yahoo.com

ABSTRACT

This study deals with the influence of uniaxial stress on the dielectric properties of electrostrictive PMN-PT ceramic. The dielectric properties of lead magnesium niobate-lead titanate prepared by a mixed-oxide method with composition ratio 9:1 were measured under uniaxial compressive stress up to 22 MPa. The experimental results revealed that the superimposed compression load significantly reduced both the dielectric constant and the dielectric loss tangent in every measuring frequency. The observations were interpreted in terms of clamping of domain walls and de-poling under the compressive loading. The change of the dielectric properties with stress was attributed to competing influences of the intrinsic contribution of non-polar matrix and the extrinsic contribution of re-polarization and growth of micro-polar regions. In addition, the results reported here also suggested a significant influence of the experimental conditions on the uniaxial stress dependence of dielectric properties of the PMN-PT ceramic.

Keywords: uniaxial stress; dielectric properties; 0.9PMN-0.1PT

INTRODUCTION

Ferroelectric lead magnesium niobate, $Pb(Mg_{1/3}Nb_{2/3})O_3$ (PMN), is widely used in devices such as actuators and transducers because of its good dielectric properties (for instance, at 100 Hz ;ε_r at room temperature ~ 13000 and ε_{max} ~ 16000) [1-3]. However, the temperature related to the maximum dielectric constant (T_{max}) of PMN is very low (~ -10 C) [3]. Thus, lead titanate ($PbTiO_3$ or PT), which has high Curie temperature (T_c ~ 490 C, ε_r at room temperature ~ 300) [3-5] is added to PMN with ratio 9:1 to enhance the dielectric properties of PMN (as well as increasing T_{max}). As a result, at 100Hz, 0.9PMN-0.1PT ceramic has T_{max} = 40 C and ε_{max} > 20000 [6]. Therefore, 0.9PMN-0.1PT ceramics have been a subject of many investigations and, more importantly, have been widely applied in actuators and transducers [1, 4, 7].

However, when used in devices specified above these ceramics are often subjected to self-induced or external stress, e.g. acoustic transducers [1,3,7]. Therefore, it is very important to obtain experimental data, as well as to better understand how these materials behave under stress. Recently, the uniaxial stress dependence of dielectric properties has been studied in materials such as PZT, PMN-PZT [8-12]. For PZT ceramics, the dielectric constant increases with increasing stress in range 0-35 MPa. After reaching a maximum value of dielectric constant at 35 MPa, it gradually decreases with further pre-stress increment [8,10,11]. On the other hand, in case of PMN-PZT ceramics, the changes of the dielectric constant with the applied stress can be divided into two different groups. For PMN-rich compositions, the dielectric constant generally decreases with increasing applied stress, while for PZT-rich compositions the dielectric constant rises slightly when the applied stress increases from 0 to 1 MPa, and becomes relatively constant when the applied stress increases further [9]. These results clearly show that the effects of stress on the dielectric properties

depend significantly on ceramic compositions and stress levels. Since PMN-PT ceramics are practically very important and there have been previous reports on the electro-mechanical properties of these ceramics under various mechanical and electrical loading conditions [13,14]. However, there has been no systematic study on the influence of an applied stress on their dielectric properties. Therefore, it is the aim of this study to determine the dielectric properties of the 0.9PMN-0.1PT ceramic as a function of uniaxial compressive stress.

EXPERIMENTAL METHOD

0.9PMN-0.1PT ceramics were prepared from starting PMN and PT powders by a mixed-oxide method. Perovskite-phase PMN powders were obtained from the columbite method, while PT powders were prepared by a simple mixed-oxide method.

To obtain the perovskite-phase PMN, the magnesium niobate powders were first prepared by mixing MgO (99.0%) and Nb_2O_5 (99.9%) powders and then calcining the mixed powders at 1100 C for 3 h, to yield a so called columbite powders ($MgNb_2O_6$). After that, the columbite powders were mixed with PbO (99.9%) by ball-milling method and calcined at 800 C for 1 h to form the perovskite-phase PMN powders. With a simple mixed-oxide route, PT powders were prepared from PbO (99.9%) and TiO_2 (99.9%) starting powders. These powders were ball-milled and calcined at 600 C for 1 h.

0.9PMN-0.1PT ceramics were prepared from starting PMN and PT powders by the same mixed-oxide method with ratio 9:1. After mixing the powders by ball-milling method and drying process, the mixed powders were pressed hydraulically to form disc-shaped pellets 12 mm in diameter and 1.5 mm thick, with 3 wt.% polyvinyl alcohol as a binder. The pellets were placed on the alumina powder-bed inside alumina crucible and surrounded with atmosphere powders of the same composition. Finally, the pellets were sintered at 1240 C

for 2 h. The phase-formation of the sintered ceramics was studied by XRD technique. The microstructure analyses were undertaken by a scanning electron microscopy (SEM: JEOL Model JSM 840A). The densities of sintered specimens were measured by Archimedes method. The detailed descriptions of the ceramic processing and characterization were presented elsewhere and will not be discussed here [15].

Before studying the dielectric properties under the uniaxial stress, the specimens were lapped to obtain parallel faces. After coating with silver paint as electrode at the faces, the specimens were heated at 750 C for 12 min to ensure the contact between the electrode and surface of ceramic. To study effects of the uniaxial stress on the dielectric properties of the ceramic, the uniaxial compressometer was constructed [9], as shown schematically in Figure 1. The specimen was laid between uniaxial stress rams. The dielectric properties were measured by LCR-meter (Instrek LCR-821). The room temperature (27 C) capacitance and the dielectric loss tangent were obtained at frequency range 1 to 200 kHz under uniaxial compressive pre-stress levels up to 22 MPa. The dielectric constant was then calculated from a parallel-plate capacitor equation, e.g. $_r$ = Cd / $_0$A, where C is the capacitance of the specimens, d and A are, respectively, the thickness and the area of the electrode, and $_0$ is the dielectric permittivity of vacuum (8.854 x 10^{-12} F/m).

RESULTS AND DISCUSSION

The dielectric constant at various frequencies of 0.9PMN-0.1PT ceramics as a function of compressive stress during loading and unloading are depicted in Figure 2. There is a significant change of the dielectric constant of the ceramic with increasing stress from 0 to 22 MPa and returning to stress-free condition. The dielectric constant decreases monotonically with increasing the compressive stress, then increases only slightly when the

compressive stress is gradually removed. The changing of the dielectric constant with increasing and decreasing the applied stress does not follow the same path. In every frequency, the dielectric constant with increasing the compressive stress is larger in value than that with decreasing stress. It is also of interest to see that the stress-free dielectric constant value decreases significantly after a stress cycle. Furthermore, as shown in Figure 2, the dielectric constant at a constant stress also changes with frequency. The dielectric constant decreases significantly when the measuring frequency increases from 1 to 200 kHz. The trend is opposite for the dielectric loss tangent (as shown in Figure 3). This is a typical characteristic of a relaxor ferroelectric, in which below the dielectric maximum temperature, the dielectric constant decreases and the dielectric loss tangent increases with increasing frequency [1-4].

As displayed in Figure 3, the results of the uniaxial compressive stress dependence of the dielectric loss tangent show a similar tendency to those of dielectric constant. At each measuring frequency, the dielectric loss tangent deceases with increasing the compressive stress and then slightly increases when the compressive stress is removed (shown in Figure 3). The dielectric loss tangent is also found to decrease significantly after a stress cycle. Since the dielectric properties change with the applied stress in very similar trend for every measuring frequency, the data at 10 kHz are selected as representatives for better comparison in Figure 4 for the fractional changes of the dielectric properties with the compressive stress. It can be seen very clearly that the dielectric constant decreases as much as 70% at the maximum applied stress and only returns to slightly less than 50% of its original value when the stress is removed. Though following the same trend, the change in the dielectric loss tangent value is less significant, as it only decreases about 50% at the maximum stress and almost returns on its original value after a stress cycle. It is also noticed that the results of this study are in parts similar to the experimental results for PMN-PZT system in earlier

investigation [9]. For 0.9PMN-0.1PZT ceramic, the dielectric constant generally decreases with increasing applied stress. However, the trend for change of the dielectric loss tangent is different. The dielectric loss tangent of 0.9PMN-0.1PZT is found to first increase when the applied stress is raised from 0 to 1 MPa, and then decrease with further increasing stress [9]. It is interesting to observe that a mixture of different normal and relaxor ferroelectrics responds to the applied stress in a similar manner.

To understand these experimental results, various effects have to be considered. Normally, the properties of ferroelectric materials are derives from both the intrinsic and extrinsic contribution [9-11]. When a compressive stress is applied to the ferroelectric materials, the domain structure in the material will change to maintain the domain energy at a minimum; during this process some of the domains engulf other domains or change shape irreversibly. Under a uniaxial stress, the domain structure of ferroelectric ceramics may undergo domain switching through non-180 domain walls, de-aging, de poling and clamping of domain walls [11,14].

In this study, since 0.9PMN-0.1PT is a relaxor ferroelectric with T_m ~ 39-40 C and the experiment was carried out at room temperature (~27 C) which is slightly below the T_m, the experimental observation, which shows decreases in both dielectric constant and dielectric loss tangent with increasing stress, can be attributed to competing influences of the intrinsic contribution of non-polar matrix and the extrinsic contribution of re-polarization and growth of micro-polar regions. Since the behavior of 0.9PMN-0.1PT depends on the ratio between the micro-polar region and the non-polar matrix, in this case the micro-polar regions dominate [9-12]. Hence, the dielectric responses of the 0.9PMN-0.1PT ceramic are observed to decrease with increasing the compressive stress, as seen in Figures 2-4.

In addition, the de-poling mechanism also plays a role in the experimental results. The decrease of both the dielectric constant and the dielectric loss tangent after a stress cycle

is believed to be the direct contribution of the partial de-poling effect under the compressive stress cycle [9-11].

More interestingly, earlier work by Viehland *et al.* [13] reported the large-signal polarization-electric field (P-E) relation under uniaxial stress of 0.9PMN-0.1PT ceramic. For comparison, one would be able to estimate from the P-E loops presented in that study the dielectric permittivity by using Eq. (1), which gives

$$\frac{\Delta P}{\Delta E} \tag{1}$$

where ΔP is the polarization difference between +2.5 and 0 kV/cm. The calculated dielectric permittivity can be called *differential permittivity*, which includes the reversible (intrinsic dielectric property) and irreversible (extrinsic domain switching related property) contributions of the materials [8,16]. The calculation shows that the differential permittivity decreases approximately 13% when the applied stress is increased from 0 to 30 MPa. This change is significantly lower than that observed in our low-field study (a decrease of more than 70% over the same stress range). Even though the reasons for the difference are still not clearly known, this observation clearly signifies the importance of the experimental conditions used to determine the dielectric properties, as well as the stress-dependence dielectric properties. More detailed study is underway and further results will be presented in future publications. Finally, the information obtained in this current work is practically very useful for design and calculation consideration of devices in low-field applications.

CONCLUSIONS

In this study, the dielectric properties of 0.9PMN-0.1PT ceramics prepared by a conventional mixed-oxide method are measured under the compressive stress from 0 to 22 MPa. The results clearly show that the dielectric constants and the dielectric loss tangent of the 0.9PMN-0.1PT ceramic decrease with increasing the compressive stress. The change of the dielectric properties with stress is attributed to competing influences of the intrinsic contribution of non-polar matrix and the extrinsic contribution of re-polarization and growth of micro-polar regions. In addition, the difference in the uniaxial stress dependence of the dielectric properties measured under low- and high-field conditions is also apparent. Finally, this study undoubtedly shows that the applied stress has significant influences on the dielectric properties of the 0.9PMN-0.1PT ceramics.

ACKNOWLEDGEMENTS

This work is supported by the Thailand Research Fund (TRF). Additional supports from Faculty of Science and Graduate School of Chiang Mai University are gratefully acknowledged. One of the authors (N.T.) also wishes to thank the Development and Promotion of Science and Technology Talents Project of Thailand (DPST) for financial support during his study.

REFERENCES

[1]. Cross, L.E., *Ferroelectric,* 1987, **76**, 241-267.

[2]. Xu, Y., *Ferroelectric Materials and Their Applications*. Elsevier Science, Amsterdam, The Netherlands, 1991.

[3]. Moulson, A. J. and Herbert, J. M., *Electroceramics*, Wiley, Chichester, 2003.

[4]. Haertling, G. H., *J. Am. Ceram. Soc.*, 1999, **82**, 797-818.

[5]. Jiang, S., Zhou, D., Gong, S. and Lu, W., *Sensors Actuat*., 1998, **A69**, 1-4.

[6]. Liou, Y. C., *J. Mater. Sci. Eng. B*., 2003, **103**, 281-284.

[7]. Safari, A., Panda, R. K. and Janas, V. F., *Appl. Ferro. Ceram. Mater.* 2000, 1-47.

[8]. Zhou, D., Kamlah, M., Munz, D., *J. Euro. Ceram. Soc.*, 2005, **25**, 425-432.

[9]. Wongsaenmai, S., Ananta, S., Meechoowas, E. and Yimnirun, R., *J. Phys. D: Appl. Phys*., 2003, **36**, 1615-1619.

[10]. Zhang, Q. M., Zhou, J., Uchino, K. and Zheng, J., *J. Mater. Res*, 1997, **12**, 226-234.

[11]. Yang, G., Liu, S. F., Ren, W. and Mukherjee, B. K., *SPIE Proceedings*, 2000, **3992**, 103-113.

[12]. Steiner, O., Tagantsev, A. K., Colla, E. L. and Setter, N., *J. Euro. Ceram. Soc.*, 1999, **19**, 1243-1246.

[13]. Viehland, D., Li, J., McLaughlin, E, Powers, J., Janus, R., and Robinson, H., *J. App. Phys.*, 2004, **95(4)**, 1969-1972.

[14]. Zhao, J. and Zhang, Q. M. *Proc. IEEE ISAF-96,* 1996, **1**, 97-974.

[15]. Udomporn, A., Ph.D. thesis, Chiang Mai University, 2004.

[16]. Yimnirun, R., Ananta, S., Ngamjarurojana, A., and Wongsaenmai, S., *Appl. Phys. A*, 2005, **81**, 1227-1231.

List of Figure Captions

Figure 1. Schematic diagram of experimental set up.

Figure 2. Uniaxial compressive stress dependence of dielectric constant ($_r$) of 0.9PMN-0.1PT ceramic at various frequencies.

Figure 3. Uniaxial compressive stress dependence of dielectric loss tangent (tan) of 0.9PMN-0.1PT ceramic at various frequencies.

Figure 4. Fractional changes of dielectric constant ($_r$) and dielectric loss tangent (tan) with uniaxial compressive stress of 0.9PMN-0.1PT ceramic (measured at 10 kHz).

Figure 1

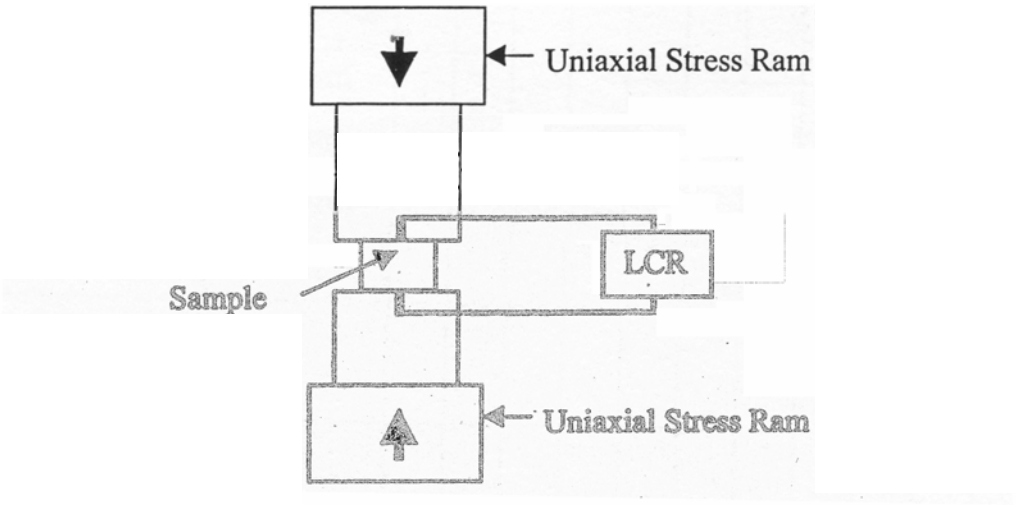

Figure 1. Schematic diagram of experimental set up.

Figure 2

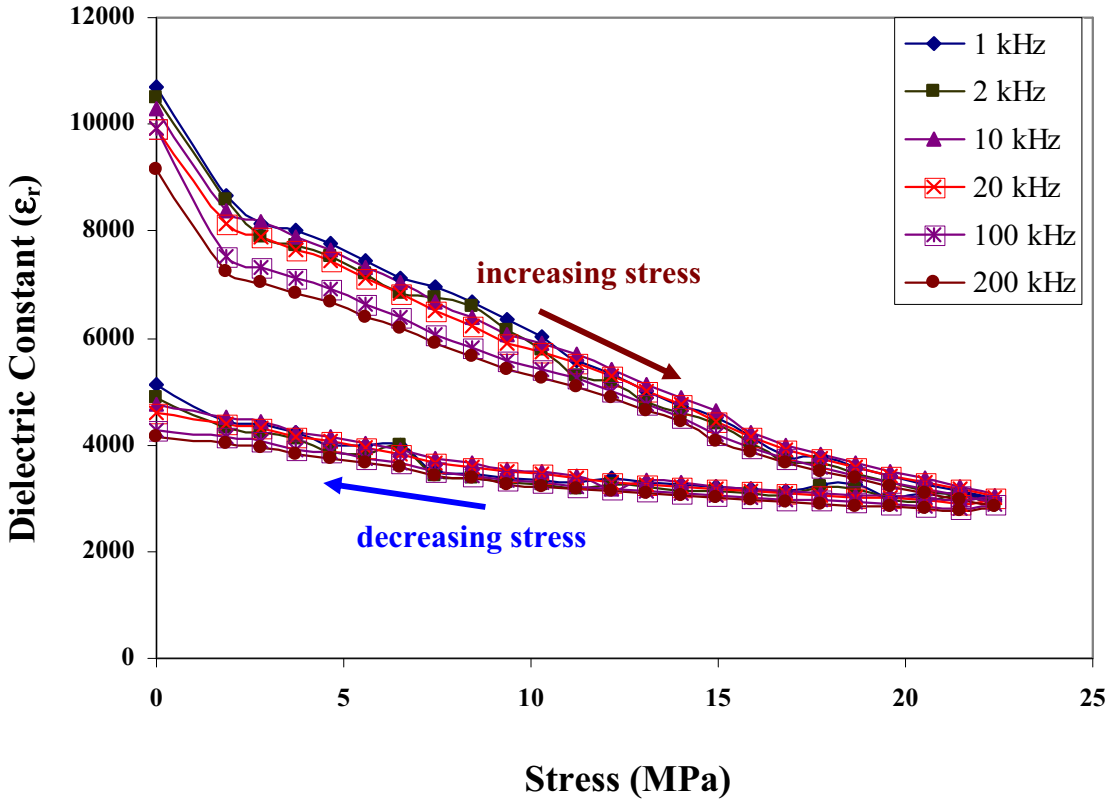

Figure 2. Uniaxial compressive stress dependence of dielectric constant ($_r$) of 0.9PMN-0.1PT ceramic at various frequencies.

Figure 3

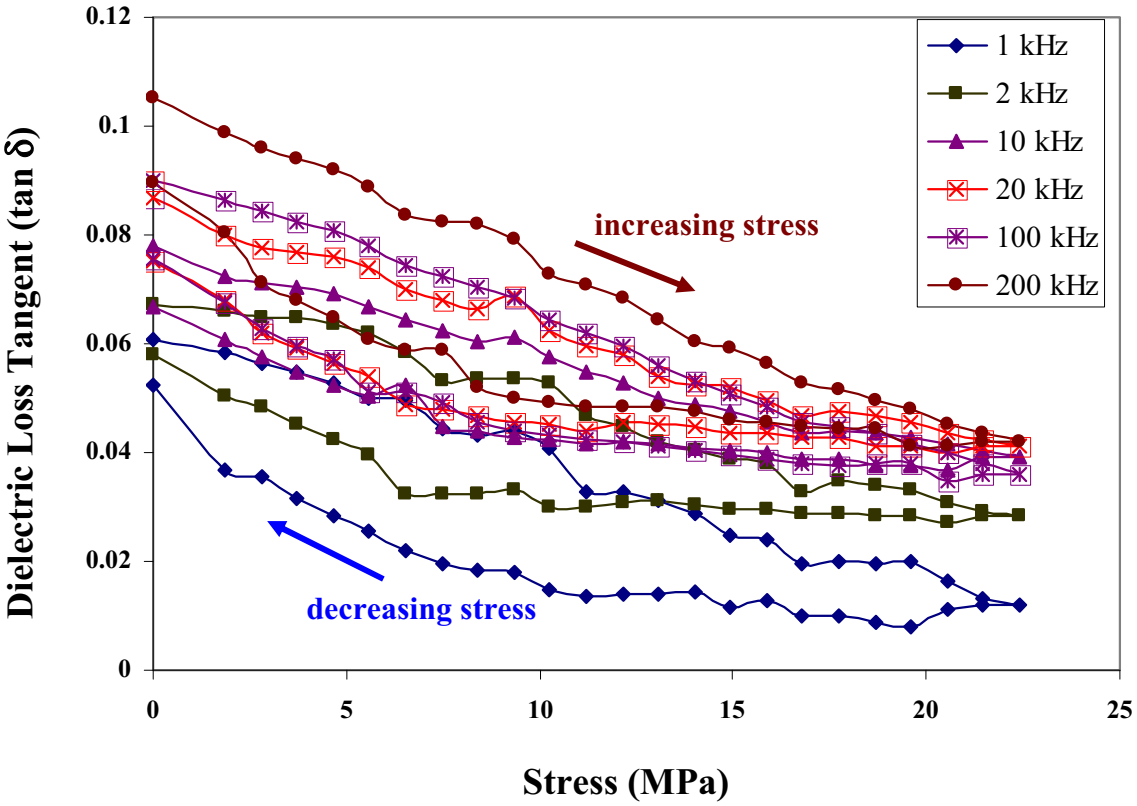

Figure 3. Uniaxial compressive stress dependence of dielectric loss tangent (tan) of 0.9PMN-0.1PT ceramic at various frequencies.

Figure 4

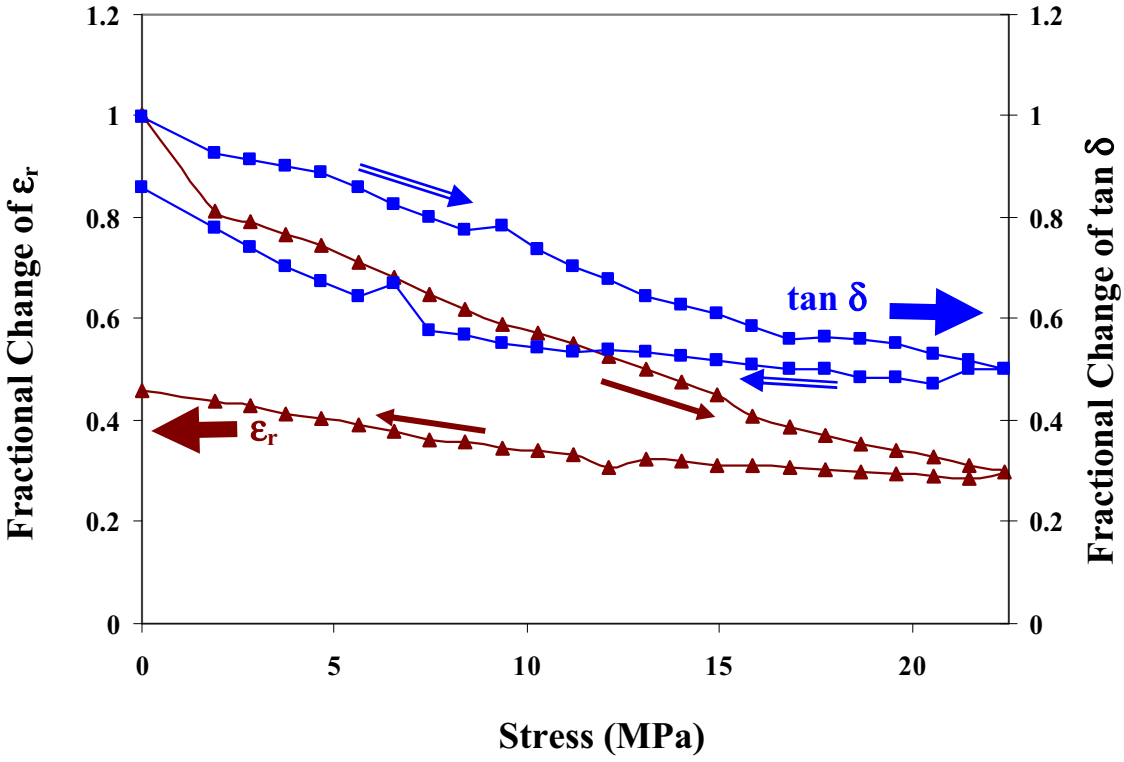

Figure 4. Fractional changes of dielectric constant ($_r$) and dielectric loss tangent (tan) with uniaxial compressive stress of 0.9PMN-0.1PT ceramic (measured at 10 kHz).

Synthesis, Formation and Characterization of Lead Zinc Niobate – Lead Zirconate Titanate Powders via a Rapid Vibro-Milling Method

A. Ngamjarurojana*, O. Khamman, S. Ananta and R. Yimnirun

Department of Physics, Faculty of Science, Chiang Mai University, Chiang Mai 50200, Thailand

***Corresponding author:** E-mail address: Ngamjarurojana@yahoo.com

ABSTRACT

In this study, an approach to synthesizing pyrochlore-free lead zinc niobate – lead zirconate titanate powders with a formula $x\text{Pb}(\text{Zn}_{1/3}\text{Nb}_{2/3})\text{O}_3$ $(1-x)\text{Pb}(\text{Zr}_{1/2}\text{Ti}_{1/2})\text{O}_3$ (when $x = 0.1\text{-}0.5$) by a mixed oxide synthetic route via a rapid vibro-milling has been developed. The formation of perovskite phase in calcined PZN-PZT powders has been investigated as a function of calcination temperature by TG-DTA and XRD techniques. Powder morphology and chemical composition have been determined with SEM and EDX techniques. The potential of a vibro-milling technique as a significant time-saving method to obtain single-phase PZN-PZT powders at low calcination temperature is also discussed. The results indicate that at calcination condition of 900 ^{o}C for 2h, with heating/cooling rates of 20 ^{o}C/min single-phase PZN-PZT powders can be obtained for every composition ratio between $x = 0.1\text{-}0.5$.

Keywords: Phase formation , Calcination ,Vibro-milling , Lead zinc niobate , Lead zirconate titanate

Introduction

Lead zirconate titanate, $Pb(Zr,Ti)O_3$ or PZT, is a well known piezoelectric that has been widely employed in a large number of sensing and actuating devices. PZT ceramics have very high Curie temperature (~ 390 ^oC). They have excellent dielectric, piezoelectric and elastic properties suitable for wide range of practical applications [1-3]. Lead zinc niobate, $Pb(Zn_{1/3}Nb_{2/3})O_3$ or PZN, which exhibits a perovskite structure and a Curie temperature ~ 140 ^oC, is one of the most important relaxor ferroelectric materials with high dielectric constant and large electrostrictive coefficient [4-5]. These characteristics make PZN a promising candidate for high performance electromechanical actuator and transducer applications. However, it has been recognized and widely accepted that inhomogeneous mixing in the conventional solid state reaction process leads to formation of pylochlore phase and subsequent deterioration of electrical properties in PZN ceramics [6-7]. The addition of other perovskite materials, such as barium titanate ($BaTiO_3$) [8], lead titanate ($PbTiO_3$) [9], or PZT [10], has been found to be effective in stabilizing PZN in the perovskite structure. However, recent work by Fan and Kim [11] has shown promise in producing only pure perovskite phase for PZN–PZT ceramics with the conventional mixed-oxide method.

The present work is aimed at synthesizing pyrochlore-free lead zinc niobate – lead zirconate titanate powders. The conventional mixed oxide synthetic route via a rapid vibro-milling has been developed with a one-step reaction of all starting materials. The rapid vibro-milling is employed for the first time in this work as a significant time-saving method to obtain single-phase PZN-PZT nano-sized powders at low temperature.

Experimental procedure

In this study, reagent grade oxides of lead oxide, PbO (Fluka Chemical, 99.9% purity), zirconium dioxide, ZrO_2 (RdH laborchemikalin, 99.9% purity), zinc oxide, ZnO (Fluka Chemical, 99.9% purity), niobium pentaoxide, Nb_2O_5 (Aldrich, 99.9% purity), and titanium dioxide, TiO_2 (RdH laborchemikalin, 99.9% purity), were used as the starting materials. PZN–PZT powders were synthesized by the solid-state reaction of these raw materials. Ground mixtures of the powders were required with stoichiometric ratios for the general composition $x\text{Pb}(Zn_{1/3}Nb_{2/3})O_3$ $(1\text{-}x)\text{Pb}(Zr_{1/2}Ti_{1/2})O_3$ where x = 0.1, 0.2, 0.3, 0.4, and 0.5. A McCrone vibro-milling technique was employed in order to combine mixing capacity with a significant time saving. The milling operation was carried out in isopropanol. High purity corundum cylindrical media were used as the milling media. After vibro-milling for 30 minutes and drying at 120 ^{o}C, the reaction of the uncalcined powders taking place during heat treatment was investigated by themogravimetric and differential thermal analysis (TG-DTA, Shimadzu) in air from room temperature up to 1350 ^{o}C. Based on the TG-DTA results, the mixture was calcined at temperatures between 750 to 950 ^{o}C for 2 hours in alumina crucible to examine the phase formation behavior of PZN-PZT powders. A heating/cooling rate of 20 ^{o}C/min was selected for all of the compositions in this system because it was shown to be effective in reducing the total amount of pyrochlore phase [12].

Calcined powders were subsequently examined by room temperature X-ray diffraction (XRD; Siemens-D500 diffractrometer) using Ni-filtered CuK radiation to identify the phases formed for the PZN-PZT powders. The relative amounts of perovskite and pyrochlore phases were approximated by calculating the ratio of the major XRD peak intensities of the perovskite and pyrochlore phases via the following equation:

$$\text{Perovskite \%} = \frac{I_{perov}}{I_{perov} \quad I_{pyro}} \quad 100$$

where I_{perov} and I_{pyro}, refer to the intensity of the (110) perovskite peak and (222) pyrochlore peak, respectively. Powder morphologies and particle sizes were directly imaged using scanning electron microscopy (SEM; JEOL JSM-840A). EDX spectra were quantified with the virtual standards peaks supplied with the Oxford Instruments eXL software. Diagram of experimental procedure is shown in Fig. 1.

Results and Discussion

Themogravimetric and Differential Thermal Analysis (TG/DTA)

TG-DTA curves obtained for powders mixed in the stoichiometric proportions of PZN and PZT powders are displayed in Fig. 2. In the temperature range 50 – 300 ^{o}C, the sample shows several large exothermic peaks in the DTA curve. These DTA peaks can be attributed to the decomposition of the organic species from the milling process. The different temperatures, intensities, and shapes of the thermal peaks are probably related to the different natures of the organic species and, consequently, caused by the removal of differently bounded species in the network [13]. In the temperature range 750^{o} – 1050 ^{o}C, both exothermic and endothermic peaks are observed in the DTA curve. The enlarge zone of this DTA curve shows that the endothermic peak centered at ~ 800 ^{o}C may result from perovskite phase crystallization, and the last exothermic peak centered at ~ 850 ^{o}C may be caused by the decomposition of lead oxide [14,15]. Above 1000 ^{o}C, TG curve indicates that higher weight loss of substance occurs. This TG result implies the upper limit of the calcination temperature for the mixed powders. Therefore, these temperatures are used to

define the ranges of calcination temperatures (750 to 950 ^{o}C) used in subsequent powder processing steps.

X-Ray Diffraction Analysis (XRD)

Powder XRD patterns of the calcined *0.5*PZN-*0.5*PZT powders at different calcination temperatures are shown in Fig. 3. The XRD results show that the pyrochlore phase $Pb_{1.88}(Zn_{0.3}Nb_{1.25})O_{5.305}$ (JCPDS No.25-0446) is dominant at the calcination temperature below 850 C for the powders. The precursor phases of PbO, ZnO, Nb_2O_5, ZrO_2, TiO_2 are also detected in the powders by XRD when calcined below 800 ^{o}C. Other compositions also show a similar trend. The pyrochlore-free *x*PZN (1-*x*)PZT powders with *x*= 0.1- 0.4 can be obtained at calcination temperatures above 850 C. Earlier study by Vittayakorn *et. al.* [16] showed similar observation. However, in that study which used a conventional ball-milling method with excess PbO 2wt% the calcination temperature was above 900 ^{o}C. This clearly indicates that a rapid vibro-milling method can lower the calcination temperature for PZN-PZT powders.

As listed in Table I, all the compositions in the present work exhibit pyrochlore-free XRD scans at calcination temperature of 900 C. It can be noticed that in most compositions the perovskite phase is formed in a sudden nature, which is significantly different from previous research [16] in which more perovskite phase was found with increasing calcination temperature. The difference could be attributed to the nano-sized mixed powders (50-300 nm) obtained from a rapid vibro-milling technique. The perovskite phase formation behavior for *x*PZN *(1-x)*PZT powders at the calcination temperature of 900 C is shown in Fig. 4. The percentage of perovskite phase in PZN-PZT powders is summarized in Table I as a function

of calcination temperature. These experimental results indicate that when the concentration of the PZN phase increases the calcination temperature must be increased to obtain single perovskite phase of PZN-PZT powders. Even though pyrochlore-free PZN-PZT powders can be obtained at calcination temperature of 900 C for all compositions (x = 0.1-0.5), it should be noted that the on-set calcination temperature for pyrochlore-free powders starts at 800 C for composition with x = 0.1. It is also very interesting to see that the on-set temperature in every composition is approximately 50 C lower that those reported earlier with the conventional ball-milling method [16]. More importantly, this study suggests that the conventional mixed oxide method helps to stabilize the perovskite phase and the calcination temperature can be lowered by a vibro-milling technique.

SEM and EDX Analysis

The morphological changes in the PZN-PZT powders formed by a mixed oxide method are illustrated in Fig. 5. In general, the particles are agglomerated and basically irregular in shape, with a substantial variation in particle size, particularly in samples with more PZN contents. Generally, particle size of all compositions can be estimated from SEM micrographs to be in range of 0.2-2 m. It should be noted that the morphology of the calcined 0.1PZN-0.9PZT and 0.3PZN-0.7PZT powders is almost similar in size and shape, while for the other compositions the size and shape of the powders are significantly different.

Finally, EDX analysis using a 20 nm probe on a large number of particles of the calcined powders confirms that the parent composition is PZN-PZT powders, in good agreement with XRD results.

Conclusions

The solid-state mixed oxide method via a vibro-milling technique is explored in the preparation of pyrochlore-free solid solution of *x*PZN-(1-*x*)PZT powders (when *x*= 0.1-0.5). The optimum calcination condition for the formation of perovskite phase PZN-PZT powders is found to be 900 ^{o}C for 2 h with heating/cooling rates of 20 ^{o}C / min. Clearly, XRD study indicates that phase pure perovskite PZN-PZT powders have been obtained in this study. The potential of a vibro-milling technique as a significant time-saving method to obtain single-phase PZN-PZT powders at lower calcination temperature has also been demonstrated.

Acknowledgements

The authors are grateful to the Thailand Research Fund (TRF), Graduate School and Faculty of Science, Chiang Mai University, and Ministry of University Affairs of Thailand for financial support.

References

[1] Jaffe, B., Cook Jr., W. R. and Jaffe, H., *Piezoelectric Ceramics*. Academic Press, London, UK, 1971.

[2] Xu, Y., *Ferroelectric Materials and Their Applications*. Elsevier Science, Amsterdam, The Netherlands, 1991.

[3] Haertling, G. H., *J.Am. Ceram. Soc.*, 1999, **82**, 797–818.

[4] Kuwata, J., Uchino, K. and Nomura, S., *Ferroelectrics*, 1979, **22**, 863–867.

[5] Park, S. E. and Shrout, T. R., *J. Appl. Phys.*, 1997, **82**, 1804–1811.

[6] Dambekalne, M., Brante I. and Sternberg,A., *Ferroelectrics*, 1989, **90**,1-14.

[7] Shrout, T. R. and Halliyal, A., *Am. Ceram. Soc. Bull.*, 1987, **66**, 704–711.

[8] Halliyal, A., Kumar, U., Newnham, R. E. and Cross, L. E., *Am. Ceram. Soc. Bull.*, 1987, **66**, 671–676.

[9] Gururaja, T. R., Safari, A. and Halliyal, A., *Am. Ceram. Soc. Bull.*, 1986, **65**, 1601–1603.

[10] Fan, H.and Kim, H. E., *J. Appl. Phys.*, 2002, **91**, 317–322.

[11] Fan, H. and Kim, H. E.,, *J. Mater. Res.,* 2002, **17,** 180-185.

[12] Vittayakorn, N., Rujijanagul G., Tunkasiri T., Tan X., Cann D.P., *J. Mater. Res*., 2003, **18**, 2882–2889.

[13] Ananta, S., Brydson, R., Thomas, N.W., *J. Eur. Ceram. Soc.*, 2000, **20**, 2325-2329.

[14] Tien, T.Y., Carlson, W.G*., J. Am. Ceram. Soc*.,1962, **45**, 567-571.

[15] Pillai, C.G., Ravindran, P.V., *Thermochim. Acta.,* 1996, **278,** 109-118.

[16] Vittayakorn, N., Rujijanagul G., Tunkasiri T., Tan X., Cann D.P., *J. Mater. Sci. and Eng. B*., 2004 **, 108,** 258–265.

Table I. Percentage of perovskite phase of (*1-x*)PZT-*x*PZN; *x = 0.1-0.5.*

Calcination Temperature(°C)	Percentage of perovskite phase				
	x = 0.1	*x = 0.2*	*x = 0.3*	*x = 0.4*	*x = 0.5*
750 °C	-	-	-	-	-
800 °C	100	78.2	-	-	-
850 °C	100	100	100	100	87.7
900 °C	100	100	100	100	100
950 °C	100	100	100	100	100

List of Figure Captions

Figure 1 Diagram of experimental procedure.

Figure 2 TG-DTA curves for the mixture of PZN-PZT powder after vibro-milling.

Figure 3 XRD patterns of 0.5PZN–0.5PZT powder calcined at various temperatures temperature for 2 h. with heating/cooling rates of 20 ^{o}C / min.

Figure 4 XRD patterns of the *x*PZN - (1-*x*)PZT powders (when x = 0.1, 0.2, 0.3, 0.4, and 0.5) calcined at 900 ^{o}C with heating/cooling rates of 20 ^{o}C/min and soaking time of 2 h.

Figure 5 SEM micrographs of the *x*PZN - (1-*x*)PZT powders calcined at 900 ^{o}C with heating/cooling rates of 20 ^{o}C/min and soaking time of 2 h for (a) x=0.1, (b) x=0.2, (c) x=0.3, (d) x=0.4 and (e) x=0.5.

Figure 1

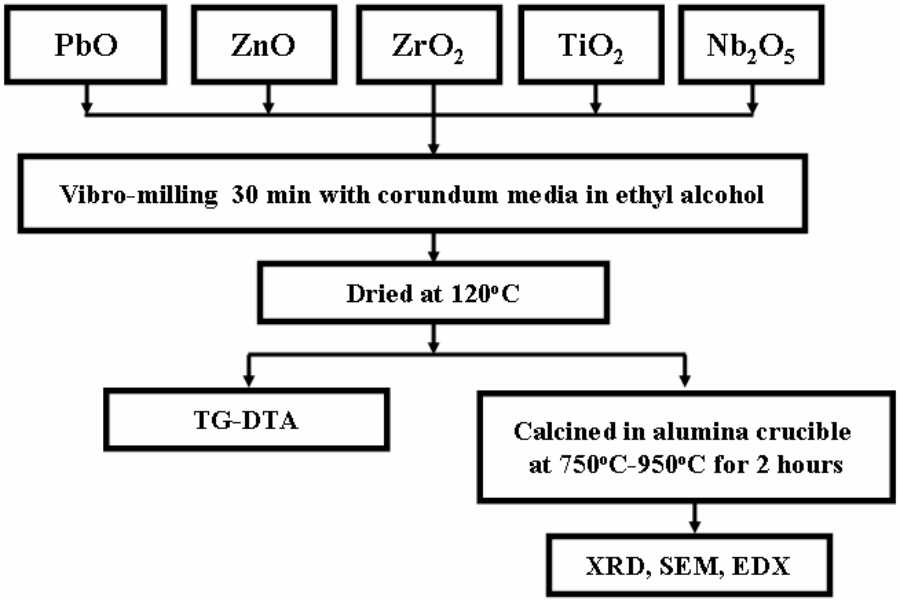
PbO
ZnO
ZrO_2
TiO_2
Nb_2O_5
Vibro-milling 30 min with corundum media in ethyl alcohol
Dried at 120°C
TG-DTA
Calcined in alumina crucible at 750°C-950°C for 2 hours
XRD, SEM, EDX

Figure 2

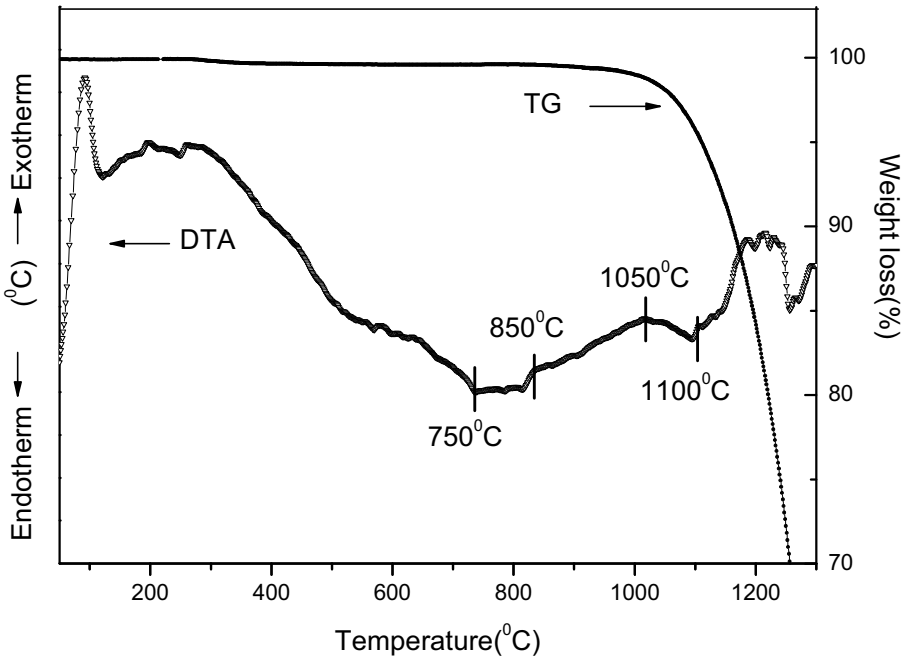
Endotherm ⟵ (⁰C) ⟶ Exotherm
Weight loss(%)
TG
DTA
1050⁰C
850⁰C
1100⁰C
750⁰C
100
90
80
70
200
400
600
800
1000
1200
Temperature(⁰C)

Figure 3

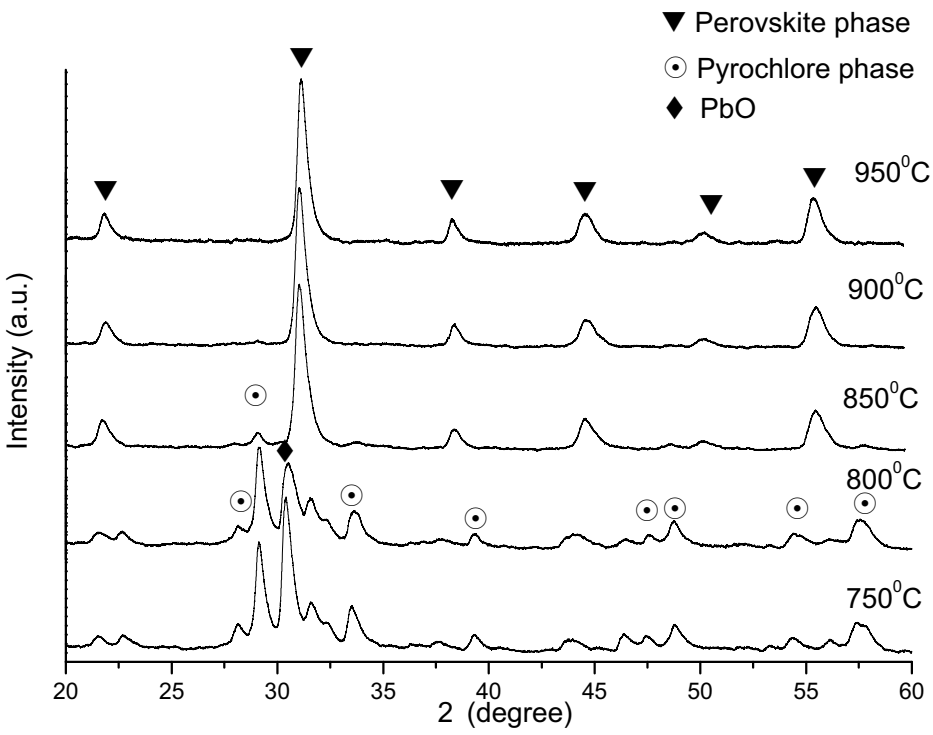
Perovskite phase
Pyrochlore phase
PbO
950^{0}C
900^{0}C
850^{0}C
800^{0}C
750^{0}C
Intensity (a.u.)
20
25
30
35
40
45
50
55
60
2 (degree)

Figure 4

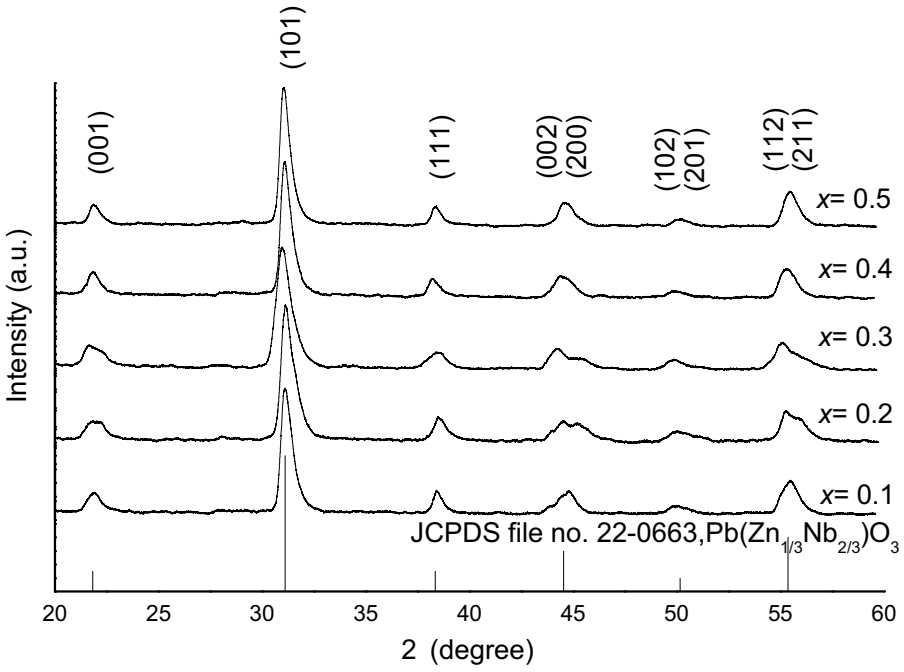
(001)
(101)
(111)
(002)
(200)
(102)
(201)
(112)
(211)
x= 0.5
x= 0.4
x= 0.3
x= 0.2
x= 0.1
JCPDS file no. 22-0663,Pb(Zn1/3Nb2/3)O3
Intensity (a.u.)
20
25
30
35
40
45
50
55
60
2 (degree)

Figure 5

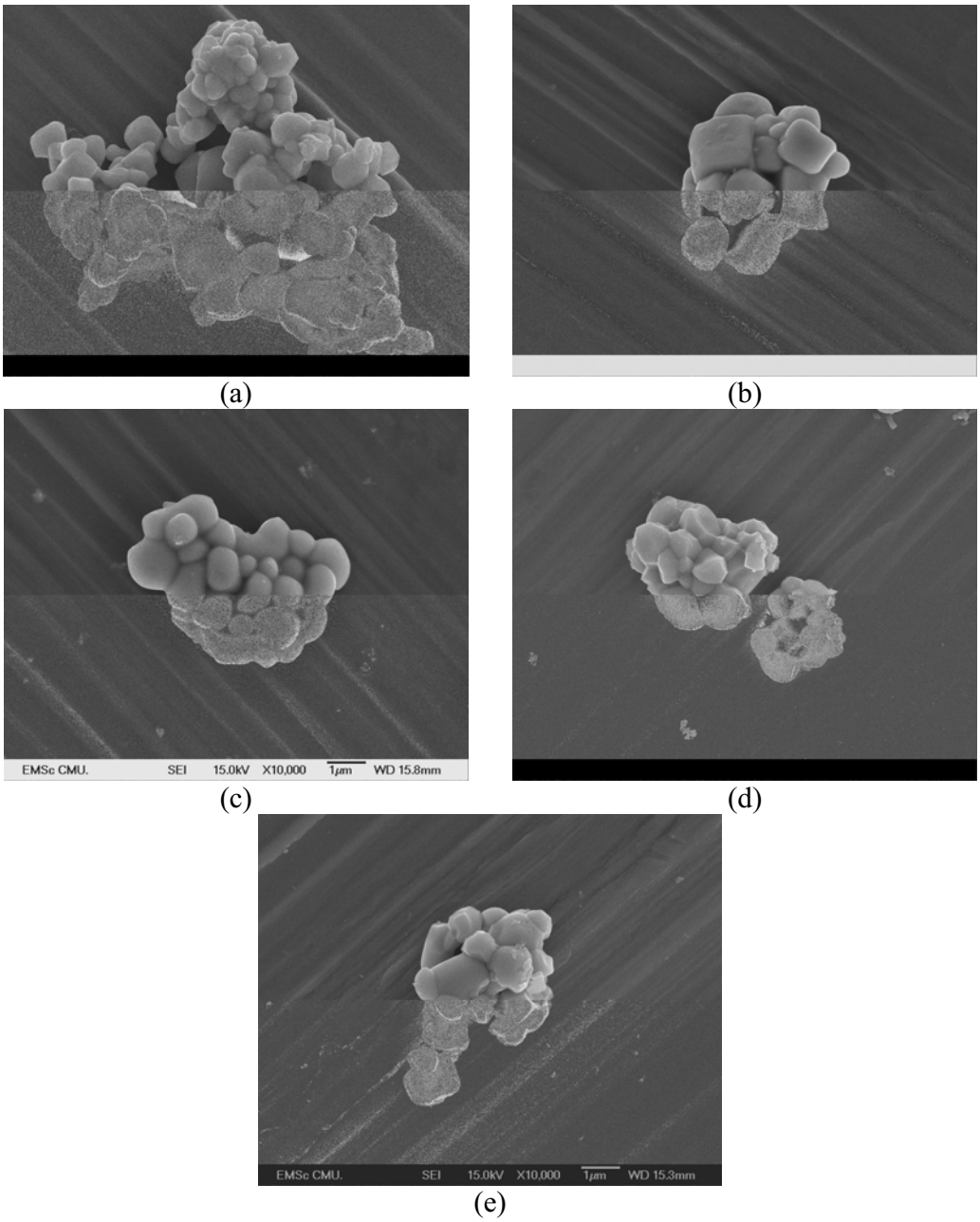

(a) (b) (c) (d) (e)

Synthesis, Formation and Characterization of Lead Indium Niobate-Lead Titanate Powders

S. Wongsaenmai, O. Khamman, S. Ananta and R. Yimnirun

Department of Physics, Faculty of Science, Chiang Mai University, Chiang Mai 50200, Thailand

Correspondence Author E-mail: wongsaenmai@yahoo.com

Abstract

In this study, powders of lead indium niobate-lead titanate (1-x)$Pb(In_{1/2}Nb_{1/2})O_3$-(x)$PbTiO_3$ (PINT) binary system near the morphotropic phase boundary (MPB) composition with x = 38mol% PT are synthesized with the conventional mixed oxide and the wolframite methods via a rapid vibro-milling technique for the first time. The preparation method and calcination temperature have been found to show pronounced effects on the phase formation behavior of the PINT powders. The stabilized perovskite phase form of PINT can be synthesized by the wolframite method, while precursor phases are still found in powders prepared by the conventional method. Finally, this study shows that the rapid vibro-milling mixing technique is effective in preparing the phase pure perovskite of PINT powders.

Keywords: PIN-PT, Conventional mixed oxide, Wolframite method, vibro-milling technique

Introduction

Lead indium niobate $Pb(In_{1/2}Nb_{1/2})O_3$ (PIN) compounds are interesting for studying the kinetics of compositional ordering [1]. It has been reported that the degrees of ordering on the B-site can be varied by thermal annealing and by forming solid solutions with perovskite compounds that exhibit normal dielectric behavior, such as $Pb(Fe_{1/2}Nb_{1/2})O_3$ (PFN), $PbZrO_3$ (PZ) and $PbTiO_3$ (PT) [2]. With different thermal treatments, the degrees of the In/Nb cation ordering on the B-site in a perovskite structure can be manipulated from a structurally disordered state into various degrees of ordering. The disorder PIN is a relaxor ferroelectric with a psudo-cubic perovskite structure. It shows the relaxor behavior with a broad dielectric maximum near 66°C, when measured at 1 kHz [3,4]. On the other hand, the ordered PIN has the antiferroelectric orthorhombic phase [5-9] with a sharp peak in the dielectric constant at 168°C [4,10]. However, pure-phase perovskite PIN ceramics free of the pyrochlore phase are very difficult to prepare using a conventional mixed oxide methode [7, 11]. This is because the tolerance and the electronegativity difference of PIN are very low compared with other perovskite compounds such as PMN [2, 12]. The wolframite method, as used by Groves [13] for the preparation of perovskite PIN ceramic, is not effective in suppressing pyrochlore phase formation. The addition of excess In_2O_3 was shown to yield higher amount of perovskite phase [13]. Recently, Alberta and Bhalla [7] were able to produce 100% phase-pure perovskite PIN ceramic with the addition of excess indium and/or lithium with wolframite method. Moreover, the solid solution with perovskite compounds such as $PbTiO_3$, can stabilize the perovskite phase of PIN and chemical ordering may be suppressed. It has also been reported that a morphotropic phase boundary of the solid solution system $(1-x)Pb(In_{1/2}Nb_{1/2})O_3$-$(x)PbTiO_3$ is located at a composition with

x=0.38 [14, 15] and this binary system near MPB composition belongs to one of the relaxor-PT systems with T_c higher than 250°C [16, 17]. Previous studies have focused on the properties of solid solution PIN-PT single crystals, while the information on PIN-PT ceramics is still limited.

This study is intended to explore a synthetics route for the pure-phase perovskite bodies of PINT binary system near MPB composition. Both the conventional mixed-oxide and the wolframite methods have been employed. More importantly, a rapid vibro-milling mixing technique is utilized to obtain phase-pure perovskite powders. Finally, the phase formation and morphology of the powders calcined at various temperatures are studied.

Experimental

For the conventional method, the starting materials of lead oxide, PbO (Fluka, 99% purity), titanium oxide, TiO_2 (Riedel-de Haën, 99% purity), niobium oxide, Nb_2O_5 (Aldrich, 99.9% purity) and indium oxide, In_2O_3 (Aldrich, 99.99% purity) were mixed in the required stoichiometric ratio for the composition (1-x)$Pb(In_{1/2}Nb_{1/2})O$-(x)$PbTiO_3$ where x = 0.38. The oxide powders were milled via a rapid vibro-milling technique for 30 min with corundum media in ethanol [18]. After drying at 120°C, the mixture was calcined at temperature between 700 to 1000 °C with dwell time of 2 h and heating/cooling rate of 10°C /min in a double crucible [19]. On the other hand, in the wolframite method the wolframite precursor was first prepared from oxide powders of niobium oxide, (Nb_2O_5) and indium oxide, (In_2O_3). The intermediate precursor $InNbO_4$ was synthesized at an optimized calcination temperature of 1100°C for 2 h [20]. The wolframite precursor was then mixed with

lead oxide (PbO) and titanium oxide (TiO_2) and re-milled. After drying, the mixture was calcined at temperature between 700 to 1000 °C with dwell time of 2 h and heating/cooling rate of 10°C/min in a double crucible.

In order to study the reaction of the uncalcined PINT powders, a differential thermal analysis (DTA) and thermalgravity analysis (TG) were performed on a DTA-TG apparatus (Perkin Elmer) using heating/cooling rate of 10°C/min in air from room temperature up to 1300°C. X-ray diffraction (XRD; Siemen-D500 diffractometer) was used to determine the phase formation behavior of the calcined powders. The microstructure was observed with a scanning electron microscope (SEM; Joel JSM-840A). The chemical compositions of the phase formed were elucidated by an energy-dispersive X-ray (EDX) analyzer with an ultra-thin window.

Results and Discussion

Initially, the DTA-TG analysis was performed on uncalcined powders to obtain thermal behavior to define the range of calcination temperature for the XRD investigation. The results from DTA-TG studies indicate that the suitable range of the calcination temperature is between 700 and 1000 °C.

Fig. 1 shows the XRD patterns of powders calcined for 2 h between 700°C and 1000°C with heating/cooling rate of 10°C/min. The differences in XRD patterns for both methods are clearly apparent. The calcination temperature of 700°C does not yield the perovskite phase for both methods. At 850°C and 800°C, respectively, the perovskite phase is found to form for the conventional and wolframite methods. The optimum calcination temperature for the formation of phase pure perovskite PINT is found to be about 900°C for the wolframite method, while the conventional method is

found to be about 850°C with PT peak. The experiment indicates that the wolframite method helps to stabilize the perovskite phase in PINT system. More importantly, though the conventional method yields the perovskite phase at lower temperature than the wolframite method, the strong PT peak is still observed in the XRD patterns of powders calcined with the conventional method as high as 1000 °C (as seen in Fig. 1a). Clearly, the significant difference between the XRD patterns is the presence of the strong PT peak at 31.5° for the powders calcined with the conventional method. As seen in Fig. 2, the diffraction peak does not match any peaks of $Pb(In_{1/2}Nb_{1/2})O_3$ (PIN) and $PbTiO_3$ (PT) compounds. Instead, the peaks closely match to those of a hypothetical solid solution formed between the two compounds. Furthermore, for the wolframite method the peaks are not a simple superposition corresponding to the two compounds, while the corresponding diffraction angle at 31.5° can be matched to maximum peak of PT for the conventional method [21]. This observation points to the formation of PT phase in the powders from the conventional method, which could be a result of better reaction of PbO and TiO_2 to form PT phase rather than PINT phase. As listed in Table 1, the quantitative analysis by energy dispersive X-ray (EDX) shows that, in addition to the PINT phase, the PIN, PT and TiO_2 phases are also present in the powders calcined by the conventional method, while only additional Nb_2O_5 phase (undetected by XRD) is possible in the powders obtained from the wolframite method. A combination of the XRD and EDX methods has indicated that the wolframite method yields XRD-phase pure PINT powders, while the conventional one results in a mixture of PINT, PIN PT, and TiO_2 (undetected by XRD) phases. This clearly emphasizes the importance of the synthetic route used to prepare the PINT powders. Moreover, effects of soaking time and heating/cooling rates have also been studied in this work. For this study, it is found that the soaking

time and heating/cooling rate do not significantly affect the phase formation behavior of PINT powders.

The morphological evolution of the calcined powders was investigated by scanning electron microscopy (SEM). Fig. 3 shows the SEM micrographs of the powders synthesized by conventional and wolframite methods. In general, the particles are agglomerated and irregular in shape. As seen in Fig. 3a, the particles synthesized by the conventional method show relatively large agglomerates ranging in diameter from about 0.5 to 2 μm. On the other hand, the particles synthesized by wolframite method, with diameter in the range ~ 0.1 to 1 μm (Fig. 3b), are lower in particle agglomeration than the conventional method.

Conclusions

The powders of a solid solution of (1-x)$Pb(In_{1/2}Nb_{1/2})O_3$-(x)$PbTiO_3$ binary system with x=0.38 was successfully prepared by both the conventional mixed oxide and the wolframite methods. The results from DTA-TG technique were use used to define the range of calcination temperature with 700°C to 1000°C. The optimum calcination temperature for the formation of phase pure perovskite was determined to be 900°C and 850°C for the wolframite, and the conventional methods, respectively, with soaking time of 2 h and heating/cooling rate of 10°C/min. Moreover, the perovskite phase was found to form at lower temperature with the conventional method than the wolframite method. However, the EDX studies showed that the stabilized perovskite phase form of PINT can be synthesized by the wolframite method, while precursor phases were still found in powders prepared by the

conventional method. Moreover, the large agglomeration and particles size were observed in powder synthesized by the conventional method.

Acknowledgement

The authors would like to express their gratitude for financial support from the Thailand Research Fund (TRF) and Graduate School and Faculty of Science, Chiang Mai University, and Ministry of University Affairs of Thailand.

.

References

[1]. A.A. Bokov, I.P. Rayevskii, V.G. Smotrakov and O.I. Prokopalo, *Phys. Stat. Sol. (a)*, **93**, 411-417 (1986).

[2]. T.R. Shrout and A. Halliyal, *Am. Ceram. Soc. Bull*., **66(4),** 704-711 (1987).

[3]. E.F. Alberta and A.S. Bhalla, *Mater. Lett*., **40**, 114-117 (1999).

[4]. E.F. Alberta and A.S. Bhalla, *J. Phys. Chem. Solids*., **63**, 1759-1769 (2002).

[5]. C.A. Randall, D.J. Barber, P. Groves and R.W. Whatmore, *J. Mater. Sci*., **23**, 3678-3682 (1988).

[6]. N. Yasuda and T. Mizuno, *Appl. Phys. Lett*., **66(5)**, 571-573 (1995).

[7]. E.F. Alberta and A.S. Bhalla, *Mater. Lett*., **29**, 127-129 (1996).

[8]. E.F. Alberta and A.S. Bhalla, *Ferroelectrics*, **188**, 96-107 (1996).

[9]. N. Yasuda, H. Ohwa, T. Mizunao, M. Iwata and Y. Ishibashi, *Appl. Phys. Lett.,* **68(24),** 3404-3406 (1996).

[10]. M. Iwata, S. Katagiri, H. Orihara, M. Maeda, I. Zusuki, H. Ohwa, N. Yasuda and Y. Ishibashi, *Ferroelectrics*., **301**, 179-183 (2004).

[11]. Y. Yoshikawa, *J. Eur. Ceram. Soc.,* **21**, 2041-2045 (2001).

[12]. Y. Guo, H. Luo, T. He and Z. Yin, *Solid. State. Commun.*, **123**, 417-420 (2002).

[13]. P. Groves, *Ferroelectrics*, **65**, 67-77 (1985).

[14]. E.F. Alberta and A.S. Bhalla, *J. Koren. Phys. Soc*., **32**, S1265-S1267 (1998).

[15]. N. Yasuda, H. Ohwa, D. Hasegawa, H. Hosono, Y. Yamashita, M. Iwata and Y. Ishibashi, *Ferroelectrics*, **270**, 247-252 (2002).

[16]. N. Yasuda, H. Ohwa, M. Kume and Y. Yamashita, *J. Appl. Phys*., **39(2A),** L66-L68 (2000).

[17]. N. Yasuda, H. Ohwa, M. Kume, K. Hayashi, Y. Hosono and Y. Yamashita, *J. Cryst. Growth,* **229**, 299-304 (2001).

[18]. R. Tipakontitikul and S. Ananta, *Mater. Lett.,* **58(3),** 449-454 (2004).

[19]. N. Vittayakorn, G. Rujijanagul, T. Tunkasiri, X. Tan and D.P. Cann, *Mat. Sci. Eng. B-Solid.,* **108**, 258-265 (2004).

[20]. N. Yasuda and M. Fujie, Jnp. J. Appl. Phys., 31, 3128-3131, (1992).

[21]. N. Yasuda, H. Ohwa, M. Kume, K. Hayashi, H. Hosono and Y. Yamashita, *J. Cryst. Growth*, **229**, 299-304 (2001).

List of Table Caption

Table 1 Chemical compositions of calcined powders from SEM-EDX analysis

List of Figure Captions

Fig. 1 XRD patterns as a function of the calcination temperature for (a) the conventional method and (b) the wolframite method

Fig. 2 XRD patterns for PINT powders at optimum calcination temperature of both methods, with comparison to standard JCPDS files for PIN and PT compound

Fig. 3 SEM micrographs of PINT powders calcined at optimum temperature for (a) the conventional method and (b) the wolframite method

Table 1 Chemical compositions of calcined powders from SEM-EDX analysis

Method	Composition (at.%)				Possible Phases
	Pb (M)	In (L)	Nb (L)	Ti (K)	
Conventional	43.9	11.3	14.4	30.4	$PbIn_{0.31}Nb_{0.31}Ti_{0.38}O_3$, $Pb(In_{1/2}Nb_{1/2})O_3$, $PbTiO_3$, TiO_2
Wolframite	46.6	11.9	21.0	20.5	$PbIn_{0.31}Nb_{0.31}Ti_{0.38}O_3$, Nb_2O_5

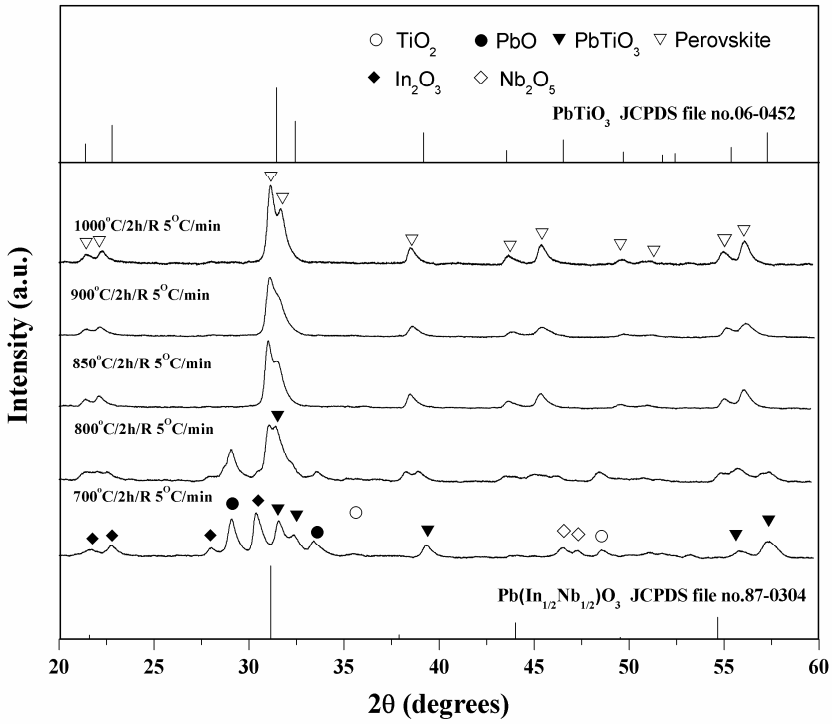

(a)

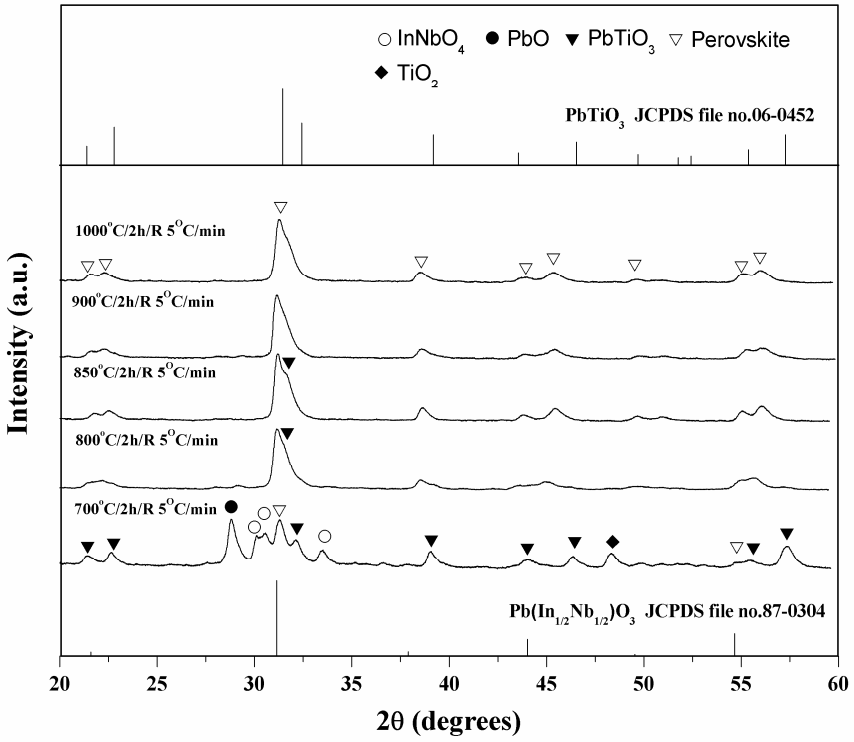

(b)

Fig.1 XRD patterns as a function of the calcination temperature for (a) the conventional method and (b) the wolframite method

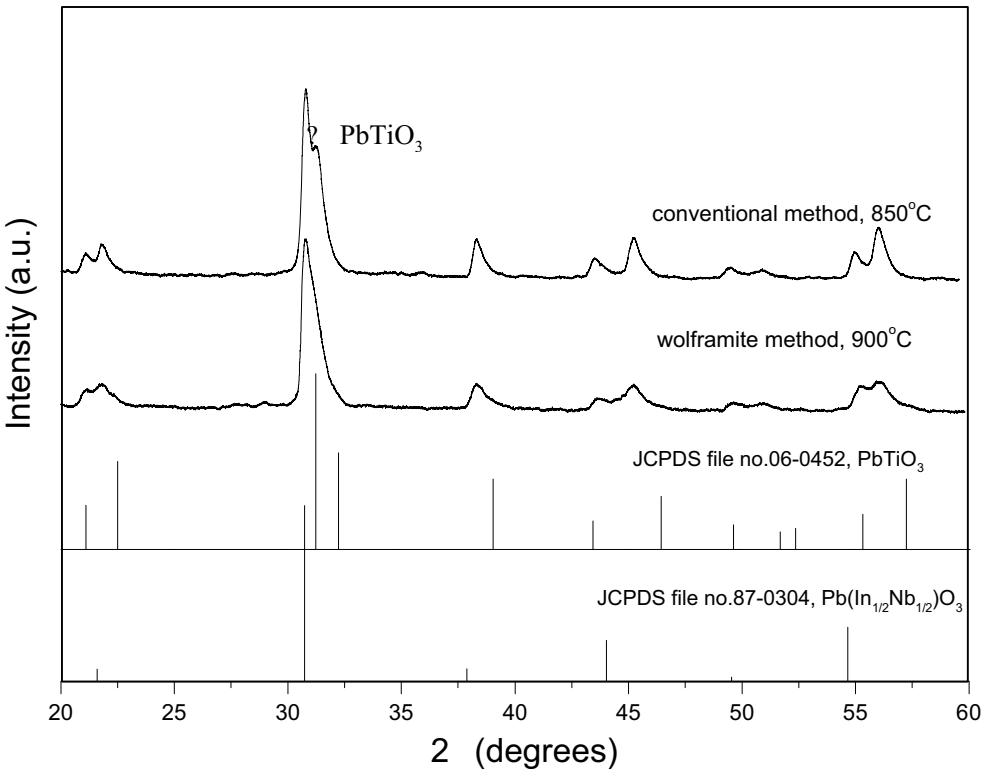

Fig. 2 XRD patterns for PINT powders at optimum calcination temperature of both methods, with comparison to standard JCPDS files for PIN and PT compounds

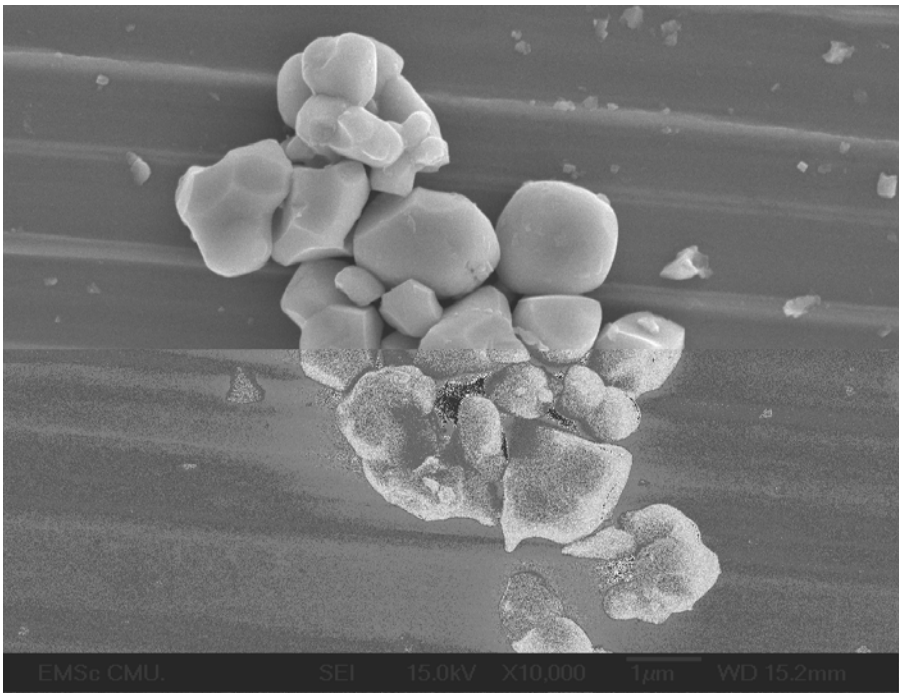

(a)

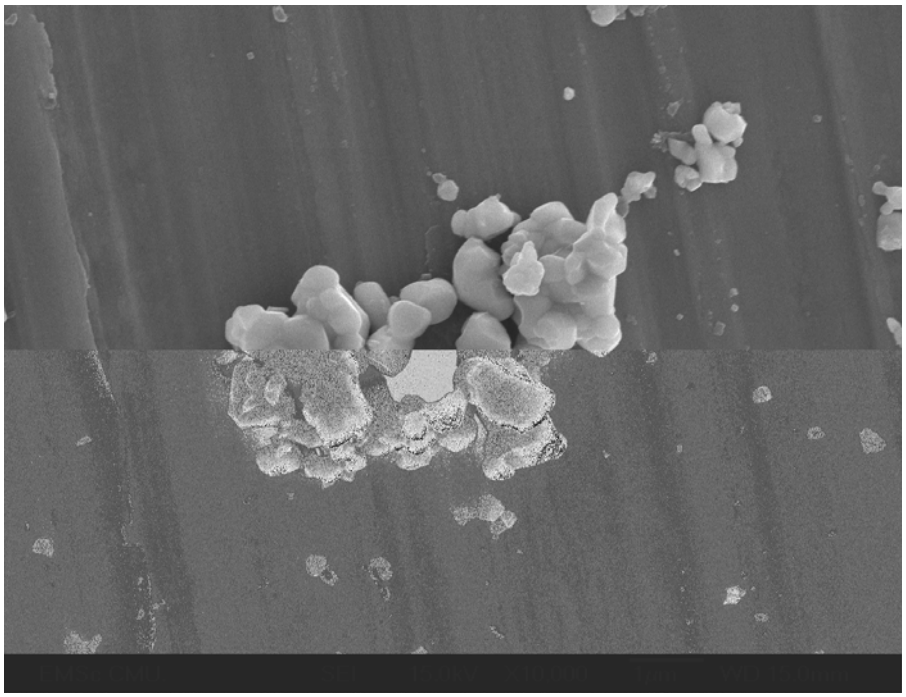

(b)

Fig. 3 SEM micrographs of PINT powders calcined at optimum temperature for (a) the conventional method and (b) the wolframite method

The Fabrication of Lead Titanate Ceramics by a Two-Stage Sintering Technique

R. Wongmaneerung*, O. Khamman, R. Yimnirun and S. Ananta
Department of Physics, Faculty of Science, Chiang Mai University,
Chiang Mai, Thailand, 50200
Email: re_nok@yahoo.com

Abstract

In this work, a two-stage sintering technique, which began with an initial heating at lower temperature and followed by higher temperature sintering, was employed in the production of $PbTiO_3$ ceramics. Effects of designed sintering conditions on phase formation, densification, microstructure and dielectric properties of the ceramics were characterized via X-ray diffraction (XRD), Archimedes method, scanning electron microscopy (SEM) and dielectric measurement, respectively. The potentiality of a two-stage sintering technique as a low-cost and simple ceramic fabrication to obtain highly dense and pure lead titanate ceramics was demonstrated. It has been found that, under suitable conditions, the perovskite phase of densified PT ceramics with reasonable dielectic properties may be achieved with equivalent to those obtained from a single-stage sintering technique.

Keyword: Lead titanate; $PbTiO_3$; Two-Stage Sintering; Perovskite; Microstructure

1. Introduction

Lead titanate ($PbTiO_3$ or PT) when combined with other oxides can form a series of ferroelectric materials that exhibit many of the most desirable dielectric, piezoelectric and pyroelectric properties for high frequency and temperature applications [1-3]. However, pure and dense PT ceramics are regarded to be one of the most difficult lead-based perovskite ferroelectric ceramics to produce due to large distortion of the tetragonal phase at room temperature (*c/a*, hereafter called tetragonality, ~ 1.06) [4]. Apart from general problems of PbO volatilization and associated high porosity, the stress induced by cooling through the phase transition can create cracking in bulk ceramics.

To overcome these problems, several techniques have been introduced, such as utilizing ultrafine powders, using additives, and carrying out appropriated milling and sintering conditions [5-7]. Amongst all the issues reported so far, most attention has been concentrated on the use of additives and powder processing, whereas investigations on modified sintering techniques have not been widely carried out [8]. Therefore, in the present study, a two-stage sintering method has been developed to resolve these problems. The overall aim of the work described here is to design the sintering scheme for fabrication of PT ceramics. The effect of the sintering conditions on phase formation, densification, microstructure and dielectric properties of materials is then investigated.

2. Experimental Procedure

Commercially available powders of PbO and TiO_2 (anatase form) (Fluka, > 99% purity) were used as starting materials. A simple mixed oxide synthetic route reported earlier [7] was employed to synthesize $PbTiO_3$ powders. Ceramic fabrication was carried out by adding 3 wt% polyvinyl alcohol (PVA) binder, prior to pressing as pellets in a uniaxial die

press at 100 MPa. Sintering was carried out with a dwell time of 2 h for each step, with constant heating/cooling rates of 1 ^{o}C/min. Variation of the single sintering temperature between 1150 and 1250 ^{o}C was carried out for the first batch of the samples. For the second batch, the first sintering temperature (T_1) was assigned at 900 ^{o}C for all cases. Variation of the second sintering temperature (T_2) from 1000 ^{o}C to 1250 ^{o}C was carried out.

Densities of the sintered products were determined by using the Archimedes principle. Sintered ceramics were examined by room temperature X-ray diffraction (XRD; Siemens-D500 diffractometer) to identify the phase formed. The lattice parameters were calculated from the XRD patterns. The microstructural development was characterized using a JEOL JSM-840A scanning electron microscopy (SEM) equipped with an energy dispersive X-ray (EDX) analyzer. Mean grain sizes of the sintered ceramics were estimated by employing the linear intercept method. The dielectric properties were measured using a HIOKI 3532-50 LCR meter.

3. Results and Discussion

X-ray diffraction patterns from the singly and doubly sintered PT ceramics are displayed in Figs. 1 and 2, respectively, indicating the formation of both perovskite and impurity phases in each case. The strongest reflections in the majority of the XRD traces indicate the formation of the perovskite phase of lead titanate, $PbTiO_3$, which could be matched with JCPDS file no. 6-452, in agreement with other works [5,7,9]. For the singly sintered PT ceramics, additional weak reflections are found in the samples sintered above 1175 ^{o}C (marked by ▼ in Fig. 1), which correlate to the starting precursor PbO (JCPDS file no.77-1971). This observation could be attributed mainly to the poor mixing of the employed powders derived from the ball-milling technique. More interestingly, a single phase of perovskite is found in most of the doubly sintered PT samples (Fig. 2), in contrast to the

observations for the singly sintered samples. This could be due to the lower firing temperature of the doubly sintered samples as compared to the singly sintered ceramics, leading to a smaller degree of lead losses and consequently avoiding the pyrochlore formation. However, many other factors come into play, e.g. homogeneity of materials, reactivity of starting powders, and processing variables.

From Table 1, it is evident that as the sintering temperature increases, the density of almost all the samples increases. The ceramic doubly sintered at 900/1150 ^{o}C having the highest relative density of about 98% with a smallest average grain size of about 0.8 m, was of the best interest for further investigations. Nevertheless, most of the samples suffered from severe stresses as a result of the high *c/a* ratio so they have broken into pieces once subjected to a cycle of high temperature measurement of dielectric properties.

Microstructural features of PT samples singly sintered at different temperatures are shown in Fig. 3. It was found that the samples subjected to low sintering temperature e.g. 1150 ^{o}C eventually burst into pieces because of the internal anisotropic stress caused by the phase transition in the ceramics as can be confirmed by the SEM images showing a loose formation of large grains (Fig. 3(a) and (b)), in consistent with high values of *c/a* given in Table 1. Additionally, average grain sizes were found to increase with the sintering temperature. For higher temperature treatments, a pronounced second phase is segregated at the grain boundaries. The EDX spectra indicated that there was more Pb and less Ti in the bright region than in the dark region. The observation of these second phase layers could be attributed to a liquid phase formation during the sintering process as proposed by Wang *et al.* and Gupta *et al.* [10,11]. It should also be noted here that the second phase could also be a result of the purity of the commercial grade starting materials and firing history used in this study. In addition, a combination of SEM and EDX techniques has demonstrated that small amounts of nano-sized (~ 1.7-2.5 m) spherical of TiO_2 inclusions (brighter phase) exits on

the surface of perovskite PT grains in some samples, as shown in Fig. 3(b) and (c). The existence of a discrete TiO_2 phase points to the expected problem of poor homogeneity of the samples arised from PbO volatilization after subjected to prolong heating scheme, although the concentration is too low for XRD detection.

Representative microstructures for doubly sintered PT ceramics are given in Fig. 4. It is seen that a uniform grain shape of typical perovskite ceramics [12] is observed, with sizes in the range of 0.4-2.0 m. It should be noted that the average grain size of the doubly sintered PT ceramics is < 1.5 m, which is less than the critical value of 3 m [13] and gives rise to a volumetric percentage enough to buffer the anisotropic stress caused by the phase transition [5]. Here, it is believed that smaller grains with random orientations result in lower internal stress in sintered samples because they compensate the anisotropy of thermal expansion coefficients.

By comparison with singly sintered PT ceramics, almost clean microstructures with highly uniform, denser angular grain-packing are generally found in doubly sintered PT samples. These microstructures are typical of a solid-state sintering mechanism. However, it should be noted that higher angulary grains were evidenced for higher second sintering temperature. The observation that the sintering temperature effect may also play an important role in obtaining a high angularity grains of perovskite ceramics is also consistent with other similar systems [14]. It is also of interest to point out that evidence has been found for the existence of microcracks (arrowed) along the grain boundaries of the samples sintered at lower second sintering temperatures (Fig. 4(a) and (b)), in consistent with other works [8,15].

Interestingly, only the samples sintered at 900 ^{o}C/1150 ^{o}C with the highest relative density and smallest average grain size of about 98% and 0.8 m, respectively, remained unbroken. It may be assumed that the ceramics consisting of very fine grains suffer less deformation, caused by the high value of *c/a* ratio, than the ceramics with significantly large

grains (Table 1). Consequently, the experimental work carried out here suggests that the optimum conditions for forming the highly dense PT ceramics in this work are double-sintering temperatures at 900 ^{o}C/1150 ^{o}C, 2 h dwell time, and 1 ^{o}C/min heating/cooling rates. The dielectric properties of PT samples sintered with different techniques are also compared in Table 2. In general, they all behave as normal ferroelectric. The Curie temperatures are about the same for all samples measured whilst the variation of dielectric constant and dielectric loss of both sets of the sintered PT ceramics seems to be somewhat related to the sintering temperatures. This observation indicates that the presence of the second phases accompanied with porosities is the key factor responsible for the dielectric response of the products. Moreover, this study demonstrated that the dielectric properties of PT ceramics are also influenced by microstructural features especially the grain boundary phase, microcracks and densification mechanism rather than by only pyrochlore phase or by grain size itself.

4. Conclusion

This work demonstrated that it was possible to obtain rather dense PT ceramics with homogeneous microstructure by the two-stage sintering technique. It has been shown that, under suitable conditions, the phase formation and densification of the ceramics are better than those obtained from the single-stage sintering. More importantly, with the two-stage sintering technique, small reductions in the maximum required sintering temperature are possible as compared to the single-stage sintering.

Acknowledgements

This work was supported by the Thailand Research Fund (TRF), Faculty of Science and Graduate school, Chiang Mai University.

References

[1]. A.J. Moulson and J.M. Herbert, *Electroceramics*, Wiley, Chichester, 2003.

[2]. G.H. Haertling, *J. Am. Ceram. Soc.*, **82**, 797-818 (1999).

[3]. S. Jiang, D. Zhou, S. Gong and W. Lu., *Sensors Actuat*., **A69**, 1-4 (1998).

[4]. G. Shirane, R. Pepinsky and B.C. Frazer, *Acta Crystallogr*., **9**, 131-140 (1956).

[5]. T. Suwannasiri and A. Safari, *J. Am. Ceram. Soc.*, **76**, 3155-3158 (1993).

[6]. J. Tartaj, C. Moure, L. Lascano and P. Duran, *Mater. Res. Bull.*, **36**, 2301-2310 (2001).

[7]. A. Udomporn, K. Pengpat and S. Ananta, *J. Eur. Ceram. Soc.*, **24**, 185-188 (2004).

[8]. S. Ananta and N.W. Thomas, *J. Eur. Ceram. Soc.*, **19**, 2917-2930 (1999).

[9]. JCPDS-ICDD Card no. 6-452. International Centre for Difraction Data. Newtown Square, PA, 2000.

[10]. H.C. Wang and W.A. Schulze, *J. Am. Ceram. Soc.*, **73**, 825-832 (1990).

[11]. S.M. Gupta and A.R. Kulkarni, *J. Mater. Res.*, **10**, 953-961 (1995).

[12]. Y.-C. Liou, *Mater. Sci. Eng.*, **B103**, 281-284 (2003).

[13]. R.W. Rice and R.C. Pohanka, *J. Am. Ceram. Soc.*, **62**, 559-563 (1979).

[14]. S. Ananta and N.W. Thomas, *J. Eur. Ceram. Soc.*, **19**, 1873-1881 (1999).

[15]. S.R. Dhage, Y.B. Khollam, H.S. Potdar, S.B. Deshpande, B.D. Sarwade and D.K. Date, *Mater. Lett.*, **56**, 564-570 (2002).

Captions of tables and figures

Table 1 Sintering behaviour of PT ceramics.

Table 2 Dielectric properties of PT ceramics.

Fig. 1 XRD patterns of PT ceramics singly sintered at various temperatures for 2 h with heating/cooling rates of 1 ^{o}C/min.

Fig. 2 XRD patterns of PT ceramics doubly sintered at various second sintering temperatures.

Fig. 3 SEM micrographs of PT ceramics singly sintered at (a) 1150 ^{o}C (b) 1200 ^{o}C (c) 1225 ^{o}C and (d) 1250 ^{o}C, for 2 h with heating/cooling rates of 1 ^{o}C/min.

Fig. 4 SEM micrographs of PT ceramics doubly sintered at (a) 900 ^{o}C/1050 ^{o}C (b) 900 ^{o}C/1100 ^{o}C (c) 900 ^{o}C/1150 ^{o}C and (d) 900 ^{o}C/1200 ^{o}C, for 2 h with heating/cooling rates of 1 ^{o}C/min.

T_1 (°C)	T_2 (°C)	Tetragonality (*c/a*)	Relative density (%)	Mean grain size* (m)
1150	-	1.064	87	10
1175	-	1.064	89	21
1200	-	1.063	92	29
1225	-	1.063	94	36
1250	-	1.063	93	41
900	1000	-	-	-
		1.060	6	1.2
		1.060	6	1.1
		1.056	7	0.8
		1.061	7	1.5
900	1250	-	-	-

* The estimated precision of the grain size is ± 1%

- Data are not available because the samples were too fragile for the measurements.

Dielectric Properties (1 kHz)	Sintering Temperature (^{o}C)	
	1225	900/1200
$_{r,\ room\ temperature}$	525	318
T_C	486	487
$_{r,\ max}$	20423	416997
$\tan\ _{max}$	2.35	0.08

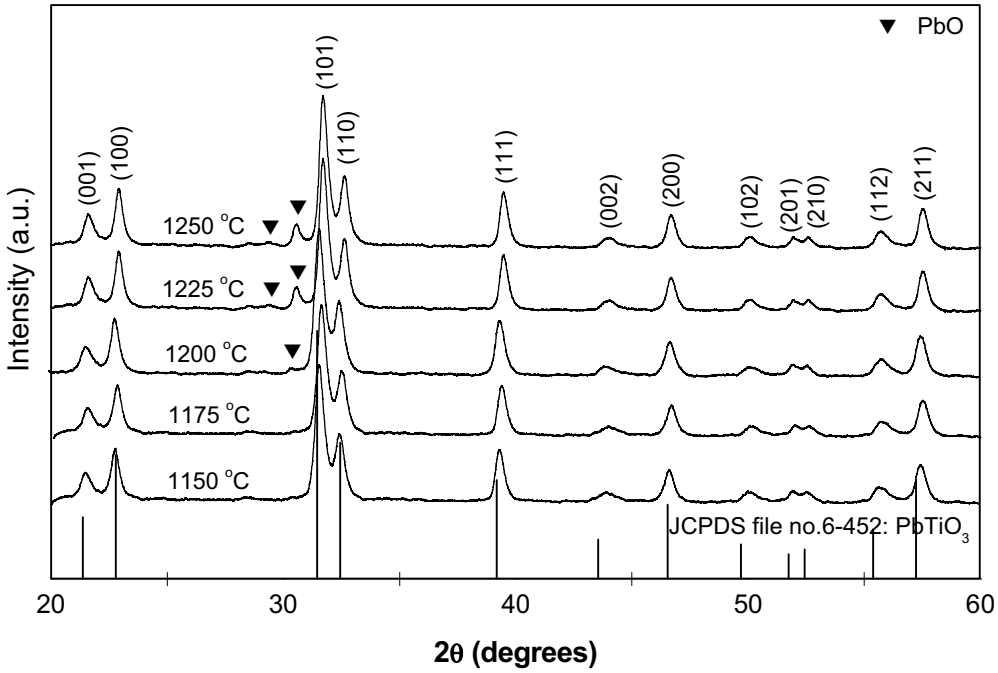
▼ PbO
(001)
(100)
(101)
(110)
(111)
(002)
(200)
(102)
(201)
(210)
(112)
(211)
1250 °C
1225 °C
1200 °C
1175 °C
1150 °C
JCPDS file no.6-452: PbTiO3
Intensity (a.u.)
20
30
40
50
60
2θ (degrees)

Fig. 1

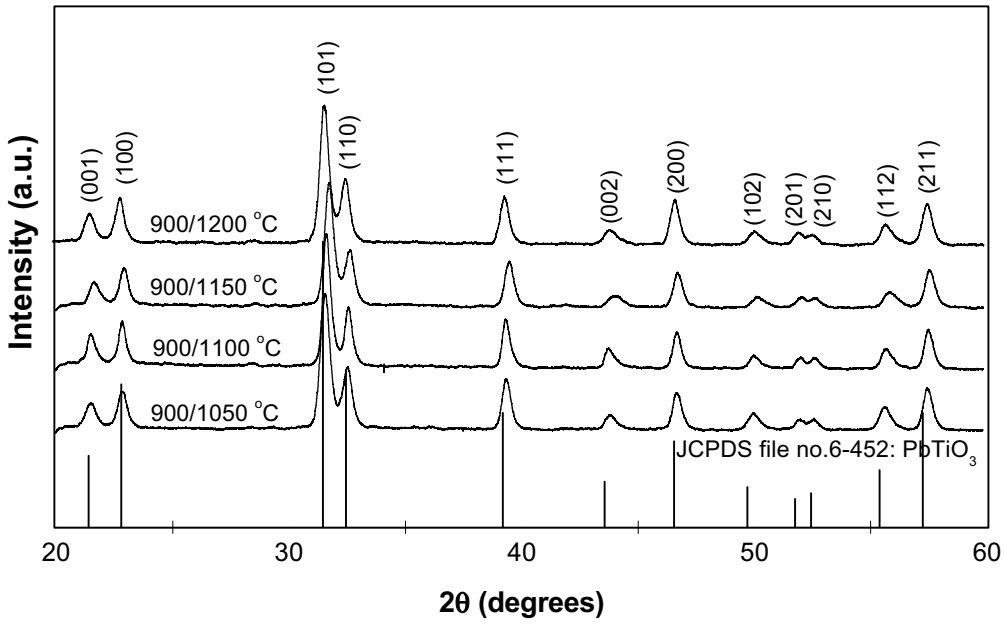
Intensity (a.u.)
(001)
(100)
(101)
(110)
(111)
(002)
(200)
(102)
(201)
(210)
(112)
(211)
900/1200 °C
900/1150 °C
900/1100 °C
900/1050 °C
JCPDS file no.6-452: PbTiO3
20
30
40
50
60
2θ (degrees)

Fig. 2

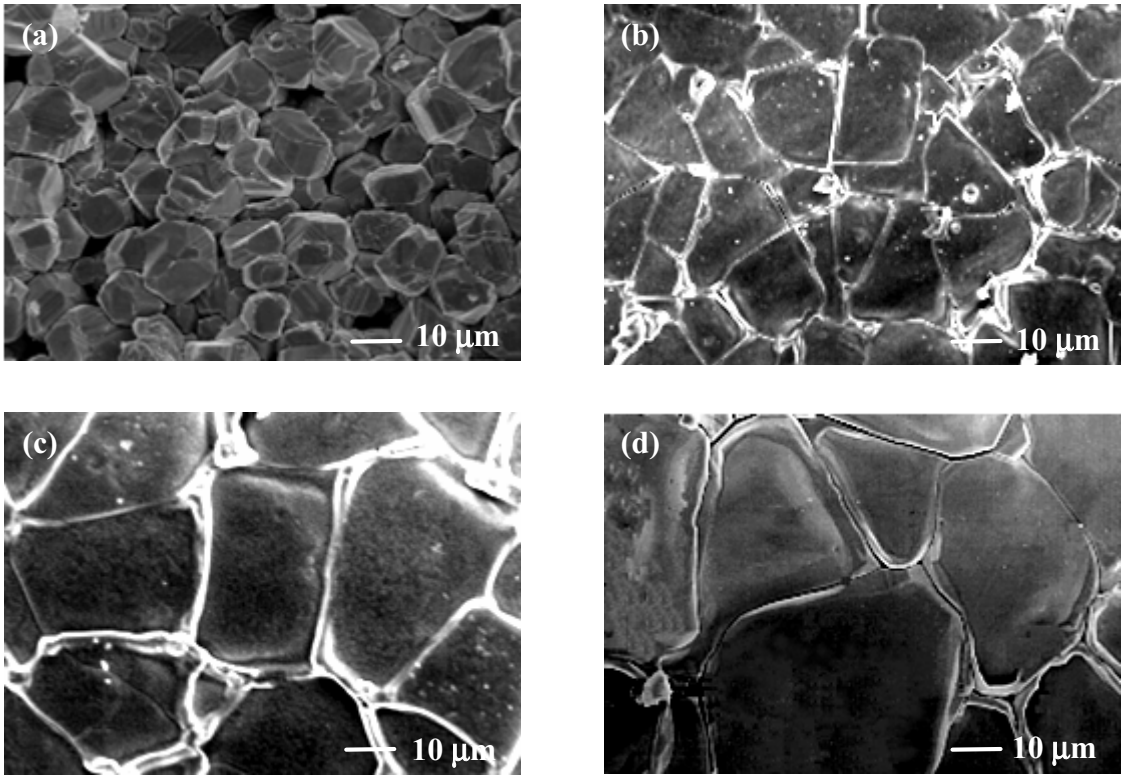

Fig. 3

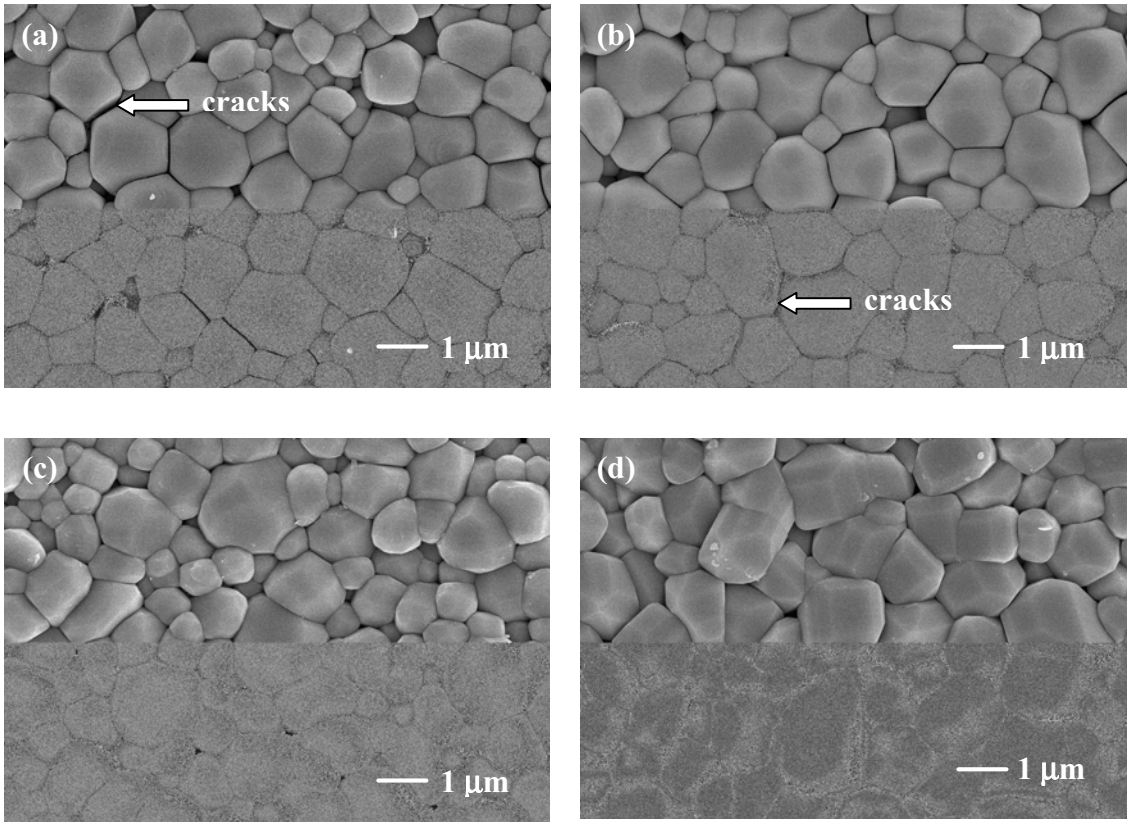

Fig. 4

Dielectric Properties of $Pb(Zr_{1/2}Ti_{1/2})O_3$–$Pb(Zn_{1/3}Nb_{2/3})O_3$ Ceramics Under Compressive Stress

Rattikorn Yimnirun, Narit Triamnak, Athipong Ngamjarurojana,

Yongyut Laosiritaworn and Supon Ananta

Department of Physics, Faculty of Science, Chiang Mai University,

Chiang Mai 50200, Thailand

Effects of compressive stress on the dielectric properties of PZT-PZN ceramics with a formula *(1- x)*$Pb(Zr_{1/2}Ti_{1/2})O_3$ *x*$Pb(Zn_{1/3}Nb_{2/3})O_3$ or *(1-x)*PZT-*(x)*PZN (x = 0.1-0.5) were investigated under stress up to 230 MPa. The experimental results revealed that the superimposed compression stress had pronounced effects on both the dielectric constant and the dielectric loss tangent of PZT-PZN ceramics. In addition, the dielectric properties were considerably lowered after a stress cycle. The observations were mainly interpreted in terms of domain switching through non-180 domain walls, clamping of domain walls, de-aging, and the stress induced decrease in switchable part of spontaneous polarization.

Keywords: dielectric properties; PZT-PZN; compressive stress

Short Title: Dielectric Properties of PZT-PZN Under Stress

INTRODUCTION

Practically, piezoelectric and feroelectric ceramics are often subjected to mechanical loading, either deliberately in the design of the device itself or because the device is used to change shapes as in many smart structure applications or the device is used under environmental stresses [1-3]. A prior knowledge of how the material properties change under different load conditions is crucial for proper design of a device and for suitable selection of materials for a specific application [4,5]. It is therefore important to determine the properties of these materials as a function of applied stress. Previous investigations on the stress-dependence electrical properties of many ceramic systems have emphasized the importance of the matter [3,6-10]. Recently, the uniaxial stress dependence of dielectric properties has been investigated in materials such as BT, PZT, PMN, PMN-PT, PZT-BT, and PMN-PZT [8-13]. The results clearly showed that the effects of stress on the dielectric properties depended significantly on ceramic compositions and stress levels.

Recently, there have been a great deal of interest in lead zirconate titanate-lead zinc niobate ($Pb(Zr_{1/2}Ti_{1/2})O_3$ $Pb(Zn_{1/3}Nb_{2/3})O_3$ or PZT-PZN) systems because of their high dielectric, piezoelectric, and ferroelectric properties [14-16]. PZN is a ferroelectric material with frequency dependent dielectric relaxation behavior, as well as diffuse phase transition at 140 °C [17]. A single crystal of PZN shows extremely high dielectric and piezoelectric constants [18]. PZT also has high piezoelectric properties, particularly compositions (Zr:Ti~52:48) close to a morphotropic phase boundary (MPB) between the tetragonal and the rhombohedral phases [19].

Therefore, PZT is the most popular ferroelectric material used in electronic devices [4,19,20]. As both PZT and PZN possess excellent electrical properties, enhanced properties can thus be expected from ceramics in PZT-PZN system. There have been many previous reports on the electrical properties of PZT-PZN ceramics [14-16]. However, there has been no systematic study on the influence of an applied stress on the dielectric properties of the PZT-PZN ceramics. Therefore, it is the aim of this study to determine the dielectric properties of the (*1-x*)PZT-(*x*)PZN ceramics as a function of compressive stress.

EXPERIMENTAL METHOD

In this study, (*1-x*)$Pb(Zr_{1/2}Ti_{1/2})O_3$–(*x*) $Pb(Zn_{1/3}Nb_{2/3})O_3$ (with x = 0.1-0.5) ceramics were prepared from starting PZT and PZN powders by a conventional mixed-oxide method via vibro-milling technique [21]. Perovskite-phase PZN powders were obtained from the columbite method with zinc niobate ($ZnNb_2O_6$) selected as the precursor, while PZT powders were prepared by a simple mixed-oxide method [22]. For optimization purpose, the sintering was carried out at temperatures between 1200 and 1250 C for 2 h. Details of the processing and characterizations were provided elsewhere [21-23].

Before studying the dielectric properties, the specimens were lapped to obtain parallel faces. After coating with silver paint as electrode at the faces, the specimens were heated at 750 C for 12 min to ensure the contact between the electrode and surface of ceramic. All the ceramics were then poled at 150 C under a field of 25

kV/cm prior to testing. To study effects of the compressive stress on the dielectric properties of the ceramics, the compressometer was constructed [8-11]. The dielectric properties were measured by LCR-meter (Instrek LCR-821). The room temperature (25 C) capacitance and the dielectric loss tangent were obtained at frequency of 1 kHz under compressive stress up to 230 MPa. The dielectric constant was then calculated from a parallel-plate capacitor equation, e.g. $_r = Cd / _0A$, where C is the capacitance of the specimens, d and A are, respectively, the thickness and the area of the electrode, and $_0$ is the dielectric permittivity of vacuum (8.854×10^{-12} F/m).

RESULTS AND DISCUSSION

The results from X-ray diffraction studies, not shown here, indicate that complete crystalline solutions of perovskite structure are formed throughout the composition range between x = 0.1 and 0.5. In general, tetragonal symmetry is observed at low PZN contents (x =0.1 and 0.2), in agreement with other workers [14,16]. By the influence of PZN, however, the rhombohedral symmetry has developed in compositions with x = 0.3. Similar microstructure characteristics are observed in these samples, i.e. uniformly sized grains with a high degree of grain close-packing, and almost no abnormal grain growth. All ceramic compositions display very similar grain size range between 1 and 3 m. Since the physical and microstructure features of all ceramic compositions are not significantly different, these parameters should not play an important role in the composition-dependent dielectric properties under the compressive stress discussed in the following paragraphs.

The dielectric properties, i.e. dielectric constant ($_r$), are measured as functions of both temperature and frequency, as shown in Fig. 1. As listed in Table 1, the maximum dielectric constant is comparatively higher in values in ceramic compositions with x = 0.1 and 0.2. With sharp phase transitions, the dielectric properties of these compositions are nearly independent of frequency, except in the vicinity of the phase transformation temperature; a typical characteristic of normal ferroelectrics [14,16]. When more PZN is added, the dielectric behavior is shifted towards that of relaxor materials. The dielectric properties of the compositions with x = 0.3 exhibit a diffuse phase transition with dielectric peak broadening [16]. All these behaviors indicate a morphotropic phase boundary (MPB) of PZT-PZN system between x = 0.2 and 0.3, as reported earlier [14]. The room temperature dielectric properties measured under stress-free condition are also listed in Table 1. It is clearly seen that dielectric constant ($_r$) of (*1-x*)PZT–(*x*)PZN ceramics increases with increasing PZN content. This observation could be attributed to a high dielectric constant of PZN and a closer to ambient temperature T_C for PZT-PZN compositions with higher PZN content [16].

The experimental results of the compressive stress dependence of the dielectric properties during loading and unloading for the ceramics in PZT-PZN system are displayed in Figs. 2 and 3. For better comparison, the dielectric properties of each composition under stress are normalized to the stress-free values. Clearly, there is a considerable change of both the dielectric constant and the dielectric loss tangent with the compressive stress. As depicted in Fig. 2, the changes of the dielectric constant with the stress can be divided into two groups. For tetragonal

compositions, the dielectric constant decreases drastically with the applied stress. The dielectric constant decreases more than 15-30% when the stress reaches 230 MPa and only returns to slightly less than 80-85% of their original values when the stress is removed. The changing of the dielectric constant with increasing and decreasing the stress does not follow the same path. On the other hand, for the rhombohedral compositions, i.e., with x values of 0.3-0.5, the change is minimal. The dielectric constant is actually rather stable within this range of the stress. The dielectric constant of these compositions initially increases then decreases with very little difference in the dielectric constant between stress-free and maximum stress conditions. In addition, the dielectric constants during loading and unloading are not significantly different. Similar trend is also observed for the compressive stress dependence of the dielectric loss tangent (tan), as shown in Fig. 3. It is also noticed that the changes in the dielectric properties with the compressive stress obtained in this study are in parts similar to those for PMN-PZT and PMN-PT systems in earlier investigations [12,13].

To understand these experimental results, at least qualitatively, various effects have to be considered. When the compressive stress is applied in the direction parallel to the poling direction, the stress will move some of the polarization away from the poling direction resulting in a change in domain structures, which may undergo domain switching through non-180 domain walls, de-aging, clamping of domain walls, and stress induced decrease in switchable part of spontaneous polarization [6,7,12,13]. It should be noted that ceramic compositions with tetragonal symmetry contain 180º and 90º domains, while those with rhombohedral symmetry consist of 180º 109º and 71º domains [4,19]. These types of domains response to the

compressive stress differently. Earlier TEM studies by Vittayakorn et al. [16] revealed mainly the 90º domain configurations in tetragonal compositions and the disrupted domains in the rhombohedral compositions.

The experimental observations, which show drastic decreases in both dielectric constant and dielectric loss tangent with increasing stress in the tetragonal compositions, i.e. 0.9PZT-0.1PZN and 0.8PZT-0.2PZN, can be attributed to the switching of 90º domains, which causes the significant decrease in the dielectric constant, as seen in Fig.2. For the rhombohedral compositions, the observed changes can be attributed to competing influences, in an opposite way, of the intrinsic contribution of domains and the extrinsic contribution of re-polarization and growth of micro-polar regions. Under the applied compressive stress, the non-180º domain wall density increases. Hence the increase of the dielectric constant is observed. The de-aging mechanism, which also increases the dielectric constant [11-13], is also expected to play a role here. Therefore, a combination of the domain switching and the de-aging mechanisms is believed to be a reason for the slight increase of the dielectric constant during low-stress application. With further increase in the stress, the stress clamping of domain walls, which results in a decrease of domain wall mobility, and the stress induced decrease in switchable part of spontaneous polarization are expected to play a role in the decrease of the dielectric constant [11,12]. Therefore, the dielectric constant of these compositions is seen to be rather stable with the applied stress. Similar observation has also been reported in PMN-PT ceramics [12]. The cause of the stress dependence of the dielectric loss tangent is a little more straightforward. As depicted in Fig. 3, the clamping of the domain walls

under the compressive stress results in a decrease of domain wall mobility and reduces the dielectric loss tangent [11]. This is a reversible effect with the domain wall mobility returning to near the original values when the applied stress is removed, as seen in Fig. 3 that the dielectric loss tangents return to near their original values after a stress cycle. In addition, a significant decrease in the dielectric constant after a full cycle of stress application in the tetragonal compositions has been observed and attributed to the stress induced decrease in switchable part of spontaneous polarization at high stress and the irreversible 90º domain switching [7,12].

CONCLUSIONS

In this study, effects of compressive stress on the dielectric properties of PZT-PZN ceramics with a formula *(1- x)*$Pb(Zr_{1/2}Ti_{1/2})O_3$ *x*$Pb(Zn_{1/3}Nb_{2/3})O_3$ or *(1-x)*PZT-*(x)*PZN (x = 0.1-0.5) have been investigated under stress up to 230 MPa. The superimposed compression stress had pronounced effects on both the dielectric constant and the dielectric loss tangent of PZT-PZN ceramics, especially in tetragonal compositions. The observations were mainly interpreted in terms of domain switching through non-180 domain walls, clamping of domain walls, de-aging, and the stress induced decrease in switchable part of spontaneous polarization.

ACKNOWLEDGMENTS

This work was supported by the Thailand Research Fund, Commission on Higher Education, Faculty of Science and Graduate School of Chiang Mai University.

REFERENCES

[1] J. Kuwata, K. Uchino, and S. Nomura, Jpn. J. Appl. Phys. 21, 1298 (1982).

[2] S. Park and T.R. Shrout, J. Appl. Phys. 82, 1804 (1997).

[3] D. Viehland and J. Powers, Appl. Phys. Lett., 78, 3112 (2001)

[4] K. Uchino, Piezoelectric Actuators and Ultrasonic Motors (Kluwer Academic, Boston, 1997).

[5] D. Stansfield, Underwater Electroacoustic Transducers (Bath University Press, Bath, 1991).

[6] D. Zhou, M. Kamlah, and D. Munz, J. Euro. Ceram. Soc. 25, 425 (2005).

[7] Q.M. Zhang, J. Zhao, K. Uchino, and J. Zheng, J. Mater. Res. 12, 226 (1997).

[8] R. Yimnirun, Ferroelectrics, 331, 9 (2006).

[9] R. Yimnirun, S. Ananta, and S. Chamunglap, Mater. Chem. Phys. (2006) in press

[10] R. Yimnirun, S. Ananta, A. Ngamjarurojana, and S. Wongsaenmai, Curr. Appl. Phys., 6, 520 (2006).

[11] G. Yang, S.F. Liu, W. Ren, and B.K. Mukherjee, Proc. SPIE Sym. Smart Struct. Mater. 3992, 103 (2000).

[12] R. Yimnirun, M. Unruan, Y. Laosiritaworn, and S. Ananta, J. Phys. D: Appl. Phys., 39, 3097 (2006).

[13] R. Yimnirun, Inter. J. Mod. Phys. B (2006) in press.

[14] N. Vittayakorn, G. Rujijanagul, T. Tunkasiri, X. Tan and D.P. Cann, J. Mater. Res. 18, 2882 (2003).

[15] H. Fan and H.-E. Kim, J. Appl. Phys. 91, 317 (2002).

[16] N. Vittayakorn, G. Rujijanagul, X. Tan, H. He, M.A. Marquardt, and D.P. Cann, J. Electroceram. 16, 141 (2006).

[17] V.A. Bokov and I.E. Mylnikova, Sov. Phys-Solid State 2 (1960), p. 2428.

[18] K. Uchino, Solid State Ionics 108, 43 (1998).

[19] Y.H. Xu, Ferroelectric Materials and Their Applications (North Holland, Los Angeles, 1991)

[20] A.J. Moulson and J.M. Herbert, Electroceramics: Materials, Properties, Applications (Wiley, Chichester, 2003)

[21] R. Yimnirun, R. Tipakontitikul, and S. Ananta, Inter. J. Mod. Phys. B, 20, (2006).

[22] A. Ngamjarurojana, O. Khamman, R. Yimnirun, and S. Ananta, Mater. Lett. 60, 2867 (2006).

[23] A. Ngamjarurojana, O. Khamman, S. Ananta, and R. Yimnirun, J. Electroceram. (2006) in press.

List of Table Caption

Table 1. Characteristics of PZT-PZN ceramics with optimized processing conditions

List of Figure Captions

Figure 1. Temperature and frequency dependence of dielectric constant of (1-x)PZT-(x)PZN ceramics (measured at 1 kHz).

Figure 2. Relative changes of dielectric constant ($_r$) with compressive stress for (1-x)PZT-(x)PZN ceramics (measured at 25 ºC and 1 kHz; solid arrows indicate loading direction).

Figure 3. Relative changes of dielectric loss tangent (tan) with compressive stress for (1-x)PZT-(x)PZN ceramics (measured at 25 ºC and 1 kHz; solid arrows indicate loading direction).

Table 1. Characteristics of PMN-PT ceramics with optimized processing conditions.

Ceramic	Sintering Temperature	Density	T_C	Stress-Free Dielectric Properties	
				$\varepsilon_{r,\,room}$	$\varepsilon_{r,\,max}$
	(^oC)	(g/cm^3)	(^oC)		
0.9PZT-0.1PZN	1250	6.95	375	1011	14676
0.8PZT-0.2PZN	1250	6.34	338	1153	18210
0.7PZT-0.3PZN	1225	7.45	306	1265	9610
0.6PZT-0.4PZN	1200	7.55	278	1349	11241
0.5PZT-0.5PZN	1200	7.75	259	1561	13181

Figure 1

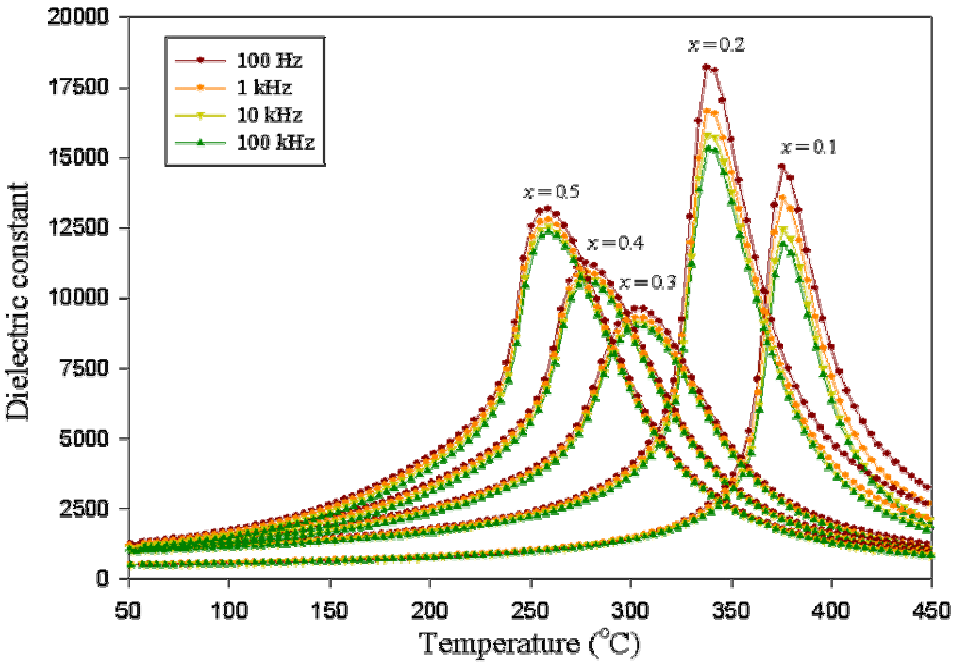
100 Hz
1 kHz
10 kHz
100 kHz
x = 0.5
x = 0.4
x = 0.3
x = 0.2
x = 0.1
Dielectric constant
Temperature (°C)
0
2500
5000
7500
10000
12500
15000
17500
20000
50
100
150
200
250
300
350
400
450

Figure 2

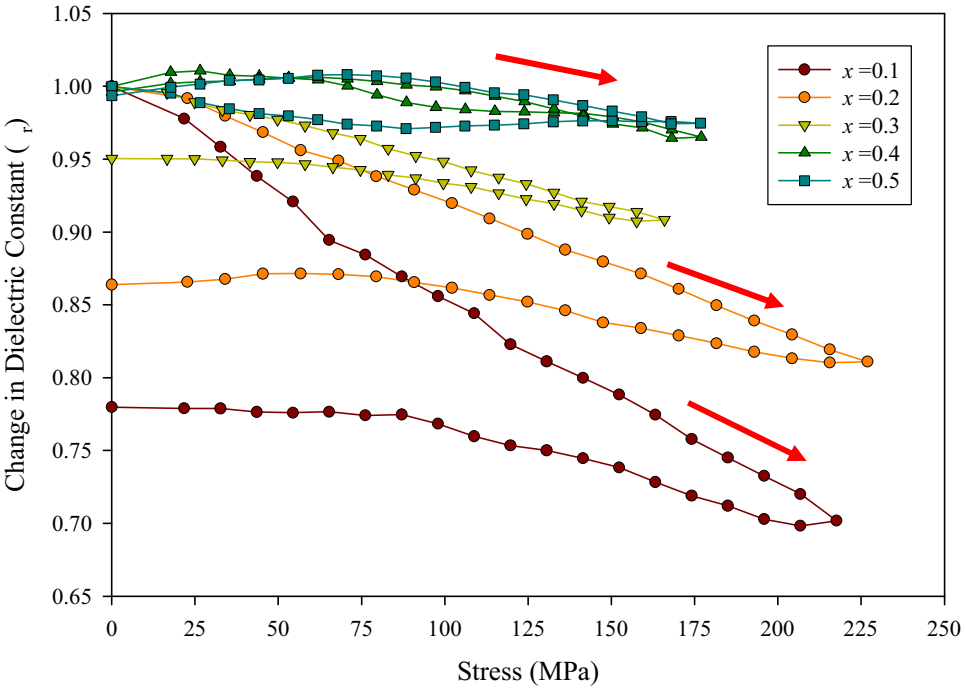
1.05
1.00
0.95
0.90
0.85
0.80
0.75
0.70
0.65
Change in Dielectric Constant (r)
0
25
50
75
100
125
150
175
200
225
250
Stress (MPa)
x =0.1
x =0.2
x =0.3
x =0.4
x =0.5

Figure 3

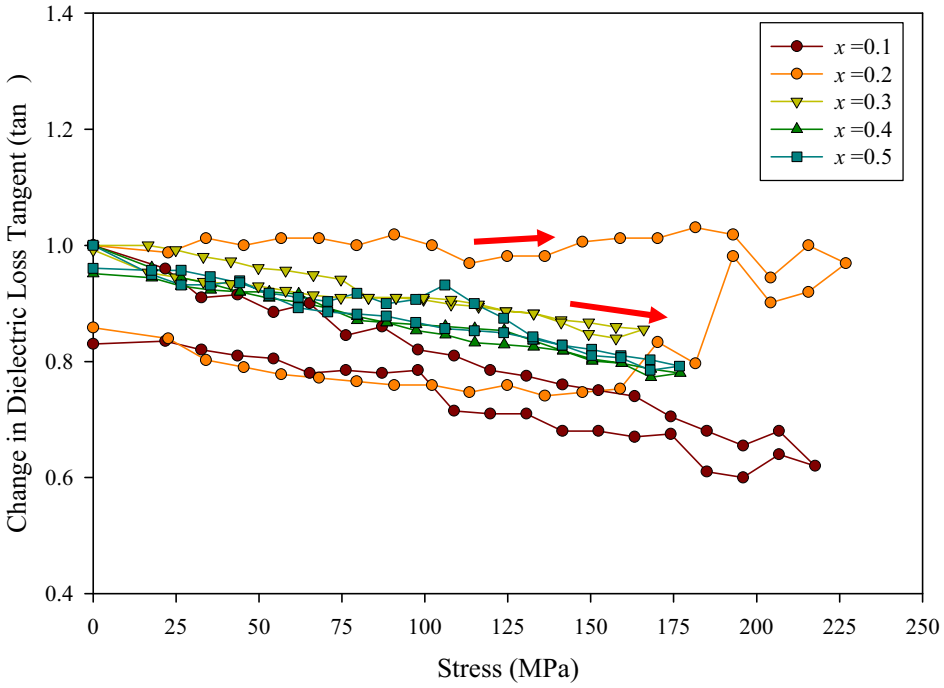
1.4
1.2
1.0
0.8
0.6
0.4
Change in Dielectric Loss Tangent (tan)
0
25
50
75
100
125
150
175
200
225
250
Stress (MPa)
x =0.1
x =0.2
x =0.3
x =0.4
x =0.5

Effects of Vibro-Milling Time and Calcination on Phase Formation and Particle Size of Lead Zirconate Nanopowders

ORAWAN KHAMMAN*, RATTIKORN YIMNIRUN,
YONGYUT LAOSIRITAWORN AND SUPON ANANTA

Department of Physics, Faculty of Science, Chiang Mai University, Chiang Mai 50200, Thailand

Effect of calcination conditions on phase formation and particle size of lead zirconate ($PbZrO_3$) powders synthesized by a solid-state reaction with different vibro-milling times was investigated. It was found that the calcination time for the formation of pure $PbZrO_3$ was lower when longer milling times were applied. More importantly, by employing an appropriate choice of the milling time and calcination conditions, $PbZrO_3$ nanopowders have been successfully prepared with a simple solid-state reaction method.

Keywords: Lead zirconate; Milling; Nanopowders; Phase formation; Particle size

1. INTRODUCTION

In recent years, some interest on the preparation of lead zirconate, $PbZrO_3$ or PZ, nanopowders and PZ-based ceramics appeared to be revived with regard to potential applications of their excellent properties for electromechanical actuators and pyroelectric sensors [1,2]. To fabricate them, a fine powder of perovskite phase with the minimized degree of particle agglomeration is needed as starting material in order to achieve a dense and uniform microstructure at the sintering temperature [1,2]. In this connection, different preparative methods have been introduced, such as co-precipitation [3], sol-gel [4], citrate combustion [5], hydrothermal [6] and microemulsion method [7]. All these techniques are aimed at reducing the temperature of preparation of the compound even though they are more expensive, involved and complicated in approach than the solid-state reaction method. Moreover, high purity of PZ nanopowders are still not available in mass quantity. Therefore, in the present work, a simple mixed oxide method employing a rapid vibro-milling technique previously advocated by the authors [8,9] has been adopted to resolve these problems. Although some research has been done in the preparation of PZ powders via a vibro-milling technique [8], to our knowledge a systematic study regarding the influence of milling time on the synthesis of PZ powders has not yet been reported. Thus, in this work, the effect of milling times on phase formation and particle size of lead zirconate powders was investigated in this connection. The potential of the vibro-milling technique as a simple method to

obtain usable quantities of single-phase PZ powders at low temperature and with nanosized particle was also examined.

2. EXPERIMENTAL PROCEDURE

The raw materials used were commercially available lead oxide, PbO and zirconium oxide, ZrO_2 (Fluka, >99% purity). The two oxide powders exhibited an average particle size in the range of 3.0 to 5.0 μm. In order to improve the reactivity of these raw materials, a McCrone vibro-milling technique [8,9] was carried out for 20 and 30 h (instead of 30 min [8]) with corundum media in isopropyl alcohol (IPA). After drying at 120 °C, various calcination conditions were applied in order to investigate the formation of $PbZrO_3$. All powders were examined by X-ray diffraction (XRD; Siemens-D500 diffractometer) using CuK_a radiation. The crystalline lattice constants and average particle size were also estimated from XRD patterns [9]. The particle size distributions of the powders were determined by laser diffraction technique (DIAS 1640) with the particle sizes and morphologies of the powders observed by scanning electron microscopy (JEOL JSM-840 A SEM).

3. RESULTS AND DISCUSSION

From Figs. 1 and 2, it is seen that for the uncalcined powders (1(a) and 2(a)), only X-ray peaks of precursors PbO ( ) and ZrO_2 (○) are present, indicating that no reaction was yet triggered during the vibro-milling process. However, after calcination at 750 °C (or 700 °C) for powders milled at 20 h (or

30 h), it is seen that the perovskite-type $PbZrO_3$ (▼) becomes the predominant phase indicating that the reaction has occurred to a considerable extent. The peaks of ZrO_2 phase were completely eliminated after calcination at 750 C for at least 3 h (or 2 h) for powders milled at 20 h (or 30 h). However, it should be noted that after calcination at 800 °C for 2 h (or 1 h) for powders milled at 20 h (or 30 h), the single phase of perovskite PZ (yield of 100% within the limitations of the XRD technique) was obtained.

In general, the strongest reflections apparent in the majority of these XRD patterns indicate the formation of $PbZrO_3$ (JCPDS file number 35-0739), consistent with other works [3,8]. In this study, it is seen that by varying the calcination temperature, the minimum dwell time at a given firing temperature for the single phase formation of each milling batch is gradually decreased with increasing milling time. This was apparently a consequence of the enhancement in crystallinity of the perovskite phase with increasing degree of mixing, in good agreement with other works [8,9].

However, there is evidence that, minor amount of the unreacted PbO phase tends to coexist along with the PZ phase, agreed with earlier works [10,11]. The appearance of PbO phase indicated that full crystallization has not occurred at relatively lower firing temperature. This could be caused by that, at low temperatures, the thermal energy is not enough to bring about the full PZ crystallization process. Therefore, in the present study, an attempt was also made to compensate the low firing temperatures with some optimum condition of calcinations, milling time and heating/cooling rates (Figs. 1 (f-h) and 2 (e-g)). In

this connection, it is shown that the yield of $PbZrO_3$ phase did not vary significantly with different heating/cooling rates ranging from 10 to 30 °C/min, in good agreement with the early observation for the $PbZrO_3$ powders subjected to 0.5 h of vibro-milling time [8]. However, one successful achievement can be obtained in this work which is that the single phase of PZ is found at lower temperature by increasing milling time (Fig. 1(e) *v.s.* Fig. 2(e)). It should be noted that no evidence of the introduction of impurity due to wear debris from the selected milling process was observed in all calcined powders, indicating the effectiveness of the vibro-milling technique for the production of high purity $PbZrO_3$ nanopowders.

The variation of calculated crystallite size of the powders milled for different times with the calcination conditions is given in Table 1. In general, it is seen that the crystallite size of lead zirconate decreases with increasing milling time or with faster heating/cooling rates. There is no obvious interpretation of these observations, although it is likely to correspond to the competition between the major mechanisms leading to crystallization and agglomeration [9]. The morphological evolution and particle size distribution during various calcination conditions of PZ powders milled with different times were investigated as shown in Fig. 3. In general, the particles are agglomerated and basically irregular in shape, with a substantial variation in particle sizes and size distribution, particularly in powders subjected to prolong milling times or with faster heating/cooling rates (Fig. 3 (b-d)). The powders consist of primary particles of 50-318 nm in size and the agglomerates measured 72-2010 nm. The

experimental work carried out here suggests that the optimal combination of the milling time and calcination condition for the production of single-phase $PbZrO_3$ nanopowders is 30 h and 800 °C for 1 h with heating/cooling rates of 30 °C/min, respectively. Moreover, the employed heating/cooling rates for $PbZrO_3$ powders observed in this work are also faster than those reported earlier [9-11].

4. CONCLUSIONS

This work demonstrated that by applying an appropriate choice of the vibro-milling time and calcination conditions, mass quantities of a high purity lead zirconate nanopowders can be successfully produced by a simple solid-state mixed oxide synthetic route.

ACKNOWLEDGEMENTS

This work was supported by the nanoscience and nanotechnology center, the Faculty of Science and the Graduate School, Chiang Mai University.

REFERENCES

[1] A. J. Moulson and J. M. Herbert, Electroceramics (Wiley, Chichester, 2003).

[2] G. Haertling, J. Am. Ceram. Soc. 82, 797 (1999).

[3] E.E. Oren, E. Taspinar and A.C. Tas, J. Am. Ceram. Soc. 80, 2714 (1997).

[4] D.M. Ibrahim and H.W. Hennicke, Trans. J. Br. Ceram. Soc. 80, 18 (1981).

[5] Y.S. Rao and C.S. Sunandana, J. Mater. Sci. Lett. 11, 595 (1992).

[6] J.Y. Choi, C.H. Kim and D.K. Kim, J. Am. Ceram. Soc. 81, 1353 (1998).

[7] J. Fang, J. Wang, S.C. Ng, L.M. Gan, C.H. Quek and C.H. Chew, Mater. Lett. 36, 179 (1998).

[8] W. Chaisan, O. Khamman, R. Yimnirun and S. Ananta, J. Mater. Sci. (2006) in press.

[9] R. Wongmaneerung, R. Yimnirun and S. Ananta, Mater. Lett. 60, 1447 (2006).

[10] M. T. Lanagan, J. H. Kim, S. Jang and R. E. Newnham, J. Am. Ceram. Soc. 71, 311 (1988).

[11] C. Puchmark, G. Rujijanagul, S. Jiansirisomboon and T. Tunkasiri, Ferroelectrics Lett. 31, 1 (2004).

Table Caption:

Table 1 Effect of milling times on the variation of particle size of PZ powders measured by different techniques.

Figure Caption:

Figure 1 XRD patterns of the 20 h milling powders (a) uncalcined and calcined with heating/cooling rates of 10 C/min at 750 C for (b) 2 h, (c) 3 h and (d) 4 h, and at 800 C for (e) 1 h and (f) 2 h, and at 800 C for 2 h with heating/cooling rates of (g) 20 C/min and (h) 30 C/min.

Figure 2 XRD patterns of the 30 h milling powders (a) uncalcined and calcined at (b) 700 C for 2 h, 750 C for (c) 2 h and (d) 4 h, and at 800 C for 1 h with heating/cooling rates of (e) 10 C/min, (f) 20 C/min and (g) 30 C/min.

Figure 3 SEM micrographs and the corresponding particle size distributions of PZ powders milled for (a) 20 h and calcined at 800 C for 2 h with heating/cooling rates of 10 C/min and (b) 30 h and calcined at 800 C for 1 h with heating/cooling rates of 10 C/min, (c) 20 C/min and (d) 30 C/min.

Table 1

Milling time (h)	Calcination condition *T/D/R* (C:h: C/min)	XRD				SEM		Laser scattering	
		A (nm)	*a* (nm)	*b* (nm)	*c* (nm)	*D* (nm)	*P* (nm)	*D* (nm)	*P* (nm)
20	800/2/10	85.39	0.8246	1.1724	0.5875	243	137-318	620	227-2010
30	800/1/10	71.42	0.8220	1.1670	0.5869	152	112-212	420	336-1200
30	800/1/20	58.91	0.8232	1.1700	0.5867	127	56-200	286	150-1050
30	800/1/30	47.50	0.8239	1.1730	0.5852	140	50-268	212	72-950

A = Crystallite size
a, b, c = Lattice parameters
D = Average particle size
P = Particle size range or distribution
T:D:R = Calcination temperature:dwell time:heating/cooling rates.

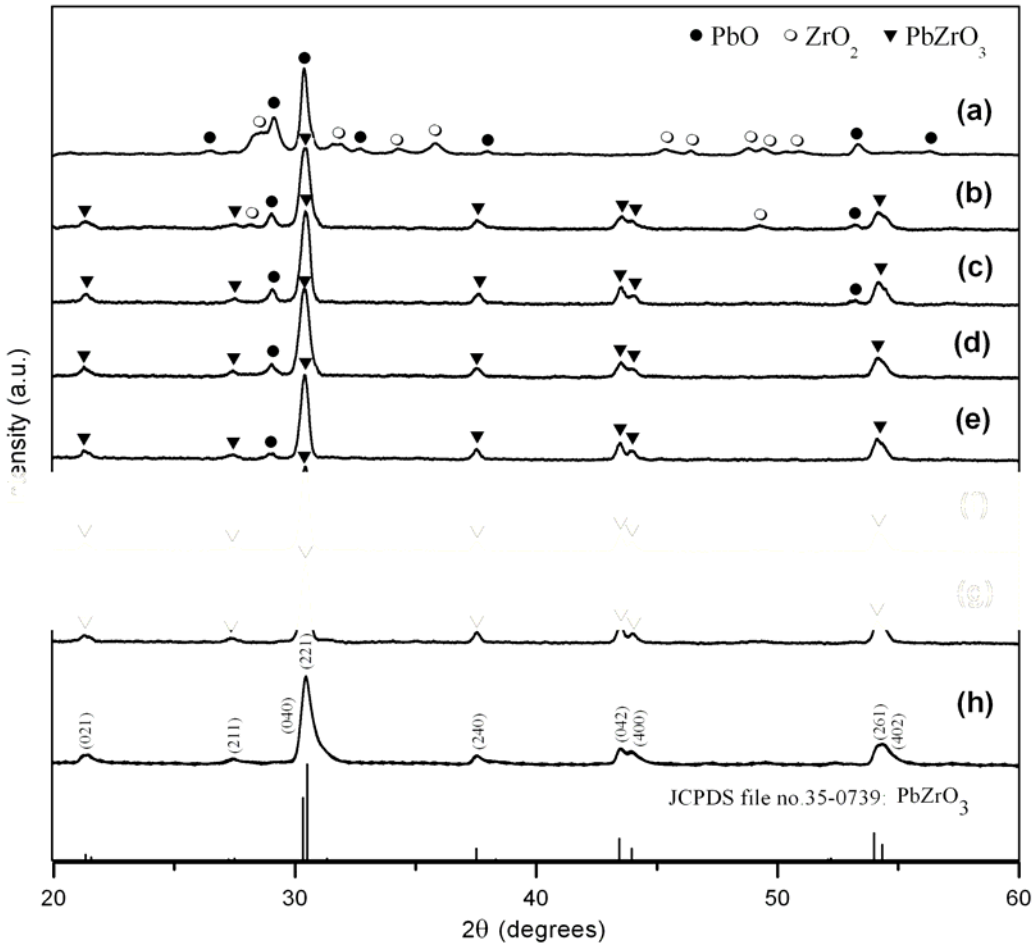
● PbO ○ ZrO2 ▼ PbZrO3
(a)
(b)
(c)
(d)
(e)
(h)
(021)
(211)
(040)
(221)
(240)
(042)
(400)
(261)
(402)
JCPDS file no.35-0739: PbZrO3
20
30
40
50
60
2θ (degrees)

Fig. 1

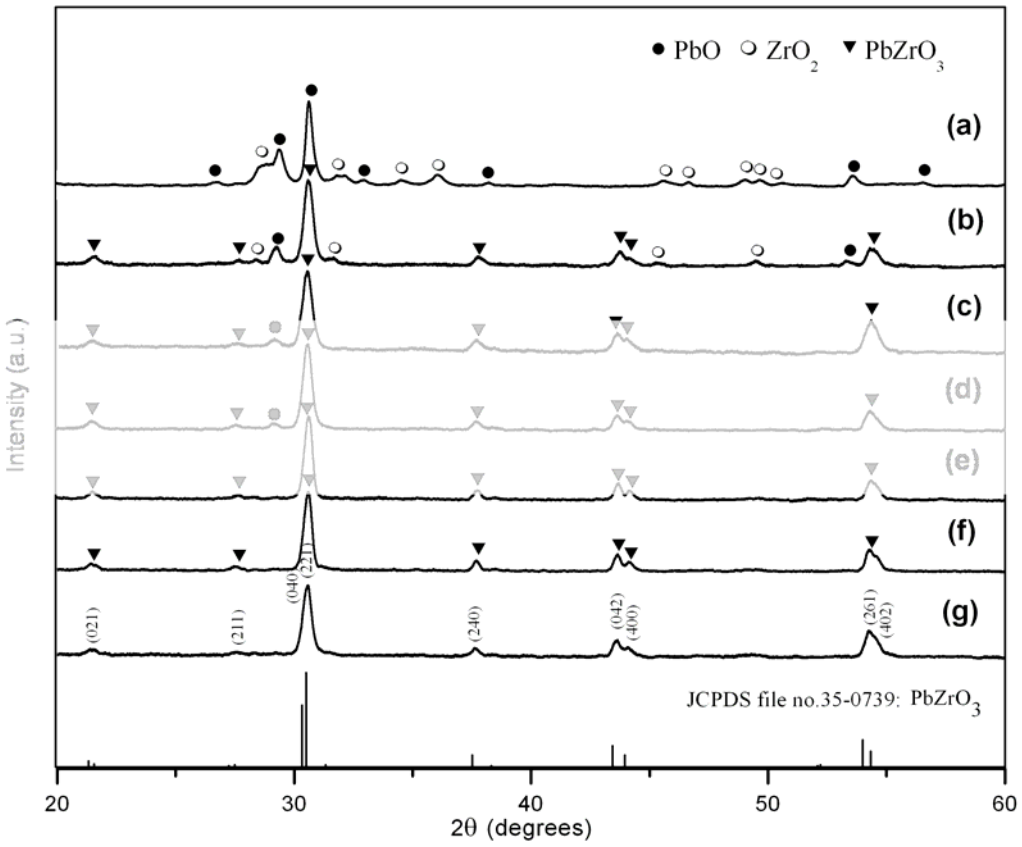
● PbO ○ ZrO2 ▼ PbZrO3
(a)
(b)
(c)
(d)
(e)
(f)
(g)
(021)
(211)
(040)
(221)
(240)
(042)
(400)
(261)
(402)
JCPDS file no.35-0739: PbZrO3
Intensity (a.u.)
20
30
40
50
60
2θ (degrees)

Fig. 2

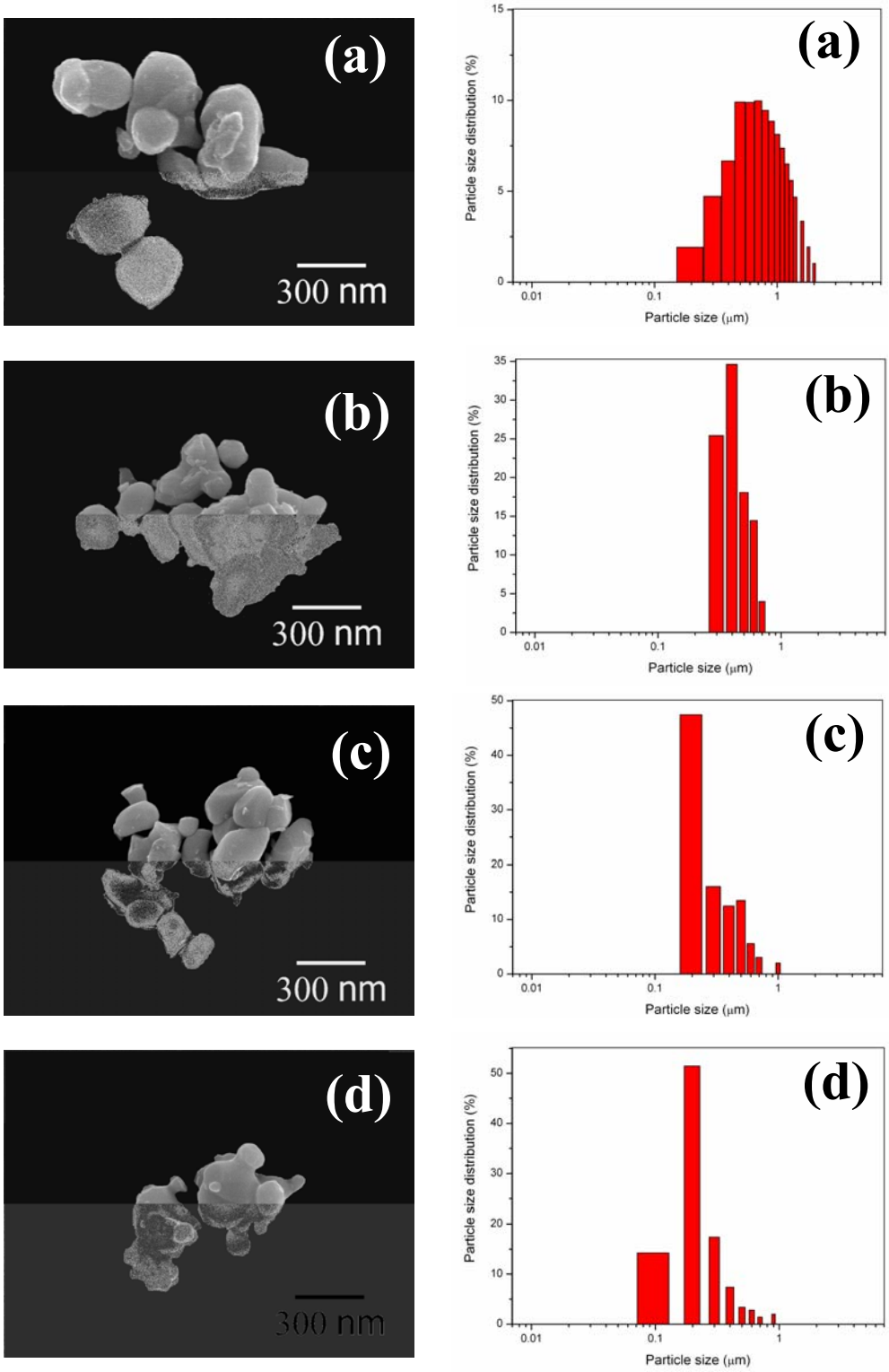
(a)
300 nm
(a)
Particle size distribution (%)
Particle size (μm)
(b)
300 nm
(b)
Particle size distribution (%)
Particle size (μm)
(c)
300 nm
(c)
Particle size distribution (%)
Particle size (μm)
(d)
300 nm
(d)
Particle size distribution (%)
Particle size (μm)

Fig. 3

Effect of Calcination Condition on Phase Formation of Zirconium Titanate Powders Synthesized by the Solid-State Reaction

ANURAK PRASATKHETRAGARN*, RATTIKORN YIMNIRUN AND SUPON ANANTA

Department of Physics, Faculty of Science, Chiang Mai University, Chiang Mai 50200, Thailand

Zirconium titanate ($ZrTiO_4$; ZT) powders have been prepared by using a solid-state reaction combined with a vibro-milling technique. The effects of calcination temperature, dwell time and heating/cooling rates on phase formation and morphology of the powders were examined. The calcination temperature and dwell time have been found to show a pronounced effect on the phase formation of the calcined zirconium titanate powders. Additionally, the minor phase of unreacted TiO_2 tends to form together with $ZrTiO_4$, depending on calcination conditions. It is seen that optimization of calcination conditions can lead to 100% yield of an orthorhombic $ZrTiO_4$.

Keywords : Zirconium titanate; Calcination; Phase formation; Solid-state reaction

1. INTRODUCTION

Zirconium titanate-based compounds have attracted great interest as dielectric resonators for microwave telecommunications [1,2]. They are also promising materials for applications in catalysis, humidity sensor and high-temperature pigment [1,3]. Moreover, zirconium titanate ($ZrTiO_4$ or ZT) is well known as the alternative precursor for the successful preparation of single-phase perovskite $Pb(Zr,Ti)O_3$ (PZT), which is becoming increasingly important for transducer, actuator and ultrasound applications [1,4].

The stoichiometry of zirconium titanate (ZT) is known to be an important factor for ensuring good properties [1,2]. Generally, the mixed oxide method involves the heating of a mixture of zirconium oxide and titanium oxide above 1200 - 1600 ^{o}C for long times [5], and has been employed intensively in the last decade [4,6]. The optimization of calcination conditions used in the mixed oxide process, however, has not received detailed attention, and the effects of applied dwell time and heating/cooling rates have not yet been studied extensively to our knowledge.

Therefore, the main purposes of this work were to explore a simple mixed oxide synthetic route for the production of $ZrTiO_4$ powders via a vibro-milling technique and to perform a systematic study of the reaction between the starting zirconium oxide and titanium oxide precursors. The phase formation and morphology of the powders calcined at various conditions will be studied and discussed.

2. EXPERIMENTAL PROCEDURE

The starting materials were commercially available zirconium oxide, ZrO_2 (baddeleyite: JCPDS file number 37-1484) and titanium oxide, TiO_2 (anatase: JCPDS file number 21-1272) (Fluka, 99.9% purity). The two oxide powders exhibited an average particle size in the range of 3.0 to 5.0 m. $ZrTiO_4$ powder was synthesized by the solid-state reaction of thoroughly ground mixtures of ZrO_2 and TiO_2 powders that were milled in the required stoichiometric ratio. Instead of employing a ball-milling procedure with ZrO_2 media under isopropanal for 24 h [7], use was made of a McCrone vibro-milling [4]. In order to improve the reactivity of the constituents, the milling process was carried out for 1 h with corundum media in isopropanal. After drying at 120 °C, the milled powders were calcined at various conditions (inside a closed alumina crucible) in order to investigate the formation of $ZrTiO_4$. The reactions of the uncalcined ZT powders taking place during heat treatment were investigated by a combination of thermogravimetric and differential thermal analysis techniques (TG-DTA, Shimadzu) using a heating rate of 10 °C/min in air. Calcined powders were subsequently examined by X-ray diffraction (XRD; Siemens-D500 diffractometer) using CuK_a radiation to identify the phases formed and optimum calcination for the manufacture of ZT powder. Powder morphologies were directly imaged using scanning electron microscopy (SEM; JEOL JSM-840A).

3. RESULTS AND DISCUSSION

The TG–DTA simultaneous analysis of a powder mixed in the stoichiometric proportions of $ZrTiO_4$ is shown in Fig. 1. The TG curve shows three distinct weight losses. In the temperature range from room temperature to ~ 100 °C, large endothermic peak (i) is observed in the DTA curve, consistent with the first weight loss. This observation can be attributed to the decomposition of the organic species from the milling process [8]. Corresponding to the second fall in the sample weight, by increasing the temperature up to ~ 900 ^{o}C, both small exothermic and endothermic peaks ((ii) and (iii)) are detected in the DTA curve. There is no obvious interpretation of these peaks, although it is likely to correspond to the anatase/rutile transformation of TiO_2, reported by a number of workers [8]. Increasing the temperature up to ~ 1400 °C, the solid-state reaction occurs between ZrO_2 and TiO_2. The broad exotherm with several small peaks in the DTA curve represents that reaction, which has maxima at ~ 900 and 1150 °C. This is supported by a third fall in sample weight over the same temperature range.

To further study the phase development with increasing calcination temperature, the powders were calcined for 4 h with heating/cooling rates of 10 ^{o}C/min in air at various temperatures followed by phase analysis using XRD. As shown in Fig. 2, for the uncalcined powder subjected to 1 h of vibro-milling, only X-ray peaks of precursors ZrO_2 (▽) and TiO_2 (▼), which could be matched with JCPDS file numbers 37-1484 and 21-1272 [8], respectively, are present, indicating that no reaction had yet been triggered during the milling process. It is

seen that fine $ZrTiO_4$ crystallites (•) were developed in the powder at a calcination temperature as low as 1000 °C, accompanying with ZrO_2 and TiO_2 as separated phases. This observation agrees well with those derived from the TG–DTA results and previous investigation [8]. As the temperature increased to 1400 °C, the intensity of the ZT peaks was further enhanced and became the predominant phase. Upon calcination at 1450 °C, an orthorhombic $ZrTiO_4$ (JCPDS file number 34-0415) is obtained. Depending on the calcination conditions, at least three minor phases were identified, i.e. baddeleyite-ZrO_2 (▽), anatase-TiO_2 (▼) and rutile-TiO_2 (+), which can be correlated with JCPDS file numbers 37-1484, 21-1272 and 21-1276, respectively. It is well established that there are a number of polymorphic forms of TiO_2 stable at different temperatures and pressures. In the work reported here, the anatase/rutile transformation of TiO_2 has been found. It is seen that a completed conversion of anatase-TiO_2 (▼) precursor to rutile-TiO_2 (+) was found after calcination at 950 ^oC, in agreement with other works [8,9].

Apart from the calcination temperature, the effect of dwell time was also found to be quite significant (Fig. 3). It is seen that the single phase of $ZrTiO_4$ (yield of 100% within the limitations of the XRD technique) was found to be possible only in powders calcined at 1400 ^oC for 6 h or at 1450 ^oC for at least 2 h. In the present study, an attempt was also made to calcine ZT powders under various heating/cooling rates. In this connection, it is found that the yield of $ZrTiO_4$ phase did not vary with the heating/cooling rates ranging from 10 to 30 ^oC/min, consistent with earlier work [4].

The morphological changes in the $ZrTiO_4$ powders formed by a mixed oxide are illustrated in Fig. 4(a-d) as a function of calcination conditions. In general, the particles are agglomerated and irregular in shape, with a variation in particle size, particularly in samples calcined at high temperature (Fig. 4(c)) or with longer dwell times (Fig. 4(b,d)). The results indicate that difference in particle size and degree of agglomeration tends to increase with calcination temperatures (Table 1). After calcination at 1500 °C for 4 h (Fig. 4(d)), the powders seem to display a significant level of necking and bonding as if they were in the initial stages of sintering. To the authors's knowledge, the present data are the first results for the morphology-calcination relationship of $ZrTiO_4$ powders prepared by the solid-state reaction. It is also of interest to point out that mass production of single-phase $ZrTiO_4$ powders with the smallest particle size ~ 0.18 m (estimated from SEM micrographs) can be achieved by employing a simple solid-state reaction combined with a vibro-milling technique.

4. CONCLUSIONS

Single-phase of zirconium titanate powders with primary particles ranging between 0.18 and 6.35 μm in diameter may be produced by employing a solid-state reaction process using oxides as starting materials. Evidence has been obtained for a 100% yield of an orthorhombic $ZrTiO_4$ at a calcination temperature of 1450 ^{o}C for 2 h with heating/cooling rates of 30 ^{o}C/min.

ACKNOWLEDGEMENTS

This work was supported by the Commission on Higher Education (CHE), Thailand Research Fund (TRF), the Faculty of Science and the Graduate School of Chiang Mai University.

REFERENCES

[1] A.J. Moulson and J.M. Herbert, Electroceramics (Wiley, Chichester, 2003).

[2] M. Leoni, M. Viviani, G. Battilana, A.M. Fiorello and M. Viticoli, J. Eur. Ceram. Soc. 21, 1739 (2001).

[3] K. Tanabe, Solid Acids and Bases: Their Catalytic Activity (Academic Press, New York, 1977).

[4] R. Tipakontitikul and S. Ananta, Mater. Lett. 58, 449 (2004).

[5] G. Wolfram and H.E. Göbel, Mater. Res. Bull. 16, 1455 (1981).

[6] Y. Park, Solid State Commun. 105, 735 (1998).

[7] C.L. Li and C.C. Chou, Integr. Ferroelectr. 55, 955 (2003).

[8] S. Ananta, R. Tipakontitikul and T. Tunkasiri, Mater. Lett. 57, 2637 (2003).

[9] P.J. Sánchez-Soto, M.A. Arilés, G. Colón, M. Macias and J.A. Navio, Mater. Lett. 20, 339 (1994).

Table Caption

Table 1 Particle size range of $ZrTiO_4$ powders calcined at various conditions.

Figure Caption

Figure 1 TG-DTA curves for the mixture of ZrO_2-TiO_2 powders.

Figure 2 XRD patterns of ZT powder calcined at various temperatures for 4 h with heating/cooling rates of 10 ^oC/min.

Figure 3 XRD patterns of ZT powders calcined with heating/cooling rates of 10 ^oC/min at 1400 ^oC for (a) 4 h, (b) 5 h and (c) 6 h, at 1450 ^oC for (d) 1 h and (e) 2 h, and (f) at 1500 ^oC for 1 h.

Figure 4 SEM micrographs of the ZT powders calcined with heating/cooling rates of 30 ^oC/min at 1450 ^oC for (a) 2 h and (b) 4 h, at 1500 ^oC for (c) 1 h and (d) 4 h.

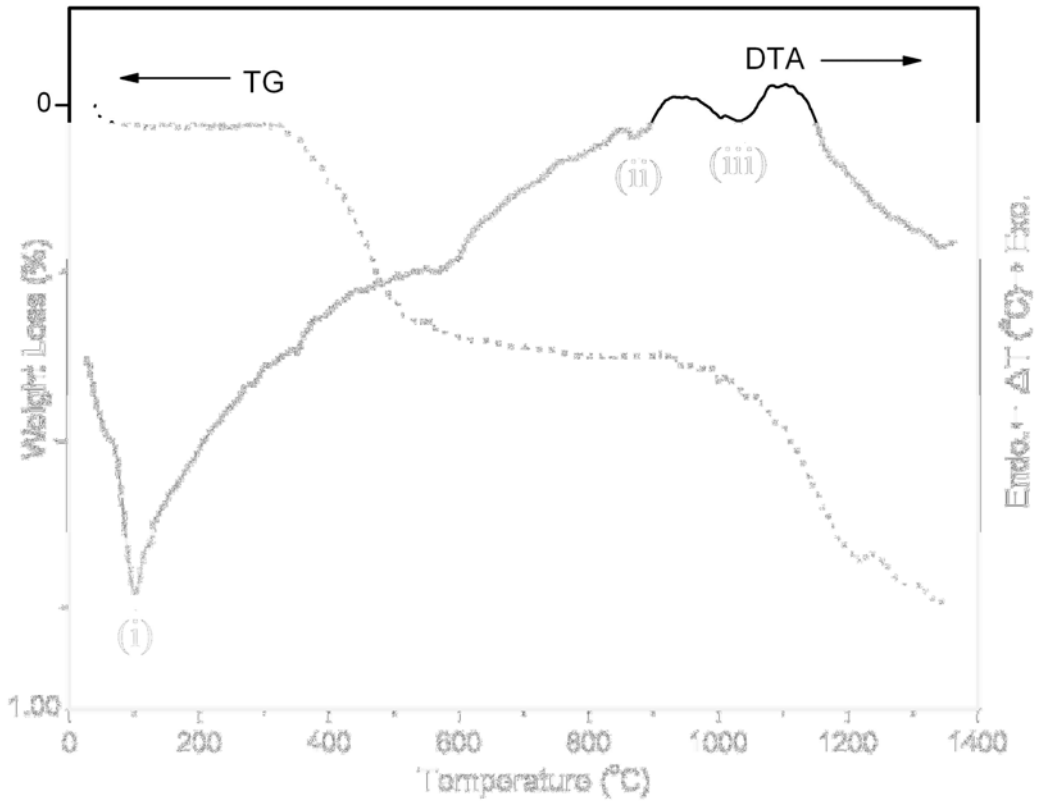
TG
DTA
0
(i)
(ii)
(iii)
Weight Loss (%)
1.00
0
200
400
600
800
1000
1200
1400
Temperature (°C)

Figure 1

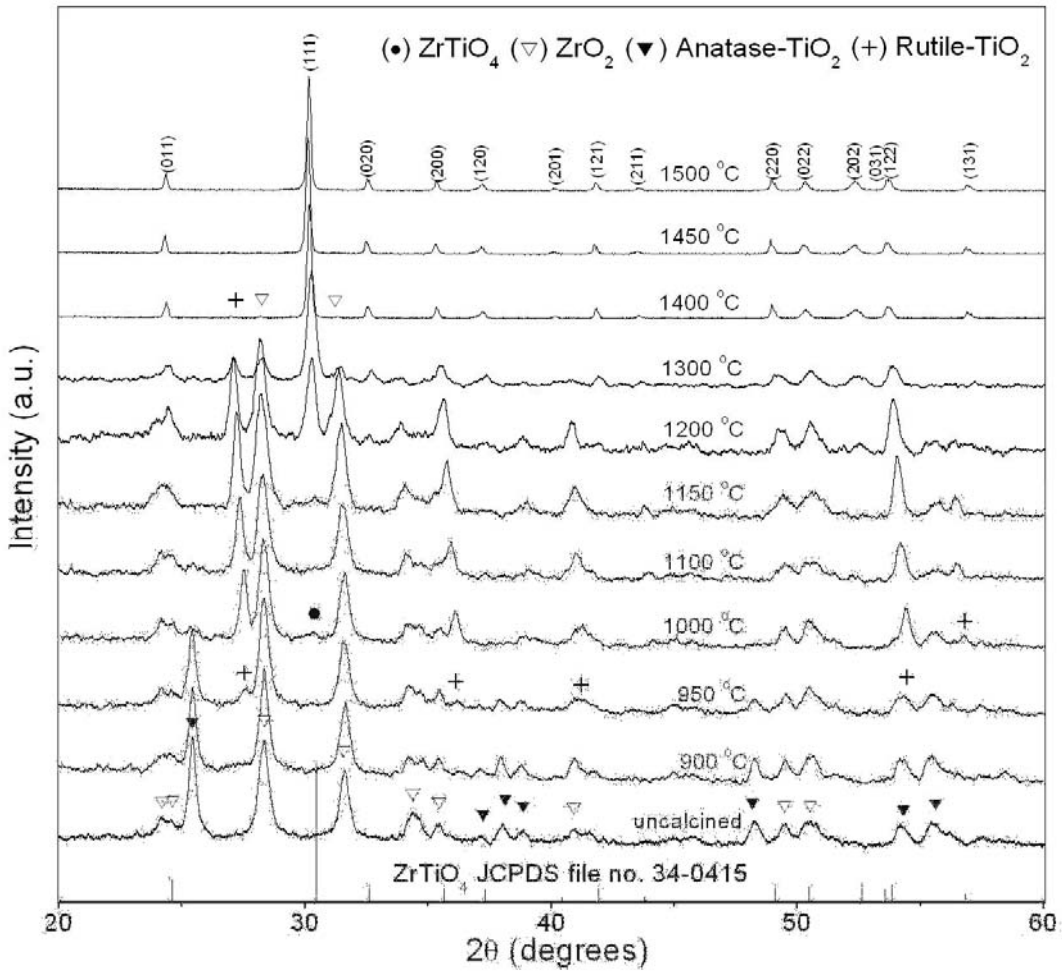
(•) ZrTiO4 (▽) ZrO2 (▼) Anatase-TiO2 (+) Rutile-TiO2
(011)
(111)
(020)
(200)
(120)
(201)
(121)
(211)
(220)
(022)
(202)
(031)
(122)
(131)
1500 °C
1450 °C
1400 °C
1300 °C
1200 °C
1150 °C
1100 °C
1000 °C
950 °C
900 °C
uncalcined
ZrTiO4 JCPDS file no. 34-0415
Intensity (a.u.)
20
30
40
50
60
2θ (degrees)

Figure 2

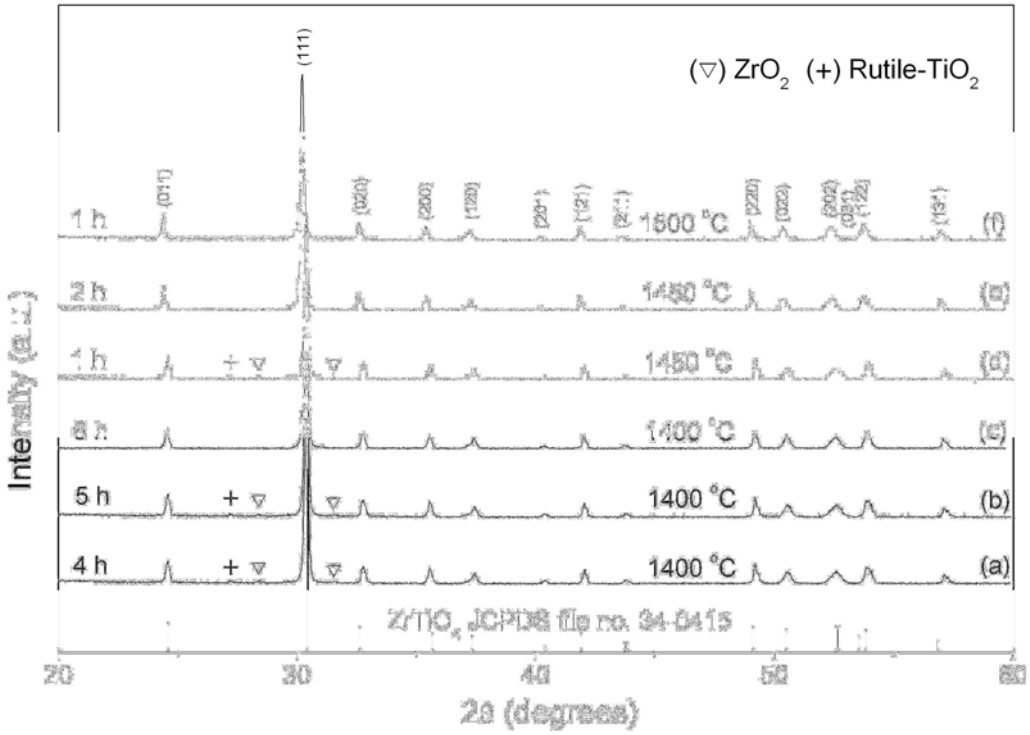
(▽) ZrO2 (+) Rutile-TiO2
(111)
1 h
1500 °C
(f)
2 h
1450 °C
(e)
1 h
1450 °C
(d)
8 h
1400 °C
(c)
5 h
1400 °C
(b)
4 h
1400 °C
(a)
Intensity (a.u.)
20
30
40
50
60
2θ (degrees)

Figure 3

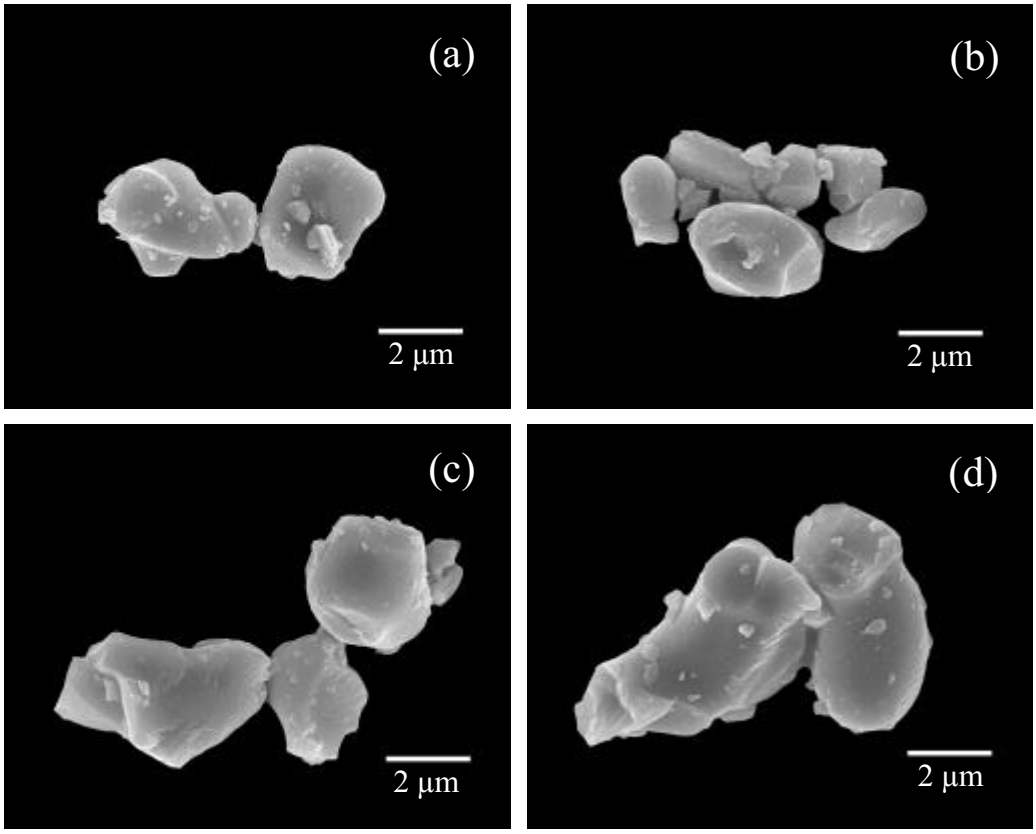

Figure 4

Table 1

Calcination conditions			Particle size range (0.05 μm)
Temperature (^{o}C)	Dwell times (h)	Heating/cooling rates (^{o}C/min)	
1450	2	10	0.25 - 3.00
1450	2	20	0.35 - 3.15
1450	2	30	0.49 - 3.16
1450	4	30	0.18 - 3.43
1500	1	30	0.78 - 5.53
1500	4	30	0.33 - 6.35

A Two-Stage Solid-State Reaction to Lead Zirconate Titanate Powders

WANWILAI CHAISAN, ORAWAN KHAMMAN, RATTIKORN YIMNIRUN AND SUPON ANANTA*

Department of Physics, Faculty of Science, Chiang Mai University, Chiang Mai, 50200, Thailand

An approach to synthesize lead zirconate titanate (PZT) powders with a modified two-stage mixed oxide synthetic route has been developed. To ensure a single-phase perovskite formation, an intermediate phase of lead zirconate ($PbZrO_3$) was employed as starting precursor. The formation of perovskite phase in the calcined powders has been investigated as a function of calcination temperature. It has been found that the perovskite $PbZrO_3$ and $PbTiO_3$ phases tend to form together with PZT, with the latter appearing in both tetragonal and rhombohedral phases, depending on calcination temperatures. It is seen that optimization of calcination can lead to 100% yield of PZT phase.

Keywords: Lead zirconate titanate; PZT powders; Solid-state reaction

1. INTRODUCTION

There has been a great deal of interest in the preparation of single-phase lead zirconate titanate, $Pb(Zr_{1-x}Ti_x)O_3$ or PZT, powders as well as in the sintering and piezoelectric properties of PZT-based ceramics [1]. The reaction sequence through which PZT is formed by solid-state reaction has been investigated by many workers but with varying approaches [2-4]. Mori *el at*. [2] were the first to study the mechanisms of a two-step reaction, initiated by the constituent oxides reacting to form a solid solution of lead titanate ($PbTiO_3$) and zirconium oxide (ZrO_2), which later homogenized to form the PZT phase. On the other hand, zirconium titanate-based compositions were also proposed as alternative key precursor for a two-step reaction sequence by other workers [3,4]. The essentially pyrochlore-free PZT powders obtained could be attributed to their high reactivity with PbO. However, high firing temperatures (> 1200 ^oC) are required for the formation of mixed-oxide derived zirconium titanate-based powders [4,5]. Moreover, the preparation of PZT using $PbZrO_3$ precursor, to date, has not been as extensive as that of PZT using $PbTiO_3$ or zirconium titanate-based precursors. Thus, the purpose of this study was to synthesize and investigate the PZT powders prepared by a

two-stage solid-state reaction with lead zirconate ($PbZrO_3$) as a key precursor.

2. EXPERIMENTAL PROCEDURE

The modified mixed oxide method was developed for preparation of $Pb(Zr_{0.5}Ti_{0.5})O_3$ powders, analogous to the synthesis of other perovskite powders [5]. Starting precursors were PbO, ZrO_2 and TiO_2 (Fluka, > 99% purity). These three oxide powders exhibited an average particle size in the range of 5.0 to 10.0 m. First, an intermediate phase of lead zirconate, $PbZrO_3$, was separately prepared by the solid-state reaction method previously reported [6]. In the second stage, TiO_2 and excess PbO were reacted with $PbZrO_3$ to give the final product of PZT:

$$PbO\ (s) + ZrO_2\ (s) \Rightarrow PbZrO_3\ (s) \quad (1)$$

$$0.5PbZrO_3\ (s) + 0.5PbO\ (s) + 0.5TiO_2\ (s) \Rightarrow Pb(Zr_{0.5}Ti_{0.5})O_3\ (s) \quad (2)$$

Instead of employing a ball-milling procedure [2], a McCrone vibro-milling was used. In order to improve the reactivity of the constituents, the milling process was carried out for 1 h (instead of 30 min [4]) with corundum media in isopropanal. After drying at 120 °C, various firing temperatures (inside a closed alumina crucible) were applied in

order to investigate the formation of PZT phase in each calcined powders. The reactions of the uncalcined powders taking place during heat treatment were investigated by a combination of thermogravimetric and differential thermal analysis techniques (TG-DTA, Shimadzu) using a heating rate of 10 °C/min in air. Calcined powders were subsequently examined by room temperature X-ray diffraction (XRD; Siemens-D500 diffractometer) using CuK_a radiation to identify the phases formed and optimum calcination temperature for the manufacture of PZT powders. Powder morphologies were directly imaged using scanning electron microscopy (SEM; JEOL JSM-840A).

3. RESULTS AND DISCUSSION

As shown in Fig. 1, in the temperature range from room temperature to ~ 150 °C, the sample shows both exothermic and endothermic peaks in the DTA curve, consistent with a drop in weight loss over the same temperature range. This observation can be attributed to the decomposition of the organic species from the milling process [4], in agreement with other works [5,6]. Increasing the temperature up to ~ 900 ^{o}C, the solid-state reaction occurred between $PbZrO_3$ and TiO_2. The broad exotherm from 300 to 750 ^{o}C in the DTA curve represents that reaction, which is not associated with a weight loss. This may correspond to a phase

transformation or to reaction between solids in this temperature range not involved with any weight change [7]. Finally, a significant drop in weight loss is also observed above 650 ^{o}C associated with the DTA peaks at the same temperature range. This may be attributed to full crystallization of PZT phase together with the PbO volatilization commonly found in the lead-based perovskites [5,6]. These data and literature [4] were used to assign the range of calcination temperatures for XRD investigation.

To further study the phase development with increasing calcination temperature, the powders were calcined for 1 h with heating/cooling rates of 10 ^{o}C/min at various temperatures followed by phase analysis using XRD. As shown in Fig. 2, for the uncalcined powder, only X-ray peaks of precursors $PbZrO_3$ (?), PbO (?) and TiO_2 (▼), which could be matched with JCPDS file numbers 77-1971, 35-0739 and 21-1272, respectively, are present, indicating that no reaction had yet been triggered during the milling process. It is seen that PZT crystallites (▽) were already found in the powders at a calcination temperature as low as 600 °C, accompanying with $PbZrO_3$ and $PbTiO_3$ as separated phases. This observation agrees well with those derived from the TG-DTA results. The occurrence of $PbTiO_3$ in this work can be attributed to the result of formation between PbO and TiO_2 precursors during firing process as proposed by Matsua and Sasaki [8].

As the temperature increased to 800 °C, the intensity of the PZT peaks was further enhanced and became the predominant phase. The optimum calcination temperature for the formation of a high purity PZT phase was found to be about 900 ^{o}C, i.e. slightly higher than the exothermic temperature in Fig. 1. In general, the strongest reflections apparent in the majority of the XRD patterns indicate the formation of two PZT phases. These can be matched with JCPDS file number 73-2022 and 33-0748 for the rhombohedral $Pb(Zr_{0.58}Ti_{0.42})O_3$ and tetragonal $Pb(Zr_{0.52}Ti_{0.48})O_3$ (Fig. 2), respectively. As is well known, the variation in composition may lead to a diffuse morphotropic phase boundary (MPB) between the tetragonal and rhombohedral PZT phases [1]. The most obvious difference between the patterns for tetragonal and rhombohedral PZT phases concerns the presence of a splitting of (002)/(200) peak at *2?* about 43^{o}-46^{o} for the former phase (inset shown in Fig. 2). It is seen that the rhombohedral PZT phase is always present in the product. This study also shows that minor amount of the intermediate phases of $PbZrO_3$ and $PbTiO_3$ tends to coexist along with the PZT phase, agreed with earlier work [9]. Upon calcination at 900 ^{o}C with heating/cooling rates of 10 or 30 ^{o}C/min, the phases of $PbZrO_3$ and $PbTiO_3$ have been found to completely disappear, and crystalline PZT of both tetragonal and rhombohedral is the only detectable phase in the powder. The finding condition is close to that

of Fernandes *et al*. [10] (900 ^{o}C for 1 h with heating/cooling rates of 5 ^{o}C/min) but with significantly faster heating/cooling rates. By increasing temperature up to 1000 ^{o}C, the yield of the tetragonal PZT phase seems to increase.

The experimental work carried out here suggests that the optimal calcination condition for single-phase PZT (with impurities undetected by XRD technique) is 900 ^{o}C for 1 h, with heating/cooling rates of 30 ^{o}C/min. The morphology of these PZT powders was also examined as illustrated in Fig. 3. In general, the particles are basically irregular in shape with substantial agglomerations. This observation is also similar to that of PZT powders synthesized by previous researchers [4,10] but with smaller particle sizes of about 74-725 nm (estimated from SEM micrographs).

4. CONCLUSIONS

Perovskite phase of PZT powders may be produced by employing a two-stage solid stage reaction process using $PbZrO_3$ as precursor. Evidence has been obtained for a pure PZT phase after calcined at 900 ^{o}C for 1 h with heating/cooling rates of 30 ^{o}C/min.

ACKNOWLEDGEMENTS

This work was supported by the nanoscience and nanotechnology center, Thailand Research Fund (TRF), Commission on Higher Education (CHE), the Faculty of Science and the Graduate School, Chiang Mai University.

REFERENCES

[1] A.J. Moulson and J.M. Herbert, Electroceramics (Wiley, Chichester, 2003).

[2] S. Mori, H. Mitsuda, K. Date, H. Hioki and T. Miyazawa, Natl. Tech. Rept. 10, 32 (1964).

[3] O. Babuhskin, T. Lindback, J.C. Lue and J.Y.M. Leblais, J. Eur. Ceram. Soc. 16, 1293 (1996).

[4] R. Tipakontitikul and S. Ananta, Mater. Lett. 58, 449 (2004).

[5] S. Ananta and N.W. Thomas, J. Eur. Ceram. Soc. 19, 155 (1999).

[6] W. Chaisan, O. Khamman, R. Yimnirun and S. Ananta, J. Mater. Sci. (2006) in press.

[7] R.N. Das, A. Pathak, S.K. Saha, S. Sannigrahi and P. Pramanik, Mat. Res. Bull. 36, 1539 (2001).

[8] Y. Matsuo and H. Sasaki, J. Am. Ceram. Soc. 48, 289 (1965).

[9] N. Chakrabarti and H.S. Maiti, Mater. Lett. 30, 169 (1997).

[10] J.C. Fernandes, D.A. Hall, M.R. Cockburn and G.N. Greaves, Nucl. Instrum. Meth. B 97, 137 (1995).

Figure Caption:

Figure 1 TG-DTA curves for the mixture of $PbZrO_3$-PbO-TiO_2 powders.

Figure 2 XRD patterns of PZT powders calcined at various conditions for 1 h (inset: enlarged XRD peaks for the tetragonal (T) and rhombohedral (R) phases as a function of calcination temperatures).

Figure 3 SEM micrograph of the PZT powders calcined at 900 ^{o}C for 1 h with heating/cooling rates of 30 ^{o}C/min.

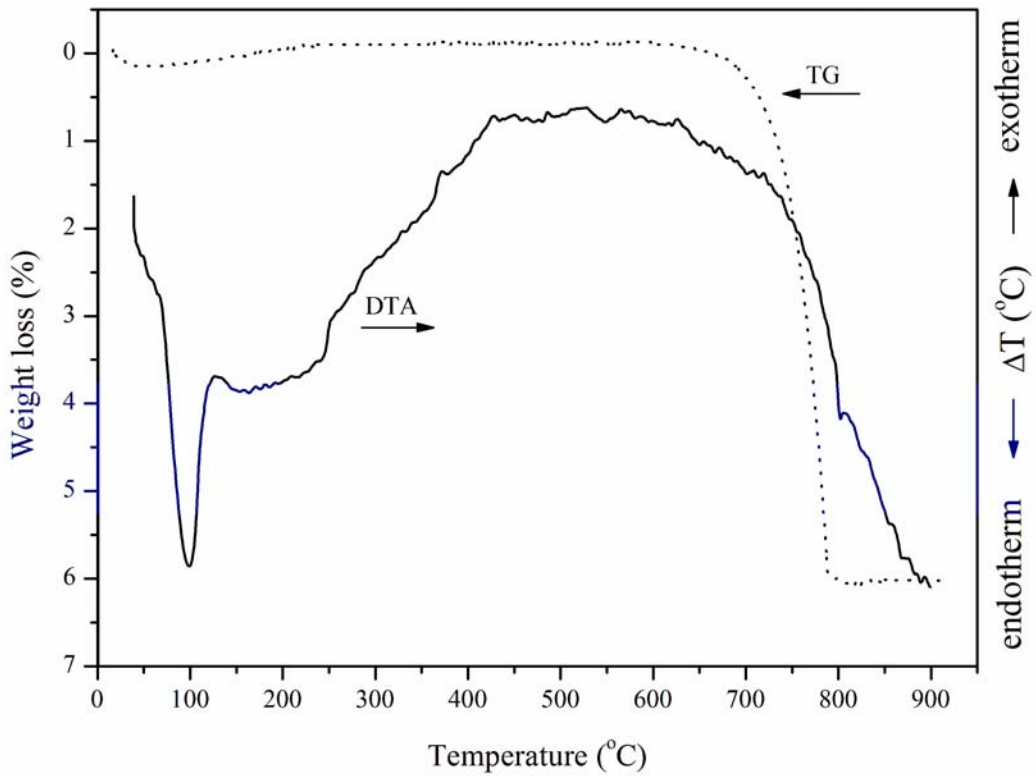
TG
DTA
Weight loss (%)
ΔT (°C)
exotherm
endotherm
Temperature (°C)
0
1
2
3
4
5
6
7
0
100
200
300
400
500
600
700
800
900

Fig. 1

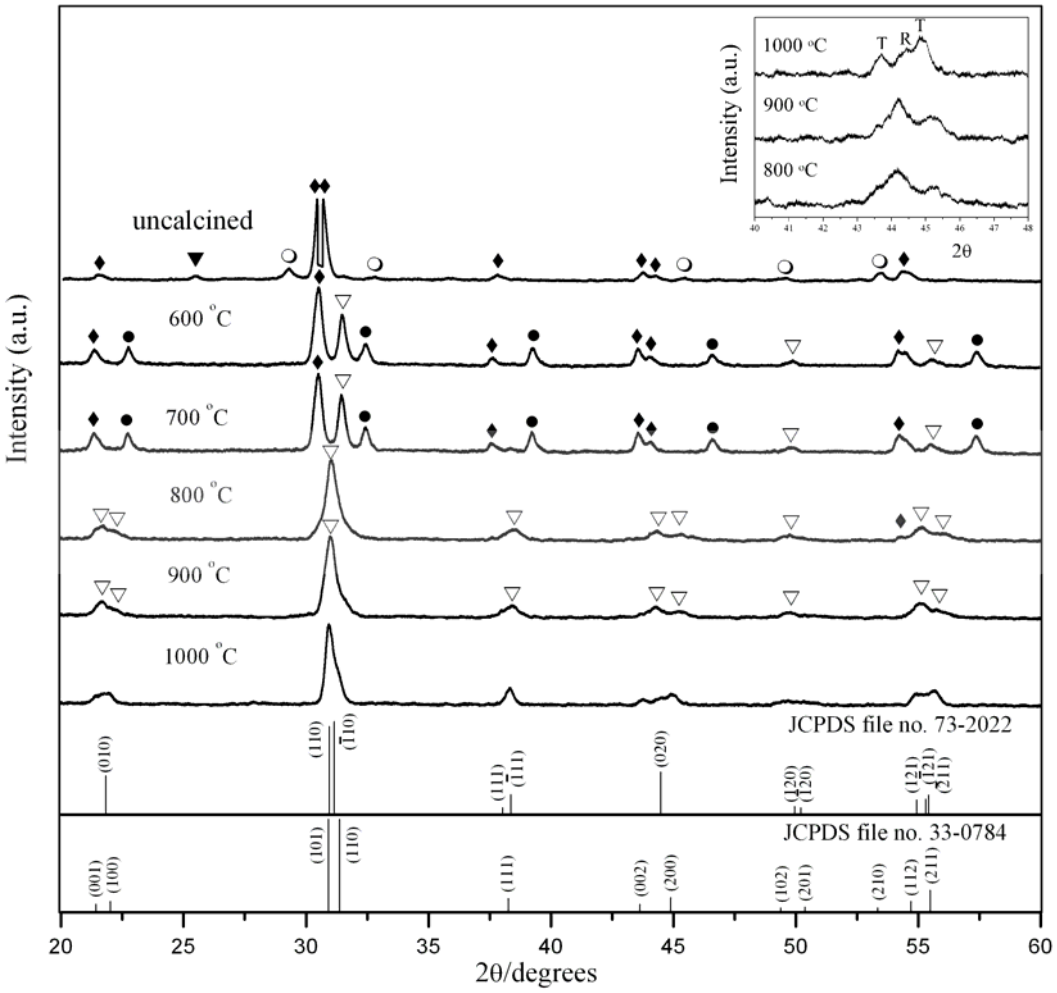
Intensity (a.u.)
uncalcined
600 °C
700 °C
800 °C
900 °C
1000 °C
1000 °C
900 °C
800 °C
T
R
T
2θ
JCPDS file no. 73-2022
(010)
(110)
(1̄10)
(111)
(11̄1)
(020)
(120)
(12̄0)
(121)
(12̄1)
(21̄1)
JCPDS file no. 33-0784
(001)
(100)
(101)
(110)
(111)
(002)
(200)
(102)
(201)
(210)
(112)
(211)
20
25
30
35
40
45
50
55
60
2θ/degrees

Fig. 2

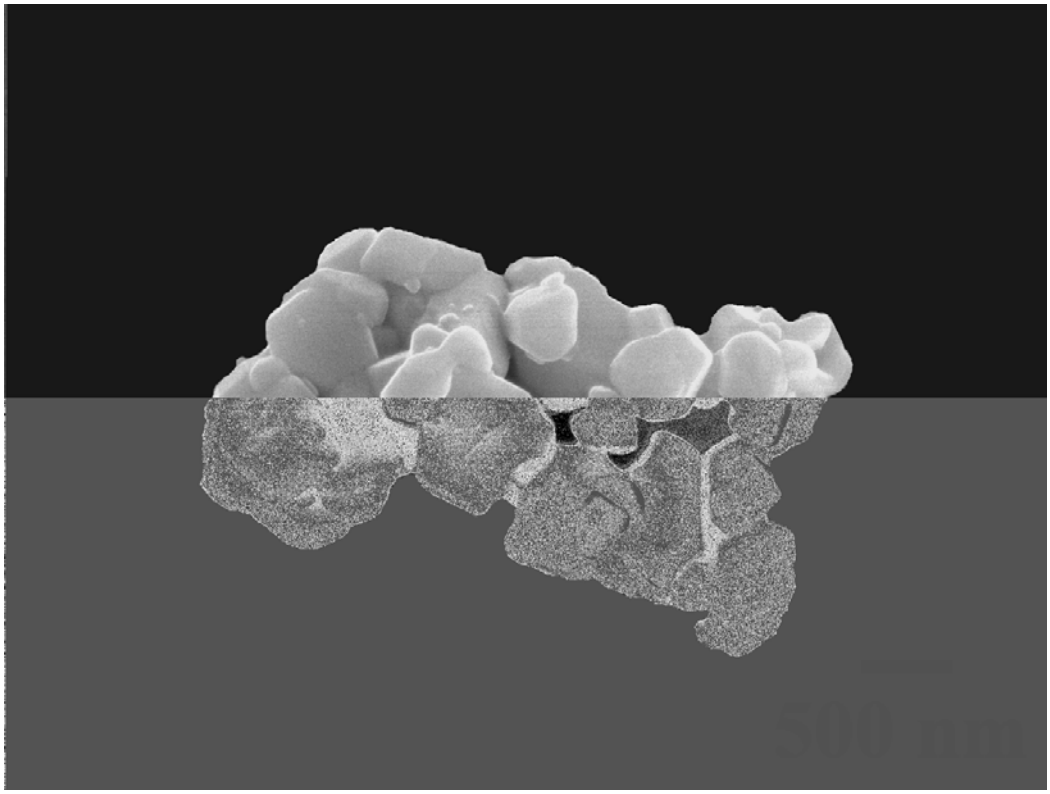

Fig. 3

Dielectric Properties of Lead Magnesium Niobate-Lead Titanate Ceramics Prepared by Mixed-Oxide Method

Rattikorn Yimnirun

Department of Physics, Faculty of Science, Chiang Mai University,

Chiang Mai 50200 Thailand

Author for correspondence, e-mail: rattikornyimnirun@yahoo.com

ABSTRACT

In this study, the (1-x)Pb($Mg_{1/3}Nb_{2/3}$)O_3–x$PbTiO_3$ (when x = 0.1, 0.3 and 0.5) ceramics were prepared from PMN and PT powders by a mixed-oxide method. The dielectric properties of the ceramics were measured as functions of both temperature (-150 - 400 °C) and frequency (100 Hz - 1 MHz). The results indicated that the dielectric properties of pseudo-cubic phase 0.9PMN-0.1PT and tetragonal phase 0.5PMN-0.5PT ceramics followed that of relaxor and normal ferroelectric behaviors, respectively, while the dielectric behaviors of a near MPB phase 0.7PMN-0.3PT ceramic showed a mixture of normal and relaxor ferroelectric behaviors. In addition, the Curie temperature (T_C) increased with increasing PT contents, while the diffusivity decreased. This confirmed a gradual transition from a relaxor ferroelectric behavior in 0.9PMN-0.1PT to a normal ferroelectric behavior in 0.5PMN-0.5PT. The difference in dielectric behaviors was attributed to the structural symmetry of the ceramics.

Key words : PMN-PT, Dielectric Properties

1. INTRODUCTION

Ceramics are one of many classes of electronic materials. The electronic industries are demanding smaller, higher packing density and higher frequency electronic devices [1]. Among those features, volume efficiency can be easily improved by reduction of the dimensions of devices and by increasing the dielectric constant of the materials used. This is particular the case for capacitor industry, in which uses of high dielectric constant ceramics are of great success. A family of materials which dominates the industry is lead-based ferroelectrics, especially lead magnesium niobate, $Pb(Mg_{1/3}Nb_{2/3})O_3$ or PMN, and its solid solution with lead titanate, $PbTiO_3$ or PT, the so-called PMN-PT compounds, which show dielectric constant in excess of 20,000, making them candidate materials for capacitors [2]. In addition, they exhibit electrostrictive behavior at temperatures above their transition temperatures. This particular feature leads to their uses in transducers and actuators [3,4].

Lead magnesium niobate (PMN) is generally established as a representative of relaxor ferroelectrics. Though the Curie temperature of PMN is well below room temperature [5], it can be easily shifted upward with PT addition, a normal ferroelectric compound which has a transition at 490 ^{o}C. A spontaneous phase transition is indicated in the solid solution PMN-PT as a result of a change in the degree of ordering induced by substitution of cationic sites. An addition of ~28% PT causes the material to revert to a normal ferroelectric tetragonal phase with $T_C \sim 130$ ^{o}C. The (1-x)PMN-(x)PT system also shows a morphotropic phase boundary (MPB) near $x \sim 0.4$, separating pseudo-cubic phase and tetragonal phases. As observed in other systems such as PZN-PT and PZT, anomalously large dielectric and piezoelectric properties are observed for compositions lying near the MPB [6]. This study is aimed

at investigating the dielectric properties, as functions of both temperature and frequency, of ceramics in PMN-PT system. In particular, three compositions, 0.9PMN-0.1PT, 0.7PMN-0.3PT, and 0.5PMN-0.5PT representing pseudo-cubic, near MPB, and tetragonal phases, respectively, are chosen for the study to examine the roles of MPB as well as to establish the structure-property relations for the PMN-PT system.

2. MATERIALS AND METHODS

The $Pb(Mg_{1/3}Nb_{2/3})O_3$-$PbTiO_3$ ceramics were prepared from PMN and PT powders by a mixed-oxide method. Perovskite-phase PMN powders were obtained via a well-known columbite method [7], while PT powders were prepared by a more conventional mixed-oxide method. For PMN powders, the magnesium niobate ($MgNb_2O_6$) powders were first prepared by mixing starting MgO (> 98%) (Fluka, Switzerland) and Nb_2O_5 (99.9%) (Aldrich, Germany) powders and then calcining the mixed powders at 1100 °C for 3 hours with the heating/cooling rates of 20 °C/min. This yielded a so-called columbite powder ($MgNb_2O_6$). The columbite powders were subsequently ball-milled with PbO (99%) for 24 hours. The mixed powders were calcined at 800 °C for 1 hour with the heating/cooling rates of 20 °C/min. X-ray diffraction analysis was employed to confirm the formation of perovskite-phase PMN. PT powders were prepared from reagent-grade PbO (99%) and TiO_2 (98.5%) starting powders (Fluka, Switzerland). These powders were ball-milled for 24 hours and then calcined at 600 °C for 1 hour with the heating/cooling rates of 20 °C/min. The (1-x)$Pb(Mg_{1/3}Nb_{2/3})O_3$-x$PbTiO_3$ powders (when x = 0.1, 0.3 and 0.5) were subsequently prepared from the precursor PMN and PT powders by a mixed-oxide technique. Initially, PMN and PT powders for a given composition were weighed and then ball-milled in ethanol for 24 hours. The mixed powders were calcined for 2 hours at 900,

800, and 750 °C for compositions with x = 0.1, 0.3, and 0.5, respectively, with the heating/cooling rates of 20 °C/min. To fabricate PMN-PT ceramics, the calcined powders were pressed hydraulically to form disc-shaped pellets 15 mm in diameter and 2 mm thick, with 5 wt.% polyvinyl alcohol (PVA) as a binder. The pellets were stacked in a covered alumina crucible. Finally, the sintering was carried out at a sintering temperature for 2 hours with 15 min/°C heating and cooling rates. The sintering temperature was optimized at 1240 °C for compositions with x = 0.1 and 0.3, and at 1220 °C for composition with x = 0.5. More details of the powder and ceramic preparation studies were described thoroughly in previous publication [8] and will not be included in this present context, which is focused on the dielectric properties of the successfully prepared ceramics.

The dielectric properties of the sintered ceramics were studied as functions of both temperature and frequency with an automated dielectric measurement system. The computer-controlled dielectric measurement system consisted of an LCR-meter (Hewlett-Packard Precision LCR-Meter HP 4284A), a temperature chamber (Delta Design 9023), and a computer system. The detailed description of this system was explained elsewhere [9]. For dielectric property characterizations, the sintered samples were lapped to obtain parallel faces, and the faces were then coated with silver paint as electrodes. The samples were heat-treated at 750 °C for 12 min to ensure the contact between the electrodes and the ceramic surfaces. The capacitance and the dielectric loss tangent were determined over the temperature of –150 and 400 °C with the frequency ranging from 100 Hz to 1 MHz. The measurements were carried out on cooling continuously. Before each cooling run, the samples were first heated up to 400 °C and then cooling run was performed at the rate of 4 °C/min. The dielectric constant was then calculated from $\varepsilon_r = Cd / \varepsilon_0 A$, where C is the capacitance of the

sample, d and A were the thickness and the area of the electrode, respectively, and ε_0 was the dielectric permittivity of vacuum (8.854 x 10^{-12} F/m).

3. RESULTS AND DISCUSSION

The experimental results on physical properties, the phase formation behavior, and microstructure features of all the sintered ceramics are presented and discussed thoroughly elsewhere [10]. Hence, these results will not be shown here. However, it should be stated here that the sintered ceramics are in perovskite phase with a pseudo-cubic crystal structure for 0.9PMN-0.1PT, and with a tetragonal crystal structure for 0.5PMN-0.5PT. It is of interest to see that 0.7PMN-0.3PT composition shows a mixed pseudo-cubic and tetragonal symmetry, which confirms that the MPB of the PMN-PT system lies between x =0.3 and 0.4 [6]. Table I includes the density and grain-size range for all ceramic compositions. It should be noted that a variation in these physical features could impose significant effects on dielectric properties. However, as seen in Table I, the density and the grain size range are not significantly different and are not expected to show marked effects on the dielectric properties of the ceramics. Therefore, in this case it is reasonable to assume that the dielectric properties of the ceramics are mainly influenced by their structural symmetry as will be discussed in the following context.

The dielectric properties, e.g. dielectric constant (ε_r) and tan δ, are measured as functions of both temperature and frequency, as shown in Fig. 1 (a-c). As listed in Table 1, the Curie temperature (T_C) (determined at measuring frequency of 1 kHz) increases from 38 °C in 0.9PMN-0.1PT to 250 °C in 0.5PMN-0.5PT. This is a direct result of PT addition to PMN (T_C ~ -8 °C) since PT itself has a Curie temperature of 490 °C [11]. The maximum dielectric constant for all the ceramics studied is in excess

of 20,000. This is clearly a reason for their potential applications in capacitors [1-4]. As shown in Fig. 1 (a), for 0.9PMN-0.1PT ceramic both dielectric constant (ε_r) and dielectric loss tangent (tan δ) exhibit strong temperature-frequency dependence below the transition temperature. This is a typical dielectric behavior of relaxor ferroelectrics [3], in which a strong temperature-frequency dependence is observed and the temperatures of maximum dielectric constant and dielectric loss tangent are shifted to higher temperature with increasing frequency. The maximum value of the dielectric constant decreases with increasing frequency, while that of the dielectric loss tangent increases. The dielectric properties then become frequency independence above the transition temperature [12-14]. PMN is a well-known relaxor ferroelectric material with diffused phase transition (DPT) as a result of a short-range ordered structure with a nanometer scale heterogeneity in composition [12]. Small addition of PT to PMN causes an increase in T_C, but the strong relaxor behavior still exists. In addition, since 0.9PMN-0.1PT ceramic has a pseudo-cubic symmetry it is therefore intrinsically electrostrictive (i.e. its electrically-induced strain is quadratically proportional to the applied electric field and is non-hysteretic) [4]. With its enhanced dielectric properties at room temperature, as listed in Table 1, it is widely employed in transducers and actuators [2-4].

Further increase in PT contents leads to more observable normal ferroelectric behavior because PT is intrinsically a normal ferroelectric [3,4]. The dielectric properties of 0.7PMN-0.3PT ceramic, as plotted in Fig. 1 (b), exhibit a mixture of both normal and relaxor characteristics, in which the transition temperature is not shifted as much as for relaxor 0.9PMN-0.1PT ceramic. Similar tendency has also been observed in several prior investigations [12-14]. It should be noted that 0.7PMN-0.3PT ceramic composition is close to MPB of the PMN-PT system. Therefore, its structural

symmetry is a mixture of pseudo-cubic and tetragonal, which in turn causes a mixture of normal and relaxor characteristics observed for dielectric properties. With a tetragonal symmetry, the 0.5PMN-0.5PT ceramic, on the other hand, exhibits a normal ferroelectric behavior with a very sharp phase transition. As plotted in Fig. 1 (c), the dielectric properties of 0.5PMN-0.5PT ceramic change significantly with temperature, but are nearly independent of frequency, except in the vicinity of the phase transformation temperature. This is a typical characteristic of normal ferroelectric ceramics with a long-range ordered structure [3,12]. It should also be noted here that the dielectric properties in all ceramics increase significantly at high temperature as a result of thermally activated space charge conduction [13,14].

When PT is added to form the binary system with PMN, the T_C increases monotonically, as shown in Table 1 and Fig. 2, and the dielectric behavior is shifted from relaxor ferroelectric towards normal ferroelectric. The degree of broadening or diffuseness is used to assess such behavior in the observed dielectric variation. This could be estimated with the diffusivity (γ) using the expression $\ln(1/\varepsilon_r - 1/\varepsilon_{max})$ vs $(T-T_{max})^{\gamma}$. The value of γ can vary from 1, for normal ferroelectrics with a normal Curie-Weiss behavior, to 2, for completely disordered relaxor ferroelectrics [13-16]. The plots in Fig. 3 show that the variation is very linear. The mean value of the diffusivity (γ) is extracted these plots by fitting a linear equation. The values of γ listed in Table 1 vary between 1.14 for 0.5PMN-0.5PT and 1.96 for 0.9PMN-0.1PT. These results confirm that diffuse phase transition occur in 0.9PMN-0.1PT ceramic ($\gamma = 1.96$) with a nearly complete disorder characteristic, while a strong normal ferroelectric behavior is observed for 0.5PMN-0.5PT ceramic with $\gamma = 1.14$. With the γ value of 1.63, 0.7PMN-0.3PT ceramic is expected to possess a mixed behavior, as is confirmed by the dielectric data plotted in Fig. 1 (b). In addition, it should also be noted that even if

it is established that the diffuseness could be caused by the decrease of grain size in a perovskite ferroelectric material [12], the observed difference of the degree of the diffuseness in this study is not a result of the grain size variation because of the uniformity of the grain size range of the ceramics studied.

4. CONCLUSIONS

The (1-x)$Pb(Mg_{1/3}Nb_{2/3})O_3$–x$PbTiO_3$ (when x = 0.1, 0.3 and 0.5) ceramics are prepared from PMN and PT powders by a mixed-oxide method. The dielectric properties of the ceramics are determined as functions of both temperature and frequency with an automated dielectric measurement system. The measurement takes place over the temperature range of -150 °C and 400 °C with measuring frequency between 100 Hz and 1 MHz. The results indicate that the dielectric properties of pseudo-cubic phase 0.9PMN-0.1PT and tetragonal phase 0.5PMN-0.5PT ceramics follow that of relaxor and normal ferroelectric behaviors, respectively, while the dielectric behaviors of a near MPB phase 0.7PMN-0.3PT ceramic show a mixture of normal and relaxor ferroelectric behavior. In contrast to an increase in T_C with increasing PT contents, the degree of broadening or diffuseness shows a decrease, which confirms a transition from a relaxor ferroelectric behavior in 0.9PMN-0.1PT to a normal ferroelectric behavior in 0.5PMN-0.5PT. The difference in dielectric behaviors is attributed to the structural symmetry of the ceramics.

ACKNOWLEDGEMENTS

The author expresses his gratitude for financial supports from the Thailand Research Fund (TRF). Helps with the sample preparation by Dr. A. Udomporn and with the dielectric measurements by Dr. Y. Somiya are gratefully acknowledged.

REFERENCES

[1] A.J. Moulson, J.M. Herbert. Electroceramics: Materials, Properties, Applications, 2nd Ed., John Wiley & Sons Ltd, New York, 2003.

[2] G.H. Haertling, J. Am. Ceram. Soc. 82(4) (1999) 797.

[3] L.E. Cross, Mater. Chem. Phys. 43 (1996) 108.

[4] S.E. Park, T.R. Shrout, Mater. Res. Innov. 1 (1997) 20.

[5] G.A. Smolenskii, A.I. Agranovskaya, Sov. Phys.-Solid State 1 (1960) 1429.

[6] S.W. Choi, J.M. Tang, A.S. Bhalla, Ferroelectrics. 189 (1996) 27.

[7] S.L. Swartz, T.R. Shrout, Mater. Res. Bull. 17 (1982) 1245.

[8] A. Udomporn ,S. Ananta, Mater. Lett. 58 (2004) 1154.

[9] Q. Jiang, Ph.D. Thesis, The Pennsylvania State University, University Park, 1992.

[10] A. Udomporn, Ph.D. Thesis, Chiang Mai University, Chiang Mai, 2004.

[11] B. Jaffe, W.R. Cook, H. Jeffe Piezoelectric Ceramics, Academic Press, New York, 1997.

[12] V. Koval, C. Alemany, J. Briancin, H. Brunckova, K. Saksl, J. Eur. Ceram. Soc., 23 (2003) 1157.

[13] R. Yimnirun, S. Ananta, P. Laoratanakul, Mater. Sci. Eng. B. 112 (2004) 79.

[14] R. Yimnirun, S. Ananta, P. Laoratanakul, J. Euro. Ceram. Soc. 25 (2005) 3225.

[15] E.F. Alberta, A.S. Bhalla, J. Phys. Chem. Solids 63 (2002) 1759.

[16] W. Chaisan, R. Yimnirun, S. Ananta, D.P. Cann, Mater. Lett. 59 (2005) 3732.

Table 1. Physical and dielectric properties of PMN-PT ceramics (at 1 kHz).

Ceramic	Density (g/cm^3)	Grain Size (μm)	T_C (°C)	Maximum Properties		Room Temp. Properties		Diffusivity (γ)
				ε_r	tan δ	ε_r	tan δ	
0.9PMN-0.1PT	7.98	0.42-3.66	38	25400	0.049	19400	0.087	1.96
0.7PMN-0.3PT	7.86	0.41-2.80	197	23500	0.011	2320	0.022	1.63
0.5PMN-0.5PT	7.78	0.48-3.76	250	23200	0.085	1010	0.025	1.14

List of Figure Captions

Fig. 1 (a). Temperature and frequency dependences of dielectric properties of 0.9PMN-0.1PT ceramic (open markers with dotted lines indicate data for the dielectric loss tangent (tan δ) at the same frequency).

Fig. 1 (b). Temperature and frequency dependences of dielectric properties of 0.7PMN-0.3PT ceramic (open markers with dotted lines indicate data for the dielectric loss tangent (tan δ) at the same frequency).

Fig. 1 (c). Temperature and frequency dependences of dielectric properties of 0.5PMN-0.5PT ceramic (open markers with dotted lines indicate data for the dielectric loss tangent (tan δ) at the same frequency).

Fig. 2. Temperature dependence of dielectric constant of PMN-PT ceramics (measured at 1 kHz).

Fig. 3. Variation of $\ln (1/\varepsilon_r - 1/\varepsilon_{max})$ vs $\ln (T-T_{max})$ of PMN-PT ceramics in the paraelectric region at 1 kHz.

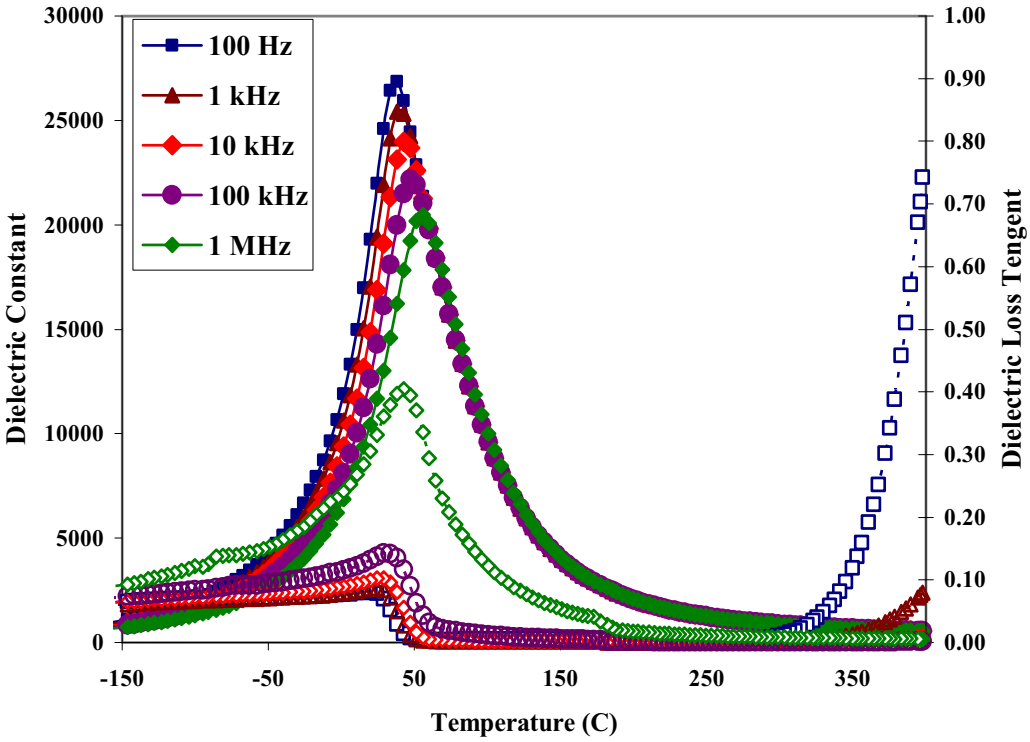

Fig. 1 (a) Temperature and frequency dependences of dielectric properties of 0.9PMN-0.1PT ceramic (open markers with dotted lines indicate data for the dielectric loss tangent (tan δ) at the same frequency)

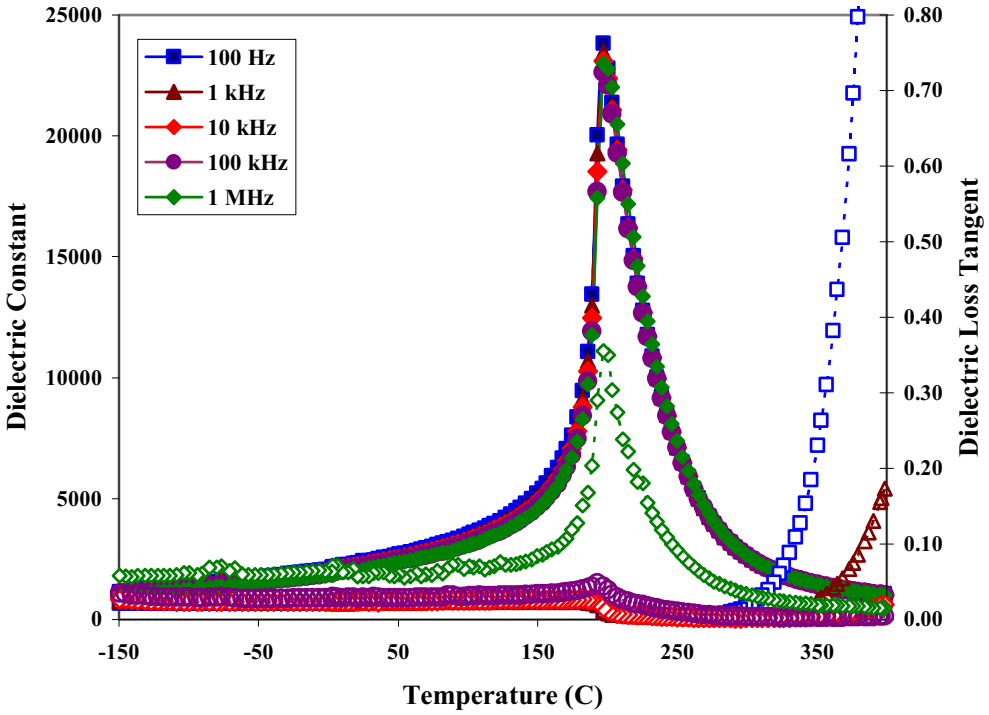

Fig. 1 (b) Temperature and frequency dependences of dielectric properties of 0.7PMN-0.3PT ceramic (open markers with dotted lines indicate data for the dielectric loss tangent (tan δ) at the same frequency)

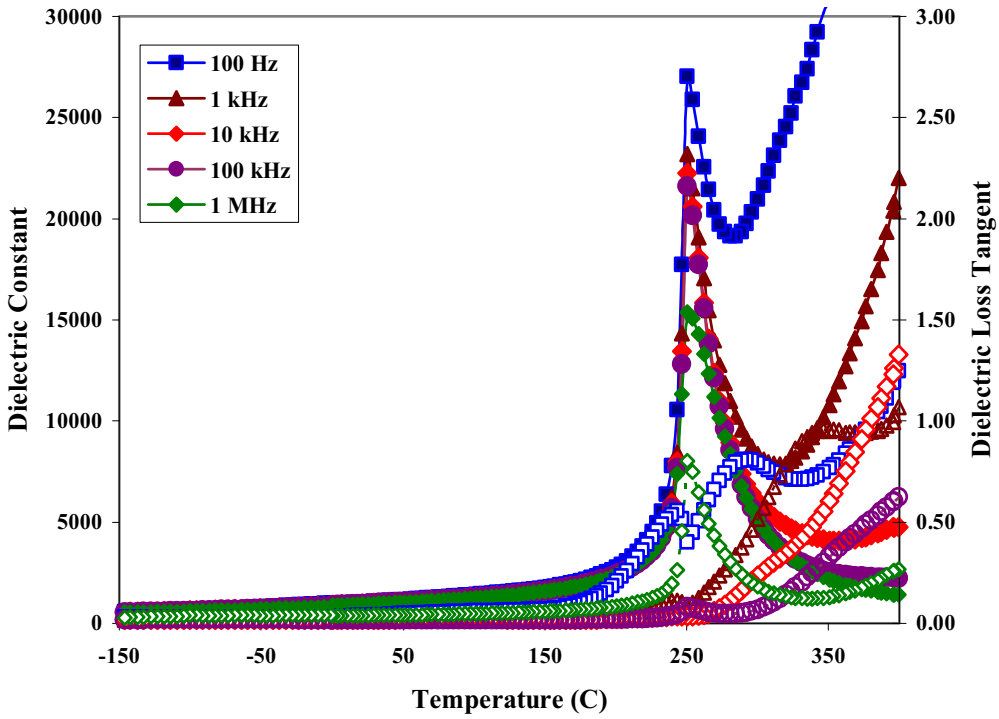

Fig. 1 (c) Temperature and frequency dependences of dielectric properties of 0.5PMN-0.5PT ceramic (open markers with dotted lines indicate data for the dielectric loss tangent (tan δ) at the same frequency)

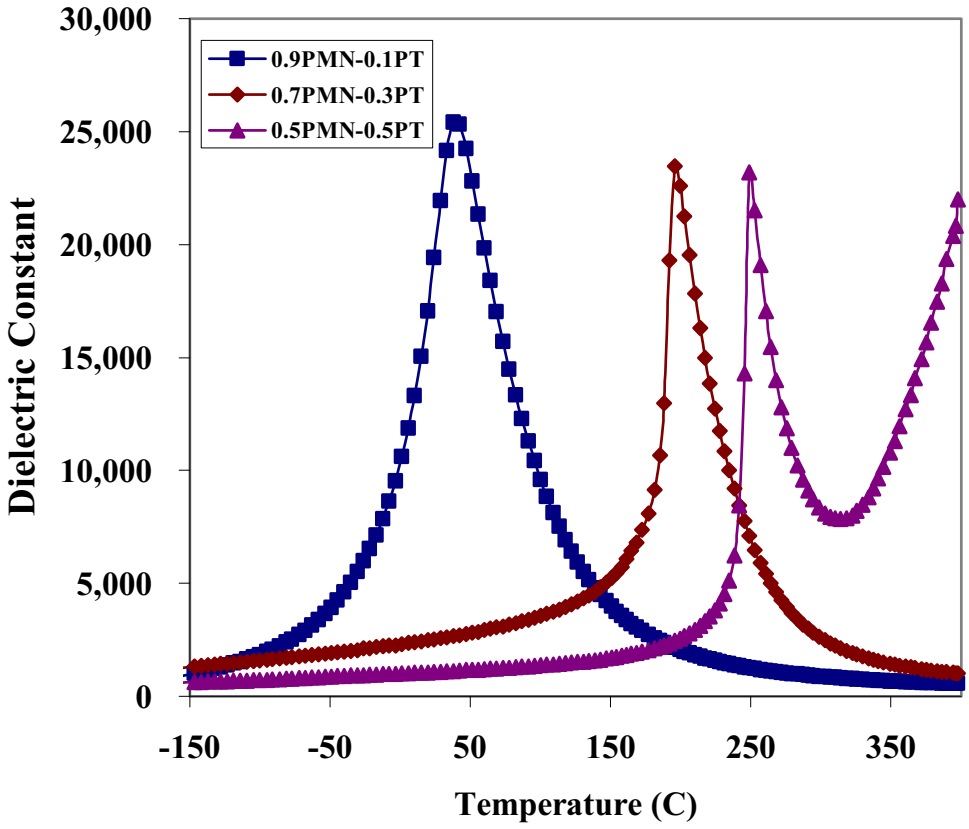

Fig. 2 Temperature dependence of dielectric constant of PMN-PT ceramics (measured at 1 kHz)

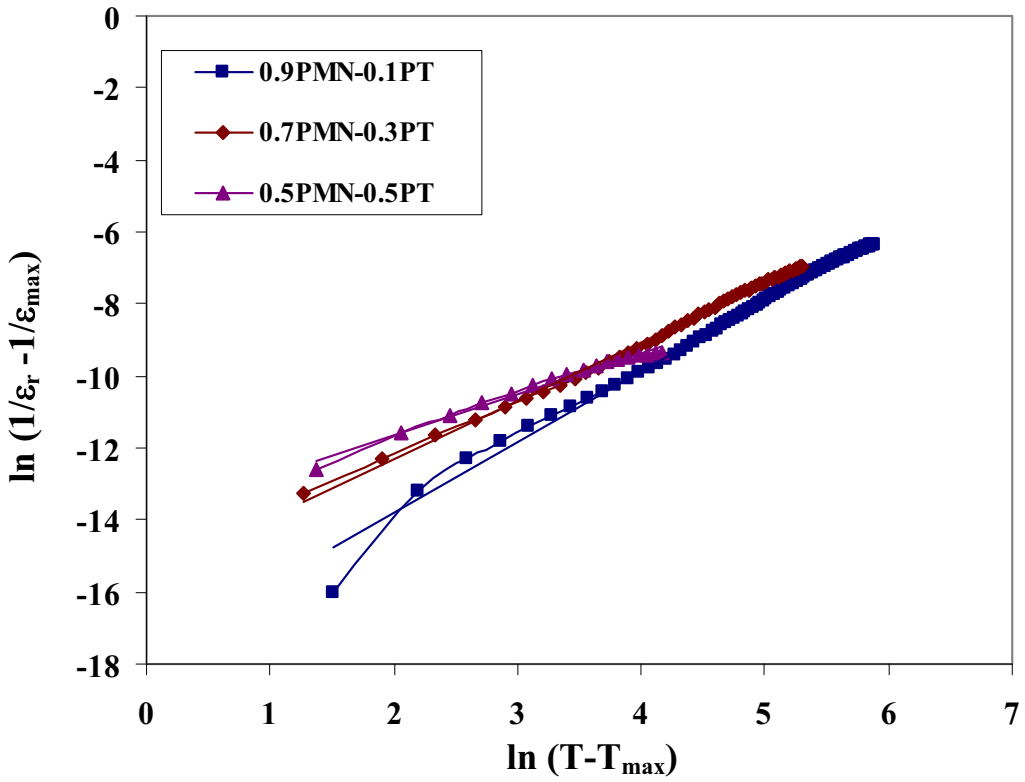

Fig. 3 Variation of ln $(1/\varepsilon_r - 1/\varepsilon_{max})$ vs ln $(T-T_{max})$ of PMN-PT ceramics in the paraelectric region at 1 kHz.

Effect of Sintering Temperature on Phase Formation, Dielectric, Piezoelectric, and Ferroelectric Properties of Nb-Doped $Pb(Zr_{0.52}Ti_{0.48})O_3$ Ceramics

PIYACHON KETSUWAN*, ATHIPONG NGAMJARUROJANA,YONGYUT LAOSIRITAWORN, SUPON ANANTA and RATTIKORN YIMNIRUN

Department of Physics, Faculty of Science, Chiang Mai University, Chiang Mai 50200, Thailand

The effects of sintering temperature on physical and electrical properties of the $Pb(Zr_{0.52}Ti_{0.48})O_3$ ceramics with addition of 1wt% Nb_2O_5 prepared by conventional mixed oxide technique were investigated. The samples were sintered over temperature rang 1200 -1300 ^oC. At lower sintering temperature, the dominant phase was rhombohedral while the tetragonal phase became dominant at higher temperature. The dielectric constant increased with increasing sintering temperature from 1200 to 1250 ^oC. Further increase in temperature resulted in a drop of the dielectric constant. Similar trend was also observed for the d_{33}-constant. For the ferroelectric properties, the electrical coercivity and remnant polarization decreased with increasing sintering temperature.

Keywords: PZT-Nb, Phase formation, Dielectric, Piezoelectric, Ferroelectric

1. INTRODUCTION

$Pb(Zr_{0.52}Ti_{0.48})O_3$ is a composition near the morphotropic phase boundary (MPB) of $Pb(Zr,Ti)O_3$, that separates rhombohedral and tetragonal ferroelectric forms with the coexistence of the 14 orientation states: 6-tetragonal and 8-rhombohedral. That is essential to allow the strong polarization for piezoelectricity. As the MPB is nearly vertical on the phase diagram, intrinsic property persists over a wide temperature range [1]. Almost all useful PZT ceramics are doped or modified to improve properties for specific applications [2]. Lead zirconate titanate solid solution modifications are controlled by aliovalent cation additions. The excess charge cation addition is called donor doped or soft PZTs, and the charge deficient cation is acceptor doped or hard PZTs. One approach of modification is off-valent donor doping, such as Nb^{5+} replacing Zr^{4+}. This makes domain wall move more easily and results in enhanced dielectric constant and coupling factor but reduced electric coercivity [3].

For PZT ceramics, a high temperature sintering process (>1200 ^oC) is normally employed to produce dense ceramics, which was the key factor for ensuring good physical and electrical properties. There have been many studies on effects of processing conditions on properties of lead-based perovskite ceramics [4-6]. Previous work on effect of sintering conditions on electric properties of PZT ceramics also showed interesting

results [7,8]. However, there have been only few reports on effect of sintering temperature of electrical properties of Nb-doped PZT ceramics prepared with conventional mixed-oxide method [9-11].

As an extension of earlier work, this study is therefore aimed at detailed and comprehensive investigation of influence of sintering temperature from 1200 to 1300 ^{o}C on phase formation, dielectric, piezoelectricc and ferroelectric properties of Nb-doped $Pb(Zr_{0.52}Ti_{0.48})O_3$ ceramics.

2. EXPERIMENTAL

The $Pb(Zr_{0.52}Ti_{0.48})O_3$ ceramics with addition of 1wt% Nb_2O_5 were prepared by conventional mixed oxide technique from PbO (Fluka 99.0%), ZrO_2 (Fluka 99.0%), TiO_2 (Fluka 99.9%) and Nb_2O_5 (Aldrich 99.9%) powders. After ball milling in ethanol for 24 h, the slurry was dried and calcined at 975 ^{o}C for 2 h [5]. Then, the calcined powder was pressed into discs (d =10 mm). The pellets were placed inside a closed alumina crucible covered with lead zirconate ($PbZrO_3$) powder to compensate the PbO volatilization and sintered at 1200-1300 ^{o}C for 2 h.

The x-ray diffraction (XRD) was used for structure and phase formation analysis. The microstructure was observed by scanning electron microscope (SEM). The bulk densities of sintered discs were measured by

the Archimedes method. The dielectric, piezoelectric and ferroelectric properties were determined by automated LCR-meter, d_{33}-meter and a Sawyer-Tower circuit, respectively. The specimens were poled under 30 kV/cm at 150 ^{o}C for 30 min in silicone oil [12,13].

3. RESULTS AND DISCUSSION

The x-ray diffraction pattern of $Pb(Zr_{0.52}Ti_{0.48})O_3$ +1wt% Nb_2O_5 ceramics with varying sintering temperature is shown in Figure 1(a). The peak intensity indicates the formation of perovskite phases, which could be matched with JCPDS file 73-2022 for rhombohedral phase of PZT and JCPDS file 33-0784 for tetragonal phase of PZT. At lower sintering temperature, the dominant phase was the rhombohedral phase which was characterized by a (020) peak between 43^{o} – 46^{o} (Figure 1(b)). The rhombohedral phase shift is also obvious for the specimens sintered at 1200 to 1250 ^{o}C for the peaks of (020). However, a distinct tetragonal splitting can be seen when sintered at 1275 ^{o}C, which was characterized by (020) and (200) peaks. Finally, the tetragonal phase became dominant at 1300 ^{o}C. The presence of rhombohedral phase is believed to be the effect of the over PbO volatilization in the lower sintering temperature from the covered lead zirconate ($PbZrO_3$) powder as the excess PbO has strong influence on the phase composition of PZT system near the MPB [14]. It

should be noticed that the ceramics sintered at 1250 ^{o}C show coexistence of tetragonal and rhombohedral phase (as shown in Figure 1(b)), which could explain enhanced properties [1], as will be discussed later.

The densification behavior of the specimens is shown in Figure 2. The density is seen to decrease with increasing temperature in the range of 1200 to1300 ^{o}C. Earlier reports also observed very similar trend [10,11]. The surface morphology of sintered ceramics was observed by using scanning electron microscope (SEM), as shown in Figure 3. The mean grain size of the ceramics was determined by using line intercept method. Also depicted in Figure 2, the mean grain size tends to increase with increasing sintering temperature. Similar observations have been reported in other systems [7,15,16]. However, the average grain size of $Pb(Zr_{0.52}Ti_{0.48})O_3$ with addition of 1 wt% Nb_2O_5 sintered at 1300 ^{o}C cannot be determined accurately due to the present of abnormal grain growth (Figure 3(e)) that is believed to be the result of the PbO loss at very high sintering temperature [17].

The maximum dielectric constant at Curie temperature(T_C) increased when the sintering temperature was increased from 1200 to 1250 ^{o}C (Figure 4(a)). Further increase in the sintering temperature resulted in a drop of the maximum dielectric constant. Similar trend is observed for the near room temperature dielectric constant (Figure 4(b)). The increased

dielectric properties with sintering temperature upto 1250 ^{o}C is belived to be a result of shifting of phase composition to near MPB, as supported by XRD in Figure 1(b). As shown in Figure 4(a) and listed in Table I, it should be noticed that over sintering temperature range of 1200 - 1250 ^{o}C the T_C is approximately 376 ^{o}C, while at higher sintering temperature (1275 ^{o}C and 1300 ^{o}C) T_C deceases to about 372 - 373 ^{o}C. Interestingly, the turning point at 1250 ^{o}C coincides with rhombohedral to tetragonal phase change identified by XRD. This observation is also observed in $Pb(Zr_{0.51}Ti_{0.49})O_3$ ceramics doped with 1 wt% MnO_2 as reported by Okazaki and Nagata [18]. The reason could be the composition shift or Pb-loss, especially at high sintering temperature, i.e. 1275 ^{o}C and 1300 ^{o}C.

In addition, as also listed in Table I, piezoelectric d_{33}-constant also increased with increasing sintering temperature from 1200 to 1250 ^{o}C, Though it is expected that the d_{33}-constant should further increase with increasing grain size [19], a drop of the d_{33}-constant was observed when the sintering temperature was further increased to 1300 ^{o}C with increasing grain size to 2 m. The explanation lies in the co-existence of two phases at 1250 ^{o}C, which results in the enhancement of d_{33}–value. Therefore, this is an evident of competing mechanism between grain size and sintering temperature in controlling the d_{33}–constant. In this case, the sintering temperature, which controls the phase formed, dominates [20].

As listed in Table I, it should be noticed that the optimum soft piezoelectric behavior with high $_r$, d_{33} and low E_c is observed in ceramics sintered at 1250 ^oC, in agreement with earlier reports [10,21,22], as also supported by the coexistence of tetragonal and rhombohedral phases discussed earlier.

The ferroelectric hysteresis behavior of $Pb(Zr_{0.52}Ti_{0.48})O_3$ with addition of 1 wt% Nb_2O_5 is shown in Figure 5. The electrical coercivity (E_c) and the remnant polarization (P_r) are seen to decrease with increasing sintering temperature. On the other hand, in the view of hysteresis behavior versus grain size, E_c is increased with decreasing grain size while the P_r decreased. These observations clearly indicate the soft piezoelectric behavior of Nb-doped PZT, as expected. Most importantly, this study shows that to achieve the optimum properties not only the starting chemical composition one also needs to obtain suitable sintering conditions.

4. CONCLUSION

The effects of sintering temperature on the physical and electrical properties of $Pb(Zr_{0.52}Ti_{0.48})O_3$ ceramics with addition of 1wt% Nb_2O_5

were investigated. The density decreased with increasing sintering temperature, while the grain size increased. The dielectric constant and d_{33}-constant reached maximum values at sintering temperature of 1250 ^{o}C. The electrical coercivity and remnant polarization decreased with increasing sintering temperature.

ACKNOWLEDGMENTS

This work was supported by the Thailand Research Fund (TRF), Graduate School and Faculty of Science, Chiang Mai University.

REFERENCES

[1] L. E. Cross, Mater. Chem. Phys., **43**, 108 (1996).

[2] G. H. Haertling, J. Am. Ceram. Soc., **82(4)**, 797 (1999).

[3] K. Okazaki, K. Nagata, J. Am. Ceram. Soc., **56**, 82 (1973).

[4] R. Wongmaneerung, R. Yimnirun and S. Ananta, Mater. Lett., **60**, 2666 (2006).

[5] W. Chaisan, R. Yimnirun, S. Ananta and D.P. Cann, Mater. Lett., **59(28)**, 3732 (2005).

[6] S. Wongsaenmai, Y. Laosiritaworn, S. Ananta and R. Yimnirun, Mater. Sci. Eng. B, **128(1-3)**, 83 (2006).

[7] R. Yimnirun, R. Tipakontitikul, S. Ananta, Inter. J. Mod. Phys. B, **20(17)**, 2415 (2006).

[8] D. A. Buckner and P. D. Wilcox, Am. Ceram. Soc. Bull., **51(3)**, 218 (1972).

[9] P. GR. Lucuta, Fl. Constantinecu, and D. Barb, J. Am. Ceram. Soc., **68(10),** 533 (1985).

[10] S.Y. Chu, T.Y. Chen, I. T.Tsai, Integra. Ferr., **58**, 1293 (2003).

[11] C. A. Randll, N. Kim, J. P. Kucera, W. Cao, T. R. Shrout, J. Am. Ceram. Soc., **81[3]**, 677 (1998).

[12] R. Yimnirun, S. Ananta and P. Laoratanakul, J. Eur. Ceram. Soc., **25(13)**, 3225 (2005).

[13] R. Yimnirun, Ferroelectrics, **331**, 9 (2006)

[14] K. Kakegawa, O. Matunaga, T. Kato, Y. Sasaki, J. Am. Ceram. Soc., **78(4)**, 1071 (1995).

[15] Y. S. Hong, H. B. Park and S. J. Kim, J. Eur. Ceram. Soc., **18**, 613 (1998).

[16] T. Y. Chen, S. Y. Chu and Y. D. Juang, Sensor. Actuat. A-Phys, **102**, 6 (2002).

[17] S. Chiang, N. Nasihoka, R.M. Fulrath and J.A. Pask, Am. Ceram. Soc. Bull., **60 (4)**, 484 (1981).

[18] K. Okazaki, K Nagata, J. Soc. Mater. Sci. Jpn. **4**, 404 (1972).

[19] K. Okazaki, K Nagata, J. Electron. Commun. Soc. Jpn. C, **53**, 815 (1970).

[20] Y. Xu, Ferroelectric Materials and Their Application (North-Holland, 1991).

[21] B. H. Chen, C. L. Huang and L. Wu, Solid. Electron., **48**, 2293 (2004).

[22] C. L. Huang, B. H. Chen and L. Wu, Solid. Commun., **130**, 19 (2004).

Table Caption

Table 1 Sintering temperature dependence of d_{33} , P_r , E_c , T_c and $_r$.

Figure Caption

Figure 1 (a) XRD pattern of $Pb(Zr_{0.52}Ti_{0.48})O_3$ +1wt% Nb_2O_5 ceramics sintered at various temperatures (b) magnification of XRD peaks near 45^o showing peaks evolution.

Figure 2 Dependence of density and grain size of $Pb(Zr_{0.52}Ti_{0.48})O_3$ +1wt% Nb_2O_5 ceramics on the sintering temperature.

Figure 3 SEM micrographs of $Pb(Zr_{0.52}Ti_{0.48})O_3$ +1wt% Nb_2O_5 ceramics sintered at (a) 1200 ^{o}C (b) 1225 ^{o}C (c) 1250 ^{o}C (d) 1275 ^{o}C and (e) 1300 ^{o}C.

Figure 4 Dielectric constant as a function of sintering temperature of $Pb(Zr_{0.52}Ti_{0.48})O_3$ +1wt% Nb_2O_5 ceramics measured at (a) Curie temperature (b) near room temperature (1kHz).

Figure 5 Sintering temperature dependence of P-E hysteresis loop of $Pb(Zr_{0.52}Ti_{0.48})O_3$ +1wt% Nb_2O_5 ceramics.

Figure 1 (a)

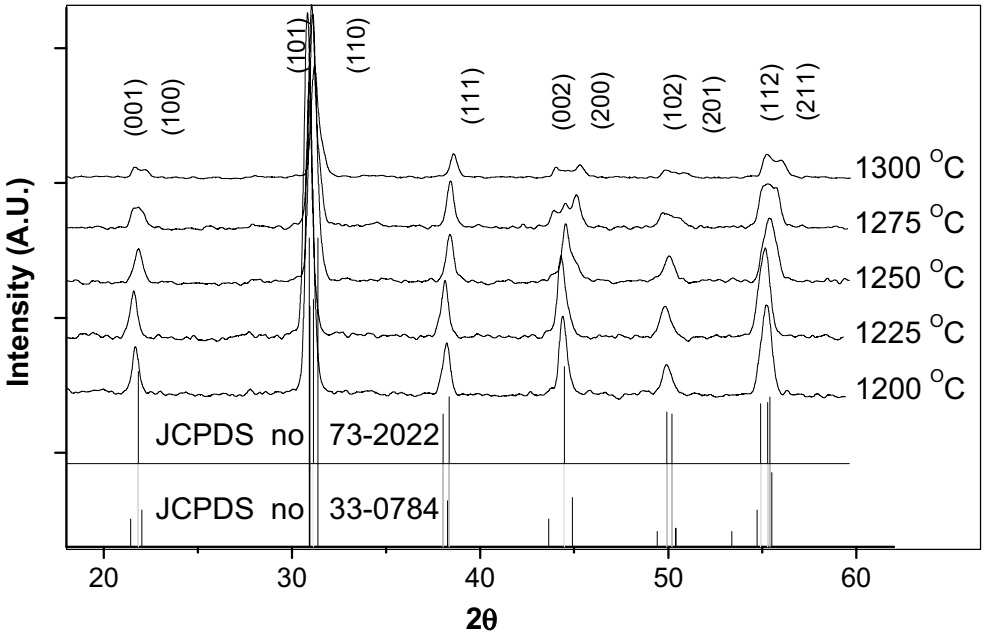
(001)
(100)
(101)
(110)
(111)
(002)
(200)
(102)
(201)
(112)
(211)
1300 °C
1275 °C
1250 °C
1225 °C
1200 °C
JCPDS no 73-2022
JCPDS no 33-0784
Intensity (A.U.)
20
30
40
50
60
2θ

Figure 1(b)

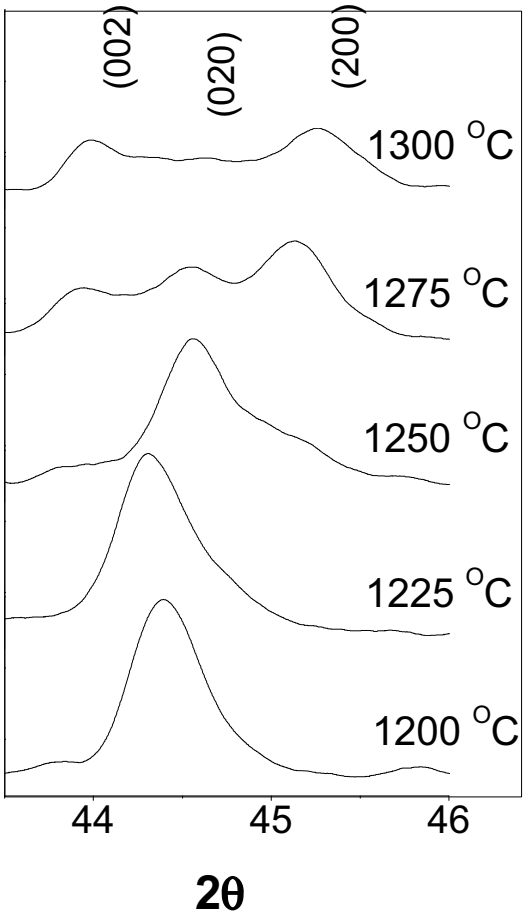

Figure 2

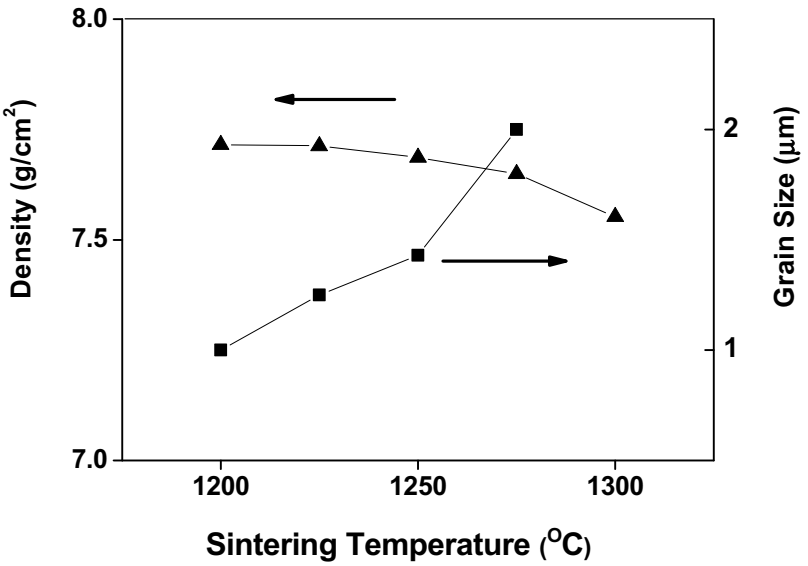
8.0
7.5
7.0
Density (g/cm^2)
2
1
Grain Size (μm)
1200
1250
1300
Sintering Temperature (^{O}C)

Figure 3

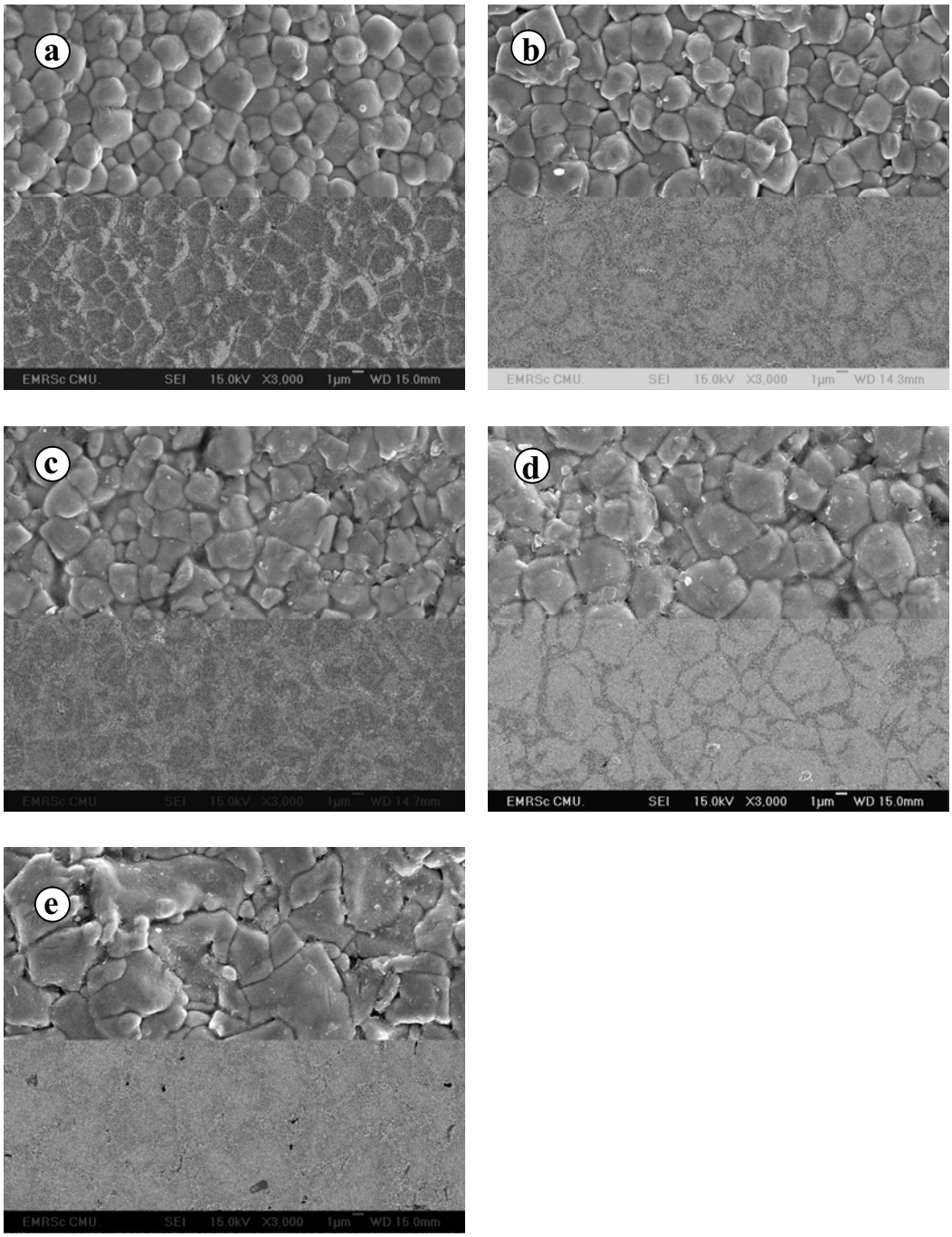
a
EMRSc CMU. SEI 15.0kV X3,000 1μm WD 15.0mm
b
EMRSc CMU. SEI 15.0kV X3,000 1μm WD 14.3mm
c
EMRSc CMU. SEI 15.0kV X3,000 1μm WD 14.7mm
d
EMRSc CMU. SEI 15.0kV X3,000 1μm WD 15.0mm
e
EMRSc CMU. SEI 15.0kV X3,000 1μm WD 15.0mm

Figure 4

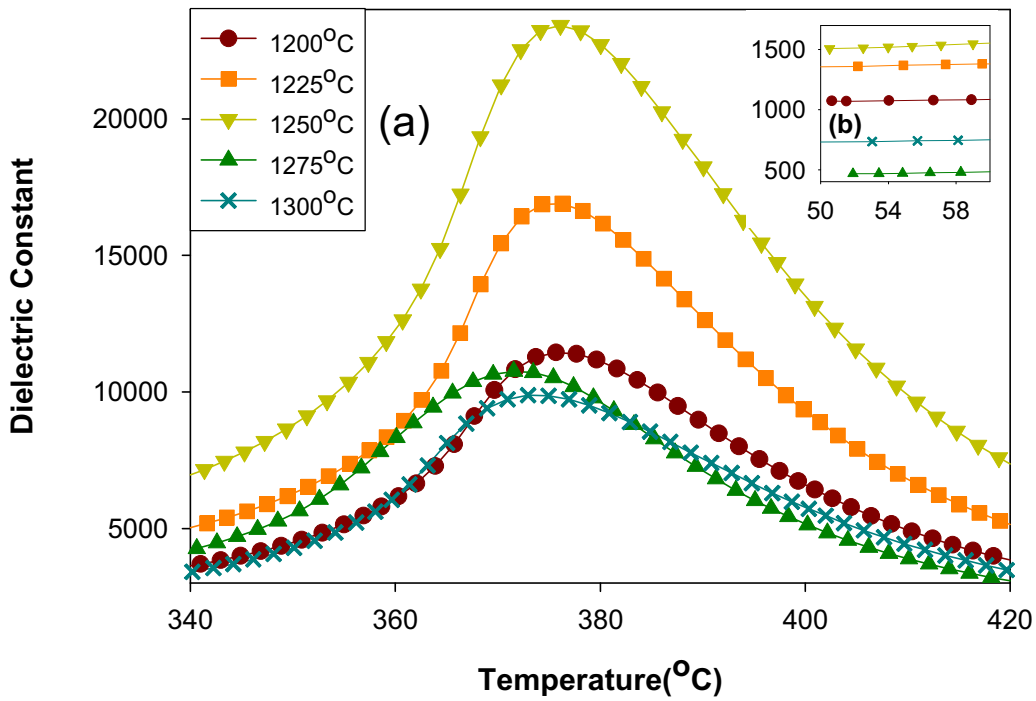
1200°C
1225°C
1250°C
1275°C
1300°C
(a)
(b)
Dielectric Constant
Temperature(°C)
20000
15000
10000
5000
340
360
380
400
420
1500
1000
500
50
54
58

Figure 5

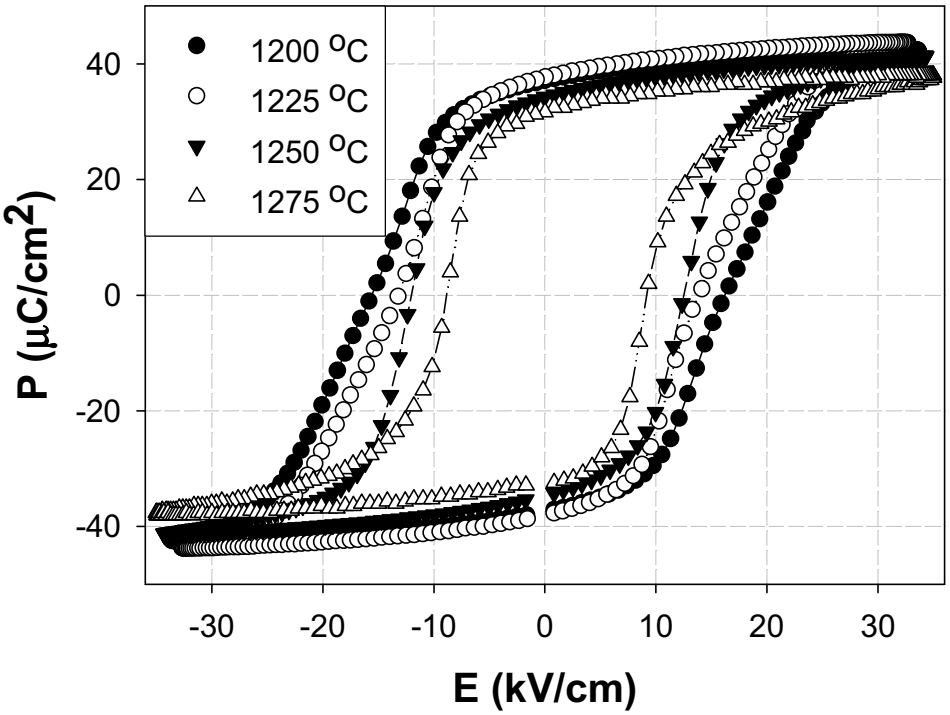
1200 °C
1225 °C
1250 °C
1275 °C
P (μC/cm2)
E (kV/cm)
40
20
0
-20
-40
-30
-20
-10
0
10
20
30

Table 1

Sintering temperature (^oC)	d_{33} (pC/N)	P_r ($\mu C/cm^2$)	E_c (kV/cm)	T_c (^oC)	ε_r(room)	ε_r(max)
1200	157	37.30	15.90	375.7	1073	11443
1225	221	37.90	13.52	376.3	1354	16895
1250	305	34.48	12.27	376.1	1508	23424
1275	206	32.23	9.00	371.6	466	10756
1300	109	-	-	373.0	730	9880

Scaling Behavior of Dynamic Ferroelectric Hysteresis in Soft PZT Ceramic: Stress Dependence

Rattikorn Yimnirun, Supon Ananta, Yongyut Laosiritaworn,

Athipong Ngamjarurojana and Supattra Wongsaenmai

Department of Physics, Faculty of Science, Chiang Mai University,

Chiang Mai, 50200 Thailand

Effects of electric field frequency, electric field amplitude, and mechanical stress on the hysteresis area were investigated on soft PZT ceramic. At stress-free condition, the investigation found the area scales with frequency and field amplitude in power law form, $A \quad f \quad E_0$; however, with different set of exponents in comparing to those in the investigation on thin films structure. On the other hand, with compressive stresses turning on, the same set of the exponents with the stress free condition is found to confirm universality. In addition, the scaling form of the area to triple parameters; i.e., frequency, field amplitude, and stress in a power law form, $\langle A \rangle \quad \langle A_{\sigma\ 0} \rangle \quad \langle A \quad A_{\sigma\ 0} \rangle \quad f^{\ 0.25} E_0 \sigma^{0.44}$, was obtained.

Keywords: Scaling, Stress, Hysteresis, soft PZT

Short Title: Stress Dependence Scaling of Soft PZT Ceramic

INTRODUCTION

In many sensor and actuator applications, as well as in more recently developed ferroelectric random access memories (Fe-RAMs), the dynamic hysteresis, i.e., hysteresis area $<A>$ as a function of the field amplitude E_0 and frequency f, characteristics have become important consideration since they present a lot of information critical for the applications whose performance is related to the signal amplitude and frequency [1-3]. Theoretical studies have been carried out to understand the dynamic response of hysteresis curves in spin systems [4-6]. In particular, attention is focused on scaling law $A \quad f^{\alpha} E_0^{\beta}$ (where a and β are exponents that depend on the dimensionality and symmetry of the system). The theoretical three-dimensional models $((F^2)^2$ and $(F^2)^3$ with O(N) symmetry (N? 8)) by Rao *et al.* and other investigators [4,6,7] proposed scaling relations applicable to the high-f limit as follows,

$$A \quad f^{\ 1} E_0 \quad \text{as} \quad f \qquad (1)$$

Apart from its theoretical importance, since reliable measurement of the hysteresis at ultra-high frequency is still a big challenge, it is technologically helpful to understand the scaling behavior so that the ultra-high frequency of the hysteresis can be predicted. Hence, there has been a great deal of interest in the

scaling behavior of the dynamic hysteresis in ferromagnetic and ferroelectric thin films [6-10]. Interestingly, some discrepancies between the theoretical predictions and the experimental results have already been reported for ferroelectric thin-films systems [9-12]. In contrast to the theoretically predicted scaling relation in Eq. (1), the experimental investigation on PZT thin films [11] has resulted in a different relation, i.e.,

$$A \quad f^{1/3} E_0 \quad \text{as} \quad f \tag{2}$$

Though bulk ferroelectric materials are useful and widely used in many applications [1-3], there has however been no report on the scaling behavior studies of ferroelectric hysteresis loops of bulk ferroelectric ceramics. It is therefore of great interest to investigate the form of this scaling relation for bulk systems. Hence, one of the aims of this present study is to investigate the scaling behavior of the dynamic hysteresis of the bulk ceramic.

More importantly, in many applications the ceramic specimens are often subjected to mechanical loading, either deliberately in the design of the device itself or because the device is used to change shapes as in many smart structure applications or the device is used under environmental stresses [1-3,13]. A prior knowledge of how the material properties change under different load conditions is inevitably crucial for proper design of a device and for suitable selection of materials for a specific application. It is therefore important to determine the

properties of these materials as a function of applied stress. Previous investigations on the stress-dependent electrical properties of many ceramic systems, such as undoped-PZT, PLZT, BT, PMN-PT, PZT-BT, PMN-PZT, and PZT and SBT thin films [14-20] have clearly emphasized the importance of the subject. This study will focus on very important bulk ceramic, i.e., donor-doped or soft lead zirconate titanate ($Pb(Zr_{1-x}Ti_x)O_3$ or PZT) ceramics. Because of the "soft" piezoelectric behaviors with higher dielectric and piezoelectric activities, soft PZT have been employed extensively in sensor and actuator applications, as well as smart systems [1-3]. Many investigations have already revealed interesting results on the electrical properties of the soft PZT ceramics under applied stress [14,17,20]. The ferroelectric properties of the soft PZT ceramics have been observed to change significantly with the applied stress [17,20]. However, it is interesting that there have been no report on the influence of the external stress on the scaling behavior of any materials. Therefore, the main aim of this study is to establish the scaling behavior of the dynamic hysteresis responses of the technically important and commercially available soft PZT bulk ceramics under the influence of the external stress.

EXPERIMENTS

The dynamic hysteresis (P E) loops of commercially available soft PZT ceramic (PKI-552, Piezo Kinetics Inc., USA) were characterized at room temperature (25 C) by using a computer controlled modified Sawyer-Tower circuit with f

covering from 2 to 100 Hz and E_0 from 0 to 18 kV/cm. The electric field was applied to a sample by a high voltage AC amplifier (Trek, model 610D) with the input sinusoidal signal from a signal generator (Goodwill, model GAG-809). The detailed descriptions of this system are explained elsewhere [18,20]. Effects of the external stress on the dynamic hysteresis were investigated with the compressometer, which was developed for simultaneous applications of the mechanical stress and the electric field [20]. Measurements were performed as a function of mechanical stress applied discretely between 0 and 24 MPa. During the measurements, a desired stress was first applied to the sample and then the electric field with varying frequency was applied. The dynamic hysteresis (P E) loop was then recorded for each applied field and frequency. The measurements reported were for the samples during their first mechanical stress cycle. It should also be noted that the reported ferroelectric parameters were obtained after a total of 10 cycles of the electric field were applied to the sample at each constant stress.

RESULTS AND DISCUSSION

The hysteresis profiles for various frequencies f, field amplitude E_0, and stress σ are obtained. Figs. 1(a) and 1(b) show examples of the hysteresis loops at different f but fixed E_0 (18 kV/cm), and at different E_0 but fixed f (100 Hz), respectively, under a stress-free condition. From Fig. 1(a), where E_0 is fixed, one sees the evolution of the pattern at different f. It is very interesting to observe

that as the frequency increases the hysteresis changes from an unsaturated loop with near square shape and rounded at the tips at low frequency (2 Hz) to well saturated loops at higher frequencies. The loop area $<A>$, remanent polarization (P_r), and coercive field (E_c) decrease with an increase of frequency. The observation that the $<A>$ decreases with increasing frequency in this high-f region is ascribed to the delayed response of the spin reversal to the varying external field [9,10]. Figure 1(b) shows the dependence of the hysteresis loop on the amplitude of the electric field. For small fields, the loop does not saturate and appears as an ellipse inclined at an angle to the E axis. An increase in the amplitude of the field E_0 makes the loop larger and increases its angle of inclination. For a given frequency of 100 Hz, as shown in Fig. 1(b), loop area $<A>$, remanent polarization (P_r), and coercive field (E_c) increase with an increase of E_0 until well saturated loop is achieved. Figure 1(c) displays the hysteresis loops of the soft PZT ceramics under different compressive stress during loading at fixed f of 100 Hz and fixed E_0 of 18 kV/cm. It should first be noticed that the area of the P E loops decreases steadily with increasing the stress. The P E loop area indicates the polarization dissipation energy of a ferroelectric material subjected to one full cycle of electric field application [18,20]. This amount of the energy loss is directly related to volume involved in the switching process during the application of electric field [17].When the mechanical stress is applied, more and more ferroelectric domains are constrained by the applied stress and cannot be re-oriented by the electric field

so as to participate in the polarization reversal. Consequently, both the saturation and remanent polarizations become lower with increasing the compressive stress [17,20]. The polarization dissipation energy is consequently found to decrease with increasing the applied stress, indicating that the sample volume contributing to polarization reversal decreases with the increasing stress. Similar observation has also been found in other investigations [17-20].

To investigate the scaling behavior under stress-free condition, we first followed the previous theoretical predictions on the loop–area by plotting the data of $\langle A \rangle$ against $f\ E_0$. This bases on an assumption that Eq. (1) is applicable, and the frequency range used in this study can be considered as the high frequency region since the loop–area decreases with increasing frequencies. The data are shown in Fig. 2(a) and the dotted line represents a fitting in terms of $A\ f^{1}E_0$. Clearly, the theoretically proposed scaling relation in Eq. (1) cannot be directly applied to the data obtained in this study.

On the other hand, earlier experimental work by Liu *et al.* [11] on the scaling behavior of PZT thin films also showed different relation, as shown in Eq. (2). In that study, the scaling takes the form of $A\ f\ E_0$. To check the validity of the relation on the bulk system, i.e., soft PZT ceramic, we plot the data of $\langle A \rangle$ against $f\ E_0$. The data are shown in Fig. 2(b) and the dotted line represents a fitting in terms of $A\ f\ E_0$. Large deviation is also observed in this case. Therefore, this implies that the scaling relations from both the

theoretical prediction and the experimental investigation are not applicable for the soft PZT bulk ceramic in this present study.

To obtain the suitable scaling relation, one can fit the data with $A \quad f^m E_0^n$ where m and n are exponents to be determined directly from the experimental data. By plotting $\langle A \rangle$ against f at fixed E_0, one obtains the exponent m. On the other hand, the exponent n can be obtained from plotting $\langle A \rangle$ against E_0 at fixed f. It should also be noted that there is more deviation from the minor loops without saturation at small field amplitudes, and these data were excluded from the fitting reported. It can be seen in Fig. 2(c) that the suitable exponent m for the frequency component has the value of –0.25 (within the limit of experimental errors), while the hysteresis area $\langle A \rangle$ is found to increase linearly with the applied field amplitude E_0, hence the exponent n should take the value of 1. Therefore, it is revealed that the data obtained under stress-free condition can be much better fitted (with R^2 = 0.97), within the measured uncertainty, by

$$A \quad f \quad E_0 \tag{3}$$

Therefore, Eq. (3) is identified as the suitable scaling relation for the soft PZT bulk ceramic under the stress-free condition.

Moreover, as evident in Fig. 1(c), at any given frequencies the hysteresis area $\langle A \rangle$ is found to decrease steadily with increasing the applied

stress. Therefore, instead of including only the field amplitude E_0 and the frequency term *f*, the scaling relation should also include the stress (σ) term, i.e.

$$A \quad f^m E_0^n \sigma^p \tag{4}$$

However, due to increasing number of exponents, to simplify the problem, we assume the validity of the scaling form $A \quad \sigma \quad f^{0.25} E_0$ for all applied stresses. Consequently, the area $\langle A \rangle$ for each stress is plotted against $f^{0.25} E_0$, as shown in Fig. 3(a). As can be seen form the least square linear fits, reasonably good linear relations can be found. As a result, the condition of universality having $m = -0.25$ and $n = 1$ in soft PZT bulk ceramic systems is confirmed whereas the proportional constant in Eq. (4) may still be a function of σ. Therefore, by discarding minor loops which usually occur at very low E_0, it is found that

$$\langle A \rangle \quad \langle A_{\sigma\ 0} \rangle \quad \langle A \quad A_{\sigma\ 0} \rangle \quad f^{0.25} E_0 \sigma^{0.44}, \tag{5}$$

where $\langle A_{s=0} \rangle$ refers to stress free hysteresis area which will be a dominant term for zero stress. Note that from the appearance of stress s, $\langle A - A_{s=0} \rangle$, referring to the difference in energy dissipation between under stress and stress free condition, increases with increasing stress suggesting a decay of $\langle A \rangle$ with s at a rate of $s^{0.44}$ as observed in experiments. As a result, from our studies, it may be concluded that in bulk ceramics, the difference of the

hysteresis area between under–stress and stress–free condition scales with frequency, field–amplitude and stress via exponents m = –0.25, n = 1, and p = 0.44. However, at a particular fixed stress, Eq. (5) yields Eq. (3) which is the original form for how the area scales with the frequency and the field–amplitude.

CONCLUSIONS

In this study, we investigated the hysteresis properties of the soft PZT bulk ceramics under the effect of mechanical stress at various frequencies and field amplitudes of the external applied electric field. Considering the scaling law for the loop area, at zero stress, the investigation found the area scales with frequency and the field amplitude in a power law function. However, the exponents to the scaling in this bulk ceramic system do not match with previous investigation on thin films structure. On the other hand, with inserting the uniaxial stress, the same set of exponents to frequency and field amplitude in stress free condition is found which confirms the condition of universality in bulk system. Furthermore, the difference of the energy dissipation between the under stress and stress free condition is found to scale with $f^{-0.25}E_0\sigma^{0.44}$.

ACKNOWLEDGMENTS

Financial supports from the Commission on Higher Education (CHE), Thailand Research Fund (TRF), and Faculty of Science and Graduate School of Chiang

Mai University are gratefully acknowledged.

REFERENCES

[1] K. Uchino, Ferroelectric Devices (Marcel Dekker, New York, 2000).

[2] B. Jaffe, W. R. Cook, and H. Jaffe, Piezoelectric Ceramics (Academic Press, New York, 1971).

[3] J.F. Scott, Ferroelectr. Rev. **1**, 1 (1998).

[4] M. Rao, H.R. Krishnamurthy, and R. Pandit, Phys. Rev. B **42**, 856 (1990).

[5] M. Acharyya and B.K. Chakrabarti, Phys. Rev. B **52**, 6560 (1995).

[6] J.-M. Liu, H.L.W. Chan, C.L. Choy, and C.K. Ong, Phys. Rev. B **65**, 014416 (2001).

[7] M. Rao and R. Pandit, Phys. Rev. B **43**, 3373 (1991).

[8] Q. Jiang, H.N. Yang, and G.C. Wang, Phys. Rev. B **52**, 14911 (1995).

[9] B. Pan, H. Yu, D. Wu, X.H. Zhou, and J.-M. Liu, Appl. Phys. Lett. **83**, 1406 (2003).

[10] J.-M. Liu, H.L.W. Chan, C.L. Choy, Y.Y. Zhu, S.N. Zhu, Z.G. Liu, and N.B. Ming, Appl. Phys. Lett. **79**, 236 (2001).

[11] J.-M. Liu, H.P. Li, C.K. Ong, and L.C. Lim, J. Appl.Phys. **86**, 5198 (1999).

[12] J.-M. Liu, H. Yu, B. Pan, and X.Y. Chen, Mater. Sci. Eng. **B118**, 2 (2005).

[13] L.E. Cross, Mater. Chem. Phys. **43**, 108 (1996).

[14] Q.M. Zhang, K. Uchino, and J. Zheng, J. Mater. Res. **12**, 226 (1997).

[15] D. Viehland and J. Powers, J. Appl. Phys. **89**, 1820 (2001).

[16] R. Yimnirun, Ferroelectrics **331**, 9 (2006).

[17] D.Zhou, M. Kamlah, and D. Munz, J. Euro. Ceram. Soc. **25**, 425 (2005).

[18] R. Yimnirun, S. Ananta, A. Ngamjarurojana, and S. Wongsaenmai, Appl. Phys. A-Mater. **81**, 1227 (2005).

[19] T. Kumazawa, Y. Kumagai, H. Miura, M. Kitano, and K. Kushida, Appl. Phys. Lett. **72**, 608 (1998).

[20] R. Yimnirun, M. Unruan, Y. Laosiritaworn, and S. Ananta, J. Phys. D: Appl. Phys. **39**, 3097 (2006).

List of Figure Captions

Fig. 1 Hysteresis loops for soft PZT ceramic (a) at various f (E_0 = 18 kV/cm and σ = 0 MPa), (b) at various E_0 (f = 100 Hz and σ = 0 MPa), and (c) at various σ (f = 100 Hz and E_0 = 18 kV/cm).

Fig. 2 Scaling of hysteresis area <A> against (a) f E_0 (b) f E_0 and (c) f E_0 for soft PZT ceramic under stress-free condition.

Fig. 3 Scaling of hysteresis area <A> against (a) f E_0 at various compressive stresses, and (b) collapse of the scaling area against f E_0 under the effect of compressive stress s for soft PZT ceramics.

Fig. 1(a)

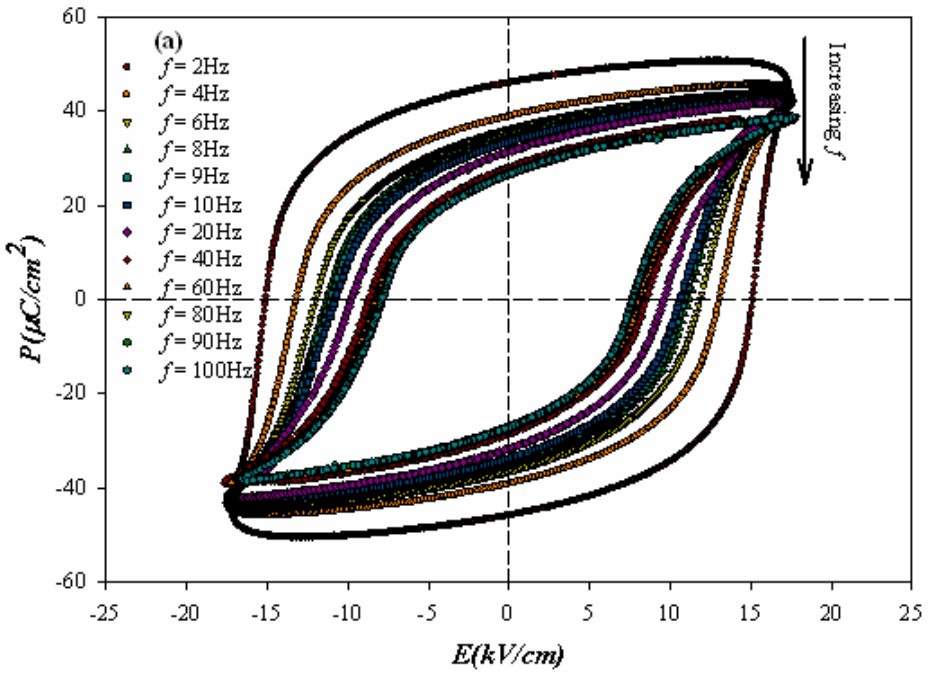
(a)
f = 2Hz
f = 4Hz
f = 6Hz
f = 8Hz
f = 9Hz
f = 10Hz
f = 20Hz
f = 40Hz
f = 60Hz
f = 80Hz
f = 90Hz
f = 100Hz
Increasing f
P(μC/cm²)
E(kV/cm)
60
40
20
0
-20
-40
-60
-25
-20
-15
-10
-5
0
5
10
15
20
25

Fig. 1(b)

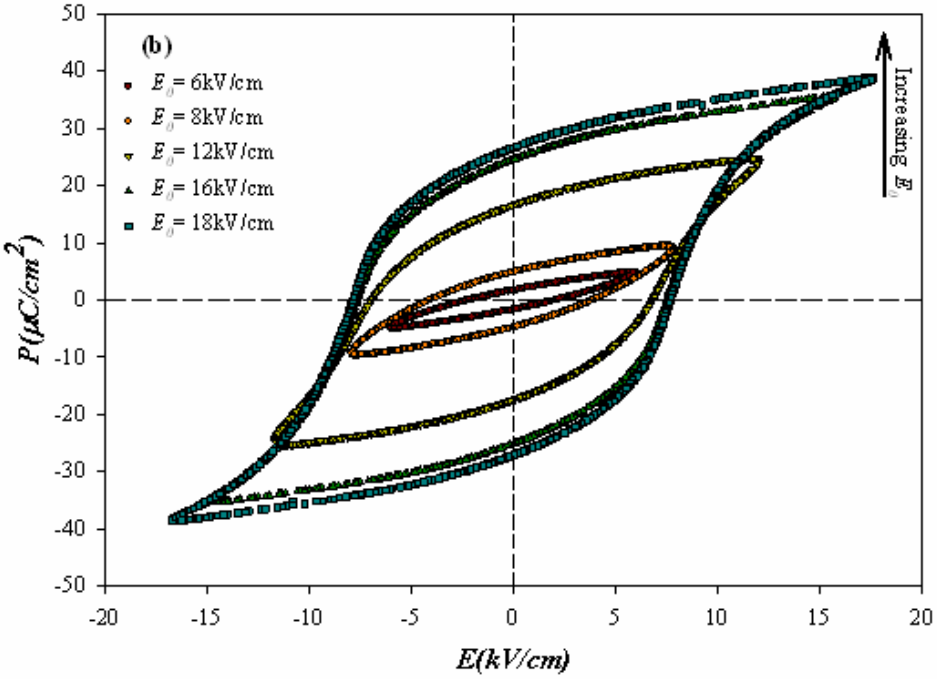
(b)
E_0 = 6kV/cm
E_0 = 8kV/cm
E_0 = 12kV/cm
E_0 = 16kV/cm
E_0 = 18kV/cm
Increasing E_0
P(μC/cm²)
E(kV/cm)
50
40
30
20
10
0
-10
-20
-30
-40
-50
-20
-15
-10
-5
0
5
10
15
20

Fig. 1(c)

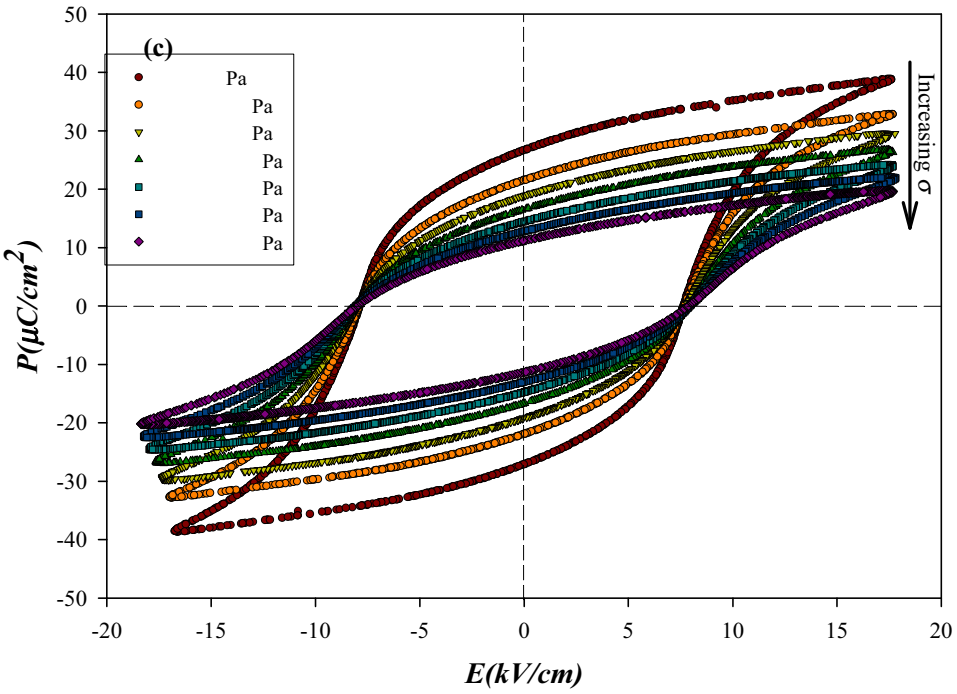
(c)
Pa
Pa
Pa
Pa
Pa
Pa
Pa
Increasing σ
P(μC/cm²)
E(kV/cm)
50
40
30
20
10
0
-10
-20
-30
-40
-50
-20
-15
-10
-5
0
5
10
15
20

Fig. 2(a)

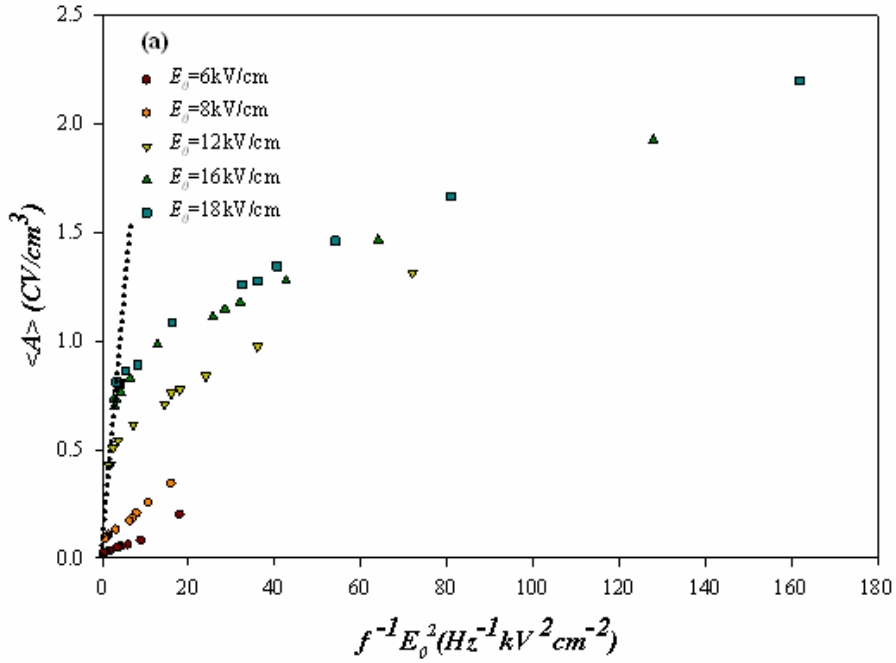
(a)
E_0=6kV/cm
E_0=8kV/cm
E_0=12kV/cm
E_0=16kV/cm
E_0=18kV/cm
<A> (CV/cm^3)
$f^{-1}E_0^2$(Hz^{-1}kV^{2}cm^{-2})
0.0
0.5
1.0
1.5
2.0
2.5
0
20
40
60
80
100
120
140
160
180

Fig. 2(b)

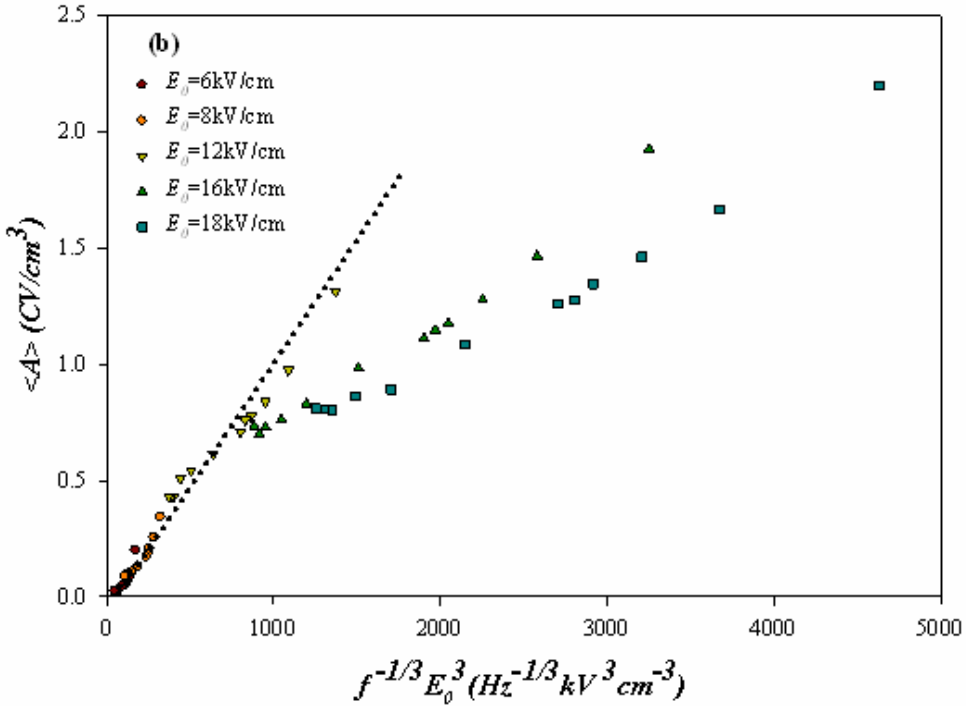
(b)
E_0=6kV/cm
E_0=8kV/cm
E_0=12kV/cm
E_0=16kV/cm
E_0=18kV/cm
<A> (CV/cm^3)
$f^{-1/3}E_0^3$ (Hz$^{-1/3}$kV^{3}cm^{-3})
0.0
0.5
1.0
1.5
2.0
2.5
0
1000
2000
3000
4000
5000

Fig. 2(c)

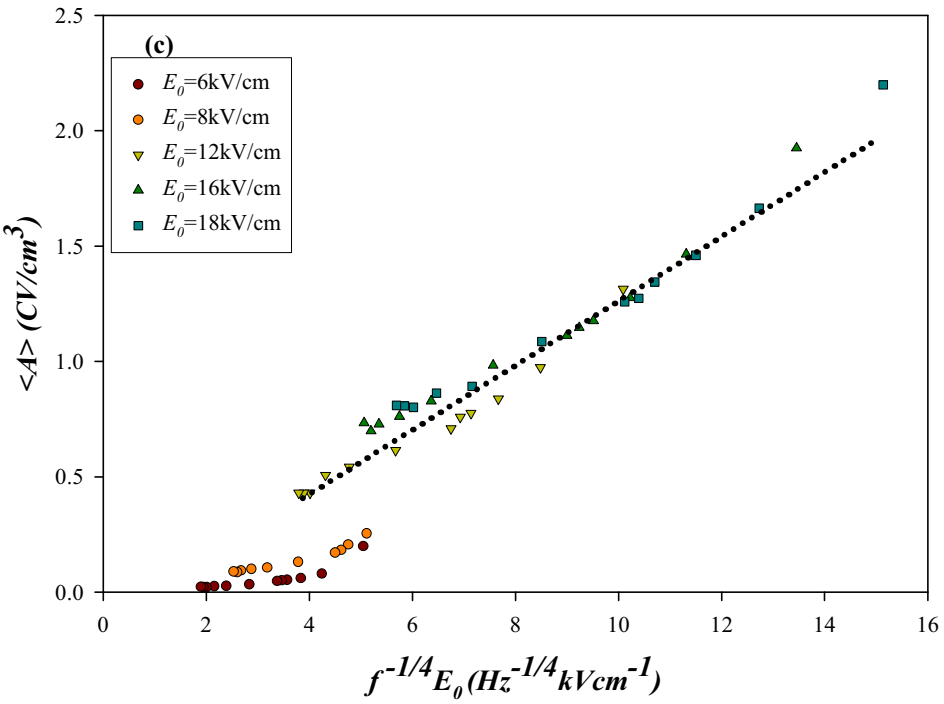
(c)
E_0=6kV/cm
E_0=8kV/cm
E_0=12kV/cm
E_0=16kV/cm
E_0=18kV/cm
<A> (CV/cm^3)
$f^{-1/4}E_0$(Hz$^{-1/4}$kVcm^{-1})
0.0
0.5
1.0
1.5
2.0
2.5
0
2
4
6
8
10
12
14
16

Fig. 3(a)

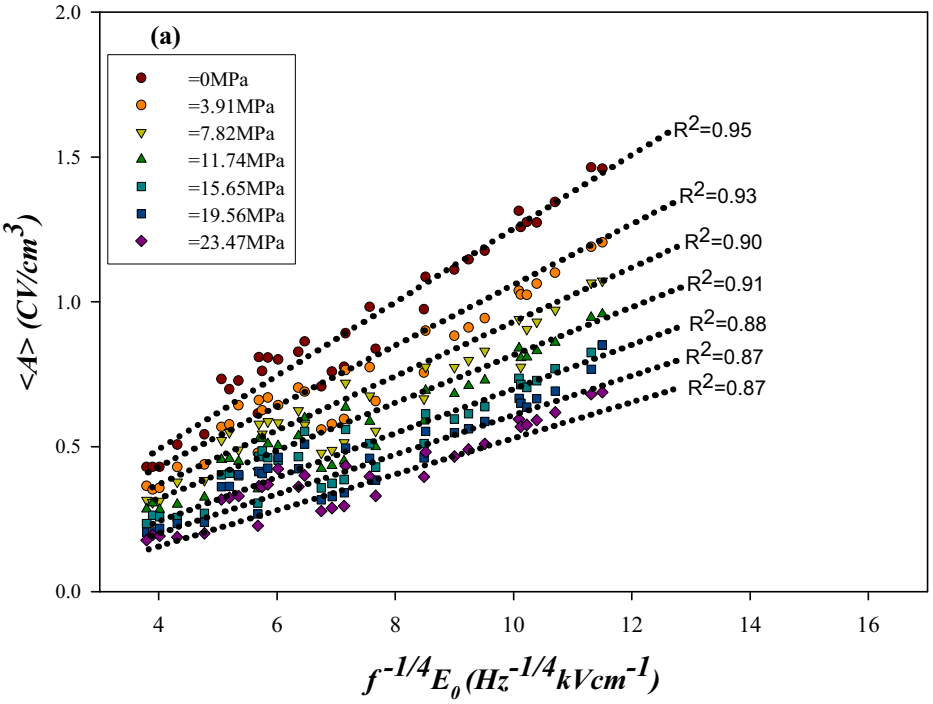
(a)
=0MPa
=3.91MPa
=7.82MPa
=11.74MPa
=15.65MPa
=19.56MPa
=23.47MPa
R2=0.95
R2=0.93
R2=0.90
R2=0.91
R2=0.88
R2=0.87
R2=0.87
<A> (CV/cm3)
f-1/4E0 (Hz-1/4kVcm-1)
0.0
0.5
1.0
1.5
2.0
4
6
8
10
12
14
16

Fig. 3(b)

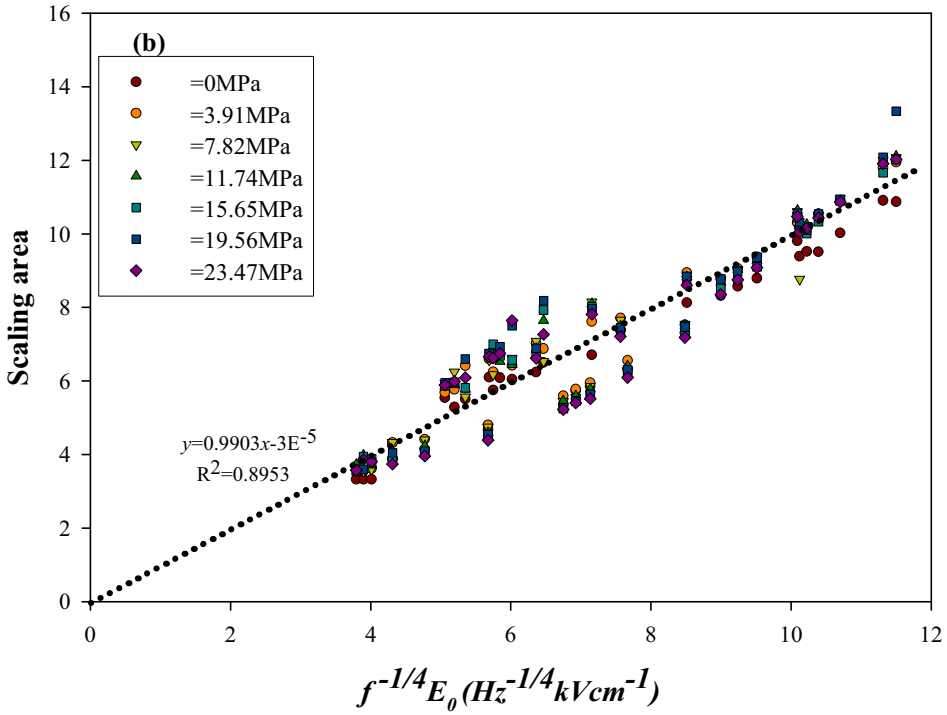
(b)
=0MPa
=3.91MPa
=7.82MPa
=11.74MPa
=15.65MPa
=19.56MPa
=23.47MPa
y=0.9903x-3E-5
R2=0.8953
Scaling area
f-1/4E0 (Hz-1/4kVcm-1)
0
2
4
6
8
10
12
14
16

Effect of Addition of BT on Relaxor Behavior of PIN-PT Ceramics

Supattra Wongsaenmai*[1], Rattikorn Yimnirun[1], Supon Ananta[1], Ruyan Guo[2] and Amar S. Bhalla[2]
[1]Department of Physics, Faculty of Science, Chiang Mai University, Chiang Mai 50200, Thailand
Tel: (6653)-943445, e-mail: wongsaenmai@yahoo.com
[2]Materials Research Laboratory, The Pennsylvania State University, University Park, PA 16802, USA
Tel: (1814)-8659232, e-mail: asb2@psu.edu

ABSTRACT: Ferroelectric ceramics with chemical formula $(1-x)Pb(In_{0.5}Nb_{0.5})O_3$-$(x)PbTiO_3$ and $(1-x)Pb(In_{0.5}Nb_{0.5})O_3$-$(x)PbTiO_3$ with 20 %mol of BT (x = 0.0, 0.1, 0.2 and 0.3) were prepared via the wolframite method. The relaxor behavior was analyzed from the dielectric properties and thermal expansion measurements. The dielectric properties were measured at frequencies between 100 Hz and 100 kHz whereas the thermal expansion was measured in the temperature range between -145°C and 500°C. It is found that the addition of BT effects the relaxor behavior of PIN-PT system. The broad and diffused dielectric constant maxima and essentially no change in Burns temperature were measured and thus suggesting the glassy polarization and relaxor behavior in the PIN-PT-BT compositions.

Keywords: PIN-PT, PIN-PT-BT, Relaxor ferroelectric, Thermal expansion, Dielectric properties

INTRODUCTION

The relaxor ferroelectric ceramics, which have the $Pb(B'B'')O_3$ complex perovskite structure, show broad dielectric transition maxima, high dielectric constant over a wide temperature range and frequency dispersion of dielectric properties [1-4]. Several models have been proposed to explain the relaxor behavior. However these models explain some features of the relaxor behavior but none can fully explain all the interesting properties observed in this class of materials. The glassy polarization behavior of relaxor ferroelectric, has been considered by Burns and Dacol's and supported by the measurements of the optic index of refraction, n(T), dependence on the temperature [5-8]. The deviation from the linear n(T) was observed starting at Burns temperature (T_d) which is much higher than the dielectric transition temperature maxima (T_m). This behavior was interpreted in term of the local polar regions of dynamic polarization (P_d), randomly orientated, small sizes with small number of unit cells, which grow with the reducing temperature. The local polarization exists above the transition temperature while disappear or become unmeasurable above Burns temperature [9]. The other techniques like Raman scattering [9], neutron powder diffraction [10] and neutron elastic scattering [11], dynamic light scattering [12], dielectric measurements [13–15], including thermal expansion technique [16] have been used to measure Burns temperature and explain the relaxor glassy behavior. There are reports on the relaxor behavior analysis by using the thermal expansion measurement in other classic relaxor ferroelectric such as PMN-PT, PMN, PZN, PLZT and tungsten bronze structure family [6, 8, 17-20], but no reported data on the glass-like behavior of order-disorder relaxor ferroelectric like PIN-based system.

PIN is of interest for the study of chemical ordering in relaxor systems. It is a member of relaxor family with a 1:1 stoichiometric B-site ordering which can be brought from disordered state into ordered state by a thermal treatment [21]. The disordered state of PIN exhibits a typical relaxor behavior which shows a broad dielectric maximum near 66 ºC [22, 23]. In contrast, the ordered state shows an antiferroelectric behavior with a sharp change in dielectric constant vs. temperature measurements at 168 ºC [23, 24]. The solid solution of relaxor ferroelectric and normal ferroelectric PT has excellent piezoelectric and electrostrictive properties [25, 26]. It is reported that the addition of BT to PMN- and PZN-based systems helps

decrease T_m of the systems and at the same time stabilizes the perovskite structure [27, 28]. Interestingly, there has been no report for the PIN-PT-BT system.

In this paper, the relaxor behavior of PIN-PT and the PIN-PT systems with addition of BT were studied for their dielectric properties and thermal expansion behavior. The broad maxima at the phase transition of dielectric constant vs. temperature were analyzed. Thermal expansion behavior of both the systems was studied and it showed deviation from the linear relationship below the Burns temperature. The local polarization (glassy behavior) was calculated from the collected thermal strain data. Both the dielectric and thermal expansion measurements suggest that the addition of PT lead to the normal ferroelectric while the addition of BT leads to the more relaxor ferroelectric like behavior.

EXPERIMENTAL

The powders of $(1-x)Pb(In_{0.5}Nb_{0.5})O_3$-$(x)PbTiO_3$ and $(0.8-x)Pb(In_{0.5}Nb_{0.5})O_3$-$(x)PbTiO_3$-$0.2BaTiO_3$ (x = 0.0, 0.1, 0.2 and 0.3, abbreviated as PIN-PT and PIN-PT-BT, respectively) were synthesized by a two-step solid solution reaction method [29]. The wolframite $InNbO_4$ was first prepared from oxide powder of In_2O_3 and Nb_2O_5 [30]. Mixed powders were milled and calcined at temperature 1100ºC for 2 hours to obtain the intermediate precursor $InNbO_4$ [31]. The wolframite precursor was then mixed with reagent grade powder of PbO, TiO_2 for PIN-PT system and PbO, $BaCO_3$, TiO_2 for PIN-PT-BT system. Excess amount of PbO (2%) and In_2O_3 (2%) were added at this stage. The mixtures were milled again following the intermediate precursor stage. After drying, the mixtures were calcined at temperature between 800ºC and 1000ºC, 1050ºC and 1250ºC with soaking time of 2 hours for PIN-PT and PIN-PT-BT, respectively [32]. Pellets were pressed with the addition of 1% PVA. The pressed pellets were sintered with the soaking time of 2 hours in a double crucible configuration at temperature from 1100ºC to 1125ºC for PIN-PT system and 1250 to 1300ºC for PIN-PT-BT system. To prevent PbO loss, the pellets were buried in protective powders.

The temperature dependence of the dielectric properties was measured with an LCR meter (HP-4284A, Hewlett-Packard, Santa Clara, CA) in conjunction with an environmental chamber (9023, Delta Design, Poway, CA). A heating rate of 2ºC/min and frequencies of 100, 1k, 10k and 100k Hz were used during measurement.

For the thermal expansion measurement, first the ceramics were cut to rectangular bars with dimensions 5mm×1mm×1mm. The temperature dependent sample expansion (strain) was measured with a linear voltage-differential transformer (LVDT) dilatometer (Series 6500, theta industries, Inc., NY). A heating rate of 2ºC/min and temperature range between -145°C and 500°C, were used for the measurements.

RESULTS AND DISCUSSION

The temperature dependence of dielectric properties, at different frequencies of PIN-PT and PIN-PT-BT systems is shown in Fig.1. The plots show the broad and diffuse phase transition temperature maxima at various frequencies. The transition temperature maxima, (T_m), shift to higher side with increasing frequency whereas the maximum of dielectric loss does the contrary. For the PIN-PT system, the dielectric constant plots show the broad peak at composition x = 0.0 and x = 0.1, then gradually change to a sharper peak with increasing PT concentration. On the other hand, the system which has 20 %mol of BT, the dielectric constant plot is broader than that of PIN-PT with the same PT content. However, the changing to the sharper maxima was

also observed with increasing PT concentration. The frequency dispersion of the dielectric properties can also be viewed as the measure of relaxor behavior. Since $T_m = T_{m,\,100kHz} - T_{m,\,100Hz}$ can be used as a rough indication of the relaxor behavior, the various T_m are calculated for the compositions and are listed in Table I. It is clear that addition of PT results in smaller T_m and thus indicates the decreasing trend of relaxor behavior and increasing fine disorder at B-site with increasing PT content [33] while with the addition of BT, T_m increases and hence the relaxor behavior. These results are in line obtained for the PT and BT additions to the PZN-based system [27].

The temperature dependences of thermal strain of PIN-PT and PIN-PT-BT ceramics are shown in Fig. 2 and 3. The plots show the nonlinear behavior at low temperature and then follow a linear relationship above Burns temperature. There is no clear correlating anomaly of the thermal expansion with the dielectric transition temperature. This behavior differs from that of normal ferroelectric which shows an abrupt discontinuity at the transition temperature and then follows linear behavior above the transition temperature in the paraelectric region. The deviation from the linear relationship below Burns temperature was observed for all the compositions. The values of Burns temperatures between 380°C to 435°C depending on the PT concentration were determine from the plots and are listed in Table II. It shows that in most cases Burns temperature is much higher than the dielectric transition maxima temperature, T_m, as observed in other relaxor ferroelectrics [7]. Also it shows that the differential between transition temperature and Burns temperature decreases with increasing PT content. For the normal ferroelectric the deviation from the straight line appears at the transition temperature for the measurements like refractive index vs. temperature and thermal strain vs. temperature [34]. The increase in Burns temperature and T_m due to the addition of PT was attributed to the higher T_c of PT [35] but; the increase of PT concentration leads to the closeness of the two transition temperatures i.e. T_m and T_d as we approach the morphotropic phase boundary (MPB) composition in PIN-PT. This result leads to the conclusion that relaxor ferroelectric nature in PIN ceramics reduces with increasing PT concentration. The PIN-PT-BT compositions show lower Burns temperature compared to the same PT concentration. From these results, it is noticed that PIN-PT-BT system is of more relaxor in nature than the PIN-PT system. From the dielectric and thermal strain results, it is suggested that addition of PT leads the behavior towards a normal ferroelectric while addition of BT leading to an enhancement in relaxor behavior.

At high temperature above Burns temperature the strain and temperature shows a linear relation. The thermal expansion coefficient ( ) defined as $\alpha_T \quad dx_T / dT$ [34], were calculated at above and below T_d and are listed in Table II. These results show small thermal expansion coefficient values and compare well with reports on other relaxor ferroelectrics [11]. The plots of thermal expansion coefficient vs. temperature, as obtained from the measurements are shown in Fig 4. The nearly linear relation between thermal expansion coefficient and temperature above Burn temperature, which decreases rapidly below Burns temperature, is evident. At composition x = 0.3, PIN-PT twice the change in slope below the Burn temperature is noticed. It is possibly due to the morphotropic phase boundary transitions in this composition which is supposed to have shown a MPB transitions. On the other hand, such abrupt change has not been observed in case of PIN-PT-BT system. It is possibly due to the addition of BT and as a result shifting of the morphotropic phase boundary of PIN-PT.

The deviations from the straight line at Burns temperature was due to the slow down of the glassy polarization effect which occur from charge differences of

ions on the B-site which are highly disordered and dynamic leading to the strongly breaking of the translational symmetry above the T_d [7]. The glassy polarization phase with local polarization (P_d) slowed down substantially below Burns temperature. Due to the dynamic nature, there is no resultant local polarization (P=0) above transition temperature, T_m, but there is a finite value as non zero square of polarization ($\overline{P}^2$?0). The dynamic local polarizations above transition temperature can be calculated through the relation of thermal expansion with the local polarization as shown below:

$$x_{11} \quad \alpha(T \quad T_0) \quad (Q_{11} \quad 2Q_{12})P^2 \tag{1}$$

Where α is the thermal expansion coefficient, T_0 is the reference temperature and Q_{11} and Q_{12} are the electrostrictive coefficients [35]. For the calculations, the electrostrictive coefficients of $PbTiO_3$ were used [36] as the electrostrictive coefficients in general are small and are almost of the same order in most perovskite structures.

The calculated values of the local polarization, P_d, of PIN-PT and PIN-PT-BT ceramics are shown along with the temperature dependence of the reversible spontaneous polarization obtained from the hysteresis measurement, in Fig. 5. The local polarization shows slowly decreasing pattern to zero at Burns temperature while the reversible polarization becomes almost zero at the dielectric transition temperature. This behavior of reversible polarization shows some gradual decrease near transition temperature where the micro clusters undergoes the higher dynamic state and redistribution of the polar nano-regions. The local polarization derived from the $\overline{P}^2$ values slows a decrease with the temperature and finally leads to zero at the Burns temperature. From the figure, the local polarization of PIN-PT-BT is higher than that of PIN-PT implies that the addition of BT strongly breaks the translation symmetry leading to a more glassy polarization phase than in the PIN-PT system. These results suggest that the addition BT to PIN-PT system leads to the enhanced relaxor behavior.

CONCLUSION

Ferroelectric ceramics with chemical formula $(1-x)Pb(In_{0.5}Nb_{0.5})O_3$-$(x)PbTiO_3$ and $(0.8-x)Pb(In_{0.5}Nb_{0.5})O_3$-$(x)PbTiO_3$-0.2BT (x = 0.0, 0.1, 0.2 and 0.3) were prepared via the wolframite method. The relaxor behavior in the two systems was analyzed from the dielectric properties and thermal expansion measurement. The dielectric properties were measured at frequencies between 100 Hz and 100 kHz whereas the thermal expansion data was collected in the temperature range between -145°C and 500°C. The broad and diffuse dielectric constant maximum show that both systems are relaxor ferroelectrics and the glassy polarization behavior differs in two systems. The glassy polarization as calculated from the thermal expansion measurements suggest that there is an enhanced relaxor behavior in the PIN-PT-BT system as a result of the addition of BT in PIN-PT.

ACKNOWLEDGEMENTS

This work was supported by the Thailand Research Fund (TRF), Commission on Higher Education (CHE), Graduate School of Chiang Mai University and Ministry of

University Affairs in Thailand. The authors are also thankful for the support from NSF/DMR through the relaxor and metamaterials grants.

REFFERENCES

1. R. E. Newnham and S. Trolier-Mckinstry, *Ceramic Transcations, 32, J. Amer. Ceram. Soc.,* **32**, 1 (1993).
2. T. R. Shrout and A. Halliyal, *Am. Ceram. Soc. Bull*., **66(4)**, 704 (1987).
3. Y. Yoshikawa, *J. Eur. Ceram. Soc.,* **21**, 2041 (2001).
4. K. Nomura, T. Shingai, S-I. Ishino, H. Terauchi, N. Yasuda and H. Ohawa, *J. Phys. Soc. Jpn.*, **68(1)**, 39 (1999).
5. G. Burns and F. H. Dacol, *Solid. State. Commun.,* **42[1]**, 9 (1982).
6. G. Burns and F. H. Dacol, *Phys. Rev.B,* **28[5]**, 2527 (1983).
7. G. Burns and F. H. Dacol, *Solid. State. Commun.,* **48[10]**, 853 (1983).
8. G. Burns and F. H. Dacol, *Ferroelectrics,* **52**, 103 (1983).
9. G. Burns, F. H. Dacol, *Solid State Commun*., **58**, 567 (1986).
10. J. Zhao, A. E. Glazounov, Q. M. Zhang, B. Toby, *Appl. Phys. Lett*., **72**, 1048 (1998).
11. D. La-Orauttapong, J. Toulouse, Z.-G. Ye, W. Chen, R. Erwin, J. L. Robertson, *Phys. Rev. B,* **67**, 134110 (2003).
12. W. Kleemann, P. Licinio, T. Woike, R. Pankrath, *Phys. Rev. Lett.,* **86**, 6014 (2001).
13. D. Viehland, S. J. Jang, L. E. Cross, M. Wuttig, *Phys. Rev. B* ,**46**, 8003 (1992).
14. V. Bovtun, J. Petzelt, V. Porokhonskyy, S. Kamba, Y. Yakimenko, *J. Eur. Ceram. Soc*., **21**, 1307 (2001).
15. J. Dec, W. Kleemann, V. Bobnar, Z. Kutnjak, A. Levstik, R. Pirc, R. Pankrath, *Europhys. Lett*., **55**, 781 (2001).
16. A. S. Bhalla, R. Guo, L. E. Cross, G. Burns, F. H. Dacol and R. R. Neurgaonkar, *Ferroelectrics*, **106**, 161 (1990).
17. A. S. Bhalla, R. Guo, L. E. Cross, G. Burns, F. H. Dacol and R. R. Neurgaonkar, *Phys. Rev. B*, **36(4)**, 2030 (1987).
18. H. Arndt and G. Schmidt, *Ferroelectrics,* **79**, 149 (1988).
19. G. Burns and F. H. Dacol, *Ferroelectrics,* **104**, 25 (1990).
20. M. V. Gorev, I. N. Flerov, P. H. Sciau, V. S. Bondarev and A. G. LehMann, *Ferroelectrics,* **307**, 127 (2004).
21. C. A. Randall and A. S. Bhalla, *Jpn. J. Appl. Phys*., **29[2]**, 327 (1990).
22. E. F. Alberta and A. S. Bhalla, *Mater.Lett*., **29**, 127 (1996).
23. E. F. Alberta and A. S. Bhalla, *J. Phys. Chem. Solids*., **63**, 1759 (2002).
24. M. Iwata, S. Katagiri, H. Orihara, M. Maeda, I. Zusuki, H. Ohwa, N. Yasuda and Y. Ishibashi, *Ferroelectrics*., **301**, 179 (2004).
25. S-E. Park, T.R. Shrout, *IEEE Trans. Ultrason. Ferroelectri. Freq. Control*., **44**, 1298 (1997).
26. S-E. Park, T.R. Shrout, *Mater. Res. Innovat*., **1**, 20 (1997).
27. A. Halliyal, U. Kumar, R.E. Newnham and L.E. Cross, *J. Am. Ceram. Soc*., **70[2]**, 119 (1987).
28. Y. S. Cho, S. M. Pilgrim, H. Giesche and K. Bridger, *J. Am. Ceram. Soc*., **10**, 2473 (2000).
29. S. Wongsaenmai, S. Ananta and R. Yimnirun, *J. Mater. Sci.*, (2006) accepted.
30. S. Wongsaenmai, S. Ananta and R. Yimnirun, *Mater. Letter.,* (2006) inpress.
31. S. Wongsaenmai, O. Khamman, S. Ananta. and R. Yimnirun, *J. Electroceram*., (2006) accepted.
32. N. Yasuda and M. Fujie, *Jnp. J. Appl. Phys*., **31**, 3128 (1992).
33. C. Lei, K. Chen, X. Zhang and J. Wang, *Solid. State. Commun*., **123**, 445 (2002).

34. G. Burns, *Phase Transition*, **5**, 261 (1985).
35. V. Mueller, L. Läger, H. Beige, H-P. Abicht and Thomas Müller, *Solid. State. Commun.,* **129**, 757 (2004).
36. L. E. Cross, S. J. Jang. R. E. Newhnam, S. Nomura and K. Uchino, *Ferroelectrics*, **23**, 187 (1980).

Table I Dielectric properties of PIN-PT and PIN-PT-BT systems.

Composition	$_m$ at 1 kHz	T_m (°C) at 1 kHz	T_m (°C)
(1-x)PIN-(x)PT:			
x = 0.0	4308	70	26
x = 0.1	6823	144	14
x = 0.2	12752	208	6
x = 0.3	15963	279	1
(0.8-x)PIN-(x)PT-0.2BT:			
x = 0.0	7591	26	30
x = 0.1	8093	85	19
x = 0.2	17366	130	15
x = 0.3	18541	155	8

Table II Thermal expansion P_d, P_s, T_d and T_m of various compositions PIN-PT PT and PIN-PT-BT systems

Composition	T_d (°C)	T_m (°C)	$T_d - T_m$ (°C)	Properties at room temperature		
				$\times 10^{-6}$ ($°C^{-1}$)	P_s C/cm^2)	P_d C/cm^2)
(1-x)PIN-(x)PT:						
x = 0.0	380	70	310	2.2	7.6	16.0
x = 0.1	391	144	247	2.9	15.2	17.7
x = 0.2	420	208	212	3.4	18.7	19.9
x = 0.3	435	279	156	4.0	23.3	24.1
(0.8-x)PIN-(x)PT-0.2BT:						
x = 0.0	360	26	334	1.1	6.1	18.0
x = 0.1	383	85	298	1.3	13.4	21.1
x = 0.2	400	130	270	1.6	23.5	24.5
x = 0.3	416	155	261	1.8	27.9	28.2

List of Figure Captions

Fig.1 Temperature dependence of the dielectric constant and dielectric loss of (a) PIN, (b) 0.8PIN-0.2PT, (c) 0.8PIN-0.2BT and (d) 0.6PIN-0.2PT-0.2BT.

Fig.2 Temperature dependence of thermal expansion and T_d for PIN-PT system.

Fig.3 Temperature dependence of thermal expansion and T_d for PIN-PT-BT system.

Fig.4 Temperature dependence of thermal expansion coefficient (for PIN-PT system (a) x = 0.0, (b) x = 0.3 and PINPT-BT which (c) x = 0.0 and (d) x = 0.3.

Fig.5 The comparison of P_d and P_s of both PIN-PT and PIN-PT-BT systems which (a) x = 0.0, (b) x = 0.1, (c) x = 0.2 and (d) x = 0.3.

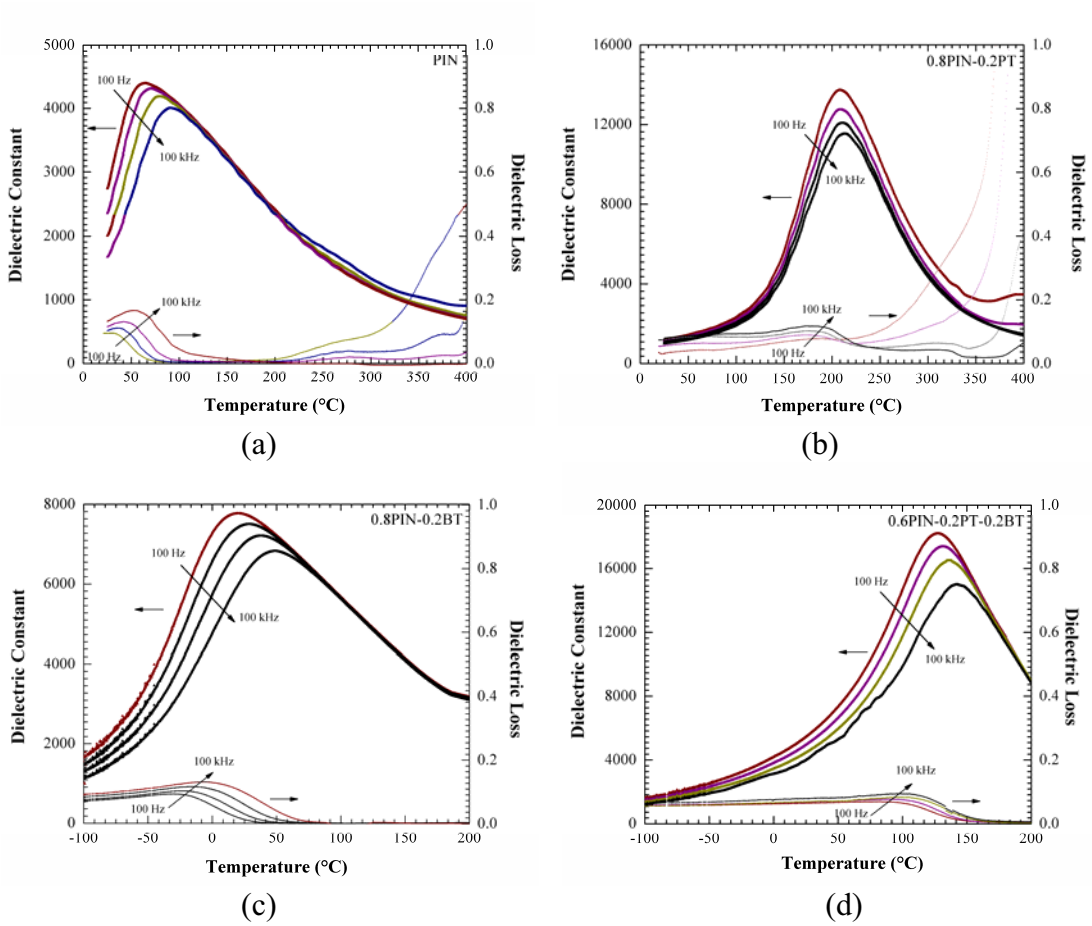
PIN
0.8PIN-0.2PT
0.8PIN-0.2BT
0.6PIN-0.2PT-0.2BT
Dielectric Constant
Dielectric Loss
Temperature (°C)
100 Hz
100 kHz
(a)
(b)
(c)
(d)

Fig.1

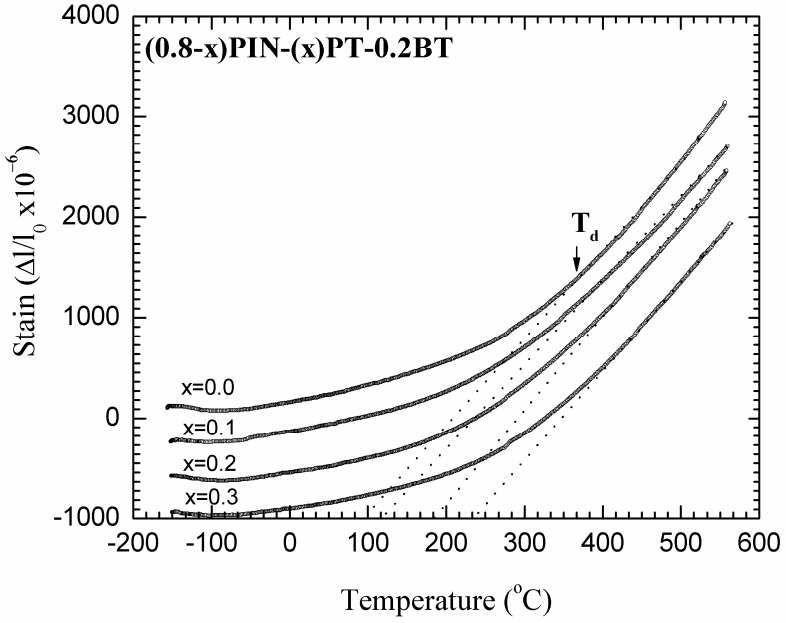
(0.8-x)PIN-(x)PT-0.2BT
Stain ($\Delta l/l_0$ x10^{-6})
Temperature (^{o}C)
T_d
x=0.0
x=0.1
x=0.2
x=0.3
4000
3000
2000
1000
0
-1000
-200
-100
0
100
200
300
400
500
600

Fig.2

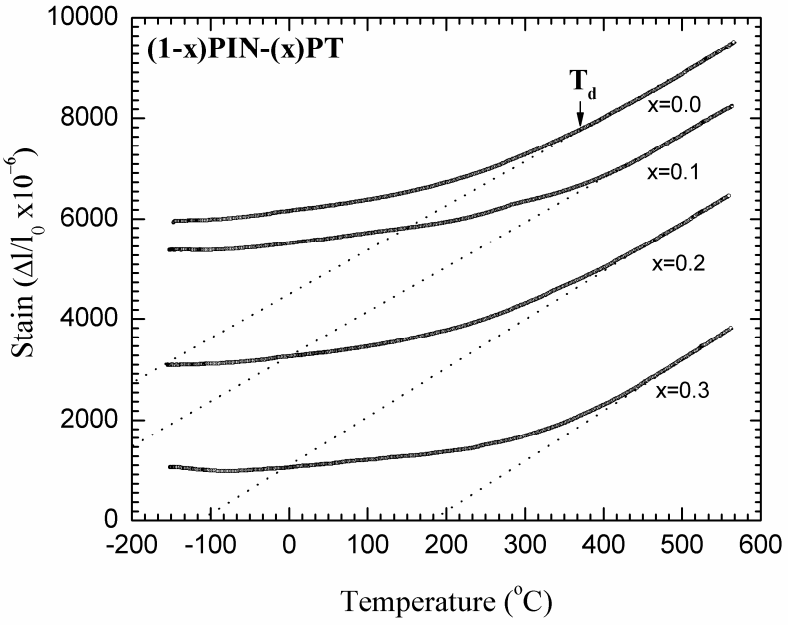
(1-x)PIN-(x)PT
T_d
x=0.0
x=0.1
x=0.2
x=0.3
Stain (Δl/l_0 x10^-6)
Temperature (°C)
10000
8000
6000
4000
2000
0
-200
-100
0
100
200
300
400
500
600

Fig. 3

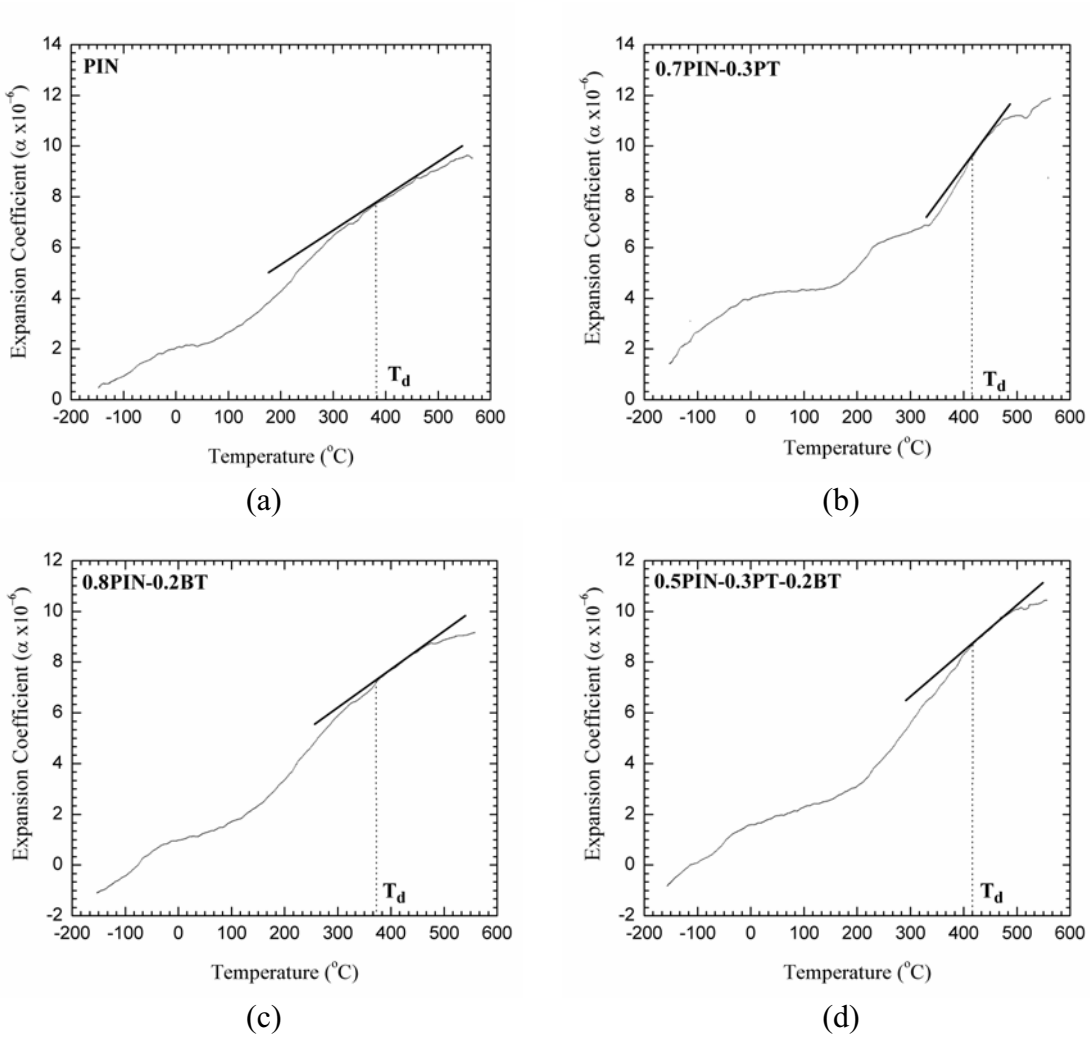
PIN
0.7PIN-0.3PT
0.8PIN-0.2BT
0.5PIN-0.3PT-0.2BT
Expansion Coefficient (α x10⁻⁶)
Temperature (°C)
T_d
(a)
(b)
(c)
(d)

Fig.4

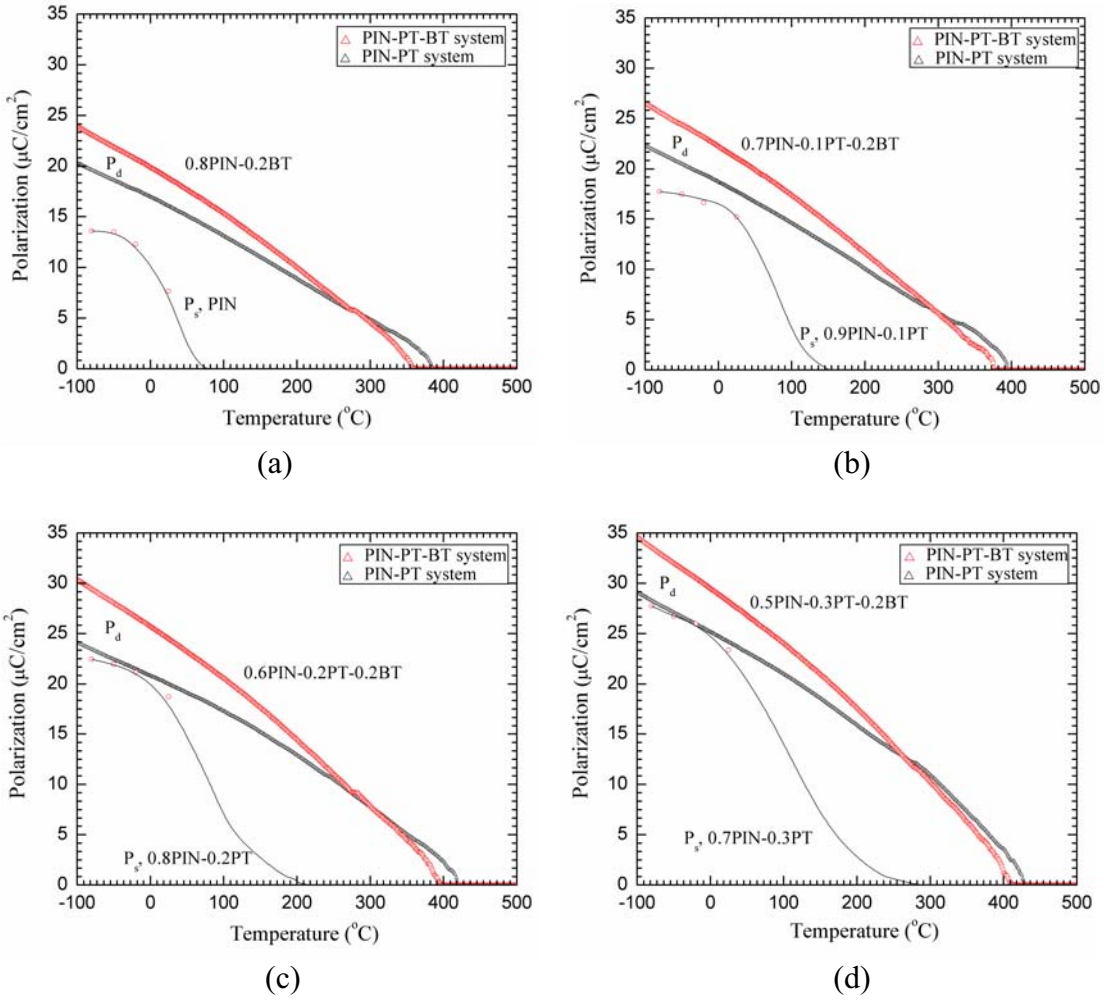
PIN-PT-BT system
PIN-PT system
P_d
0.8PIN-0.2BT
P_s, PIN
Polarization (μC/cm²)
Temperature (°C)
(a)
PIN-PT-BT system
PIN-PT system
P_d
0.7PIN-0.1PT-0.2BT
P_s, 0.9PIN-0.1PT
Polarization (μC/cm²)
Temperature (°C)
(b)
PIN-PT-BT system
PIN-PT system
P_d
0.6PIN-0.2PT-0.2BT
P_s, 0.8PIN-0.2PT
Polarization (μC/cm²)
Temperature (°C)
(c)
PIN-PT-BT system
PIN-PT system
P_d
0.5PIN-0.3PT-0.2BT
P_s, 0.7PIN-0.3PT
Polarization (μC/cm²)
Temperature (°C)
(d)

Fig.5

Dielectric Properties and Relaxor Behavior of PIN Based System

Supattra Wongsaenmai*[1], Supon Ananta[1], Rattikorn Yimnirun[1], Ruyan Guo[2]and Amar S. Bhalla[2]
[1]Department of Physics, Faculty of Science, Chiang Mai University, Chiang Mai 50200, Thailand
Tel: (6653)-943367, e-mail: wongsaenmai@yahoo.com
[2]Materials Research Laboratory, The Pennsylvania State University, University Park, PA 16802, USA
Tel: (1814)-8659232, e-mail: asb2@psu.edu

ABSTRACT: Several compositions in the two PIN based systems (1-x)$Pb(In_{0.5}Nb_{0.5})O_3$-(x)$PbTiO_3$ and (0.8-x)$Pb(In_{0.5}Nb_{0.5})O_3$-(x)$PbTiO_3$-0.2$BaTiO_3$ (x = 0.0, 0.1, 0.2 and 0.3) were synthesized via the wolframite method. Dielectric properties were measured in the frequency range between 100 Hz and 100 kHz and were analyzed for understanding relaxor behavior in the system. The temperature dependence of the dielectric properties was analyzed by studying the deviation from the Curie-Weiss law while the frequency dependence of the dielectric properties was analyzed by the Vogel-Fulcher relation. The results showed that the addition of BT increased the dielectric constant and decreased the shift of the maximum dielectric constant temperature (T_m) of (1-x)PIN-(x)PT compositions. Finally, the analysis also confirmed that, when added to PIN, PT decreased and BT increased the relaxor behavior of the PIN-based ceramics.

Keywords: PIN-PT, PIN-PT-BT, Dielectric Properties, Curie Weiss Law, Vogel-Fulcher Relation

INTRODUCTION

The relaxor ferroelectric ceramics, which have the $Pb(B'B'')O_3$ complex perovskite structure, show broad ($_r$ vs. T) transitions, high dielectric constant frequency dispersion of dielectric properties [1-4] over a wide temperature range. These excellent properties persuaded various researchers to investigate these behaviors for high performance applications. Several models have been proposed to explain these relaxor behaviors. The composition fluctuation model proposed by Smolenskii [5] suggests that the different local Curie temperatures lead to broad diffuse phase transition. Cross proposed the polarization mechanism analogous to the superparamagnetic clusters in magnetic materials [6]. This model considered no interaction between each polar nano-regions or clusters. The clusters have two states of polarization orientation separated by energy barrier. The thermal energy affects the flipping of polarization reorientation; therefore frequency of flipping can be explained by an Arrhenius equation:

$$\varpi \quad \varpi_0 \exp \frac{E_a}{kT} \tag{1}$$

where E_a is the activation energy for flipping, ϖ_0 is the Debye frequency and T is the absolute temperature. The broad distribution and frequency dispersion of dielectric properties originate from slowing down of polarization reorientation in each cluster. The interaction between clusters can be analogous with magnetic spin glass model [7]. The freezing temperature was defined as the macroscopic polarization emergence. The relation of this was fitted with Vogel-Fulcher equation:

$$\varpi \quad f_0 \exp \frac{E_a}{k(T_m \quad T_f)} \tag{2}$$

where f_0, E_a and T_f are the Debye frequency, the activation energy and the static freezing temperature, respectively [7]. Though these models attempted to explain the relaxor behavior, none can completely explain their interesting properties.

PIN is of interest for its chemical ordering study. It is a member of relaxor family with a 1:1 stoichiometric of B-site ordering which can be brought from disordered state into ordered state by thermal treatment [8]. The disordered state of PIN exhibits relaxor behavior which shows broad dielectric maximum near 66 ºC [9, 10]. In contrast, the ordered state shows antiferroelectric behavior with a sharp peak in dielectric constant vs. temperature curve observed at 168 ºC [10, 11]. The solid solution of relaxor ferroelectric and normal ferroelectric PT has excellent piezoelectric and electrostrictive properties [12, 13]. The electrostrictive property with no hysteresis and low mechanical loss above the temperature of maximum dielectric constant (T_m) of ceramics has been considered for high performance application devices such as electostrictive transducer and actuator. It has been reported that the PIN-PT system has high temperature performance of electromechanical coupling factor at temperatures up to 200 ºC [14]. However, the most applications have generally been at near room temperature, thus it is also important to look for the new systems which have T_m near room temperature and at the same time maintain their low hysteresis behavior. From the published literature, it was noticed that the addition of BT to PMN- and PZN-based systems helps decrease T_m of the systems and at the same time stabilizes the perovskite structure [15, 16]. There have been no details or reports for the characteristic of PIN-PT-BT system.

In this paper, the relaxor behaviors of PIN-based system have been reported. The dielectric properties have been measured in PIN-PT and PIN-PT-BT complex systems. It was anticipated that an addition of PT would increase the dielectric properties whereas added BT could shift T_m closer to room temperature and increase disorder phase leading to extended relaxor behavior.

EXPERIMENTAL

The powders of $(1-x)Pb(In_{0.5}Nb_{0.5})O_3$-$(x)PbTiO_3$ and $(0.8-x)Pb(In_{0.5}Nb_{0.5})O_3$-$(x)PbTiO_3]$-$0.2BaTiO_3$ (x = 0.0, 0.1, 0.2 and 0.3, abbreviated as PIN-PT and PIN-PT-BT, respectively) were synthesized by a two-step solid solution reaction method [17]. The wolframite $InNbO_4$ was first prepared from oxide powder of In_2O_3 and Nb_2O_5 [18]. Mixed powder was milled and calcined at temperature 1100ºC for 2 hours to obtain the intermediate precursor $InNbO_4$ [19]. The wolframite precursor was then mixed with reagent powder of PbO, TiO_2 for PIN-PT system and PbO, $BaCO_3$, TiO_2 for PIN-PT-BT system. Excess amount of PbO (2%) and In_2O_3 (2%) were added at this stage. The mixtures were milled again following the intermediate precursor stage. After drying, the mixtures were calcined at temperature between 800ºC and 1000ºC, 1050ºC and 1250ºC with soaking time of 2 hours for PIN-PT and PIN-PT-BT, respectively [20]. Pellets were pressed with 1% PVA. The pressed pellets were sintered with the soaking time of 2 hours in a double crucible configuration at temperature from 1100ºC to 1125ºC for PIN-PT system and 1250 to 1300ºC for PIN-PT-BT system. To prevent PbO loss, the pellets were buried in protective powders.

The temperature dependence of dielectric properties was measured with an LCR meter (HP-4284A, Hewlett-Packard, Santa Clara, CA) in conjunction with an environmental chamber (9023, Delta Design, Poway, CA). A heating rate of 2ºC/min and frequencies of 100, 1k, 10k and 100k Hz were used during measurement.

RESULTS AND DISCUSSION

The temperature dependences of dielectric constant at frequencies of 100 Hz to 100 kHz are shown in Figs. 1 and 2 for PIN-PT and PIN-PT-BT systems, respectively. The broad dielectric curves are observed for compositions x = 0.0 and 0.1, then changing slightly to sharper peak with further increase in PT contents. In addition, the frequency dispersion in their dielectric properties was also considered. Since $T_m = T_{m,100kHz}-T_{m,\ 100Hz}$ can be used as a rough estimate for more relaxor behavior with higher T_m, as listed in Table I, addition of PT results in smaller T_m. These results indicate the decreasing of relaxor behavior with increasing PT content [21]. Moreover, as shown in Fig, 2, the dielectric behavior of PIN-PT-BT system shows a stronger frequency dispersion and broader dielectric maximum than observed in PIN-PT system. This implies that addition of BT promotes the distribution of polar nano-regions and then leads to relaxor behavior while the addition of PT leads to normal ferroelectric. The parameters of dielectric properties are summarized in Table I, show that with the same PT content the dielectric constant of PIN-PT-BT ceramic is higher than that of PIN-PT ceramic. The addition of BT also decreases the maximum dielectric constant temperature (T_m), as clearly evident from a comparison between 0.8PIN-0.2PT and 0.8PIN-0.2BT with T_m of 208 ºC and 26 ºC, respectively. Similar effect of PT and BT additions on the dielectric properties of PZN-based system has been reported earlier [15].

It is known that in the normal ferroelectric ceramics the dielectric constant follows the Curie-Weiss law above temperature of maximum dielectric constant (T_m) whereas the relaxor ferroelectrics could follow the modified Curie Weiss behavior up to the temperature much higher than T_m [22]. The deviation from Curie-Weiss law can be shown to follow the Curie-Weiss square law [23] as

$$\frac{1}{\varepsilon} \quad \frac{1}{\varepsilon_m} \quad \frac{T \quad T_m}{C}^{\gamma} \tag{3}$$

where and C' are constants. With = 1 for normal ferroelectric, the equation (3) reduces to the normal Curie-Weiss law, while = 2 leads to the quadratic law for relaxor behavior. The plotting of ln(1/ -1/ $_m$) vs. ln(T-T_m) of both systems are shown in Figs.3 and 4. By fitting these graphs with equation (3), the parameter which indicates degree of relaxor behavior, is obtained from slopes of these plots, The empirical parameter of all compositions is listed in Table I showing the maximum values of = 1.89 and 1.98 at x = 0.0 and minimum value of = 1.66 and 1.82 at x = 0.3 for PIN-PT and PIN-PT-BT system, respectively. Decreasing trend of value with increasing of PT content observed in both systems agrees with the previous study [24]. However, PIN-PT-BT system shows higher value than that of PIN-PT system. This provides support for the observation in the early discussion that the addition of BT leads to increasing relaxor behavior.

The dependence of temperature of maximum dielectric constant (T_m) on frequency of PIN-PT and PIN-PT-BT systems was also fitted with Vogel-Fulcher equation. An example of the fitting curve is shown in Fig.5 with solid line indicating plotting of equation (2) and solid circles indicating the experimental data. This plot shows that the experimental data can be fitted with the Vogel-Fulcher equation which suggests that the relaxor behavior of PIN-PT and PIN-PT-BT systems follow the glass-like behavior. The Debye frequency, the activation energy and the static freezing temperature obtained by fitting the experimental data with equation (2) are

listed in Table II. Similar observation has also been reported in the case of other relaxor-based systems [25]. From equation (2), it is known that the activated energy is an internal energy (minus sign) of the cluster, which concerns with an anisotropy energy, K_{anis} and the cluster volume, V [23]. The fitting results show that the activation energy increases with increasing PT content for both systems, indicating that PT induces the increase of the anisotropic energy and influence the cluster volume. It can be implied that size of isolated cluster or ordering change with increasing PT contents. For relaxor ferroelectrics, the value of Debye frequency relate with size of polar nano-region and interaction between polar nano-regions. In general, the stronger interaction and larger size show the smaller of the Debye frequency value. However, the addition of BT shows larger Debye frequency and smaller activation energy, as compared to the PIN-PT system, indication of smaller ordering or existence of distribution of ordering. From the experimental result and fitting of Vogel-Fulcher relation, it can be implied that the increasing PT content shows marked effect in decreasing relaxor behavior by increasing interaction between polar nano-regions. Meanwhile, the addition of BT tends to increase the relaxor behavior in PIN-based system, in good agreement with the observations discussed earlier.

CONCLUSION

The (1-x)$Pb(In_{0.5}Nb_{0.5})O_3$-(x)$PbTiO_3$ and (0.8-x)$Pb(In_{0.5}Nb_{0.5})O_3$-(x)$PbTiO_3$-0.2$BaTiO_3$ (x = 0.0, 0.1, 0.2 and 0.3) ceramics were prepared via the wolframite method. The dielectric properties of the ceramics were investigated as functions of both temperature and frequency. The dielectric properties were measured at frequency between 100 Hz and 100 kHz and used for relaxor behavior analysis. The temperature dependence of the dielectric properties was analyzed by the deviation from the Curie-Weiss law while the frequency dependence of the dielectric properties was analyzed by the Vogel-Fulcher relation. The results showed broaden phase transition at x = 0.0 and 0.1 for both systems. From the Curie-Weiss square law fitting plots, the maximum values of of 1.89 and 1.98 were observed for PIN-PT and PIN-PT-BT systems, respectively, and the value decreases with increasing PT content. Moreover the addition of BT leads to an increase of the value. These observations implied that in PIN-based system the addition of BT leads to the relaxor behavior while the addition of PT leads to the normal ferroelectric. Moreover, the Vogel-Fulcher relation analysis showed that PIN-PT and PIN-PT-BT systems are relaxor ferroelectrics with glass-like behavior.

ACKNOWLEDGEMENTS

This work was supported by the Thailand Research Fund (TRF), Commission on Higher Education (CHE), Graduate School of Chiang Mai University, Ministry of University Affairs in Thailand, and NSF/DMR relaxor and metamaterials grants at MRI, Penn State USA.

REFFERENCES

1. R. E. Newnham and S. Trolier-Mckinstry, *Ceramic Transcations, 32, J. Amer. Ceram. Soc.,* **32**, 1 (1993).
2. T. R. Shrout and A. Halliyal, *Am. Ceram. Soc. Bull*., **66(4)**, 704 (1987).
3. Y. Yoshikawa, *J. Eur. Ceram. Soc.,* **21**, 2041 (2001).
4. K. Nomura, T. Shingai, S-I. Ishino, H. Terauchi, N. Yasuda and H. Ohawa, *J. Phys. Soc. Jpn.*, **68(1)** 39 (1999).
5. G. A. Smolenskii, *Jpn. J. Appl. Phys*., **28**, 1970 (1970).
6. L. E. Cross, *Ferroelectrics*, **76**, 246 (1987).
7. D. Viehland, S-J. Jang and L. E.Cross, *J. Appl. Phys*., **68[6]**, 2916 (1990).
8. C. A. Randall and A. S. Bhalla, *Jpn. J. Appl. Phys*., **29[2]**, 327 (1990).
9. E. F. Alberta and A. S. Bhalla, *Mater.Lett*., **29**, 127 (1996).
10. E. F. Alberta and A. S. Bhalla, *J. Phys. Chem. Solids*., **63**, 1759 (2002).
11. M. Iwata, S. Katagiri, H. Orihara, M. Maeda, I. Zusuki, H. Ohwa, N. Yasuda and Y. Ishibashi, *Ferroelectrics*, **301**, 179 (2004).
12. S-E. Park, T. R. Shrout, *IEEE Trans. Ultrason. Ferroelectri. Freq. Control*., **44**, 1298 (1997).
13. S-E. Park, T. R. Shrout, *Mater. Res. Innovat*., **1**, 20 (1997).
14. N. Yasuda, H. Ohwa, M. Kume and Y. Yamashita, *Jpn. J. Appl. Phys*., **39**, 5586 (2000).
15. A. Halliyal, U. Kumar, R. E. Newnham and L. E. Cross, *J. Am. Ceram. Soc*. **70[2]**, 119 (1987).
16. Y. S. Cho, S. M. Pilgrim, H. Giesche and K. Bridger, *J. Am. Ceram. Soc*. **10**, 2473 (2000).
17. S. Wongsaenmai, S. Ananta and R. Yimnirun, *J. Mater. Sci.*, (2006) accepted.
18. S. Wongsaenmai, S. Ananta and R. Yimnirun, *Mater. Letter.,* (2006) inpress.
19. S. Wongsaenmai, O. Khamman, S. Ananta. and R. Yimnirun, *J. Electroceram*., (2006) accepted.
20. N. Yasuda and M. Fujie, *Jnp. J. Appl. Phys*., **31**, 3128 (1992).
21. C. Lei, K. Chen, X. Zhang and J. Wang, *Solid. State. Commun*., **123**, 445 (2002).
22. K. Uchino and S. Nomura*, Ferroelectric Lett.*, **44**, 55 (1982).
23. D. Viehland, S-J. Jang, L. E.Cross and M. Wutting*, Phys. Rev.B*, **46[13]**, 8003 (1992).
24. M. Kuwabara, S. Takahashi, K. Goda, K. Oshima and K. Watanabe, *Jpn. J. Appl. Phys.*, **31**, 3241 (1992).
25. G. Singh, V. S. Triwari and V. K. Wadhawan, *Solid. State. Commun.,* **129**, 665 (2004).

Table I The dielectric properties and calculated parameters for PIN-PT and PIN-PT-BT systems.

Composition	$_m$ at 1 kHz	T_m (K) at 1 kHz	T_m (K)		C
(1-x)PIN-(x)PT:					
x = 0.0	4308	343	26	1.89	1.9×10^5
x = 0.1	6823	417	14	1.86	1.7×10^5
x = 0.2	12752	481	6	1.71	2.4×10^5
x = 0.3	15963	552	1	1.66	4.2×10^5
(0.8-x)PIN-(x)PT-0.2BT:					
x = 0.0	7591	299	30	1.98	5.6×10^5
x = 0.1	8093	358	19	1.90	10.4×10^5
x = 0.2	17366	403	15	1.87	12.6×10^5
x = 0.3	18541	428	8	1.82	16.1×10^5

$T_m = T_m(100Hz)-T_m(100kHz)$, C = calculated Curie constant value

Table II The parameters obtained from fitting Vogel-Fulcher equation for PIN-PT and PIN-PT-BT systems.

Composition	T_m (K) at 1 kHz	T_f (K)	T_m-T_f	f_0 (Hz)	$_a$ (eV)
(1-x)PIN-(x)PT:					
x = 0.0	343	268	75	4.4×10^{10}	0.051
x = 0.1	417	389	28	3.1×10^{10}	0.036
x = 0.2	481	467	14	2.7×10^{10}	0.024
x = 0.3	552	548	4	1.2×10^{10}	0.005
(0.8-x)PIN-(x)PT-0.2BT:					
x = 0.0	299	248	51	6.2×10^{10}	0.068
x = 0.1	358	316	42	4.7×10^{10}	0.057
x = 0.2	403	379	24	3.9×10^{10}	0.035
x = 0.3	428	414	14	2.6×10^{10}	0.020

List of Figure Captions

Fig.1 Temperature dependence of dielectric constant for (1-x)PIN-(x)PT system with (a) x = 0.0, (b) x = 0.1, (c) x = 0.2 and (d) x = 0.3.

Fig.2 Temperature dependence of dielectric constant at for (0.8-x)PIN-(x)PT-0.2BT system with (a) x = 0.0, (b) x = 0.1, (c) x = 0.2 and (d) x = 0.3.

Fig.3 Plots of ln(1/ -1/ $_m$) vs. ln(T-T_m) on (1-x)PIN-(x)PT system.

Fig.4 Plots of ln(1/ -1/ $_m$) vs. ln(T-T_m) on (0.8-x)PIN-(x)PT-0.2BT system.

Fig.5 Temperature of maximum dielectric as a function of frequency for 0.8PIN-0.2BT ceramic.

PIN-PT system

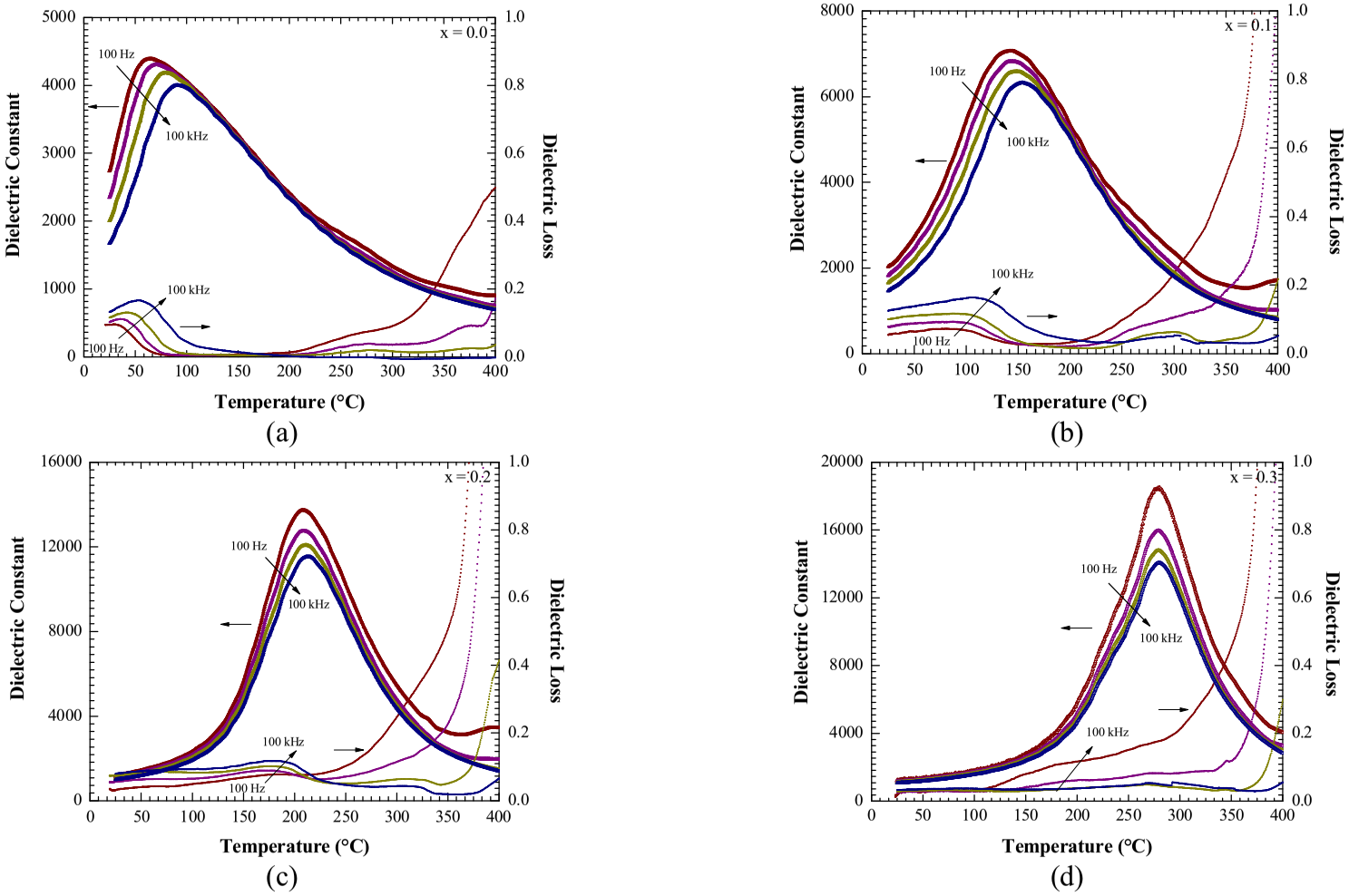

Fig. 1

PIN-PT-BT system

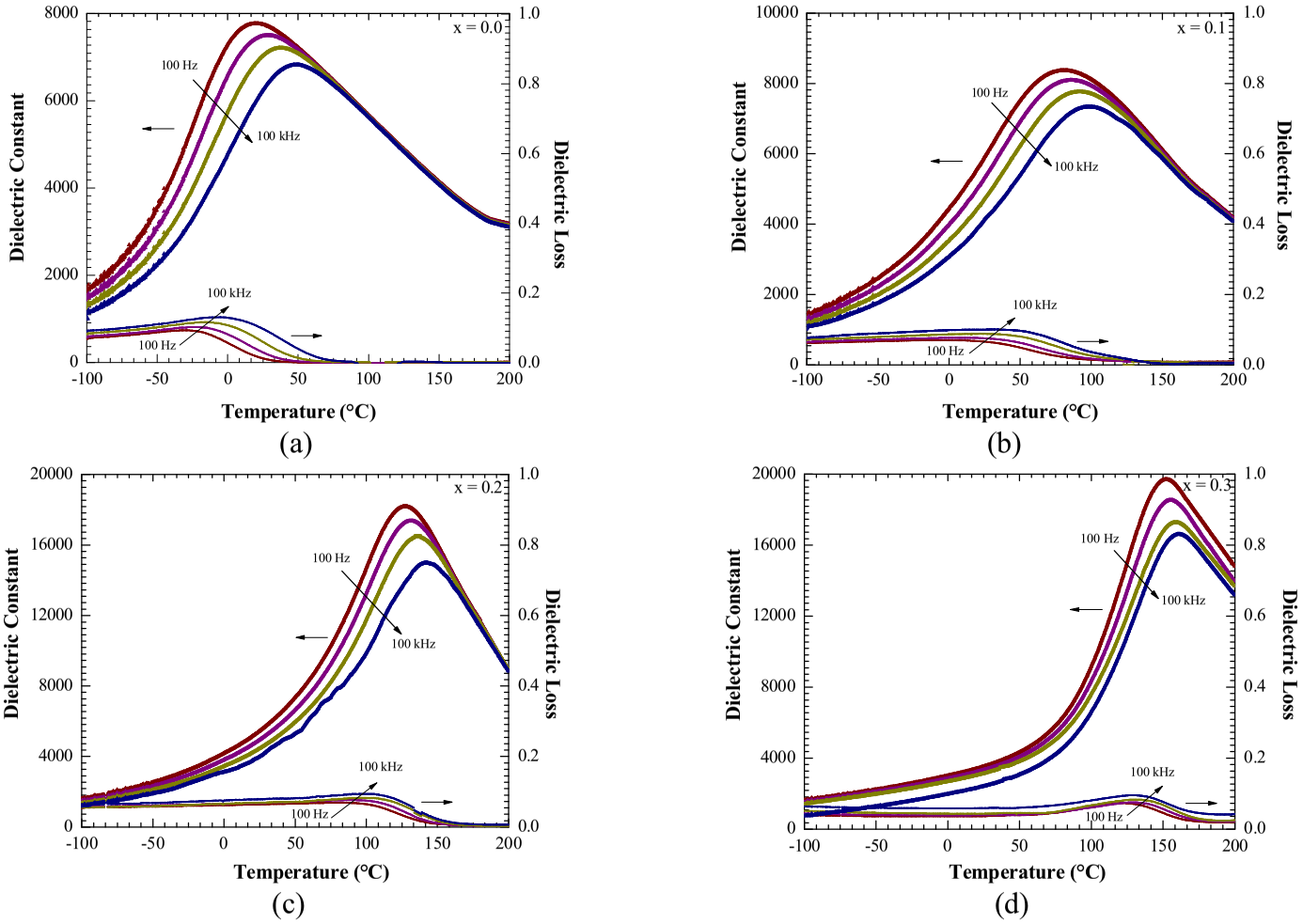

Fig.2

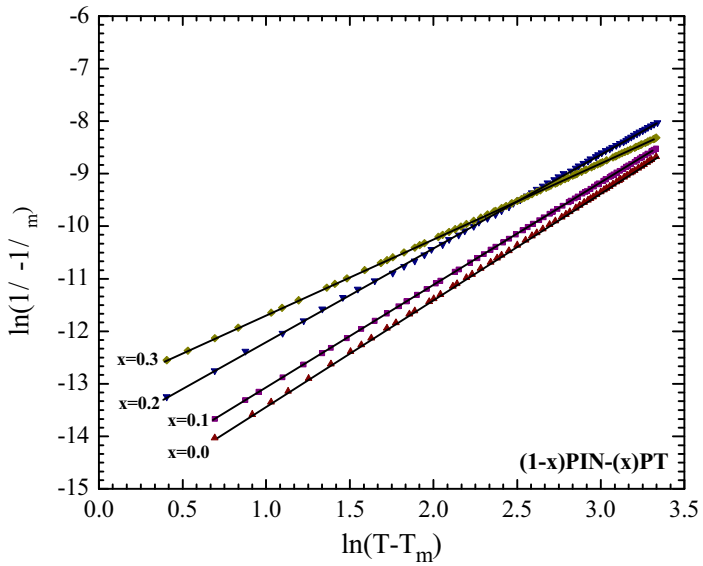
ln(1/ -1/ m)
ln(T-Tm)
x=0.3
x=0.2
x=0.1
x=0.0
(1-x)PIN-(x)PT

Fig.3

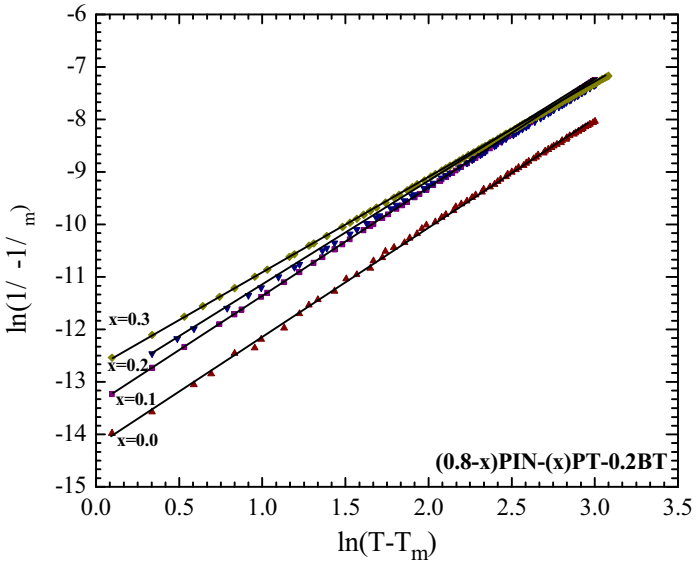
ln(1/ -1/ m)
ln(T-Tm)
x=0.3
x=0.2
x=0.1
x=0.0
(0.8-x)PIN-(x)PT-0.2BT

Fig.4

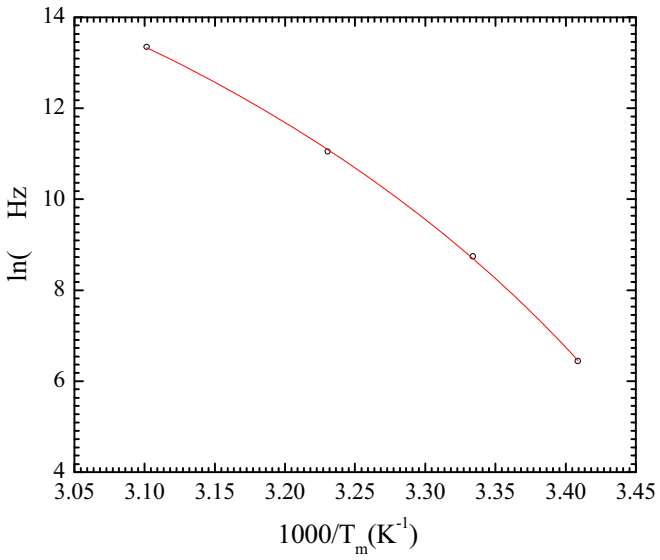

Fig.5

Editorial Manager(tm) for Journal of Materials Science
Manuscript Draft

Manuscript Number: JMSC5763R1

Title: Effects of Milling Time and Calcination Condition on Phase Formation and Particle Size of Lead Zirconate Nanopowders Prepared by Vibro-milling

Article Type: Manuscript

Section/Category:

Keywords: Lead zirconate; Perovskite; Nanopowders; Calcination; Phase formation

Corresponding Author: Dr. S. Ananta, PhD

Corresponding Author's Institution:

First Author: S. Ananta, PhD

Order of Authors: S. Ananta, PhD; O. Khamman; T. Sarakonsri; T. Sarakonsri; A. Rujiwatra; Y. Laosiritaworn; Rattikorn Yimnirun, PhD

Manuscript Region of Origin:

Abstract: Effect of calcination conditions on phase formation and particle size of lead zirconate ($PbZrO_3$) powders synthesized by a solid-state reaction with different vibro-milling times was investigated. A combination of the milling time and calcination conditions was found to have a pronounced effect on both the phase formation and particle size of the calcined $PbZrO_3$ powders. The calcination temperature for the formation of single-phase perovskite lead zirconate was lower when longer milling times were applied. More importantly, by employing an appropriate choice of the milling time and calcination conditions, single-phase $PbZrO_3$ nanopowders have been successfully prepared with a simple solid-state reaction method.

*** Response to Reviewer Comments**

Supon Ananta, Ph.D.
Associate Professor of Materials Science

Department of Physics, Faculty of Science
Chiang Mai University
Chiang Mai 50200 THAILAND

Telephone: (6653) 943-376
Fax: (6653) 357-512
E-mail:
suponananta@yahoo.com

February 1, 2007

Dear Editor;

Enclosed please find a *revised* manuscript being re-submitted for publication in **Journal of Materials Science**.

Based on very kind and useful comments from the reviewers on our submission, considerable changes have been incorporated into the revised manuscript (Marked in Red). The following points are responses (in bold) to the reviewer's comments;

COMMENTS FOR THE AUTHOR:

Reviewer #1: The authors report on the formation of PbZrO3 nanoparticles using Vibro-milling, and study the time-temperature range in which single phase PZ nanoparticles can be obtained. This peer reviewer find the data obtained in the said study useful as it delineates a commercially feasible way of preparing PZ nanoparticles. However, some improvements on the manuscript are called for. It is a well-established fact that ferroic nanoparticles undergo what is called a finite-size effect. Namely, at a certain particle size called the critical size, the high-temperature paraelectric phase is stabilized at room temperature. Prior reaching that size, the lattice paramaters as well as the paraelectric-ferroic phase transition temperature changes. Given these facts, the authors should do the following so as to enhance the interpretation of their data:

1) Plot lattice paramaters as a function of particle size for single phase powder and show systematic variation of the same with particle size

Fig.9 has been added to show these plots with discussions (in Pages 10-11).

2) Attempt to extrapolate from the smallest paricle size lattice parameter data so as to estimate a critical crystallite size.

The crystallite size is estimated from the plots in Fig. 9, as suggested (Pages 10-11).

3) If would also be desirable to show the variation of unit cell volume with decreasing particle size.

Fig.9 has been added to show these plots with discussions (in Pages 10-11).

4) Mention size effect phenomena that is already in the literature in relation to the work presented therein.

More discussions have been added to address this issue in Pages 10-11 with new references [21-29].

5) Clearly discuss that the nanoparticles are indeed polycrystalline and not single domain single crystalline as in the case of PbTiO3 nanoparticles reported in the literature. The comparison of X-ray crystallite size with SEM apparent crystalite size shows that the nanoparticles have imperfections (polycrystalline). Hence, comment on the possibility of introducing excess crystalline defects through milling.

More discussions have been added to address this issue in Pages 8-9.

6) Is it possible tha Vibro-milling causes local melting? For instance the 25 hrs sample in Fig 5 seems to show "necking" which is known to be thermally induced. The authors should clarify this point. Is there a hidden thermal history due to milling? If so, what is its extend?

More discussions have been added to address this issue in Page 9.

7) The abstract should also convey the important numerical results as well. Please do insert your most important results.

The abstract has been modified to include numerical results and important findings.

The authors should address these points, revise their manuscripts and then resubmit it for a second round of peer review.

All the issues have been addressed with proper references.

Reviewer #2: This paper reports a study on the effects of vibro milling (time) on the phase formation and particle characteristics of lead zirconate upon calcination at different temperatures. In the study, authors established a correlation between particle size and milling/calcination conditions. Although lead titanate has been widely investigated, the authors studied the correlations between processing conditions and the resulting particle characteristics in a rather systematic manner, which are of interest to the community working on electroceramic materials. I therefore recommend that the manuscript be published subject to minor improvement, as detailed as follows:

(1) Properly index all the main peaks for oxides and lead zirconate in figures 1-3, where some of the peaks are very close to each other;

Figs 1-3 have been properly modified, as suggested.

(2) The conclusion section is too short. Author shall list some details in the conclusion.

The abstract has been modified to include numerical results and important findings.

(3) Formation of pervoskite phase from mixed oxides by mechanical activation has been reported, for example, by S.E. Lee, et al, Acta Materialia, 47 (1999) 2633; and J.M. Xue, et al, Journal of the American Ceramic Society, 82 (1999) 1687, which shall be included in the introduction section, for a complete picture of the subject area.

This has been added in Introduction (refs. [9,10]).

Thank you very much for your valuable time and very kind consideration. Should you have any questions regarding the revised manuscript, please feel free to contact me. I am looking forward to hearing from you very soon.

Sincerely yours,

Supon Ananta
Department of Physics, Faculty of Science,
Chiang Mai University, Chiang Mai 50200
THAILAND
E-mail: suponananta@yahoo.com

*Corresponding author:
Dr. S. Ananta
Department of Physics,
Faculty of Science
Chiang Mai University
Chiang Mai 50200 Thailand
Tel: (00) 53 943367; fax: (00) 53 943445
E-mail: *suponananta@yahoo.com*

Effects of Milling Time and Calcination Condition on Phase Formation and Particle Size of Lead Zirconate Nanopowders Prepared by Vibro-milling

O. Khamman[a], T. Sarakonsri[b], A. Rujiwatra[b], Y. Laosiritaworn[a], R. Yimnirun[a] and S. Ananta[a*]

[a]*Department of Physics, Faculty of Science, Chiang Mai University, Chiang Mai 50200, Thailand*
[b]*Department of Chemistry, Faculty of Science, Chiang Mai University, Chiang Mai 50200, Thailand*

Abstract

Effect of calcination conditions on phase formation and particle size of lead zirconate ($PbZrO_3$) powders synthesized by a solid-state reaction with different vibro-milling times was investigated. A combination of the milling time and calcination conditions was found to have a pronounced effect on both the phase formation and particle size of the calcined $PbZrO_3$ powders. The calcination temperature for the formation of single-phase perovskite lead zirconate was lower when longer milling times were applied. The optimal combination of the milling time and calcination condition for the production of the smallest nanosized (~28 nm) high purity $PbZrO_3$ powders is 35 h and 750 °C for 4 h with heating/cooling rates of 30 °C/min, respectively.

Keywords: Lead zirconate; Perovskite; Nanopowders; Calcination; Phase formation

1. Introduction

Lead zirconate, $PbZrO_3$ or PZ, is one of the widely investigated antiferroelectric materials with a perovskite structure. The unique properties such as high transition temperature (~ 230 °C), free of remanant polarization and double hysteresis behaviour make it an interesting candidate for many applications especially for energy storage, low-loss linear capacitors, microelectronics and actuators [1,2]. There has been a great deal of interest in the preparation of single-phase PZ powders as well as in the sintering and electrical properties of PZ-based ceramics [2,3]. To fabricate them, a fine powder of perovskite phase with the minimized degree of particle agglomeration is needed as starting material in order to achieve a dense and uniform microstructure at the sintering temperature [1-3]. Some typical processes to synthesize perovskite lead-based powders are the microemulsion [4], the sol-gel technique [5], the co-precipitation [6], the hydrothermal reaction [7], mechanical activation [8,9], and the solid-state reaction or mixed oxides [10].

Recently, ultrafine powders (< 100 nm in diameter) are promising starting materials in the fabrication of advanced nanoceramics [2,3]. However, the evolution of a method to produce nano-sized powders of precise stoichiometry and desired properties is complex, depending on a number of variables such as starting materials, processing history, temperature, etc. The advantage of using a solid-state reaction method via mechanical milling for preparation of nano-sized powders lies in its ability to produce mass quantities of powder in the solid state using simple equipment and low cost starting precursors [11,12]. Although our earlier work has been done in the

preparation of PZ powders via a vibro-milling technique [13], a detailed study considering the role of both milling times and firing conditions on the preparation of PZ nanopowders has not been reported yet.

Therefore, the present work has been undertaken to investigate the effects of vibro-milling time together with calcination conditions on phase formation and particle size of lead zirconate powders synthesized by solid-state reaction method. The powder characteristics of the vibro-milling derived $PbZrO_3$ have also been thoroughly investigated.

2. Experimental procedure

The raw materials used were commercially available lead oxide, PbO (JCPDS file number 77-1971) and zirconium oxide, ZrO_2 (JCPDS file number 37-1484) (Fluka, > 99% purity). The two oxide powders exhibited an average particle size in the range of 3.0 to 5.0 μm. $PbZrO_3$ powder was synthesized by the solid-state reaction of these raw materials, in analogous with other similar lead-based perovskites as described in our previous works [12,14]. A McCrone vibro-milling technique [11,12] was employed for preparing the stoichiometric $PbZrO_3$ powders. In order to improve the reactivity of the constituents, the milling process was carried out for various milling times ranging from 15 to 35 h (instead of 30 min [13]) with corundum media in isopropanol. After drying at 120 °C for 2 h, various calcination conditions, i.e. temperature ranging from 550 to 800 °C, dwell times ranging from 1 to 6 h and heating/cooling rates ranging from 10 to 30 °C/min, were applied (the

powders were calcined in air inside a closed alumina crucible) in order to investigate the formation of $PbZrO_3$ [13].

All powders were subsequently examined by room temperature X-ray diffraction (XRD; Siemens-D500 diffractometer) using Ni-filtered CuK_α radiation, to identify the phases formed, optimum milling time and firing conditions for the production of single-phase $PbZrO_3$ powders. The crystalline lattice constants and average particle size were also estimated from the diffraction peak (240) of the perovskite pattern using Scherrer equation [15]. The particle size distributions of the powders were determined by laser diffraction technique (DIAS 1640 laser diffraction spectrometer) with the particle sizes and morphologies of the powders observed by scanning electron microscopy (JEOL JSM-840A SEM). The structures and chemical compositions of the phases formed were elucidated by transmission electron microscopy (CM 20 TEM/STEM operated at 200 keV) and an energy-dispersive X-ray (EDX) analyzer with an ultra-thin window. EDX spectra were quantified with the virtual standard peaks supplied with the Oxford Instrument eXL software. Powder samples were dispersed in solvent and deposited by pipette on to 3 mm holey copper grids for observation by TEM. In addition, attempt was made to evaluate the crystal structures of the observed compositions/phases by correcting the XRD and TEM diffraction data.

3. Results and discussion

Powder XRD patterns of the calcined samples after different milling times are given in Figs. 1-3, with the corresponding JCPDS patterns. As

shown in Fig. 1, for the uncalcined powder subjected to 15 h of vibro-milling and the powders calcined at 550 °C, only X-ray peaks of precursors PbO (•) and ZrO_2 (○) are present, indicating that no reaction was yet triggered during the vibro-milling or low firing processes, in agreement with literatures [13,16]. However, it is seen that crystalline phase of the perovskite $PbZrO_3$ (▼) was found as separated phase in the powders calcined at 600 °C, and became the predominant phase in the powders calcined at 700 °C. Further calcination at 800 °C with dwell time of 1 h does not result in very much increase in the amount of $PbZrO_3$ whereas the traces of unreacted PbO could not be completely eliminated. This could be attributed to the poor reactivity of lead and zirconium species [10,13]. However, it should be noted that after calcination at 800 °C for 2 h (Fig. 1 (f)), the single phase of perovskite $PbZrO_3$ (yield of 100% within the limitations of the XRD technique) was obtained. In general, the strongest reflections apparent in the majority of these XRD patterns indicate the formation of $PbZrO_3$. These can be matched with JCPDS file number 35-0739 for the orthorhombic phase, in space group *P2cb* (no. 32) with cell parameters *a* = 823.1 pm *b* = 1177 pm, and *c* = 588.1 pm [17], consistent with other works [7,13,16]. For 15 h of milling, the optimum calcination temperature for the formation of a high purity $PbZrO_3$ phase was found to be about 800 °C.

To further study the phase development with increasing milling times, an attempt was also made to calcine mixed powders milled at 25 h and 35 h under various conditions as shown in Figs. 2 and 3, respectively. In this connection, it is seen that by varying the calcination temperatures and dwell

times, the minimum firing temperature or dwell time for the single perovskite phase formation of each milling batch is decreased with increasing milling time (Figs. 1-3), in good agreement with other perovskite systems [12,14,18]. The main reason for this behavior is that a complete solid-state reaction probably takes place more easily when the particle size is milled down by accelerating an atomic diffusion mechanism to meet the suitable level of homogeneity mixing. It is thought that the reduction in the particle sizes significantly reduces heat diffusion limitations. It is therefore believed that the solid-state reaction to form perovskite $PbZrO_3$ phase occurs at lower temperatures or shorter dwell times with decreasing the particle size of the oxide powders [11,12].

As expected, there is evidence that, even for a wide range of calcination conditions, single-phase $PbZrO_3$ cannot easily be produced, in agreement with literatures [13,16]. In the work reported here, evidence for the minor phase of PbO which coexists with the parent phase of $PbZrO_3$ is found after calcination at temperature 600-750 °C, in agreement with literature [13,16]. This second phase has an orthorhombic structure with cell parameters a = 589.3 pm, b = 549.0 pm and c = 475.2 pm (JCPDS file number 77-1971) [19]. This observation could be attributed mainly to the poor reactivity of lead and zirconium species [13] and also the limited mixing capability of the mechanical method [11,12]. A noticeable difference is noted when employing the milling time longer than 15 h (Figs. 2 and 3), since an essentially monophasic $PbZrO_3$ of perovskite structure was obtained at 800 °C for 1 h or 750 °C for 6 h (or 4 h) for the milling time of 25 h (or 35 h). This was apparently a consequence of the enhancement in crystallinity of the

perovskite phase with increasing degree of mixing and dwell time, in good agreement with other works [12,18].

In the present study, an attempt was also made to calcine the powders with different milling times under various heating/cooling rates (Figs. 1-3). In this connection, it is shown that the yield of $PbZrO_3$ phase did not vary significantly with different heating/cooling rates ranging from 10 to 30 °C/min, in good agreement with the early observation for the $PbZrO_3$ powders subjected to 0.5 h of vibro-milling times [13]. The variation of calculated crystallite size of the $PbZrO_3$ powders milled for different times with the calcination conditions is given in Table 1. In general, it is seen that the calculated crystallite size of $PbZrO_3$ decreases with increasing heating/cooling rates for all different milling times. These values indicate that the particle size affects the evolution of crystallinity of the phase formed by prolong milling treatment. It should be noted that no evidences of the introduction of impurity due to wear debris from the selected milling process was observed in all calcined powders, indicating the effectiveness of the vibro-milling technique for the production of high purity $PbZrO_3$ nanopowders. Moreover, it has been observed that with increasing milling time, all diffraction lines broaden, e.g. (261) and (402) peaks, which are an indication of a continuous decrease in particle size and of the introduction of lattice strain (Fig. 4) [15].

For $PbZrO_3$ powders, the longer the milling time, the finer is the particle size (Fig. 4 and Table 1). Also the relative intensities of the Bragg peaks and the calculated crystallite size for the powders tend to decrease with the increase of milling time. However, it is well documented that, as Scherer's analysis provides only a measurement of the extension of the coherently

diffracting domains, the particle sizes estimated by this method can be significantly under estimated [15,18]. In addition to strain, factors such as dislocations, stacking faults, heterogeneities in composition and instrumental broadening can contribute to peak broadening, making it almost impossible to extract a reliable particle size solely from XRD [15,20].

In this connection, a combination between scanning electron microscopy and laser diffraction techniques was also employed for particle size measurement (Table 1). The morphological evolution and particle size distribution during various calcination conditions of $PbZrO_3$ powders milled with different times were investigated as shown in Fig. 5. At first sight, the morphological characteristic of $PbZrO_3$ powders with various milling times is similar for all cases. In general, the particles are agglomerated and basically irregular in shape, with a substantial variation in particle sizes and size distribution, particularly in powders subjected to prolong milling times. Fracture is considered to be the major mechanism at long milling times. The powders consist of primary particles of nanometers in size and the agglomerates measured ~ 0.75-6.00 μm. In addition to the primary particles, the powders have another kind of very fine particle (brighter particles) with diameter of about 30 nm. However, as unidentified by the XRD technique, a combination of SEM and EDX techniques has demonstrated that unreacted PbO phases (Fig. 6(b)) (circled in the micrographs in Fig. 5) exist in neighbouring to the parent $PbZrO_3$ phase. In general, EDX analysis using a 20 nm probe on a large number of particles of the calcined powders confirmed the parent composition to be $PbZrO_3$ (Fig. 6(a)). As listed in Table 1, the

comparison of XRD crystallite size with SEM apparent crystallite size indicates that the nanoparticles of PZ obtained in this study are indeed polycrystalline, not single-domain single crystalline as in the case of PbTiO3 nanoparticles [21]. This clearly suggests the possibility of introducing excess crystalline defects through vibro-milling.

The effect of milling time on particle size distribution was found to be significant, as shown in Fig. 5. After milling times of 15 and 25 h, the powders have a similar particle size distribution. They exhibit a single peak covering the size ranging from 35 to 2000 nm. However, upon further increase of milling time up to 35 h, a bimodal distribution curve with peak broadening between 10 and 6000 nm is observed. This behavior is believed to arise mainly from particle agglomeration, consistent with SEM result where the strong interparticle bond within each aggregate is evident by the formation of a well-established necking between neighbouring particles (Fig. 5). This observation could be attributed to the mechanism of surface energy reduction of the ultrafine powders, i.e. the smaller the powder the higher the specific surface area [22]. However, it should also be noticed in Fig. 5 that there is a possible necking is observed in long milling time, i.e. 25 h. This necking could be a result of local melting caused by vibro-milling technique. This statement is also supported by the large agglomeration at longer milling time, i.e. 35 h, detected by laser diffraction. Nonetheless, even with the possibility of thermally induced necking, the nano-sized particles could still be obtained with the vibro-milling technique, as seen in Fig. 5.

Bright field TEM images of the calcined $PbZrO_3$ powders derived from milling time of 35 and 25 h are shown in Figs. 7(a) and 8(a), respectively. By

employing a combination of both selected area electron diffraction (SAED) and crystallographic analysis, the major phase of orthorhombic $PbZrO_3$ (Figs. 7(b) and 8(b)) was identified, in good agreement with the XRD results. It is interesting to note that limited evidence for the presence of the unreacted precursor PbO (Fig. 8(c)), in good agreement with the SEM results, was also found in the TEM-SAED investigation, even though this could not be detected by XRD. It is, therefore, intriguing to note the advantage of a combination between TEM-SAED and SEM-EDX techniques, which lies in its ability to reveal microstructural features often missed by the XRD method which requires at least 5 wt% of the component [7,15].

The experimental work carried out here suggests that the optimal combination of the milling time and calcination condition for the production of the smallest nanosized high purity $PbZrO_3$ powders is 35 h and 750 °C for 4 h with heating/cooling rates of 30 °C/min, respectively. Moreover, the employed heating/cooling rates for $PbZrO_3$ powders observed in this work are also faster than those reported earlier [13,16]. This investigation indicates a strong relationship between the vibro-milling process, the calcination condition and the yield of $PbZrO_3$ nanopowders.

Furthermore, it is a well-established fact that ferroelectric nanoparticles undergo what is called a finite-size effect [21,23]. Namely, at a certain particle size called the critical size, the high-temperature paraelectric phase is stabilized at room temperature. Prior to reaching that size, the lattice parameters as well as the paraelectric-ferroelectric phase transition temperature changes. However, there has been much controversy concerning the critical size at room temperature. The critical crystallite size has been

reported to range between 25 to 200 nm [21,23-29]. In particular, earlier report has shown that the critical crystallite size in PZ is approximately 100 nm [23,24]. In view of this connection, an attempt has been made to determine the critical crystallite size for the PZ nanoparticles produced in this study. As shown in Fig. 9, the critical crystallite size for the PZ seems to be around 30-35 nm. It should also be noticed that there is an increase in lattice parameters and unit-cell volume at smaller particle size, which could be attributed to crystallite aggregation, as reported earlier in $BaTiO_3$ [25] and also in good agreement with SEM results (Fig. 5) which show aggregated clusters. It is also to be noted the critical crystallite size obtained in this study is significantly lower than previously reported values [23,24]. This is mainly due to the range of the particle size used for the critical size determination is limited to 27-60 nm, as compared to 30-250 nm in previous studies [23-29]. Therefore, more accurate value can be obtained with wider range of particle sizes.

4. Conclusions

This work demonstrated that by applying an appropriate choice of the vibro-milling time, calcination temperature and dwell time, mass quantities of a high purity lead zirconate nanopowders can be successfully produced by a simple solid-state mixed oxide synthetic route without the use of high purity starting precursors. A combination of the milling time and calcination conditions was found to have a pronounced effect on both the phase formation and particle size of the calcined $PbZrO_3$ powders. The calcination temperature for the formation of single-phase perovskite lead zirconate was

lower when longer milling times were applied. The optimal combination of the milling time and calcination condition for the production of the smallest nanosized (~28 nm) high purity $PbZrO_3$ powders is 35 h and 750 °C for 4 h with heating/cooling rates of 30 °C/min, respectively.

Acknowledgement

This work was supported by the National Nanotechnology Center (NANOTEC), the Thailand Research Fund (TRF), the Commission on Higher Education (CHE), Faculty of Science, and the Graduate School of Chiang Mai University.

References

[1] B. Jaffe, W.R. Cook, H. Jaffe, Piezoelectric Ceramics, Academic Press, New York, 1971.

[2] A.J. Moulson, J.M. Herbert, Electroceramics, 2nd ed., Wiley, Chichester, 2003.

[3] G.H. Haertling, J. Am. Ceram. Soc. 82 (1999) 797.

[4] Y.S. Rao, C.S. Sunandana, J. Mater. Sci. Lett. 11 (1992) 595.

[5] D.M. Ibrahim, H.W. Hennicke, Trans. J. Br. Ceram. Soc. 80 (1981) 18.

[6] E.E. Oren, E. Taspinar, A.C. Tas, J. Am. Ceram. Soc. 80 (1997) 2714.

[7] A. Rujiwatra, S. Tapala, S. Luachan, O. Khamman, S. Ananta, Mater. Lett. 60 (2006) 2893.

[8] M.T. Lanagan, J.H. Kim, S. Jang, R.E. Newnham, J. Am. Ceram. Soc. 71 (1988) 311.

[9] S.E. Lee, J.M. Xue, D.M. Wan, J. Wang, Acta Mater. 47 (1999) 2633.

[10] J.M. Xue, D.M. Wan, S.E. Lee, J. Wang, J. Am. Ceram. Soc. 82 (1999) 1687.

[11] A. Ngamjarurojana, O. Khamman, R. Yimnirun, S. Ananta, Mater. Lett. 60 (2006) 2867.

[12] R. Wongmaneerung, R. Yimnirun, S. Ananta, Mater. Lett. 60 (2006) 1447.

[13] W. Chaisan, O. Khamman, R. Yimnirun, S. Ananta, J. Mater. Sci. (to be published).

[14] S. Ananta, N.W. Thomas, J. Eur. Ceram. Soc. 19 (1999) 155.

[15] H. Klug, L. Alexander, X-Ray Diffraction Procedures for Polycrystalline and Amorphous Materials, 2nd ed., Wiley, New York, 1974.

[16] C. Puchmark, G. Rujijanagul, S. Jiansirisomboon, T. Tunkasiri, Ferroelectric Lett. 31 (2004) 1.

[17] Powder Diffraction File No. 35-0739. International Centre for Diffraction Data, Newtown Square, PA, 2000.

[18] R. Wongmaneerung, R. Yimnirun, S. Ananta, Mater. Lett. 60 (2006) 2666.

[19] A. Revesz, T. Ungar, A. Borbely, J. Lendvai, Nanostruct. Mater. 7 (1996) 779.

[20] J.S. Reed, Principles of Ceramic Processing, 2nd ed. Wiley, New York, 1995.

[21] S. Chattopadhyay, P. Ayyub, V.R. Palkar, M. Multani, Phys. Rev. B 52 (1995) 13177.

[22] Powder Diffraction File No. 77-1971. International Centre for Diffraction Data, Newtown Square, PA, 2000.

[23] S. Chattopadhyay, P. Ayyub, V.R. Palkar, A.V. Gurjar, R.M. Wankar, M. Multani, J. Phys.: Condens. Matter 9 (1997) 8135.

[24] S. Chattopadhyay, NanoStructured Mater. 9 (1997) 551.

[25] M.R. Leonard, A. Safari, IEEE ISAF. 2 (1996) 1003.

[26] K. Uchino, E. Sadanaga, T. Hirose, J. Amer. Ceram. Soc. 72 (1989) 1555.

[27] B.D. Begg. E.R. Vance, J. Nowotny, J. Amer. Ceram. Soc. 77 (1994) 3186.

[28] K. Saegusa, W.E. Rhine, H.K. Bowen, J. Amer. Ceram. Soc. 76 (1993) 1505.

[29] X. Li, W.H. Shih, J. Amer. Ceram. Soc. 80 (1997) 2844.

Table Caption

Table 1 Effect of calcination conditions on the variation of particle size of $PbZrO_3$ powders milled for different times.

Figure Caption

Fig. 1 XRD patterns of $PbZrO_3$ powders milled for 15 h (a) uncalcined, and calcined for 2 h with heating/cooling rates of 10 $^{\circ}$C/min at (b) 550 (c) 600 and (d) 700 $^{\circ}$C, at 800 $^{\circ}$C for (e) 1 and (f) 2 h, and at 800 $^{\circ}$C for 2 h with heating/cooling rates of (g) 20 and (h) 30 $^{\circ}$C/min.

Fig. 2 XRD patterns of $PbZrO_3$ powders milled for 25 h and calcined for 2 h with heating/cooling rates of 10 $^{\circ}$C/min at (a) 600 (b) 700 and (c) 750 $^{\circ}$C, at 750 $^{\circ}$C for (d) 5 and (e) 6 h, and at 750 $^{\circ}$C for 6 h with heating/cooling rates of (f) 20 and (g) 30 $^{\circ}$C/min, and (h) at 800 $^{\circ}$C for 1 h with heating/cooling rates of 30 $^{\circ}$C/min.

Fig. 3 XRD patterns of $PbZrO_3$ powders milled for 35 h and calcined for 2 h with heating/cooling rates of 10 $^{\circ}$C/min at (a) 600 (b) 700 and (c) 750 $^{\circ}$C, at 750 $^{\circ}$C for (d) 3 and (e) 4 h, and at 750 $^{\circ}$C for 4 h with heating/cooling rates of (f) 20 and (g) 30 $^{\circ}$C/min, and (h) at 800 $^{\circ}$C for 1 h with heating/cooling rates of 30 $^{\circ}$C/min.

Fig. 4 Enlarged zone of XRD patterns showing (261)/(402) peaks broadening of $PbZrO_3$ powders milled for (a) 15 h (Fig. 1(h)), (b) 25 h (Fig. 2(h)) and (c) 35 h (Fig. 3(g)).

Fig. 5 SEM micrographs and particle size distributions of $PbZrO_3$ powders milled for (a) 15 h (Fig. 1(h)), (b) 25 h (Fig. 2(h)) and (c) 35 h (Fig. 3(g)).

Fig. 6 EDX analysis of (a) the major phase $PbZrO_3$ and (b) the minor phase PbO (some signals of C and Cu come from coated electrodes and sample stubs, respectively).

Fig. 7 (a) TEM micrograph and (b) SAED pattern ($[13\bar{1}]$ zone axis) of $PbZrO_3$ powders milled for 35 h (Fig. 3(g)).

Fig. 8 (a) TEM micrograph of $PbZrO_3$ powders milled for 25 h (Fig. 2(h)) and SAED pattern of (b) major phase $PbZrO_3$ ($[\bar{1}02]$ zone axis) and (c) minor phase PbO ($[\bar{2}00]$ zone axis).

Fig. 9 Values of (a) a (■) and b (▲) lattice parameters, (b) c (●) lattice parameter, (c) tetragonal distortion (c/a), and (d) unit cell volume as a function of the particle size (XRD crystallite size) in single-phase $PbZrO_3$ powders.

Table
Click here to download Table: Table 1.doc

Table 1

Milling time (h)	Calcination condition *T/D/R* (°C:h:°C/min)	XRD (nm, ± 2.0)				SEM (nm, ± 10)		Laser scattering (nm, ± 200)	
		A	*a*	*b*	*c*	*D*	*P*	*D*	*P*
15	800/2/10	60.44	0.8255	1.1679	0.5873	306	65-522	720	40-2000
15	800/2/30	60.41	0.8257	1.1682	0.5875	280	53-692	700	35-2000
25	800/1/10	38.38	0.8242	1.1723	0.5877	235	36-415	190	35-800
25	800/1/30	35.11	0.8239	1.1720	0.5875	223	31-400	170	35-750
35	750/4/10	32.45	0.8227	1.1672	0.5870	160	39-420	1600	10-4500
35	750/4/20	30.94	0.8231	1.1769	0.5868	152	36-390	1580	10-5000
35	750/4/30	27.50	0.8235	1.1729	0.5854	121	31-228	1570	10-6000

A = Crystallite size
a, b, c = Lattice parameters
D = Average particle size
P = Particle size range or distribution
T/D/R = Calcination temperature, dwell time and heating/cooling rates.

New Figure 1
Click here to download Figure: Fig 1.doc

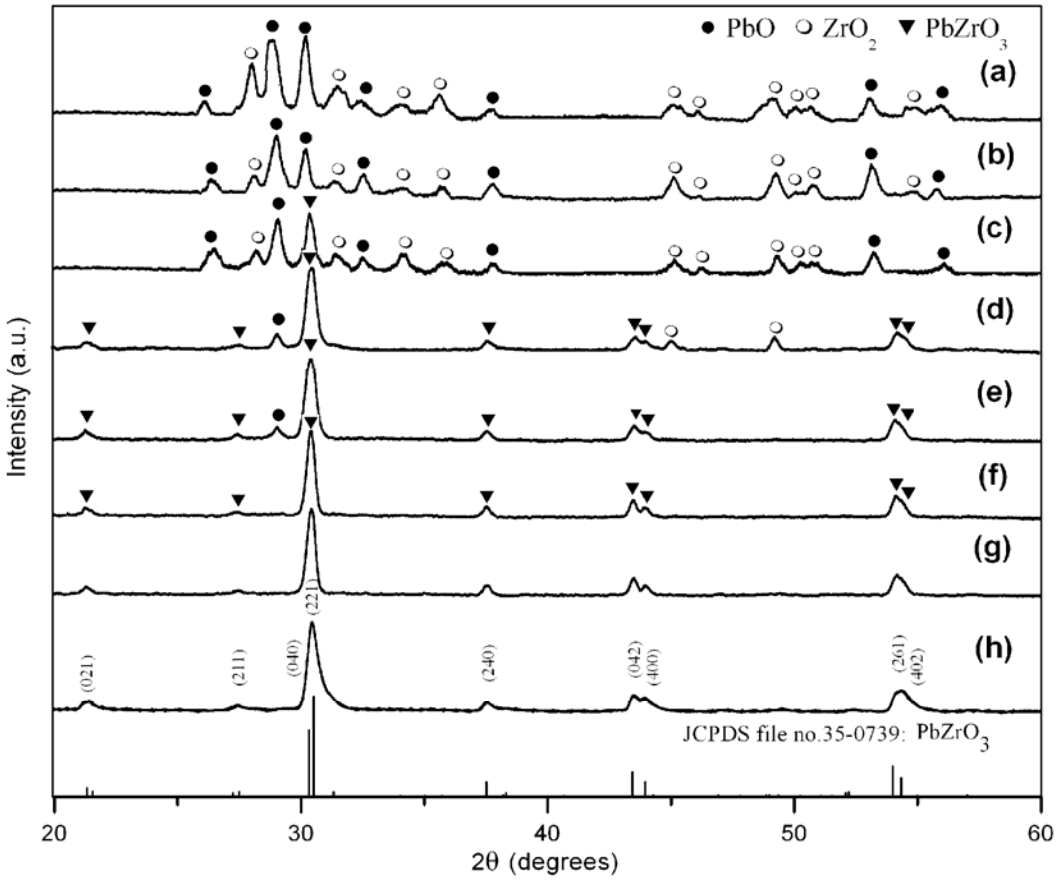

Fig. 1

New Figure 2
Click here to download Figure: Fig 2.doc

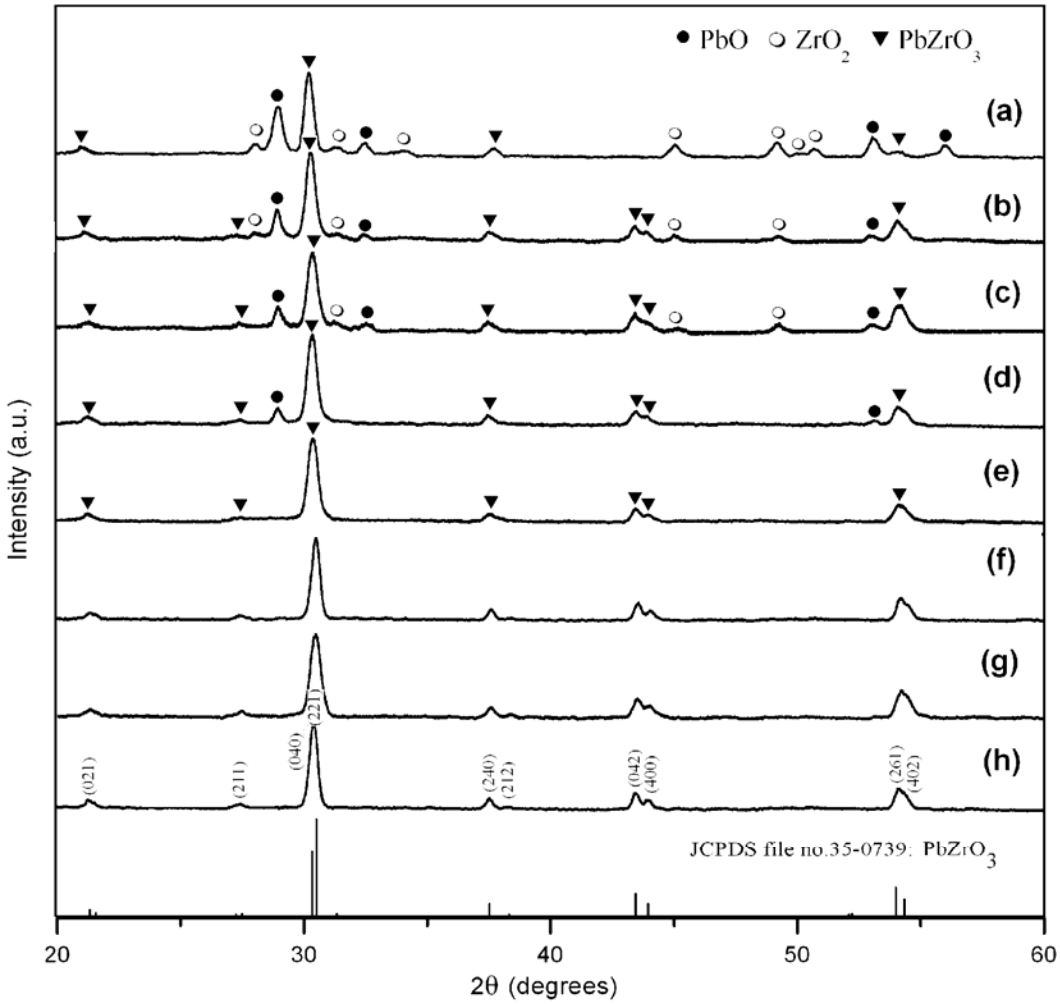

Fig. 2

New Figure 3
Click here to download Figure: Fig 3.doc

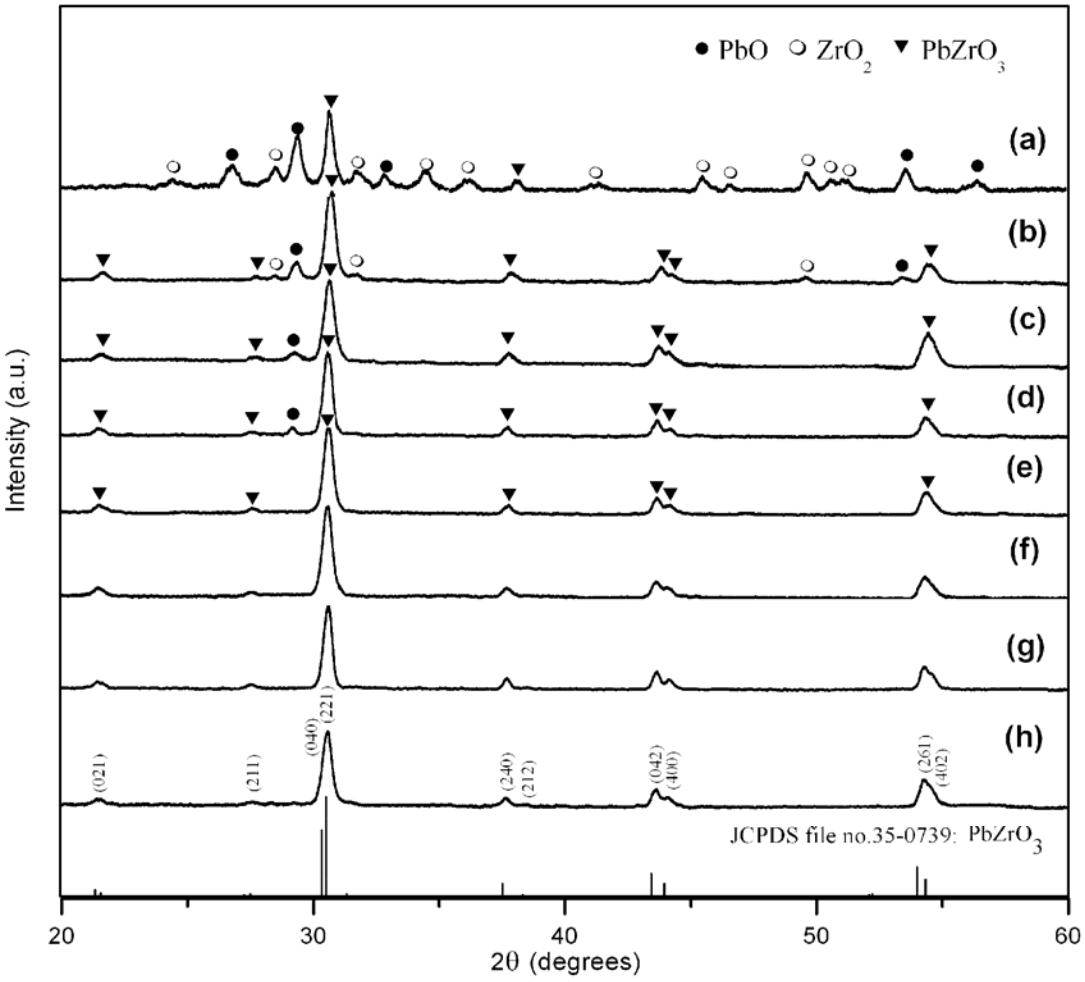

Fig. 3

Figure 4
Click here to download Figure: Fig 4.doc

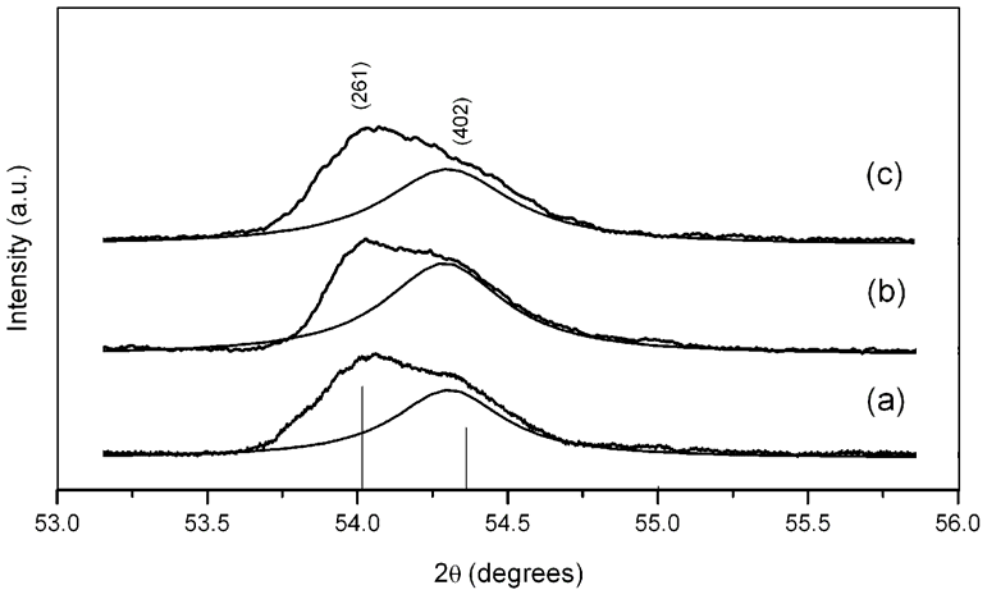

Fig. 4

Figure 5
Click here to download Figure: Fig 5.doc

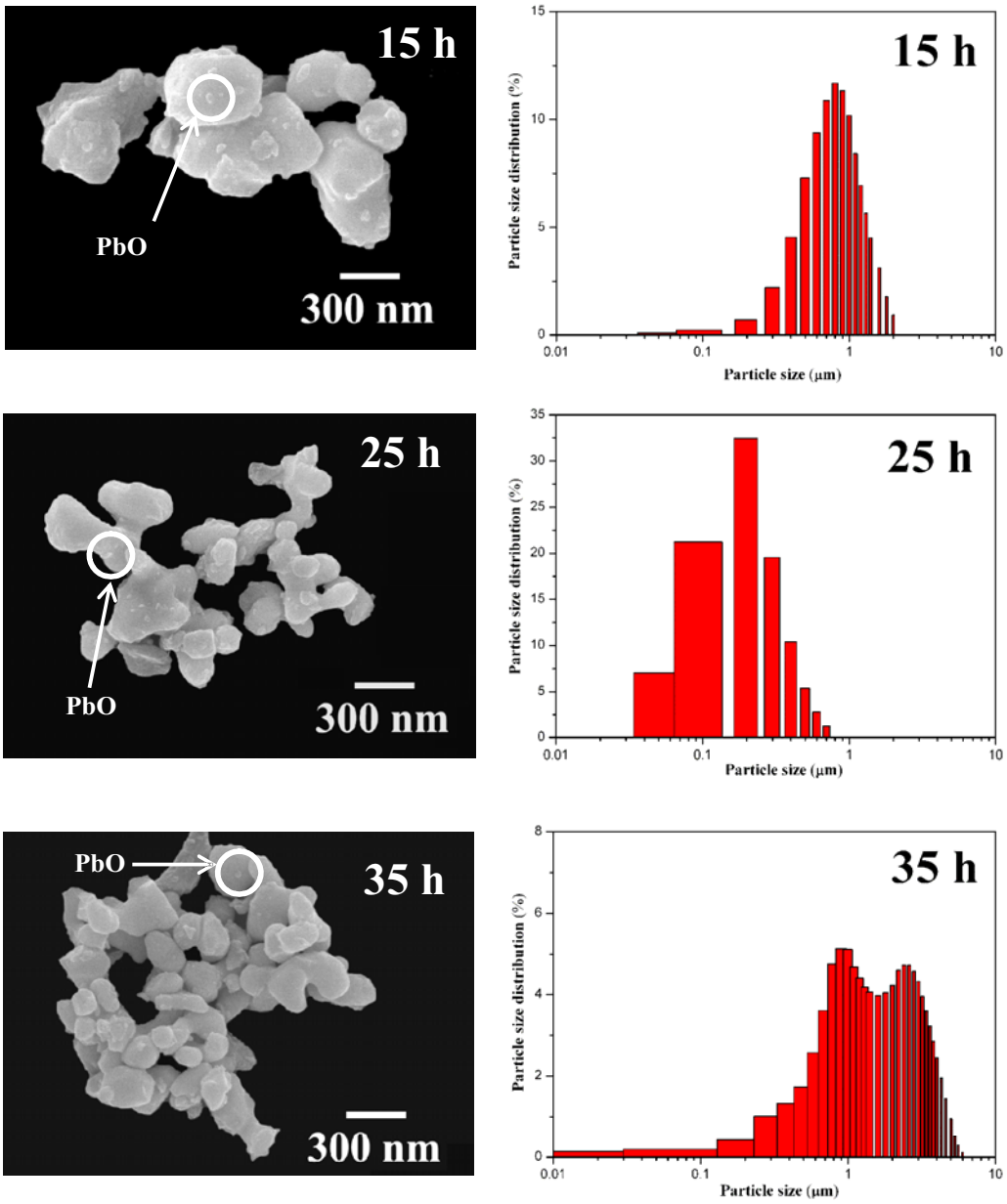

Fig. 5

Figure 6
Click here to download Figure: Fig 6.doc

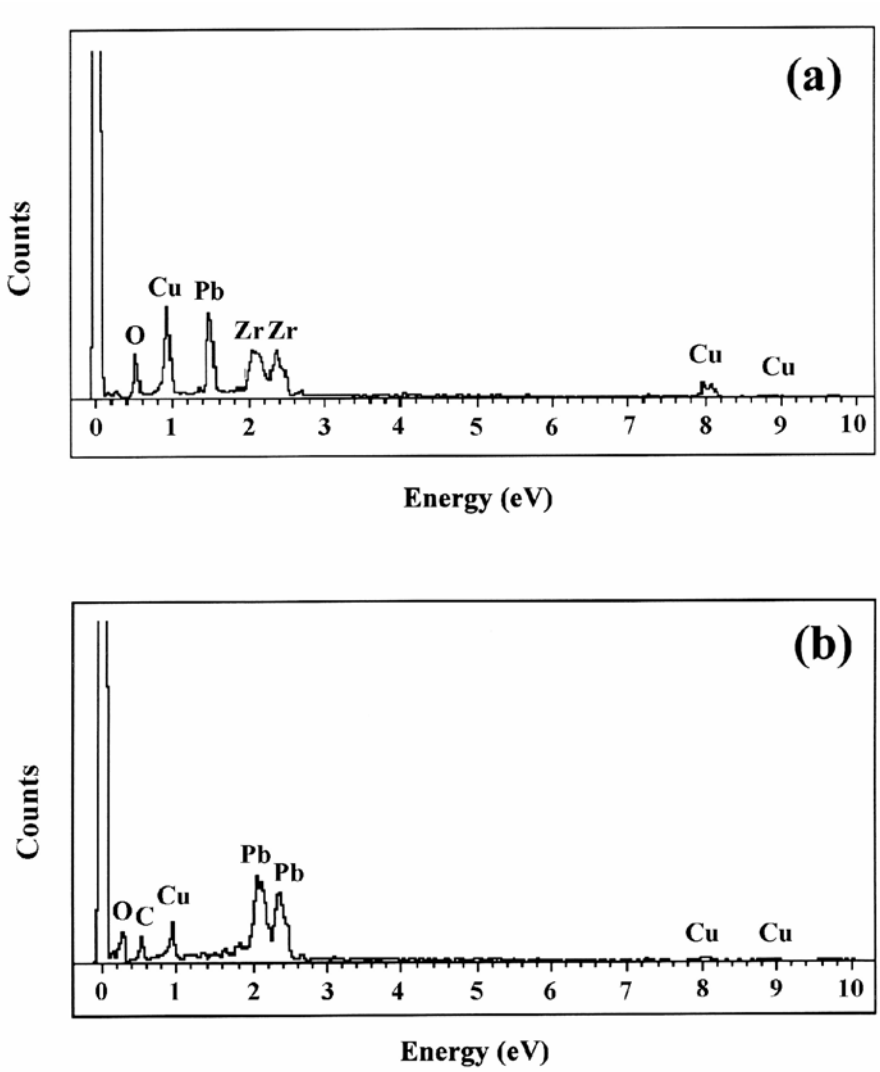

Fig. 6

Figure 7
Click here to download Figure: Fig 7.doc

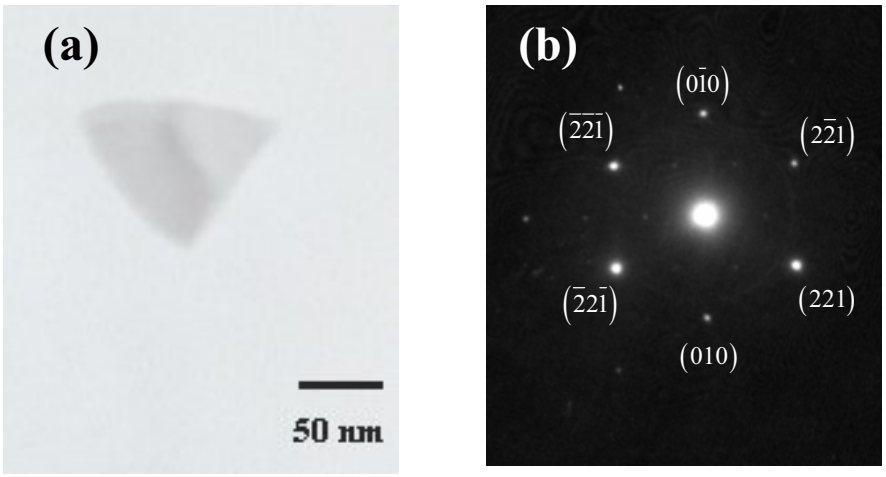

Fig. 7

Figure 8
Click here to download Figure: Fig 8.doc

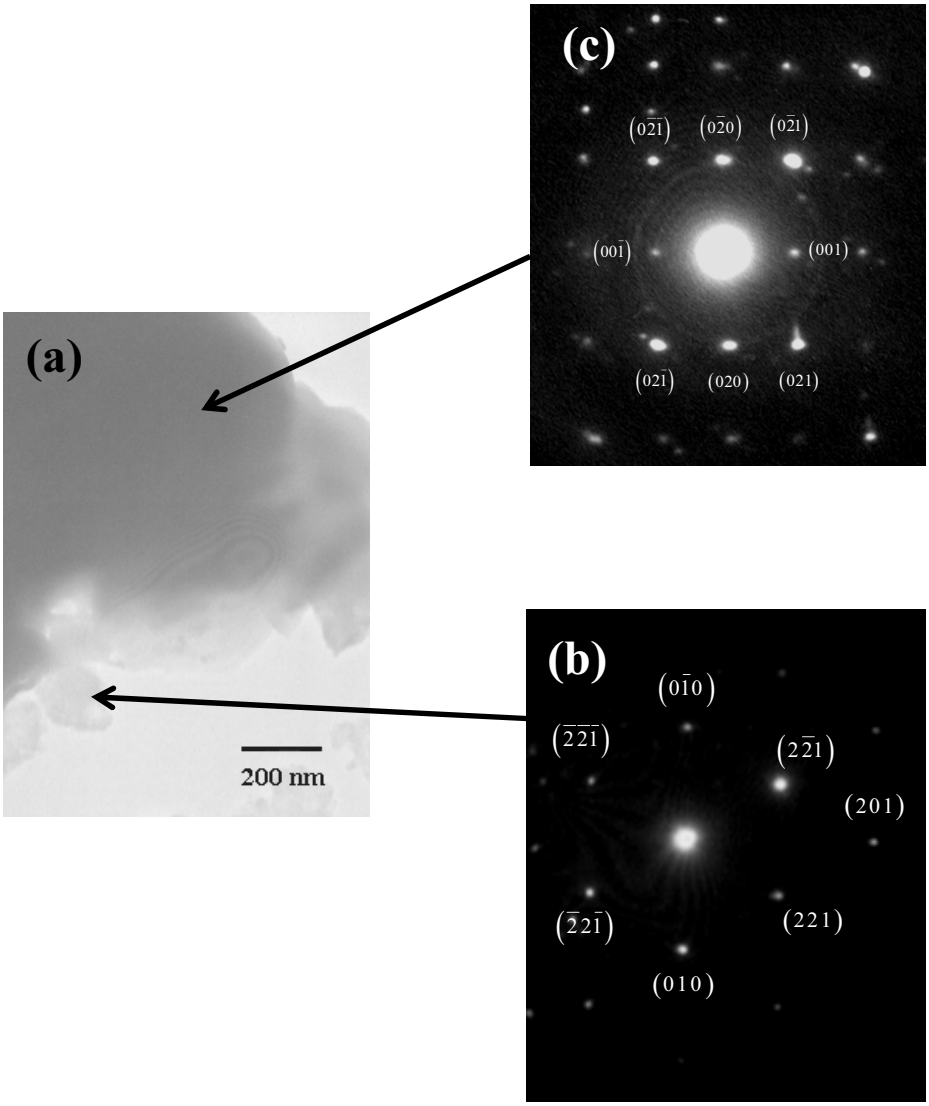

Fig. 8

Figure 9-New
Click here to download Figure: Fig 9.doc

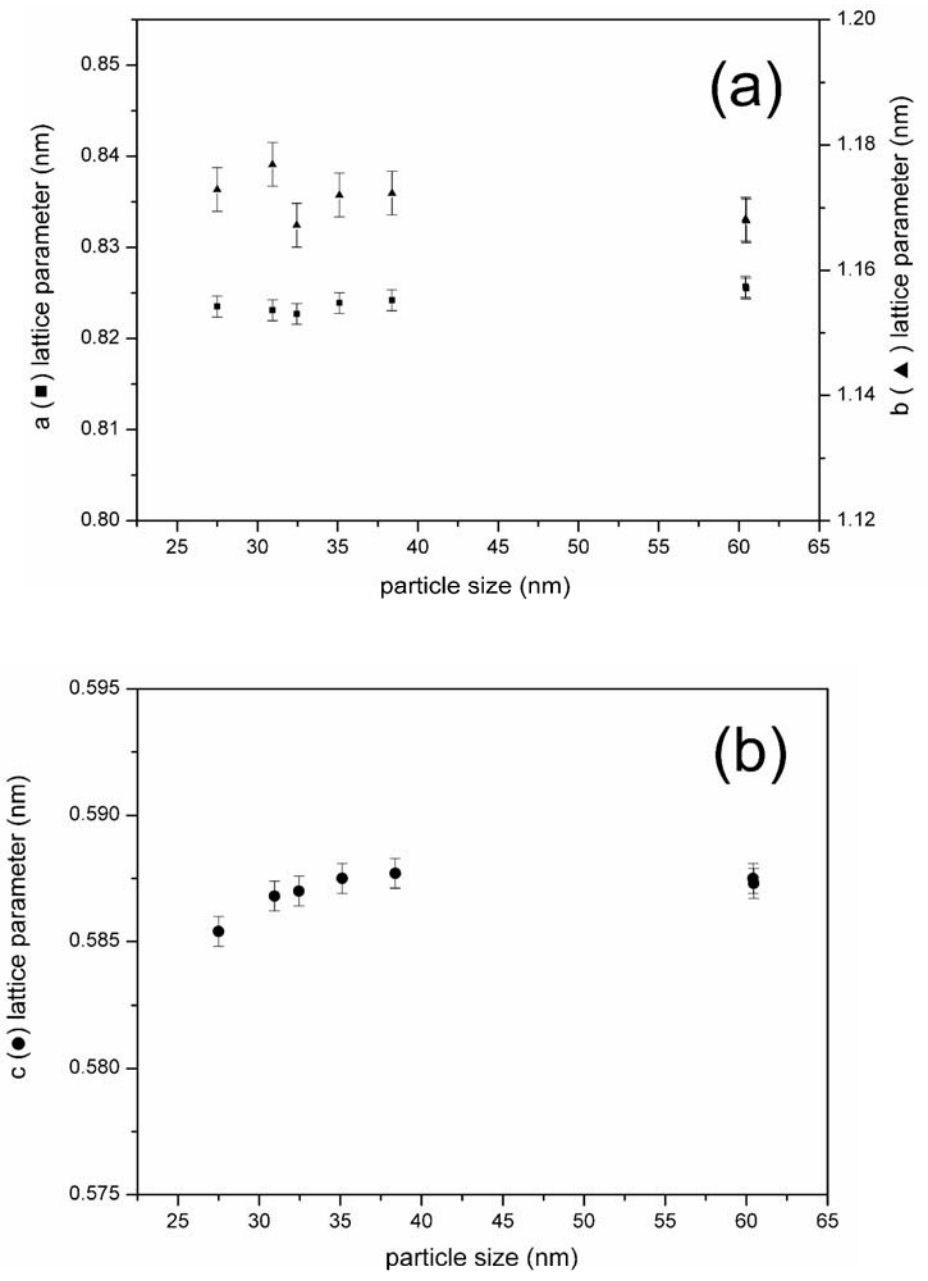

Fig. 9

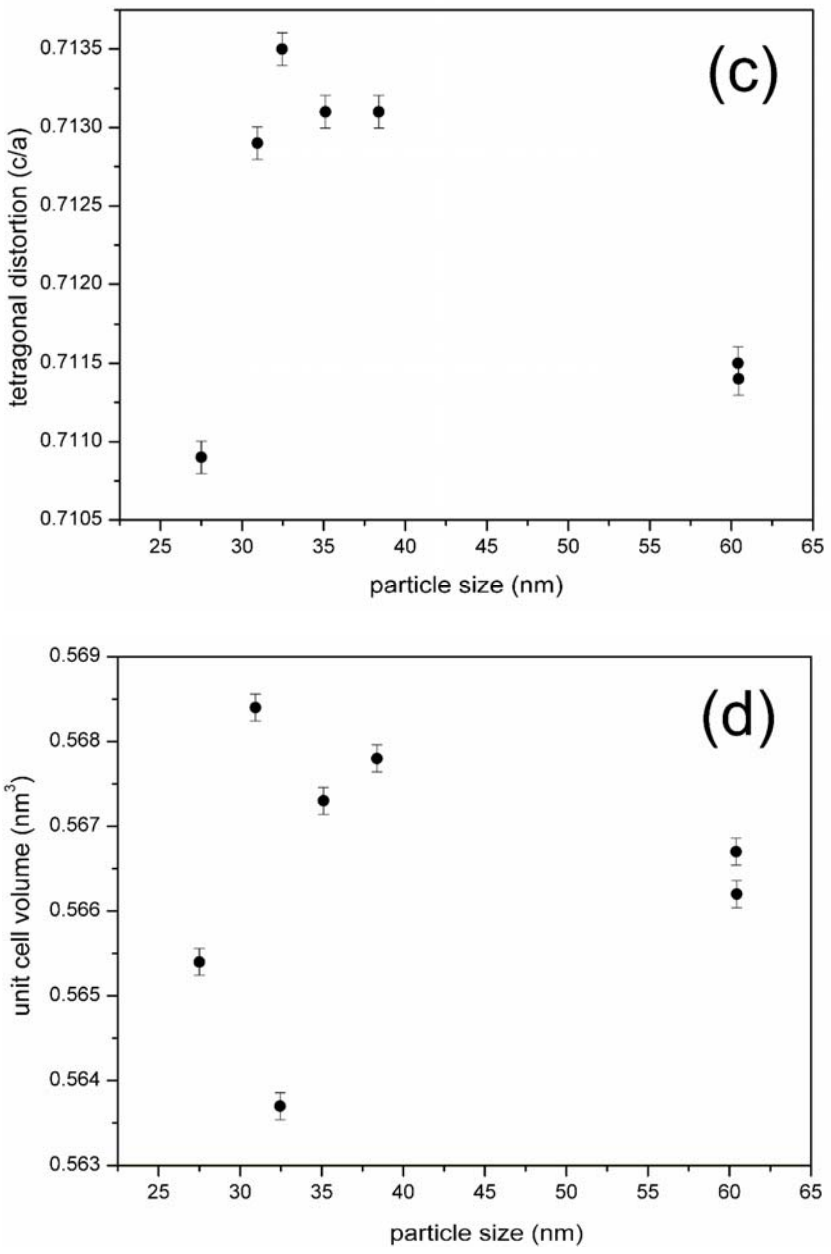
(c)
tetragonal distortion (c/a)
0.7135
0.7130
0.7125
0.7120
0.7115
0.7110
0.7105
25
30
35
40
45
50
55
60
65
particle size (nm)
(d)
unit cell volume (nm^3)
0.569
0.568
0.567
0.566
0.565
0.564
0.563
25
30
35
40
45
50
55
60
65
particle size (nm)

Fig. 9